europhysics conference abstracts

24th European Physical Society Conference on

Controlled Fusion and Plasma Physics

Berchtesgaden, 9th-13th June 1997

Editors: M. Schittenhelm, R. Bartiromo and F. Wagner

Contributed Papers, Part II

Volume 21A
Part II

24th European Physical Society Conference on

Controlled Fusion and
Plasma Physics

24th Fusion
Berchtesgaden
1997

Kongresshaus Berchtesgaden, Germany

9 - 13 June 1997

Editors: M. Schittenhelm, R. Bartiromo and F. Wagner

97-1034

europhysics conference abstracts

24th European Physical Society Conference on

Controlled Fusion and Plasma Physics

Berchtesgaden, 9th-13th June 1997

Editors: M. Schittenhelm, R. Bartiromo and F. Wagner

Contributed Papers, Part II

Preface

The 24th European Physical Society Conference on Controlled Fusion and Plasma Physics, under the auspices of the Plasma Physics Division of the European Physical Society, was hosted by the Max-Planck-Institut für Plasmaphysik Garching, Germany. Following the guidelines of the Board of the EPS Plasma Physics Division, the 1997 Conference included topics from the areas of: Tokamaks; Stellarators; Alternative Magnetic Confinement Schemes; Magnetic Confinement Theory and Modelling; Plasma Edge Physics; Plasma Heating; Current Drive and Profile Control; Diagnostics; Basic Collisionless Plasma Physics; Highly Compressed and Non Stationary Plasmas.

The scientific programme and paper selection were the responsibility of the International Programme Committee appointed by the Board of the EPS Plasma Physics Division. The Programme Committee selected 523 contributed papers (out of 651 submitted abstracts) for presentation as posters in four sessions at the meeting. Guideline for the composition of the poster session was to display the various contributions of larger teams in one session and to place teams of similar goals and interests into different sessions.

As in the past, the Proceedings are printed after the meeting, giving authors the opportunity to present their latest results in four-page papers. According to EPS Plasma Physics Division regulations, the Conference Proceedings contain the four-page papers of all those contributions for which at least one author was a registered participant at the Conference. All submitted papers satisfy this condition. 51 papers were not presented at the Conference and not submitted to the Scientific Secretary though they had originally been accepted by the Programme Committee. This caused some problems in the organisation of the poster sessions. As only in a few cases the cancellation had technical reasons, it is strongly recommended for future conferences that along with the submission of an abstract a guarantee has to be provided that an accepted paper will be presented

The four volumes of the proceedings will be mailed to all registered participants of the Conference. The papers of the 8 Review Lectures and 20 Topical Lectures will be published in a Special Issue of the journal 'Plasma Physics and Controlled Fusion', which will also be mailed to all registered participants.

M. Schittenhelm, R. Bartiromo and F. Wagner

July 1997

V

Programme Committee

R. Bartiromo	IGI del CNR, Italy - Chairman
E. Ascasibar	CIEMAT, Madrid, Spain
D. Gresillon	LPMI/EP, Palaiseau, France
R.D. Hazeltine	Texas University, USA
F. Hofmann	CRPP/EPFL, Lausanne, Switzerland
A. Litvak	IAP, Nizhny Novgorod, Russia
L. Stenflo	Umea University, Sweden
F. Sluijter	Eindhoven University, Netherlands
D.F.H. Start	JET Joint Undertaking, Abingdon, U. Kingdom
U. Samm	Forschungszentrum Jülich, Germany
F. Serra	Universidad Technica, Lisboa, Portugal
T. Todd	UKAEA Fusion, Abingdon, United Kingdom
F. Wagner	IPP, Garching, Germany
R. Weynants	ERM, Brussels, Belgium

Local Organising Committee

F. Wagner	Chairman
G. Zankl	Vice Chairman
M. Schittenhelm	Scientific Secretary
A. Eggeling (Ms)........	Conference Secretary
T. Geist	
H. Jahreiss	Finance Officer
Ch. Stahlberg (Ms)	
K.-H. Steuer	

Acknowledgements

Contents of
Europhysics Conference Abstracts
Volume 21A (Part I - Part IV)

Index of Contributed Papers

Contributed Papers

Contents of Part I (Poster Session 1)

Contents of Part II (Poster Session 2)

Contents of Part III (Poster Session 3)

Contents of Part IV (Poster Session 4)

H-mode confinement on ASDEX Upgrade

Disruptive Beta Limits for High Performance Discharges in JT-60U

S. Ishida, S. Takeji, A. Isayama, N. Isei, Y. Ishii, T. Ozeki,
T. Fujita, Y. Kamada and Y. Neyatani

Japan Atomic Energy Research Inst., Naka Fusion Research Establishment
Naka-machi, Naka-gun, Ibaraki-ken, 311-01 Japan

1. Introduction

High-β_p H-mode and reversed shear discharges in JT-60U have achieved a highest fusion triple product of $n_D(0)\tau_E T_i(0)=1.5\times10^{21}m^{-3}$ •s•keV[1] and an equivalent fusion amplification factor of $Q_{DT}^{eq}=1.05$ [2], respectively, at q_{95}~3. In such a high current low-q region, the discharges tend to be disruptively terminated when a fast β collapse occurs near ideal stability limits. The purpose of this paper is to clarify the observed disruptive β limits investigating internal MHD characteristics with fast ECE measurements and analyzing the ideal stability in the JT-60U high performance regimes. Figure 1 shows attainable normalized beta as a function of q_{95} (safety factor at the 95% flux) with toroidal fields around 4 T. In the high-β_p regime, the stability is improved in combination of the high-β_p mode with an H-mode edge. The β limits for the reversed shear regime, which has an L-mode edge, appears to be similar to that for the high-β_p mode regime.

Fig.1 Normalized beta as a function of q_{95} for high poloidal beta and reversed shear regimes.
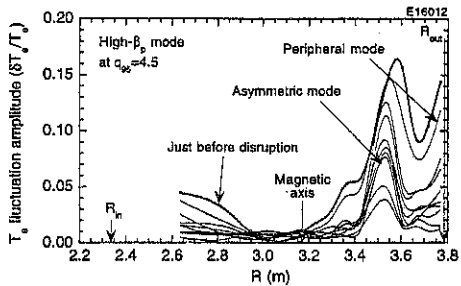
Fig.2 T_e fluctuation amplitude as a function of the major radius; t=4.7580-4.7599 s (plotted every 2 ms).

2. High-β_p Regime

The β_p collapse was originally discovered as a non-disruptive fast β collapse for a long pulse high-β_p discharge naturally producing a reversed magnetic shear configuration due to a high bootstrap current fraction in JT-60[3]. In JT-60U, the β_p collapse was also observed for high-β_p mode discharges with a weak central magnetic shear and a central q (q_0) slightly above unity. The high-β_p mode is characterized by the presence of an internal transport barrier (ITB)[4]. As a precursor mode prior to the collapse, in-out asymmetric modes like ballooning modes were observed to be localized near the ITB only at the low field side and characterized by low-n mode numbers (m/n=3/2, 2/1 or 4/3) and a variety of growth times (~100μs-10 ms)[5]. For higher current or lower safety factor region, the collapse tends to result in a fast major disruption. It should be emphasized here that the in-out asymmetric modes are accompanied with peripheral modes. The fluctuation amplitude of electron temperature is shown to grow until the collapse occurs in Fig.2. This suggests that the

collapse results in a major disruption when the MHD perturbations are so globally extended within the plasma.
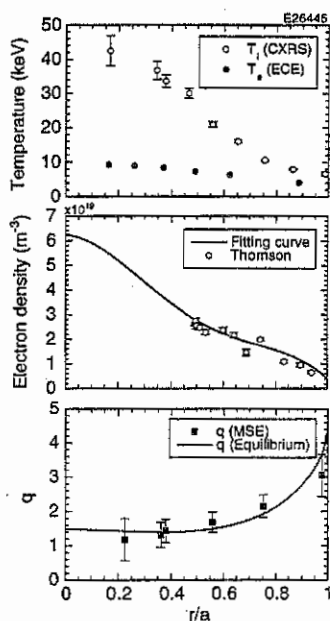
Fig.3 Temperature, density and safety factor profiles for a high-β_p H-mode discharge.

Fig.4 T_e fluctuation profiles just before a disruption for a high-β_p H-mode discharge.

Fig.5 Fourier component profiles of the ideal kink-ballooning modes for a high-β_p H-mode discharge.

For a typical high performance high-β_p H-mode discharge at $q_{95} \sim 3.3$, the temperature, density and safety factor profiles are shown in Fig.3 where the q profile is measured from motional Stark effect spectroscopy. As shown here, the ITBs tend to almost disappear while the edge transport barrier is formed as an H-mode edge. So, the ITB is considered to destabilize the asymmetric modes as the modes do not appear without clear ITB. In the low-q region around $q_{95} \sim 3$, the precursor oscillations are most often observed as in-out *symmetric* modes like kink modes during ELM-free phase. Figure 4 shows the T_e fluctuation profiles for a typical high performance high-β_p H-mode discharge disrupted at $q_{95} \sim 2.8$ and $\beta_N = 1.9$. The internal mode observation reveals the simultaneous destabilization of $m/n = 1/1$, $2/1$ and $3/1$ modes with almost the same frequency. Here, an $m/n = 1/1$ mode is found to be dominantly destabilized though the q=1 surface is absent in the plasma.

The ERATO-J code analysis of ideal kink-ballooning modes are made for the current and pressure profiles obtained from the high-β_p discharges. The observed β limits are found to close to the ideal stability limits predicted from the stability analysis. As shown in Fig.5, the Fourier components of the displacement eigen function show that internal and external modes are destabilized with significant toroidal mode couplings, which are calculated for the plasma conditions of Fig.4. Apart from the growth time, the observed fluctuation profile appears to be consistent with the ideal n=1 kink ballooning mode analysis. It should be remarked, however, that the asymmetric modes could not be reproduced from the ideal kink-ballooning mode analysis. The stability analysis and experimental observations suggests that the collapse
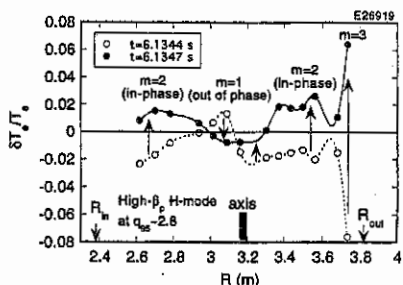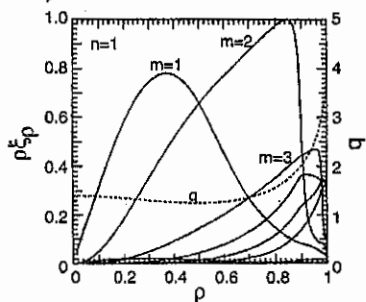
can result in major disruptions when both internal and external modes are destabilized. This is so significant in the low-q region that the high performance discharges can become highly disruptive.

3. Reversed Shear Regime

High performance reversed shear discharges with an L-mode edge have been achieved in which the ITB is observed to be at a large minor radius around $r/a \sim 0.6$ in density and temperature profiles near the minimum safety factor (q_{min}) region as shown in Fig.6 [2, 6]; a JT-60U record stored energy of 10.9 MJ, a high neutron rate of 4.5×10^{16} /s and an equivalent Q_{DT} value of 1.05 are achieved in this shot [2]. When the q_{min} closely approaches 2, the reversed shear discharges are disruptively terminated due to a fast β collapse at $\beta_N \sim 2$ for the low q of $q_{95} \sim 3$. No high performance discharges have been yet attained with q_{min} below ~ 2.
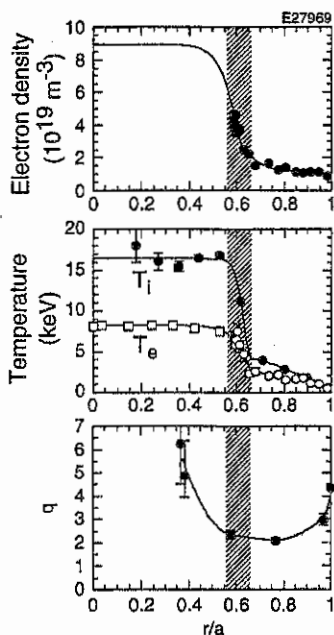
Fig. 6 Density, temperature and safety factor profiles for a typical reversed shear discharge.
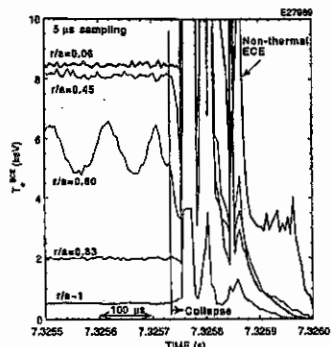
Fig.7(a) T_e evolutions around a disruption for the reversed shear discharge of Fig.6.
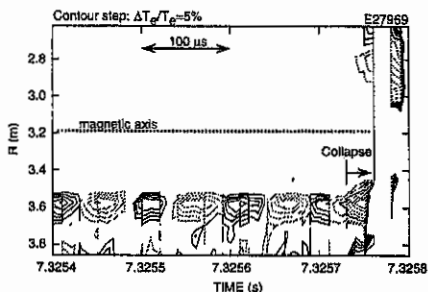
Fig.7(b) Time evolution of the T_e fluctuation profile; the solid and broken curves indicate positive and negative to the mean temperature, respectively.

Electron temperature evolutions near the disruption are measured from a 20-channel ECE grating polychromator with a sampling time of 5 μs for the discharge of Fig.6 as shown in Fig.7(a). It is found that precursor oscillations are observed with a slow growth time of ~10 ms and the collapse explosively grows from the ITB region ($r/a \sim 0.6$) with a very fast growth time of the order of ~10 μs. From the time evolution of the fluctuation profiles in Fig.6(b), the precursor oscillations are found to appear in the ITB region with a high pressure gradient only at the low field side like the asymmetric modes observed in the high-β_p mode discharges.

The observed β limits for the reversed shear discharges are found to be close to the ideal

stability limit for low-n kink-ballooning modes as predicted from the ERATO-J code analysis in which conducting wall effects would substantially improve the stability. Fourier components of the displacement eigen function are shown in Fig.8 for experimental pressure and current profiles with $q_{min} \sim 2$ and $q_{95} \sim 2.9$. As similarly observed in the high-β_p discharges in Fig.4, the internal and external modes are destabilized with significant mode couplings. The stability analysis of the reversed shear discharges shows that the external modes are destabilized even at a high q region such as $q_{95} \sim 5$ unlike the high-β_p mode discharge probably because the current density profile leans toward the surface. The combination of the internal and external modes may be a reason why the disruptions are frequent in reversed shear discharges tends to be followed by disruptions even at the high-q region.
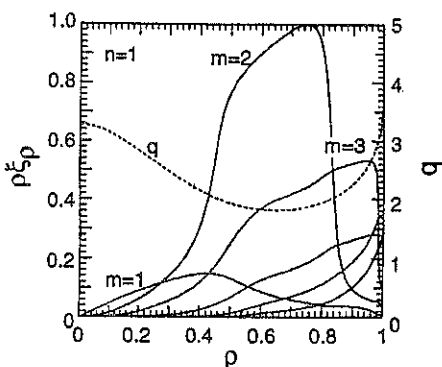
Fig.8 Fourier component profiles of the ideal kink-ballooning modes for a high-β_p H-mode discharge.

4. Discussions and conclusions

As for the precursor phase, the asymmetric modes like ballooning modes are commonly observed in the high-β_p mode and reversed shear discharges where the presence of the ITB plays an important role. Such a strong asymmetry observed in the precursors can not be quantitatively reproduced from the stability analysis even if a relation of $\delta T_e/T_e \sim \xi_r (dp/dr)/p$ is considered. The growth time of the asymmetric mode is often observed as relatively slow unlike an ideal mode growth. While the following explosive growth process in the collapse phase is partly masked by strong non-thermal ECE for both high performance discharges, no clear inconsistency to the predictions is found in the MHD activity at a timing very close to the collapse phase.

In conclusion, the β limits in the two high performance regimes are close to the ideal stability limits for low-n kink-ballooning modes, where the MHD activity in the collapse phase looks consistent to the theoretical predictions. It is suggested that the collapse can result in disruptions under the conditions where internal and external modes are destabilized with strong mode couplings. As decreasing q and increasing β, the low-q high performance discharges could be apt to suffer from a major disruption possibly due to the enhancement of the effects.

References

[1] S. Ishida et al., paper IAEA-CN-64/A3-1 in Plasma Physics and Controlled Nuclear Fusion Research, Motreal 1996 (International Atomic Energy Agency, Vienna, 1997).

[2] Y. Koide et al., to be published in Phys. of Plasmas; S. Ishida et al., submitted to Phys. Rev. Lett.

[3] S. Ishida et al., Phys. Lev. Lett., 68, 1531(1992).

[4] S. Ishida et al., in Plasma Physics and Controlled Nuclear Fusion Research, Würzburg 1992 (International Atomic Energy Agency, Vienna, 1993), Vol.1, p.219.

[5] Y. Koide et al., Phys. Rev. Lett., 72, 3662(1994).

[6] T. Fujita et al., Paper IAEA-CN-64/A1-4, ibid. in [1].

Behaviour of Radiation Power Loss from Radiative Divertor with Reversed Shear Plasmas in JT-60U

Hiroshi TAMAI, Shigeru KONOSHIMA, Nobuyuki ASAKURA, Kiyoshi ITAMI,
Satoru HIGASHIJIMA, Akira SAKASAI, Nobuyuki HOSOGANE, and the JT-60 Team

Japan Atomic Energy Research Institute, Naka Fusion Research Establishment
Naka-machi, Naka-gun, Ibaraki-ken 311-01, JAPAN

1. Introduction

The compatibility of the radiative cooling in dense and cold divertor plasmas with the enhanced confinement in the main plasma is one of key issues in ITER Physics R&D. The way to control the radiative divertor in the steady-state has been tested in many tokamaks.[1]-[5]. Trials for producing the radiative divertor plasma compatible with reversed shear plasmas have been demonstrated in the JT-60U tokamak[6],[7]. This paper describes the investigation of radiation power from the divertor plasma that has the compatibility with the reversed shear plasma.

2. Diagnostics

Radiation power from the divertor region is observed by two bolometer arrays, which are labelled as the top array and the side array respectively. Total radiation power from the divertor is estimated by summing up the signals from six central channels of the top array.

Bolometer arrays are installed on a toroidal port sections apart from the location of a gas valve, which injects the impurity gas into the divertor region. Therefore, the bolometric measurement is not affected from the toroidal asymmetry caused by the intense impurity gas puffing.

3. Compatible radiative divertor with the reversed shear configuration

Successful radiative divertor with the reversed shear plasma has been documented in ref.[6]. Figure 1 shows again the typical plasma parameters in that discharge. Divertor gas puff of neon is injected at 5.5s to a reversed shear plasma, then the divertor radiation power increases. Although neon is puffed with only short duration of 0.3s, the intensity of line emission of NeX from the main plasma is kept almost constant after the neon puff at 5.5s due to its high recycling rate. After the additional puff of the hydrogen is injected at 6.5s, the divertor radiation power increases twice with remarkable reduction of the heat load on the divertor plates[6]. The internal transport barrier (ITB) is maintained until 7.7s, where the radiative divertor is compatible with the reversed shear configuration for about 1s.
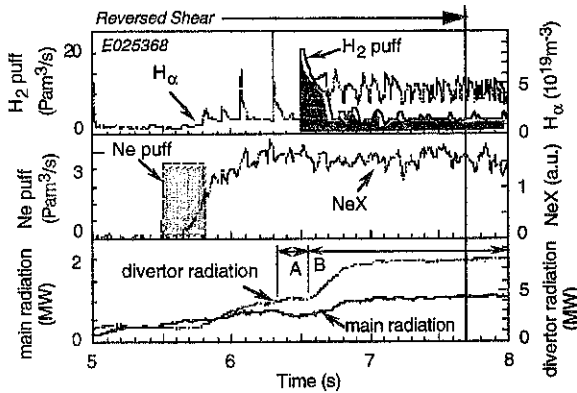
Fig.1 Temporal behaviour of plasma parameters in the
remote radiative plasma in a reversed shear configuration.

4. Profile of the radiation power

Figure 2 shows the divertor radiation profile integrated along the line of sight of each bolometer channel. The equiflux surface around the divertor x-point and the each chord of bolometer channel are also illustrated. A peak in the side array and in the top array locates below the X-point at 6.4s. This period corresponds to the first flat top of the divertor radiation power appeared in the Fig.1 (shown as A). At the second flat top (B) during the additional hydrogen puff (7.0s), the intense radiation region further locates above the X-point inside the separatrix. The intense radiation around X-point is stably kept both at the same intensity and at the same position during the co-existence of neon and hydrogen.
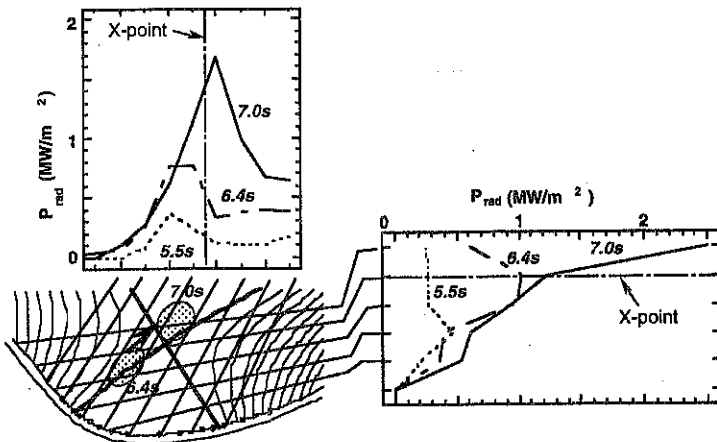
Fig.2 Profile of the divertor radiation integrated along the line of sight, measured by the top
and the side bolometer arrays. The timing is 5.5s(.......), 6.4s(_._._.), and 7.0s(_____).

Figure 3a shows the time evolution of the radiation profile in the main plasma. Plots are at 5.5s (before gas puff), at 6.4s (after neon puff), and at 7.0s (after hydrogen puff). After the gas puff, radiation power in the peripheral plasma (r/a>0.6) gradually increases, up to as three times of that before gas puff. Profiles of temperature and density, measured by the Thomson scattering drastically change after the hydrogen gas puff, which is plotted in Fig.3b. Radial position of the ITB locates inward at 7.0s. In another shot of the same plasma operation without divertor gas puff, the radial position of the ITB does not shift. In Fig.3, Z_{eff} and the radiation power by Bremsstrahlung are also plotted, which are estimated from the visible Bremsstrahlung emission with tangential viewing chords. Intensity of the Bremsstrahlung emission from the centre agrees with the bolometric measurement within an accuracy of order of magnitude. Radiation power from the plasma centre is still low during the radiative divertor phase with reversed shear plasma.
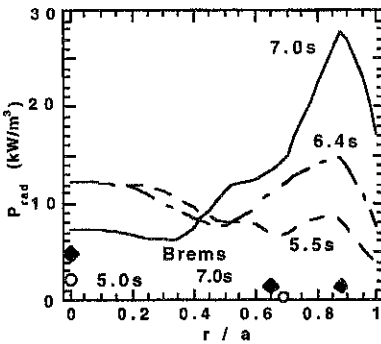
Fig.3a Radiation profile of the main plasma at 5.5s, 6.4s, and 7.0s. Bremsstrahlung intensity at 5.5s and 7.0s is also plotted.
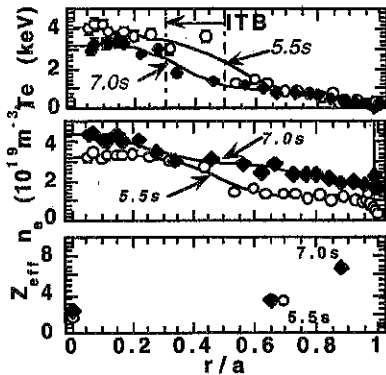
Fig.3b Profile of the electron temperature and density at 5.5s and at 7.0s, and the Zeff at 5.5s and at 7.0s.

5. Contribution of neon to the increase in the radiation power

In order to investigate the contribution of neon to the radiation power in the peripheral plasma and to the position of the ITB, the radiation rate by neon is estimated. The radiation rate, P_z, is assumed to be described by Corona model as

$$P_z = n_e n_z L_z, \qquad (Eq.1)$$

where n_e, n_z, and L_z, are electron density, impurity ion density, and the cooling rate of impurity, respectively. Impurity ion density is obtained from two methods for the cross check. One is the estimation of the neon density, n_z, from Z_{eff} measured by the visible Bremsstrahlung emission, and the other is that from the measurement of the charge exchange recombination spectroscopy (CXRS). Impurity cooling rate is calculated by the polynomial fitting with electron temperature[7].

Figure 4 shows the calculated results for the radiation rate of neon at 7.0s. Both the results from CXRS and Bremsstrahlung measurement are in good agreement, therefore, the impurity radiation of neon is low inside the plasma, on the other hand, from the edge region neon radiation is about three times as large as that from the central. Edge radiation by neon is roughly consistent with the radiation power at the periphery ($0.7<r/a<0.9$) with in a accuracy of factor 2.
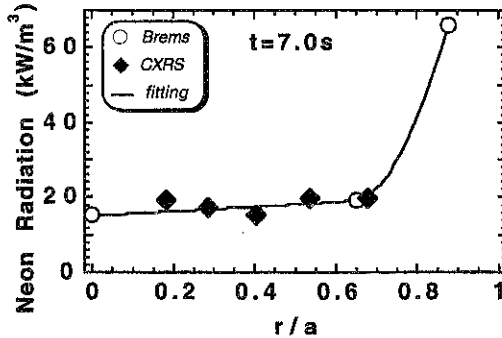
Fig.4 Profile of the impurity radiation by neon, at t=7.0s.estimated from the visible Bremsstrahlung and CXRS measurement.

Summary

Radiation power is investigated for the radiative divertor with reversed shear plasma. At the successful radiative divertor phase by the neon and additional hydrogen gas puff, intense peak in diverter radiation profile appears above the X-point. In the periphery of main plasma ($0.7<r/a<0.9$) radiation power increases as three time as that before gas puff, which is mainly contributed from the neon fraction. On the other hand, radiation from the plasma centre is mainly by the Bremsstrahlung emission, and kept relatively low. W-shaped pumped divertor experiments[8], just started at this moment, is expected to find out a way to control the radiative divertor with various improved plasma configuration.

References

[1]   J.Winter, *et al.*, *Phys.Rev.Lett.* **71**, 1549 (1993).

[2]   A.Kallenbach *et al.*, *Nucl.Fusion* **35**, 1231 (1995).

[3]   S. Allen, *et al.*, *J.Nucl.Mater.* **220-222**, 336 (1995).

[4]   M.Keilhacker, *Plasma Phys.Control.Fusion* **37**, A3 (1995).

[5]   N.Asakura, *et al.*, *Nucl.Fusion* **36**, 795 (1996).

[6]   K.Itami, *et al.*, *Phys. Rev. Lett.* **78**, 1267 (1997).

[7]   D.E.Post, *et al.*, *Atomic Data and Nuclear Data Tables* **20**, 397 (1977).

[8]   N.Hosogane, *et al.*, *in the 16th IAEA Fusion Energy Conf.* IAEA-CN-64/GP-11 (1996).

Analysis of Transient Transport Processes on JT-60U Tokamak

S.V. Neudatchin*, H. Shirai, T. Takizuka, T. Fujita,

S. Takeji, N. Isei, S. Ishida, Y. Kamada

Japan Atomic Energy Research Institute, Naka Fusion Research Establishment

Naka-machi, Naka-gun, Ibaraki-ken 311-01, Japan

*Russian Research Center "Kurchatov Institute", Moscow, Russia

1. Introduction

Recent success of JT-60U Reversed Shear (RS) experiments has been reported [1,2]. The good confinement performance of these plasmas attributed the formation of the Internal Transport Barrier (ITB). The aim of the present paper is to highlight some features of the ITB formation for the reversed shear plasmas as well as for the normal shear plasmas.

The transport analyses of normal shear discharges with ITB and especially of RS discharges are complicated because of their small ITB width. In the RS discharges, the new type of ITB with clear pedestals of T_i, T_e, and n_e was observed [1,2]. Usually only one channel of the ECE measurement of T_e and one channel of the charge-exchange recombination spectroscopy for T_i measurement are located in the ITB region with steep temperature gradient.

The time variation of the diagnostic positions "traveling through the ITB" due to the preprogrammed plasma motion enables us to measure the thin structure of the ITB. Reconstruction of the these features of T_e, and T_i profiles is performed. Discontinuous change of the conductivity around the ITB is estimated, and the position of the "shoulder" of ITB is determined with the high space resolution.

The physics of the ITB in normal shear plasmas has not fully been known yet. So-called Barrier Localized Modes (BLM) [3] cause the fast time scale heat outflux to the plasma periphery. The BLM-induced L-H-L transitions in a high β_p pulse are studied. The relationship between the ITB transport property and the edge confinement is investigated. The electron conductivity jump is estimated during the fast-time-scale ITB recovery.

2. Analysis of ITB in RS Discharges

We discuss here the phase of the preprogrammed motion in the RS pulse E27969 with I_p/B_t = 2.8 MA/4 T (the highest Q_{DT}^{eq} shot [2]). Waveforms of this discharge is shown in Fig. 1. The plasma center moves in the major-radius direction with an inward velocity, $|dDR/dt| \approx 10$ cm/s for $t \geq 6.0$ s. Different behaviors of T_{e13} and T_{e14} are clearly seen, where T_{ek} denotes the electron temperature measured by the k-th channel. The gradual heating is seen for both channels during 6.0 s $< t < 6.6$ s. The decrease of T_{e14} was obvious for 6.6 s $< t < 7.0$ s, which corresponds to the radial gradient of the ITB.

Evolution of spatial positions and T_e values for 13th and 14th channels are shown in Fig. 2. Points on a curve are plotted at every 0.1 second from $t = 6.0$ s to 7.3 s. The relation between the "real" temperature gradient and the "measured" gradient from a curve of T_k is given by

$$\frac{\partial}{\partial r} T(r, t) = \frac{d}{dr} T_k(r_k(t), t) - \frac{1}{v_k} \left(\frac{\partial}{\partial t} T(r, t) \right), \tag{1}$$

where r_k is the k-th channel position moving with the radial velocity v_k. The $\partial T_e/\partial r$ values, which are estimated by the differential approximation with T_{e14} and T_{e13}, are -10 eV/cm for $r <$ 0.5 m, -60 ev/cm near the inner "shoulder" of ITB, and -380 eV/cm in the ITB region. The "measured" T_e gradient (first term in RHS of eq. (1)) in the ITB region is about - 450 eV/cm. The correction part (second term in RHS of eq. (1)) is evaluated by taking account of T_e evolution on neighboring channels, and is found to be from 0 ev/cm to -160 eV/cm. The maximum gradient in the ITB region is 450 eV/cm $< | \nabla T_e |_{ITB} < 610$ eV/cm.

It is obvious from all the above results that the discontinuous change of ∇T_e is occurred in the distance shorter than 3 cm, which is the spatial resolution of T_e measurement. Because the spatial change of the absorbed power density is smaller than that of ∇T_e, the value of electron heat diffusivity χ_e is almost inversely proportional to the ∇T_e value. We expect the discontinuous change of χ_e at the ITB "shoulder", and very small χ_e value in the ITB region which is about 1/10 of that just outside the ITB.

Evolution of T_i are also shown in Fig. 1. Tracks of T_i for 8th, 9th and 10th channels are plotted in Fig. 2. The similar behavior of T_{i9} with T_{e14} is found. The channel 10 was already on the ITB at the beginning $t = 6.0$ s. The T_{i9} arrived at the inner "shoulder" at $t \approx 6.5$ s, while T_{i8} remains outside of ITB. The ITB widths for T_i and T_e seem almost the same ≤ 10 cm.

Interestingly, a small difference is observed in the ITB locations between for T_e and T_i. The T_{i9} reaches the ITB boundary at $t \approx 6.5$ s on $r \approx 0.45$ m, while the T_{e14} reaches the ITB boundary at $t \approx 6.7$ s on $r \approx 0.54$ m. Possible reasons are 1) physical difference of ITB positions, 2) physical difference of ITB gradient due to banana size, and 3) different resolutions between T_i (~6 cm) and T_e (~3 cm). This problem should be clarified in future.

The increase of T_{i9} for $t > 7.0$ s with $v_{i9} \approx 0$ suggests the outward motion of ITB region, whose location is seen by drawing a line from a point of $T_{i9}(t)$ to a point of $T_{i10}(t)$ in Fig. 2.

3. Study of BLM-induced Transitions

It was found that the BLM relaxes the temperature profile inside the ITB and causes the increase of peripheral temperature [3]. Waveforms of the high β_p discharge E23612 of normal shear plasma with $I_p/B_t = 1.4$ MA/4 T [4] are shown in Fig. 3. Fast time-scale T_e data are presented in Fig. 4. Sudden decay of T_e is induced by the BLM at $t = 5.895$ s as clearly seen on T_{e6} and T_{e7} located inside the ITB, $r/a < 0.6$, while the fast jump of of T_{e5}, T_{e16} and T_{e17} outside the ITB, $r/a > 0.6$. The D_α signal drops correlating with the BLM and the density increases gradually. These phenomena suggest an L-H transition induced by the BLM.

Twenty ms after the BLM, the Te profile inside ITB is reconstructed as almost the same as that before BLM. At $t = 5.921$ s, the T_e starts to decay simultaneously with D_α jump by an H-L back transition. A time delay of the T_e response is seen for inner region $r/a < 0.4$.

From these observations we find that the BLM does not deteriorate the improved transport property near the ITB, and that the H-L back transition affects globally the improved transport feature. The latter fact has already been reported [5,6]. The jump of χ_e, $\delta\chi_e$, can be estimated from the change of dT_e/dt at the transition [5]. The estimated value of $\delta\chi_e$ for $0.4 < r/a < 0.6$ is about $0.6 \sim 1.0$ m^2/s.

This degraded transport is soon varied to the improved one. The discontinuous changes in the time derivative dT_e/dt are clearly seen twice on T_{e6} and T_{e7} simultaneously at $t = 5.968$ s and at $t = 6.015$ s. The evolution of W_{dia} is also discontinuous at $t = 5.921$ s, 5.968 s and 6.015 s. On the other hand in region $r/a > 0.6$, change in the T_e evolution is small. The absolute values of $\delta\chi_e$ near $r/a = 0.5$ at $t = 5.968$ s and 6.015 s for recovery phase are $1/2 \sim 1/3$ of that at $t = 5.921$ s (H-L transition). Therefore, after $t = 6.015$ s the value of χ_e becomes again as small as that before the H-L transition. We suppose that the ITB properties are recovered. Above transient processes seem to have global natures rather than diffusive natures.

4. Conclusion

Some features of the ITB formation for reversed shear plasmas as well as for normal shear plasmas in JT-60U are studied through the analysis of transient transport processes.

Reconstruction of the thin features of the T_e and T_i profiles in a RS plasma is done for the preprogrammed-motion phase. The position of the "shoulder" of ITB is determined with high space resolution. The width of the ITB is smaller than 10 cm. The discontinuous change of χ_e within 3 cm distance at the ITB "shoulder" is found and the χ_e value in the ITB region is about 1/10 of that just outside the ITB. A small difference is observed in the ITB locations between for T_e and T_i. This reason should be clarified in future.

The BLM-induced L-H transition and the H-L back transition in a high β_p plasma with normal shear are studied. The BLM suddenly relaxes the T_e profile but does not deteriorate the improved transport property. The H-L back transition causes the simultaneous degradation of transport near the ITB region. The χ_e jump is estimated as about 1 m^2/s. After the back transition, the transport is discontinuously improved in time and the ITB properties are recovered. Global natures of these transient processes are noticeable.

References

[1] T. Fujita, S. Ide, H. Kimura et al., 16th IAEA Fusion Energy Conference, Montreal, 1996, IAEA-CN-64/A1-4.

[2] Y. Koide, JT-60 Team, 38th APS Anual Meeting, 1996, to be published in Phys. Plasmas.

[3] S. Takeji, Y. Kamada, T. Ozeki et al., Proc. 22nd EPS Conf. Bournemouth, 1995, Vol. 19C, Part IV, EPS, Geneva (1995) 33.

[4] Y. Koide, T. Takizuka, S. Takeji et al., Plasma Phys. Control. Fusion **38** (1996) 1011.

[5] S.V. Neudatchin, T. Takizuka, H. Shirai et al., Jpn. J. Appl. Phys. **35** (1996) 3595.

[6] H. Shirai, T. Takizuka, M. Sato et al., Proc. 23rd EPS Conf. Kiev, 1996, Vol. 20C, Part I, EPS, Geneva (1996) 339.
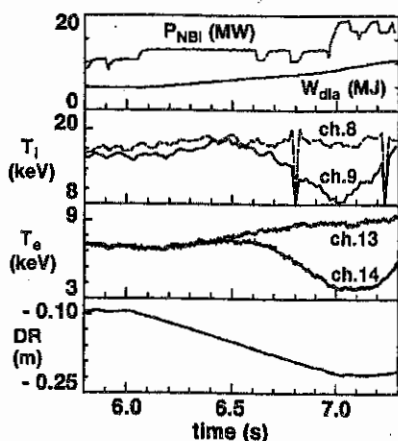
Fig. 1 Time evolution of NBI power P_{NBI}, stored energy W_{dia}, ion temperature T_i (ch.8 and 9), electron temperature T_e (ch. 13 and 14), and displacement of plasma column in the major radius direction from the center of vacuum vessel DR, in the RS shot (E27969).
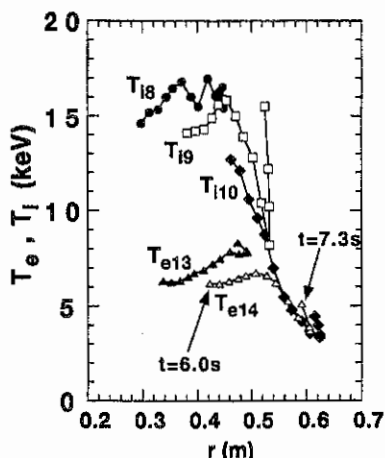
Fig. 2 Motion of measuring points in the plasma column for electron temperature T_e (ch.13, 14) and ion temperature T_i (ch.8, 9, 10) in the RS shot (E27969). ITB features are seen on tracks of T_{e14} and T_{i9}.
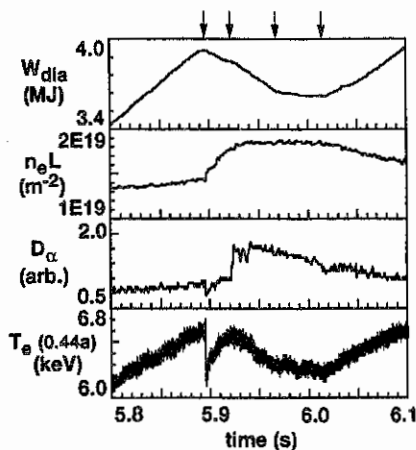
Fig. 3 Time evolution of W_{dia}, line integrated electron density n_eL, D_α signal and $T_e(0.44a)$ in the high β_p shot (E23612). Arrows indicate times of interest: BLM, H-L back transition, the first improvement recovery and the second recovery.
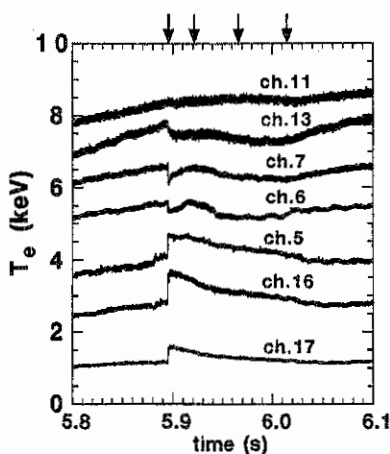
Fig. 4 Time evolution of T_e at $r/a=0.14$ (ch.11), 0.33 (ch.13), 0.44 (ch.7), 0.56 (ch.6), 0.68 (ch.5), 0.79 (ch.16) and 0.98 (ch.17) in the high β_p shot (E23612).

Suppression of Runaway - Electrons Generation during Disruptive Discharge - Terminations in JT-60U

Y. Kawano, R. Yoshino, Y. Neyatani, T. Kondoh, N. Isei, S. Ishida,
K. Tobita, T. Hatae, K. Itami, A. Sakasai, and the JT-60 team

Japan Atomic Energy Research Institute, Naka Fusion Research Establishment
801-1 Mukoyama, Naka-machi, Naka-gun, Ibaraki-ken, 311-01, Japan

Abstract

The generation of runaway electrons during fast discharge terminations has been suppressed. Electrons accelerated by a loop voltage spike during current quench are eliminated by large magnetic fluctuations due to "burst" (minor disruption) and "n=1" mode before they run away, resulting in the avoidance of the generation of high energy runaway electrons. External helical magnetic field coils are applied to enhance magnetic fluctuations. A typical threshold value of magnetic fluctuations for the suppression is; $\widetilde{B}_{r\_n=1} \sim 18 \times 10^{-4}$ T ($\widetilde{B}_{r\_n=1}/B_t \sim 0.07$ %) for current quench rate d $I_p/dt \sim -100$ MA/s .

1 Introduction

Energetic runaway - electrons (REs) are often observed in fast discharge - terminations due to the normal disruption and the killer-pellet injection. Because first wall materials can be irradiated and damaged by runaway electrons, those generation must be suppressed in tokamak fusion reactors like as ITER. Recently, it has been found that the REs generation is suppressed when spontaneous magnetic - fluctuations are large enough [1]. Based on this result, a series of experiments has been performed to establish the runaways - free fast discharge - termination [2].

2 Experimental setup

In the experiment, the JT-60U ohmically heated discharges are terminated by the killer - pellet injection (KPI). The discharge conditions are the plasma current I_p=1.7MA, the toroidal magnetic field at the center of the vacuum vessel B_t= 2.5T~3T and the safety factor at the 95% of total flux q_{95}=3.35~4. The relatively low electron density n_e=0.6~0.8x10^{19}m^{-3} and the high electron temperature T_e(0) ~2keV are selected for the shallow deposition of the pellet, which can easily generate runaways. A neon - ice - pellet (ϕ4mm x L4mm) is injected into the plasma as the killer pellet with the velocity of 600~1000m/s, which causes the disruptive discharge - termination with fast current quench, where the maximum current quench rates are; dI_p/dt = -50 ~ -160MA/s. Except of slowest two cases (< ~ -60MA/s), the generation of REs which produce current tail (REs tail) is usually observed during early phase of the current quench. The external helical field is provided by four sets of sector coils named DCW [3]. When DCW coils are energized with the coil current of I_{DCW} =15kA, additional radial error field; B_{r_DCW} is ~ 4x10^{-3}T at the plasma center and ~ 2x10^{-2}T at the plasma edge at inboard side. Based on the dominant toroidal number of the coils of 4, and they

are energized to produce B_r with opposite direction at every 90 deg, the DCW coils can produce m/n=3/2 magnetic field [4] with the radial magnetic field component of ~7x10⁻⁴T at the plasma center. Small magnetic field of m/n=4/3, 4/2 can be also produced.

3 Results

3.1 Suppression of REs generation by energizing DCW coils

By energizing DCW coils, REs which induces the REs tail are successfully suppressed for discharges of $I_p/B_t = 1.7$MA/2.5T as shown in Fig. 1. The DCW coils are energized from t=13s (~500ms before pellet injection). In the cases of I_{DCW}=0kA and 7kA, clear REs tails are produced. In contrast with above results, no REs tails are observed for I_{DCW}=11kA and 14kA. With the increase in I_{DCW}, the intensity of REs (hard X-ray intensity with energy of >1MeV) is substantially reduced. The generation timing of REs is also significantly delayed, which resulted in the suppression of REs tail. The maximum current quench rates are as fast as dI_p/dt=-90MA/s~-130MA/s, which are fast enough to produce the REs tail for usual case.

The mechanism of the suppression of REs is attributed to enhancement of magnetic fluctuations due to energizing of DCW coils. Figure 2 and 3 show typical waveforms with and without energizing DCW coils. In the case of without DCW (I_{DCW}=0kA), the quick generation of REs is observed just after the current quench starts. In Fig. 2, fluctuations of poloidal magnetic field measured by a pick-up coil ($d\widetilde{B}_\theta/dt$,at the divertor) and the absolute amplitude of the radial field fluctuation of n=1 component ($d\widetilde{B}_{r\_n=1}/dt$) measured by saddle loop coils are shown. By comparison between discharges with and without DCW, enhancement of magnetic fluctuations are observed for I_{DCW}=14kA (see Fig. 3). We found the "burst" like fluctuations in the $d\widetilde{B}_\theta/dt$ signal, which are attributed to minor disruption. The period when the bursts are last, we call the period as the "burst phase". Both the amplitude of "burst" and the duration of "burst phase" are increased with I_{DCW}. The super-thermal electrons (indicated by relatively low energy ($E < 1$MeV) hard X-ray signal) generated just after the KPI disappear during the "burst phase". This means that super-thermal electrons are eliminated During "burst phase", the $d\widetilde{B}_{r\_n=1}/dt$ signal is also enhanced with disturbed feature. After the end of the "burst phase", $d\widetilde{B}_{r\_n=1}/dt$ signal becomes quiescent and begins decaying gradually. Afterwards, generation of low intensity REs is observed. We call this relatively quiescent phase as the "burst-free phase".

3.2 Regimes of REs suppression

Figure 4 shows a comparison of $\widetilde{B}_{r\_n=1}$ amplitudes for different I_{DCW}. The $\widetilde{B}_{r\_n=1}$ amplitude is increased due to " bursts" and is kept at a relatively higher level during " burst" phase. Additionally, the maximum $\widetilde{B}_{r\_n=1}$ amplitude is increased with I_{DCW}. The $\widetilde{B}_{r\_n=1}$ amplitude during "burst" phase for the case of I_{DCW}=14 kA is reached up to ~ 2.4x10⁻³ T, which is two times larger than that for the case of I_{DCW}= 0kA. These large n=1 activities can suppress the REs generation even during fast current quench. Figure 5 and 6 show regimes of REs suppression and generation. The REs tails are observed at the absolute value of d I_p/dt is ~70 MA/s and the $\widetilde{B}_{r\_n=1}$ ~5x10⁻⁴T ($\widetilde{B}_{r\_n=1}/ B_t$ ~0.02 %). In more faster cases, REs tails are generated at higher $\widetilde{B}_{r\_n=1}$ regime. On the other hand, when the $\widetilde{B}_{r\_n=1}$ amplitude becomes larger value above the threshold of REs generation, the quick generation of

REs which causes REs tail is avoided. A typical threshold value for d I_p/dt of ~ -100 MA/s is $\widetilde{B}_{r\_n=1}$ ~18×10⁻⁴ T ($\widetilde{B}_{r\_n=1}$ / B_t ~0.07 %). (A time trace of the the case of I_{DCW}= 14kA for Bt=2.5T is drawn in Figs. 5 and 6.)

4 Discussions

Generally, the Dreicer evaporation process is considered to be the basic mechanism of REs generation [5]. In future work, though measurements of plasma parameters are not easy during fast current quench, the Dreicer normalized field should be introduced instead of the current quench rate for further comprehensive understanding of REs suppression.

Acknowledgment

References

[1] R. Yoshino, et. al., Plas. Phys. and Cont. Fusion, **39**, 313 (1997).

[2] Y. Kawano, et. al., **IAEA-CN-64/A3-4** in 16th Fusion Energy Conf., Montreal 1996.

[3] H. Ninomiya, et. al., Plas. Devices and Oper. **1**, 43 (1990).

[4] Miura S., JAERI-M report **93-057**, 287 (1993).

[5] Knoepfel H. and Spong D. A., Nucl. Fusion, **19**, 785 (1979).
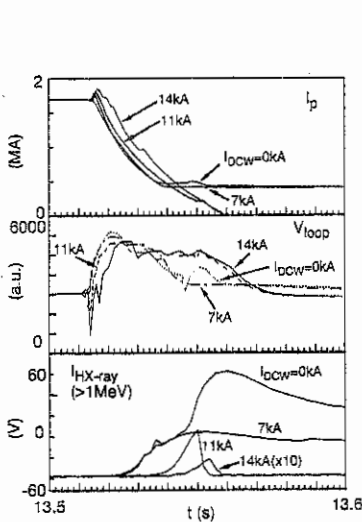
Fig. 1   Effect of energizing DCW coils on the generation of REs.
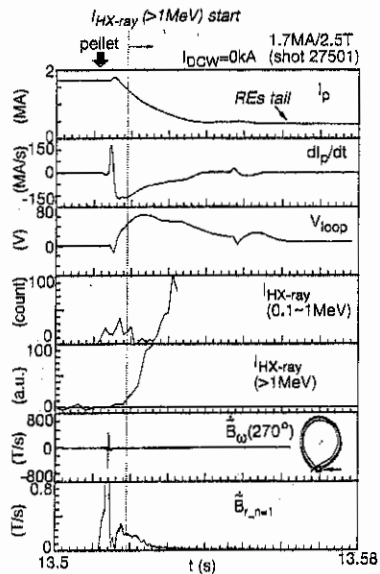
Fig. 2   Typical waveforms for without DCW.
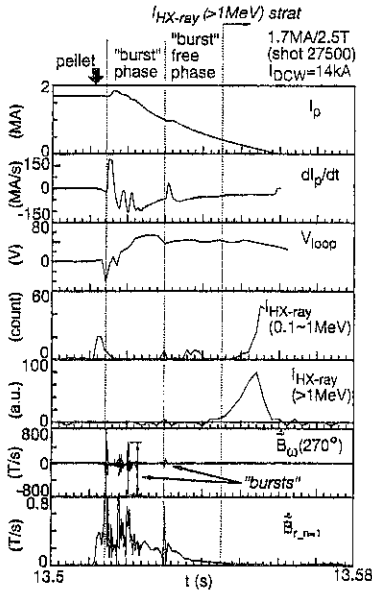
Fig. 3 Typical waveforms for I_{DCW} = 14kA.
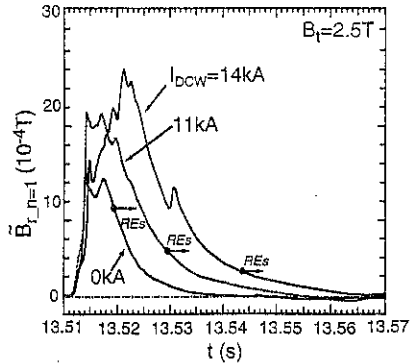
Fig. 4 Enhancement of magnetic fluctuation of n=1 mode by DCW coils.
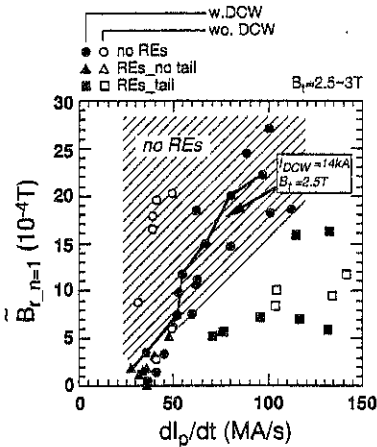
Fig. 5 Regime of $\widetilde{B}_{r\_n=1}$ amplitude for suppression and generation of REs.
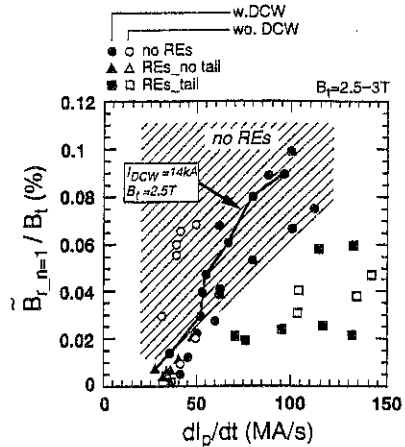
Fig. 6 Regime of $\widetilde{B}_{r\_n=1}/B_t$ for suppression and generation of REs.

Analysis of JT-60U Divertor Plasma Using "B2-Eirene" Code

A.Hatayama[*1], R.Schneider[*2], D.P.Coster[*2],
N.Hayashi[*1,*4], M.Sugihara[*3], M.Ogasawara[*1],
K.Shimizu[*4], N.Asakura[*4] and T.Hirayama[*4]

*1: Faculty of Science and Technology, Keio University Yokohama 223, Japan
*2: Max-Planck-Institut fur Plasmaphysik, Garching, FRG.
*3: ITER JCT, IPP Garching,
*4: Japan Atomic Energy Research Institute, Naka, Ibaraki, Japan

1. Introduction "B2-Eirene" code [1-4] has been successfully applied to the analyses for the present divertor experiments and the predictive study for the future reactors. The present study is the first attempt to apply the "B2-Eirene" code to the analysis of JT-60U divertor plasma. In Ref.[5], extensive studies of recycling, particle flux and divertor plasma parameters have been made for JT-60U L-mode discharges. The relation between total recycling particle flux and the main plasma parameters, such as NBI heating power P_{NBI}, effective safety factor q_{eff}, line averaged electron density $\bar{n}_e$, has been investigated for the wide range of experimental condition. Comparison of "B2-Eirene" results with the above global feature of particle flux in JT-60U has been done in this study. In addition, we compare numerical results for n_e, T_e and CII-line radiation profiles in the SOL/divertor region with the experimental results, taking a JT-60U shot (shot#E19059) [6] as an example.

2. Numerical Model The main aspects of "B2-Eirene" code package have been described in detail in Refs.[1-4]. Here, we briefly summarize numerical model used in the present study. Bulk ion species D^+ and all carbon impurity ion species (C^+-C^{6+}) are described by the "B2" multi-fluids code[2]. This plasma description is self-consistently coupled[1] to the "Eirene" Monte-Carlo-code[3],[4] for the neutrals. Essential features of neutral kinetics for D, D_2 and C are taken into account. Figure 1 shows JT-60U configuration and numerical grid. Sight lines of optical fiber array (38 ch.) are also shown in Fig.1. MHD equilibrium data for the grid generation is taken from the shot#E19059 (I_p=2MA, B_t=4T, and q_{eff} =5.05). Time evolution of this example shot (#E19059) is shown in Fig.2 from Ref.[6]. We use

Fig.1 JT-60U configration and numerical grid
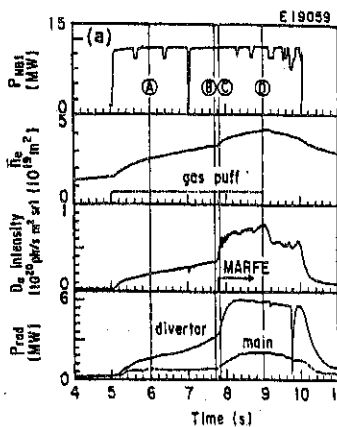
Fig.2 Time history of shot #E19059
(from Ref.[6])

constant transport coefficient model for anomalous radial transport. Three different cases [(a):D=1.0m²/s, χ_e=χ_i=0.3m²/s, (b):D=1.0m²/s, χ_e=χ_i=2.0m²/s, (c): D=0.5m²/s, χ_e=χ_i=2.0m²/s] have been considered. Taking into account loss mechanisms in the main plasma, we set total input power as P_{in}=9MW throughout this study and equally distributed in the cells at inner most flux surface in Fig.1. The remaining set of boundary conditions is the almost same as those in Ref.[1].

3. Global feature of particle flux In Ref.[5], the relation between total particle flux Φ^D and the main plasma parameters has been investigated for wide range of experimental conditions. As shown in Fig.3[5], Φ^D has been scaled as $\Phi^D = C_1 \exp(\bar{n}_e q_{eff}/C_2)$, where C_1 and C_2 are the fitting parameters and depend mainly on geometrical factor, e.g., plasma volume, X-point height. Before proceeding to the detailed comparison with the shot #E19059, we have done the preliminary density scan in order to compare with the above global feature. In this series of run, deuterium density at bulk plasma side has been changed as n_D=0.5, 1.0, 2.0, 3.0 and 3.5 x10¹⁹m³, respectively. For the radial transport coefficients, the case(a) above has been used. Since the numerical grid shown in Fig.1 is produced from the MHD equilibrium for shot#E19059, magnetic configuration is not exactly the same as those in Fig.3. However, plasma parameters of $I_p = 2MA$, $B_t = 4T$ and $q_{eff} = 5.05$ are very similar and also P_{in} (=9MW) is within the range of experimental parameter scan in Fig.3. Figure 4 shows the "B2-Eirene" results. In Fig.4, Φ^D at the divertor plate is plotted as a function of $n_e^{sep} q_{eff}$ instead of $\bar{n}_e q_{eff}$, where n_e^{sep} is calculated separatrix electron density at the outer mid-plane. Basically the same tendency as in Fig.3 can be seen. The total particle flux Φ^D increases almost linearly with $n_e^{sep} q_{eff}$ in logarithmic scale, expect for the highest density case. In the highest density case, main radiated region by the carbon was not localized in the divertor region, but near X-point inside the separatrix. Therefore, this highest density case is close to Marfe onset(or in the Marfe state, depending on the definition of Marfe). In order to make more exact comparison with Fig.3, the relation between n_e^{sep} and $\bar{n}_e$ is needed. If we roughly assume $\alpha = \bar{n}_e/n_e^{sep} \approx 2.5$ from Thomson scattering data at r/a =0.97, the "B2-Eirene" results in Fig.4 can be re-plotted as a function of $\bar{n}_e q_{eff}$ and well fitted by $\Phi^D = C_1 \exp(\bar{n}_e q_{eff}/C_2)$ with
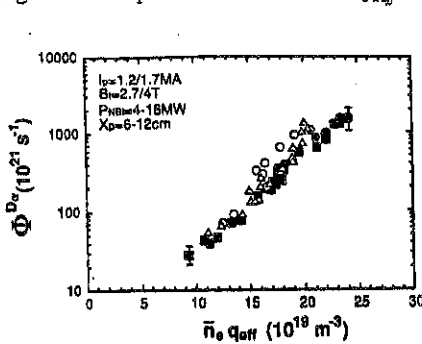
Fig.3 Φ^D as a function of $\bar{n}_e q_{eff}$

(from Ref.[5])

$n_e^{sep} q_{eff}$ (10¹⁹m⁻³)
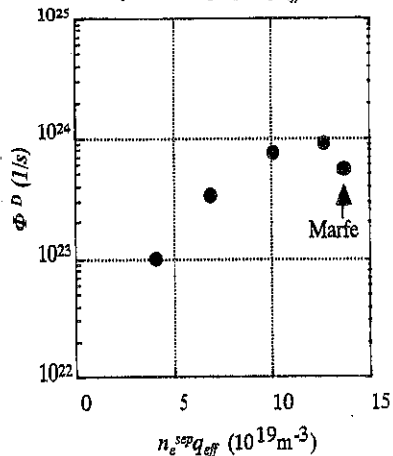
Fig.4 Depenedence of Φ^D on $n_e^{sep} q_{eff}$

$C_1 = 30.0$ and $C_2 = 8.7$. Compared with the experimental fit, C_2 is quite close, while C_1 is about 2.5 times larger. However, above fitting is based on the crude estimate for α and α is fixed constant for all n_D. Generally, α becomes smaller as density increases. If we take account of this feature, more close agreement can be obtained.

4. Analysis of shot#E19059   In the present study, we concentrate on the low density phase "A" in Fig.2. For this low density phase, we set as $n_D = 0.5 \times 10^{19} \mathrm{m}^{-3}$. Figure 5 shows T_e profile at the outer mid-plane as a function of the distance d from the separatrix. Curve (a) and (b) correspond to the result for the different transport, the case (a) and the case (b) in Sec.2, respectively. In both cases, T_e drops quickly from the separatrix but then decreases more gradually. A long tail, i.e., a "second SOL" is formed. This behavior can be explained by the strong dependence of parallel classical heat diffusivity $\chi_{//}$ on T_e and consistent with theoretical prediction[7]. Unfortunately, there is no experimental measurement of T_e profile for this shot. Quite recently, the same behavior of T_e profile has been reported in JT-60U[8] by the reciprocating probe measurement. Similar "second SOL" was observed for similar discharge conditions (L-mode discharge with I_p=1.8MA, B_t=3.5T, q_{eff}=4.7), but higher density regime ($\bar{n}_e$=1.9-4.3x10^{19}m^{-3}) and lower input power(P_{NBI}=4MW). Temperature decay length l_T for the first SOL in Fig.5 becomes (a) l_T=0.5cm and (b) l_T=1.7cm, respectively, while 2.2-2.5cm in the above experiments. Density profiles are shown in Fig.6. Unlike the T_e profile, there is no "second SOL". In the above experiments[8], a "second SOL" has been also observed for n_e profile. In addition, the typical density decay length for the first SOL became 1.4cm-1.7cm. Density decay lengths in Fig.6 are apparently larger than these values. We have also used smaller D [case (c):D=0.5m^2/s in Sec.2]. However, we couldn't obtained such a drastic change to explain the above experimental observations, although l_n becomes smaller. Comparison with these recent experimental findings suggests that some different model of radial transport (for example, including pinch effect in the model) is necessary to
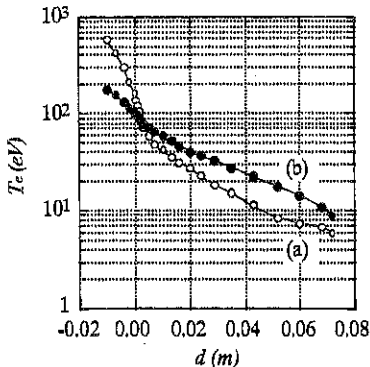
Fig.5 Te-Profile at outer mid-plane.   *Fig.6 ne-profile at outer mid-plane*
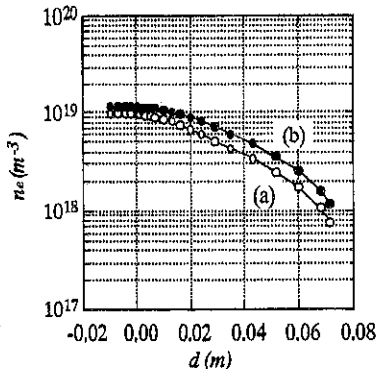
simulate JT-60U SOL and divertor plasmas. Figure 7 shows CII-line intensity for each channel of sight lines in Fig.1. Solid line is "B2-Eirene" result for the case(b) in Sec.2, while closed circles are experimental results from Ref.[6]. CII-line intensity profile of the numerical result is broader than the experimental result. This feature is related to the broad density profile in the SOL discussed above. Comparison of CII-line intensity profile here again suggests that more wide range and systematic study for the radial particle transport, together with the recycling property, will be needed in the future. In addition, peak value of the numerical results about 2.5 times larger than that of experimental results. As pointed out in

Ref.[6], chemical sputtering is important, not only in the high density regime, where physical sputtering is relatively less important, but also in the low density regime as in the present study. Shimizu, *et al*[6] found that only 10% of target-produced CD_4 reaches C^+, taking into account methane dynamics. Also in Ref.[9], with the use of the Monte-Carlo DIVIMP code, it has been shown that chemically sputtered hydrocarbons only contributes 10% of C^+ to explain the observed CII-line intensity profile. "B2-Eirene" code can take into account methane dynamics. However, in the present study, slow C-atoms launch at the target with the given chemical sputtering yield as in the Ref.[9]. Thus, we have implicitly assumed that 100% of hydrocarbon contribute to C^+ generation and it may be possible to overestimate C^+ concentration. To examine this, a simple test calculation, in which chemical sputtering yield at the plate is set to be zero, has been done. The result is shown by dotted line in Fig.7. Although the profile is still broad, its peak value well agrees with the experimental result.
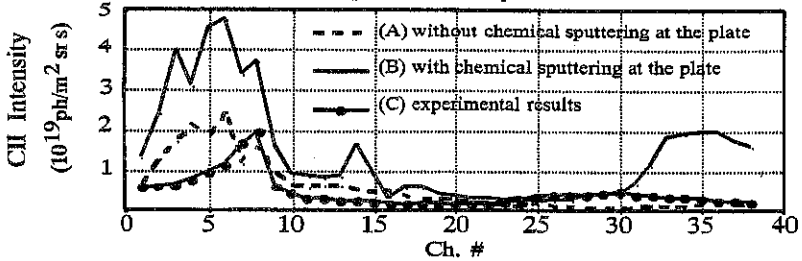
Fig. 7 CII line intensity profiles

5. Summary   Dependence of total particle flux at the plate on the upstream n_e has been compared with the experimental result in Ref.[5]. "B2-Eirene" results reproduce the essential feature in the experiments. Effects of the radial transport and chemical sputtering on the numerical results are also studied, taking shot#E19059[6] as an example. A clear 2nd SOL of T_e-profile has been observed in the simulation as in the recent experiment[8]. Decay length of 1st SOL almost agrees with the experimental value of Ref.[8] for $\chi_e=2.0m^2$/s. However, to explain experimental n_e-profile, smaller D-value or different model of radial transport (ex. pinch effect) seems to be necessary. More systematic and wide range of parameter survey is now going on. Comparison of CII-line intensity suggests that only a small fraction of target-produced CD_4 can reach C^+ to explain the observed CII-line intensity. This "B2-Eirene" result supports the result in Ref.[6] by IMPMC Monte-Carlo code for impurity transport.

References
[1] R.Schneider, D.Reiter, H.P.Zehrfeld, B.Braams, *et al*: J.Nucl.Mater., 196-198(1992)810.
[2] B.Braams: NET report No.68 (EUR-FU/XII-80/87/87/68), 1987.
[3] D.Reiter: J.Nucl.Mater., 196-198(1992)80.
[4] D.Reiter, *et al*: Plasma Physics and Controlled Fusion, 33(1991)1579.
[5] N.Asakura, *et al*: Nucl.Fusion 35(1995)381.
[6] K.Shimizu, *et al*: *Plasma Physics and Controlled Fusion Research*, 1994, Vienna, IAEA 1995, Vol.2, p.431.
[7] F.Wagner and K.Lackner : in *Physics of Plasma Wall Interaction in Controlled Fusion*, p.931, Plenum, 1986.
[8] N.Asakura, *et al*: J.Nucl.Mater. 241-243(1997)559.
[9] H.Y.Guo, *et al*: *Proc. 22nd EPS Conf. on Contr. Fusion and Plasma Phys.*, Part II, p.273, 1995.

Behavior of Neutral Deuterium and Helium Atoms in the Divertor Region of JT-60U

H. Kubo, H. Takenaga, T. Sugie, S. Higashijima,

S. Suzuki, K. Shimizu, A. Sakasai and N. Hosogane

Naka Fusion Research Establishment, Japan Atomic Energy Research Institute,

Naka-machi, Naka-gun, Ibaraki 311-01, Japan

1. Introduction

Understanding of behavior of neutral deuterium and helium atoms in divertor regions is necessary to control fueling and pumping in fusion plasmas. The velocity distribution of neutral atoms determines their penetration depth into plasmas and includes the information on the basic recycling processes. Understanding emission processes of the atoms is necessary to use the spectroscopic measurement for plasma diagnostics.

In the divertor region of JT-60U, the Doppler broadening of $D\alpha$ and He I (667.8 nm) lines has been observed [1] and analyzed to investigate the velocity distribution and the recycling and emission processes.

2. $D\alpha$ line profile

$D\alpha$ line profile was measured with a wavelength resolution of 0.011 nm. The profile was simulated with a two-dimensional neutral particle transport code (DEGAS) [2] using the electron temperature and density measured with Langmuir probes at the divertor tiles. The code uses reflection model based on TRIM calculation [3]. The code has been modified to obtain the line shape and all of the molecular data used in it has been revised.

Measured and simulated $D\alpha$ spectra around the outboard strike point are shown in Fig.1. The measured line profile was well reproduced by the simulation. As shown in the lower figure, the reflection model overestimates the reflection by a factor of 2 - 3.

Composition of the simulated $D\alpha$ spectrum is shown in Fig. 2. The spectrum is asymmetric, because the spectrometer faces the divertor tiles and the atoms moving toward the divertor tiles arrive at the tiles in a short time. The proportion of emission from atoms excited at the dissociation is 41 % of the total emission. Therefore, it is necessary to consider the emission from atoms excited at the dissociation for analysis of $D\alpha$ line intensity. The decay time of the excited state is so short that the atoms excited at the dissociation emit $D\alpha$ line before escaping the divertor plasmas. On the other hand, high-energy atoms produced by reflection and charge exchange escape from the divertor plasma in a short time, and the ratio of the emission to the flux is low in low density plasmas like the present case. For estimation of the ion temperature from the broadening of the blue wing of the spectrum, it is necessary not only to chose the viewing chord to reduce the effect of the reflected atoms but also to consider the escape of high-energy atoms produced by charge exchange.
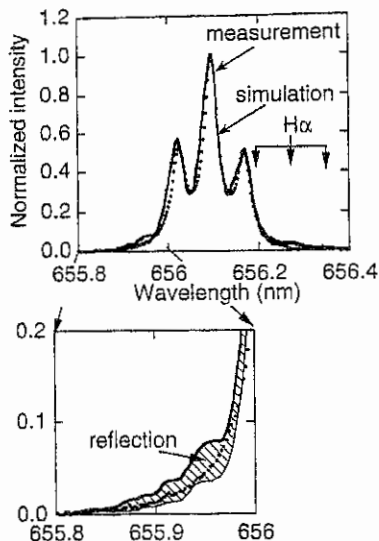
Fig. 1. Measured (points) and simulated (line) Dα spectra around the outboard strike point in a L-mode discharge with NB heating of 5 MW. The electron temperature and density in the divertor were 72 eV and 2.6×10^{18} m^{-3}, respectively. In the lower figure, the shaded area indicates the emission from reflected atoms.
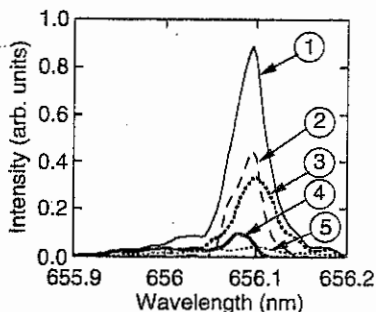
Fig. 2. Composition of the simulated Dα spectrum (① total emission, ② emission from atoms excited after dissociation, ③ emission from atoms excited at dissociation, ④ emission from reflected atoms, ⑤ emission from atoms produced by charge exchange). Here the Paschen-Back effect was not considered.

3. Broadening of He I line

Time evolution of a discharge for this study is shown in Fig. 3. The helium ion density in the main plasma was estimated to be about 4 % of the electron density. The electron density near the separatrix decreased rapidly at 6.1 s due to the occurrence of partial detachment. The profile of He I line has been observed with a wavelength resolution of 0.014 nm. Fig. 4 shows the spectra of the He I line observed at the outboard strike point at times of 5.25 s and 7.75 s of the discharge. At 5.25 s, the spectrum is similar to the instrumental function. It suggests that helium atoms are dominantly desorbed with energy about the surface temperature of the divertor tiles (about 0.05 eV). On the other hand, at 7.75 s, the spectrum is obviously broader than the instrumental function and the temperature corresponding to the width is 1.3 eV. In this paper, we fit the spectrum by a sum of two Gaussian components convoluted by the instrumental function. It is assumed that the width of the narrow component corresponds to the surface temperature of the divertor tiles. The time evolution of the intensities of the two components and the temperature corresponding to the width of the broad component are shown in Fig. 3. The intensity of the narrow component decreases and the intensity of the broad component increases, as the electron density increases and the electron temperature decreases. The broad

component is dominant in the partially detached plasma. The temperature of the broad component is 1 - 2 eV.

 A possible heating mechanism to explain the broad component is the elastic collision with deuterium ions. In a temperature range lower than 20 eV, as the temperature decreases, the ionization rate decreases rapidly while the elastic collision rate increases gradually. It can qualitatively explain the tendency that the line width increases as the temperature decreases. Here we define an average temperature of helium atoms as (T (narrow) × I (narrow) + T (broad) × I (broad)) / (I (narrow) + I (broad)). The relation between the average temperature and the electron temperature near the strike point is shown in Fig. 5. The datum in a partially detached plasma is tentatively plot at an electron temperature of 10 eV according to the electron temperature

Fig. 3. Time evolution of a discharge with a He puff. The line-averaged electron density in the main plasma and the NBI power are shown in the first row. The puff rates of He and D_2 are shown in the second row. The third row shows the electron temperature and density obtained by a Langmuir probe near the outboard strike point. The forth and the fifth show intensities of the broad and narrow components and the temperature corresponding to the width of the broad component of He I line at the strike point.

estimated from intensity ratios of He I lines [4]. The average temperature increases as the electron temperature decreases. When helium atoms are heated by the elastic collision before their ionization in an infinite area with temperature: T, and density: n, the average temperature of helium atoms to be observed: T_{He} (calculation), is expressed as

$$\overline{T_{He}} \text{ (calculation)} = \frac{\int_0^\infty T_{He}(t) \exp\left(-S\left(T_e\right) n_e t\right) dt}{\int_0^\infty \exp\left(-S\left(T_e\right) n_e t\right) dt},$$

$$\frac{dT_{He}}{dt} = R\left(T_{He}, T_{D^+}\right) n_{D^+},$$

where S and R are the ionization rate coefficient and the temperature relaxation rate coefficient by the elastic collision, respectively. The temperature relaxation rate coefficient is calculated using the diffusion crosssection for the elastic collision [5]. When the ion temperature is equal to the electron temperature and the deuterium ion density is equal to the electron density, the average temperature is given as a function of the temperature as shown in Fig. 5. The calculated

average temperature increases like the measured average temperature, as the plasma temperature decreases. The calculated temperature is, however, lower than the measured temperature in the temperature range from 20 to 60 eV. The discrepancy may be attributed to the spatial distribution. Moreover, it may be attributed to the definition of the average temperature, because the spectral line does not have a Gaussian profile and the width is close to the width of the instrumental function.

Since in the discharge the probability of penetration into the main plasma is estimated to be 0.1 % and 2.7 % for helium atoms with energies of 0.05 and 2 eV, respectively, the broad component affects significantly helium contamination of the main plasma. The high-energy atoms corresponding to the broad component have much higher mobility than the low-energy atoms corresponding to the narrow component and it is expected to affect the pumping efficiency of He ash.

Acknowledgment
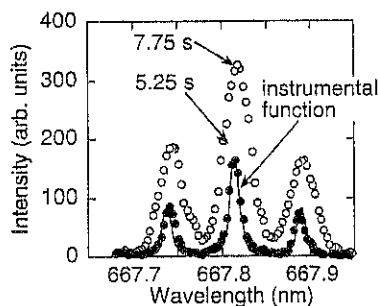
Fig. 4. Spectra of the He I line. The solid and the open circles indicate the spectra observed at the outboard strike point at times of 5.25 and 7.75 s of the discharge shown in Fig. 3, respectively. The line indicates the instrumental function of the spectrometer.
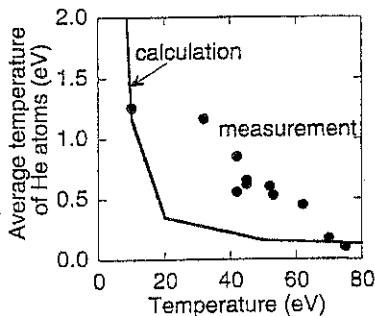
Fig. 5. Average temperatures of the helium atoms as functions of plasma temperature. The points indicate the measurement and the line indicates the calculation.

References

[1] H. Kubo et al., to be published in Fusion Eng. Des.

[2] D. B. Heifetz, in Physics of Plasma-Wall Interactions in Controlled Fusion, eds. D. E. Post and R. Behrish (Plenum, New York, 1986) 695.

[3] W. Eckstein and H. Verbeek, Max-Planck-Institut Report IPP 9/32 (1979).

[4] H. Kubo, et al., Japan Atomic Energy Research Institute JAERI-Research 96-018 104 (1996).

[5] P. Bachmann and H. J. Belitz, Max-Planck-Institut Report IPP 8/2 (1993).

Heating and Current Drive Experiments with Negative-ion-based Neutral Beam on JT-60U

Y. Kusama, T. Oikawa, M. Nemoto, T. Fujita, O. Naitoh, K. Tobita, Y. Kamada, K. Ushigusa, M. Kuriyama, C.B. Forest* and JT-60 Team

Naka Fusion Research Establishment, Japan Atomic Energy Research Institute, Naka-machi, Naka-gun, Ibaraki, 311-01 Japan

Injection of negative-ion-based neutral beams (NNB; designed parameters of 500 keV and 10 MW with two ion sources) began for the first time on JT-60U in March 1996. It will be used to sustain high performance plasmas and will demonstrate the physics basis of plasma heating and neutral beam current drive for the International Thermonuclear Experimental Reactor (ITER). A current drive efficiency of 0.8×10^{19} m^{-2}A/W has been achieved with NNB, approximately twice that obtained with 90 keV beams (PNB). Sawtooth stabilization has been observed, resulting in efficient electron heating, and classical slowing-down of NNB-injected ions has been confirmed in 1996 [1]. This paper presents recent progress in heating and current drive studies with NNB and in the performance on beam power and pulse length of NNB.

Systematic study of beam current drive were carried out with a combination of hydrogen NNB and PNB in hydrogen plasmas. Figure 1 shows time traces of the typical discharge: I_p=1.8 MA at the flat top, $\bar{n}_e$~1×10^{19} m^{-3}, V_p=73 m3, q_{eff}≈4. The NNB of 2.7 MW was injected at 350 keV after loop voltage, electron density end temperature became almost constant. A counter-PNB for the motional Stark effect spectroscopy (MSE) measurements [2] was injected just after the initiation of the plasma together with a co-PNB to cancel plasma current induced by MSE beam. Prior to the NNB injection, another PNB was also applied for CXRS measurements.

A NNB-driven current profile was reconstructed with the total current density and loop voltage profile using EFIT code [3, 4] and MSE measurements, following a next method. A radial distribution of loop voltage profile in the plasma is obtained from time dependent equilibrium reconstructed with magnetic diagnostics; magnetic probes, flux loops and the MSE measurements. Assuming neoclassical conductivity [5], inductive plasma current profile is calculated with the electric field profile. Non-inductive plasma current is reconstructed by subtracting the inductive current from the total plasma current density. Finally, NNB-driven current profile is deduced by subtraction of non-inductive current without NNB from that with NNB.

For the discharge shown in Fig. 1, the NNB-driven current profile was deduced from two time slices, just before the NNB injection (8 s) and just before the termination of NNB (8.4 s). Figure 2 presents the obtained profile of plasma current density. A small fraction of

uncancelled PNB driven current and increment of bootstrap current due to the increase of electron temperature by NNB heating are included actually in the current density profile. A hollow NNB-driven current profile consistent with the theoretical predictions using the ACCOME code was confirmed within uncertainty. Total current driven by NNB is integrated to be 125 kA ($\sim$7% of I_p) and is comparable to that calculated from ACCOME (100 kA). I has been confirmed that the measurements show total driven current and a current density profile reasonably agreed with the theoretical predictions using the ACCOME code [6]. The establishment of evaluation scheme for the current drive performance associated with the energetic beams would significantly contribute to ongoing ITER Physics R&D activities.

As a future prospect of non-inductive full current drive performance using the NNB assisted by PNB, total beam driven current for currents is shown in Fig. 3. The target plasma is a quasi-steady-state high-β_p H-mode one [7] and 10 MW of NNB is injected simultaneously with 5 MW of co-PNB and 10 MW of perp-PNB. The figure shows a possibility of achieving non-inductive full current drive of $\sim$2.7 MA.

Interaction between toroidicity-induced Alfvén eigenmodes (TAE modes) exited by ICRF heating (102 MHz, $2\omega_{CH}$) and hydrogen NNB was investigated in helium plasmas. Figure 4 shows a contour plot of TAE modes frequency against time together with other plasma parameters. TAE modes of toroidal mode number n=12-5 were destabilized by the ICRF-driven energetic protons before sawtooth crash, followed by other high frequency modes considered to be ellipticity-induced Alfvén eigenmodes (EAE modes) [8]. The NNB(350 keV/1.6 MW) was injected into the similar discharge and its interaction with TAE and EAE modes was investigated. Similar TAE modes were excited also in the case of NNB injection and no significant change was observed in TAE modes comparing with the case with NNB. On the other hand, EAE modes observed in the discharge without NNB almost disappeared. In the plasma with n_{He}=1×10^{19} m^{-3} ($n_e\sim$2×10^{19} m^{-3}) and B_{t0}=3.3 T, the velocity of hydrogen beam energy of 350 keV in a toroidal field direction corresponds to $\sim$0.6v_A (v_A=Alfvén velocity), which is slightly higher than $v_{//}\approx$0.5v_A of the EAE mode resonance. It means that NNB-injected ions can resonate with EAE modes and beam ion Landau damping can play an effective role for the mode stability. One of important mechanism of disappearance of EAE modes is thought to be the beam ion Landau damping. Concerning the effect of TAE modes on confinement of NNB-injected ions, no clear degradation of the confinement was observed from the charge-exchange measurements [9] in a range of 130-500 keV.

Multi-step ionization of energetic beam atoms has been evaluated because of its importance for determining the beam energy in ITER and for knowing the absorbed energy of NNB in a plasma. The density dependence of the shine-through of NNB was measured in a fixed plasma configuration using thermocouples installed in armor tiles of the NNB facing first wall. Reference heat flux in the case without plasma was measured by injecting short-pulse NNB (0.2 s). The analysis shows that measured shine-through is smaller than that

expected from single-step ionization processes. Figure 5 compares NNB-chord-averaged enhancement factor estimated from the experimental shine-through with one obtained from shine-through calculated using the enhanced cross-section evaluated by Janev [10]. It seems that the Janev's cross-section is larger than that evaluated experimentally. Much more data are necessary for more careful comparison with Janev's cross section .

The performance on beam power and pulse length is being progressed together with its application to heating and current drive experiments using NNB. Recent achievements of 3.2 MW/source of power at 350 keV of beam energy and a pulse length up to ~2 s at 300 keV are promising for early demonstration of the full injection performance.

In summary, the profile of currents driven by the energetic beams from NNB was for the first time identified from the MSE measurements, which reasonably agrees with the theoretical prediction. This result indicates that evaluation scheme for the current drive performance associated with the energetic beams has been established. The interaction between NNB and TAE and EAE modes was investigated. It is thought that one of the important stabilizing mechanisms is the beam ion Landau damping. The density dependence of the shinethrough of NNB in plasmas were measured and the averaged enhancement factor evaluated with Janev's cross-section appears to be larger than that estimated experimentally. The heating and current drive experiments using the NNB with full performance in the new divertor configuration would significantly contribute to ongoing ITER Physics R&D activities.

References

[1] K. Ushigusa and JT-60 Team, 16th IAEA Fusion Energy Conference, Montreal 1996, F1-CN-64/O1-3.

[2] T. Fujita et al., to be published in Fusion Eng. Design.

[3] L.L. Lao at al., Nucl. Fusion **30**, 1035 (1990).

[4] C.B. Forest et al., Phys. Rev. Lett. **73**, 2444 (1994).

[5] M. Kikuchi et al., Nucl. Fusion **29**, 343 (1990).

[6] T. Oikawa et al., paper in preparation.

[7] S. Ishida et al., Phys. Rev. Lett. 68, 1531 (1992).

[8] G.J. Kramer et al., submitted to Phys. Rev. Lett.

[9] Y. Kusama et al., to be published in Fusion Eng. Design.

[10] R.K. Janev et al., Nucl. Fusion **29**, 2125 (1989).

* General Atomics, San Diego, CA 92186-9784, USA. (present address: University of Wisconsin-Madison)
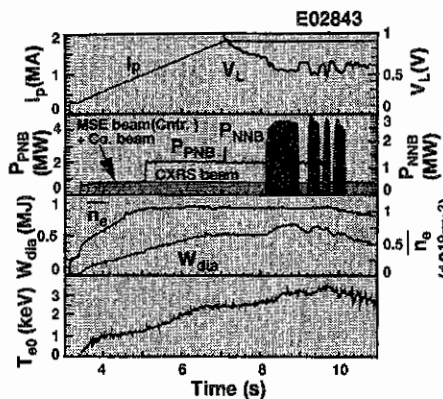
Fig. 1: Time traces of plasma current (I_p), loop voltage (V_L), neutral beam power (P_{NNB}, P_{PNB}), line-averaged density ($\overline{n_e}$), diamagnetic stored energy (W_{dia}) and central electron temperature (T_{e0}).

Fig. 2: The measured profile of NNB driven current and predicted one with ACCOME code. Uncertainty of the measurement is also shown.
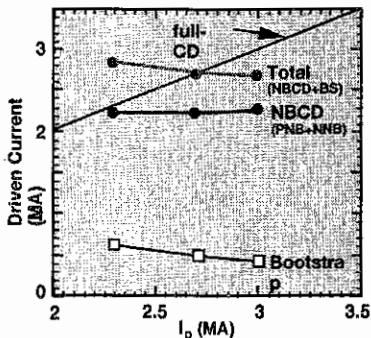
Fig. 3: Total driven current (beam driven + bootstrap) vs I_p. Used plasma parameters are $n_{e0}=5.3\times10^{19}$ m^{-3}, $T_{e0}=10.6$ keV and $T_{i0}=31.6$ keV.

Fig. 4: Contour plot of TAE modes frequency, ICRF power P_{IC} (3.8 MW), NB power P_{NB} (1.5 MW) for MSE and CXRS, W_{dia} and T_{e0} against time.
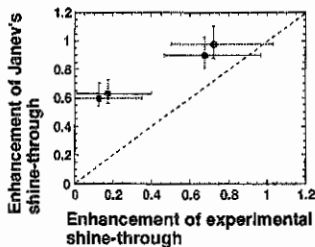
Fig. 5: Comparison between NNB-chord-averaged enhancement factor estimated experimentally and one obtained using Janev's cross-section.

Nonlinear Fokker-Planck analysis of ion temperature in JT-60U hot ion plasma

M. Yamagiwa, J. Koga, S. Ishida

Japan Atomic Energy Research Institute, Naka, Ibaraki, Japan

Abstract. A two-dimensional nonlinear Fokker-Planck code is applied to evaluate the ion (deuteron) temperature in a JT-60U hot ion plasma in which the measured carbon impurity temperature reached up to 45 keV with the 90 keV beam injection. The deuteron bulk temperature is found to exceed the carbon temperature, indicating that the impurity temperature measurement does not lead to overestimation of the ion temperature. The effective temperature based on the average energy is, however, almost the same as the carbon temperature, and the D-D fusion reactivity is also around a value given by a Maxwellian distribution with its temperature equal to the carbon temperature, which can be regarded as an equivalent ion temperature.

1. Introduction

A very high ion temperature of ~45 keV was recently achieved under the intense neutral beam injection (NBI) power of 37 MW and the beam energy (E_b) of 90 keV in a JT-60U hot ion plasma, where the fusion triple product $n_i(0)\tau_E T_i(0)$ reached ~1.5×10^{21} m^{-3} s keV [1]. The ion temperature was measured by the charge exchange recombination spectroscopy of carbon impurity ions. Usually the energy input to an impurity ion is much larger than that to a main plasma ion, because the power transferred from beam ions to background k-species ions is proportional to the ratio, Z_k^2 / A_k, with Z_k and A_k being the charge and mass numbers. Therefore, the temperature of the impurity ions is considered to be higher than that of the main plasma ions in most cases. In the case where the resultant ion temperature is comparable to the beam injection energy as in the JT-60U discharge, however, the aforementioned simple picture of the power transfer from a test particle to the background ions may not hold: When the ion temperature is close to the beam energy, it is difficult to distinguish the fast ion component from the bulk ion component and the effect of self collisions among the main plasma ions on the bulk and tail formation becomes important in the slowing-down process of the beam ions. Consequently, the impurity temperature may not be necessarily higher than the main plasma ion temperature, which is required to evaluate. The purpose of the present work is to obtain the deuteron distribution function and evaluate the deuteron temperature for the JT-60U hot ion plasma parameters. We use a two-dimensional nonlinear Fokker-Planck code in order to take into account the effect of deuteron self heating. The deuteron bulk temperature is estimated by the slope of the numerically obtained energy spectrum, while the carbon temperature is given as a parameter. In Section 2 a model Fokker-Planck equation is described. In Section 3 numerical results are presented. Section 4 contains the conclusions.

2. Model equation

Use is made of the following two-dimensional nonlinear Fokker-Planck equation

$$\frac{\partial f_D}{\partial t} = \sum_j C(f_D, f_j) + \frac{1}{2} \frac{1}{v^2} \frac{\partial}{\partial v}\left(v^3 \frac{f_D}{\tau_E}\right) - \frac{f_D}{\tau_p} + S_D \tag{1}$$

where $f_D(v, \theta)$ is the deuteron distribution function with v and θ being the particle speed and pitch angle, $C(f_D, f_j)$ the nonlinear collision term between deuterons and j-species particles [2], τ_E the energy loss time, τ_p the particle loss time, and S_D the particle source due to beam injection, respectively. The dependences of τ_E and τ_p on particle energy, E, are taken to be $\tau_E = \tau_E^0 \left[1 + (E/E_*)^{1.5}\right]$ and $\tau_p = \tau_p^0 \left[1 + (E/E_p)^{1.5}\right]$, respectively. Quantities E_* and E_p are characteristic energies for energy and particle losses, respectively. The value of τ_E^0 can be given somewhat arbitrarily, while that of τ_p^0 is determined so as to conserve the number density. Confinement of the fast ions is assumed to be better than that of the thermal ions, as was found in combined beam and radio-frequency wave heating experiments in JT-60 [3, 4]. In addition, it is assumed that there is no MHD-induced loss of fast ions since no strong MHD fluctuations have been observed. The electron and carbon distribution functions are assumed to be Maxwellian with the temperature T_e and T_C, respectively. Parameters used are pertinent to the JT-60U hot ion discharge [1]: $T_C = 45\pm5$ keV, $T_e = 10$ keV, $n_e = 5.2\times10^{19}$ m^{-3}, $Z_{eff} = 2.2$, $P_{NBI} \sim 1.6$ MW/m^3, which correspond to the values at r/a ~ 0.16, and $E_b = 90$ keV. The distribution function obtained is averaged over the pitch angle in velocity space to get the energy spectrum. The bulk temperature T_D is evaluated from the slope of the energy spectrum in the low energy region. The effective temperature, T_{eff}, based on the average energy is also studied.

3. Numerical results

First we study the dependence of the power transfer from deuterons to carbon ions and from carbon ions to electrons on the carbon temperature. The parameters concerning the energy loss are chosen to be $E_* = \infty$ and $\tau_E^0 = \infty$, indicating that no energy loss is assumed except for the energy sink due to the fixed temperatures of the electrons and carbon ions. Regarding the particle confinement of deuterons, E_p is taken to be 50 keV. It is shown in Fig. 1 that the power density transferred from carbon ions to electrons, P_{Ce}, naturally increases with T_C, while that from deuterons to carbon ions, P_{DC}, decreases with T_C. At $T_C \sim 49$ keV, for this case, the energy balance of the carbon breaks; for $T_C > 49$ keV the power loss (to electrons) exceeds the power gain (from deuterons), indicating that the carbon energy confinement time is negative. Therefore, $T_C \sim 49$ keV is the upper limit of the possible carbon temperature for the case of E_p = 50 keV.

Figure 2 shows the τ_E^0 dependence of the power density transferred from deuterons to carbon ions, P_{DC}, that from carbon ions to electrons, P_{Ce}, and the deuteron bulk temperature,

T_D, for $T_C = 45$ keV, $E_p = 50$ keV, and $E_* = 50$ keV. When τ_E^0 tends to a critical value of τ_{Ec}^0 $\lesssim 1.2$ sec, at which the energy flow from deuterons to carbon ions is balanced with that from carbon ions to electrons, P_{DC} approaches P_{Ce}, and the carbon energy confinement time goes to infinity. For $\tau_E^0 < \tau_{Ec}^0$, no steady state exists. At $\tau_E^0 \sim \tau_{Ec}^0$, $T_D \sim 52$ keV.
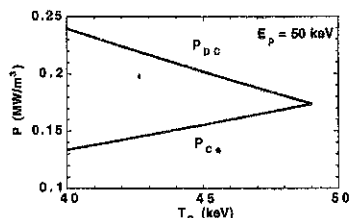
FIG. 1. Dependence of the power density transferred from deuterons to carbon ions, P_{DC}, and from carbon ions to electrons, P_{Ce}, on T_C for $E_* = \infty$, $\tau_E^0 = \infty$, and $E_p = 50$ keV.
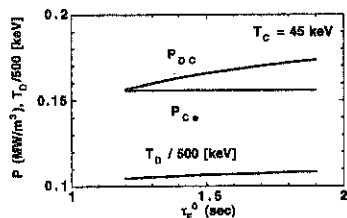
FIG. 2. Dependence of the power density transferred from deuterons to carbon ions, P_{DC}, that from carbon ions to electrons, P_{Ce}, and the deuteron bulk temperature, T_D, on τ_E^0 for $T_C = 45$ keV, $E_p = 50$ keV, and $E_* = 50$ keV.

Figure 3 shows the T_C dependence of T_D (solid curves) and T_{eff} (dashed curves) at $\tau_E^0 \sim$ τ_{Ec}^0 (for each T_C). The straight line indicates the case where $T_D = T_C$. It is seen that the deuteron bulk temperature, T_D, exceeds the carbon temperature, while the effective temperature, T_{eff}, is comparable to T_C. The difference between the cases of $E_* = 25$ keV (circles) and E_* $=\infty$ (squares) is slight. Therefore, variation of E_*, which has been chosen arbitrarily, is expected not to have so significant effect on the results.

Figure 4 shows the deuteron energy spectrum at $\tau_E^0 \sim \tau_{Ec}^0$ for $T_C = 45$ keV and $E_* =$ $E_p = 50$ keV. The bulk temperature, T_D, is ~ 52 keV. For comparison, Maxwellian distributions with temperatures of 45 keV and 52 keV are also shown by dash-dotted and dashed curves, respectively. For such a high bulk temperature, the slowing-down tail is not so clearly distinguished from the bulk slope: The slowed-down deuterons are assimilated with the bulk deuterons near the injection energy, $E_b = 90$ keV. As a result, the bulk temperature becomes higher than the carbon temperature. On the other hand, the tail for $E > E_b$ degrades as compared to the Maxwellian tail: In a sense the tail ions are cooled by beam injection. The effective temperature based on the average energy remains almost the same as the carbon temperature because of this tail degradation. Nevertheless, it is from deuterons to carbon ions that the power should be transferred, since the external power input is only due to the deuteron beam injection. So, the bulk temperature may be higher than the carbon temperature. Accordingly, the present result, $T_D > T_C$, is not unreasonable. The tail degradation leads to reduction of the D-D fusion reactivity as well. The amount of reduction is 17 % of that for the Maxwellian distribution with the temperature of 52 keV: The value of the reactivity is almost

the same as that for the Maxwellian distribution with the temperature of 45 keV. Therefore, the equivalent deuteron temperature may be regarded as 45 keV in terms of the average energy and the D-D neutron production rate.
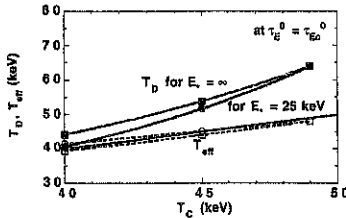
FIG. 3. Dependence of T_D (solid curves) and T_{eff} (dashed curves) at $\tau_E^0 \sim \tau_{Ec}^0$ on T_C for $E_p = 50$ keV. The straight line indicates the case where $T_D = T_C$. The cases of $E_* = 25$ keV and $E_* = \infty$ are shown by circles and squares, respectively.
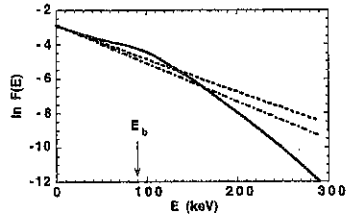
FIG. 4. Deuteron energy spectrum at $\tau_E^0 \sim \tau_{Ec}^0$ for $T_C = 45$ keV and $E_* = E_p = 50$ keV. Maxwellian distributions with temperatures of 45 keV and 52 keV are shown by dash-dotted and dashed curves, respectively.

4. Conclusions

The deuteron temperatre in a beam heated hot ion plasma containing carbon impurities in JT-60U has been studied by using a two-dimensional nonlinear Fokker-Planck code. The deuteron bulk temperature has been evaluated from the slope of the numerically obtained energy spectrum. The resultant bulk temperature has been found to exceed the carbon temperature, indicating that the measurement of the impurity temperature in experiment does not lead to overestimation of the ion temperature. The effective temperature based on the average energy is, however, almost the same as the carbon temperature because of the tail degradation above the beam injection energy. The D-D fusion reactivity is also close to a value which would be given if the deuteron distribution was Maxwellian with the temperature same as the carbon temperature. Therefore, the carbon temperature may possibly be regarded as an equivalent ion temperature in terms of the average energy and the D-D neutron production rate.

References

[1] S. Ishida, et al., in Plasma Physics and Controlled Nuclear Fusion Research 1996 (Proc. 16th Int. Conf. Montréal, 1996), IAEA, Vienna (in press) Paper F1-CN-64/A3-1.

[2] J. Killeen, K.D. Marx, Methods in Computational Physics, Vol. 9, Academic Press, New York (1969).

[3] H. Kimura, et al., Nucl. Fusion **31**, 83 (1991).

[4] M. Yamagiwa, et al., Plasma Phys. Control. Fusion **30**, 943 (1988).

Statistical Study of TCV disruptivity and H-mode Accessibility

Y. Martin, Ch Deschenaux, J.B. Lister, A. Pochelon

Centre de Recherches en Physique des Plasmas,
Association EURATOM - Confédération Suisse,
Ecole Polytechnique Fédérale de Lausanne, CH-1015 Lausanne, Switzerland

INTRODUCTION

Optimising tokamak operation consists of finding a path, in a multidimensional parameter space, which leads to the desired plasma characteristics and avoids hazardous regions. Typically the desirable regions are the domain where an L-mode to H-mode transition can occur, and then, in the H-mode, where ELMs and the required high density can be maintained. The regions to avoid are those with a high rate of disruptivity. On TCV, learning the safe and successful paths is achieved empirically. This will no longer be possible in a machine like ITER, since only a small percentage of disrupted discharges will be tolerable. An *a priori* knowledge of the hazardous regions in ITER is therefore mandatory. This paper presents the results of a statistical analysis of the occurrence of disruptions in TCV.

For the H-mode accessibility, it is usually admitted that a minimum auxiliary power is required, and that this power threshold depends on some plasma parameters. On TCV, since the H-mode was achieved with Ohmic heating only, such a power threshold can not be determined. Plasma shape, current and densities as well as the vacuum vessel conditioning are known to play a role in the H-mode accessibility. Discriminant analysis, a powerful statistical method, has been used to estimate a probability of being close to an L-mode to H-mode (LH) transition, which could be used to guide the plasma discharge towards the LH transition, with the help of an advanced and intelligent control system.

PLASMA DISRUPTIVITY IN TCV

In order to quantify the disruption rate in TCV, we have defined the disruptivity as the number of disruptions observed in a multidimensional cell of the operational domain, divided by the total plasma operation time spent in that cell. This latter time is provided by a database containing time slices taken every 50 ms in every plasma discharges produced over more than two years of operation, a total of over 60'000 time slices. The disruptions have been visually

classified according to their operational context, such as during an L-mode or H-mode phase or in the presence of locking modes, etc. This allows us to analyse the disruptivity in different contexts separately and also to remove disruptions provoked by technical failures or feedback control experiments, which have nothing to do with the underlying physics of disruptions. The aim of such an approach is to identify the high disruptivity zones without *a priori* knowledge. For instance, the q=2 limit naturally emerges from the analysis as a hard limit, with only a slight increase in disruptivity for 2<q<3.

To answer the question whether the Greenwald density limit is a strong limit or not, we plot the disruptivity in the Greenwald diagram for 4 different contexts (fig 1). In the stationary case, in L-mode or H-mode or soon after a HL transition, the Greenwald limit (G=1) is not exceeded. However, the disruptivity does not increase with the Greenwald parameter (G). This limit then appears like a soft limit for the low currents in L-mode, in the sense that the plasma itself avoids going to higher density, but without disrupting. For higher plasma current values, the disruptivity simply increases with the plasma density, not with G. In H-mode plasmas, the disruptivity also increases with the density with only a weak dependence on the Greenwald parameter (Ip/a^2). During the current decay phase, the limit is exceeded, but with a high disruptivity. In this case the Greenwald density limit appears as a strong limit.
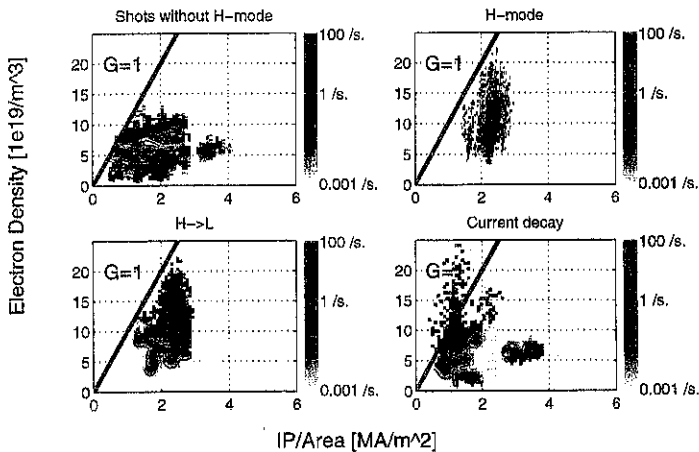
Fig 1: Disruptivity at the Greenwald density limit in different contexts
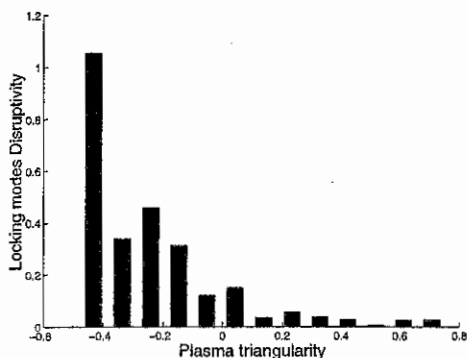
Fig 2: *Disruptivity due to locking modes decreases with the triangularity*

Although no clear dependence on the plasma shape is observed when all disruptions are taken together, either in a Hugill or li:q diagram, the disruptions due to locking modes are found to occur mainly at low triangularity, as shown in Fig. 2. This decrease of disruptivity at high positive triangularity is commonly used on TCV to cross q=3. For instance, even if the desired final plasma has a negative triangularity, its formation goes through a high triangularity phase ($\delta>0.2$). With such a formation path, we performed 180 similar shots, one every morning, with a disruption rate lower than 1 %.

H-MODE ACCESSIBILITY

L-mode to H-mode transitions have been observed in TCV in a wide variety of ohmically heated plasma configurations (limited, single null, double null), plasma shapes (triagularity, elongation, gaps, ...), plasma currents, plasma densities and magnetic fields. Initially, the vacuum vessel conditioning appeared to play an important role in the reproducibility of the H-mode access. Since physics explanations of the effect of the conditioning remain unclear, a statistical approach, discriminant analysis, has been chosen, with the aim of extracting those parameters which are important for characterising the closeness to the LH transition.

Discriminant analysis consists of a multidimensional (R^n) coordinate transformation which minimises the intercorrelation between data groups while maximising the intracorrelation within a data group. In the case of a discrimination between two groups of data, only one variable, called the classification variable, is necessary to reveal the separation, if any. From that new variable, we define a probability of belonging to one or to the other of the two groups.

We calculated the classification variable, as well as the associated probability for two groups of data. One contains the time slices in L-mode before the transition and the other contains the time slices taken right at the LH transition. In a first step, the input parameters were the

the plasma shape, current and density. This set of input parameters did not lead to a clear classification variable. We had to include the Ohmic power, the plasma temperature and a measure of the gas flux inside the machine to obtain a good enough classification variable, as shown in Fig. 3. The necessity of using this latter variable indicates the importance of the recycling on the H-mode accessibility.

Figure 4 shows the discriminant analysis results between L-mode and ELM free H-mode time slices, with the same input parameters. The probability curve clearly shows that a predictor can be easily calculated in this case.

Fig 3: Dα trace shows a L-mode to H-mode transition, the discriminant variable and the associated probability reveals the imminence of the transition by the increase of the transition probability

CONCLUSIONS

The disruptivity analysis reveals the importance of the plasma shaping during its formation in order to avoid disruptions due to locking modes. The Greenwald limit does not appear as a strong limit during the stationary phases.
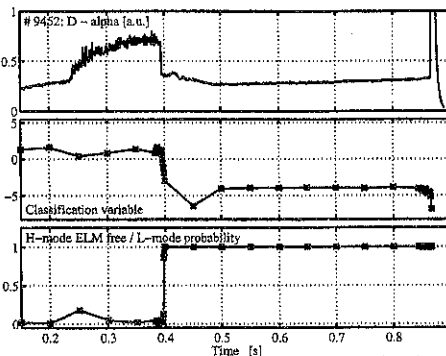
Fig 4: Dα trace of a typical TCV H-mode plasma, the discriminant variable and the associated probability showing the prediction to be in the H-mode

Resulting from a discriminant analysis, a linear combination of plasma parameters, including information about the wall recycling, gives a probability of LH transition which is verified to increase and reach unity as the transition is approached.

ACKNOWLEDGEMENT

Stability and Energy Confinement of Highly Elongated Plasmas in TCV

F. Hofmann, R. Behn, M.J. Dutch, Y. Martin, J.-M. Moret, C. Nieswand,
Z.A. Pietrzyk, H. Reimerdes, D.J. Ward

Centre de Recherches en Physique des Plasmas
Ecole Polytechnique Fédérale de Lausanne
Association EURATOM - Confédération Suisse
CH- 1015 Lausanne, Switzerland

1. Introduction

One of the principal aims of TCV [1] is the creation and active stabilization of highly elongated plasmas, $\kappa \leq 3$. This implies high growth rates of axisymmetric modes and a very low stability margin. To stabilize such modes, TCV is equipped with a vertical position control system using a combination of slow coils outside the vacuum vessel (response time $\approx$ 1ms) and a fast coil inside the vessel (response time $\approx$ 0.1ms). The fast coil became operational in August 1996 and this paper describes the first experiments using both fast and slow coils for vertical stabilization.

2. Axisymmetric Modes

The dominant axisymmetric mode in an elongated tokamak is basically a vertical displacement of the entire plasma. The open-loop growth rate of this instability depends primarily on plasma elongation but also on a number of other parameters, such as triangularity, squareness, vertical position within the vessel, plasma wall distance, internal inductance, poloidal beta, etc. [2,3].
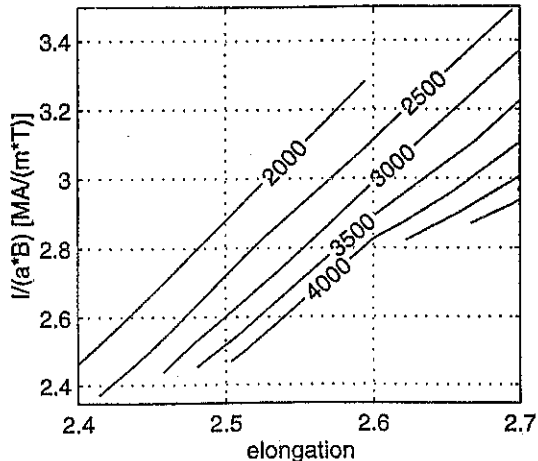
Fig.1.: n=0 growth rate [sec^-1] for D-shaped plasmas in TCV

If these other parameters are optimized to give the minimum growth rate for a given elongation, and if we assume Ohmic current profiles and low beta ($\beta_{tor} \approx 2\%$), we can express the vertical growth rate as a function of elongation and normalized current (Fig.1). The results presented here have been computed with the NOVA-W code [4]. Vertical instability growth rates have also been measured in TCV and excellent agreement with NOVA-W results was found [3].

3. Experiments with Slow Coils Only

The power supplies which drive the slow coils in TCV i.e. the shaping coils outside the vacuum vessel, have a response time, Δt, of approximately 1ms. This imposes an upper limit on the growth rate that can be stabilized with these coils, $\gamma < (\Delta t)^{-1}$ [5]. In fact, plasmas with vertical growth rates up to 1000 sec^{-1} have been successfully stabilized in TCV with the slow coils only [3]. An upper limit on the growth rate implies an upper limit on elongation for any given plasma current, as is evident from Fig.1.

4. Experiments with Slow and Fast Coils

The fast coil in TCV is mounted inside the vacuum vessel and consists of 6 turns connected in series, 3 positive turns on the bottom and 3 negative turns on the top of the vessel. The coil is driven by a power supply capable of producing a maximum current of 2kA at 550V with a response time of less than 0.1ms. Initial experimemts with the fast coil were done on plasmas with low current (250kA), low triangularity and large plasma-wall distance (Fig.2a). Under these conditions, the growth rate of the vertical instability is large, even at moderate elongation ($\kappa=1.9$). Derivative feedback was applied to the fast coil and four outboard slow coils, whereas proportional feedback was only applied to the slow coils. This scheme ensures that the time-averaged current in the fast coil always remains close to zero. Optimization of the three feedback gains (slow proportional gain, slow derivative gain and fast derivative gain) allowed us to stabilize plasmas with vertical growth rates up to 4400 sec^{-1}, corresponding to a stability margin, f=1.028.

After the system had been shown to work satisfactorily at low plasma current, a second series of experiments was launched with the aim of maximizing the plasma current. For this purpose, the triangularity was increased, the plasma was moved to the top of the vessel and the plasma current was increased to a value close to the q=2 limit. The feedback scheme was the same as the one used for the low current experiments. Using a toroidal field of 1.43 T, a maximum current of 1.02MA was reached at an elongation of $\kappa=2.28$ (Fig. 2b). This plasma had a relatively modest vertical growth rate, $\gamma = 1200$ sec^{-1}.
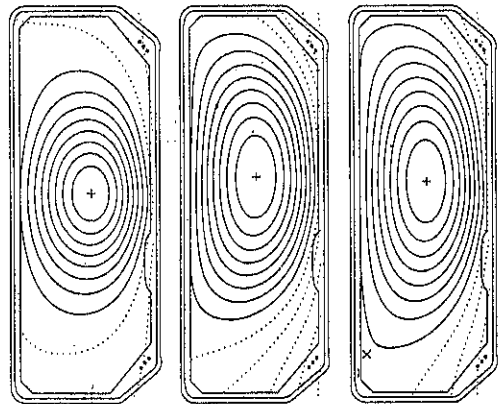
Fig.2.: Reconstructed equilibria of TCV discharges

(a)	(b)	(c)
$I_p=257kA$	$I_p=1.024MA$	$I_p=726kA$
$B_t=1.43T$	$B_t=1.43T$	$B_t=1.00T$
$\kappa=1.93$	$\kappa=2.28$	$\kappa=2.58$

A third series of experiments was then undertaken to explore the limits on elongation. This was done at a lower toroidal field, 1.0T, in order to minimize the risk of damage to the fast coil during vertical disruptions. The feedback setup was still the same as was used for the previous experiments, but the vertical position observer was slightly modified such as to minimize its sensitivity to the fast coil current. These experiments led to the successful stabilization of D-shaped plasmas with elongations up to 2.58 (Fig.2c) and vertical instability growth rates up to 2700 sec^{-1}.

5. Current Limit at High Elongation

During the experimental campaign described above, it was found that the maximum normalized current that can be stably confined increases with elongation, as expected, up to $\kappa \approx 2.3$. However, for $\kappa > 2.3$, the maximum normalized current remains roughly constant, $I_p/(a*B) \approx 3.0*10^6$ (Fig.3.). As soon as we try to increase the current above this limit, non-axisymmetric modes appear and lead to a disruption. The modes have been analyzed using toroidal and poloidal arrays of fast pick-up coils and mode numbers m/n=3/2 or m/n=2/1 are observed just before the disruption. This result is consistent with theoretical predictions [6,7] indicating that the current limit at zero pressure is approximately

given by $I_p/(a*B) <$ $3.2*10^6$ at an elongation $\kappa=2.5$ and remains constant up to $\kappa=3.0$. Based on these results, we can now draw operational limits in κ-I_p space and we find that the maximum elongation that can be produced in TCV depends on the maximum vertical growth rate that can be stabilized.
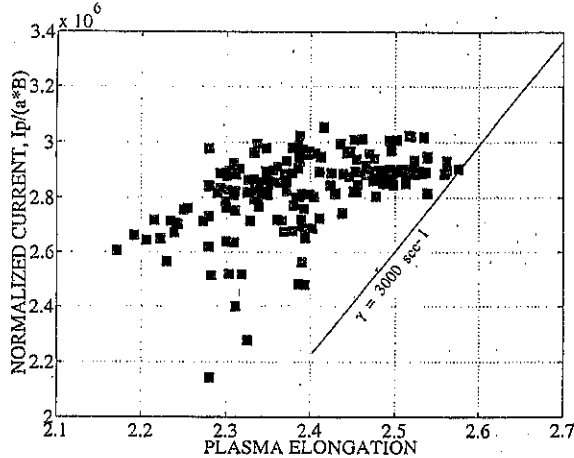
Fig.3.: Normalized current vs. elongation for TCV plasmas

Since the fast coil has a response time of less than 0.1ms, it is possible to stabilize very high growth rates, of the order of 5000 sec^{-1}. However, for a growth rate of this magnitude, the stability margin is extremely small, f=1.025, and a very slight change in plasma position or current profile (ELMs, sawteeth) can then push the plasma beyond the ideal limit (f=1). In order to avoid this extreme sensitivity, we assume, as a practical limit, f≥1.042, which implies $\gamma \leq 3000 \text{ sec}^{-1}$ in TCV. Together with the current limit mentioned above, this leads to an upper limit on elongation, $\kappa \leq 2.6$ (Fig.3.). This limit is, of course, only valid for conventional D-shaped plasmas and does not apply to more exotic shapes such as doublets [8] or triplets [9].

6. Confinement at High Elongation

The experiments with highly elongated plasmas have produced an additional, rather unexpected result. It was observed that, above a certain elongation, the plasma undergoes a slow transition, typically within 200ms, to a new mode of operation. This new mode is characterized by higher electron density, higher electron temperature, slightly lower loop voltage and a higher energy confinement time. A typical example is shown in Fig.4. The transition takes place during the current plateau, between 300 and 500ms. It is likely that the transition is associated with a change in current profile, as the internal inductance is increasing (Fig.4.).
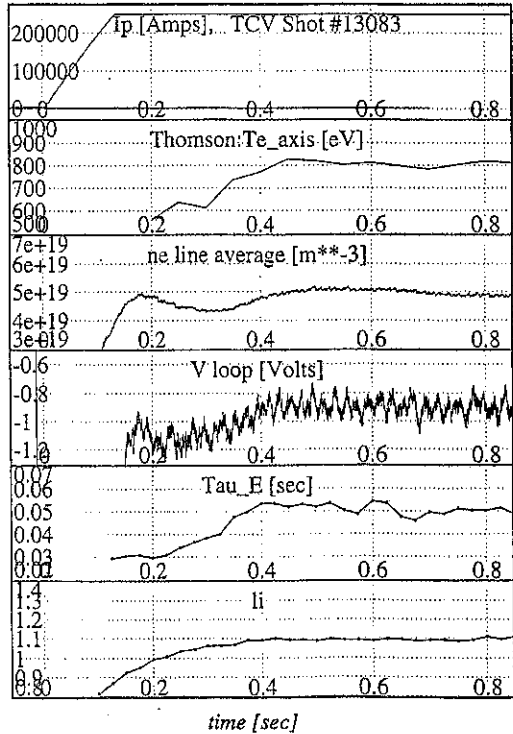
Fig.4.: Transition to a state of improved Ohmic confinement

Acknowledgements

References

[1]   Hofmann, F. et al., Plasma Phys. Control. Fusion **36** (1994) B277.

[2]   Ward, D.J. et al., Nuclear Fusion **33** (1993) 821.

[3]   Hofmann, F. et al., Nuclear Fusion **37** (1997) 681.

[4]   Ward. D.J. et al., J. Comput. Phys. **104** (1993) 221.

[5]   Noll, P. et al., in Controlled Fusion and Plasma Heating (Proc. 17th Europ. Conf. Ansterdam, 1990), Part I, Vol. 14B, 419.

[6]   Turnbull, A.D. et al., Nuclear Fusion **29** (1989) 629.

[7]   Eriksson, G. et al., in Plasma Physics (Proc. 1992 Int. Conf. Innsbruck), Vol. 16C, Part I, European Physical Society (1992) 343.

[8]   Wesley, J.C. et al., in Plasma Phys. Contr. Nuclear Fusion Research 1980 (Proc. 8th Int. Conf. Brussels, 1980) Vol 1, IAEA (1981) 35.

[9]   Hofmann, F., Plasma Physics and Controlled Fusion **29** (1987) 1053.

Confinement Optimisation by Plasma Shaping on TCV

J.-M. Moret, R. Behn, S. Franke, F. Hofmann, H. Weisen

Centre de Recherches en Physique des Plasmas
Association EURATOM - Confédération Suisse
École Polytechnique Fédérale de Lausanne
CH-1015 Lausanne, Switzerland

Any improvement in the energy confinement time of a tokamak reactor may facilitate its access to ignition. TCV has the unique capability of creating a wide variety of plasma shapes and can therefore investigate to which extent an appropriate choice of the plasma shape can improve the energy confinement time. For simple shapes defined only by their elongation and triangularity, it has already been observed on TCV that the confinement properties of the plasma depend strongly on the shape [1,2]. This previous work has now been extended to include more complex shapes and higher elongations, in order firstly to test the applicability of the previously proposed explanation for the shape dependence of the confinement time and secondly to propose new shapes which offer a substantial gain on their confinement characteristics.

Experiments. TCV plasma shape is controlled by 16 independent poloidal coils. The present work is based on equilibria whose outer shape is defined by the analytical contour

$$(R, Z) = (R_0, Z_0) + a(\cos(\theta + \delta\sin\theta - \lambda\sin 2\theta), \kappa\sin\theta) \tag{1}$$

where (R_0, Z_0) is the geometric axis position, a the minor radius, κ the elongation, δ the triangularity and λ the squareness. A negative λ tends to define a lozenge shape while a positive value gives the contour a rectangular shape. The studied shapes are divided in three sets: a systematic

	κ	δ	λ	q_a	$\bar{n}_e$ [10^{19}m^{-3}]
(κ,δ) scan	$[1.0,1.9] \times [-0.45,0.80]$		0.00	$[2.3,6.0] \times [2.9,8,8]$	
(δ,λ) scan	1.5	$[-0.25,0.35] \times [-0.10,0.30]$		$[2.3,5.1]$	5.3
high κ	$[1.9,2.6]$	$[0.30,0.50]$	$[0.05,0.25]$	$[2.5,3.9]$	$[2.7,8.5]$

scan in the (κ,δ) plane at fixed λ; a systematic scan in the (δ,λ) plane at fixed κ; a set of highly elongated shapes for which κ and λ increase simultaneously at fixed δ. The value of the shape parameters κ,δ,λ comes from a fit of the contour (1) to the last closed flux surface (LCFS) de-

duced from the equilibrium reconstruction and may differ slightly from the usual definition based on the contact points of the circumscribed rectangle. For each shape a plasma current scan allows to separate the influence of the current itself, the safety factor, q_a, the shape and the ohmic input power, P_{oh}. All data points are obtained during stationary ohmic L-modes with $R_0 = 0.88\,\text{m}$, $a = 0.25\,\text{m}$, 1.43T, D_2. The confinement properties of these plasmas are quantified by the electron energy confinement time, $\tau_{Ee} = W_e/P_{oh}$, where the total electron thermal energy, W_e, is obtained by vol-

Fig. 1   Shape dependence of the electron energy confinement time for 3 $< q_a < 4$ and $4 \times 10^{19}\ m^{-3} < n_e < 5.5 \times 10^{19}\ m^{-3}$. Left: from the ($\kappa,\delta$) scan and high κ, ● $\kappa = 1.2$, ▲ $\kappa = 1.37$, ▼ $\kappa = 1.55$, ◆ $\kappa = 1.72$, ★ $\kappa = 2.5$. Right from the (δ,λ) scan, white $\delta = -0.18$, grey $\delta = 0$, black $\delta = 0.3$.

ume integration of Thomson scattering measurements at 10 to 25 spatial positions. At fixed q_a and fixed line average density, $\bar{n}_e$, the following variations in τ_{Ee} when the shape parameters are scanned are observed (fig. 1): (i) no significant modification with the elongation, even when comparing a circular plasma with an elongation as high as $\kappa = 2.5$; (ii) a marked degradation at positive triangularity compared with zero or slightly negative triangularity, which can reach a factor 3 at the highest densities; (iii) a substantial improvement for rectangular shapes when λ is increased from 0 to 0.3.

Local transport. To understand these observations, it is necessary to determine the influence of the shape on the heat conduction, the main loss channel. A simplified radial power balance has then been established in which: (i) radiation losses, localised near the plasma edge, have been neglected; (ii) in the absence of a measurement of the ion temperature profile, ion and electron heat conduction fluxes are not separated. This yields the following heat flux equation:

Fig. 2   Plot of the energy flux versus the temperature gradient in the region $r/a = 0.8$ for $5.5 \times 10^{19}\ m^{-3} < n_e < 7 \times 10^{19}\ m^{-3}$: ▼ from the ($\kappa,\delta$) scan, ■ from the ($\delta,\lambda$) scan, ★ from high κ.

$$(q_{in} = -n\chi_{eff}\langle\nabla T_e\rangle),\ \chi_{eff} = \chi_e + \chi_i\frac{\nabla T_i}{\nabla T_e} \qquad (2)$$

where q_{in} is the input energy flux and $\langle\nabla T_e\rangle$ the electron temperature gradient averaged on a

flux surface. A plot of q_{in} versus $\langle \nabla T_e \rangle$ for a fixed density but a wide variety of plasma shapes indicates that the effective thermal diffusivity does not depend on the shape. There is however a non linear relationship between these parameters, indicating a dependence of χ_{eff} on $\langle \nabla T_e \rangle$. The second factor entering the conduction flux is the temperature gradient. A first direct consequence of shaping is a local modification of the flux surface separation and incidentally of the temperature gradient. To quantify this effect the latter can be written as

$$\nabla T = \frac{dT}{dr}\frac{dr}{d\psi}\nabla\psi \tag{3}$$

where ψ is the poloidal magnetic flux and r the distance from the magnetic axis measured at the outer midplane and normalised such that $r = a$ on the LCFS. This particular coordinate has been chosen instead of ψ because different ψ distribution can define the same geometry and because the Shafranov shift depends closely on the shape. Appropriate shaping creates large volume where the gradient geometrical factor, $\frac{dr}{d\psi}\nabla\psi$, is small and hence conduction losses reduced.

Shape Enhancement Factor. The gradient geometrical factor and the fact that the thermal diffusivity does not depend on the shape can be combined to quantify the influence of the geometry on the global energy confinement time. To do so, the confinement time of a shaped plasma is compared to that of cylindrical plasma (indexed o) with the same thermal conduction and the same input energy flux. It is then convinient to introduce a "Shape Enhancement Factor" (SEF) as the ratio of these two confinement times:

$$H_s = \frac{S_o \int\limits_0^a n \int\limits_r^a \frac{q_{in}d\psi}{n\chi dr}\langle\nabla\psi\rangle^{-1}dr'dV}{S\int\limits_0^a n \int\limits_r^a \frac{q_{in}}{n\chi}dr'dV_o} \tag{4}$$

where S is the LCFS area. In the results presented here, the SEF has been computed using a flat
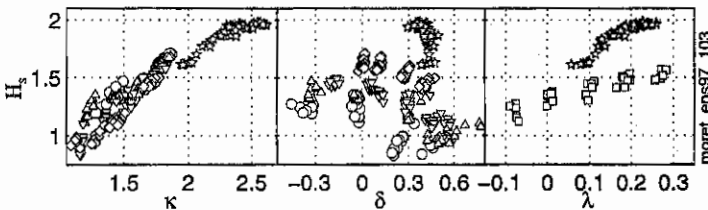
Fig. 3 Value of the Shape Enhancement Factor for different shapes. Left: from the (κ,δ) scan with ●▼▲◆ representing increasing δ and ★ from high κ. Middle: from the (κ,δ) scan with ●▼▲◆ representing increasing κ and ★ from high κ. Right: ■ from the (δ,λ) scan and ★ from high κ.

density profile and a canonic profile for $\frac{q_{in}}{n\chi}$, so that H_s depends only on the geometry via the ψ distribution. In the derivation of the expression for H_s, the thermal diffusivity was assumed independent of ∇T or $\langle \nabla T \rangle$. This hypothesis can be relaxed without noticeable modification in the H_s value [2]. Variation of the SEF with the three shape parameters κ,δ,λ is shown in figure 2. It increases continuously with κ but saturates at a limiting value of 2 for high elongation. It decreases markedly for high positive δ compared to its value around $\delta = 0$; computation on theoretical equilibria with very negative δ indicates that the SEF should reach a maximum for slightly negative values of δ; this remains to be experimentally verified. The SEF finally displays a substantial improvement for rectangular shapes with a large λ, typically 25% over the explored range.

Obviously the variations in the SEF correspond to that observed in the energy confinement time. Thus dividing the confinement time by H_s should cancel the shape dependence. There remains however a decrease of τ_{Ee}/H_s when κ and δ increase, but this persisting variation can easily be interpreted as a heat flux degradation effect (fig. 3), $(P_{oh}/S)^{-0.5}$, since increase both in κ and δ are accompanied by an increase in P_{oh} [1,2].

Fig. 4   Energy flux degradation of the corrected confinement time. Symbols and data selection as in fig. 2.

Conclusion. In summary, no influence of the plasma shape on the transport mechanism has been found for the explored shapes and operational regimes. Global energy confinement can however be considerably improved by plasma shaping, which by geometrical effects reduces the temperature gradient and the associated conduction losses. The formulation of this improvement in term of a Shape Enhancement Factor has proved to apply also to more complex shapes and to high elongations. It can therefore be safely used as a criterion for optimising the shape effects. Study of the influence of high order shape parameter, such as the squareness, shows that even if engineering or physical constraints may restrict the choice of the basic shape parameters, there remains room for a substantial gain in the confinement properties with an appropriate shaping.

[1] J.-M. Moret, S. Franke, H. Weisen et al., LRP 560/96, submitted for publication in Physical Review Letters.
[2] H. Weisen, J.-M. Moret, S. Franke et al., LRP 571/97, accepted for publication in Nuclear Fusion.

Toroidally Asymmetric ELM Precursor Oscillations in the TCV Tokamak

H. Reimerdes, A. Pochelon, W. Suttrop†, Ph. Guittienne, H. Weisen

Centre de Recherches en Physique des Plasmas, Ecole Polytechnique Fédérale de Lausanne, Association EURATOM - Confédération Suisse, CH-1015 Lausanne

†Max-Planck Institut für Plasmaphysik, IPP - EURATOM Association, D-85748 Garching

Introduction

In TCV (R=0.89 m, a=0.25 m, I_p<1.2 MA, B_ϕ<1.5 T) ohmic H-modes have been obtained in diverted single-null (SND), double-null (DND), and elongated limited plasma configurations. In ELM-free H-modes the particle density rises continously until the discharge usually terminates with a high density disruption. Quasi-stationary H-modes have been obtained in the presence of ELMs. The observed ELM spectrum is continuous and ranges from clearly identifiable *type III ELMs* to low frequency, *large ELMs* [1]. The necessity of ELMs for particle control of H-mode plasmas while causing high peak-power loads on strike points makes the control of their level and nature desirable and motivates the study of the underlying MHD-instability.

Prior to ELMs in TCV coherent magnetic oscillations, that indicate a rapidly growing MHD instability, have been observed. The structure of these precursor oscillation is investigated with TCV's Mirnov probe arrays. In particular an observed toroidal asymmetry in the growth of the instability has to be explained.

Mirnov Probes on TCV

Toroidal and poloidal arrays of magnetic pick-up coils, measuring the poloidal magnetic field, have been installed inside TCV's vaccum vessel. For high-n mode analysis there are two complete toroidal arrays of 16 and 8 equally spaced probes, located on the equatorial low field side (LFS) and high field side (HFS) respectively. Poloidal arrays each with 38 probes were installed in 4 equidistant sectors. Data can be sampled up to a rate of 1 MHz. To maximize the signal amplitude, in spite of multipole field decay, toroidal and poloidal measurements have been performed on two different plasma configurations. For toroidal measurements a single null upper divertor (SNU) plasma on the midplane (z=0), allowing a minimal distance of down to 5 cm on the HFS and 7.5 cm on the LFS between the plasma edge and the toroidal array, is investigated (Fig. 1a). To allow maximum poloidal phase information the poloidal measurements have been performed on SNU plasmas, which were moved as close to the bottom as was possible during H-mode. A minimum distance of 10 cm to the probes at the bottom of the vessel has been achieved (Fig. 1b).
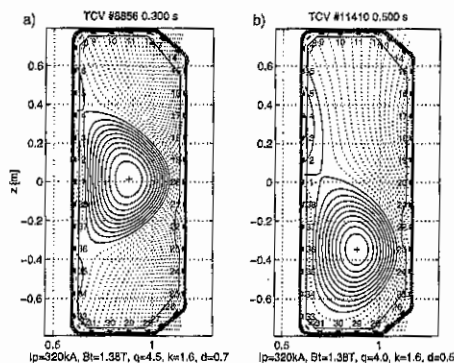
Figure 1: Poloidal cross section showing the position of the magnetic probes and the plasma configurations used: a) SNU configuration for toroidal mode number analysis. The toroidal arrays are located in the equatorial plane corresponding to positions 1 (HFS) and 20 (LFS). b) SNU configuration for poloidal mode number analysis.

Toroidal Measurements

The ELMs obtained in the discharges with fast toroidal measurements have caused a moderate particle loss of 2-4% and an energy loss of 2-6% of the total plasma content, which are typical figures for type III ELMs in TCV. Their repetition frequencies range from 120-300 Hz. For many ELMs a coherent precursor oscillation has been detected several 100 μs before the onset of the enhanced particle transport phase corresponding to the rise of the D_α-signal. The precursor is first detected on the LFS where it's amplitude is generally higher than on the HFS, even though the distance between probes and plasma is greater. The instability first develops at a toroidally localized position (Fig. 2). This precursor then grows both in amplitude and toroidal extent with a typical growth time of $\tau_{prec} = 50\,\mu s$. At the same time the frequency f_{prec} decreases from typically 120 to 70 kHz. When the precursor encompasses the whole toroidal circumference, the increased transport of energy and particles begins. The D_α signal increases rapidly, the magnetic oscillations lose their coherence while the fluctuation amplitude strongly rises. Due to the toroidal rotation of the precursor, measurements with a toroidally fixed probe show characteristics of beating as has been observed on other experiments [2,3].

The spatial measurements of $\dot{B}_\theta$ have been expanded into a Fourier series yielding toroidal mode numbers of $n = 0 \ldots 8$. It is clearly seen that the precursor consists of high n=5-8, predominantly 7 and 8, components (Fig. 2), but spatial aliasing could mask higher mode numbers such as 9 or 10. The amplitude of the n=8 component shows an oscillation with the precursor frequency due to the missing phase information at the Nyquist wave number. It is remarkable that a similar oscillation is also observed on lower n mode amplitudes.

There are several possible reasons for this toroidal asymmetry. For example the presence of two modes with $\Delta n=1$ show a spatial beating, that corresponds to a toroidal envelope of n=1. Nevertheless that does not explain either the oscillating amplitude of A_n for $n \leq 7$ or the existence of more than two toroidal mode components of the precursor.

A toroidal localization of an n=8 mode can explain these observations. Assuming a
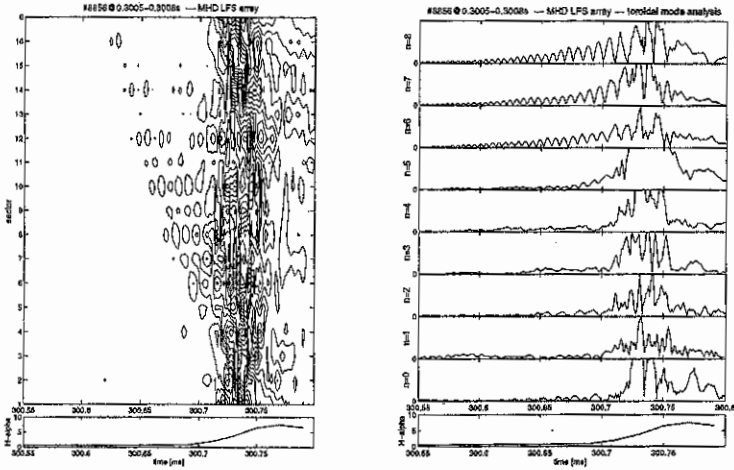
Figure 2: ELM-precursor oscillations seen with the toroidal array on the LFS. Left: Contour lines of $\dot{B}_\theta$ show the toroidally localized onset of the precursor. Right: Amplitude of the n=5-8 components grow before the beginning of the transport phase determined by the D_α-signal, which is shown below.

Gaussian toroidal weight of the amplitude of the pertubation field

$$\dot{B}(\phi,t) = A(t) \cdot e^{-\frac{1}{2}\frac{(\phi - \phi_{max})^2}{\sigma_\phi^2}} \cdot \sin(8\phi - \phi_0) \tag{1}$$

the expected mode spectra show approximately a convolution of the n=8 spectrum with a Gaussian of half width $\sigma_n = 1/\sigma_\phi$. This is consistent with the observed mode spectrum (Fig. 2) and explains the oscillation of the amplitudes of $n \neq 8$.

Since the toroidally localized onset of the precursor differs for different ELMs, a localization due to errors in the measurements (i.e. hardware misalignment, gains) and a triggering of the ELM due to an asymmetry of the TCV assembly can be excluded.

Poloidal measurements

The ELMs obtained during discharges in the configuration shown in Fig. 1b) caused a higher particle loss of 4-7% and high energy losses of up to 11% of the total energy content, which is typical for *large ELMs*. The repetition frequency varied from 80-200 Hz. The probes on the LFS show coherent precursor oscillations with a frequency of $f_{prec} \approx 50$ kHz and a typical growth time of $\tau_{prec} \approx 50$ μs. The observed local mode number of the precursor oscillation $m_{local} = \Delta\phi/\Delta\theta$ shows a dependence on the poloidal angle θ. The poloidal spacing of the probes limits the resolution ($m_{Ny} = \pi/\Delta\theta_{probes}$). Both vary strongly with the poloidal angle from $m_{Ny} \approx 8$ to $\gg 20$. If we assume a poloidally constant local

mode number $m_{local} = n \cdot q$ above the Nyquist mode number, the mode detected by aliasing would also vary with θ. Therefore the poloidal observations are consistent with high poloidal mode number of m≈16-20, but are, due to small signal amplitude, not unambiguous.

Conclusion

TCV ELMs believed to be type III ELMs and large ELMs both show magnetic precursor oscillations. Both precursors are strongly localized on the LFS. They both show similar growth rates and frequencies, which are in the range of values found for type III precursors on ASDEX-Upgrade [2] confirming the identification of TCV's type III ELMs and suggesting that TCV's *large ELMs* are large *type III ELMs.*

A toroidal mode analysis reveals high toroidal mode numbers. High n and a strong localization on the bad-curvature side support a ballooning-like instability as has previously been proposed for ELMs in various experiments [4]. The onset of the precursor is toroidally localized. Since asymmetries in the machine have been ruled out as a cause, this asymmetry must be intrinsic. A possible cause could be a low-n resistive mode located in the high pressure gradient region close to the plasma edge. It has been shown [5] that ideal ballooning modes are less stable on flux surfaces close to a magnetic island. A bunching of field lines close to the x-point can reduce the stabilizing shear and pressure gradients are enhanced near the island. This could give rise to a localized high n instability as has been observed prior to high-β disruptions in TFTR [6]. Weak low n mode activity has been observed, but a correlation between its phase and the onset of the precursor could not be retrieved.

The localized instability itself does not significantly enhance the radial transport over the separatrix. It is its encompassing of the entire toroidal circumference, that seems to be linked to the typical loss of particles and energy.

Acknowledgments

References

[1] H. Weisen et al., Plasma Phys Control. Fusion **38** (1996) 1137.

[2] T. Kass et al., this conference.

[3] R. J. Buttery et al., Proc. 22nd EPS Conf. in Bournemouth 1995, Vol III p273.

[4] H. Zohm, Plasma Phys. Control. Fusion **38** (1996) 105.

[5] C. C. Hegna and J. D. Callen, Phys. Fluids B, **4** (1992) 3031.

[6] E. D. Fredrickson et al., Phys. Plasmas **2** (1995) 4216.

Heating and Confinement Studies with ECRH in the TCV Tokamak

A.Pochelon, T.P.Goodman, M.Henderson, Z.A.Pietrzyk, M.Q.Tran, I.Furno, F.Hofmann, JP.Hogge, JM.Moret, F.Perthuisot, H.Reimerdes, O.Sauter, H.Weisen, S.Alberti, R.Behn, F.Bühlmann, S.Coda, M.J.Dutch, B.P.Duval, S.Franke, R.W.Harvey*, B.Joye, J.B.Lister, Y.Martin, P.Mandrin, Ch.Nieswand, R.A.Pitts, J.Rommers, W.van Toledo, G.Tonetti

Y.V.Esipchuk[†], A.A.Martynov[†], K.A.Razumova[†], I.N.Roy[†]

Centre de Recherches en Physique des Plasmas, Ecole Polytechnique Fédérale de Lausanne, Association EURATOM-Confédération Suisse, CH-1015 Lausanne, Switzerland
[†]Kurchatov Institute of Atomic Energy, 123182 Moscow, RF
*CompX, Del Mar, Ca., USA

Introduction - ECRH experiments have recently started on the TCV tokamak with the use of 1 MW, X2 heating. The ECW system installation is continuing and will eventually provide 3 MW X2 and 1.5 MW X3 [1]. The study of the effects of different heating localization is possible using *1)* the mobile mirrors of the launcher, *2)* the large vertical room for displacing the plasma in the TCV vessel and *3)* the radial displacement of the cyclotron resonance with magnetic field. Initial studies of heating and confinement have concentrated mostly on close-to-circular plasmas to allow the largest variation of beam-plasma geometry and to allow comparison with earlier results on other machines - a necessary first step before investigating more strongly shaped plasmas. For TCV parameters ($R = 0.89$ m, $a = 0.25$ m, $I_p < 1.2$ MA), the nominal field of $B = 1.44$ T and the frequency of 82.7 GHz of X2 gyrotrons places the resonance position on the high-field side (HFS) of the magnetic axis ($\Delta = -0.16$ to -0.2); while the frequency of 118GHz of X3 gyrotrons results in a slightly low-field side (LFS) resonance position.

Central MHD-activity - Different types of sawtooth activities are observed while scanning the safety factor q, the injected power P_{EC} or triangularity δ. The standard sequence observed when increasing q, P_{EC}, or decreasing δ, with a heat deposition close to $q=1$, starts from *1)* ohmic-like, normal sawteeth (NST), of the standard triangular shape, passing
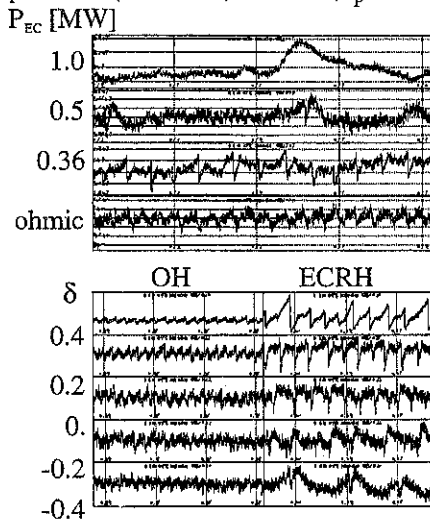
Fig.1   Change of central sawtooth activity in a a) power scan, b) triangularity scan

through 2) saturated sawteeth (SST), where the temperature saturates after the fast reheat following the sawtooth crash and 3) humpback sawteeth (HBST), earlier seen in ECCD experiments on T-10 [2] to 4) complete substitution of sawtooth activity by a kind of "hilling activity" (HA), resembling HBST but where the crashes have completely disappeared. An example of these different types of sawteeth is shown in Fig. 1a) for a power scan and Fig. 1b) for a triangularity scan. A decrease of D_α emission during HBST and HA suggests improved particle confinement.

A study of the change of ST period and reheat after crash with heating close to or inside of q=1, has been performed by the three different swept deposition methods. Sweeping the plasma vertically through a fixed ECH beam keeps the incidence angle on the resonance constant but changes slightly the magnetic configuration. Sweeping the B-field at constant q is also non-stationary, but provides a sweep of the resonance location along the major radius. Whilst a sweep of the mirror angle θ in the poloidal plane produces a scan along the resonance in the vertical direction in a stationary magnetic configuration, albeit with a varying incidence angle on the resonance. For all three sweeps, a maximum of the ST period occurs when heating close to the ST inversion radius obtained from soft X-ray tomography, see Fig. 2 for the example of a vertical, z-sweep. The rate of reheating increases when heating inside of the inversion radius. Moving the deposition further towards the magnetic axis produces longer, giant ST of high, but strongly fluctuating, temperature.

The saturation of the electron temperature after the fast reheat occurring with deposition between q=1 and the axis as suggested by soft X-ray emission signals, has been confirmed by Thomson

Fig. 2 Radial deposition z-sweep showing initial sawtooth reheat slope and sawtooth period maximal close to q=1

scattering measurements. The saturation seems to be linked with the appearance of n=2 mode activity on q=1, measured both from magnetic probes (Fig. 3) and from soft X-rays, prior to the usual (1,1) mode. When the (1,1) mode vanishes for central enough heating, the central pressure rises again in the final stage of the sawtooth development, producing giant sawteeth.

Optimization of confinement versus localization (B,q) and versus (P,n_e) - An initial confinement study was carried out on a small target plasma placed in front of the launcher with quasi-horizontal launch in order to minimize effects related to the launch geometry with regard to refraction ($\theta=18^\circ$, z=38, $\kappa=1.31$, $\delta=0.15$). Scan domains were: $1.32 < B < 1.45T$, representing a 20% radial displacement of the resonance around q=1;

Fig. 3 Central temperature saturation and $n = 2,1,0$ activity during a single sawtooth.
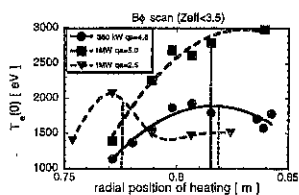
a) electron temperature
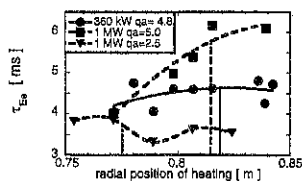
b) confinement time τ_{Ee}

Fig. 4 Radial deposition during a B-field scan: both a) and b) have the q=1 position indicated.

$1.5 \times 10^{19}\text{m}^{-3} < n_{eo} <$ over-dense (X2 cut-off at 4.25); $2.2 < q < 6$; $P_{EC} \leq 1\text{MW}$. This power led to a ratio P_{tot}/P_{oh} during ECRH from 3 to 14 in the q-scan for 1MW power injection.

In a B-field scan, for high-q (~5) moderate-power (0.5MW) shots, the plasma temperature response depends strongly on the radial location of the power deposition relative to the q=1 surface. The *central* electron temperature is maximum with deposition close to (but perhaps slightly outside) the q=1 surface (Fig. 4a) as determined from the sawtooth inversion radius from the soft X-ray camera data. The central temperature decreases slightly as the deposition location moves inside the q=1 surface but again rises as the deposition location moves further towards the center. The electron confinement time does not show such a strong dependence on localization during this scan; although, low-q high-power shots show an increase (as with T_e) for this location close to q=1 (Fig. 4b). As a function of the safety factor q, the dependence is much stronger, with τ_{Ee} increasing with q, maximizing at q~5.5 and dropping beyond q~6 (Fig. 5).
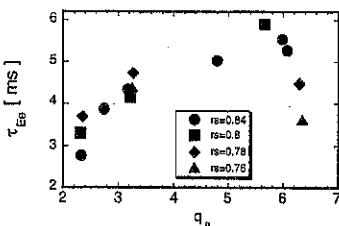
Fig. 5 τ_{Ee} versus q, for different deposition radii in a Bϕ scan.

The power degradation exponent α_P, ($\tau_{Ee} \sim P^{-\alpha_P}$), is weaker than usually expected: $-0.5 < \alpha_P < -0.4$, as measured for q=5 at $n_{eo}=2$ and $3 \times 10^{19}\text{m}^{-3}$ (see Fig. 6), and at q=2.5 for a density close to $2 \times 10^{19}\text{m}^{-3}$. This low confinement degradation may originate from the impact of heating on profiles and MHD-activity (in particular the sawtooth period) during slightly off-axis heating. When considering only power scans up to 0.5MW, higher degradation exponents are obtained. This yields similar power and density exponents as obtained earlier in T-10 electron cyclotron heating [3]. At the opening of the vessel following the campaign, a verification of the launchers revealed that one of the launchers had a non-zero toroidal angle, thus some features of the heating results, with $P_{EC} > 500\text{kW}$, may contain an ECCD component.
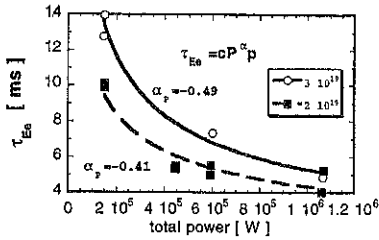
Fig. 6 τ_{Ee} power degradation for two densities, q=5

Transport simulations of TCV discharges - ECRH heated discharges have been simulated using the ASTRA transport code. The T-10 transport model in the ASTRA code was benchmarked against TCV ohmic data in order to reproduce the central temperature evolution. In the ohmic regime, the measured temperature profiles $T_e(r)$ of TCV are well described (accuracy ±10%) by the T-10 model (i.e. similar electron transport and confinement laws can be used). Early discharges had q=3.1, κ=1.26, differing oblique beam incidence angles on the resonance (15°<θ<45°) to correspond to the z-sweep and static plasmas with saturated sawteeth when heating inside q=1. To simulate correctly the measured central temperature during ECRH, it was necessary to use an absorption efficiency factor k~0.65<1 (where P_{ab} = k P_{input} or more correctly, P_{ab} = k P_{ab}^{TORAY}), as in other ECRH experiments [4]. Thus, under the condition P_{ab} = 0.65 P_{in}, the T-10 model correctly describes (in the stationary case) not only values and profiles of $T_e(r)$ and $n_e(r)$ but also the temperature responses for different power deposition profiles. Simulating more recent shots, with high q~6, κ=1.32, n_{eo}=2×10^{19}m^{-3} in quasi-horizontal launch (θ=18°), where T_{eo}=3keV was obtained with 0.5MW, a higher k-factor, close to unity was appropriate.

Conclusions - Heating effects, MHD-activity and to a lesser degree confinement, are shown to depend strongly on the localization of the EC power deposition location. This has been shown in sweeps and scans of mirror angle, vertical plasma position and magnetic field. Sawteeth and mode activity are stabilized/de stabilized depending on the location of the power deposition relative to the q=1 surface. Dramatic changes in central temperatures occur when heating is close to q=1 or towards the magnetic axis. A similar trend, though weaker, exists for confinement time. Confinement increases significantly with q, culminating at q~5-6, before dropping at higher values. The effect of q on confinement is more dramatic than the effect of B-field variation, displacing the resonance in the range of ±3-4cm around q=1 surface. The power degradation exponent has a value between -0.4 and -0.5, a weaker degradation than generally expected, which may originate from effects improving confinement, like sawteeth stabilization or reduced shear due to the slightly off-axis deposition.

References
[1]   T.P Goodman et al., 19th SOFT, Lisbon, Sept. 1996; A. Pochelon et al., 20th EPS
       Conf on contr. Fus. and Plasma Phys., Vol. 17C, Part III (1993)1029;
       and T.P Goodman et al., Proc. EC-10 Conf., presented by M.Q. Tran, Ameland 1997
[2]   D.A Kislov et al., 22nd EPS Conf on contr. Fus. and Plasma Phys., Vol. 19C, Part I
       (1995) 369
[3]   Y. Esipchuk et al., J. Moscow Phys. Soc. 1(1991)119 and ITER-IL-PH-4-9-5-10(1991)
[4]   V.V. Alikaeev et al., Proc. 10th Int. Conf. on Plasma Phys. and cont. nucl. Fus., Vol I
       (1985) 419; and V.V. Abrakov et al. Nucl. Fus. 37 (1997) 233

Comparison of the CREATE-L Plasma Response Model With Experiments on TCV

P. Vyas[1], F. Villone[2], J.B. Lister[1], R. Albanese[3]

[1] CRPP-EPFL, Association EURATOM-Suisse, CH-1015 Lausanne, Switzerland
[2] Associazione EURATOM/ENEA/CREATE, Dip. di Ing. Industriale,Univ. di Cassino,
I-03043, Cassino (FR), Italy

[3] Associazione EURATOM/ENEA/CREATE, DIEMA,
Univ. di Reggio Calabria, I-89125, Reggio Calabria, Italy

Abstract Experiments have been performed on the TCV tokamak to evaluate the response of Ohmic, L-Mode, limited and diverted plasmas to changes in the poloidal field coil voltages. The resulting closed loop plasma responses have been compared with the CREATE-L linearized MHD equilibrium model of TCV. The simulated responses show excellent agreement with the experiments in both the time and frequency domains. Tests with models derived using different assumptions indicate that the underlying physical assumptions of the nominal model are appropriate.

Introduction The CREATE-L plasma response model is derived by linearizing the equilibrium equation and Ohm's law in the active and passive conductors and in the plasma. In this model, the plasma is assumed to be in permanent MHD equilibrium and the plasma current density profile is kept fixed, whereas the total plasma current is allowed to vary. The boundary and magnetic axis fluxes are also allowed to vary. The model can be used to predict the plasma current, shape and position response to voltages applied to control coils and is being used to design the ITER Poloidal Field Coil control system. In ITER only small margins in power, coil voltages and currents are available for plasma shape control and it is important that the model used to design the feedback control loop should be accurate.

TCV discharges were fully simulated by the CREATE-L model, including details of the 18 external poloidal field coils, their power supplies, the passive vessel structure, the poloidal magnetic field and flux sensors as well as the plasma equilibrium for the particular discharges used. Selected limited and diverted plasmas have been examined.

This paper describes the experimental details of the comparisons and presents the results of comparisons for various plasma parameters. Models based on different physical assumptions are also compared.

Experimental set-up Experiments were performed on two plasma equilibria. An up-down symmetric, centred, limited L-mode configuration ($\kappa=1.44$, $\delta=0.3$, $I_p=200kA$, $q_a=5.5$) and an L-mode, noncentred, single-null diverted plasma ($\kappa=1.44$, $\delta=0.38$, $I_p=200kA$, $q_a=7.3$). The
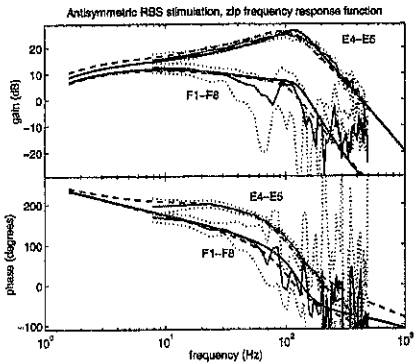
Fig.1 *Response of limited plasma to antisymmetric RBS stimulation for expt. (light solid with dotted confidence bounds), CREATE-L (dark solid), and RCDM (dashed)*

plasma position and shape responses were excited by adding stimulation voltages to the poloidal field control coils. Responses to 50ms square pulses were examined in the time domain to provide a simple visual test of the model-experiment agreement. Random binary sequences (RBS) were applied to provide data for spectral analysis for frequency domain comparison over a wider bandwidth.

The symmetry of the limited plasma was exploited to improve the signal to noise ratio. Up-down antisymmetric coil-pair stimulation was used to excite the plasma vertical position, and symmetric pair excitation was used to excite other parameters. Single coil excitation was used for the diverted plasma.

All experiments were performed in closed loop with feedback on five control variables constructed from linear combinations of poloidal flux, field and poloidal field coil currents. These were the vertical flux imbalance (P_VERT) which provides a measure of radial position; the outboard field curvature (TRI_OUT) and in the inboard field curvature (TRI_IN) which together provide a measure of plasma elongation and triangularity; the vertical position current moment (zI_p); and the plasma current (I_p). An additional parameter related to the radial current moment (PSI_R) which was not controlled was also compared and is the difference between the $R^2 I_p$ current moment and $R_0^2 I_p$ where R_0 is the unperturbed major radius. A set of coefficients for the linear combination of fields, fluxes, and currents were also derived for this parameter. A least squares straight line fit was removed from both the experimental data and simulation responses to remove their offsets and linear drift. This is because the low frequency disturbance or drift experienced by the plasma was not modelled.

Limited Plasma The closed loop time domain responses of a limited plasma to antisymmetric stimulations were first compared to a rigid current displacement model (RCDM) in [1]. The agreement was found to be good and showed that the coils close to the centre and on the inboard side were best coupled to fast vertical motion of the plasma. The RBS data was reanalysed to produce frequency response estimates which were compared with the RCDM and CREATE-L models (Fig.1). Both models agree with the estimated responses and clearly lie within the estimated confidence bounds. It is also confirmed that coil-pair E4-E5 has a much larger closed loop amplitude response at frequencies above 10Hz than the pair F1-F8 and has a smaller phase lag.

Symmetric excitation first introduced in [2] was used to examine up-down symmetric parameters. The RCDM cannot model these outputs and instead the CREATE-L model and a plasmaless CREATE-L model were compared to the experiment. Since the TCV controller design was based on a plasmaless model the latter was thought to be a useful comparison. The CREATE-L model is within good agreement for all coils and parameters in both the time and frequency domains. The plasmaless model does not provide a meaningful signal in the case of the plasma current moment parameters but is reasonable when compared to the P_VERT, TRI_OUT and TRI_IN signals.

Diverted plasma The analysis was repeated for a single-null diverted plasma with single coil excitation. The CREATE-L model proved to be in good agreement with all the parameters except zI_p (Fig.2). The model follows the experimental trace

Fig.2 Response of SND plasma to square pulse stimulation for expt. (dark solid), CREATE-L (light solid) and plasmaless model (dashed)

except for oscillations in the experiment which occur when the plasma radial position moves a significant distance. This can be explained by nonlinear coupling of the zI_p dynamics to the position of the plasma. As the plasma moves radially outwards the vertical gradient of the radial field ($\delta B_R/\delta z$) causes an increase in the plasma vertical position instability growth rate. The closed loop plant becomes highly underdamped and begins to oscillate at the resonant frequency (130Hz).

The response of the separatrix was considered important and was compared. Plasma equilibrium parameters and the plasma contour were reconstructed using the LIUQE inverse equilibrium code [3] from both experimental and simulated measurements of the poloidal field, flux and control coil currents. Parameters such as l_i, β_p and q_a were in agreement (Fig.3) as well as shape parameters such as κ, δ and the plasma contour itself.

Model assumptions Two variants of the CREATE-L model were tested on the diverted configuration in order to examine the effect of the basic assumptions. First the sensitivity of the responses to the shape of the plasma was examined. An up-down asymmetric limited plasma model was created with a similar shape to the diverted plasma. Comparing the simulations to the diverted experiments shows (Fig. 4) that the directly measured parameters are modelled as well as the diverted model except PSI_R. The radial current moment proved to be a sensitive indicator of the model accuracy.

Fig.3 Response of SND plasma to square pulse stimulation for expt. (dark solid) and CREATE-L model (light solid)
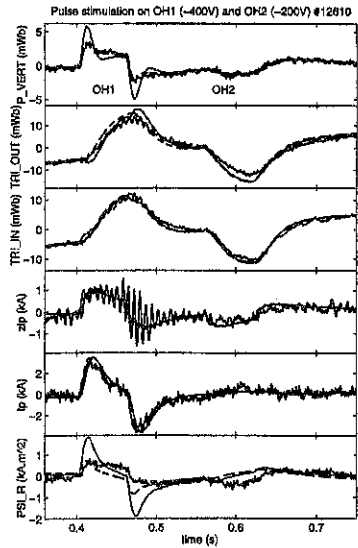
Fig.4 Response of SND plasma to square pulse stimulation for expt. (dark solid), frozen flux CREATE-L (light solid) and limited asymmetric CREATE-L model (dashed)

A second CREATE-L model was created for the diverted plasma assuming that flux at the plasma boundary was frozen. The model agreement with the radial position signals is poor particularly when OH coil stimulation causes large I_p changes to occur. This suggests that this assumption is not reasonable for the closed loop square pulse responses of the plasma.

Conclusions So far no disagreement has been found between any of the closed loop experimental data and the CREATE-L simulations. This suggests that the assumptions made in the derivation of the model are appropriate for plasma position and shape response simulations for the discharges studied.

References

[1] J.B.Lister, Y.Martin and J.-M.Moret, Nuclear Fusion, **36**, 1547 (1996)

[2] F.Villone, P.Vyas, J.B.Lister, R.Albanese, Lausanne Report 569/97 (1997) (submitted to Nuclear Fusion)

[3] F.Hoffman, G.Tonetti, Nuclear Fusion, **28**, 1871 (1988)

X-Ray measurements of MHD activity in shaped TCV plasmas.

I. Furno, H. Weisen, J.M. Moret, P. Blanchard and M. Anton*

Centre de Recherches en Physique des Plasmas, Association EURATOM-Confédération Suisse
EPFL,CH-1015 Lausanne, Switzerland

*present address: Max Planck Institut für Plasmaphysik, D-8046 Garching, Deutschland.

1 . Introduction

The ability of TCV to produce a wide variety of plasma shapes has allowed an investigation of MHD behaviour in a large number of limited ohmic L-mode discharges in which the elongation κ and the triangularity δ have been varied over a wide range: $\kappa=1.1$->2.5, δ=-0.3->0.7.

A 200 channel soft X-ray tomography system in conjuction with toroidally spaced soft X-ray diodes has been used to study the structure of internal disruptions and MHD modes. A strong reduction of sawtooth amplitude is observed as the plasma triangularity is decreased together with an increase in mode activity. The reduced sawtooth amplitudes are not correlated with any significant changes of the inversion radius and hence are not simply due to changes in current profiles; the inversion radius however is strongly correlated with the Spitzer conductivity profile and with the edge safety factor.

2 . Diagnostics

The soft X-ray tomography on TCV consists of ten cameras placed in a poloidal plane looking at the plasma through a curved Beryllium filter of 47 μm of thickness; each camera is equipped with a linear array detector of 20 photodiodes providing a total of 200 lines of sight and allowing a spatial resolution of about 3 cm. The acquisition frequency of the system is 10 kHz.

The line integrated signals are tomographically inverted using the Minimum Fisher Information method and the reconstructed poloidal emissivities are analyzed with the help of *Singular Value Decomposition* (SVD), allowing the determination of MHD mode structures and the sawtooth inversion radius [1].

The soft X-ray emissivity from the plasma is also monitored by four silicon photodiodes, equipped with a Beryllium filter of 50 μm thickness, placed at the top of the vessel and equally spaced in the toroidal direction. The viewing lines of these detectors cut the poloidal midplane $\cong$7 cm from the centre of the vessel in the direction of the major axis. The availability of these 4 photodiodes allows us to distinguish between n=1 or n=3 (by aliasing) and n=2 modes.

3 . MHD and sawtooth behaviour

The most important feature of shape on MHD behaviour is observed as the triangularity is changed. Shots at high triangularity are characterized by large sawtooth amplitude and low level MHD modes; as the triangularity is reduced the sawtooth activity decreases and the MHD modes become persistent (Fig. 1, top).
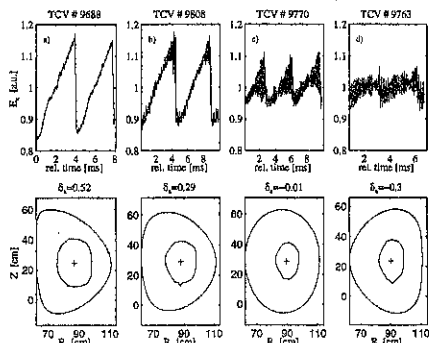
Fig.1. Raw X-Ray signals (top of the figure) with Sawtooth and Mirnov oscillations. Sawtooth inversion radius (bottom of the figure) and LCFS for four different triangularities. All discharges had $q_a=3.5$ $n_e=5.0$ 10^{19} m^{-3}, $\kappa_a=1.4$.

The SVD analysis in conjunction with the toroidal Fourier analysis has allowed the identification of MHD mode structures.
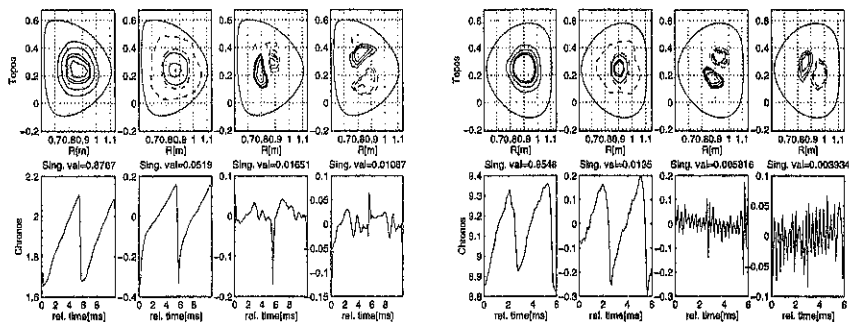
Fig. 2: SVD analysis of the shot 9688 (a) and 9763 (b). Contour plots of the different Topos are shown at the top of the figure with the LCFS; dotted lines correspond to negative value of the Topos. At the bottom the corresponding Chronos normalized to the sawtooth singular value are shown.

As can be seen in Fig. 2, for $\delta>0$ the MHD activity is mainly due to non-axisymmetric modes localized near the q= 1 surface. These modes, presumably tearing modes, are present only as brief precursors or postcursors of the sawtooth crash, being almost absent during the sawtooth

ramp. For δ<0 MHD activity becomes continuous and appears as a rotating m=1/n=1 mode. The maximum of the mode amplitude is reached during the sawtooth crash and the rotation is in the direction of the electron diamagnetic drift. At very negative triangularity these modes can lead to a loss of confinement and cause disruptions by mode locking.

As the elongation is increased beyond 2 an m=2/n=2 locked or slowly rotating mode becomes important (Fig. 3), reaching maximum amplitude during the sawtooth crash. The amplitude of these mode increases with the elongation and, at fixed shape, increases as the edge safety factor is reduced. The presence of this mode is consistent with the observation of an m=3, n=2 mode in the soft X-ray emissivity and in the Mirnov probes during major disruptions in TCV [3-4].
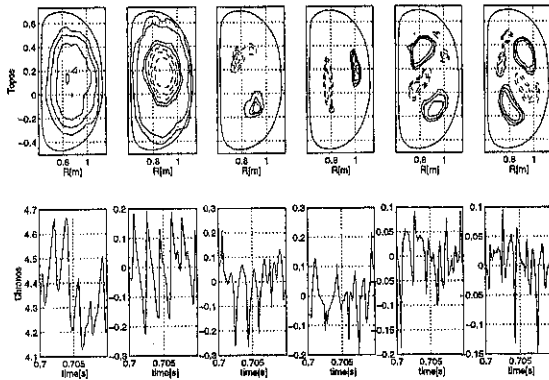
Fig. 3: SVD analysis of TCV SHOT# 11832 at t=0.7-0.71. The shot parameters are:I_p=0.7 MA, κ_{95}=2.38, δ_{95}=0.28. At the top of the figure, the Topos with the LCFS are shown together with the corresponding Chronos (bottom). Topos #3 and #4 show the normal 1/1 activity, while Topos #5 and #6 show the superposed slowly rotating 2/2 mode

The amplitude of the sawtooth crash varies strongly with triangularity, being largest at positive triangularity and sometimes vanishing at negative triangularity [2]. This behaviour can be explained by the fact that any reduction in the ohmic input power, caused either by reduction of current density (high q_a discharges) or by an improvement in energy confinement as observed for δ<0, leads to a reduction of sawtooth reheat power. In Fig. 4 we see that plasmas with highest confinement times have lower ohmic heating power and hence small sawtooth amplitudes.

The sawtooth inversion radius, defined as $\rho_{inv}=(V_{inv}/V)^{1/2}$ where V_{inv} is the plasma volume inside the inversion contour, correlates very well with the cross sectional area averaged current density. This is shown in Fig. 5 where as abscissa we use the non-dimensional average current density $\langle j \rangle^*=\mu_0 R_0 \langle j \rangle/B_T$; symbols refer to classes of δ_a showing that there is no intrinsic de-

pendence of the inversion radius on triangularity. This good correlation could be explained by assuming that the effect of sawtoothing is to flatten the current profile inside the inversion radius, preventing the current density from rising to a value higher than that corresponding to $q\cong1$ for $r \leq r_{inv}$.
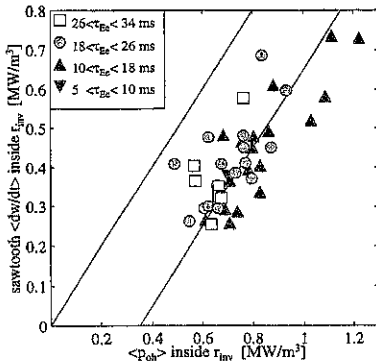
Fig. Sawtooth reheat power versus central ohmic heating power inside inversion radius for $n_e=6.3*10^{-19}$ m^{-3}. The upper line corresponds to $<dw_0/dt>_{inv}=<p_{oh}>_{inv}$, the lower line to $<dw_0/dt>_{inv}=<p_{oh}>_{inv}-0.35$ MW/m^3. Symbols refer to classes of confinement time.
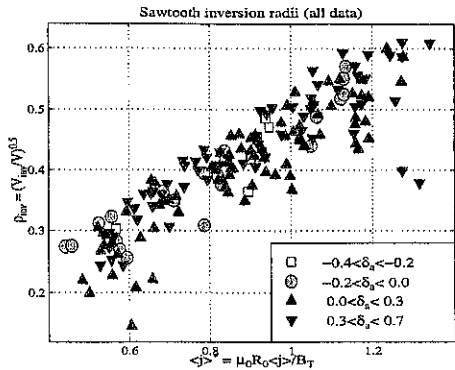
Fig. 5. Normalized sawtooth inversion radius versus non-dimensional average current density. Symbols refer to classes of triangularity.

The reduction of the ohmic input power with δ_a may explain, at least partly, the increase of mode activity. This reduction leads to lower edge electron temperatures [2], which may contribute to destabilizing resistive modes. High amplitude modes are unlikely to develop with $Te(0.9a)>200$ eV but are frequent at lower temperature. This suggests that the mode observed by X-ray tomography at the q=1 surface may be induced by mode coupling with m>1,n=1 which are destabilized near the plasma edge.

Acknowledgement

References
[1] M. Anton *et al, Plasma Phy. and Control. Fusion 38, 1849-1878 (1996).*

[2] H. Weisen *et al, Effect of plasma shape on confinement and MHD behaviour in TCV Tokamak* submitted for publication to Nuclear Fusion, available as LRP 571/97.

[3] O. Sauter *et al,* this conf.

[4] F. Hofmann *et al,* this conf.

Measurement of the Effective Plasma Ion Mass in Large Tokamaks

J.B. Lister, L. Villard and G. de Ridder

Centre de Recherches en Physique des Plasmas

Association Confédération Suisse-EURATOM, CRPP-EPFL, CH - 1015 Lausanne

ABSTRACT There is not yet a straightforward method for the measurement of the D-T ratio in the centre of a tokamak plasma. One of the simpler measurements put forward in the past is the interpretation of the MHD spectrum in the frequency range of the Global Alfvén Eigenmodes (GAE). However, the frequencies of these modes do not only depend on the plasma mass, but are also quite strongly dependent on the details of the current and density profiles, creating a problem of deconvolution of the estimate of the plasma mass from an implicit relationship between several measureable plasma parameters and the detected eigenmode frequencies. This method has been revisited to assess its likely precision for the JET tokamak. The low n GAE modes are sometimes too close to the continuum edge to be detectable and the interpretation of the GAE spectrum is rendered less direct than had been hoped. We present a statistical study on the precision with which the D-T ratio could be estimated from the GAE spectrum on JET.

1. Introduction The ratio of deuterium to tritium ions (D-T ratio) should be close to unity in the plasma core to maximise the thermal fusion power. Different sources of deuterium and
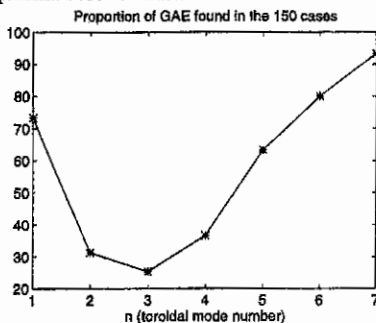
Fig. 1 Percentage of GAEs found in 150 test runs, as a function of the toroidal mode number.

GAE_PROP : 10-Feb-87

tritium from neutral beam injection, pellet injection, gas fuelling and recycling from walls and the divertor make the D-T source ratio difficult to estimate. Different radial transport time constants might further confuse the control of the D-T ratio. For these reasons a direct measurement of the D-T ratio is highly desirable. In the absence of a clear candidate for this measurement, we have revisited the use of Global Eigenmodes of the Alfvén Wave (GAE) for determining the core D-T ratio in the JET tokamak.

A method of estimating the effective mass, defined as $A_{eff} = \Sigma A_i n_i / n_e$ summing over all ion species, was developed on the TCA tokamak [1,2,3]. The method relies on the dispersion relation for Shear Alfvén Waves, given in the cylindrical approximation and up to second order in ω/ω_{ci} by:

$$\omega_{nm}^2(r) = \omega^o_{nm}{}^2(r)/A_{eff}(r)[1+\{\omega^o_{nm}{}^2(r)/\omega_{cH}^2\}\{\Sigma n_i(r)A_i^3/n_e(r)Z_i^2\}/A_{eff}(r)^2],$$

where $\omega^o_{nm}{}^2(r) = B_\phi^2(n+m/q(r))^2/\mu_0 n_e(r) m_p R^2$, n and m are the toroidal and poloidal mode numbers, ω_{cH} is the cyclotron frequency of hydrogen and the summation is over all ion species. The GAE frequencies lie close to but below the minimum of this continuum frequency. Many GAE's can be detected using a wide-band frequency sweep and A_{eff} could be estimated from the full spectrum of observed GAE's. On TCA, about 60 W were launched by a small poloidal emitting antenna and the system was used to measure the dynamic behaviour of the effective mass following the influx of cold H^0 into a D^+ discharge [2] and to feedback control the H-D ratio [3]. These encouraging results leave us with two open

questions. Firstly, we needed to assess the likely precision for JET and secondly we needed to assess whether the physics of the GAE would be different on a much larger device.

2. Method The uncertainties in using the GAE frequency as a diagnostic lie in its known sensitivity to the precise details of both the plasma current and density profiles which have considerable experimental uncertainty. Although the value of the Shear Alfvén Wave continuum frequency on axis, $\omega_{nm}(0)$, is a local quantity, the separation between $\omega_{nm}(0)$ and the eigenmode frequency ω_{GAE} is not and we must infer the value of this separation from the experimental data available. In order to assess the extent to which the usually measured quantities allow us to estimate this separation, we embarked on a Monte-Carlo based approach to this proposed diagnostic, which required several steps:

- determination of a suitable plasma profile parametrisation
- determination of the realistic parameter ranges
- determination of inter-parameter correlations providing additional constraints
- generation of a large volume of Monte-Carlo plasma parameters
- adjustment of the multi-dimensional population to simulate a realistic distribution
- generation of a small subset of data, creating 150 plasmas to be analyzed.
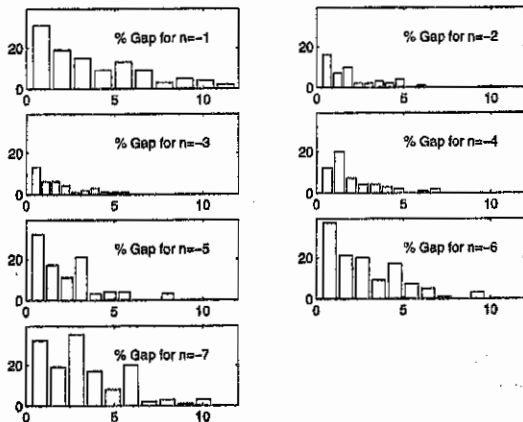
GAP_PROB : 11-Feb-97

Fig. 2 Histogram of the variation of $\delta\omega/\omega$ for different toroidal mode numbers.

The resulting "representative" JET discharges were then simulated in the 1-D ISMENE code [4] to calculate the GAE frequency for modes $n = -1...-7$ and $m = -1$. In ISMENE we consider a cold, magnetized, current carrying, bounded plasma, including several ion species and various mass and current density profiles. All 150 plasmas were analysed in this way giving 1050 eigenfrequencies. Full details of the results are to be found in [5].

3. Results A first inspection of the raw results was disappointing due to the large number of gaps in the results where the code had failed to locate a GAE peak in the plasma response, either because the GAE does not exist, or its eigenfrequency is too close to the continuum edge. Figure 1 shows the proportion of the 150 runs producing a separated GAE resonance, as a function of n. The values of $\delta\omega/\omega$ found are histogrammed for different n in Fig. 2, showing a significant variation.

Figure 3 shows the percentage GAE separation as a function of n, for three representative cases. Figure 4 shows the results from a frequency scan across the modes $n = -1...-7$, $m = -1$ for one case. The vertical bar indicates the continuum edge, $\omega_{min} = $ minimum of $\omega_{nm}(r)$, since the continuum may be at the edge of the plasma or at a local off-axis minimum. The frequency scans are shown over the range $(0.86 - 1.01) \times \omega_{min}$. The widths and heights of the GAE peaks are defined by an artificial damping term introduced into the cold plasma model. In the case shown, the GAE disappears into the continuum for $n = -2, -3, -4$ but subsequently

reappears. Runs of ISMENE using a 1-D hot model expanded to second order in ion Larmor radius showed the same disappearance into and reappearance from the continuum.

Separation of the GAE from the Continuum for 3 Test Cases
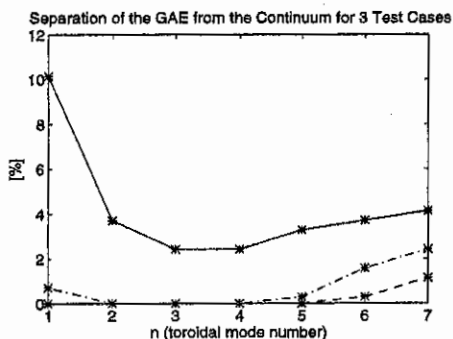
GAE_GAP : 10-Feb-87

Fig. 3 GAE separation $\delta\omega/\omega[\%]$ as a function of toroidal mode number for the 3 test cases. The solid line is case No 1, the dashed line is case No 14 and the dot-dashed line is case No 12.

We have cross-checked a few cases to confirm the cylindrical model, by performing computations with the finite element LION code [6,7]. LION differs from ISMENE not only by its finite aspect ratio, but also in the fact that no assumption is made on the ratio $B_{0\,pol}/B_{0\,tor}$, whereas ISMENE relies on a first-order expansion in $B_{0\,pol}/B_{0\,tor}$. The proper modelling of $B_{0\,pol}/B_{0\,tor}$ in LION has even more dramatic effects, in particular for the lowest frequency modes and low n modes. Indeed, the first order approximation in $B_{0\,pol}/B_{0\,tor}$ is not valid for $\omega/\omega_{ci} \approx 0$ or for $n = 0$. In simple analytical cases (e.g. $n = 0$, $q = const$, $\omega/\omega_{ci} \approx 0$) the first order model predicts the existence of GAEs whereas the exact model predicts no GAE. The relatively high fraction (50%) of $n = -1$ cases with GAEs as predicted by ISMENE might therefore be exagerated by an artifact of the first order expansion in $B_{0\,pol}/B_{0\,tor}$.

Finite aspect ratio effects have also been checked. The eigenfrequency of the GAE is more affected by toroidicity for low n than for high n. But even for $n = -1$ we found the GAE eigenfrequency changed by less than 3%. Finite aspect ratio also leads to continuum damping of the GAEs through toroidal coupling of shear Alfvén resonance surfaces with different poloidal mode numbers.

To summarise, we have found a smaller fraction of identifiable GAE resonances than initially hoped on the basis of TCA experimental results. The underlying reason is that TCA operated with significant values of the GAE frequency compared with the ion cyclotron frequency $\omega_{nm}/\omega_{ci} \sim 20\text{-}30\%$. On the other hand the physical size of JET implies ω_{nm}/ω_{ci} of the order of a few percent. Since the ω/ω_{ci} terms push the GAE below the continuum, adding to the separation due to field line curvature effects, the separation between the GAE and the continuum in JET is significantly reduced. ITER would have an even smaller value of ω_{nm}/ω_{ci}. Moreover, the smaller aspect ratio and larger elongation of JET, compared with TCA, increases the toroidal and elliptical coupling of the GAE to Alfvén resonant surfaces of different poloidal mode numbers, thereby increasing the continuum damping of GAEs [6,7]. The response is broadened and flattened and therefore detection of GAEs in JET is almost certainly more difficult than in TCA. The ISMENE results are confirmed as reasonable, provided the probably spurious reappearance of low n modes is ignored.

4. Analysis As a first interpretative step, we fit an MLP (Multi-Layer Perceptron) to the mapping {plasma parameters : $\delta\omega/\omega$}, where the plasma parameters are: [k-j, b-j, k-n, b-n, q*], q* being the cylindrical equivalent (Ip R/a^2 B) and k-j, k-n, b-j, b-n define the radial profiles via the parabolic exponents and edge pedestals respectively. The MLP provides a

generalised functional fitting of an {input:output} multi-dimensional mapping [8]. The values of $\delta\omega/\omega$ for $n = -6$ and $n = -7$ show a high correlation. This implies that little additional information can be obtained by using two adjacent eigenmodes and the analysis was performed just for $n = -7$. The root mean square residual for the full data is ~ 14.8% of its maximum range of 11%, i.e. a statistical precision in ω of 1.6%. The root mean square residual of the actual values of $\delta\omega/\omega$ is 21% of the full range, namely 2.4%. The non-linear MLP prediction of $\delta\omega/\omega$ has therefore only reduced its uncertainty by a factor of 1.5.
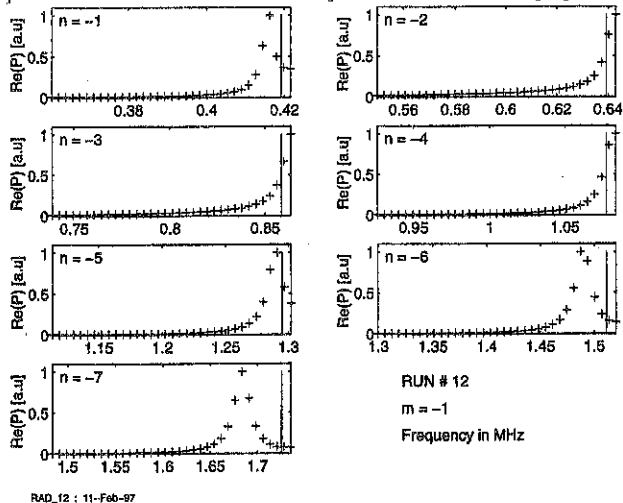
Fig. 4 Spectral scan over the test case # 12.

A simple linear estimation of A_{eff} is obtained if we assume that $n_e(0)$ is experimentally available and we assume $q^0 = 1.0$. The resulting value, A_{eff}^0 can be fitted by linear regression to the known $A_{eff}(0)$. This relationship between $A_{eff}(0)$ and the estimated A_{eff}^0 has an RMS residual of $\sigma = 0.087$. Since the range of $A_{eff}(0)$ is about unity, this corresponds to an RMS residual of 8.7%. An MLP was fitted to the input variables li, k_n, q95, A_{eff}^0 to see to what extent an MLP could reduce the uncertainties further. Over the whole dataset for $n = -7$ the full-scale residual was reduced from 5.6% to 5.1% by varying the number of MLP hidden nodes from 1 to 4, illustrating the lack of improvement.

We conclude that the MLP fit to the input data only reduces the uncertainty by a factor of 1.3. We estimate the uncertainty of $A_{eff}(0)$ as being of the order of 7% for the GAE mode $n = -7$, $m = -1$, chosen since it was observed for 140 out of 150 test runs.

REFERENCES
[1] G.A. Collins, A.A. Howling, J.B. Lister, Ph. Marmillod, Plasma Phys. and Contr. Fusion 29, 323 (1987)
[2] T. Dudok de Wit, B.P. Duval, B. Joye, J.B. Lister, Nuclear Fusion 32, 359 (1991)
[3] T. Dudok de Wit, J.B. Lister, B.P. Duval, B. Joye, Ph. Marmillod, Nucl. Fusion 30, 1493 (1990)
[4] K. Appert and J. Vaclavik, in Plasma Physics 24, 551, (1983)
[5] J.B. Lister, L. Villard, G. de Ridder "GAE detection for mass measurement for D-T ratio control", LRP 574/97 (1997)
[6] L. Villard, K. Appert, R. Gruber, and J. Vaclavik, Comput. Phys. Rep. 4, 95 (1986)
[7] L. Villard, S. Brunner, J. Vaclavik, Nuclear Fusion 35 (1995) 1173
[8] J.B. Lister, H. Schnurrenberger, Ph. Marmillod, LRP 398/90 (1990)

MHD stability of configurations with distorted toroidal coils

W. A. Cooper and A. Ardelea

CRPP/EPFL, Association Euratom/Confederation Suisse,
Lausanne, Switzerland

1. Introduction

One of the principal advantages of tokamak/torsatron hybrids is that vacuum flux surfaces exist prior to the current ramp-up and subsequent to the current ramp-down phases. This can facilitate plasma breakdown, reduce volt-second consumption making it possible to lengthen the duration of a discharge and more easily control the termination stages of shots. The added flexibility of an externally applied transform is another favourable consideration, but it is realized at the expense of a nonaxisymmetric deformation of the plasma which can cause the guiding centre drift orbits of particles to escape the confinement zone. Moroz has proposed a compact stellarator/tokamak device [1], but the ideal magnetohydrodynamic (MHD) stability properties of such a concept have not previously been reported. In this paper, we examine the ballooning mode stability and the Mercier criterion of the EPEIUS compact tokamak/torsatron hybrid proposal [2]. We model the EPEIUS coils by single straight filament segments located at their respective centres. The EPEIUS coil set, as shown in Fig. 1, consists of 8 nonplanar toroidally distorted D-shaped coils with $360kA$ current in each. These coils impose an eightfold toroidal periodicity on the system. In addition, there are 3 pairs of vertical field coils. In the absence of a toroidal plasma current in vacuo, the magnetic field lines generate bean-shaped flux surface with varying ellipticity E and triangularity δ depending whether the cross section lies roughly under the plane of a coil (largest E, smallest δ) or between two coils (smallest E, largest δ).

The vacuum magnetic fields are determined using the Biot-Savart law and serve as input for the free boundary version of the three dimensional (3D) VMEC equilibrium code [3]. With vanishing toroidal current, the equilibrium computed reproduces to a very high approximation the last closed flux surface calculated tracing vacuum magnetic field lines. We have studied sequences of equilibria at finite β with zero net toroidal current within each flux surface and with $50kA$ peaked toroidal current. We have also considered a sequence with variable hollow toroidal current fixed at 180 kA and constant $\beta = 6.75\%$. The inverse rotational transform q at the plasma edge is slightly larger than 2 for these values of current and β. The local ideal MHD stability properties of these configurations have been investigated with the relevant modules of the 3D TERPSICHORE code [4].

2. Local ideal MHD stability

The sequence that has zero net toroidal current is obtained with vertical field coil currents $I_v = (120, 180, 180)kA$. The vertical field coil pair that carry $120kA$ have the largest radii at $r_v = 1.06m$. The pairs of concentric coils with centres farthest from the geometric origin each carry $180kA$. The plasma mass profile is prescribed as $M(s) = M(0)(1-s)^3$, where $0 \leq s \leq 1$ is proportional to the toroidal magnetic flux (hence to the plasma volume enclosed). To obtain the corresponding pressure profile, we have chosen the adiabatic index $\Gamma = 5/3$. The q-value increases slightly with β

only near the plasma edge; it decreases slightly for $s \leq 0.6$. The ballooning eigenvalue and the Mercier criterion predict stability up to $\beta \sim 0.8\%$. The edge region $s > 0.6$ tends, however, to remain very spiky. The most unstable ballooning structures localise on the outside edge of the cross section that lies equidistantly between two coils. The sequence with $50kA$ peaked toroidal plasma current has $I_v = (132, 198, 198)kA$ with the plasma mass profile prescribed as $M(s) = M(0)(1 - s)^2$ and the toroidal plasma current profile precribed as $2\pi J'(s) = 2\pi J'(0)(1 - s)^2$. In this case, the local ideal MHD modes predict basic stability to $\beta \sim 1.2\%$. Locally unstable spikes remain that are closely aligned with resonant values of the inverse rotational transform per field period $1/(qL) = n/m = 1/14, ..., 1/18$, where $L = 8$ is the number of periods. At $\beta \sim 1.4\%$, ballooning modes are unstable for $s > 0.4$. We concentrate in this paper on the $\beta = 6.75\%$, $180kA$ sequence with varying hollow toroidal current profiles. For this sequence, the vertical field coil currents were $I_v = (180, 270, 270)kA$, the plasma mass profile is prescribed as $M(s) = 0.5M(0)[(1 - s)^3 + (1 - s)^2]$ and the toroidal current profile is prescribed as $2\pi J'(s) = 2\pi J'(0)[c(1 - s^5)^2 + (1 - c)(1 - s^4)^2]$, where the parameter c controls the degree of hollowness of the current profile. We have chosen values of $c = 1, 10, 15, 20, 15$ in this work. The case with $c = 1$ corresponds to a broad monotonically decreasing profile and increasing c enhances the hollow nature of the profile. The toroidal current profiles described this way and the corresponding q profiles are displayed in Fig. 2. The Mercier criterion profiles and the ballooning eigenvalue profiles are shown in Fig. 3. The plasma is unstable for $c \leq 15$. The configuration with $c = 20$ becomes marginally stable to the local stability criteria except at a few isolated and radially very localised surfaces in the outer half of the plasma volume that remain Mercier unstable. The radial location of the point where ballooning stability becomes marginal occurs in the region of vanishing global magnetic shear close to the plasma boundary $s \sim 0.92$. We have verified that the 15 poloidal transit domain of integration for the ballooning calculation on the most unstable field line suffices to resolve the mode structure more than adequately at this radial position.

3. Summary and discussion

In summary, we have investigated the local ideal MHD stability properties of a compact tokamak/torsatron configuration that models the proposed EPEIUS device. The β limits imposed by the Mercier criterion and ballooning modes approach 1% in $50kA$ peaked toroidal current and in current-free cases. A sequence at $\beta = 6.75\%$ is demonstrated to become marginally stable to local modes when the $180kA$ toroidal current prescribed becomes sufficiently hollow that the maximum value of the inverse rotational transform q_{max} exceeds 5 and the minimum value q_{min} near the plasma edge approaches 2. The stabilisation mechanism is associated with the shape of the flux surface average of the parallel current density $< \sigma >$. A $< \sigma >$ profile that increases in magnitude radially exercises a strong stabilising influence on the energy principle [5]. In the outer half of the plasma volume, the Mercier criterion (and to a lesser extent the ballooning eigenvalue) displays very local unstable spikes that align with rational values of $1/(qL)$. We interpret this as a potential for pressure-driven island formation rather than a strict stability limit. This phenomenon requires more detailed investigation using equilibrium codes that can study magnetic island structures. Global internal and external mode stability properties must also be examined, particularly for hollow current profile cases where the large toroidal plasma current concentrated near the plasma edge could destabilise external modes.
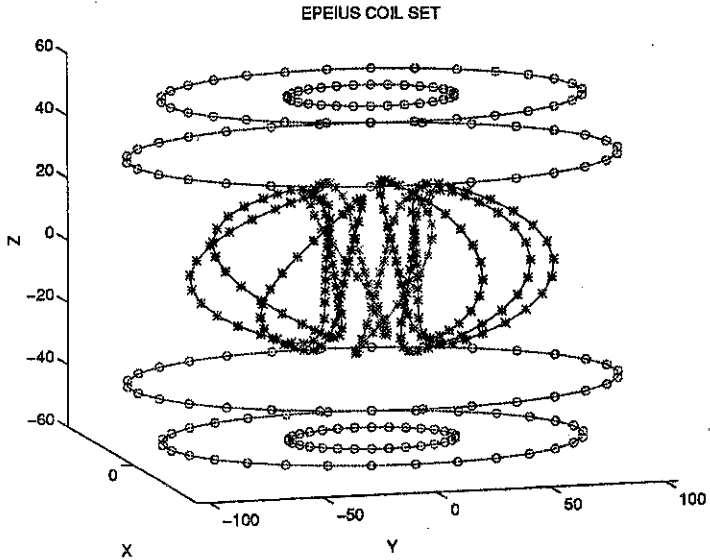
EPEIUS COIL SET

Fig. 1. The EPEIUS coil set consists of 8 identical distorted toroidal coils and 9 pairs of vertical field coils. The coils are modelled by a single filament at their respective centres.

References
[1] P. E. Moroz, *Phys. Rev. Lett.* **77** 651 (1996)
[2] D. W. Ross et al., *Proc. US/Japan JIFT Workshop, Columbia Univ.* (1996)
[3] S. P. Hirshman et al., *Comput. Phys. Commun.* **43** 143 (1986)
[4] D. V. Anderson et al., *Int. J. Supercomp. Appl.* **4** 34 (1990)
[5] W. A. Cooper, *Nucl. Fusion* **34** 729 (1994)
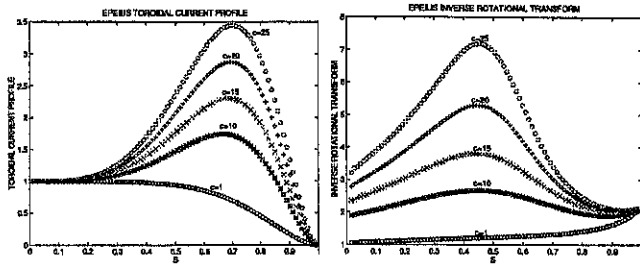
Fig. 2. *The toroidal current profiles $2\pi J'(s)$ (left) and the corresponding inverse rotational transform profiles $q(s)$ (right) in an EPEIUS configuration at $\beta = 6.75\%$ with varying degrees of hollowness controlled by the parameter $c = 1(o), 10(*), 15(\times), 20(+)$ and $25(o)$. The toroidal current is $180kA$.*
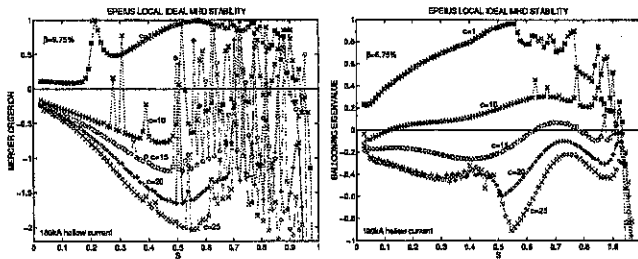
Fig. 3. *The Mercier criterion (left) and the ballooning eigenvalue (right) profiles in an EPEIUS configuration with $180kA$ hollow toroidal current at fixed $\beta = 6.75\%$ for values of $c = 1(*), 10(\times), 15(o), 20(+)$ and $25(*)$. Positive values denote instability.*

Fast Edge Mode observed during Enhanced D_α phase in Alcator C-Mod

I.H.Hutchinson, R.S.Granetz, A.Hubbard, J.A.Snipes, S.M.Wolfe

Plasma Science and Fusion Center, MIT, Cambridge, MA, USA

Abstract. An $n = 1$, $m = 4$ perturbation has been observed during the Enhanced-D_α H-mode phase on Alcator C-Mod. It is resonant just a few millimetres inside the separatrix and rotates extremely rapidly in the direction counter to the plasma current. This Fast Edge Mode is either an indicator of an extremely large negative radial electric field at the edge, or it is a mode rotating at about 4 times the estimated local diamagnetic velocity.

Introduction. The "Enhanced D_α" H-mode [1] on Alcator C-Mod occurs at high density and heating power, and appears to represent an attractive operational regime in which the impurity accumulation, characteristic of the ELM-free H-mode, is prevented without large ELMs. The energy confinement during D_α enhancement is slightly lower than ELM-free H-mode, but the edge particle confinement is much reduced. A search for the cause of the particle confinement reduction has revealed the presence in many enhanced D_α phases of an n=1 magnetic fluctuation with high frequency: 60 - 90 kHz. This "Fast Edge Mode" is unusual in comparison with other large-scale MHD fluctuations in that it rotates in the electron diamagnetic direction, or equivalently the counter-I_p direction. At present, these two characteristics (speed and direction of rotation) are regarded as the defining features of this low-m mode.

General observations. Fast edge modes sometimes occur in bursts lasting typically one millisecond that coincide with rises in the hydrogen light, and with slight rises in the plasma pressure observed by divertor embedded Langmuir probes at the separatrix. These bursts do not resemble ELMs of any previously identified type, being much more benign. Figure 1 shows an example of this behaviour. As indicated by the ECE T_e measurements, the fluctuation bursts show little or no (time-averaged) perturbation on the edge or central temperature and occur at a different time from the sawteeth. Some tendency has been observed for the bursts to occur shortly after sawteeth, when the edge temperature is near its maximum. In any case, the Fast Edge Modes occur interspersed with sawteeth whose precursors rotate in the opposite direction (co-I_p) with frequencies typically ten times smaller, thus demonstrating a "shear" in the mode rotation velocity.

Other Enhanced $D\alpha$ plasmas show quasi-continuous periods of Fast Edge Mode oscillations, and some show no clear coherent modes. Occasional Fast Edge Modes have been observed in what appear to be ELM-free H-modes. The magnetic fluctuations show no significant statistical coherence with the fluctuations observed on reflectometry[2], but both fluctuation levels are higher in Enhanced D_α phases.

Mode Structure Identification. Because of the very high frequency of the modes, their data are at present unaliased only on a subset of the magnetics diagnostics, primarily the coils mounted in the outboard limiter plus a few on the inboard wall. The

Fast Edge Mode Episode
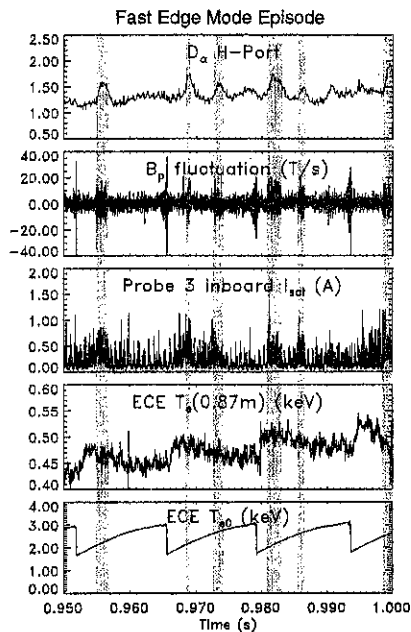
Figure 1: *Bursts of Fast Edge Mode fluctu-ations appear on D_α, magnetics and separa-trix probes but not ECE.*
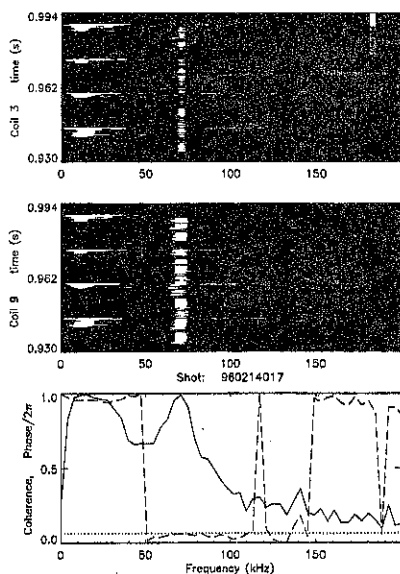
Figure 2: *Frequency spectra evolution and cross coherence (solid) and phase (dashed) for magnetic coils separated by 10 degrees toroidally, during a continuous Fast Edge Mode.*

limiter coils are installed in two limiters separated by a toroidal angle of 156 degrees. Each limiter has coils in pairs at the same poloidal position and separated by 10 degrees toroidally. This arrangement enables an unequivocal identification of the toroidal mode number of large coherent Fast Edge Modes as $n = 1$. In addition, spectrally resolved cross-correlation analysis is able to verify this identification in many cases when it is not visible by inspection. Figure 2 shows an example of this analysis. The spectra of two adjacent magnetic pick-up coils measuring $\dot{B}_\theta$ is shown together with their cross-coherence and cross-phase averaged over this time period. At the frequency of the Fast Edge Mode (70 kHz), the coherence is very high and the phase difference is about plus 10 degrees. For these two adjacent coils this indicates counter-rotation of an $n = 1$ mode. At the lower frequencies, bursts of sawtooth precursors can be seen. Their cross phase is minus 10 degrees (equivalent to plus 350 degrees), showing opposite (i.e. co-) rotation.

Because the plasma is strongly shaped, naive "poloidal angle" fits of the poloidal mode structure are misleading, and because of the sparseness of the fast magnetics data in poloidal angle, it is not possible simply to count nodes and antinodes. Instead, a value of safety factor, q_s, is specified, and on the flux surface of the equilibrium reconstruction

corresponding to this safety factor, the field-line is followed in 3-dimensions around the torus, tracing out a poloidal contour. At intervals on this contour corresponding to constant increments of toroidal angle, and hence of toroidal mode phase difference at constant poloidal position, are placed filaments with current proportional to $\exp(-i\delta\phi)$, where $\delta\phi$ is the phase difference. The poloidal projection then has filaments with positions and phases corresponding to modelling the perturbation as currents following field-lines on this rational surface. The values of the field perturbation arising at the magnetic measurements from these filaments are then calculated and compared with the experimental observations. (The influence of the conducting vacuum vessel is ignored at present). The resonant q_s is that which gives the best fit by this process. Figure 3 gives an example.

The measured values of the amplitudes and phases of the mode at the measurements can sometimes be obtained by inspection. However, when their amplitude is small, statistical methods are needed to recover the corresponding values from the noise. The approach used is to form the cross correlation matrix for all the relevant measurements in the frequency band of interest. The largest principle component (i.e. eigenvector with largest eigenvalue) of this matrix is then taken as the experimental mode structure.

For the cases analysed so far, the fast edge mode is found to be quite well fitted by the field-aligned current model with $m = 4$ (and $n = 1$). The coils on the outboard limiters are by themselves unable to distinguish between $m = 1 - 5$ because it is observed that the modelled phase variation across them is hardly different for the different poloidal mode numbers. This is a feature of the field structure as a function of flux surface. Actually

Figure 3: Fit of perturbation mode (stick arrows) to observed magnetics (filled arrows). The amplitude and phase at the probe locations are shown by arrow size and orientation. The second limiter coils are shown shifted right. The model filament phase is also given by arrow orientation on the resonant flux surface.

there is a small discrepancy observable in Fig 3, in that the modelled phase difference from top to bottom of the limiter is $\sim 30\%$ less than the measured phase difference (for all modelled m-numbers). This is believed to be because the mode does not exactly follow the field-line in shaped-cross-section plasmas; a small amount of field bending is preferred. The critical measurements for mode identification, then, are the inboard

coils. Their amplitude in addition to their phase, is quite well matched (by $m = 4$). This fact indicates there is no appreciable "ballooning" character to the mode.

Analysis and Discussion. The Fast Edge Mode is clearly different from the type III ELM precursors previously observed on Alcator C-Mod [3] and elsewhere, and from, for example, the "Quasi Coherent Mode" observed on PDX [4] in that it has $n = 1$, not large ($n \sim 10$ in ref [3]).

The $q = 4$ surface is only 4 mm from the separatrix, at the midplane, in these plasmas, so this mode is resonant within the steep gradient region of the H-mode "pedestal" or thermal barrier. The mode amplitude is quite small. The typical poloidal field perturbation at the coils is $\sim 2 \times 10^{-5}$ T. A crude estimate of the size of any magnetic island at the resonant surface may be obtained by supposing that a radial field of this magnitude exists on the resonant surface. In that case an island width of only ~ 1 mm would result using the standard island width formula $4\sqrt{(rq_s\tilde{B}_r/mq'_s B_p)}$.

The frequency and mode number of the mode tells us its velocity perpendicular to the field, assuming the mode is essentially field-aligned. If the velocity were all toroidal, it would be typically 4×10^5 m/s; whereas if it were all poloidal it would be 5×10^4 m/s. These speeds should be compared with the typical ion sound-speed of $\sim 10^5$ m/s in the vicinity of the mode rational surface. It seems unlikely that the rotation could be toroidal; if it were, it would be at about Mach 4.

The speed of the mode may be discussed in terms of the standard radial pressure balance (for ions) $E_r = (1/Zen_i)\partial p_i/\partial r - v_{ip}B_\phi + v_{i\phi}B_p$, where E_r is the radial electric field, n_i, p_i and v_i are the ion density, pressure and velocity. If we suppose the mode rotation to be due to $E \wedge B$ drift (the E_r term) alone, we deduce an extremely large *equivalent* negative radial electric field, $E_r \approx -350$ kV/m.

The mode probably is not at rest in the frame moving at the $E \wedge B$ velocity. Resistive modes tend to move with the electron drift velocity, which is moving relative to this frame at the electron diamagnetic velocity. Our knowledge of the diamagnetic drift velocity in the H-mode edge barrier is limited so far by insufficient spatial resolution (about 1 cm) of diagnostics. But even a generous estimate of about 0.5 keV in 0.5 cm (100 kV/m) is about four times too low to account for the observed rotation in terms of diamagnetic drifts. Moreover, if the velocity were to be attributed to pressure gradients – much steeper than presently estimated – the gradients would have to exceed the first ballooning limit by a substantial factor.

The Fast Edge Modes then, are highly edge-localized, n=1, perturbations whose rapid rotation shows either that they exist in a region with a very large negative radial electric field, or that the mode is a peculiar, as yet unidentified, instability.

References.

[1] Y. Takase *et al*, Phys. Plasmas **4** 1647 (1997).

[2] P. C. Stek *Reflectometry Measurements on Alcator C-Mod* PhD Thesis, MIT, (1997).

[3] J. A. Snipes *et al*, Plasma Phys. Control. Fusion **38** 1127 (1996).

[4] R. Slusher *et al*, Phys. Rev. Lett. **53** 667 (1984).

Analysis of ICRF Heating on Alcator C-Mod*

Y. Takase, P. Bonoli, S. Wukitch, C. Fiore, A. Hubbard,

A. Mazurenko, P. O'Shea, M. Porkolab, J. Reardon, C. Rost

MIT Plasma Science and Fusion Center, Cambridge, Massachusetts 02139 U.S.A.

1. Introduction

Alcator C-Mod [1] ($R = 0.67$ m, $a = 0.22$ m, lower single-null, $\kappa = 1.7$ typical) is a compact high field tokamak. The first wall consists of all metallic (mostly molybdenum) plasma facing components. Experiments described in this paper were performed with boronized walls. The heating scenario employed was hydrogen minority heating in deuterium majority plasmas at 5.3 T with RF powers in the range 1.5–3 MW at 80 MHz [2,3].

2. Power absorption in L-mode plasmas

A density scan at an RF power level of 1.5 MW was performed in L-mode plasmas. In order to avoid H-mode at this power level, the toroidal field was reversed so that the ion ∇B drift was directed away from the active X-point. The density scan was repeated at two values of plasma current, 0.8 MA and 1.1 MA (the density range for the 1.1 MA scan was limited to $\bar{n}_e > 1.6 \times 10^{20}$ m^{-3}). The hydrogen concentration was less than 3%.
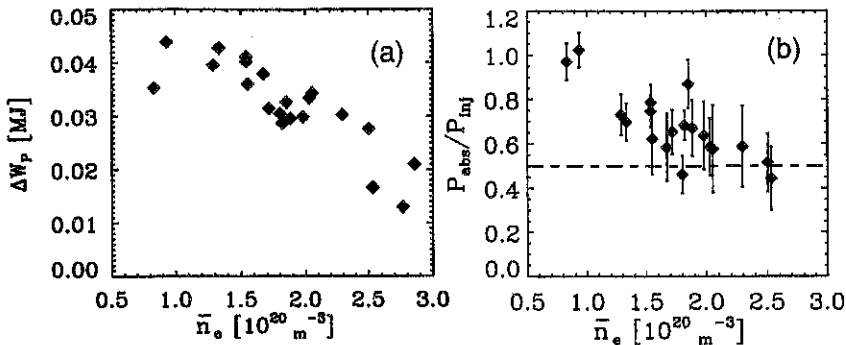
Fig. 1: (a) Stored energy increase and (b) power absorption efficiency as functions of density. L-mode plasmas, $B_T = 5.3$ T, $I_p = 0.8$, 1.1 MA, $n_H/n_e \leq 3\%$, $P_{RF} = 1.5$ MW.

Heating, as measured by the stored energy increase ΔW, degrades by roughly a factor of two as the density is increased as shown in Fig. 1(a). The absorption efficiency, estimated from the discontinuity in slope of the diamagnetic stored energy, also

---

degrades with density from 100% to 50%, as shown in Fig. 1(b). The incremental confinement time, $\Delta W/\Delta P$ is approximately constant at 0.045 s. The heating degradation at higher density is therefore attributed to lower power absorption efficiency. The cause of degraded absorption efficiency for high density L-mode plasmas is presently not well understood, but may be related to the higher edge plasma and neutral densities. In contrast, power absorption in high density ($\overline{n}_e > 3 \times 10^{20} \, \mathrm{m}^{-3}$) H-mode plasmas is nearly 80%.

3. Power absorption profiles

In D(H) minority heating, most of the RF power is absorbed by the hydrogen minority ions. Electrons and bulk deuterium ions are heated by collisional power transfer from the heated hydrogen minority ions. A small fraction of the RF power can be absorbed directly by the majority deuterium ions by second harmonic damping. The central electron heating rate can be derived from the central electron reheat rate after a sawtooth crash. The contribution from the ohmic heating power must be subtracted to obtain the contribution from RF heating. The central ion heating rate can be measured from the discontinuity in slope of the central ion temperature. Both the central electron heating rate and the central ion heating rate increase with density, as shown in Fig. 2. The increase of the central electron heating rate with density may be counter-intuitive, but this can be explained by the more localized power deposition at higher density. The central (averaged over $r/a \leq 0.25$) power transfer densities to electrons and ions calculated by TRANSP[4]/FPPRF[5]/SPRUCE[6] are shown for comparison. The fraction of power transferred to electrons averaged over the whole plasma volume (compared to power transferred to bulk ions) does decrease with density.
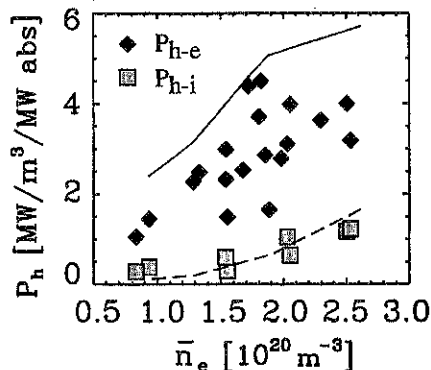
Fig. 2: Central electron and ion heating power densities as functions of density. Same parameters as Fig. 1. The solid line and the dashed line are central electron and ion heating power densities calculated by TRANSP/FPPRF/SPRUCE.

There are two mechanisms responsible for localization of power deposition at higher density. The first is the wave focusing effect. At higher densities the radial wavelength of the fast wave becomes small compared to the minor radius of the plasma, and the wave field becomes more tightly focused. At lower densities the radial wavelength becomes comparable to the minor radius and diffraction becomes important. This effect will determine the power deposition width in the vertical direction along the cyclotron resonance. The second effect is due to Doppler broadening of the ion cyclotron resonance in the horizontal direction. At lower densities the average energy of the minority ions becomes larger, thus increasing the radial width of power deposition. A comparison of power absorption contours calculated by the FPPRF/SPRUCE code for low density and high density plasmas are shown in Fig. 3. Because the vertical extent is generally larger than the horizontal extent, power deposition width is determined mainly by the wave focusing effect.
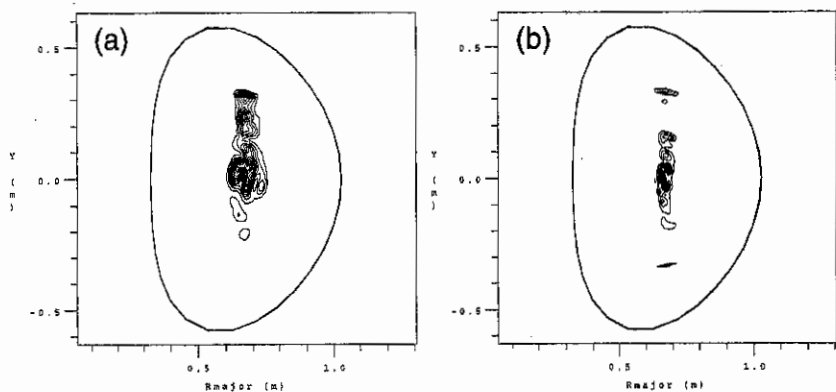
Fig. 3: Total power absorption contours at two densities: (a) $\overline{n}_e = 0.9 \times 10^{20}\,\mathrm{m}^{-3}$, (b) $\overline{n}_e = 2.6 \times 10^{20}\,\mathrm{m}^{-3}$. Same parameters as Fig. 1.

The energy stored in the energetic minority ions is 30% of the total stored energy at the lowest density in this scan, but decreases to 5% at the highest density. At the lowest density in this scan, fast ion orbit loss is calculated to be significant (about 20% of the absorbed RF power), but is negligible at higher densities.

4. Second harmonic damping

In high power H-mode plasmas, β of the main ions becomes significant. The central ion beta of $\beta_{i0} = 1.5\%$ has been obtained at 5.3 T. Under such a condition, second harmonic damping on the majority deuterium ions can dominate over hydrogen minority ions for low hydrogen concentrations. Calculations show that switch-over to dominant second harmonic deuterium damping takes place for $n_H/n_e \leq \beta_{i0}$, as shown

in Fig. 4 where the central (integrated up to $r/a \leq 0.35$, the sawtooth inversion radius) power absorption by second harmonic deuterium, fundamental hydrogen, and mode conversion are plotted for a high-density high-power H-mode as functions of hydrogen concentration n_H/n_e. Such concentrations have been achieved after an extended period (1–2 months) of deuterium plasma operations. Second harmonic deuterium heating may be useful for enhancing the fusion reactivity in high performance plasmas such as high power, high density H-mode or PEP mode plasmas[3].
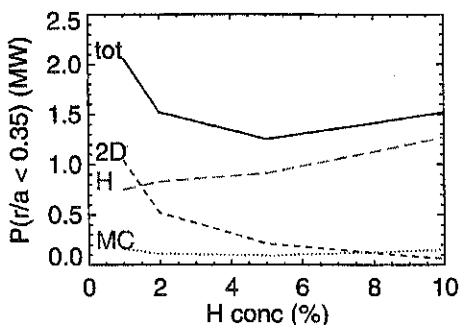
Fig. 4: Central power absorption by second harmonic deuterium, fundamental hydrogen, and mode conversion in high-density high-power H-mode as functions of hydrogen concentration n_H/n_e. $B_T = 5.3$ T, $I_p = 1.0$ MA, $P_{RF} = 2.7$ MW, $\overline{n}_e = 4.2 \times 10^{20}$ m^{-3}.

5. Conclusions

A degradation of heating (stored energy increase) was observed in high density L-mode plasmas, which was attributed to a degradation of the absorption efficiency by a factor of 2. In high density H-modes, power absorption was substantially higher (nearly 80%). Both central electron and ion power densities increased with density due to more localized power absorption. In high density H-mode plasmas, second harmonic absorption can become important at low hydrogen concentrations $n_H/n_e \lesssim \beta_{i0}$.

References

[1] I.H. Hutchinson, et al., Phys. Plasmas 1, 1511 (1994).

[2] Y. Takase, et al., Plasma Phys. Control. Fusion 38, 2215 (1996).

[3] Y. Takase, et al., Phys. Plasmas, 4, 1647 (1997).

[4] R. J. Hawryluk, in *Physics of Plasmas Close to Thermonuclear Conditions*, Vol. 1 (CEC, Brussels 1980) p. 19.

[5] G. W. Hammett, Ph. D. Thesis, Princeton University (1986).

[6] D. N. Smithe, et al., Nucl. Fusion 27, 1319 (1987).

Enhanced D_α H-modes in Alcator C-Mod

J. A. Snipes, R. Boivin, C. Fiore, J. A. Goetz, A. Hubbard, I. H. Hutchinson,
J. Irby, B. LaBombard, B. Lipschultz, E. S. Marmar, J. Rice,
P. C. Stek, Y. Takase, J. L. Terry, S. M. Wolfe
MIT Plasma Science and Fusion Center, Cambridge, MA USA

Introduction A new and potentially reactor relevant high confinement regime has been found on Alcator C-Mod at high electron density ($\bar{n}_e > 2 \times 10^{20}$ m^{-3}) with ICRF heating, called the Enhanced D_α H-mode (EDA H-mode) [1]. These H-modes reach a steady state density and total radiated power, yet remain free of discrete ELMs throughout the ICRF heating phase. The D_α emission drops initially as the plasma enters H-mode, then rises rapidly, often returning to L-mode levels at the midplane and in the divertor as the density reaches a steady state. The energy confinement of Enhanced D_α H-modes is slightly lower than that of the best ELM-free H-modes, but can still reach and maintain confinement enhancement factors up to two relative to L-mode. High frequency (50 - 100 kHz) density and magnetic fluctuations are often observed during EDA H-modes.

Method of Operation Enhanced D_α H-modes were first obtained after closing off some divertor bypass leaks, which increased the divertor/midplane neutral compression ratio from a range of 10-100 to a range of 50-250 in H-mode. The first moderately enhanced D_α H-modes were obtained before the machine was boronized by operating at high density ($\bar{n}_e > 2.5 \times 10^{20}$ m^{-3}) and high ICRF heating power ($P_{ICRF} > 2.5$ MW) with strong gas puffing.

After boronization with B_2D_6, EDA H-modes were obtained at high density without strong gas puffing. While high ICRF power is usually required to achieve EDA H-mode, some were achieved immediately after boronization with $P_{ICRF} < 1$ MW. The divertor pressure in EDA H-mode is usually 2 - 10 Pa, but after a fresh boronization, EDA H-modes can occur with divertor pressures from 0.25 - 1 Pa. Boronization widens the operational range of EDA H-mode through lower core radiation and increased particle inventory.

Particle and Energy Confinement EDA H-modes have somewhat lower core particle and energy confinement than ELM-free H-modes in C-Mod. The core impurity particle confinement time was measured with trace scandium injection during an ELM-free H-mode that became an EDA H-mode before the scandium left the plasma (Fig. 1). In the ELM-free phase, the scandium did not decay, indicating an impurity confinement time much greater

than 0.2 sec. In the Enhanced D_α phase, the scandium left the plasma with a characteristic decay time of 0.1 sec. By comparison, in the L-mode phase, the scandium decay time was about 30 msec. So, in EDA H-mode, the core impurity confinement time is about three times higher than L-mode, but at least two times lower than ELM-free H-mode.

The reduced particle confinement of EDA H-mode relative to ELM-free H-mode leads to reduced impurity accumulation in EDA H-mode. The radiated power saturates in EDA H-mode at a

Fig. 1. Scandium injection at 0.7 sec to measure particle confinement in ELM-free and EDA H-mode.

steady state value with $0.2 < P_{rad}/P_{tot} < 0.6$ rather than continuing to increase as in ELM-free H-mode (Fig. 2). The total radiated power profile across the main plasma, measured by bolometers, is substantially lower in EDA H-mode than in ELM-free H-mode. By contrast, the divertor radiation is substantially higher in EDA H-mode than in ELM-free H-mode. Z_{eff} is also lower in EDA H-mode than in ELM-free H-mode.

The peak energy confinement in EDA H-mode is generally slightly lower than in ELM-free H-mode, but can still reach $2 \times$ L-mode. Values of the thermal energy confinement time in EDA H-mode $\tau_{Eth}^{EDA} > 60$ msec have been achieved compared to ELM-free values up to $\tau_{Eth}^{EFH} \approx 80$ msec. The advantage of EDA H-mode over ELM-free H-mode is that the confinement remains high in steady state for as long as the ICRF pulse because the impurities do not accumulate and radiate away the thermal energy. This is accomplished without the large perturbations of Type I ELMs. So, EDA H-mode has the improved confinement of Type I ELMy H-mode, without the problems associated with large ELMs.

Divertor Physics Fast Scanning Probe upstream and outer divertor domed Langmuir probe measurements indicate that the EDA H-mode is in the High Recycling Divertor regime [2], where the measured electron pressure is approximately constant along the field, but the electron temperature falls between the upstream location and the divertor plate. The EDA H-

Fig. 2. Comparison of a) ELM-free H-mode and b) Enhanced D_α H-mode showing the line averaged density, divertor D_α emission, central electron temperature, stored energy, total radiated power and ICRF power.

mode occurs at high density when the power conducted to the divertor plate is sufficiently high (Fig. 3). Here $P_{plate} = P_{in} - dW/dt - P_{rad}^{main} - P_{rad}^{div}$ is the power that arrives at the divertor plate after subtracting the change in stored energy and both main chamber and divertor radiation. Figure 3 shows an EDA H-mode that turns into a detached divertor H-mode through intense nitrogen gas puffing. The enhanced D_α emission returns to ELM-free levels when the power conducted to the plate drops due to increased radiation, just as the divertor detaches.

Edge Fluctuations High frequency magnetic and density fluctuations are often observed during EDA H-mode.
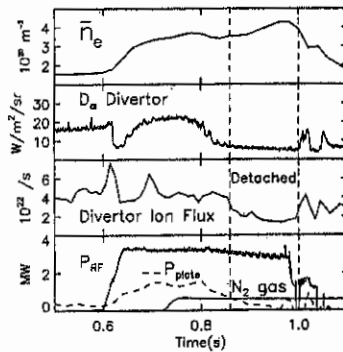
Fig. 3. Detached divertor H-mode with nitrogen puffing. The D_α emission is suppressed as the power to the plate drops.

The magnetic perturbations are covered in a companion paper in these proceedings [3]. The density fluctuations are observed with an AM reflectometer at 88 GHz with a density cutoff in the steep gradient region at 1.5×10^{20} m^{-3}. In EDA H-mode, there is an increase in the broadband fluctuations out to the 400 kHz anti-aliasing filter of the diagnostic and often
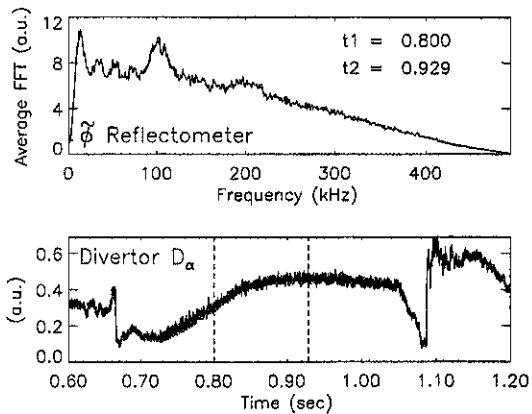
Fig. 4. Average between 0.8 and 0.929 sec of the Fourier transform of the density phase fluctuations from the reflectometer during an Enhanced Da H-mode showing a clear peak in the fluctuations at about 100 kHz.

an additional coherent peak at typically 100 kHz (Fig. 4). Although the magnetic fluctuations are often at about the same frequency and time, there is no clear coherence between the magnetic and density fluctuations.

Conclusion   The Enhanced D_α H-mode regime may prove to be a good compromise for ITER operation to obtain high confinement, avoid large ELMs, and maintain low Z_{eff} with high divertor radiation in steady state. In comparison with ELM-free H-modes, impurity accumulation is substantially reduced in EDA H-modes leading to lower Z_{eff} values and lower total radiated power across the main plasma and a factor of two higher radiated power in the divertor. The energy confinement is comparable in both types of H-mode. High frequency edge density and magnetic fluctuations are observed during EDA H-mode, though the role they play has not yet been determined.

References

[1] Y Takase, et al., Phys. Plasmas **4** (1997) 1647.

[2] B LaBombard, et al., Phys. Plasmas **2** (1995) 2242.

[3] I H Hutchinson, et al., this conference.

Reversed Shear Experiments in Alcator C-Mod with Current Ramp and ICRF Heating*

M. Porkolab, R. Boivin, P.T. Bonoli, C. Fiore, M. Greenwald, A. Hubbard,
I.H. Hutchinson, Y. In, E. Marmar, P. O'Shea, J. Ramos, J. Rice, J.C. Rost,
J.A. Schachter, J. Snipes, Y. Takase, S.M. Wolfe, and the Alcator C-Mod Group

MIT Plasma Science and Fusion Center, Cambridge, MA,02139, USA

A. Bondeson, Chalmers University, Goteborg, Sweden

Initial scoping experiments were performed to obtain the enhanced reversed shear (ERS) mode in Alcator C-Mod[1] using current ramp and early ICRF heating in the D(H) minority heating regime. Alcator C-Mod is a relatively modest size ($R = 0.67$ m, $a = 0.22$ m), but high power density and high field ($B_t \leq 9.0$ T, $I_p \leq 1.5$ MA) tokamak with a divertor and substantial elongation ($\kappa \leq 1.8$), which should provide valuable data regarding ERS operation with purely RF heating in a plasma with comparable T_e and T_i. In these experiments up to 2 MW of ICRF power at 80 MHz were injected using a pair of two strap antennas, each phased at 180° between adjacent straps[2]. The volumetric power density exceeded 2 MW/m^3, and the surface power density exceeds the H-mode threshold in the steady current phase of the discharge beyond the first sawtooth crash at 0.23 s, a substantial fraction of the resistive skin time. Typical plasma parameters at the end of the 0.23 s sawtooth free period were $\bar{n}_e = 1 \times 10^{20}$ m^{-3}, $B_t = 5.3$ T, $T_{e0} = 5$ keV, $T_{i0} = 2.5$ keV, $n_H/n_e \simeq 0.04 - 0.05$, and $I_p = 0.8$ MA. Calculations with a combined Fokker Planck - ICRF heating code FPPRF [3] indicate for these parameters approximately 70% of the rf power carried by the minority (H) tail is transferred collisionally to the background electrons. During the initial plasma phase ($t \lesssim 0.12$ s), the coupled power from the two ICRF transmitters varies between 0.8 - 1.8 MW. Beyond this time, both transmitters couple well into the target plasma, providing a continuous power of 1.8 MW. During the ramping phase, 0.08 − 0.1 s into the discharge initiation phase, MHD oscillations were observed on both poloidal field pick-up coils and ECE diagnostics. The short bursts of coherent low frequency ($1 - 10$ kHz) MHD oscillations lasting for 10 ms were observed just as $q_{\psi_{es}}$ dropped below 5. The correlated oscillations were observed on several ECE grating polychromator signals which measures T_e at 9 radial locations along the midplane. The diagnostic is sampled at 20 kHz and has a radial resolution of 0.9 cm, with 2.0 cm separation between channels. As shown in Fig. 1, clear perturbations can be seen on several channels during the current rise, indicating a relatively wide mode structure, typically in the range $0.4 \leq r/a \leq 0.9$. The peak in the fluctuations varies from $r/a = 0.75 - 0.85$ (see Fig. 2). Equilibrium reconstruction using the EFIT code [4] was also done in an attempt to establish the main plasma equilibrium quantities, including the q-profiles. At least three distinct equilibria were established, each with somewhat different current and q-profiles. These q-profiles are also plotted in Fig. 2, two of them being a clear reverse shear profile
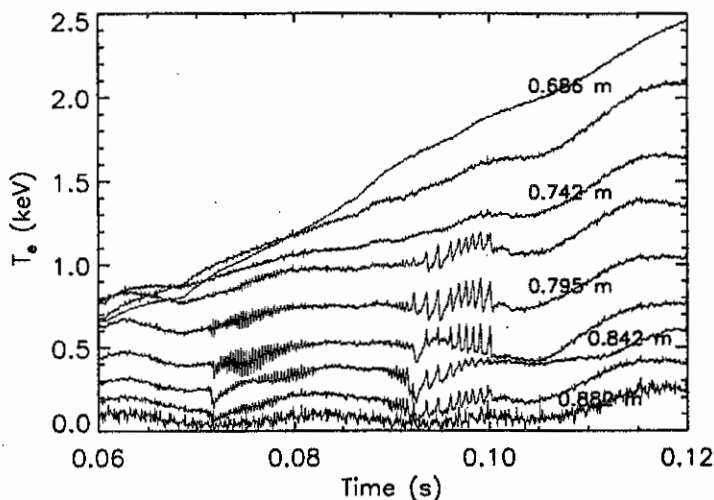
Figure 1: Electron temperature versus time from GPC for C-Mod Shot 960223047.

with $q_0 = 4.2 - 4.7$, $q_{min} = 3.2 - 3.1$, $q_{95} = 4.5$, while the third profile tended to be flat in the inner half of the plasma, with $q_{min} = 3.0$, and $q_{95} = 4.5$. One of the reversed shear q-profiles, with $q_0 = 4.7$, $q_{min} \simeq 3.1$ was characterized by substantial edge current pedestals, with significant MHD stability consequences, as is discussed below.

The poloidal and toroidal mode numbers of the oscillations were determined by comparing the measured phase of the oscillations on poloidal field pick-up coil signals from the outboard limiter and the inner wall at different toroidal locations. The mode numbers were found to be $m = 5$, $n = 1$ on shot 960223047 at both 0.08 s and 0.09 s, which corresponds to a flux surface that passes from $r/a = 0.96$ to $r/a \sim 1$ as the current rises. A current filament code was also run to compare the measured phases with the expected phases from a perturbation at the $q = 5$ surface and good agreement was found between the expected and measured phases.

We have carried out a detailed MHD analysis of the 960223047 discharge during its current ramp phase in an attempt to explain the observed $n = 1$ fluctuations. We have concentrated on a time point of 0.092 s that corresponds to the beginning of the second burst of MHD activity. The MHD stabiliy has been investigated with the linear code MARS [5] for resistive modes. It is important to realize that the MHD stability results are sensitive to equilibrium details that cannot be resolved with the available diagnostics of pressure and current profiles. In particular significant uncertainties exist regarding the

inner shape of the current or q-profiles, and regarding the precise values of the current density and its gradient at the plasma edge. For the case under consideration we have investigated all three different EFIT equilibria shown in Fig. 2.
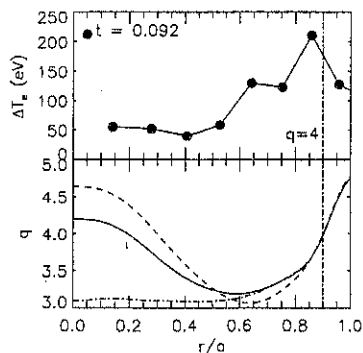
Figure 2: Electron temperature fluctuation profile for Shot 960223047 (top curve). Profiles of safety factor (q) for three distinct EFIT equilibrium reconstructions of Shot 960223047 (bottom curves).
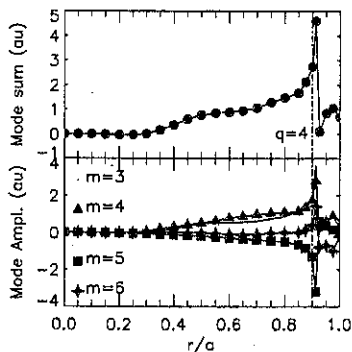
Figure 3: Resistive MHD mode analysis for non-monotonic q-profile in Fig. 2 with $q_0 = 4.2$. Eigenfunction for $n = 1$ resistive mode.

The MHD analysis of the first equilibrium (flat q-profile) using the MARS code yields an $n = 1$ resistive (tearing) instability localized at the $q = 4$ mode resonant surface near the plasma edge. The growth rate of this mode is low, with an estimated e-folding time of the order of 10 ms. This result should be taken only as a rough approximation because the MARS code uses only a simple expression for the temperature profile of the form $(T/T_0) = (p/p_0)^\alpha$, $(n/n_0) = (p/p_0)^{1-\alpha}$, and $Z_{eff} = 1$ when evaluating the plasma resistivity. In our calculation we took the experimental values for $T_0 = 1.6$ keV and $n_0 = 0.7 \times 10^{20}$ m^{-3}, and a simple guess $\alpha = 0.6$. Thus this model may yield a value of the plasma resistivity at the edge near the $q = 4$ mode resonant surface significantly different from the actual one . The second equilibrium is found unstable to a very similar $n = 1$ resistive mode whose eigenfunction is (with $q_0 = 4.2$) diplayed in Fig. 3. This is a single tearing mode localized at the outer $q = 4$ resonant resonant surface, despite the fact that this equilibrium has a non-monotonic q-profile with two $q = 4$ surfaces within the plasma. The absence of a double tearing mode can be understood because the two $q = 4$ surfaces are far apart and the inner one is in a high temperature region, so that the resistive mode only grows at the colder, outer resonant surface. The growth rate of this instability is

very close to the one in the first equilibrium where q is monotonic.. The structure of the eigenfunction is also very similar but the enhancement of the $m = 3$ component in the central region of flat $q \simeq 3$ of the first equilibrium is now absent. We can conclude that the modification of the internal current density profile from the first EFIT reconstruction to the second one has little effect on this resistive mode.

The third equilibrium ($q_0 = 4.7$) is found unstable to an $n = 1$ ideal external mode, that appears to be driven by the larger edge current density (not shown here) and current density gradient of this equilibrium fit, combined with the presence of a $q = 5$ mode resonant surface in the vacuum just outside the plasma. This ideal mode has a growth rate about 100 times faster than those of the resistive modes in the first two equilibria, with an e-folding time of the order of 0.1 ms independent of the resistivity. Its eigenfunction peaks near the outside vacuum region.

Comparison with the signature of the experimentally observed fluctuations is not conclusive. The fact that the observed fluctuation amplitudes seem to exhibit a maximum about $q = 4$, favors the interpretation in terms of the resistive mode rather than the edge kink-mode. The discharge is not disrupted, and the main impact of these modes is that the electron temperature is "clamped" in regions of large mode amplitudes. These modes become stabilized as the discharge evolves toward higher temperatures.

In these preliminary experiments no evidence of the ERS confinement regime was observed yet. As the discharge evolves, at ~ 0.15 s high frequency, ($\sim 300 - 400$ kHz) narrow bandwidth modes were observed, which are believed to be TAE modes driven by the hydrogen minority tail. Future experiments, including $D(^3He)$ minority heating and pellet injection, should favor increased ion heating and hence the enhanced reversed shear (ERS) mode. In addition, off-axis mode-conversion current drive will be carried out in an attempt to "clamp" the reversed shear equilibrium.

References

[1] HUTCHINSON, I.H., et al., Phys. Plasmas 1, 1511 (1994).

[2] TAKASE, Y., et al., *Proc. 14th IEEE/NPSS Symp. Fusion Engineering* (San Diego, CA, 1992) p. 118.

[3] HAMMETT, G.W., "Fast Ion Studies of Ion Cyclotron Heating in the PLT Tomamak", PhD Diss., University Microfilms Int. No. GAX86-12694, Princeton University (1986).

[4] LAO, L.L., et al., Nucl. Fusion 30, 1035 (1990).

[5] BONDESON, A., et al., Phys. Fluids B, 1989 (1992).

VOLUME RECOMBINATION IN ALCATOR C-MOD DIVERTOR PLASMAS

J.L. Terry, B. Lipschultz, D. Lumma, B. LaBombard, and D. Pappas

Plasma Science and Fusion Center, MIT, Cambridge, MA, 02139, USA

1 Introduction

Volume recombination has been predicted to be a significant process in tokamak divertors under detached conditions. These predictions arise from a number of considerations - from modelling [1,2], as the mechanism for removing a large fraction of ion flux [3,4,2], and as a probable consequence of the ~1 eV electron temperatures observed in the detached divertor plasmas of DIII-D [5] and Alcator C-Mod[6]. The first experimental measurements of significant volume recombination in a tokamak divertor were on Alcator C-Mod[7], where the ion sink due to recombination was observed to be comparable to the ion loss to the plates. In addition, recent measurements on a linear device[8] have also shown the importance of recombination during simulations of plasma detachment. The observations are consistent in a broad sense with the theoretical considerations and modelling. However, more detailed experiments and comparisons with the modelling are required before the role of recombination in the physics of plasma detachment is understood and can be exploited to achieve the heat and momentum dissipation required in future fusion reactors.

In this paper a more streamlined analysis technique, which relates the number of recombinations occurring within a field-of-view to the number of Balmer series photons emitted within that view, is presented. This technique is then exploited to determine the spatial distribution of the volume recombination occurring in the Alcator C-Mod divertor region when the inner divertor plate is detached, while the outer divertor plate is still attached.

2 Recombinations per Balmer Series Photon

For the determination of the recombination rates in Alcator C-Mod, measurements of the Balmer series lines of D_0 are used. An example of such a spectrum, containing the $n=6,7,8...11 \rightarrow 2$ lines is shown in Fig. 1. Measurements of D_α ($n=3\rightarrow2$) along the same view are also made at the same time. From the spectra it is apparent that the Balmer lines are Stark broadened, with line widths, consistent within a given spectrum, which correspond to electron densities as high as $\sim 2 \times 10^{21} \mathrm{m}^{-3}$. In addition, the measurements typically show that the scaling of the upper level population densities of these transitions is consistent with a population distribution which is a result of recombination. They are inconsistent with population by excitation. This can be shown using a collisional-radiative model like that of Johnson and Hinnov[9] or Fujimoto et al. [10]. Since the scaling of the observed line brightnesses is that of population-by-recombination, the same collisional - radiative model has been employed to relate the volume emission rate of those measured lines to the total volume recombination rate, as long as the electron density and temperature are also known. The number of recombinations per photon of any Balmer series line has been calculated vs T_e and n_e for a recombining plasma. ($n_e = n_i$ is assumed.) This is the the recombination analog for what Johnson and Hinnov [9] have done in the *ionizing* case, where curves showing the number of ionizations per D_α photon for an ionizing plasma were generated. We have generated curves which give the number
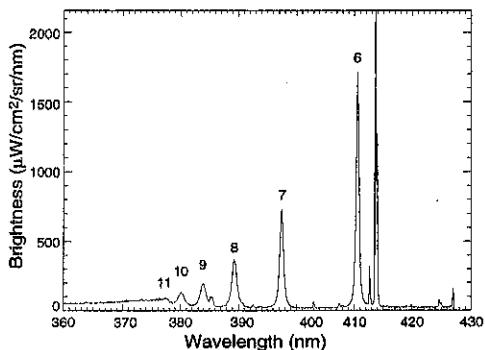
Figure 1: *The higher n D_0 Balmer series lines (n=11, 10, ...6 → 2). The widths of the Stark broadened lines correspond to a density of ~ 1.5×10^{21} m^{-3}. The view for this spectrum is of the inner, detached divertor plate.*

of recombinations per Balmer-series-line photon, with the condition that the upper level of the line be populated by recombination. Examples of this quantity vs T_e are shown in Fig. 2 at two different densities. Here we have used the model of Ref. [10], although use of Ref. [9] gives essentially the same results.
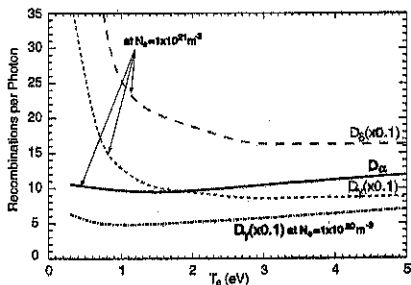
Figure 2: *The number of recombinations per photon for three Balmer series lines, calculated in a recombining plasma and showing the relatively weak T_e dependence for $T_e \gtrsim$ ~0.8 eV. $n_e = 10^{21}$ m^{-3} and 10^{21} m^{-3} for the second D_γ curve.*

3 Spatially Resolved Measurements of Recombination

In order to provide more detailed measurements of the connection between recombination and detachment, we have used the formalism described above to analyse the spatial distribution of the recombination during an Alcator C-Mod discharge when the inner divertor
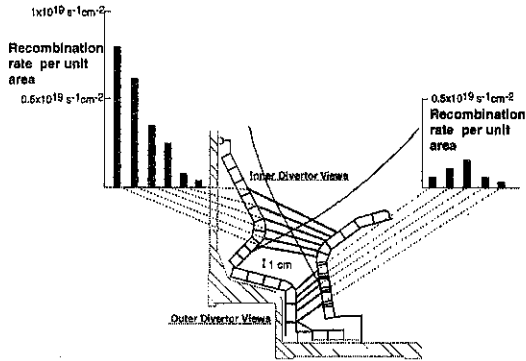
Figure 3: *The recombination rate per unit area determined for different viewed areas of the inner and outer divertor plates. The inner divertor plate is detached, while the outer is not. Also shown are the viewing chords, the LCFS, and the strike points.*

plate was detached, but the outer plate was not. Other plasma parameters were $I_p=1.0$ MA, $P_{ICRF}=1$ MW, $\overline{n_e} = 3.5 \times 10^{20} \mathrm{m}^{-3}$, with H-mode confinement. The line brightnesses of the $n=3,6\text{-}11 \rightarrow 2$ are measured along the viewing chords (with diameters of $\sim 1 \mathrm{cm}$) shown in Fig. 3. The chords have diameters of ~ 1 cm. Radial profiles of D_α emission, measured from a separate array, viewing the divertor from above, show that the emission is is strongly peaked between the inner divertor plate and the x-point, but falls to about 20% of its peak value along the outer (attached) divertor plate. These measurements lead us to ascribe the photons detected by those views to recombination occurring near the inner divertor. Similarly, we take the measured D_0 emission along the chords labeled 'outer-divertor-view' to be due to recombination at the outer plate. After verifying that the Balmer lines ($n=3, 6, 7 \rightarrow 2$) exhibit the characteristic recombination scaling with n, curves similar to those of Fig. 2 (but generated for the plasma densities measured from the line widths) are used to measure the recombination rate per unit area of plasma surface viewed. Since the recombinations per photon varies little with T_e at higher temperatures, the T_e needed for the evaluation is only an issue if it is $\lesssim 0.8$ eV, in which case the ratio between the 3-2 and 6-2 lines can be used to estimate the temperature. In fact all of the analyses are consistent with $T_e \gtrsim 0.8$ eV. The results of the evaluations are also shown in Fig. 3. The 'inner-divertor-views' show that the recombination increases as the inner - detached - strike point is approached. The more extensive array of D_α views shows that the emission, and, by implication, the recombination rate are peaked at or close to the strike point. However, rates for those views are not shown, since the other Balmer lines were not measured. The integration providing the total recombination rate in front of the inner plate has been done after interpolating poloidally between the views by assuming toroidal symmetry. This 'inner plate' recombination was then compared to the rate at which ions were being collected at the plate, measured by a set of five probes embedded in the inner plate. The recombination rate ($\sim 2.7 \times 10^{22}$ s^{-1}) is approximately a factor of two greater than the ion current ($\sim 1 \times 10^{22}$ s^{-1}) to this detached plate. The

time histories of each rate show that this ratio stays fairly constant for the entire time the inner plate is detached, which is essentially the duration of the diverted discharge. An analogous evaluation has also been done for the outer - attached - plate. As shown, the recombination is much reduced here, although the rate is similarly peaked close to the outer strike point. The ion current collected by the outer plate ($\sim 4 \times 10^{22}$ s^{-1}) is about 20 times the recombination rate there.

4 Summary and Discussion

Significant volume recombination of the majority ions is been observed in the divertor region of Alcator C-Mod under detached conditions. This determination is made by analysis of the visible spectrum from the divertor, in particular the Balmer series line emission. After verification that the upper levels of the measured lines are populated primarily by recombination, the recombination rate within the field-of-view has been found from curves relating the number of recombination per Balmer-series-line photon. These curves are relatively insensitive to T_e and n_e, although n_e is measured from the Stark-broadened line-widths. The distribution of the recombination is found for a case where the inner divertor plate is detached, while the outer plate is not. The recombination rate in the detached region in front of the inner divertor plate is approximately a factor of two higher than the rate of ion collection at the plate. For the attached plate, the recombination occurring in front of it is still small in comparison to the ion current to the plate. For both plates the recombination is peaked near the strike points. This may be a result of the fact that at this time for this discharge n_e is highest and T_e lowest at the strike point locations. It is interesting also to speculate about the effects of the detached/attached asymmetry between the plates and the resulting, observed asymmetries in recombination and ion currents. We note that the total ion sink (recombination plus ion current) is still approximately balanced between the plates, so that neutral density made up of recombined *and* recycled neutrals may be balanced as well. It is still possible, however, that differences in neutral density distributions may arise due to the volume source nature of recombination. Such differences may give rise to complicated ion/neutral flow patterns in the SOL.

Finally, we discuss the possible opacity of Lyman series lines. The analysis and Fig. 2 assume that all lines are optically thin. In fact, Ly$_\alpha$ is probably thick along some paths, and there is evidence on other, higher density shots that Ly$_\beta$ is somewhat self-absorbed. The Balmer series lines are optically thin. The greatest effect of Ly$_\alpha$ self-absorption will be an enhancement of the $n=2$ level and a possible over-estimate of the recombination rate.

References
[1] F. Wising et al., Contrib. Plasma Phys. 36, p 136 (1996)
[2] S.I. Krasheninnikov et al., Phys Plasmas 4, p 1638 (1997)
[3] A. Loarte, Proc. 12th PSI Conf, J. Nucl. Mater (1996) I9, in press
[4] K. Borrass et al., Proc. 12th PSI Conf, J. Nucl. Mater (1996) A41, in press
[5] S. L. Allen et al., Proc. 12th PSI Conf, J. Nucl. Mater (1996) B37, in press
[6] B. LaBombard et al., Phys Plasmas 2, p 2242 (1995)
[7] D Lumma et al, Phys Plasmas (1997), in press
[8] J. Park et al., submitted to PRL 1997
[9] L.C. Johnson and E. Hinnov, JQSRT 13, p 333 (1973)
[10] T. Fujimoto et al., Nucl Fus 28, p 1255 (1988)

Study of Balmer spectrum near the photo-recombination edge in Alcator C-Mod divertor plasmas

A. Yu. Pigarov, J. L. Terry and B. Lipschultz

PSFC, Massachusetts Institute of Technology, Cambridge, MA 02139, U.S.A.

Introduction. Recent experimental [1] and theoretical [2] investigations have demonstrated that volumetric plasma recombination plays a crucial role in divertor plasma detachment. Important experimental evidence for the strong recombination of the majority ions in the divertor comes from the analysis of the plasma emission spectrum. Under detached conditions in Alcator C-mod tokamak, the measured spectra [1] show merging of Balmer series lines and a photo-recombination (PR) continuum edge which is not a sharp step. This phenomenon, known as a smooth discrete-to-continuum (D-C) spectrum transition, is typical only for high density ($N_e \geq 10^{21} m^{-3}$) and low temperature ($T_e \approx 1$ eV) plasmas [3]. In this paper we describe a theoretical model capable of explaining the main features of measured spectrum, the smooth D-C transition in particular. The changes in spectral characteristics with plasma density and temperature variation will be discussed. The calculated and measured spectra for a typical detached divertor discharge in C-Mod will be compared.

D-C spectrum transition. Fig.1 illustrates the smooth D-C transition in a fragment of Balmer spectrum calculated for a deuterium plasma. The basic components of spectrum are shown: Balmer series of lines D_k (index k corresponds to the radiative transition from level $n' = k + n^{pr}$ to level $n^{pr} = 2$, n with any index is the principle quantum number), Balmer (BPRC) and higher-series (HPRC) photo-recombination continua, and bremsstrahlung (BR). As seen, in the direction of shorter wavelengths (λ) the intensities of lines gradually decrease, the lines become increasingly broader, overlap and finally immerse into the continuum. At the same time the BPRC extends above its ideal limit (at $\lambda^{bprc} = 364.6$ nm) towards longer λ. To explain the observed spectra it is not enough to incorporate the Stark broadening of the spectral lines [4]. It is also necessary to take into account the mechanisms which reduce the intensities of lines near the series limit and simultaneously make allowance for continuum emission at wavelengths above the ideal PR limit. Such mechanisms have been found to be connected with the decay of atomic levels caused by statistical plasma microfields (SPM) and have been discussed in many papers [3,5,6] with respect to the separation of free and bound states and obtaining the convergent expression for atomic partition function.

Collisional radiative model for D-C transition. Our theoretical model is comprised of three parts: (i) a collisional-radiative (CR) model for population densities of excited states, (ii) atomic structure and collision rates for an atom affected by SPM, and (iii) a model for calculating the line profiles and the extended PR continuum.

The population model is based on the CR theory developed by Bates et al [7]. The Collisional Radiative Atomic Molecular code, CRAMD [8], solves a system of coupled rate equations which describe the kinetics of population and de-population of quantum states (n resolved) of an atom in the quasi-stationary approximation [7] and under assumptions that plasma is transparent to all radiation and that the local velocity dis-

tribution functions of plasma and gas particles are Maxwellian. An important feature of the CRAMD code is a self-consistent incorporation of SPM effects in a manner discussed below.

SPM effect on atomic structure. The energy u and ionization frequency γ of each Stark component are strong functions of the parabolic quantum numbers q and the electric field strength f. To describe these dependencies we use the analytical expressions $u(q, f)$ and $\gamma(q, f)$ derived in [9]. There exists a certain critical value f_c for the external field at which the potential barrier for a bound electron in an atom disappears. We calculate f_c by solving the equation: $\gamma(q, f_c) = \nu_o(q)$, where ν_o is the Bohr frequency of electron revolution. It is well established [3,6] (i) that with respect to field ionization, the SPM produced by ions are quasi-static; (ii) that the distribution function $\theta(pp, f)$ of SPM is described by a Hooper distribution [10] with implicit dependence on a set pp of plasma parameters, and (iii) that the existence of microfields with $f \geq f_c$ results in the reduction of the statistical weight (SW) of a level. We introduce the SW correction factor δ_q as the survival probability of sublevel q in SPM. It is calculated by integration of $\theta(f)$ over microfield strengths from 0 to $f_c(q)$. The correction factor δ_n of level n is a sum over all its Stark components divided by $2n^2$. The highest existing level m is that with $4m^2\delta_m \approx 1$. The dependence of δ_n on ion density N_i is given in Fig.2. A strong decrease in SW occurs when the ion separation ρ_i $(4\pi\rho_i^3 N_i/3 = 1)$ is about the radius of n-th Bohr orbit.

SPM effect on collision rates. An important part of the CR model is a set of semiempirical formulae representing the rates of state-to-state excitation, ionization and recombination, and the probabilities of radiative transitions. For hydrogen the CRAMD code incorporates the complete and consistent set of rate formulae developed in [11]. To include the SPM effects these formulae are modified by taking the advantage of the ions microfields being statistical and quasi-stationary. In the most simplified version the ionization rate takes the form $r_n^{ion}(pp) = (\delta_n)^{-1} \sum_{i=n}^{m}(\delta_i - \delta_{i+1})R_i^{ion}(T_e \mid i + 1)$, PR rate $r_n^{pr}(pp) = \sum_{i=n}^{m}(\delta_i - \delta_{i+1})R_i^{pr}(T_e \mid i+1)$, and excitation rate $r_{n,n'}(pp) = (\delta_n - \delta_{n'})R_{n,n'}(T_e \mid m)$, where $R(T_e \mid n_d)$ denotes Johnson's [11] rate expression derived under the condition that the ionization threshold is lowered to n_d level. The modified expressions take into account both the increase of the oscillator strength coupled to the continuum and the reduction of ionization potential. Thus the effective rates are functions of many plasma parameters pp. The destruction of upper levels causes an increase in the ionization and recombination rates for lower levels.

Profiles of lines and the continuum. Standard theory [12] of line broadening by plasma is used in the calculation of Stark profile. The contribution of ions is described in the quasi-static (QS) approximation. The QS profile, obtained by using the ion SPM distribution $\theta(f)$ and the inverse function $\hbar\omega_{q \to q'} = u(q', f) - u(q, f)$ within the range $0 < f < f_c(q)$, includes the multi-Stark broadening effects. The impact approximation is used to calculate the electron contribution. The Stark profile of spectral line is a sum over all dipole transitions between the Stark components of an appropriate pair of quantum levels. Here we assume complete mixing between Stark components within the n_q level, that is, sublevels are populated according to their real SW. The total profile of

a spectral line is calculated as a simple convolution of profiles caused by Stark, Doppler, electrodynamic and instrumental broadening mechanisms. The final profile of a given line is renormalized to have the integral intensity equal to the intensity calculated by the CRAMD code. In the presence of SPM the PR continuum, associated with free-bound transition to n^{pr} level, splits into multiple continua. Each subcontinuum corresponds to the destruction of n-th level ($n^{pr} < n < m+1$) with probability $(\delta_{n-1} - \delta_n)$ and to the ionization potential lowering up to this level. In the calculation of its spectral distribution we use Johnson's [11] formulae and take into account the instrumental broadening.

Results. The previous analysis [1] of Balmer spectrum, measured from the detached plasma in C-Mod divertor has shown that in the R-region (where the strong plasma recombination occurs) $T_e = 0.75 \div 1.5$ eV and $N_e = (0.8 \div 1.6)10^{21} m^{-3}$. For N_e and T_e in this range we use the CRAMD code to calculate, under different model assumptions, the population densities (PD) of excited states for deuterium atom. The dominant population mechanism of states with $n > 3$ is the conventional 3-body recombination (C3BR). Excitation of atoms from the ground state and molecular activated recombination [8] can strongly effect on the population of lower states. The effect of plasma microfields on densities of excited states populated by C3BR is shown in Fig.3. Without SPM the population densities monotonously increase with level number n. Exactly the same behavior gives the Saha-Boltzmann (SB) distribution for levels for $n > 3$. As expected, the incorporation of SPM results in a strong decrease in the density of upper states with $n > 15$ with respect to SB population. The destruction of atomic states with $n > 8$ significantly increases the intensity of PR above λ^{bprc} as it is shown in Fig.4. With the increase in plasma density, more and more radiation from Balmer lines transforms into the continuum radiation, and, in the limit of ultra-high densities, the BPRC can spread to the whole series range. At the same time, for $N_e < 10^{22} m^{-3}$ the ratio of continuum intensities in the points 452 and 358 nm, used in [1] for plasma temperature estimation, is a strong function of T_e and depends slightly on N_e. Finally, we performed a series of runs in order to fit the measured C-Mod spectrum arround the λ^{bprc} PR edge. The best agreement with experimental data (see Fig.5) is provided the run with the following plasma parameters in R-region: $T_e = 0.8$ eV and $N_e = 2 \times 10^{21} m^{-3}$. The correction of about 0.13 units of continuum is made for contribution of radiation that comes from the core plasma and from the hotter region of the divertor plasma ($T_e \geq 2$ eV and $N_e \leq 10^{21} m^{-3}$).

References: [1] D. Lumma et al, to appear in July, *Phys. Plasmas* (1997). [2] S.I. Krasheninnikov et al, *Phys. Plasmas* 4, 1638 (1997). [3] V.E. Fortov, I.T. Yakubov, *Physics of Nonideal Plasma*, chapter 7, NY, Hemisphere Pub. (1990). [4] B.L. Welch et al, *Phys. Plasmas* 2, 4246 (1995). [5] V.S. Vorob'ev et al, *Sov. J. Plasma Phys.* **3-4**, 499 (1977). [6] V.T. Gurovich et el, *Sov. Phys. JETP* 45, 232 (1977). [7] D.R. Bates et al, *Proc. Roy. Soc.* 267 A, 297 (1962). [8] A.Yu. Pigarov et al, *Phys. Lett. A* 222, 251 (1996). [9] N.Hoe et al, *Phys. Lett. A* 85, 41 (1965). [10] C.F. Hooper, *Phys. Rev.* 149, 77 (1966). [11] L.C. Johnson, *Astroph. J.* 174, 227 (1972). [12] H. Griem, *Spectral Line Broadening by Plasmas*, Academic, NY (1974).
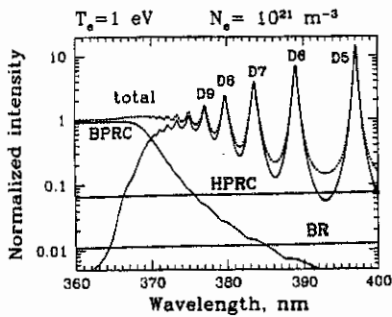
Fig. 1
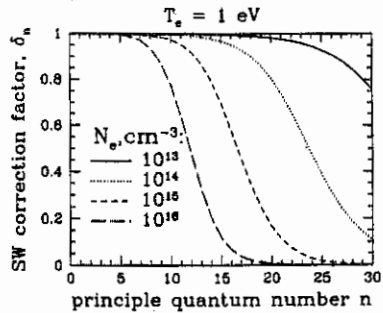
Fig. 2
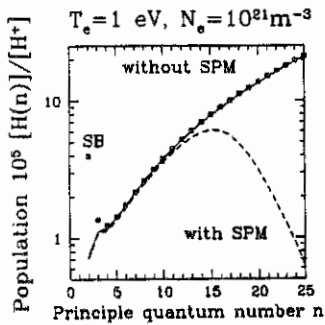
Fig. 3
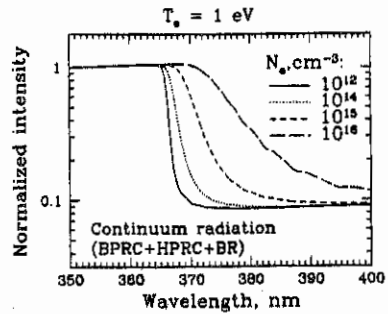
Fig. 4
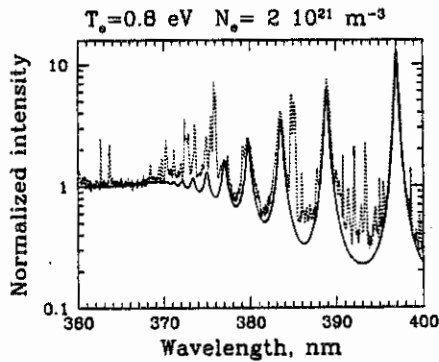
Fig. 5

SOL POWER AND PRESSURE BALANCE IN ALCATOR C-MOD

C. S. Pitcher, J A Goetz, B LaBombard and B Lipschultz

MIT, Plasma Science and Fusion Center, NW17, Cambridge, MA, 02139, USA

1. Introduction

In this paper we compare the results of a simple model of scrape-off layer (SOL) power and pressure balance, with detailed plasma measurements in the Alcator C-Mod tokamak. The model is based on the commonly used 'Two-Point Model', but includes significant additions (described in detail in a recent review article [1]). The present paper should be considered as a companion to an earlier publication [2], where similar data from the ASDEX-Upgrade tokamak was presented.

2. Power Balance

We assume that power flows along field lines in the SOL with a density q_u from the upstream stagnation location to the divertor by electron heat conduction,

$$T_u^{7/2} - T_t^{7/2} \simeq \frac{7 q_u L}{2 \kappa_0} \tag{1}$$

where L is the connection length ($\simeq 8m$), T is the plasma temperature (we assume $T_i = T_e$), κ_0 is a constant and 'u' and 't' denote the upstream (we assume outer mid-plane) and (outer) target plate locations, respectively.

In Eqn. 1 we have assumed that the parallel power is nearly constant over most of the length of the flux tube. This is approximately valid, as detailed calculations have indicated, even in cases with high radiation on open surfaces, since such radiation tends to be localized near the divertor where densities are elevated. Although simple analytic estimates of such radiative loss based on 1-D modelling can be used [1,2], assuming for example, constant impurity radiation coefficients and impurity fractions, the associated error is significantly larger than other uncertainties implicit in the simple modelling. We therefore take the experimentally determined radiative loss near the divertor as an input to the model, i.e. q_{rad}.

The boundary condition at the target plate is

$$q_t = n_t c_{St}(\gamma T_t + \epsilon_{pot}) \tag{2}$$

where, q_t is the parallel power density at the target plate ($q_t = q_u - q_{rad}$), c_{St} is the ion acoustic speed and $\gamma = 7$ is the sheath power transmission factor. ϵ_{pot} is the potential energy associated with each ion reaching the plate, including atomic and molecular recombination ($\epsilon_{pot} \simeq 16eV$).

3. Neutral Dynamics

We allow for the loss of plasma pressure by ion neutral friction in a thin recycling region close to the divertor plate. The pressure loss factor, f_m, is given by,

$$f_m \equiv \frac{2 n_t T_t}{n_u T_u} = 2\left(\frac{\alpha}{\alpha + 1}\right)^{\frac{\alpha+1}{2}} \tag{3}$$

where,

$$\alpha \equiv \frac{< \sigma v >_i}{< \sigma v >_i + < \sigma v >_m} = f(T_t) \tag{4}$$

where $< \sigma v >$ are the rate coefficients for ionization (i) and momentum loss (m), including both elastic and charge-exchange collisions, given by [3]. Eqns. 3 and 4 were originally derived for gas discharge theory [4]. We assume an isothermal plasma temperature in the recycle region.

The neutral density in the recycle region n_H is related to the parallel scale-length of the region L_H, according to [1],

$$n_H L_H = F(T_t) \equiv \frac{c_{St}}{< \sigma v >_i + < \sigma v >_m} \left(\frac{\alpha + 1}{\alpha^{1/2}} \arctan \alpha^{-1/2} - 1 \right) \tag{5}$$

The parallel scale-length is determined using,

$$L_H = \frac{\lambda_H}{sin\theta} \tag{6}$$

where θ is the field line pitch angle at the plate and λ_H is the poloidal penetration distance from the plate of recycled neutral atoms based on charge-exchange diffusion [5],

$$\lambda_H = \left(\frac{8T_t}{3\pi m < \sigma v >_i < \sigma v >_m} \right)^{1/2} \frac{1}{n_r} \tag{7}$$

where $n_r = 2n_t/f_m$ is the density at the entrance of the recycle region.

Typically in experiments, rather than n_H in the plasma, one diagnoses the molecular gas adjacent to the divertor fan,

$$\phi_{mol} = \frac{\phi_H}{2} = \frac{1}{8} n_H \bar{c}_H \tag{8}$$

where the ϕ's are the molecular ('mol') and atomic ('H') flux densities and $\bar{c}_H$ is the mean thermal speed of atoms in the fan based on the plasma temperature T_t. We have assumed that atom fluxes out of the fan are balanced by molecular fluxes back into the fan and that other net particles sources and sinks are small in comparison to this exchange.

4. Experiment

The model is compared with experimental results from the Alcator C-Mod tokamak. The SOL plasma density and temperature are measured at the upstream and outer target plate locations with Langmuir probes. The molecular flux density outside of the plasma fan in the divertor is determined using an absolutely calibrated capacitance manometer. The radiated power in the divertor is deduced using multiple chords of bolometer cameras. The experimental results presented here consist of Ohmic discharges at various densities without boronization with $I_p = 0.8MA$, $B_t = 5.4T$ and vertical outer plate geometry.

In Fig. 1 we compare the experimentally determined pressure loss factor f_m at the outer plate on a number of flux surfaces (denoted by their ρ values, mapped to the outside mid-plane) with the prediction of Eqns. 3 and 4. Reasonable agreement between model and experiment is obtained, with strong pressure loss for $T_t < 5eV$ and no pressure loss for $T_t > 10eV$. In particular, the rapid decrease in f_m at low T_t is strong evidence that atomic physics processess are responsible. In the case of neutral friction, this results from the rapid decrease in ionization rate $< \sigma v >_i$ compared with charge-exchange rate $< \sigma v >_m$. Fig. 1, however, may also be consistent with other atomic processes being responsible, for example, volume recombination, which

also has a strong temperature dependence and whose signature has recently been observed in C-Mod [6,7].

The fact that f_m values on different fluxes surfaces are coincident, is perhaps surprising, given the 1-D nature of the model. This is reasonable, however, since plasma flow in the recycling region is primarily along field lines, from ionization source close to the plate to the surface sink, with cross-field transport of plasma being of minor importance.

The full model is now compared with experiment in Fig. 2, as a function of line-average density $\overline{n}_e$ for conditions on a flux surface near the separatrix, $\rho = 1mm$. Two fitting parameters are used in this modelling – the radiated power, as mentioned above, is taken from experiment, and the relation between the upstream density and $\overline{n}_e$, where we make the approximation $n_u = \overline{n}_e/3$. Thus, the 'good fit' between model and experiment in Figs. 2a and 2b is artificial. From global power balance and measurements of the mid-plane radial plasma profiles, $q_u \simeq 75 MWm^{-2}$, which is assumed fixed in the modelling, approximately consistent with experiment.

Fig. 2c, 2d, 2e give the model prediction and experimental results for the target plate conditions, n_t, T_t and p_t, and the upstream conditions T_u and p_u, where $p_{t,u}$ are the total electron pressures. The data clearly exhibits three characteristic regimes – the linear/sheath-limited regime at low density, the high recycling regime at moderate density and the detached regime at high density [1,8]. The linear regime has nearly isothermal conditions between the upstream location and the target plate, with $n_t \propto \overline{n}_e$ and no pressure loss along field lines. In the high recycling, large parallel temperature gradients develop, the target density rises rapidly with discharge density, $n_t \propto \overline{n}_e^3$, and no pressure loss is observed, since $T_t > 10eV$. In the detached regime, the T_t drops below 5 eV and significant pressure loss becomes possible, which results in a 'roll-over' of the target plate density n_t.

The model also gives the molecular flux density outside of the fan, ϕ_{mol}. One notes this continues to rise, throughout all regimes, following in the linear regime $\phi_{mol} \propto \overline{n}_e$, $\phi_{mol} \propto \overline{n}_e^3$ in the high recycling and continuing to rise in the detached regime. It may be, at first sight, surprising that atomic and molecular fluxes should continue to increase in the detached regime, despite a decrease in plasma ion density (and fluxes) at the target plate. The high neutral density is explained, after consideration of ion particle continuity, by the need to supply enough ionization in the face of a strong decrease in the ionization rate at low plasma temperatures [1,9].

References

[1] C S Pitcher and P C Stangeby, Plas Phys Contr Fus (1997), in press

[2] C S Pitcher et al, EPS Proceedings (Bournemouth, 1995) III-245

[3] R K Janev et al, Elem Proc in H-He Plas, Springer-Verlag, Berlin (1987)

[4] S A Self and H N Ewald, Phys. Fluids 9 (1966) 2486.

[5] B Lehnert, Physica Scripta 12 (1975) 327

[6] D Lumma et al, Phys Plas (1997), in press

[7] J L Terry et al, these proceedings

[8] B LaBombard et al, Phys Plas 2 (1995) 2242

[9] A Niemczewski et al 37 (1997) 151

Fig. 1

Fig. 2

Figures showing f_m versus T_t (eV) with model fit (Fig. 1), and panels (a)–(f) plotting $P_{rad,div}/P_{SOL}$, n_u (m^{-3}), n_t (m^{-3}), T_e (eV), p_e (Pa), and ϕ_{mol} ($m^{-2}s^{-1}$) versus $\bar{n}_e$ (10^{20} m^{-3}), each divided into linear, high recycle, and detached regions.
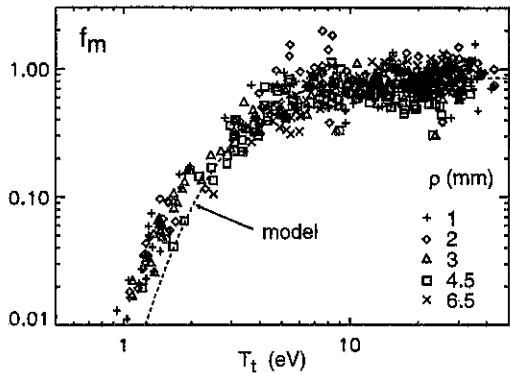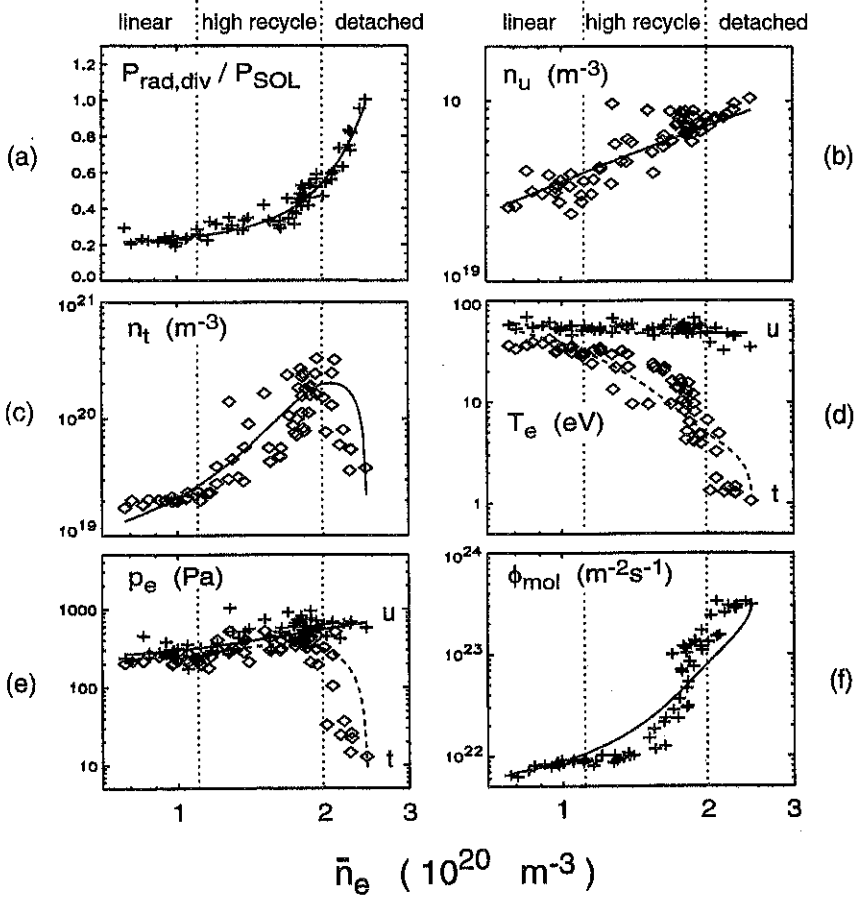
Transport Barriers and Bifurcations in off-axis ECR heated discharges in RTP

M.R. de Baar, P. Galli[1], G.M.D. Hogeweij, N.J. Lopes Cardozo, P. Mantica[2], A.A.M. Oomens, F.C. Schüller and the RTP team

FOM-Instituut voor Plasmafysica "Rijnhuizen", Association Euratom-FOM, Trilateral Euregio Cluster
P.O. Box 1207, 3430 BE Nieuwegein, the Netherlands
[1] INFM and Dipartimento di Fisica, Università degli Studi di Milano, Milano, Italy
[2] Instituto di Fisica del Plasma, Ass. EURATOM-ENEA-CNR, Milano, Italy

This paper focuses on recent experiments with strong off-axis ECH in RTP. Such discharges show very sharp transitions in confinement with minor variations in either the plasma current I_p or the (normalized) ECH deposition radius ρ_{dep}. [1]
CW Off-axis heating
In Fig. 1 an experiment ($I_p = 80\,\text{kA}$, $n_e(0) \approx 4. \times 10^{19}\text{m}^{-3}$) is presented in which ρ_{dep} is ramped by increasing the toroidal magnetic field B_ϕ within one discharge. By focussing, the cross-section of the micro-wave beam has been reduced to a diameter of 2 cm. The central electron temperature $T_e(\rho = 0)$ as obtained from ECE is plotted vs. time. If electron thermal transport were a smooth function of plasma parameters and position, a steady decrease of $T_e(0)$ would be observed as ρ_{dep} is gradually moved outwards. However, stepwise changes in $T_e(0)$ are observed: intervals with nearly constant $T_e(0)$ end in sudden drops. The oscillation in $T_e(0)$ between 220 to 250 ms is due to MHD-activity. The position observed by the ECE-channels changes with B_ϕ; $T_e(0)$ was obtained from spline interpolation of a few channels. Distinct classes of $T_e(\rho)$ can be identified. [1] A few of them are shown in Fig. 2.
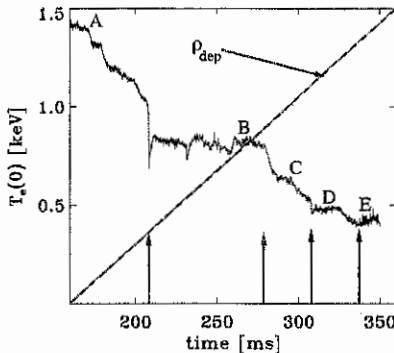
FIG. 1. $T_e(0)$ and ρ_{dep} for a discharge in which ρ_{dep} is being swept through the plasma and varies between 0.2 and 0.6. Note, that the adaption of the T_e- profile occurs within small intervals of the steering parameter (arrows). ECH is switched off outside the presented time-window.
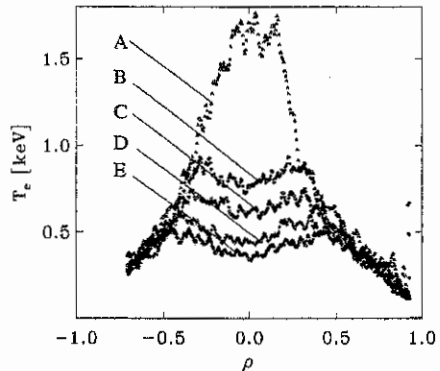
FIG. 2. $T_e(\rho)$ as measured by Thomson scattering for different phases of a ramped ρ_{dep} experiment. Note that the outer part of the profiles remains unchanged during the experiment.

As the off-axis ECH is applied at sufficiently large ρ_{dep}, $\rho_{\text{dep}} > 0.4$, the current density profile $j(\rho)$ broadens, the central Ohmic power deposition decreases and $T_e(0)$ decreases until $T_e(\rho)$ becomes hollow and the plasma develops negative central shear (NCS). The remainder of this paper focuses on the regimes (b) to (e) in Fig. 2. Fig. 3 shows $T_e(\rho = 0, t)$ traces for seven subsequent shots close to the transition between (d) and (e). Initially, the

traces form a continuum, but after 30 ms two discrete levels in $T_e(0)$ are formed. These two levels in $T_e(0)$ correspond to two distinct classes of hollow $T_e(\rho)$. Whether the plasma takes the high or low branch is determined by the value ρ_{dep}, where the transition from one class to the other is as sharp as $\delta\rho_{dep} < 0.01$, corresponding to $< 2\,mm$ in the plasma (see Fig. 4). The T_e and p_e profiles show a narrow transport barrier (a thin region in which the turbulent transport is quenched) in the high confinement branch (d), which is absent in the low branch (e) [3].
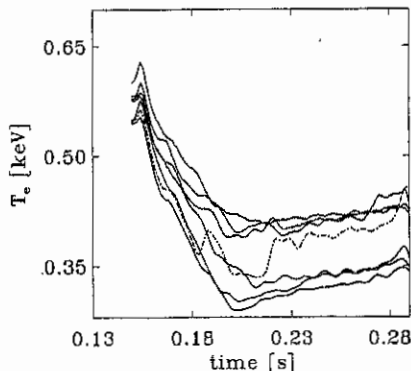
FIG. 3. Evolution of $T_e(0)$ as measured by ECE in 7 nearly identical discharges after switch on of ECH at $t = 150\,ms$, showing the two levels of confinement. The subtlety of the distinction between these levels is illustrated by one discharge (dash-dotted) that crosses over from the low to the high branch.
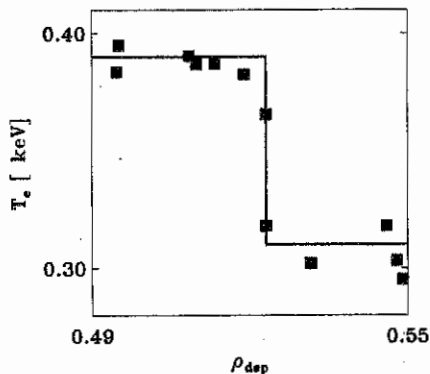
FIG. 4. High $(T_e(0) \approx .4\,keV)$ and low $(T_e(0) \approx .3\,keV)$ branch of confinement discharges are separated by ρ_{dep}. The sharp transition corresponds to a difference of ρ_{dep} of 0.01. The discharge that crosses over sits exactly at this transition.

When fixing ρ_{dep} and varying the plasma current similar transitions can be induced on the plasma. As an example, in Fig. 5 $T_e(0, t)$-traces are presented for discharges in which ρ_{dep} is fixed and I_p varies in the range from 80 to 101 kA. The ECH-system is switched-on at $t = 175\,ms$. Before switch-on the differences in Ohmic input power lead to differences in $T_e(0)$. Again the system evolves into two separate regimes after switch-on. Fig. 6 shows $T_e(0, t = 280\,ms)$ vs. I_p. The transition is again extremely sharp, $\delta I_p \leq 2\%$ separating the two regimes. The discharges with $I_p \leq 93\,kA$ evolve to hollow $T_e(\rho)$, and the discharges with $I_p \geq 93\,kA$ evolve to flat $T_e(\rho)$. After switch-off, the two regimes remain separated. Two equilibrium profiles exist for the Ohmic phase of the discharge. The the low I_p-discharges develop profiles that are flat within $\rho < .3$, whereas the high I_p-discharges develop 'normal' T_e profiles for Ohmic discharges.

Modulated Off-axis heating

Heat pulse analysis complements the steady-state power balance analysis [4]. It allows the separation of components of the heat flux driven by diagonal and off-diagonal elements in the transport matrix. Modulated ECH has been used to further investigate the transport barriers. For this purpose, the gyrotron was modulated 100%, with a duty cycle of 80%. In this way the net heating effect was almost the same as with CW ECH, while heat pulses of sufficient amplitude were induced. The modulation frequency of the gyrotron was 312.5 Hz

In Fig. 7 the outcome of a ramped ρ_{dep} experiment is presented for $T_e(\rho = 0.0)$ (dashed) and $T_e(\rho = 0.5)$ (full). The sharp transitions in confinement were clearly borne out by the heat pulse propagation. Sudden changes in the propagation of the MECH-induced heat pulses were observed, indicative of changes in electron thermal transport. These sudden

changes coincide with the sudden drops in $T_e(0)$ as presented in Fig. 1. Interestingly, the amplitudes of the two traces show an asymmetric behavior: At the instant of changes in thermal transport, the amplitude of the central temperature modulation decreases and the amplitude of the temperature modulation at half radius increases. This behavior indicates that also here a barrier is crossed and lost.
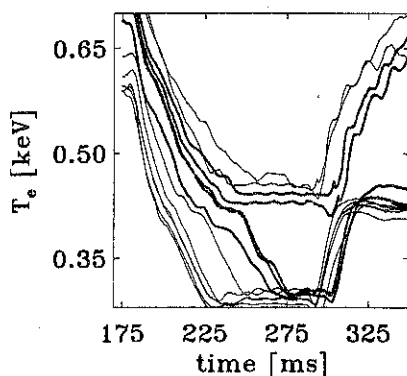
FIG. 5. Evolution of $T_e(0)$ as measured by ECE in discharges for which ρ_{dep} was fixed and I_p was scanned. ECH was switched on at $t = 150$ ms. Again two levels of confinement develop.
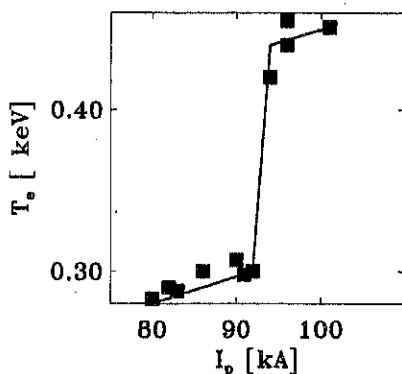
FIG. 6. High $(T_e(0) \approx .4$ keV$)$ and low $(T_e(0) \approx .3$ keV$)$ branch of confinement discharges are separated by ρ_{dep}. The sharp transition corresponds to a difference of $\delta I_p \leq 2\%$.

Figure 8 shows a comparison of the phase and amplitude profiles as measured with ECE, for two discharges in the profile classes B and C, respectively (see Fig 1). These measurements provide evidence for a transport barrier near $\rho = 0.25$, i.e. in between the amplitude maxima (or the phase minima). The evidence consists of the large phase jump and amplitude attenuation when the heat pulse crosses the barrier, which is observed for deposition both inside and outside the barrier.
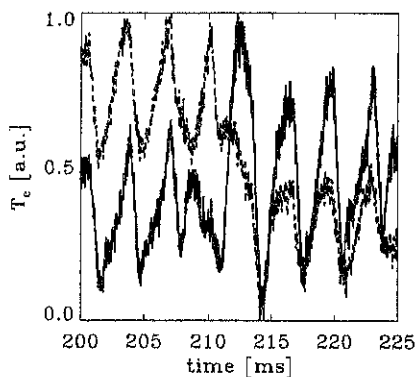
FIG. 7. $T_e(0)$ (dashed) and $T_e(0.5)$ (full) during a ramped ρ_{dep} experiment with increasing ρ_{dep}. The ECH-power was modulated. Note, that before the transition at $t = 210$ ms, $T_e(0)$ shows large excursions as compared to the excursions after the transition. The time average of $T_e(0)$ decreases after the transition. For $T_e(0.5)$, the excursions and the timeaverage increase after the transition.

Summary and Discussion

The presented observations evidence a non-linear response of the plasma to the off-axis heating, and cannot be explained with a local transport model featuring a smooth profile of the diffusivity. Sharp transitions have been reported for slight I_p variations, slight ρ_{dep}

variations and the ρ_{dep}-ramp.

The T_e-profiles show that outside ρ_{dep} the profiles do not change after the transitions in confinement. The heat flow is constant, ∇T_e and n_e remain unchanged and consequently χ_e remains unchanged. Sofar, the data indicates that for all of the regimes, barriers for thermal transport exist or are formed, crossed and lost as ρ_{dep} is shifted through the plasma. A local transport model in which $\chi_e(\rho)$ features sharp dips near rational q-surfaces in regions of low shear, can be used to analyse these data.

A first attempt has been put forward to classify several regimes in terms of transport barriers. The ρ_{dep}-scan indicates a wide variety of classes of T_e-profiles to exist [1], all of which have to be analysed. The analysis will benifit form the ECE-imaging system currently being installed at RTP.
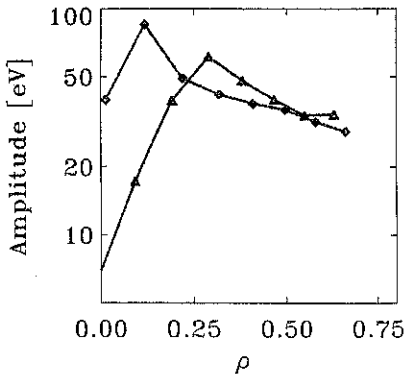
FIG. 8. Amplitudes (first harmonic) of B-type (diamonds) and C-type profiles (triangles). The data evidences a transport barrier between the amplitude maxima around $\rho = 0.25$.
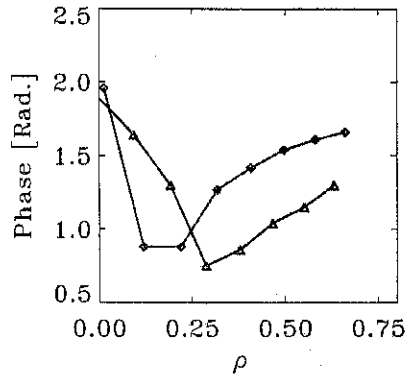
FIG. 9. Phase profiles for B-type and C-type profiles. The existence of the barrier is corroborated by the significant phase jump, which is observed for deposition both inside and outside the barrier

[1] N.J. Lopes Cardozo et al, this conference
[2] G.M.D. Hogeweij et al, Phys.Rev.Lett. **76** (1996) 632
[3] M.R. de Baar et al, Accepted for publication in Phys.Rev.Lett.
[4] P. Mantica et al, Nucl. Fusion **36** (1996) 1317

Disruption Studies with Active Triggering of Thomson Scattering in RTP

F. Salzedas†, S. Hokin†, M.N.A. Beurskens, H.J. van der Meiden,
A.A.M. Oomens, Th. Oyevaar, F.C. Schüller, and the RTP team

FOM-Instituut voor Plasmafysica `Rijnhuizen', Association EURATOM-FOM, Trilateral
Euregio Cluster, Nieuwegein, The Netherlands
† Alfvén Laboratory Division of Fusion Plasma Physics, Association EURATOM-NFR,
Royal Institute of Technology, Stockholm, Sweden

Introduction It is well known that if the electron density in a limiter tokamak discharge is increased freely, a sequence of instabilities will develop in the plasma in such a way that the discharge is abruptly terminated with a density limit disruption. Although the general picture of the time evolution of the density limit disruption is more or less clear, the details of the interaction between the instabilities, the changes in the complex structure of the plasma that lead to the disruption, are still unclear [1].

In experiments done with the purpose to study the energy quench phase of an Ohmic density limit disruption, a set of advanced electron diagnostics available on RTP such as a high spatial resolution Thomson scattering system (TS) [2] and a 20 channel ECE radiometer with a temporal resolution of 2 μs, were used.

To achieve the disruptions the density was ramped in He discharges, using a methane gas puff with I_p=100 kA, B_φ=2.15 T and q_a=4. The TS system was triggered on a magnetic signal, representative of the m=2 power, which increases prior to disruption.

During these discharges MHD activity developed in two distinct ways. One with slow growth of MHD activity and other with fast growth of MHD activity that ends at a much higher density than the former. Since the nature of the second type is not yet clear, we will concentrate on the first type. These disruptions were always preceded by a radiative contraction of the current channel, which strongly destabilized the q=2 surface, allowing a big m=2/n=1 magnetic island to grow slowly and destabilize a m=1/n=1 mode in the core of the plasma. Attention will be focused on thermal quenches, since their study is the main objective of this work.

The presence on the electron temperature profile of a m=3/n=2 mode in the precursor phase of the thermal quench was observed at RTP. This mode, predicted by Bondeson *et al.* [3] was also observed in other tokamaks, however by other diagnostics [4,5].

Minor disruption In fig.1 the time evolution of the ECE radiation temperature, along with the oscillatory component of $B_\theta(r=a,\theta=0)$, obtained along a horizontal chord, is shown during 2 ms. The first 0.5 ms show clearly an m=1/n=1 mode in the hot core of the plasma, surrounded by a big and cold m=2/n=1 island situated at 0.5≤ |r/a|≤1. The two modes evolve in time such that the hot part of the 1/1 mode is aligned with the cold O point of the 2/1 cold island at the high field side (HFS). In between them the plasma exhibits a steep temperature gradient as shown by the closely distributed equal-interval isothermals around |r/a|=0.4. This region acts as a thermal barrier, separating the hot plasma core from the surrounding colder plasma.

At 236.62 ms the thermal quench of the minor disruption starts, with the characteristic decrease of central temperature and consequent increase at the edge. Three points are worth noticing at this stage. Firstly, a few microseconds before the thermal quench, isothermals start leaving the thermal barrier indicating that it is already leaking heat. According to Bondeson *et al.* [3], the good flux surfaces that form the thermal barrier start to be damaged at this moment. Secondly, the core of the hot m=1/n=1 mode remains hot for ~ 40 μs after the quench, indicating that the magnetic structure of the mode is still good enough to provide energy confinement, while the surrounding plasma is cooling. Thirdly,

the amplitude of the magnetic signal from the m=2/n=1 island only diminishes gradually after the quench, although the island is being crossed by a heat wave coming from the core of the plasma. After the quench the thermal barrier closes again and the core is able to reheat.
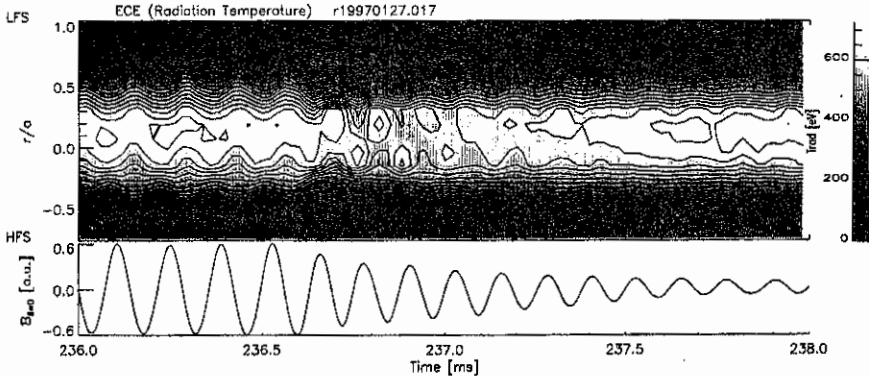
Fig.1- Time evolution of ECE radiation temperature and $\tilde{B}_\theta(r=a,\theta=0)$, during a minor disruption.

Major disruption As in fig.1, fig.2 shows the time evolution of electron radiation temperature, before and during the thermal quench of a major disruption.
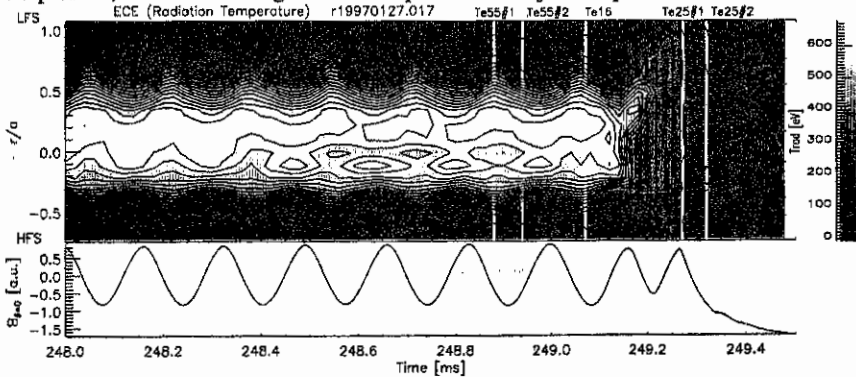
Fig.2- Time evolution of ECE radiation temperature and $\tilde{B}_\theta(r=a,\theta=0)$, during a major disruption. The 5 vertical lines across the ECE profile, indicate the relative position between the thermal quench and the time of the Thomson profiles of the indicated discharges.

At RTP the rotating MHD modes never lock completely to the wall. However the quench occurs when the 2/1 mode, which starts rotating with a frequency of ~10 kHz, slows down to a frequency of ~ 5 kHz. Apart from this, the global picture is in all identical to the minor disruption, except for the fact that the thermal barrier is now completely destroyed. Bondeson et al. conclude that the non linear coupling of large 1/1,3/2 and 2/1 modes breaks up the good magnetic surfaces isolating the q≈1 region from the stochastic region around q=2.

Due to low spatial resolution, it is impossible to recognize on the ECE temperature profile of fig.2 any kind of pattern that could indicate the presence of a 3/2 mode. A 3/2 structure can be resolved, however, by high-resolution TS, as demonstrated by Te profiles

in fig.3 a) and 4 a) taken before the energy quench. These profiles are along a vertical chord that is toroidally displaced 15° from the ECE diagnostic, and 180° from the Mirnov coils. Fig.2, 3 and 4 a) belong to three separate discharges that ended with similar Ohmic density limit disruptions.
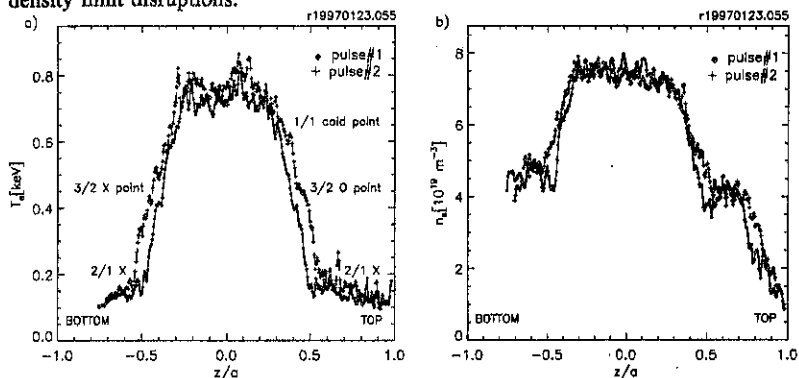
Fig.3- Electron, temperature (a) and density (b) Thomson scattering profiles before a major disruption with a time interval between the two pulses of 60 μs. For clarity, the location of the modes is indicated just for the second pulse.

The two profiles of fig.3 a) belong to the same discharge and were obtained with the double pulse TS, with a time interval between pulses of 60 μs. Since the period of rotation of the 2/1 mode is 170 μs and the pulse #1 was taken at the time the O point of the 2/1 mode passed in front of the TS, pulse #2 shows the profile half way between the 2/1 O point and the closest 2/1 X point. The Te#2 profile is therefore broader. Relative to the 1/1 mode, the Te#1 was taken when the 1/1 cold point was at the HFS and, consequently, the 1/1 hot point at the LFS. Since TS measures across a vertical chord the Te#1 profile of the 1/1 mode should be symmetric. After 60 μs Te#2 should show the 1/1 cold point above the 1/1 hot point on the Te profile. That is observed, as indicated in fig.3 a).

Having localized the 1/1 and 2/1 modes, knowing q_a and using the fact that the modes are phase locked, if a 3/2 mode exists it should show its O points at |r/a|~0.4 on Te#1, and due to the deformation caused by the 2/1 X point, Te#2 should show the 3/2 O point on top and 3/2 X point on bottom. That is indeed what is observed as is signed in fig.3 a). It is also visible that the 3/2 mode on Te#2 is pulled outwards, due to the deformation induced by the big 2/1 mode and is lifted up indicating that close to the 2/1 X point the 3/2 O point is hotter than when it passes close to the 2/1 O point. A temperature gradient exists along the 3/2 mode.

On the Te TS profile of fig.4 a) the presence of the 3/2 mode is even more clear. This profile was obtained just 160 μs before the onset of the thermal quench (approximately one period of the 2/1 mode).

In fig.3 b) the electron density TS profiles, from the corresponding Te TS of fig.3 a) are shown. A clear density minimum can be observed at the inner separatrix of the 2/1 island which implies a local density maximum at the center of the island, as has been observed at TEXTOR [6]

Returning to the ECE temperature profile of fig.2, it shows an asymmetry in the evolution of the thermal quench, also called the 'erosion' of the temperature profile which has been observed in other tokamaks [1]. Following the time evolution of the 1/1 mode, it comes out that the hot plasma in the core which keeps its temperature the longest during the thermal quench, is part of the hot core of the 1/1 mode. As in the minor disruption, this indicates that the structure of the 1/1 mode is still able to provide energy confinement,

while the surrounding plasma is cooling faster. Since, at RTP, the modes do not lock to the wall this hot 'tip' of the 1/1 mode can be in any position, depending on the phase of the 1/1 mode on the onset of the thermal quench.
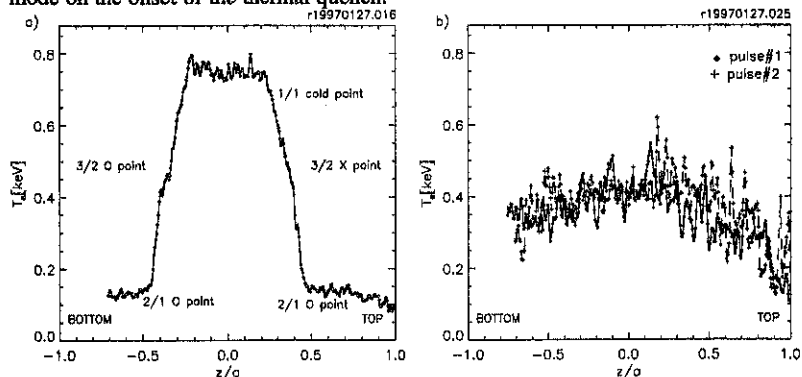
Fig.4- Electron, temperature Thomson scattering profiles a) 160 µs before the onset of the thermal quench and b) at the end of the 'erosion' phase of the thermal quench.

· Fig.4 b) shows the electron temperature profile of the end of the 'erosion' phase of the energy quench. As expected the profile is almost flat along all the TS line of sight, except for the upper part, where the plasma is already cooling. It should be noted that the temperature of 400 eV is higher than the 200 eV measured by ECE. This discrepancy has been observed in all the thermal quenches and it is not yet understood.

Conclusions Using the geometrical structure of the m=2/n=1, m=3/n=2 and m=1/n=1 MHD modes, together with the ECE radiation temperature profiles, the magnetic signals from the Mirnov coils and the fact that the modes are phase locked, it was possible to identify the presence of the m=3/n=2 MHD mode. This shows up in the electron temperature profiles, taken immediately before the energy quench of a density limit disruption, with a high resolution Thomson scattering diagnostic. The 3/2 mode in the precursor phase of a density limit disruption has been detected in other tokamaks, more indirectly with magetics [4] and soft X rays [5].

A decrease of the electron density has been observed at the inner side of the O point of the m=2/n=1 mode.

At the end of the 'erosion' phase the Te profile is completely flat but the TS measures a temperature two times higher than the ECE.

References

[1] F.C. Schüller Plasma Phys. Control. Fusion **37**, A135, (1995)

[3] A. Bondeson *et al.*, Nucl. Fusion **31**, 1695, (1991).

[2] M.N.A. Beurskens *et al.*, EPS-Kiev, 1996.

[4] F. Alladio *et al.*, Nucl. Fusion **26**, 11, (1986)

[5] S. Tsuji *et al.*, Nucl. Fusion **25**, 305, (1985)

[6] de Vries *et al.*, submitted to Nucl. Fusion

Acknowledgments

Evidence for fast radial transport during pellet ablation in the RTP Tokamak as measured by Thomson Scattering

J. de Kloe, M. N. A. Beurskens, G. M. D. Hogeweij, J. Lok,

N. J. Lopes Cardozo, A.A.M. Oomens and the RTP Team

FOM-Instituut voor Plasmafysica 'Rijnhuizen', Association Euratom-FOM, Trilateral
Euregio Cluster, P.O. Box 1207; 3430 BE Nieuwegein, The Netherlands .

Introduction

One of the basic assumptions in most pellet ablation theories is that on the time scale of the ablation process, lasting typically 200-400 μs , only transport parallel to the magnetic field lines is important and that cross-field transport does not play an important role (after ionisation of the ablatant). If furthermore the plasma configuration is described using flux-surfaces, the calculations can be done in one dimension only.

In this contribution it will be shown that the above assumption is not always true. From the measured time evolution of both the electron temperature, T_e , and the electron density, n_e , profiles after injection of a pellet in the RTP tokamak, it can be concluded that radial transport is important in some cases. It will be shown that changes in T_e or n_e occur for regions not yet traversed by the pellet. The changes take place on a timescale much shorter than for phenomena that are usually referred to as non-local.

Experimental setup

The measurements in RTP have been done under the conditions: $R_0 = 0.72$ m, $a = 0.164$ m, $I_{pl} = 75 - 120$ kA, $B_{tor} = 2.1 - 2.3$ T, central density $n_{e,0} = 4.0$-7.0×10^{19}m^{-3}, central temperature $T_{e,0} = 0.7 - 1.0$ keV, edge safety factor $q_a = 3.4 - 5.5$, H_2 plasmas and boronized vessel. The pellet injector was built by the Risø National Laboratory [11]. The pellet velocity and time of arrival in the plasma are measured with two optical detectors when the pellet is in free flight. The pellet mass is measured using a microwave resonance cavity. The emitted H_α radiation is used to estimate the ablation rate and to check the pellet position. Earlier results of experiments with this equipment have been reported in [5, 7, 10]. For this investigation, H_2 pellets with a particle content of $1.6 - 1.9 \times 10^{19}$ atoms, which is a few times the particle content of the plasma, and a velocity of 570-760 m/s have been used. The pellets have been injected in the stationary phase of an ohmic discharge and the effects were observed with a Thomson scattering (TS) setup, which yields T_e -, n_e - and p_e -profiles along a vertical chord through the plasma center, with a spatial resolution of 1.7-2.5 mm [1, 2]. The laser of the TS system can be fired twice during the ablation process, on a pre-programmed position of the pellet. In this way the reaction of the plasma to the pellet can be scanned on a shot-to-shot base. Also some results were obtained using a five-camera soft X-ray (SXR) tomography setup [4]. Each camera consists of 16 channels with a time resolution of 5 μs and a spatial resolution of 20 mm in radial direction. The spacing between the viewing chords of the different channels is 20 mm in the plasma center.

file: r970124.020
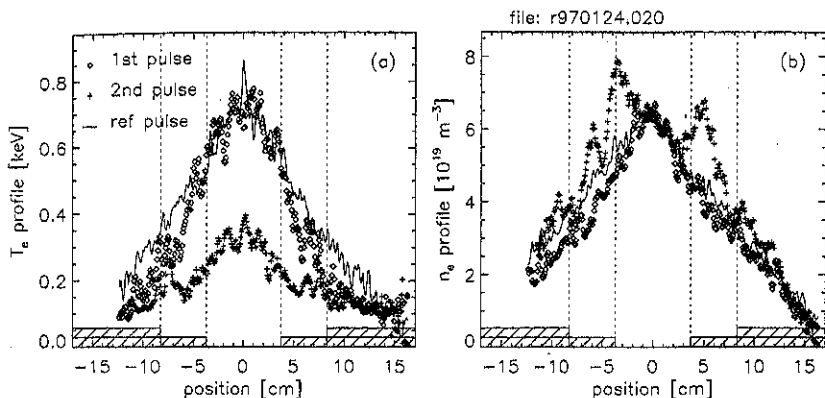
Figure 1: T_e (a) and n_e (b) profiles measured by double pulse TS (pulse separation 60 μs) compared to a reference shot without pellet. There is a dramatic drop in central temperature although the pellet has not yet reached this part of the plasma. ($I_{pl} = 77.2$ kA, $B_{tor} = 2.26$ T, $q_a = 5.46$, $n_{e,0} = 6.7 \times 10^{19} m^{-3}$)
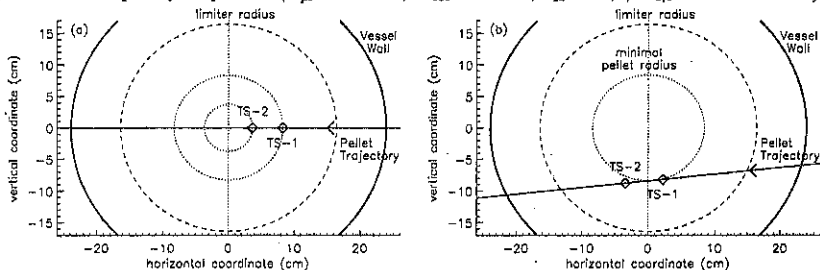
Figure 2: poloidal cross-section of the Tokamak at the position of the pellet injector showing the geometry of the experiment with a horizontally injected pellet (a) (for which some results are shown in fig. 1) and an obliquely injected pellet (b) (for which some reults are shown in fig. 3). The pellet positions at the time of both TS pulses are indicated by the two diamonds.

Measurements

The first evidence for enhanced radial transport is shown in fig. 1. It gives the T_e - and n_e -profiles as measured by double pulse TS taken when a horizontally injected pellet (see fig. 2a) was at radii of 82 mm and 36 mm (indicated by the bars at the bottom of the plot). The time difference between the first and second pulse was 60 μs . In the plasma center the temperature drops, compared to both the undisturbed reference profile and to the profile measured by the first TS pulse, even though the pellet has not yet penetrated to the plasma center. This collapse happens when the pellets is in the vicinity of q=1 [5].

More evidence is obtained for an obliquely injected pellet. The pellet trajectory, and the pellet positions at the time of both TS pulses, separated by 100 μs , are indicated in fig. 2b. The T_e - and n_e -profiles are shown in fig. 3. This obliquely injected pellet has its closest approach to the plasma center at 84 mm (see the vertical dashed lines) assuming that the pellet travels along a straight line, which is supported by photographs taken from the ablation process.

In the n_e -profile a clear rise is visible in the profile measured by the second TS pulse,

file: r970428.025
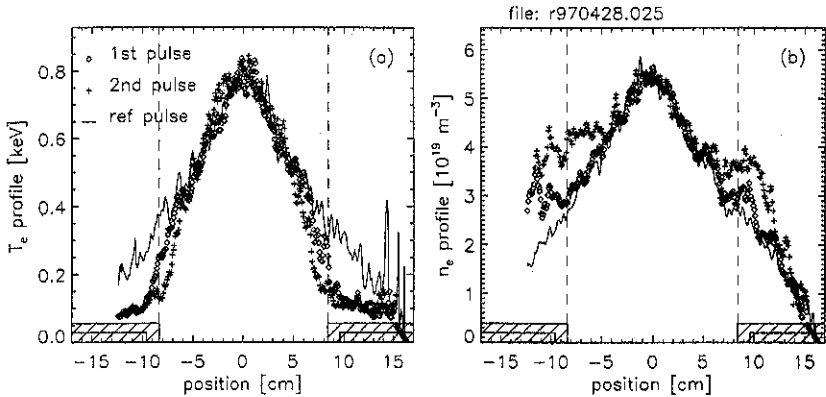
Figure 3: T_e *(a) and* n_e *(b) profiles measured by double pulse TS (pulse separation 100* μs *) compared to a reference shot without pellet for an obliquely injected pellet. The closest approach of the pellet to the plasma center is indicated by the vertical dashed lines. There is a clear density increase up to a radius of 50 mm although the pellet has not and will never reach this part of the plasma (* $I_{pl} = 80.2$ *kA,* $B_{tor} = 2.19$ *T,* $q_a = 5.10$, $n_{e,0} = 5.5 \times 10^{19} m^{-3}$ *).*

in comparison with the results of the first pulse and the reference discharge, even for radii up to 50 mm that are not, and never will be reached by the pellet.
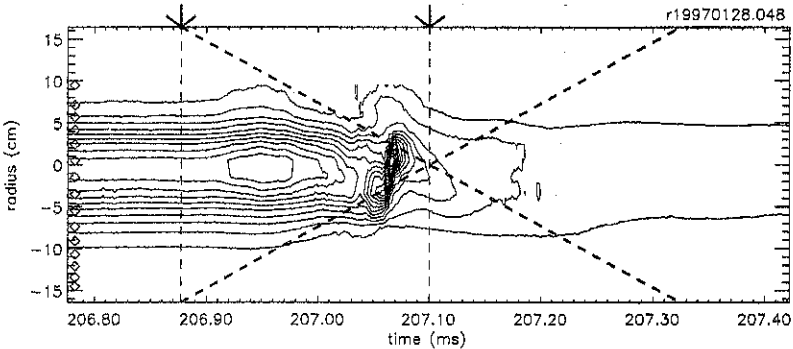
Figure 4: contour plot of the SXR emission detected by one of the cameras of the SXR setup. On the vertical axis the impact parameter of the different chords of the camera, each indicated by a diamond, is plotted. The dashed lines are explained in the text. All channels start to increase when the pellet is at a radius of ≈ 14 *cm (206.91 ms) including the ones viewing the plasma center (* $I_{pl} = 117$ *kA,* $B_{tor} = 2.16$ *T,* $q_a = 3.44$, $n_{e,0} = 4.1 \times 10^{19} m^{-3}$ *).*

The third piece of evidence is seen for some conditions in which a very fast increase on most channels of the SXR system occurs when the pellet just enters the plasma. An example of this is shown in fig. 4. The dashed vertical lines and the arrows indicate when the pellet reaches the limiter radius and the plasma center respectively (not taking into account that it might be fully ablated before that time). The dashed diagonal lines indicate the radial position of the pellet. In this contour plot it is clearly seen that most channels start to increase significantly when the pellet is at a radius of about 14 cm

(206.91 ms), especially the central ones. All five cameras show the same behaviour, so the emission is clearly not localised at the edge of the plasma. We have not yet been able to determine whether this increase in SXR emission is due to an n_e increase or a non-thermal part of the electron population, but a T_e increase has been excluded by taking TS profiles of this effect. Further experiments are planned to determine what is happening here.

Interpretation

In the previous section three different cases of fast radial transport were shown. It must be noted that all these cases are much faster (occurring 50-200 μs after the pellet entered the plasma) than non-local phenomena published before, which occur 1-5 ms after the pellet has entered the plasma (for an example at this conference see P. Mantica [9]).

The first case of a fast central T_e-drop has been observed before on several Tokamaks and is generally known as precooling (see for example [3]). There is no model yet that explains this phenomenon. The second case of fast radial n_e transport has never been seen before on this timescale, although it was known already that the symmetrisation of the n_e-profile after the end of the ablation is remarkably fast [6]. For both cases a diffusivity for the region not traversed by the pellet can be calculated from the two profiles. This results in an electron thermal diffusivity χ_e much larger than usually observed in undisturbed plasmas for the first case (fig. 1a yields $\chi_e > 30$ m^2/s). For the second case the electron inward convection v_ϕ also is far above the expected value (fig. 3b yields $v_\phi > 400$ m/s). This indicates that these fast transport processes are probably not diffusive, although it can not be excluded that the fast n_e transport is diffusive since a very localised density increase maybe is not seen by the TS diagnostic. The third case is even faster because here the pellet just starts to penetrate the plasma when the effects in the center become visible. Although it is not known if a change in n_e is causing this effect it might be connected to the extremely fast charge exchange precooling that is described by Liu [8] which would cause besides a central cooling also a small central density increase. Finally it must be noted that though all three processes are very fast they probably do not have a common explanation.

Acknowledgement

References

[1] C. J. Barth et al., Rev. Sci. Instrum. 63 p. 4947, 1992.

[2] M. N. A. Beurskens et al., this conference, p2.028

[3] A. D. Cheetham et al., 14th EPS Conf., Madrid, Vol. 11D, part 1, p.205, 1987.

[4] D. F. da Cruz et al., Rev. Sci. Instrum., 65 p.2295, 1994.

[5] D. F. da Cruz et al., Phys. Rev. Letters, 75, p.3685, 1995.

[6] M. Greenwald et al., 10th Int. Conf. London, IAEA-CN-44/A-I-3, p.45, 1984.

[7] J. de Kloe et al., 23rd EPS Conf. Kiev, Vol. 20C, part 1, p.368, 1996.

[8] W. Liu et al., Nucl. Fusion, 34, p.337, 1994.

[9] P. Mantica et al., this conference (post deadline)

[10] A. A. M. Oomens et al., 22nd EPS Conf. Bournemouth, Vol. 19C, part 1, p.129, 1995.

[11] H. Sørensen et al., 17th Symp. on Fusion Technology 1992, Rome, Vol. 1, p.647, 1992.

Dynamics of small scale T_e, n_e and p_e structures; Thomson Scattering at RTP.

M.N.A. Beurskens, C.J. Barth, N.J. Lopes Cardozo, H.J. van der Meiden,
and the RTP-team

FOM-Instituut voor Plasmafysica 'Rijnhuizen', Association Euratom-FOM,
P.O. Box 1207, 3430 BE Nieuwegein, The Netherlands. Trilateral Euregio Cluster.

Introduction

The research program of the Rijnhuizen Tokamak Project (RTP; $R/a = 0.72/0.16\,\mathrm{m}$, $B_T \leq 2.5\,\mathrm{T}$, $I_p \leq 150\,\mathrm{kA}$, $q_a \geq 2$) is concentrated on transport physics. For a typical Ohmic plasma ($q_a = 5$), without additional heating, the central electron temperature (T_e) is $\sim 1\,\mathrm{keV}$ at a density (n_e) of $5 \times 10^{19}\,\mathrm{m^{-3}}$. Additional heating of the plasma is performed by Electron Cyclotron Heating (ECH) at 60 and 110 GHz.

One of the research goals is to study small-scale structures on the T_e, n_e and p_e profile. In this paper only p_e profiles are shown because they feature the most clear structures. Fig. 1 gives an overview of the structures which have been observed with the multi-position Thomson scattering diagnostic[1,2] at RTP. In the center of the plasma high p_e peaks have been observed during additional ECH. These peaks, so-called filaments, have a typical width of 5-10 mm. Additionally heated plasmas also show steep p_e gradients near the sawtooth inversion region. The p_e profile also shows small scale, odd and even, steps and bumps. These are interpreted as higher odd and even MHD modes and appear in both Ohmic and additionally heated plasmas. High n_e discharges show large $m/n=2/1$ islands. The size of these islands can be up to 1/4 of the plasma radius. Also with off-axis ECH strong $m=2$ activity can be induced.

A double pulse multi-position Thomson scattering diagnostic has been installed[3,4] to study the dynamics of the structures. This diagnostic measures T_e and n_e profiles along a vertical chord covering 85 % of the diameter. The spatial resolution is ~ 1 % of the plasma diameter. T_e can be measured with an accuracy of ≤ 5 % in the range 50 eV–6 keV for $n_e \approx 2 \cdot 10^{19}\,\mathrm{m^{-3}}$ and a laser energy of 10 J. The error on n_e is a factor 1.5 less. A 50-100 % observational error is reached at $n_e \sim 10^{18}\,\mathrm{m^{-3}}$. The double pulse feature enables measurements of two profiles during one plasma discharge with a temporal separation (Δt) of 20–800 μs. Fig. 2 shows that there is good agreement between the measured profiles for Δt=0 μs. Small scale p_e structures are discussed in the following order: $m/n = 2/1$ islands, small odd and even MHD modes, and finally the filaments.
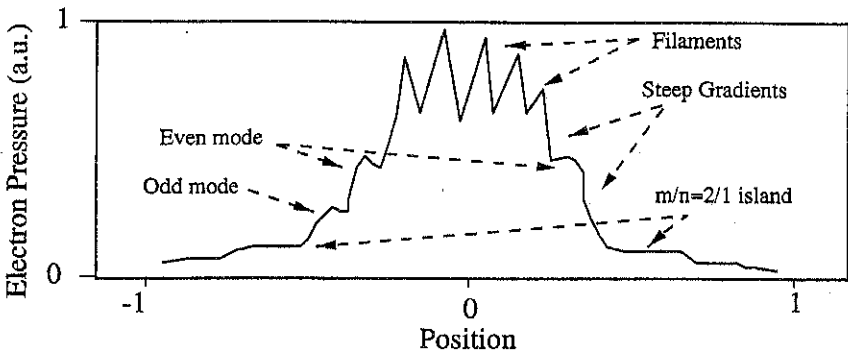
Figure 1: Overview of the most striking structures observed by Multi-position Thomson scattering

Identification of MHD modes using the plasma rotation.

Fig. 3 (a) shows two Thomson scattering profiles taken in a high n_e discharge, in which a large m=2 mode was present. The m=2 island is clearly visible in the profiles. In this case, Δt was set equal to the rotation period (τ_{MHD}) of the mode, as measured by magnetics. Comparing the two profiles, it is clear that the m=2 island is very similar. Moreover, also smaller structures, most strikingly the odd mode in the steep gradient, but also the complicated T_e structure in the center, appear very similar in two measurements taken with $\Delta t = (\tau_{MHD})$. the fact that these structures appear in the same relative positions after a single toroidal turn demonstrates that the constellation may be ragarded as a solid rotator.

Using the plasma rotation and setting Δt to a fraction of τ_{MHD}, allows a mode analysis of the structures seen on the profiles. An example is given in Fig. 3 (b), which shows how after $\Delta t = 0.5 \times \tau_{MHD}$ the m=2 island has rotated from showing its x-points to showing its O-points. Interestingly, the O-point of the odd mode in the steep gradient has returned to the same position, demonstrating that this mode must have n=even, with n=2 as the most likely candidate.

In Fig. 4 the plasma rotation is again used, with $\Delta t = 0.5 \times \tau_{MHD}$. In these profiles, a 3/2 and a 4/3 mode could be identified using the rotation, in combination with the q-profile calculated using neo-classical resistivity and including the bootstrap current.

A more extensive database will be created containing a Δt scan, such that even higher MHD modes can be identified.

Filaments

Two p_e profiles of an additionally heated low density $(n_e(0) \approx 2 \times 10^{19} \, m^{-3})$ discharge are shown in Fig. 5. The separation time $\Delta t = \tau_{MHD}$ 90μs is obtained from m/n=2/1 rotation. A reproduction of the position of the filaments can be seen, however, the amplitude varies. This is not surprising in view of the very peakedness of the filaments. When τ_{MHD} is missed by Δt by a few percent, the laser-beam crosses the filaments differently and two subsequent p_e profiles show peaks with varying amplitude. Topologically, filaments are interpreted as snake-like m/n = 1/1 modes.

Summary

At RTP small scale structures on T_e, n_e and p_e can be measured with a very high spatial resolution using the Thomson scattering system at RTP. Taking the MHD rotation frequency into account the mode number of MHD modes can be identified. Filaments seem to reproduce after one rotation period.

Acknowledgement.

References

1. N.J. Lopes Cardozo, et al., Phys Rev. Letters 73 (1994) 256-259.
2. C.J. Barth, et al., Accepted for publication in Rev. Sc. Instrum.
3. M.N.A. Beurskens, et al., Rev. Sci. Instrum. 68 (1) (1997) 721-724.
4. M.N.A. Beurskens, et al., Proc. 23nd EPS Conf. on Contr. Fusion and Plasma Phys., Kiev (1996) Vol. III. f034, 1088-1091. 1-724.
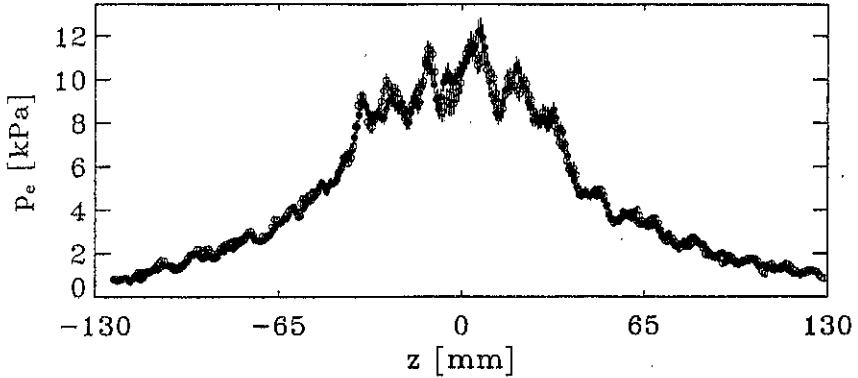
Figure 2: Double detection: two p_e profiles measured with $\Delta t = 0\,\mu s$. The profiles agree within the error bars. For this discharge $n_e(0) = 2 \cdot 10^{19} m^{-3}$. Note the relatively small error bars.
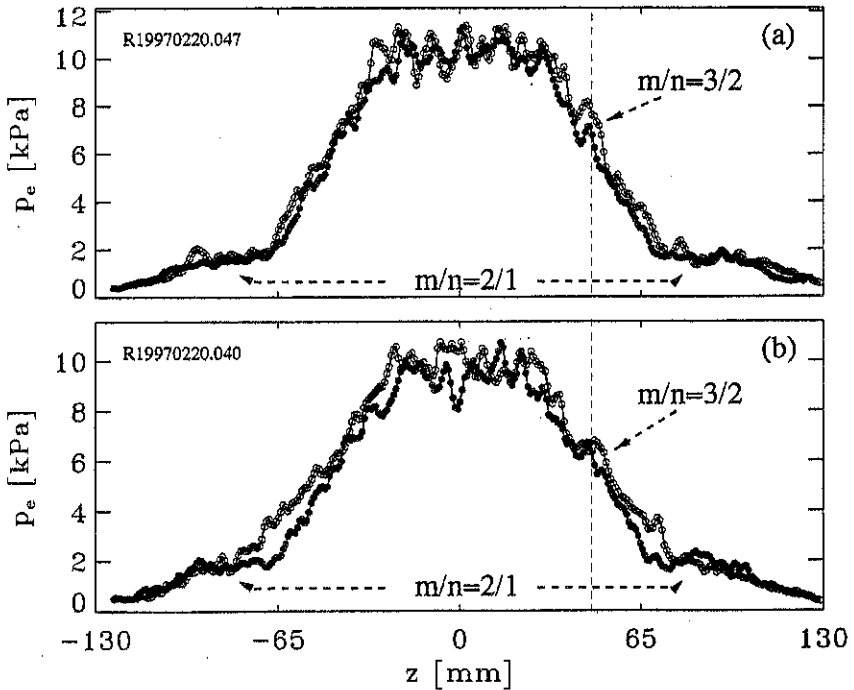
Figure 3: (a) Two profiles showing reproduction of $m/n=2/1$ and $m/n=3/2$ islands $1 \times \tau_{MHD}$ separated in time $(150\,\mu s)$. (b) Profiles $0.5 \times \tau_{MHD}$ separated. The $m/n=3/2$ mode shows an O-point in both profiles, while the $m/n=2/1$ island shows an O- and an X-point respectively.
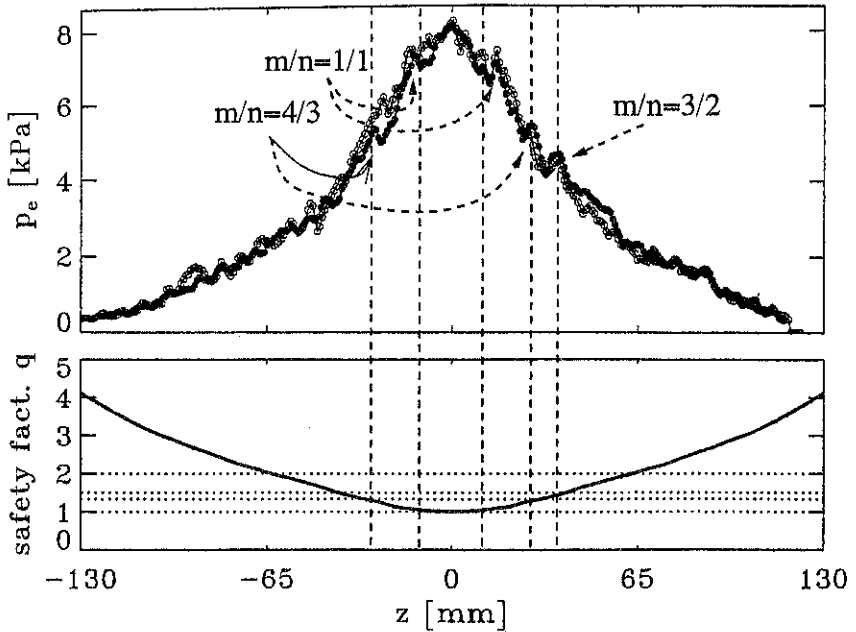
Figure 4: Two profiles showing reproduction of m/n=3/2, O- and X-points of a 4/3 mode, and a 1/1 mode. All agree very well with the calculated q-profile
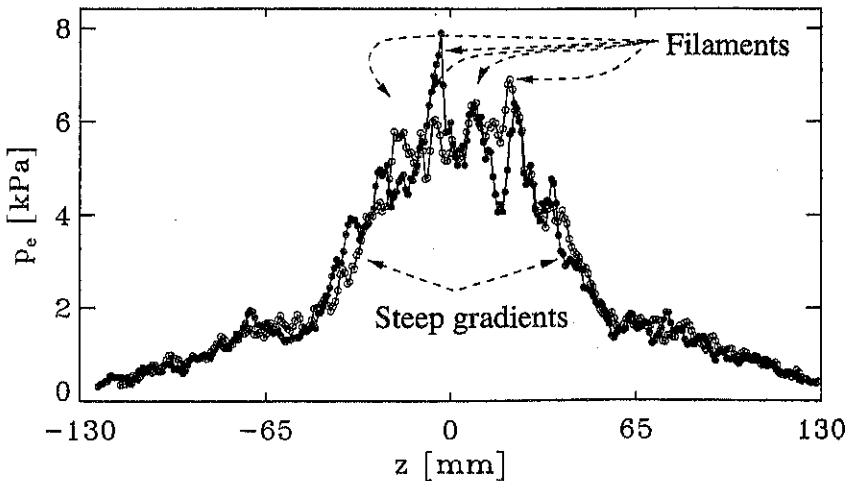
Figure 5: Two p_e profiles of an additionally heated plasma, $1 \times \tau_{MHD}$ separated. The positions of the filaments in the center reproduce.

Magnetohydrodynamic stability analysis of negative shear plasmas in the KSTAR tokamak.

A.J.C. Beliën[1], B. van der Holst[1], J.P. Goedbloed[1], B.G. Hong[2], S.K. Kim[2]

[1]FOM-Institute for Plasma Physics 'Rijnhuizen', Association Euratom-FOM,
P.O. Box 1207, 3430 BE Nieuwegein, The Netherlands

[2]Korean Atomic Energy Research Institute, Taejon, South-Korea

Introduction

The good confinement and transport properties of tokamak plasmas with negative central shear and large positive shear near the edge have attracted a lot of interest since it opens up the possibility for smaller tokamak reactors. MHD stability analysis of such plasmas is performed to obtain insight in the maximum obtainable beta values that can be achieved. Plasmas with inverted shear are potentially unstable with respect to internal low-n pressure driven infernal modes that often pose more severe limits on achievable beta values than high-n ballooning modes [7, 3]. However, low-n external modes are generally the most severe instabilities in plasma with inverted shear, see for example [1].

We have performed an MHD stability analysis for KSTAR tokamak plasmas with inverted shear. KSTAR is a tokamak that is currently being designed by the Korean Atomic Energy Research Institute and Korean universities. Its design parameters are $R = 1.8\,\text{m}$, $a = 0.5\,\text{m}$, ellipticity $\kappa = 2.0$, triangularity $\delta = 0.8$, $B = 3.15\,\text{T}$, $I \leq 2.0\,\text{MA}$. A large fraction of the plasma current will be driven non-inductively and off-axis giving rise to inverted shear profiles. In this paper we focus on the $n = 1$ stability analysis of KSTAR plasmas with high shear at the plasma edge, i.e., $q_1/q_{\min} \simeq 6$–8. We especially look at equilibria with $1.0 \leq q_{\min} \leq 2.0$ to investigate the stability requirements with respect to $m/n = 1/1, 2/1$ modes.

Equilibrium construction

Static equilibria are constructed with the HELENA code [5] using 81 radial grid points and 129 poloidal grid points. For the specification of the equilibrium we use a typical averaged current density and pressure profile as obtained by the JETTO transport code in the modeling phase of the profile control experiments [4]. The pressure profile is described by 21 grid points and is optimized for stability against the first region of stability by locally adapting the pressure gradient. The optimal toroidal beta reached for $I = 2.04\,\text{MA}$ is $\beta_t = 6.4\%$ and $\beta_p = 1.8$. For the $n = 1$ stability study the equilibria are recalculated with 101 radial grid points and 257 poloidal grid points to obtain better resolved better converged growth rates and eigenfunctions. Also, lower poloidal betas are considered because the optimal ballooning stable betas are, generally, violently unstable with respect to $n = 1$ modes. For $\beta_p = 1.1$ the profiles of the safety factor q and pressure profiles are shown in Fig. 1.

$n = 1$ stability analysis

Low-n stability is studied with the resistive MHD stability code CASTOR [6]. For the stability study 101 radial grid points and 25 poloidal Fourier harmonics are exploited. Convergence studies show these resolutions to give growth rates within a percent of the converged growth rates. The plasma is surrounded by a vacuum and enclosed by a ideal conducting wall having
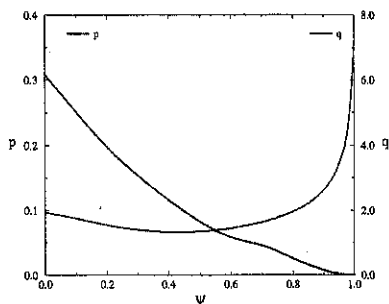
Figure 1: Safety factor and pressure profile for a tokamak plasma with KSTAR specifications ($a/R = 0.278$, $\kappa = 2.0$, $\delta = 0.8$, $B = 3.15\,T$, $I = 2.2\,MA$). The minimum in the safety factor profile $q_{min} = 1.33$ is located at $\psi = 0.42$. The safety factor at the edge $q_1 = 7.17$. The poloidal and normalized toroidal betas are $\beta_p = 1.1$ and $\beta_N = 2.7$, respectively.

the same shape as the last closed flux surface. The vacuum magnetic configuration is solved using 101 radial grid points and 25 poloidal Fourier harmonics.

In Fig. 2a and Fig. 2b, we have plotted the two largest ideal growth rates versus q_1, and also versus q_{min}, for three different positions (normalized to the small tokamak radius a) of the ideal conducting wall and for three values of the poloidal beta. These scans over q_1 are obtained by scaling the equilibrium through q_0. $\tau_a \equiv R_M \sqrt{\mu_0 \rho_M}/B_M$ is the usually Alfvén time scale, where R_M is the radius of the magnetic axis and ρ_M and B_M are the magnitudes of the density and the magnetic field on axis.
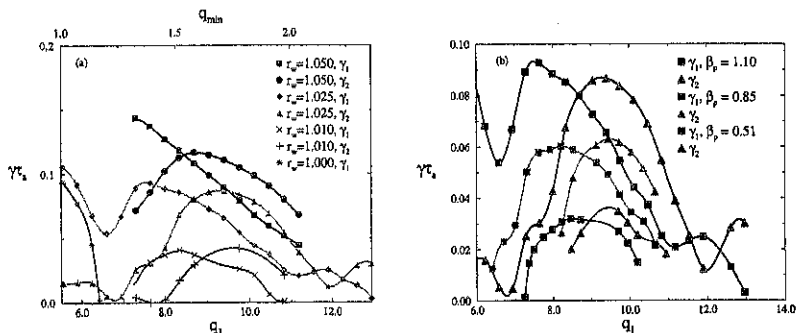
Figure 2: Ideal growth rates of the two largest instabilities versus q_1 for (a) four different values of the position of the ideal conducting wall ($\beta_p = 1.10$) and (b) for three different values of the poloidal beta ($r_w = 1.025$).

The growth rates are huge and these external instabilities can be made stable by bringing the wall well within 1% distance of the plasma edge, measured in terms of the small tokamak radius a, as can be extrapolated from Fig. 2a. Decreasing the poloidal beta lowers the growth rates, but even for $\beta_p = 0.51$ they are still considerable as is the width of the unstable q_1 window. Note that around $q_{min} = 1.0$ the internal $m/n = 1/1$ instability is located, which we have only plotted for $r_w = 1.025$ and $r_w = 1.0$ (wall on the plasma). These instabilities are localized at

the plasma-vacuum interface in the region of high shear. The most dominant m-modes are the ones corresponding to the highest two rational q-surfaces located within the plasma. In Fig. 3a we have plotted the radial mode structure for γ_2 at $q_1 = 9.41$ and for $r_w = 1.025$ for v_1, i.e. the radial component. Table 1 shows that the growth rates of these modes decrease with increasing resistivity.
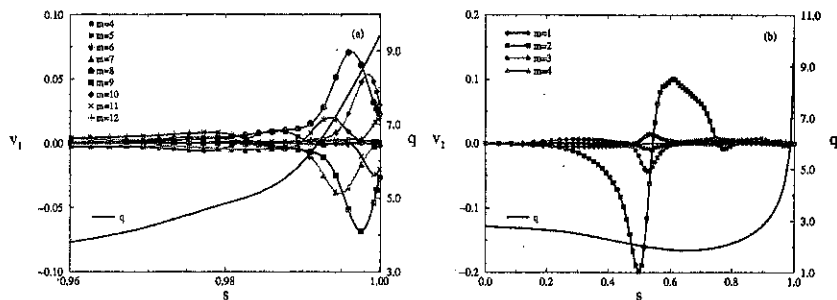
Figure 3: (a) Radial mode structure ($s \equiv \sqrt{\psi}$) near the plasma edge of the v_1 component of the γ_2 external instability of Fig. 2a at $q_1 = 9.41, r_w = 1.025$. (b) Radial mode structure of the v_1 component of the largest resistive internal instability at $q_1 = 10.12$. Only the few largest poloidal Fourier harmonics are shown in both figures. The safety factor profile is also shown.

Up till now, we have only discussed free boundary or ideal and resistive external instabilities. Resistive internal modes do occur but their growth rates are generally smaller except for the $m/n = 1/1$ internal kink. However, for larger values of the resistivity, i.e. $\eta \geq 10^{-6}$, their growth rates are larger than the external instabilities. Table 2 contains the growth rates for the two largest resistive instabilities at $q_1 = 9.41$ as a function of the resistivity η. Both growth rates scale as $\eta^{\frac{1}{3}}$ indicating the interchange character of the modes [2]. The radial mode structure of the fastest of these resistive interchange instabilities is shown in Fig. 3b for $q_1 = 10.12$ and $\eta = 10^{-6}$. The double mode resonant $m = 2$ behaviour around the $q = 2$ surfaces is clearly visible. We have also found resistive modes with growth rates that scale with the tearing mode scaling, but the growth rates are always smaller than the resistive interchange ones mentioned here. Hence, for the considered equilibrium, these double resistive interchange modes are more important than the double tearing mode.

η	$\gamma_1 \tau_a$	$\gamma_2 \tau_a$
1×10^{-5}	1.019×10^{-3}	7.584×10^{-3}
1×10^{-6}	2.802×10^{-3}	1.868×10^{-2}
1×10^{-7}	6.654×10^{-3}	5.537×10^{-2}
1×10^{-8}	8.051×10^{-2}	5.871×10^{-2}
1×10^{-9}	8.524×10^{-2}	6.364×10^{-2}
0	8.674×10^{-2}	6.563×10^{-2}

Table 1: Growth rates of the two largest external, edge localized modes at $q_1 = 9.41$ of Fig. 2a as a function of the resistivity η. For $\eta = 0$ the mode structure of γ_2 is plotted in Fig. 3a.

η	$\gamma_1 \tau_a$	$\gamma_2 \tau_a$
10^{-5}	1.998×10^{-2}	9.029×10^{-3}
10^{-6}	6.543×10^{-3}	3.291×10^{-3}
10^{-7}	2.983×10^{-3}	1.436×10^{-3}
10^{-8}	1.457×10^{-3}	6.795×10^{-4}
10^{-9}	7.056×10^{-4}	$< 3.0 \times 10^{-4}$
0	stable	stable

Table 2: Growth rates of the two largest resistive internal modes at $q_1 = 10.12$ as a function of the resistivity η. Both growth rates scale as $\eta^{\frac{1}{3}}$ indicating the interchange character of these modes. For $\eta = 10^{-6}$ the mode structure of γ_1 is plotted in Fig. 3b.

Conclusions

In this paper we have investigated the $n = 1$ MHD stability of negative central shear plasma with large positive shear near the plasma edge. The stability study has been performed for KSTAR tokamak plasmas. A major result is that for $1.5 \leq q_{\min} \leq 2.5$ stability is not determined by low-m internal modes but by high-m ($m = 6$–9) external modes which are localized near the plasma edge. These modes can be made stable only by bringing an ideal conducting wall very close to the plasma edge. Typically, the distance of the wall to the plasma edge should be below 1% of the minor radius. Furthermore, the growth rate decreases with increasing resistivity and decreasing poloidal beta. These modes appear to be related to the high shear at the plasma edge. Plasmas with flatter q-profiles, such as, for example, the ones studied in [1], appear to have better stability properties.

References

[1] P.T. Bonoli, M. Porkolab, J.J. Ramos, W. Nevins, and C. Kessel, *Negative central shear modes of operation in the Alcator C-mod tokamak near the beta limit*, Plasma Phys. Control. Fusion **39** (1997), 223.

[2] H.P. Furth, J Killeen, and M.N. Rosenbluth, *Finite resistive instabilities of a sheet pinch*, Phys. Fluids **6** (1963), 459.

[3] H.A. Holties, G.T.A. Huysmans, J.P. Goedbloed, W. Kerner, V.V. Parail, and F.X. Söldner, *Stability of infernal and ballooning modes in advanced tokamak scenarios*, Nucl. Fusion **36** (1996), 973.

[4] H.A. Holties, G.T.A. Huysmans, W. Kerner, J.P. Goedbloed, F.X. Söldner, and V.V. Parail, *MHD stability of advanced tokamak scenarios*, 21st EPS Conf. on Controlled Fusion and Plasma Physics (Montpellier) (E. Joffrin, P. Platz, and P.E. Scott, eds.), 27 June - 1 July 1994, p. 234.

[5] G.T.A. Huysmans, J.P. Goedbloed, and W. Kerner, *Isoparametric bicubic hermite elements for solution of the Grad-Shrafranov equation*, Proc. CP90 Conf. on Comp. Phys. Proc., World Scientific Publ. Co., 1991, p. 371.

[6] ———, *Free boundary resistive modes in tokamaks*, Phys. Fluid **B5** (1993), 1545.

[7] J. Manickam, N. Pomphrey, and A.M.M. Todd, *Ideal MHD stability properties of pressure driven modes in low shear tokamaks*, Nucl. Fusion **27** (1987), 1461.

Second Harmonic ECCD Experiments in RTP

R.W. Polman, J. Lok, E. Westerhof, B. de Groot, O.G. Kruyt,
A.A.M. Oomens, F.C. Schüller, and the RTP-team

*FOM-Instituut voor Plasmafysica 'Rijnhuizen', Association Euratom-FOM,
Trilateral Euroregio Cluster, P.O. Box 1207, 3430 BE Nieuwegein, The Netherlands.*

Abstract

Second harmonic Electron Cyclotron Current Drive (ECCD) experiments on the Rijnhuizen
tokamak RTP have been performed utilizing 110 GHz waves launched from the low field side of
the torus. Considerable fractions (up to more than 50%) of the plasma current have been driven
in a very localized way. This results in large effects on current density and consequent MHD
activity. The dependence of the ECCD efficiency on the position of the cold resonance layer, on
the plasma current I_p, on the toroidal launch angle, and on the ECH power has been measured.
The efficiency - $\langle n_e \rangle_{19} R I_{cd} / P_{rf}$ - for 2nd harmonic ECCD in RTP is $(0.05 \pm 0.015) \times 10^{19}$ A/Wm^2.

The experimental results for position and angle scans are compared with quasi-linear Fokker-
Planck predictions. The linear predictions partly agree with experimental results.

Introduction and experimental set-up

The RTP tokamak (R_0 = 0.72 m, a_{lim} = 0.165 m, $B_T \leq 2.5$ T, $I_p \leq 150$ kA, iron core, boronized
SS first wall, carbon limiters) is equipped with two 60 GHz, 200 kW, 100 ms gyrotrons, and a
single 110 GHz, 200 ms, 500 kW gyrotron for ECRH and ECCD. Both 60 GHz gyrotrons are
connected to RTP by wave guide transmission lines: one to the low field side (LFS) for bulk
heating, the other to the high field side (HFS) to achieve heating and current drive. The 110 GHz
rf power is transmitted quasi-optically, as a linearly polarized Gaussian beam. The beam is
injected from the LFS. A recent system extension [1] allows oblique injection via a steerable
mirror, as required for ECCD experiments. The center of the launching mirror is 0.105 m below
the equatorial plane, and at 0.23 m from the plasma center. Near the resonance zone the diameter
of the rf beam is a few cm. So, the power deposition is very localized. The polarization of the
launched EC power is linear. The coupling efficiency to 2X-mode is estimated to be 65% for 30°
off-perpendicular launching, and better for smaller angles.

ECCD has been obtained in two ways in RTP: by launching 60 GHz waves from HFS [2],
and by launching 110 GHz waves from LFS. In both cases the X-mode polarization has been
used. The 110 GHz oblique injection from LFS yields second harmonic ECCD through the up-
shifted resonance scheme. This paper describes the first 110 GHz ECCD results.

In standard operation an injected power level of 300 kW during 150-200 ms, and a plasma
current $I_p \approx 60$ kA have been used. Absorption of 2nd harmonic X-mode waves increases with
density. Experiments were performed at $\langle n_e \rangle = (1 - 2) \times 10^{19}$ m^{-3}, to get the combination of low
density and sufficient absorption. For such waves, obliquely launched from LFS, the Doppler-
shifted absorption zone is to the low field side of the cold resonance position, which is at 1.96 T
for 55 GHz.

Linear theory predicts the scaling I_{ECCD} (:) $P_{rf} T_e / R_0 n_e (Z_{eff} + 5)$ [3]. This scaling suggests that it is advantageous to experiment at low densities and to use the full power to obtain the highest EC driven currents. Through T_e, the driven current will depend on B_T.

Density and plasma current are feedback controlled. The working gas is hydrogen. Standard diagnostics, a 19-channel interferometer/polarimeter, 20-channel ECE, a high-resolution multi-position Thomson Scattering system and other multi-channel diagnostics are available [2].
The established current drive has not been large enough to drive all of I_p, and a residual loop voltage is observed. As at RTP no direct methods are available at the moment to determine the driven current in detail, the EC driven current has been estimated indirectly from a comparison of the residual loop voltages during co-drive (V_{co}) and counter-drive (V_{cntr}) [4]. For zero bootstrap current this method relates: $I_{ECCD} / I_p = (V_{cntr} - V_{co})/(V_{cntr} + V_{co})$.

Results
The dependence of the current drive efficiency on the location of the resonance layer, the plasma current, the toroidal launch angle, and the ECH power, has been measured. The experimental results are compared with Fokker-Planck code predictions.

Fig. 1 shows an example of V_{loop} for co- and counter current drive ($I_p = 42$ kA, $q(a) = 8.8$, $P_{ECH} = 285$ kW, injection $\pm 17.5°$, $B_T = 1.98$ T). The estimated driven current fraction is 55%, i.e. $I_{ECCD} = 23$ kA. Note that in co-drive the Ohmic power is as low as 5 kW, less than 2% of the total input.

Results of B_T scans are given in Fig. 2. The cold resonance is at 1.96 T and B_T was varied between 1.9 and 2.3 T. Experiments with oblique angles of $\pm 25°$ and densities $\langle n_e \rangle = (1.7 \pm 0.2) \times 10^{19} m^{-3}$ showed driven currents of around 10 kA ($I_p = 60$ kA) in a surprisingly broad B_T window and up to higher B-values than expected from the simple up-shifted resonance picture. The use of lower densities ($\langle n_e \rangle = 1.2 \times 10^{19} m^{-3}$) and steeper injection angles ($\pm 20°$) resulted in a doubling of I_{cd} in a narrower field range. A further step down in density ($\langle n_e \rangle = (1.1 \pm 0.2) \times 10^{19} m^{-3}$) and injection angle ($\pm 17.5°$) yielded a further increased current: $I_{cd} = 25$ kA. This all illustrates the role of the local temperature (the rf power both heats and drives current). Though the estimated currents are higher than for first harmonic current drive with lower power [2], the efficiencies - $\langle n_e \rangle_{19} R I_{cd}/P_{rf}$ - are much the same: typically $(0.05 \pm 0.015) \times 10^{19}$ A/Wm². Linear Fokker-Planck calculations for 25° off-perpendicular injection in a plasma with parabolic density profile and $n_e(0) = 2.0 \times 10^{19} m^{-3}$ predict maximum driven currents around 15 kA for $T_e(0) = 1.5$ keV, and around 40 kA for $T_e(0) = 3$ keV for 300 kW injected power. These values correspond fairly to the experimental results, however the B-window is different (1.85-1.95 T). Quasi-linear effects are very large for the pertinent parameter regime, due to the high power density. These should give rise to a strong increase (up to a factor of 2) of the predicted current. The predicted non-linear improvement of the efficiency has not been observed up to now.

The launch angle is another determining parameter of current drive. Figure 3 shows the loop voltage as a function of that parameter for a 60 kA discharge ($P_{ECH} = 300$ kW, $B_T = 1.97$ T, and $\langle n_e \rangle = 1.1 \times 10^{19} m^{-3}$). At the start of the ECH pulse $V_l = 1.30$ V. The voltage difference between oblique and perpendicular injection (heating only) is symmetric in this scan. Hence, I_{ECCD} increases linearly with off-perpendicular injection angle up to 15°; upwards the efficiency decreases. Linear Fokker-Planck calculations predict an increase up to 25°.

A power scan shows an increase of I_{cd} with increasing power. The efficiency I_{cd}/P_{rf} is plotted against power in Fig. 4; conditions are close to optimal. For $P_{ECH} > 175$ kW the efficiency is around 0.04 A/W. At lower power the efficiency decreases, partly as a result of lower plasma temperatures. The driven current also shows a dependence on I_p. Data obtained with narrow power deposition in the center of the discharge ($P_{rf} \approx 285$ kW, $B_T = 1.98$ T) showed a driven current fraction of more than 50 % at 40 kA ($\langle n_e \rangle = 1.1 \times 10^{19} m^{-3}$, see Fig. 1), while at 90 kA ($\langle n_e \rangle = 1.5 \times 10^{19} m^{-3}$, q(a) = 4, see Fig. 5) only 4 kA was estimated to be driven. The reduction of the current drive efficiency as observed for the 90 kA discharge is worth investigating further.

The large fractions driven at $I_p = 40 - 60$ kA, in combination with the very localized power deposition of the focused rf beam, thus very localized current drive, have interesting implications. Simple considerations show that current density profiles will be very different for co-and counter-drive for moderate driven current fractions, and that the total current density in the center could even become reversed in a counter-driven discharge. In consequence, the localized current drive strongly modifies the q-profile, and thus the MHD behaviour, of RTP discharges. (On the other hand, if large fractions are driven, and if such different current density profiles could result, then the applicability of the simple $\Delta V/\sum V$ formula becomes questionable). Though the magnitudes and profiles of I_{cd} are presently not really known, the RTP discharges show many signatures of substantially modified q-profiles. As an example, in the co-drive case of Fig. 1 ($I_p = 42$ kA, q(a) = 9) the discharge shows sawtoothing behaviour during ECCD. The onset of this behaviour reveals that the central q(0) is driven below 1 in this high-q(a) discharge.

Fig. 5 shows a discharge with small sawteeth in the Ohmic phase ($I_p = 90$ kA, q(a) = 4). After application of ECCD an increase of the sawteeth occurs in the co-drive case, while in the counter-driven discharge the sawteeth are stabilized. If current profiles are strongly modified through ECCD, unusual behaviour of the plasma is observed, depending on launching and discharge parameters. An example is given in Fig. 6. These time traces from the same ECE channel apply to 60 kA discharges with $\langle n_e \rangle = 1.2 \times 10^{19} m^{-3}$ in which an estimated co- and counter-ECCD of 30% is established. In the co-drive familiar sawteeth are produced. The frequency of the channel corresponds to a position outside the inversion radius ($B_T = 2.00$ T, $R_{ECE} = 0.687m$). The counter-drive case ($B_T = 1.98$ T, $R_{ECE} = 0.681m$) shows quite different and more virulent MHD behaviour as evidenced from position control, loop voltage, and spiky behaviour of the HXR-signal. Finally it should be mentioned that surprisingly the temperature profiles can be broader for co-drive than for counter-drive, which also indicates a strong q-profile modification through ECCD.

References

[1] A.A.M. Oomens et al., Proceedings EC-10 Workshop, Ameland, 1997 (to be published)
[2] A.J.H. Donné et al., in Plasma Physics and Controlled Nuclear Fusion Research 1996 (Proc. 16th Int. Conf., Montréal), IAEA-CN-64/EP-8 (IAEA, Vienna, to be published)
[3] N.J. Fisch and A.N. Boozer, Phys. Rev. Lett. **45**, 720 (1980)
[4] V. Erckmann and U. Gasparino, Plasma Phys. Control. Fusion **36**, 1869-1962 (1994)
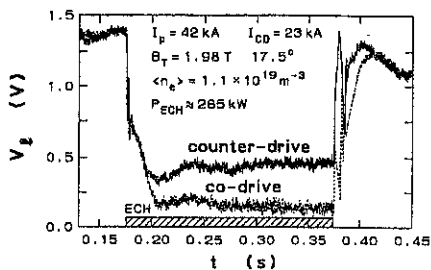
Fig. 1
V_{loop} time traces for co- and counter-drive

$I_P = 42$ kA $I_{CD} = 23$ kA
$B_T = 1.98$ T   17.5°
$\langle n_e \rangle = 1.1 \times 10^{19}$ m^{-3}
$P_{ECH} \approx 265$ kW

counter-drive
co-drive
ECH
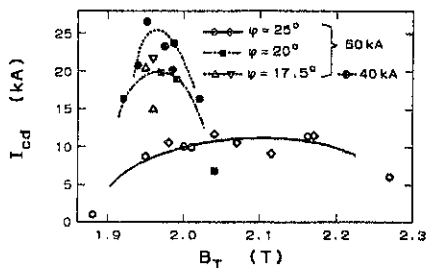
Fig. 2
Experimental I_{ECCD} as a function of B_T, for 25°, 20°, and 17.5° off-perpendicular injection ($P_{ECH} \approx 285$ kW, different densities, see text).

$\varphi = 25°$
$\varphi = 20°$ 60 kA
$\varphi = 17.5°$ 40 kA
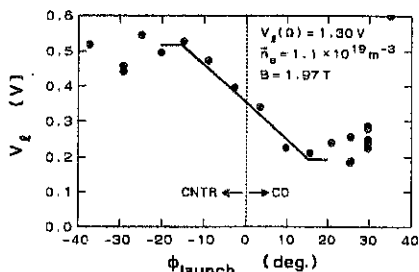
Fig. 3
V_{loop} as a function of off-perpendicular injection angle
($I_p = 60$ kA, $P_{ECH} = 300$ kW)

$V_\ell(0) = 1.30$ V
$\bar{n}_e = 1.1 \times 10^{19}$ m^{-3}
$B = 1.97$ T

CNTR ← → CO
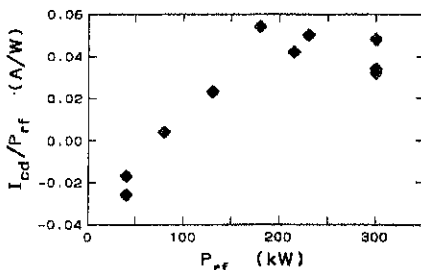
Fig. 4
Power scan: I_{ECCD}/P_{ECH} versus P_{ECH}.
(Machine settings close to optimal, $B_T = 1.95$ T,
$\langle n_e \rangle = 1.1 \times 10^{19}$ m^{-3})
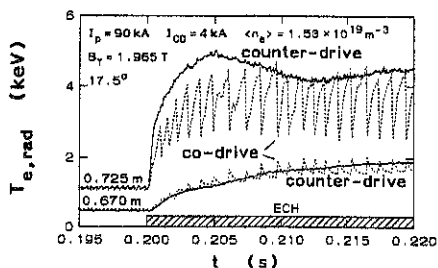
Fig. 5
Suppressed or intensified sawteeth by central counter- or co-drive, respectively (4 kA driven in a 90 kA discharge)

$I_P = 90$ kA $I_{CD} = 4$ kA $\langle n_e \rangle = 1.53 \times 10^{19}$ m^{-3}
$B_T = 1.965$ T
17.5°
counter-drive
co-drive
counter-drive
0.725 m
0.670 m
ECH
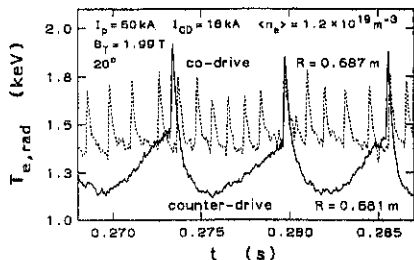
Fig. 6
Usual sawteeth and unusual MHD behaviour induced by co- and counter-drive, respectively, in a 60 kA RTP plasma.

$I_p = 60$ kA $I_{CD} = 18$ kA $\langle n_e \rangle = 1.2 \times 10^{19}$ m^{-3}
$B_T = 1.99$ T
20°
co-drive   R = 0.687 m
counter-drive   R = 0.661 m

VUV measurements of impurity behaviour on RTP

F.G. Meijer* , M.G.N. Breuls and the RTP-team
FOM-Instituut voor Plasmafysica 'Rijnhuizen',
Association Euratom-FOM, Trilateral Euregio Cluster,
P.B. 1207, 3430 BE Nieuwegein, The Netherlands
e-mail : f.g.meijer@rijnh.nl
*also Faculteit WINS, Universiteit van Amsterdam, Amsterdam, The Netherlands

1. Introduction

The vacuum ultraviolet (200 – 1 nm) is very suitable for the study of impurities in a fusion plasma. Besides $L\alpha$, the resonance line of hydrogen, the main transitions in almost all ions are emitted in this wavelength range. This insures lines of relatively high intensity and allows access to the ground level. The resolution required for a certain accuracy is however directly related to the wavelength of the light emitted and therefore spectrometers with a large dispersion and thus a large size are needed. By measuring the linewidth, ion temperatures can be deduced and line shifts provide us with ion velocities through the Doppler effect. Variation of the line of sight allows us to obtain information on the spatial distribution of these ions and their properties.

2. Experimental setup

A 6.65m normal incidence vacuum spectrometer [1,2] is used to obtain spectra at fairly high temporal and spectral resolution. The light emitted by the RTP tokamak is collected by a two mirror system in a coma–free setup. The size of the mirrors is 100×100 mm^2 and their focal lengths are 4000 and 2000 mm respectively. The mirror facing the plasma can be rotated around a horizontal axis in its plane [see fig. 1]. In this way the line of sight can be moved up and down through the plasma.
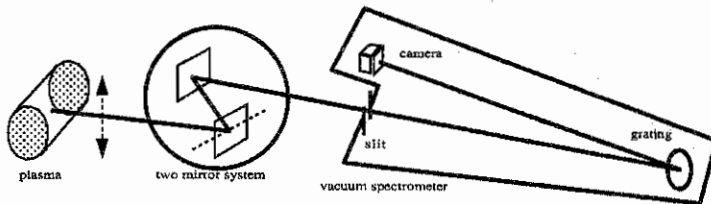
fig.1 scheme of the instrumental setup

The instrument is equipped with a 1200 lines/mm grating of 250 mm diameter, covering a wavelength range from 250 to 110 nm. In a photographic setup, this instrument has reached a resolving power of more than 100 000. To monitor the tokamak plasma a microchannel plate is used as detector, coupled via a phosphor screen to a linear CCD–camera. The CCD–array consists of 2048 pixels of 14x500 μm^2. The electronic camera control system allows storage of 1200 spectra with a smallest sample time of 0.2 ms. An example of the development of such a spectrum in time is given in fig. 2. When using this photo–electric detection system the performance seems limited to a somewhat lower level by the microchannel plate detector. This allows a velocity resolution of 100 m/s.

The focus of the instrument is corrected for the deviation of the Rowland circle[3], which for gratings of this large radii can amount to mm or even cm[4] and is caused by a varying groove spacing.
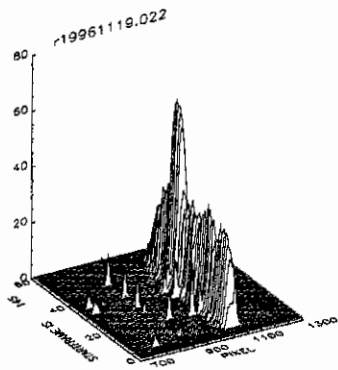
fig. 2 typical spectrum, x_axis : wavelength, y–axis :time (units 10 ms), z–axis intensity
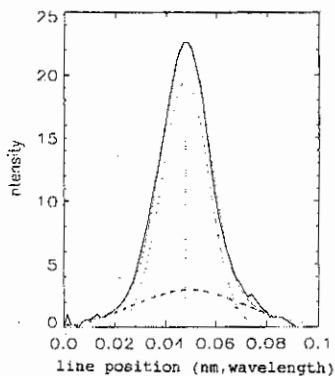
fig. 3 two hydrogen populations with different temperatures and velocity observed with L_a at 122 nm

3. First experimental results

First results were obtained from the L_α line. The temperature during the normal phase of a discharge, 5.9(1) eV, resulting from the Franck–Condon energy, increased to 7.4(1) eV during ECR heating. Switching the heating on and off shows a clear influence on the poloidal rotation (see fig.6a). Another discharge showed, after the heating was switched off, two different populations of hydrogen, one with a temperature of 10 eV and a cooler one (6.7 eV), the latter moving with the original speed, while the hot one had a velocity differing about 5 km/s from the other one [see fig. 3]. Also the emitted intensity increases about twofold during heating.

The measurement of ion impurities started with a C IV doublet at 123 nm , which could not directly be resolved. Again a rise of temperature could be seen during ECRH. Fitting the resulting line shape with two Gaussians [see fig. 4] provided a temperature rise from about 27 eV to 39 eV during heating.Also displacements of this doublet could be seen, but this effect is partly blurred by the fact that the intensity ratio of these two lines is not perfectly constant during exposure, due to the low intensity.
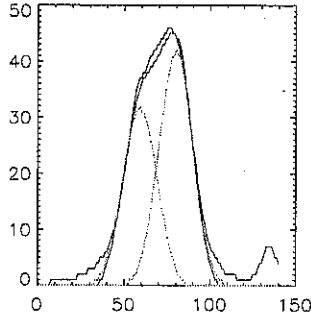
fig.4 unresolved C IV doublet at 123 nm, fitted with two Gaussians; the wavelength scale is given in pixels, where one pixel is 0.0025 nm; the intensity is in arbitrary units

4. Rotation caused by gas puffing

More suitable for the study of C IV is the resonance doublet at 155 nm. To enhance the amount of carbon in the discharge CH_4 was injected during 10 ms every 40 ms. The effect is a cooling of the plasma during injection, followed by an increase in intensity, but more interesting is an increase in poloidal rotation during gas puff as can be seen in fig. 5. We are looking 160 mm below the axis of the plasma and the line shifts clearly to lower wavelength at each event, corresponding to a change in velocity of about 1400 m/s. This has to be compared with an average poloidal speed at this radius of 3500 m/s.
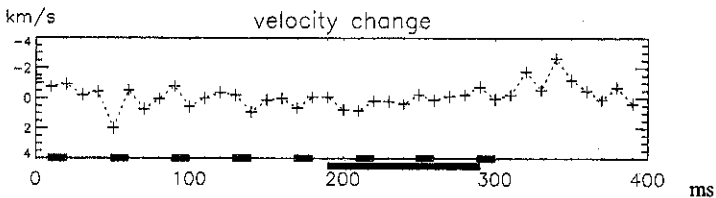
fig. 5 change in velocity of C IV ions during gas puff (indicated by the small bars)

5. Rotation at pellet injection

Also the injection of an hydrogen pellet changes the rotation of the plasma. As can be seen from fig. 6, again looking 160 mm below the axis, the wavelength shifts downwards upon arrival of the pellet, which means that the poloidal rotation speeds up. From the linewidth a cooling down of the C IV ions can be deducted.
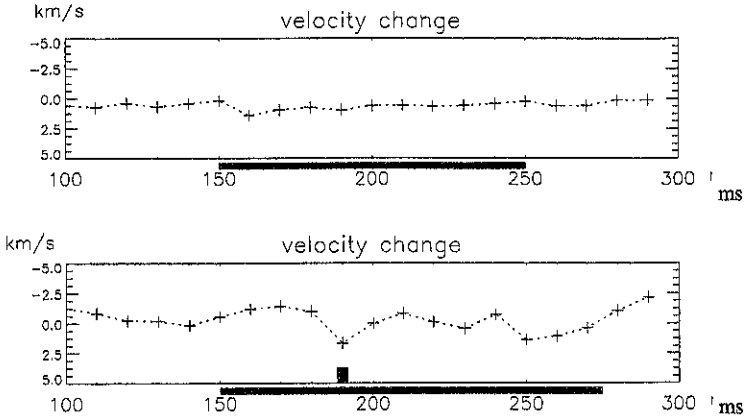
fig. 6 the upper figure shows the change in rotation above axis during ECRH (━━━━);
the lower one spin–up of the rotation due to a pellet injected below axis (■, 190 ms)

6. Conclusions

From the results given above it is clear that we can obtain a rotation velocity resolution of 100 m/s. ECRH, gas puff and pellet injection all influence the poloidal rotation of the plasma, as well as the temperature. Scanning the imaging mirror system up and down allows to study the spatial profile of a given impurity. By choosing different spectral lines is it possible to observe the plasma at different radii. All those data together allows to build up a rotation profile in the poloidal plane. These experiments can be done with a temporal resolution down to 0.2 μs, depending on the strengths of the lines involved, and a spatial resolution of about 1 cm.

This work was performed with financial support from NWO and Euratom.

[1] Th. A. M. van Kleef and Schroder, Appl. Sci Res. B11, 465–478, 1964

[2] F.G. Meijer, 28th EGAS Conference, Graz, Austria, 1996.

[3] F.M. Gerasimov, E.A. Yakovlev, I.V. Peisakhson and B.V. Koshelev, Opt. Spectrosc. 28, 423 426, 1970.

[4] F.G. Meijer, Opt. Appl. XVII, 256–263, 1987

Transonic MHD flows:
Stationary states and spectrum

J.P. Goedbloed[1], R.J. Nijboer[1], A.E. Lifschitz[2]

[1]FOM-Institute for Plasma Physics, Association Euratom-FOM,
P.O. Box 1207, 3430 BE Nieuwegein, The Netherlands

[2]University of Illinois at Chicago, Chicago, U.S.A.

1. Introduction

Whereas most of tokamak stability theory is based on the assumption of static equilibrium, neutral beam heating causes the plasma to spin and particle and energy extraction in divertors results in the supersonic flow of a narrow plasma layer on the outside of the tokamak. These kinds of flow present an enormous challenge, both with respect to the construction of stationary flow patterns, with possible transitions to super-Alfvénic flows, and with respect to the investigation of the different oscillations and new types of instabilities. In astrophysics, plasma flows have been investigated for a much longer time since they are prominent in a wide range of important phenomena, like stellar winds, rotating accretion disks, jets from extragalactic nuclei, etc. Therefore, the construction of the different types of plasma flows is a problem of common interest to the fusion and astrophysics communities [1]–[3].

Plasma flows imply a major complication in the field of MHD spectroscopy [4], which demands the construction of stationary equilibrium states and their spectral study. These theories are well developed for static equilibria but for stationary flow they still require an enormous effort. In fusion research, opening up of the magnetic geometry and high speed flows in pumped divertors pose problems of a similar nature as transonic flows in astrophysics. There, an important question is: How does *super* fast/Alfvén *flow* connect onto *sub* Alfvén/slow *flow*? One of the problems encountered is the presence of *limiting line internal singularities* where one set of characteristics in the hyperbolic flow domains starts to develop envelopes. It has been assumed that the other set of characteristics crosses these lines and, thus, facilitates the construction of continuous stellar wind solutions [5]. Our analysis shows this conclusion to be false.

In Sec. 2 we discuss the stability of incompressible flows with an X-point. In Secs. 3 and 4 we are concerned with the construction and classification of the different types of MHD flows. Particular attention is paid to the transitions from elliptic to hyperbolic flows, to the existence of limiting lines, and the implications for flow patterns in global magnetic geometries. The limiting line singularities are resolved by means of the explicit construction of symmetric discontinuous solutions.

2. Spectrum of X-type flows

Equilibrium flows have major consequences for the MHD spectral problem. The self-adjoint spectral property of static equilibrium is lost and the analysis becomes quite involved. Only the spectrum of simple equilibria can be calculated analytically. We have computed the spectrum of incompressible MHD equilibria with an X-point making simplifying assumptions on the plasma profiles. The work is an extension of the investigation of the spectrum of these kinds of flow without magnetic field [6].

Applying special Fourier transforms, it is found that the MHD spectral problem for 2D configurations with linear flow profiles can be reduced to a system of ODE's in Fourier space. This facilitates the analytic solution for the continuous spectrum, whereas the discrete spectrum may be solved numerically.

We find that the introduction of a magnetic field is stabilizing in the two-dimensional case: whenever the magnetic field dominates $(M^2 < 1)$ the flow the plasma is stable whereas it becomes unstable when flow dominates $(M^2 > 1)$.

3. Continuous stationary flows

Stationary $(\partial_t = 0)$ symmetric $(\partial_z = 0)$ MHD flows are described in terms of a flux function ψ, related to $\mathbf{B}_p$, and a stream function $\chi(\psi)$, related to $\mathbf{v}_p$. The five arbitrary flux functions χ', H, S, I, Ω may be collapsed to three: $\Pi_{1,2,3}(\psi)$. The poloidal Alfvén Mach number is defined by $M^2 \equiv \rho v_p^2 / B_p^2 = \chi'^2 / \rho$. The core problem [3] then involves a *nonlinear PDE* for the flux $\psi(x,y)$:

$$\nabla \cdot \left[(1 - M^2)\, \nabla\psi \right] + \frac{\Pi_1{}'}{M^2} - \frac{\Pi_2{}'}{\gamma M^{2\gamma}} + \frac{\Pi_3{}'}{1 - M^2} = 0,$$

end *the Bernoulli equation* for $M^2(x,y)$:

$$\tfrac{1}{2} |\nabla\psi|^2 - \frac{\Pi_1}{M^4} + \frac{\Pi_2}{M^{2(\gamma+1)}} + \frac{\Pi_3}{(1 - M^2)^2} = 0.$$

Assuming *one master profile* with two constants, A (entropy) and B (longitudinal field), i.e.

$$\Pi_1 = \pi(\psi), \quad \Pi_2 = A\,\pi(\psi), \quad \Pi_3 = B\,\pi(\psi), \qquad \pi = \psi^{2-2/\lambda},$$

and making the Ansatz of *self-similarity*,

$$M^{-2} = X(\theta), \qquad \psi = r^\lambda Y(\theta)$$

the problem reduces to two ODE's. Differentiating the Bernoulli equation, $F(X, Y, Z) = 0$ with $Z \equiv (1 - 1/X)Y'$, we obtain a system of three ODE's:

$$\frac{dX}{d\theta} = \frac{H(X,Y)}{(1 - 1/X)\, J(X,Y)}\, Z, \qquad \frac{dY}{d\theta} = \frac{1}{1 - 1/X}\, Z, \qquad \frac{dZ}{d\theta} = G(X,Y),$$

where H, J, and G are complicated functions of X and Y. The singularities $J = 0$ represent the limiting lines.

In general $(B \neq 0)$ seven flow regimes are obtained from the Bernoulli equation, indicated by $\mathcal{H}_{ff}(1^+)$, $\mathcal{H}_f(1^-)$, $\mathcal{E}_f(2)$, [Alfvén gap at $X_A = 1$], $\mathcal{E}_s(3)$, $\mathcal{H}_s(4^-)$, $\mathcal{H}_{ss}(4^+)$, $\mathcal{E}_{ss}(5)$. Here $\mathcal{H}$ and $\mathcal{E}$ indicate the hyperbolic and elliptic domains, and ff, f, s, and ss indicate the super fast, fast, slow, and sub slow speed regimes, respectively.

For $B = 0$, the region 2 disappears and the resulting phase plane with the trajectories (solutions $Q(X)$) is shown in Fig. 1. Here, Q is a simple function of Y involving the profile parameter λ. The trajectories appear to cross all the obstacles (fast and slow limit lines and the Alfvén singularity) smoothly, but the corresponding flow patterns shown in Fig. 2 are not smooth at all. In fact, the flow 'reverses' direction at the limit lines (physically impossible), indicating that there are multiple solutions that cannot be connected smoothly. The only way out is to permit discontinuous solutions.
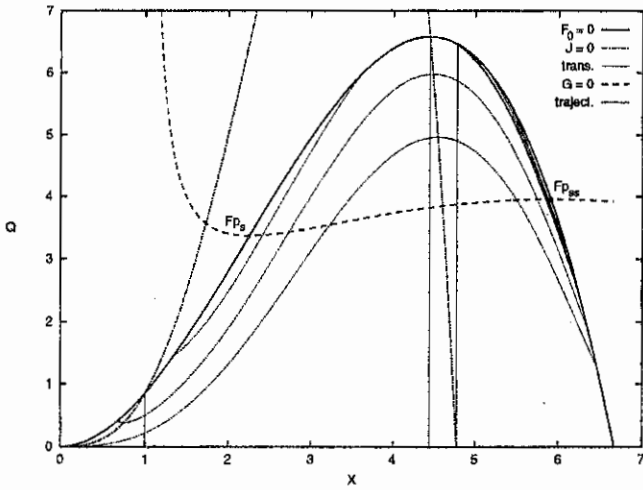
Figure 1. Trajectories in the X–Q phase plane for $A = 0.15$, $B = 0$, $\lambda = 0.5$, $\gamma = 2.0$.
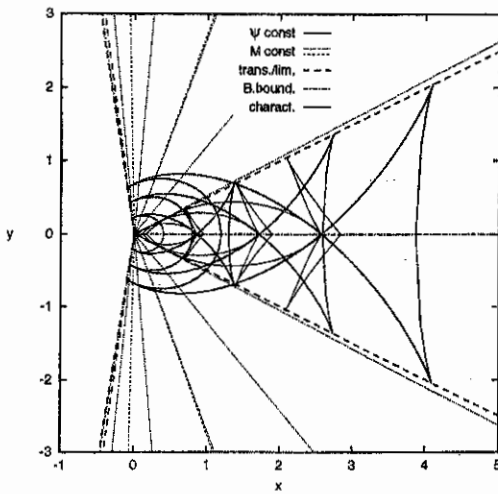
Figure 2. Flow patterns in the physical plane corresponding to the trajectory $X_i = 0.4$ of Fig. 1. Superposed are super-fast 1^+ (outer) & fast-slow $1^-, 3, 4^-$ (inner) & sub slow $4^+, 5$ (innermost) flows.

4. Discontinuous stationary flows

The following jump conditions are obtained for the self-similar solutions:

– Y and B continuous: $\quad [\![Y]\!] = 0, \quad [\![B]\!] = 0,$

– X and A discontinuous:

$$[\![(1 - 1/X)\,Y']\!] = 0, \qquad [\![1/X]\!]\,\lambda^2 Y^{2/\lambda} + \left[\!\left[X^2 + (1 - 1/\gamma - X)\,AX^\gamma \right]\!\right] = 0,$$

– Entropy condition: $[\![A]\!] \leq 0$.

At the shock positions, the following five variables can be distinguished: $\hat{X}_1 \neq \hat{X}_2$, $\hat{Y} \equiv \hat{Y}_1 = \hat{Y}_2$, $A_1 \neq A_2$. The procedure is then first to eliminate A_2 giving the *distilled jump condition*, $f_1(\hat{Y}, \hat{X}_1, \hat{X}_2, A_1) = 0$, and next to substitute A_2 in the entropy condition giving the *distilled entropy condition*, $f_2(\hat{Y}, \hat{X}_1, \hat{X}_2, A_1) \geq 0$. For given $(\hat{Y}, A_1)$, the possible shocks are then selected by plotting f_1 and f_2 in the $\hat{X}_1$-$\hat{X}_2$ plane. This gives an enormous number of possible shocks, of all categories (fast, intermediate, and slow) [3]. This provides the necessary solutions jumping across the limiting lines and resolving the mentioned paradox in astrophysical flows.

5. Conclusions

- *There are four flow regimes, separated by the limit lines and the Alfvén gap and not connected by continuous flows.*

- *The limiting line signals the expiration of continuous solutions and guarantees the existence of discontinuous solutions jumping across.*

- *Fast shocks jump across the fast limiting line Lf, intermediate shocks jump across the Alfvén gap A, and some also jump across the slow limiting line, slow shocks jump across the slow limiting line Ls.*

- *The three obstacles just create the right conditions to produce the three kinds of strongly discontinuous flow which may be considered as the nonlinear counterpart of the weak discontinuities of linear MHD.*

- *This resolves the paradox in transonic astrophysical MHD flows.*

References

[1] J.P. Goedbloed and A.E. Lifschitz, "Symmetry of magnetohydrodynamic flows", *Astrophys. Lett. and Comm.* **36**, 267 (1996).

[2] A.E. Lifschitz and J.P. Goedbloed, "Transonic magnetohydrodynamic flows", *J. Plasma Phys.*, to appear (1997).

[3] J.P. Goedbloed and A.E. Lifschitz, "Stationary symmetry magnetohydrodynamic flows", *Phys. Plasmas*, to appear (1997).

[4] J.P. Goedbloed, G.T.A. Huysmans, H. Holties, W. Kerner, S. Poedts, "MHD spectroscopy: Free boundary modes (ELM's) and external excitation of TAE modes", *Plasma Physics and Controlled Fusion* **35**, B277–292 (1993).

[5] T. Sakurai, "Magnetohydrodynamic solar/stellar wind models", *Computer Physics Reports* **36**, 247–273 (1990).

[6] A.E. Lifschitz, "On the spectrum of hyperbolic flows", *Phys. Fluids*, submitted (1997).

Ray-Tracing near Cyclotron Resonance Using Warm Plasma Dispersion

E. Westerhof

FOM-Instituut voor Plasmafysica 'Rijnhuizen', Association EURATOM-FOM
Postbus 1207, 3430 BE Nieuwegein, Nederland

1. Introduction

A standard approach to propagation of electro-magnetic waves in the electron cyclotron range of frequencies is by ray-tracing calculations on the basis of the cold-plasma Appleton-Hartree dispersion relation. Absorption and emission then are evaluated along the 'cold-plasma' trajectories, using the relevant warm plasma kinetic expressions. This has been implemented in many ray-tracing codes for Electron Cyclotron Heating (ECH) and Emission (ECE). An example of the former is TORAY [1,2]. However, warm plasma kinetic effects not only affect the imaginary part of the dispersion relation describing absorption, but also affect the real part of the wave vector. In particular, the dispersion of the perpendicular O-mode near cyclotron resonance and of the perpendicular X-mode near the second harmonic are affected significantly: in both cases one finds a minimum in the perpendicular refractive index $N_\perp$ almost at the resonance and a maximum on the high field side of the resonance. These differences with respect to the cold-plasma dispersion also lead to changes in the wave propagation. Previous studies [3-7] have shown, for example, reflections of X-mode at the position of the second harmonic resonance [3,6], and a focussing of O-mode waves propagating vertically near the fundamental resonance [7].

Warm plasma ray-tracing, however, is complicated by the fact that near cyclotron (harmonic) resonances the dispersion relation is complex. To calculate ray trajectories, the complex dispersion relation is substituted by a real approximation. This cannot be done by neglecting the anti-Hermitian part of the dielectric tensor: near resonance the anti-Hermitian part is very large, and its neglect would lead to nonsensical results [4,5]. Also the method proposed by Friedland and Bernstein [8] for ray-tracing in weakly dissipative media, based on an expansion of the dispersion relation near its real frequency root, breaks down for parameters of practical interest to EC wave propagation [9].

No approximation is necessary, when one first solves the full, complex dispersion relation $D(x, \mathbf{k}, \omega) = 0$ for complex $k_\perp$ and real $k_\parallel$ and ω, which is possible by writing D as a biquadratic equation for $k_\perp$ [10]. Since ray trajectories are determined by the real part of $\mathbf{k}$, they are obtained exactly using the following ray Hamiltonian [9]:

$$D' = k^2 - {k'_\perp}^2(\mathbf{x}, k_\parallel) - k_\parallel^2(\mathbf{x}, \mathbf{k}) = 0, \tag{1}$$

in which $k_\parallel$ and $k'_\perp$ are *functions of the wave vector* $\mathbf{k}$ *and the local equilibrium*: $k_\parallel$ is the projection of $\mathbf{k}$ along the equilibrium magnetic field, and $k'_\perp$ is the real part of the corresponding solution of the full, complex dispersion relation. Ray tracing on the basis of Eq. (1) has been implemented in a new version of TORAY.

2. Results of Warm Plasma Ray-Tracing

The largest differences with respect to cold plasma dispersion are found in the warm plasma dispersion for (nearly) perpendicular propagation of both the fundamental harmonic Ordinary (O-)mode and the second harmonic eXtraordinary (X-)mode. In both cases the perpendicular refractive index $N_\perp$ exhibits a minimum almost at the resonance and a maximum on the high field side of the resonance. As shown in Ref. [9], the dependence of this oscillation on the parallel refractive index $N_\parallel$ is responsible for an oscillation of the ray path in the direction along the magnetic field when crossing the resonance. This effect is recovered in the present ray-tracing calculations, but in all cases studied the related excursion from the cold plasma trajectory was small and did not affect significantly the projection of the ray path on the poloidal plane nor the power deposition. In fact, as is noted in Ref. [9], the optical depth is given in terms of the imaginary part of the perpendicular wave vector as $\tau = \int 2k''_\perp \cdot ds$, and is practically independent of the details of the trajectory parallel to $\boldsymbol{B}$.

In Ref. [6] ray-tracing results were shown in which effects of warm plasma dispersion led to an anomalously low absorption of O-mode for (nearly) perpendicular propagation. This result is not reproduced in our warm plasma ray-tracing calculations, and is also in conflict with our previous remark concerning the optical depth. This discrepancy is probably due to the application in Ref. [6] of the approximation of Friedland and Bernstein well outside its regime of validity for this case.

Two effects of warm plasma dispersion are recovered in our ray-tracing calculations: (1) reflection at the position of the second harmonic of X-mode waves injected perpendicularly toward the magnetic axis from close to the top or the bottom of the plasma [3,6]; (2) focussing of a vertically propagating O-mode beam for frequencies just above or slightly below the cyclotron frequency [7]. The latter effect has been invoked to explain a peak on the high frequency side of the resonance in the vertical O-mode transmission spectrum on Tore Supra [7]. Both effects are easily explained by the behaviour of the perpendicular refractive index as sketched above: the rays are reflected from the local minimum in $N_\perp$ at the resonance. Note that the spatial gradient in $N_\perp$, caused by this resonant effect, is along the major radial direction. Apart from density effects, the vertical gradient of $N_\perp$ vanishes and, consequently, N_{vert} is approximately conserved. When a ray is injected such that N_{vert} is larger than the minimum in $N_\perp$ near resonance, the ray will be reflected there. This is demonstrated in Figs. 1a and b, which show the warm plasma trajectories of nearly vertically injected 60 GHz O- and 110 GHz X-mode, respectively. The parameters are typical of a small tokamak (RTP, $R_0 = 72$ cm, $a = 16.5$ cm), with plasma density and temperature $n_e(r) = 3.0 \times 10^{19}(1 - (r/a)^2)^{.25}\,\text{m}^{-3}$, $T_e(r) = 1.0(1 - (r/a)^2)^2$ keV. In both cases the resonance is at $R = R_0$ (i.e. (a) $B_0 = 2.14$ T, (b) $B_0 = 1.96$ T). In all cases, the corresponding cold plasma trajectories would be almost straight lines through the magnetic axis. For these parameters the 60 GHz O-mode waves are reflected from the resonance if their injection angle differs by less than about 25° from vertical, while the 110 GHz X-mode waves are reflected for angles less than about 35°.

We also studied the effects of warm plasma dispersion in typical ECRH or ECCD scenarios for ITER. An equilibrium with peaked pressure profile has been used that corresponds to a full performance ITER reference discharge as obtained with the PRETOR code [11]. Figures 2a and b show the projection on the poloidal plane of the trajectories for rays injected from a typical range of positions as considered for ECRH or ECCD: i.e., horizontal injection in the range from 50 cm below to 50 cm above the plane through the magnetic axis, or vertical injection from a top port. Figure 2a shows an example of ray paths for perpendicular injection of O-mode at 170 GHz for heating to ignition (the central temperature is taken to be 10 keV in this case). Figure 2b refers to obliquely injected O-mode at 170 GHz for ECCD during full performance (central $T_e = 30$ keV). Injection is at a toroidal angle of 30° for the waves launched horizontally and of 50° and 60° respectively for the waves launched from the top. A flat density profile with central density $n_e = 1.5\,10^{20}\mathrm{m}^{-3}$ has been used with steep gradients at the edge. The dashed curves represent the corresponding cold plasma wave trajectories. The regions of wave absorption along the warm trajectories are indicated by the black diamonds. Significant differences between cold and warm plasma trajectories are again only seen for waves injected almost vertically from the top, which suffer reflection. Where waves along the cold trajectory would be fully absorbed, only partial absorption occurs for the reflected rays: 90% and 45% absorption for the perpendicular (a) and oblique (b) top rays, respectively.

Note that the density used in the calculations for ITER is relatively high: for lower densities the effects of dispersion are much smaller.

REFERENCES
[1] A.H. Kritz, et al., proceedings of the 3rd Intern. Symposium on Heating in Toroidal Plasmas, Grenoble (France), 22–26 March (1982) Vol. II, p. 707.
[2] E. Westerhof, Rijnhuizen Report RR 89–183 (1989).
[3] H. Bindslev, in *EC-9, Proceedings of the* 9th *Joint Workshop on ECE and ECH*, Borrego Springs (CA), 23–26 Jan. 1995, Ed. J. Lohr, World Scientific, p. 585 (1995).
[4] S. Pesić and A. Stojić, 14th Int. Conference Plasma Physics and Controlled Nuclear Fusion Research, Würzburg, 30 September–7 October 1992, IAEA Vienna (1993) Vol. 2 p 273; S. Pesić and A. Stojić, J. Phys. Soc. Jpn. **62**, 2359 (1993).
[5] S. Pesić, Europhys. Lett. **35**, 349 (1996).
[6] A. Pochelon, et al., 20th *EPS Conference on Controlled Fusion and Plasma Physics*, Lisboa (1993), Part III p 1029.
[7] J.L. Ségui, et al., in *EC-9, Proceedings of the* 9th *Joint Workshop on ECE and ECH*, Borrego Springs (CA), 23-26 Jan. 1995, Ed. J. Lohr, World Scientific, p. 223 (1995).
[8] L. Friedland and I.B. Bernstein, Phys. Rev. A **22**, 1680 (1980).
[9] E. Westerhof, to be published in Plasma Phys. Contr. Fusion **39**, June (1997).
[10] I. Fidone, G. Granata and R.L. Meyer, Phys. Fluids **25**, 2249 (1982).
[11] D. Boucher, et al., Proc. IAEA TCM on Advances in simulation and modelling of thermonuclear plasmas, Montreal, Canada, 5–18 June 1992, p. 142 (1993).
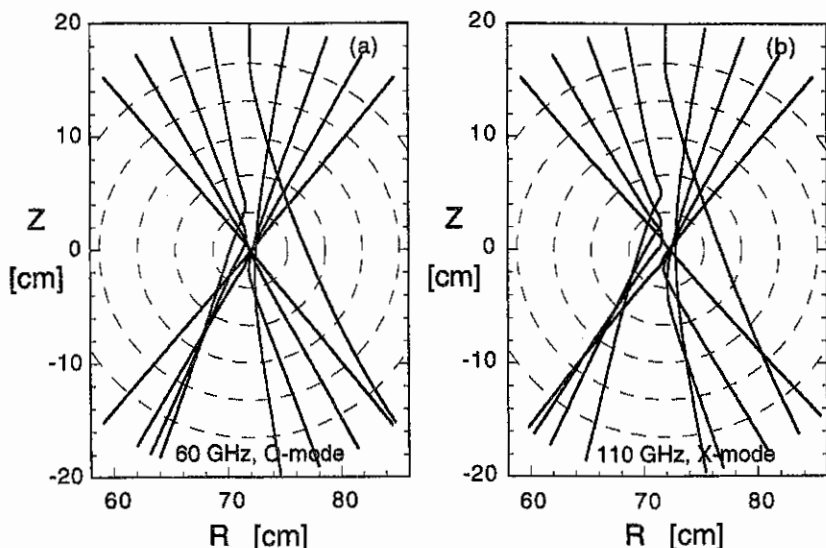
Figure 1. Trajectories of 60 GHz first harmonic O-mode (a), and 110 GHz second harmonic X-mode (b) injected perpendicularly in RTP (for parameters see text). Subsequent rays, launched from $r = 20$ cm at the top of the vessel, differ by $10°$ in poloidal injection angle and are directed exactly toward the axis.
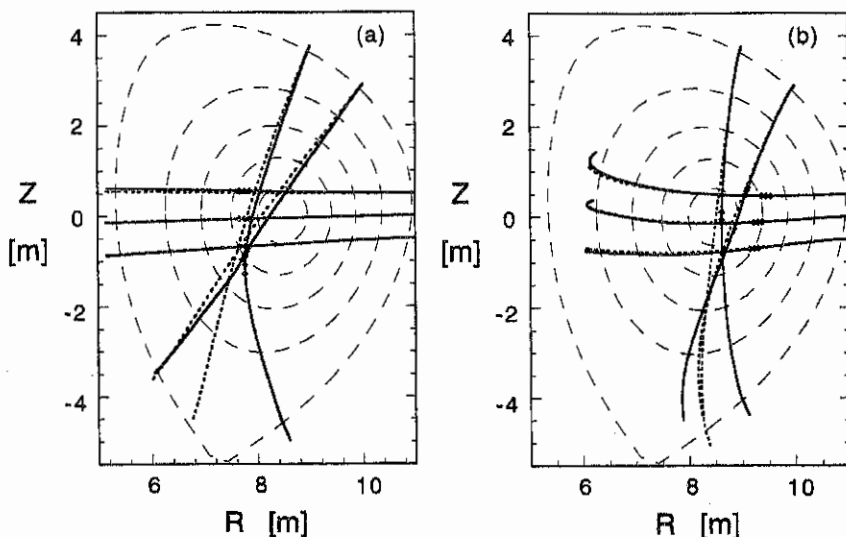
Figure 2. Trajectories in the poloidal plane of 170 GHz first harmonic O-mode waves in ITER. (a) perpendicularly injected waves for central heating; (b) obliquely injected waves for central current drive ($N_{\parallel} = 0.4 - 0.5$ at injection).

Current density profiles measured with multi-position tangential Thomson scattering in the RTP tokamak

F.A. Karelse, M. de Bruijne, M.N.A. Beurskens, C.J. Barth, G.M.D. Hogeweij,
N.J. Lopes Cardozo, H.J. van der Meiden, F.J. Pijper and the RTP team

*FOM-Instituut voor Plasmafysica 'Rijnhuizen', Association Euratom-FOM,
Trilateral Euregio Cluster, P.O.Box 1207, 3430 BE Nieuwegein, The Netherlands*

Introduction

The Rijnhuizen Tokamak Project (RTP; $R/a = 0.72/0.164$ m, $B_T \leq 2.5$ T, $I_p \leq$ 150 kA) is devoted to transport physics. One of the key issues is to understand the role of the current density j in transport phenomena. Because j determines the internal magnetic structure, it may strongly determine the plasma behaviour, and knowledge of j may open ways to regimes of better confinement.

To study j profiles, a new tangential detection branch has been installed on the double-pulse multi-position Thomson scattering diagnostic [1,2] (see figure 1). The tangential detection branch measures the electron temperature (T_e) and density (n_e), collecting ruby laser light (wavelength $\lambda_0 = 694.3$ nm) scattered along a vertical chord through the plasma (20 cm for tangential, 30 cm for radial observation). Additionally, an extra Doppler shift $\Delta\lambda_d$ is measured, caused by the toroidal electron drift velocity v_d. From the measured $\Delta\lambda_d$, j can be derived.
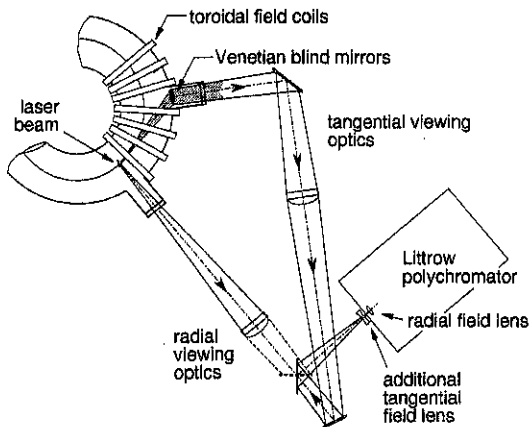
Figure 1: *Layout of the RTP Thomson scattering system.*

The performance of the tangential detection branch is comparable to the radial one: T_e can be determined in the range of 50 eV–6 keV with a typical error of 8 %, at $n_e = 2 \cdot 10^{19}$ m^{-3} and a laser energy of 15 J for a scattering volume of 1.7 mm. The double pulse recording allows accurate plasma background correction. Venetian blind mirrors [3] are used to reflect the scattered light into the diagnostic port. The overall transmission is three times lower than in the radial branch. The statistical error on v_d is in the order of 1.5 nm, for each z-position of 1.7 mm, and $n_e = 5 \cdot 10^{19}$ m^{-3}. This corresponds typically to a 100 % error on j. By averaging 10 spatial elements and 15 plasma discharges, this error can be brought down to less than 10 %. This yields 11 independent measurements of j.

In this paper the first results are presented.

Data analysis

Two analysis methods were developed: 1) a 3 parameter least squares fit of a shifted Mattioli distribution [4] to the measured spectra. This method assumes that that the spectrum is only shifted and that the plasma is thermal; 2) Momentum method [5]. The relativistic spectrum is reshaped to a Gaussian spectrum. The Mattioli fit is only used to get the temperature as an input for the relativistic correction. This method is more sensitive to distortions in the tails of the spectrum. Both methods are tested on simulated data. The results of both methods are in agreement, and the errors are comparable. The results match well within the error bars to the input of the simulation. However, the addition of disturbances such as plasma light and Poisson noise, gives an offset red shift to the results. The plasma disturbances are measured using the double pulse recording. Furthermore, the red offset can be removed by subtracting the measurements of discharges with positive and negative currents. Results in this paper are obtained with method 1.

Results

Figure 2 shows the comparison of the Mattioli distribution with the data, averaged over 34 ohmic negative current shots. Method 2 is applied to the data as well as the theoretical curve. The data are equal to the Mattioli form within the error bars, which means that the Mattioli distribution is justified.
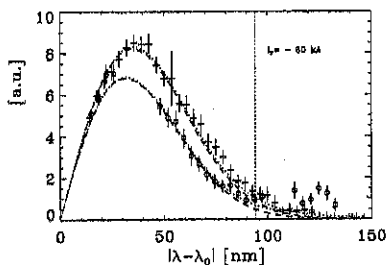
Figure 2: *j contribution per wavelength for the red wing(+) and the blue wing (○). The spectrum is averaged over all negative current shots. The area between the curves corresponds to the net j. The line indicate the Mattioli fit. The vertical dotted line indicates $2\Delta\lambda_e$.*

To assess the accuracy and limitations of the tangential Thomson scattering (TTS) set-up, measurements were made in a series of ohmic discharges ($q_a = 7$, $T_e(0) \sim 600$ eV). The density was scanned ($1 - 9 \cdot 10^{19} \text{m}^{-3}$) and the current was reversed in half of the discharges.

To deduce the spectral shifts from the measured spectra, $\Delta\lambda_d$ is averaged over 17 mm in z-direction and over all discharges of equally signed current(17 discharges with +60 kA, 34 with −60 kA, density corrected). The average shifts of the plus and minus current shots are subtracted. In figure 3 the resulting j and safety factor q profiles are shown. The dotted lines indicate the calculated results from neo-classical resistivity. The measured data show good agreement with the dotted lines. The estimated error is 9%.

The averaged plus and minus shift have a common red offset as expected from the simulations. This offset is slightly increasing with $1/n_e$, because the noise increases with $1/n_e$. It should be noted that the offset of the shift profiles varies with position beyond the fit errors. However, the shift profile corrected for the offset does not show this effect, so probably this is a constant instrumental effect. The wavelength calibration of the CCD chip could be varying with z.
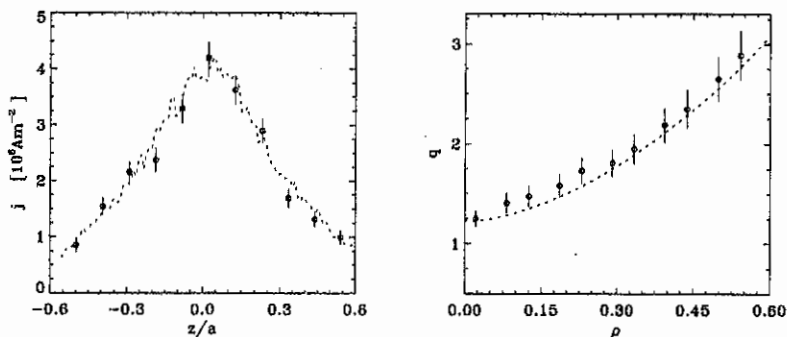
Figure 3: *j for ohmic plasmas, and the corresponding q profile, respectively. Dashed lines are computed with neo-classical resistivity.*

NCS Discharges

Recent experiments at RTP have shown bifurcations in confinement in hollow T_e profile discharges [6,7]. These profiles are achieved with strong off-axis Electron Cyclotron Heating (ECH)(deposition radius $\rho_{dep} = 0.4 - 0.6$, $P_{ECH} \sim 5 \cdot P_n$). q-profiles based on neo-classical resistivity indicate Negative Central Shear (NCS), but have a large uncertainty in the plasma center. TTS can provide additional information on the central q.
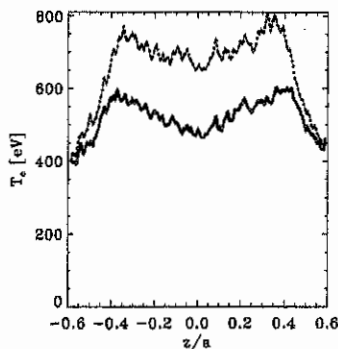
Figure 4: T_e for the averaged low $(-)$ and high $(\cdot\cdot)$ confinement NCS shots.
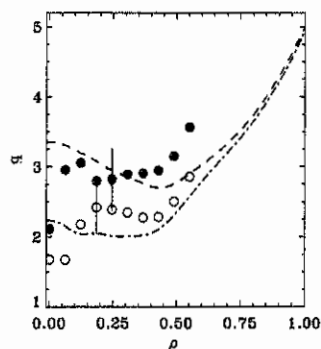
Figure 5: *q for the low $(\bullet)$ and high $(\circ)$ confinement NCS shots. The lines are the q-profiles from neo-classical resistivity.*

A series of 47 TTS profiles was taken in steady state hollow T_e plasmas with currents of both signs, so that the shift difference can be determined. ρ_{dep} was changed between 0.40 and 0.46 ± 0.02. Hence, the discharges fall into two classes of confinement

with distinct central temperatures. In figure 4, the averaged $T_e(z)$ for the low and the high confinement discharges are plotted. The T_e profiles are almost equal outside ρ_{dep}, whereas inside ρ_{dep} they are separated by 200 eV. In figure 5, the q-profile measurements are shown for the high and the low branches, as well as the corresponding q-profiles from neo-classical resisitivity.

It should be noted that the shear is about zero up to ρ_{dep} in both cases. However, the q are separated significantly. For the low branch q is above $5/2$, and for the high branch just below $5/2$. This confirms the existence of a q-related thermal barrier as proposed in [7]. The agreement with neo-classical resisitivity is reasonably good in the region just inside ρ_{dep}. At $z = 0$ the measurements show a significant decrease. The cause of this is unclear.

Conclusion

Unique measurements of the tangential Thomson scattering diagnostic at RTP were presented, giving local current density measurements in the inner 20 cm of the plasma (60 % of a) with an accuracy < 10 %, after averaging 10 z-positions and ~ 15 shots. Two analysis methods were evaluated, giving very similar results. In a test series of ohmic shots, TTS gave results in agreement with neo-classical resistivity. Furthermore, the Mattioli fit function turned out to be justified. For NCS discharges, TTS measures two distinct q profiles for the two classes of confinement, confirming the q-related thermal barriers close to the deposition radius. Unfortunately, TTS could not provide reliable information on the central q.

In this paper the ion toroidal velocity has not been accounted for yet. For ohmic shots this velocity is ± 5 % of v_d, for NCS discharges, it could be even more. In absence of accurate measurements, this question remains open.

In the near future we hope to investigate j during Electron Cyclotron current drive, especially counter current drive. Neo-classical calculations of the current density indicate that in this case $j(0)$ might be strongly reduced. The variation in the offset in $\Delta\lambda_d$ should be investigated furtherand the question will be adressed whether the fluctuations on the individual shift profiles of the order of the statistical error have any plasma physical cause.

References

[1] C. J. BARTH et al., A high resolution multiposition Thomson scattering for the RTP tokamak, *Acc. by Rev. Sci. Instrum.*

[2] M.N.A. BEURSKENS et al., Double pulse Thomson scattering system at RTP, *Rev. Sci. Instrum.* **68**, 721 (1997).

[3] C. J. BARTH, B. J. J. GROBBEN AND G. C. H. M. VERHAAG , A mirror system for collecting Thomson-scattered light in a tangential direction, *Appl. Opt.* **33**, 6062 (1994).

[4] M. MATTIOLI, Incoherent light scattering from high temperature plasmas, *EUR-CEA-FC-752 (1975)*.

[5] A. C. A. P. VAN LAMMEREN et al., *Nucl. Fus.* **32**, 655 (1992).

[6] M.R. DE BAAR et al., *Acc. by Phys. Rev. Lett.* and this conference.

[7] N.J. LOPES CARDOZO, invited at this conference.

Analysis of electrostatic and magnetic fluctuations on the CASTOR tokamak

J. Stöckel, V. Dhyani, K. Jakubka, L. Kryška, F. Žáček
Institute of Plasma Physics, Prague, Czech Republic
I. Ďuran, M. Hron, J. Petržílka
Faculty of Mathematics and Physics, Charles University, Prague

Spatial-temporal characteristics of turbulent structures are investigated on the CASTOR tokamak ($R = 0.4\ m$, $a = 0.06\ \&\ 0.085\ m$, $B_t = 0.5 \div 1.1\ T$, $I_p = 5 \div 20\ kA$, $\tau \leq 50\ ms$). The experimental tools are arrays of electric and magnetic probes that can be placed in SOL or even inserted into the core plasma during short and low-I_p discharges.

Electrostatic fluctuations in the edge plasma are measured by an array of 16 Langmuir probes oriented in the poloidal direction. The odd tips measure the floating potential ($\sim$plasma potential), the even ones are biased and measure the ion saturation current ($\sim$density). This arrangement allows to correlate the signals of the same kind as well as to compute the mutual correlation between the plasma density and potential [1]. An example of the spatial-temporal correlation functions is shown in Fig. 1.
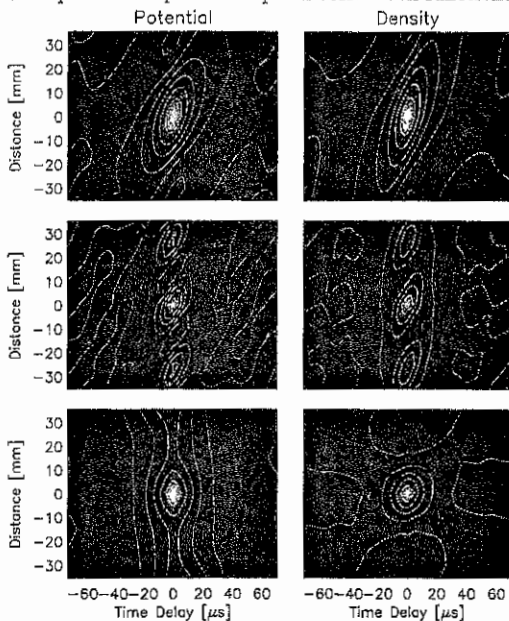
Fig. 1: *Correlation portrait of potential (left) and density (right) fluctuations. Bright and dark regions represent the positive and negative correlation, respectively.*
Top row: *"Standard" turbulent structures similar to those observed on ASDEX [2].*
Middle row: *Short wavelength structures are observed in regimes with the aspect ratio $A = 4.7$ and $q_a > 11$.*
Bottom row: *Spatial decorrelation of potential and density fluctuations is observed in regimes with the aspect ratio $A=6.7$ and $q_a > 7.4$. The probe array is close to the velocity shear layer in this particular case.*

In most cases, the correlational analysis reveals structures of density and potential similar in character. Their lifetime is $\sim 10 \div 20\mu s$, the correlation length is $\sim 1 \div 2\ cm$ and they are seen propagating in the poloidal direction with $v_p \leq 1\ km/s$. The structures exhibit a poloidal periodicity ($\lambda = 8 \div 10\ cm$), while they are aperiodic in time. A relatively high level of mutual correlation between the density and potential fluctuations indicates forming of "eddies"[1]. Such turbulent structures are similar to those reported from the

ASDEX [2], in spite of the quite different size of the experiment. Under some discharge conditions (in particular, in shots with high q_a), the poloidal dimension of the structures is dramatically reduced, as also demonstrated in Fig. 1.

The fluctuation induced flux is derived from the probe data as a product of the local density and poloidal electric field (see Fig. 2). The resulting mean flux $\bar{\Gamma}$ is directed always outwards, typically in the range of $\sim 10^{20}\ m^{-2}s^{-1}$.
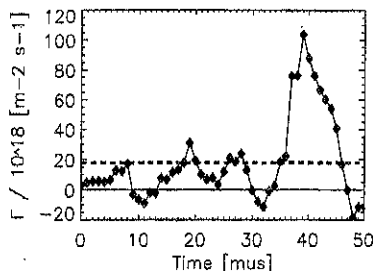
Fig. 2: *Evolution of the fluctuation-induced flux $\Gamma(t)$. Dashed line — the mean value, $\bar{\Gamma}$.*
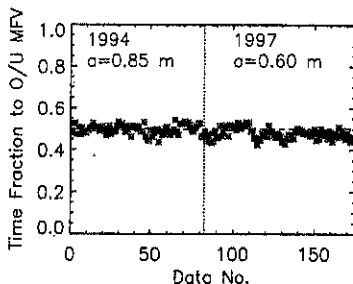
Fig. 3: *Ratio of the time fractions in which $\Gamma(t)$ is above and below the mean value for 178 shots.*

Among many parameters characterizing the fluctuation induced flux, we compute also the time fractions $T_{\Gamma(t)<\bar{\Gamma}}$ and $T_{\Gamma(t)>\bar{\Gamma}}$ corresponding to the time of $\Gamma(t)$ spent below and above its mean value. Their ratio $T_{\Gamma(t)>\bar{\Gamma}}/T_{\Gamma(t)<\bar{\Gamma}} \approx 0.5$ is found to be invariant on the discharge conditions, as shown in Fig. 3. This may indicate that the fluctuation induced flux could be an implicit function of a random variable x as $\Gamma \sim x^4$.

Magnetic Fluctuations are measured by an array of eight absolutely calibrated coils with spatial resolution 6.7 mm in the radial direction. In short discharges ($t \leq 10\ ms$) with a reduced plasma current ($I_p \leq 7\ kA$), the whole array can be inserted into the plasma column without any serious plasma disturbance. An example of the frequency spectra ($10 < f < 120\ kHz$) of the $\tilde{B}_r$ fluctuations measured at $0.65 \leq r/a \leq 1.2$ are shown in Fig. 4.
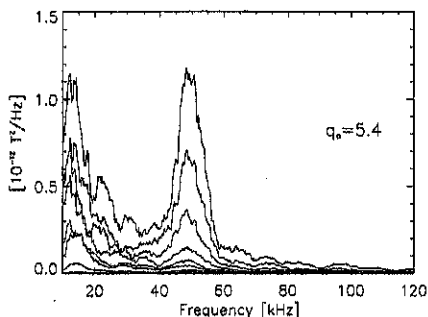
Fig. 4: *Frequency spectra of $\tilde{B}_r$ fluctuations in a shot (# 3020) with $q_a = 5.4$. $B_t = 0.5\ T$, $I_p = 10\ kA$, $\bar{n}_e = 8 \cdot 10^{18} m^{-3}$. Spectra are evidently a superposition of broadband spectra decaying as $\sim f^{-(2+3)}$ and a narrow peak. The highest spectral power density in measured by the innermost coil.*

The frequency resolved correlational analysis of the coil signals indicates that the spectrum

is a superposition of incoherent broadband fluctuations and a coherent mode (see Fig. 5). The radial correlation length of the broadband fluctuations is in the range of 2 cm over the whole length of the probe array and, interestingly, their radial propagation in the outward direction can be identified from this correlational portrait.
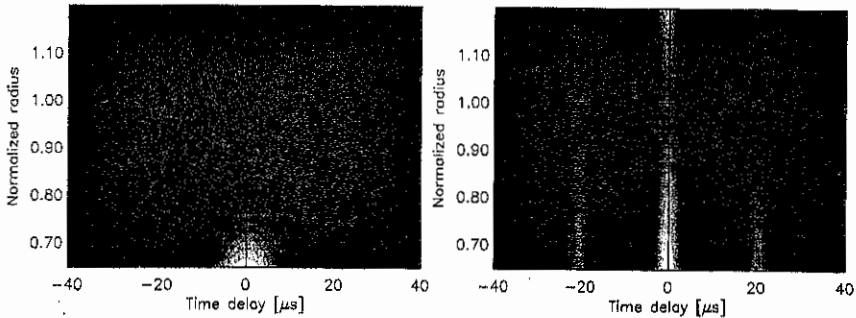
Fig. 5

Correlational portrait of B_r fluctuations in the frequency band $10 \div 35\ kHz$ (microturbulence), # 3020.

Correlational portrait of B_r fluctuations in the frequency band $35 \div 60\ kHz$ (coherent mode), # 3020.

The dominant poloidal number of the coherent fluctuations was identified as $m = 2$ by an array of Mirnov coils. The frequency resolved radial profiles of B_r fluctuations differ in form as shown in Fig. 6.
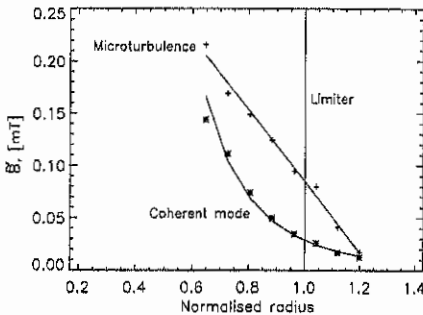
Fig. 6: *Radial profile of broadband fluctuations and of the coherent mode with $m=2$, # 3020. The level of the coherent fluctuations decays radially as $\sim r^{-4}$. Position of the resonant surface $m=2$ is estimated to be around $r/a \sim 0.5 \div 0.6$ assuming a reasonably peaked current profile.*

Fluctuations of Electric Current

A possible link of electrostatic and magnetic fluctuations in the SOL was recently suggested in [2]. The proposed model tries to explain the plasma turbulence by a flute-like instability developed at the low field side of the torus due to unfavorable curvature of the magnetic field lines, using approach described in [3]. The model predicts dipole current tubes (poloidally spaced) connected to each other via the limiter surface. Fluctuating parallel currents are expected to be in phase with the potential fluctuations and, consequently, their character should be similar.

We try to measure fluctuations of the parallel electric current directly by a miniature Rogowski coil with the spatial resolution 7 mm. Simultaneously, the floating Langmuir probe is placed in the center of the Rogowski coil to have the possibility to correlate the

current and potential fluctuations. This combined probe is movable on a shot-to-shot basis. Results of preliminary measurements are shown in Fig. 7.
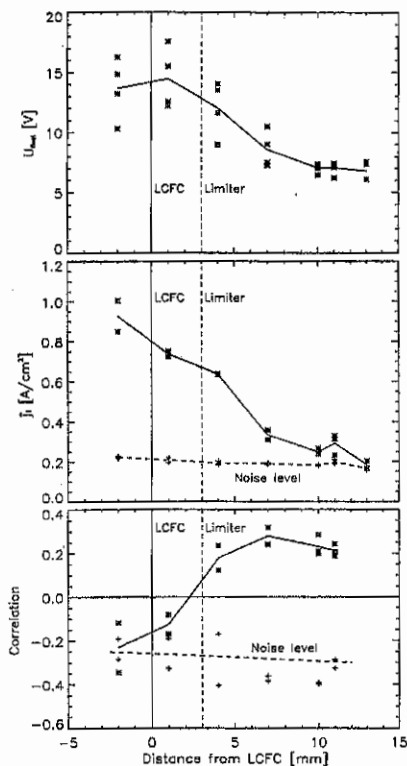
Fig. 7: *Current fluctuations in the limiter shadow, #5000-30.*

Top: *Radial profile of the floating potential is measured to determine the position of the Last Closed Flux Surface.*

Middle: *RMS value of electric current fluctuations versus normalized radius r/a. The noise level is determined under similar discharge conditions by closing the active space of the Rogowski by two metallic plates. This prevents the current flow through the coil.*

Bottom: *Cross-correlation of the current and potential fluctuations.*
The correlation is not too high, probably due to a noise component in the Rogowski coil signal. Nevertheless, the opposite sign of the correlation coefficient within and behind the LCFC is apparent.

As seen from the figure, the radial profile of $\tilde{j}_\parallel$ exhibits a characteristic plateau extended a few mm behind the LCFC. This plateau is well above the noise and its level $\tilde{j}_\parallel \sim 0.5 \ A/cm^2$ is in the range of prediction [2], which is $\tilde{j}_\parallel = enc_s\frac{e\tilde{\phi}}{kT_e} \approx 1 \ A/cm^2$ for typical CASTOR edge plasmas.

A relatively low correlation between $\tilde{j}_\parallel$ and $\tilde{\phi}$ is observed, but its sign changes on crossing the LCFC. However, the definite statement about the mutual link of these quantities needs to further reduce of the noise.

References:

[1] *Stöckel J. et al: In Proc. of 1996 ICPP Conference, Vol. 1, p. 322, Nagoya, 1996*

[2] *Endler M. et al: Nuclear Fusion, 35, 1995, p. 1307*

[3] *Nedospasov A.V.: Sov. J. Plasma Phys., 15, 1989, p. 659*

Characteristics of low intensity LHW launched in tokamak CASTOR by a quasioptical grill

Žáček F., Jakubka K., Klíma R., Kryška L., Nanobashvili* S., Pavlo P., Preinhaelter J., Stöckel J.

Institute of Plasma Physics, Za Slovankou 3, 182 00 Prague 8, Czech Republic
*Institute of Physics, Taramashvili 6, 380077 Tbilisi, Georgia

INTRODUCTION

To avoid difficulties with the complexity of lower hybrid waveguide grills used currently for generation of electric current in large tokamaks, the idea of a much more simple quasioptical launcher (*"quasioptical grill"*) has arisen [1]. It has been the goal of the experiments carried out recently on tokamak CASTOR ($R/a = 0.4/0.1m, B \leq 1T, I_p \leq 20kA, \tau \leq 40ms$) to prove the viability of this idea.

A direct identification of slow lower hybrid wave (LHW) inside the tokamak plasma (not the current generation itself) has been chosen as a physical proof of the method applicability on the basis of conclusions of the First Meeting on Advanced Launchers [2]. For these experiments, a short pulse magnetron ($\tau \leq 1.5ms$) working on the frequency $9.3GHz$ and yielding a relatively low power of several kW only has been used. For the RF measurements inside the plasma, a movable (through the whole plasma cross-section) coaxial double probe detecting the wave amplitudes and phases in two points separated $6mm$ toroidally and RF circuit for determination of the wave phase velocity v_z along the toroidal magnetic field have been developed and realized [3]. As launchers, two quasioptical antenna systems have been developed and applied. The first one (an *"open"* grill with output dimensions $76mm$ in toroidal and $100mm$ in poloidal directions [3]) was based on the original idea [1] of oblique illumination of sufficiently large system of rods by a plane wave. The second one (a *"closed"* grill with dimensions $68 \times 52mm$), having many advantages, has been suggested quite recently, see [4,5]. In this case, the grill rods form the end part of an oversized waveguide. Due to this fact, all the boundary conditions are taken into account and the problem (i.e. enumeration of the power spectrum and coupling) is solved exactly by full wave method. The movable RF probe has been placed in CASTOR plasma cross-section $45°$ toroidally away from the launcher. This position has been chosen according to the LHW ray tracing, taking into account all the parameters of the experiment (i.e. wave frequency, tokamak magnetic field, density profile and N_z expected from the theory).

This contribution brings an attempt to analyze the characteristics of LHW launched into the CASTOR tokamak plasma using the quasioptical antennas and measured by double RF probe as mentioned above.

EXPERIMENTAL RESULTS

The first striking observation during the LHW measurements inside the plasma was a high level of the wave amplitude turbulent modulation in time as well as in space [3]. It may be reasonably considered that such situation is caused by plasma density fluctuations. However, detailed measurement of local density fluctuations in the place of RF probes [3] as well as in front of the grill [5] don't reveal any correlation between these local density fluctuations and the wave's amplitude fluctuations (in the both cases of "open" as well as "closed" antennas). Moreover, it was found in [6] after a modification of the phase evaluating schema for such conditions that not only the amplitude, but also the phase of the wave fluctuates in a very high degree. An example of this wave behaviour at $r = -65mm$ is shown in Fig.1 for RF pulse $P_{inc} \simeq 3kW$ with a length of $150\mu s$ (electron density at radius $r = -65mm$ $n \geq n_{crit} \doteq 1 \times 10^{18}m^{-3}$ for $f = 9.3GHz$). U_1 and U_2 in Fig.1 are quantities proportional to the squares of the electric fields in two points separated $6mm$ toroidally (signals from detecting diodes), φ is the mutual phase of these two fields.

The following conclusions can be drawn from this figure:

1. amplitude of the field inside the plasma is modulated almost up to 100%;

2. there is no regular time correlation between the peaks of both amplitudes (some peaks seem to be correlated, however, some others are not);

3. mutual phase fluctuates in a time scale of several hundreds of kHz up to $\pm 90°$; it is clear that such high level of phase fluctuations hinders the N_z determination.

#3688, r=−65mm
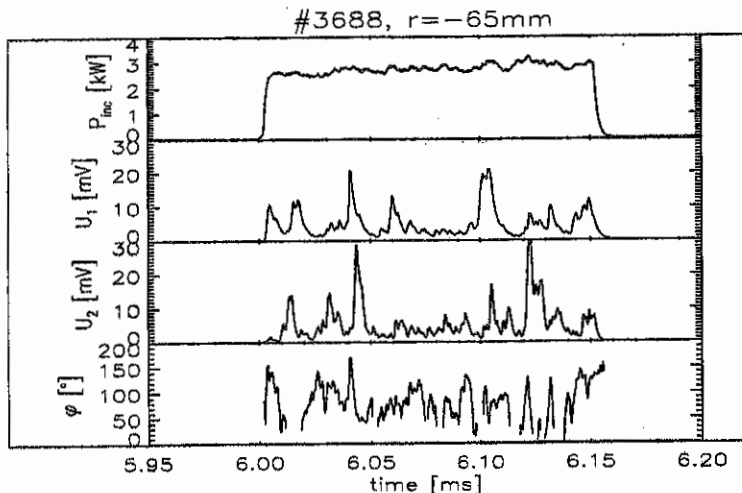
Figure 1: Time dependences of incident RF power P_{inc}, amplitudes of RF fields U_1, U_2 at the radius $r = -65mm$ and mutual phase φ of these fields.

DISCUSSION

During the previous measurements with quasioptical grill carried out on tokamak CASTOR two important facts have been proved:

1. amplitude of the wave launched in tokamak exhibits a clear concentration in the region of lower hybrid conus predicted by LHW ray tracing [3];

2. the measured dependence of wave's reflection on the electron density in front of the grill corresponds very well to the theory prediction [5].

Both these facts support our opinion that the wave launched by the quasioptical grill and observed inside the tokamak plasma is really the LHW.

Nevertheless, the main goal of the work, i.e. determination of N_z, has not been reached up to now. Namely, in the presence of a fluctuating tokamak plasma the observed wave exhibits a strong turbulent character hindering the phase evaluation. It was shown in [3,5] that the strong amplitude and phase fluctuations observed are neither correlated with local fluctuations of the plasma density in the measuring probe position nor in front of the grill. This fact indicates that the local behaviour of RF field inside the plasma is determined by fluctuations of the refractivity index along the whole ray of the wave from launching antenna to the measuring RF double probe. In this way the observed RF field behaviour is determined by the spatial integration of an instant picture of the plasma density fluctuations along the whole wave's path. Because density fluctuations along the wave's path are uncorrelated, it can well happen that two or more rays originating in quite different points of launching antenna interfere in the same place. A computer simulation of such possibility is given in Fig.2 in terms of ray tracing, where the effects of density fluctuations (all possible real k_r have been considered) and non-zero width of N_z spectrum ($\Delta N_z = 0.5$ is supposed) are depicted. In this figure, "images" of five points $[h, z = 0]$ of CASTOR launching antenna are shown at three successive radii in the vicinity of the first reflection (on the layer with $n \leq n_{crit}$) of the LHW rays on the tokamak high field side (not to speak of the possible multiple reflections). It may be seen from the figure that "images" are defocussed to partially overlapping areas with dimensions up to several cm. Note that the toroidal position of the depicted areas corresponds just to the location of RF probes (about 45° toroidally from the antenna). It follows from this facts that the interference of the rays radiated from the antenna at poloidal distance of several cm is highly probable. Note that such distance is well comparable with dimensions of poloidally rotating turbulent density formations, observed in [5]. In this way, the turbulence of tokamak plasma results in localized, quickly changing (more quickly than local density changes) standing waves pattern hindering a direct N_z determination. The question is whether the picture observed is not a common picture of the LHW propagation in the fluctuating plasma without any deteriorating effect on the current generation efficiency.
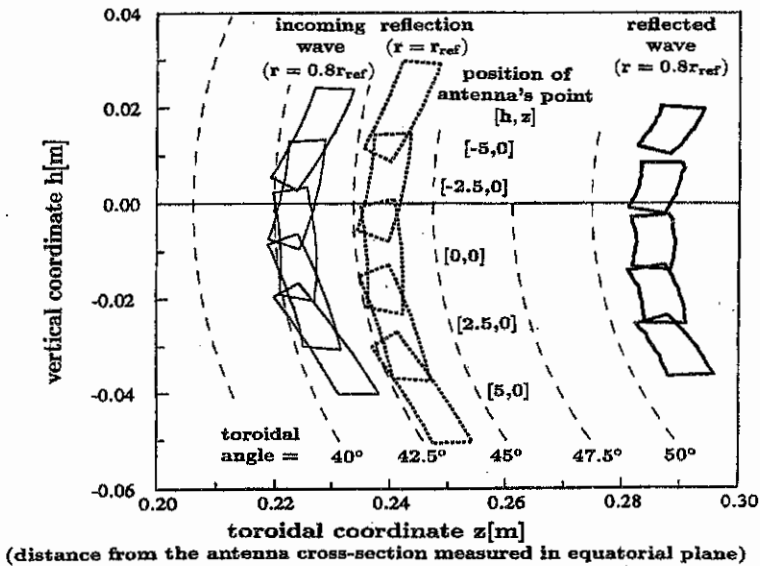
Figure 2: Defocussation of *LHW* rays due to the plasma density fluctuations and due to the finite N_z ($N_z = 3 \pm 0.25$) in tokamak CASTOR; $r_{ref} = r(n = n_{crit}) \doteq -70mm$.

References:

[1] Petelin M.I., Suvorov E.V.: Sov. Tech. Phys. Lett. 15 (1989), 882

[2] "Quasioptical LHCD Launchers: Status and Development Programme", Minutes of Meeting on Advanced Launchers, Frascati 1993

[3] Žáček F., Jakubka K., Kletečka P., Klíma R., Krlín L., Kryška ., Nanobashvili S., Pavlo P., Preinhaelter J., Stöckel: "Experiments with quasioptical grill on tokamak CASTOR", 22 EPS Conf. on Controlled Fusion and Plasma Physics, Proc. IV-373, Bournemouth 1995

[4] Preinhaelter J., "QOG mounted in hyperguide", Nucl. Fus. 36 (1996), 593

[5] Žáček F., Stöckel J., Jakubka K., Klíma R., Kryška L., Nanobashvili S., Nanobashvili I., Pavlo P., Preinhaelter J.: "Turbulent characteristics of plasma in front of quasi-optical grill on CASTOR tokamak", 1996 Int. Conf. on Plasma Physics, Proc. I, p. 1030, Nagoya 1996

[6] Žáček F., Stöckel J., Jakubka K., Klíma R., Kryška L., Nanobashvili S., Nanobashvili I., Pavlo P., Preinhaelter J.: "Detection of LHW in tokamak CASTOR", IAEA TCM on Research Using Small Tokamaks, Prague 1996

Space Resolved Investigation of USX Radiation of Low-Z Impurities in CASTOR Tokamak

J. Badalec, J. Moravec, V. Piffl

Institute of Plasma Physics, Za Slovankou 3, P.O.B. 17, 182 00 Prague 8, Czech Republic

Introduction

Study of the impurity in the tokamak plasma issues mostly from spectroscopic data of impurity radiation. Carbon and Oxygen were identified as the dominant low-Z impurities in the CASTOR tokamak ($R = 0.4$m, $a = 0.085$m, $n_e = 10^{18} \div 10^{19}$ m^{-3} , Ip $\leq$ 20 kA). The high charge stages of low-Z impurities radiate predominantly in the ultrasoft-X-ray (USX) spectral range. The spectral radiance of the H- and He-like ions of Carbon and Oxygen along the central line-of-sight were measured routinely on the CASTOR [1,2] using the high throughput multilayer-mirror (MLM) spectrometer.

In the present work the spectral radiance has been measured with a spatial resolution in vertical direction. For this purpose, the MLM spectrometer used on the Castor tokamak was modified and tested during last months. The line-of-sight was possible to be changed within ±8.5cm measured in the plasma centre.

Using space resolved measurements of the spectral radiances, the radial profiles of the spectral intensity could be reconstructed. Finally, the radiative losses by the USX radiation of C^{4+}, C^{5+}, O^{6+} and O^{7+} ions were evaluated.

The spectrometer

The two channel MLM spectrometer has been manufactured in IPP Prague earlier [2]. Both the channels are designed on the use of a combination of the filter technique and the dispersive spectroscopy. Suitable submicron metallic film works as a band filter and the flat multilayer mirrors (MLM) are chosen as the high reflecting dispersive elements.

The first channel is fixed to a certain spectral line and can be only tuned while the monochromator vacuum vessel is opened. A vacuum-tight clock-like mechanism of the second channel allows the mirror and the detector to be set separately at the angle α and 2α, respectively, without vacuum break. The spectrometer alignment and the accurate proof of the mirror/detector position has been performed by a He-Ne laser.

A new equipment has been designed that makes possible all the spectrometer to be mechanically tilted within a range of about $\pm 10°$ related to the horizontal plane. That allows the radiance to be measured shot-to-shot through different chords all over the plasma cross-section of the CASTOR tokamak. The spatial resolution of about 1 cm in the center of plasma is determined mainly by the set of collimators.

Experiments

The experiments were performed in several regimes of Ohmic discharge in CASTOR tokamak which differed mainly in plasma current (and consequently in electron temperature). An other serie was performed with a reduced plasma column diameter as a smaller circular limiter was inserted during plasma fluctuation measurements.

The impurity spectral radiance was measured with a shot-to-shot step of the tilt of the spectrometer that corresponded typically to 0.5 cm shift of the line-of-sight in the center of plasma column. The time resolution was about 1 ms. The tokamak discharge parameters were hold possibly the same during the serie of measurements.
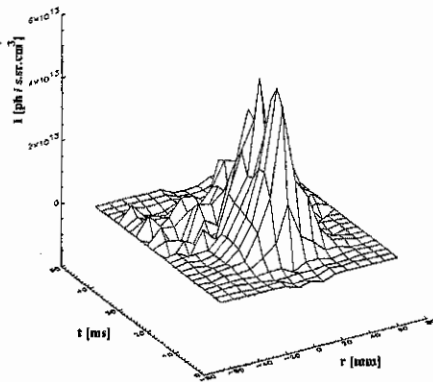
Fig. 1: Time and space evolution of spectral intensity of Oxygen OVII (574eV) line

The measured data of the spectral radiance were processed by a modified Abel transform with aim to obtain the spatial distribution of the spectral intensity. At the first approach the poloidal symmetry of the spectral intensity was assumed for these calculations. As the measured radiance was rather asymmetrical in some cases, a modified Abel transform was employed later based on the method of a weight function [4] that allowed the asymmetrical profile to be processed. The time and space evolution of the O^{VII}(574 eV) spectral intensity is drawn in Fig.1

Profile of the spectral intensity was estimated from the spectral radiance supposing symmetrical profiles both of the electron density and temperature. The central electron density was measured by a microwave interferometer. The central electron temperature was estimated by two-foil method [4]. The radial profile of the spectral intensity at the time of the

steady state period of discharges is drawn in Fig.2 for Carbon and in Fig.3 for Oxygen. While the Carbon ions radiation profile is more or less flat all over the cross-section, both the profiles of Oxygen lines O^{VII} and O^{VIII} are peaked in the CASTOR condition due to the higher excitation energy of the ion.
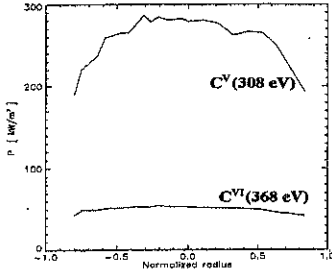
Fig. 2: Radial profile of Carbon spectral intensity   *Fig. 3: Radial profile of Oxygen spectral intensity*
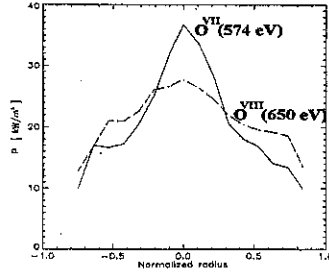
It is seen that C^V (308eV) radiation dominates; its intensity is four times higher than the intensity of the higher ionization stage of the same (Carbon) ion. The intensities of the Oxygen lines are less than of the Carbon.

The dominant contribution of Carbon could be explain by rather high concentration of Carbon ions because of a poor clearness of the tokamak chamber and/or by the low electron temperature, which was evaluated to be app. 200 eV in these measurements. The low electron temperature could imply the higher population of the ions with lower ionization energy and higher excitation rate (that is valid within the energy range similar to CASTOR).
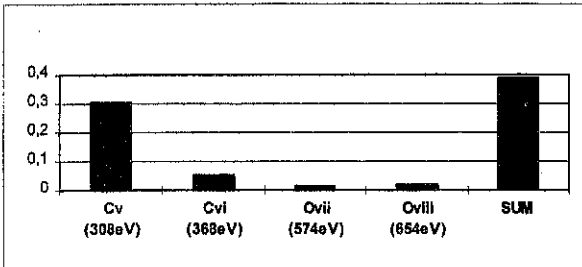
Fig. 4 : Relative radiative power P_RAD / P_OH

Under the assumption of toroidal symmetry, the global (from all the tokamak volume) radiative losses via C^V(308eV), C^{VI}(368eV), O^{VII}(574eV) and O^{VIII}(654eV) spectral radiances were

evaluated. The results are presented in Fig.4 relatively with respect to Ohmic heating power. It is obvious that more than 30% of Ohmic heating power is lost by C^V radiation while the effect of the other 3 lines is lower than 5%. However, in case of relatively low temperature of the plasma (that is probably the case of our discharges in the CASTOR), some art of radiative losses is released through radiation of the lower ions.

Conclusion

The new tilting equipment of the two-channel MLM spectrometer allowed the space resolved measurement of the radiance of USX spectral lines that yielded a more complex information on the low-Z impurities in CASTOR tokamak. This work presents results of the first sets of the space resolved measurements for several pairs of spectral lines of Carbon and Oxygen. The space resolved measurement of the radiance allowed the radiative power due to the impurity to be estimated.

The next work will be focused on simultaneous measurement in USX and VUV spectral ranges with aim to obtain a complex description of the behavior of light impurities. A more complex model would be employed that would include diffusive processes of light impurities in tokamak plasmas.

Acknowledgments

References

[1] Piffl V., Badalec J., Golubev A.V., Bobashev S.V.: IPPCZ-340, IPP Prague, 1994
[2] Badalec J., Moravec J., Piffl V.: Proc. 22nd EPS Conf.on Plasma Phys., Bournemouth, p.II-373, 1995
[3] Weinzettl V. et al: 18th Symposium on Plasma Phys., Prague, June 17-20, 1997
[4] Yasutomo Y. et al: IEEA Trans. on Plasma Sci., Vol.PS-9, No.1, 18-21, 1981

THE PLASMA BEHAVIOR WITH MOLECULAR BEAM AND PELLET INJECTION IN HL-1M

L.H.YAO, Y.LIU, D.Q.LIU, Z.G.XIAO, N.Y.TANG, Z.Y.CUI, D.M.XU, X.T.DING,
Z.C.DENG, Y.ZHOU, J.L.LUO, J.F.DONG, X.P.CHEN, L.W.YAN, C.H.CUI, Y.LIANG,
G.C.GUO, X.Y.FENG,S.K.YANG, D.H.YAN, E.Y.WANG
Southwestern institute of physics, P.O.Box 432, Chengdu, Sichuan 610041,China

HL-1M is a circular cross-section tokamak with $R = 1.02$ m, $a = 0.26$ m, $B_t \leq 3$ T, $I_p = 350$ kA and two full graphite limiters located at the toroidally symmetrical sections. The pellet injection line is just on the equator plane of the torus and along the major radius, the molecular beam injection line is parallel to the pellet injection line and 9 cm below the plane.

1. Supersonic molecular beam

Pulsed molecular beams are of great advantages for having high instantaneous intensity, high speed, small spread of velocity and small angular distribution. Gas pules lasting tens and hundreds of milliseconds are commonly used in this work and satisfy the requirements of HL-1M gas fueling which reduced the edge recycling[1].

The pulsed molecular beam source and its measurement arrangement[2] for the analogue of HL-1M vacuum chamber are shown in Fig.1: about 6×10^{19} gas particles from the gas source at a pressure of 1×10^5 Pa have passed through the nozzle and got into the beam source chamber at pressure of less than 1×10^{-3} Pa. The mean flying velocity of hydrogen molecular beam at a distance of 1 m is about 500 m/s under previous condition of pressure difference, but the local sonic velocity is about 260 m/s, so the Mach number of the beam M≈ 2.

2. Pellet fueled in HL-1M

Multiple hydrogen pellets (diameter $\phi = 1$ mm) injection was performed on HL-1M with velocity of up to 700 m/s and total particle number $N \approx 4.5 \times 10^{19}$. The typical time interval between pellets is 20 ms. Three PIN diode arrays were used for measurement of soft x-ray (SX) intensities allowing a spatial resolution of 1 cm and a time resolution of 10 μs.

3. Penetrating injection and density peaking

The peaked-density profiles are the results of MBI and PI fueling, and recycling control at the edge plasma. Hydrogen recycling was decreased by degassing procedures employing siliconization and pure helium glow discharge cleaning that remove hydrogen entrapped in the graphite limiters. In order to reduce recycling at the plasma edge, helium was selected as working gas for pulsed molecular beam. Normally, helium MBI fueling was carried out at low target density of hydrogen plasma, for example, in shot 4116 $\bar{n}_e = 4 \times 10^{18}$ m^{-3}, the ramp-up of line-average electron density $d\bar{n}_e/dt$ is as high as 3.1×10^{20} m^{-3} s^{-1} during injection and the resulting plasma density after 100 ms injection reaches to $\bar{n}_e = 5.4 \times 10^{19}$ m^{-3} with steady state. One of the features for MBI fueling is that the peaking density profiles could be remained stationary for a long time, as shot 4118 shown in Fig.2, in which the peaking factor of density profile $Q_n = n_e(0)/<n_e>$ reaches 1.5 and retains this value for 400 ms. Up to 12 cm depth of the helium particle penetration is observed by the PIN diode(He I 587.6 μm) detector array and treated by Abel inversion.

With the pellet injection, the density profile has a peaking factor $n_e(0)/<n_e> = 1.6$-1.8 with the central value of $n_e(0) \approx 5 \times 10^{19} m^{-3}$, and the energy confinement time was enhanced up to 30% higher than that of the target plasma as shown in Fig.3. After pellet injection,

sudden drop (< 4 ms) of the electron temperature was detected by ECE, and hence on soft x-ray signal. Apart from the perturbation, $\delta n_e / n_e$, introduced by the pellet, the MHD activity of plasma was greatly influenced by the pellet penetration depth. In centrally fueled discharge of pellet injection where the initial density is about $\bar{n}_e \leq 2.0 \times 10^{19} m^{-3}$, the sawtooth activity can be completely suppressed in period of 20-50 ms with a simultaneous increase of central soft X-ray radiation. The pressure gradient saturates at a certain value and degrades suddenly when a large sawtooth emerges. In Fig.4 the evolution of the SX signals around the first large sawtooth crash are shown, the peaked SX profile is broadened at the crash.

4, Central magnetohydrodynamic activity after pellet injection

Furthermore, the central magnetohydrodynamic activities are strong affected by pellet injection. A snake-like oscillation has been observed to arise immediately after the onset of sawtooth crash in discharges. The centrally peaked pressure is degraded in a slow time scale compared to that for the usual sawtooth crash. The first large sawtooth crash time is typically about $400 \, \mu s$-$600 \, \mu s$, which is much longer than that of gas fueled discharge (100-$200 \, \mu s$). The most conspicuous feature is that the increasing of m=1 mode merges into a snake-like oscillation just at the former stage of the crash as shown in Fig.5. The time evolution of SX profiles during the phase of density variation from t = 291.00 ms to t = 291.07 ms is shown in Fig.6, the snake-like oscillation rotates in the electron drift direction. Such m=1/n=1 oscillation associated with a density perturbation will enhance the crash period. Normally, the density perturbation should decay on a time scale of r_s^2 / D. In the central region of plasma the typical values are $r_s \cong 5$ cm and $D = 0.3 \pm 0.1 \, m^2 s^{-1}$. If increasing D by one order of magnitude during the crash phase, the decay time will decrease to several hundred microseconds and it is comparable to the decay time of the snake-like oscillation as observed in HL-1M experiment.

5. Hollow profile of T_e and electron heat transport

There are obvious variations of the electron temperature profile during the MBI, for example in shot 4116 as shown in fig.7, the helium MBI begins at t = 160 ms. The hollow profiles of electron temperature have been indeed observed to be asymmetrical in HL-1M by ECE diagnostics 190 ms after helium MBI. The peak of electron temperature profiles is around R = 1.02 m, but the center of the hollow drifts off the center of the temperature profiles at R = 1.06 m and remains stationary till the end of discharge. According to the sawtooth signal variation with time measured by the SX-ray array, the period of sawtooth increases with electron density and the inversion radius of q = 1 surface is $r_{s1} \leq 5$ cm after MBI. The hollow may be the results of density peaking outward rather than impurity accumulation. The comparison of the profiles of the electron heat transport coefficient χ_e between two different fueling modes has been obtained from the method of energy balance. At the range of plasma radius r = ± 10 cm, the χ_e value of the plasma with MBI varies from 0.3 to 0.7 m^2/s; it is smaller than that with GP plasma, especially in the side of strong magnetic field.

6. Improved confinement with MBI

In the experiment of HL-1M, the hydrogen plasma with GP fueling τ_E increases linearly with the density at $\bar{n}_e \leq 2 \times 10^{19} m^{-3}$, when the density is further increased, τ_E increases slowly with the density. If the working gas is the mixture of H2+He, the critical density will increase to $2.5 \times 10^{19} m^{-3}$, beyond which τ_E continuously but slowly increases. In the experiment of MBI fueling with helium into the hydrogen plasma, τ_E increases with

increasing plasma density till $n_e = 6 \times 10^{19} m^{-3}$, and is 30% longer than that of previous GP results at the same density range. A comparison of the variation of τ_E versus $\bar{n}_e$ with GP and MBI is as shown in Fig.8 .

7. Discussion

The process of pellet injection is very strongly dependent on the electron temperature and only slightly on the electron density. The pellet could inject into the plasma center, which benefits by the protective layer composed of cold particles that shields the pellet from the incoming electron collisions. Three slow pellets with velocity 200 m/s were injected into an ohmically heated deuterium plasma with starting density $\bar{n}_e = 1.3 \times 10^{19} m^{-3}$, and the penetration of up to 7 cm and energy confinement time enhanced up to 30% were observed, which experiment was carried out in ASDEX [3]. The experimental results of the slow pellet fueling are similar to that of the MBI fueling in this paper. Whether the protective layer appears during MBI is under investigation.

References

[1] Yao L H, Diao G.Y, Wang Z H, et al., in   Controlled Fusion and Plasma Physics
    (Proc.20th Europ.Conf.. Lisboa, 1993), Vol. 17 C(I), European physical society (1993) 303.
[2] Yao L H, Tang N Y, Feng X Y, Nucl. Fusion and Plasma Phys. 17 (1997) 61.
[3] Kaufmann M, Buchl K, Fussmann G, et al., Nucl. Fusion 28 (1988) 827.
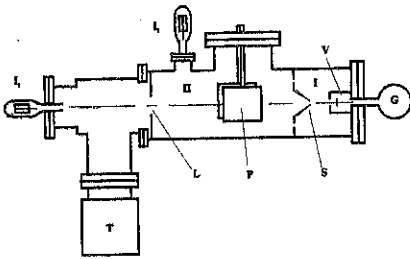
*Fig.1 The pulsed molecular beam source
and its measurement arrangement*

I_1___*ion gage 1 for beam detection,* I_2___*ion
gage 2 for backgrond pressure measurement,*
T___450l/s turbomolecular pump,
L___limiter,   P___parallel electrodes,
S___skimmer,   V___fast electromagnetic valve,
G___gas source,   I___beam source chamber,
II___collimator chamber
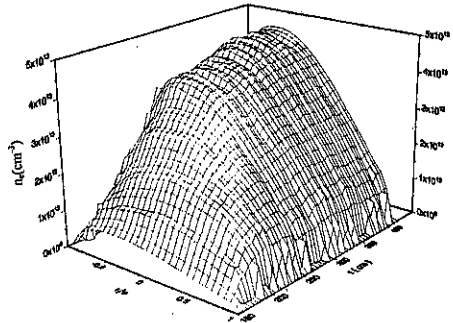
*Fig.2 Density profile of shot 4118
after He MBI, $Q_n = 1.5$*
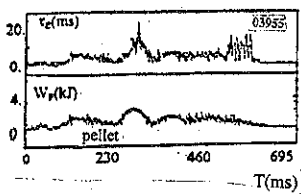
Fig.3 τ_e and the total stored energy W_p for a pellet-fuelle 100kA Omic heated discharge.
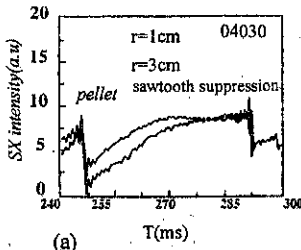
(a)
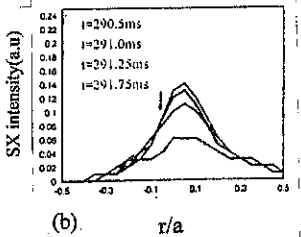
(b)

Fig.4 (a) Time evolution of central SX signals during pellet injection.(b)The profile evolution of Abel inverted SX emission around the first large sawtooth crash.
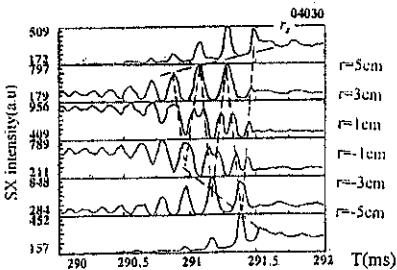
Fig.5 Time evolution of the central SX signals around the first large sawteeth crash.
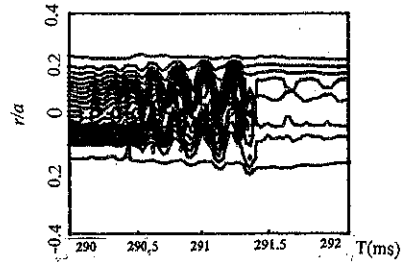
Fig.6. Contour lines of SX intensity in the central region from t=291- 292 ms.
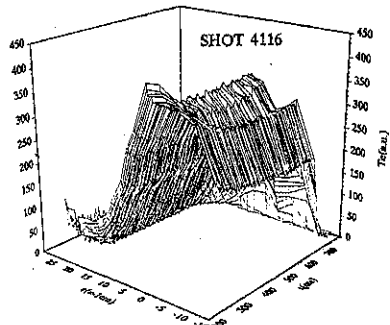
Fig.7 Hollow profile of T_e during He MBI in shot 4116
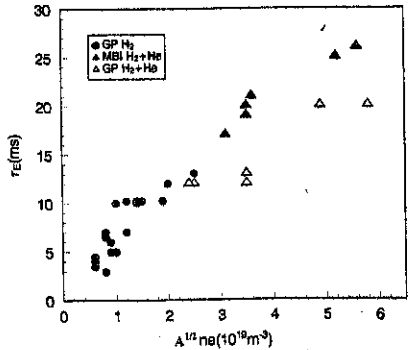
Fig.8 A comparison of the variation of τ_E and $\bar{n}_e$ with GP and MBI

GP H_e___ normal gas puffing with hydrogen, GP H_2+He ___gas puffing with mixture gas of H_2+He,   MBI H_2+He___ herium MBI into hydrogen plasma, A___reduced mass number of H_2 and He, It is1.6 in this experiment.

ENHANCED CONFINEMENT IN INTERNAL AND EDGE REGIONS OF HL-1M H-MODE PLASMA

L. B. Ran, E. Y. Wang, D. M. Xu, J. Y. Cao, Z. Y. Cui, X. Y. Feng, W. Y. Hong, L. W. Yan, J. Chen, Z. C. Deng, G. Y. Diao, Y. Zhou, G. C. Guo, Y. C. Zhong, J. F. Dong, K. H. Li, C. X. Luo, H. N. Zou, J. L. Luo, M. L. Shi, S. K. Yang, Q. W. Yang, J. W. Yang X. W. Deng, J. C. Yan and HL-1M team

Southwestern Institute of Physics
P. O. Box 432, Chengdu 610041 P. R. China

I. INTRODUCTION

Experiments on many tokamks have shown that the H-mode can be actively triggered by an externally added electric field with a biased electrode[1,2]. This kind of H-mode has been observed and studied on the HL-1 tokamak[3,4,5] and studied again on the HL-1M tokamak with wall boronization, fast ramp-up of the bias voltage and fast ramp-down of the plasma current, and some enhanced confinement features have been observed in the internal and edge regions by some newly installed diagnostics.

II. EXPERIMENT AND RESULTS

The HL-1M tokamak is the modified version of the HL-1 tokmak after the thick copper shell was moved and the minor radius was inceased from 0.20m to 0.26m, and has been operated up to I_p =320kA and B_t=2.8T with current and displacement feed back control after wall boronization in helium glow discharge.

The electrode has a graphite head of 44mm diameter, been installed at the top of the vacuum chamber and inserted into the plasma by 2-3.5cm as V_b is applied to the plateau phase of the plasma current. When V_b is higher than 300-350V the characteristics of H-mode-like can be observed: drop of the $H\alpha$ intensities around the device measured by the visible and VUV spectrometers, increase of the plasma density measured by the HCN laser interferometer, increase of the diamagnetic flux by the re-design diamagnetic coils, suppression of the fluctuations at the edge measured by Langmuir probes, similar to the observation on HL-1[3,4,5].

An ECE frequency-scan heterodynes receiver (f=117-182GHz, time resolution 4ms) has been installed to measure the electron temperature profile, a laser blow-off system has been built up to study the particle confinement and impurity transport, and March probes have been used to study the poloidal and toloidal plasma motions at the plasma edge. With these new diagnostics, some new plasma features have been observed and the enhanced confinement has been obtained in the internal and edge plasma regions.

As the H-mode is achieved, the energy confinement time τ_E, obtained from the diamagnetic measurement, is increased from 4-12ms in the L-mode to 11-15ms in H-mode as density $\bar{n}_e$ changes from $0.6\times10^{13}/cm^3$ to $2.0\times10^{13}/cm^3$ at the plasma currents of 90-140kA with B_t=2.2-2.4T, as shown in Fig. 1. The H factor $\tau_E/\tau_E^{ITER-89P}$ of 1.1-1.8 has been obtained in the H-mode, as shown in Fig. 2.

The measurements of the ECE frequency-scan heterodynes receiver show that the electron temperature profile $T_e(r)$ becomes steepend as the H-mode is achieved. The typical $T_e(r)$ profiles in the L- and H-mode are shown in Fig. 3 for a typical discharge #3231 in which I_p=140kA and B_t=2.4T. In Ohmic phase (L-mode) at 230ms the relative central electron temperature $T_e(0)$ is about 950, the radial gradients $dT_e(r)/dr$ are 50/cm and 25/cm in the regions of r≈5-15cm (r/a≈0.2-0.6) inboard and outboard respectively. As I_p begins to decrease with the rate of ~1MA/s and a fast rising-up V_b (~2ms to its maximum 450V) is used at about 235ms, the normal H-mode characteristics are observed, the electron temperature $T_e(r)$ rises up inside r=10cm (r/a≈0.4) and drops down outside r=10cm, indicating that the electron temperature $T_e(r)$ becomes steepend and the confinement is enhanced in the internal region. After about 18ms later, at 253ms, the central electron temperature $T_e(0)$ reaches its maximum ~1100, increasing ~10-20% than in L-mode, $dT_e(r)/dr$ are ~70/cm and ~90/cm in the region of r=5-15cm inboard and outboard respectively, implying that a transport barrier probably exists in this area, and the radial gradient of the electron temperature is increased more outboard than that inboard. After bias, the $T_e(r)$ profile at 276ms is similar to the $T_e(r)$ profile at 230ms, indicating plasma returns to L-mode.

From the steepend $T_e(r)$ it can be derived that the central plasma current density rises up and its profile becomes steepend, and also the plasma current density can be steepend when the plasma current I_p is reduced as B_t is kept constant.

After $T_e(0)$ was calibrated by the results of the ruby-laser scattering measurement, a simulation with an one dimensional transport code has been performed and the radial electron heat conductivity χ_e has been obtained, that is χ_e=4.0-5.0m^2/s and χ_e=4.0-7.5m^2/s inboard and outboard respectively in the internal region of r=5-15cm in the L-mode. In the H-mode, however, in the same r-region χ_e is 2.0-3.9m^2/s inboard and 2.0-3.5m^2/s outboard[6], much smaller than in the L-mode, and the Hχ factor $\chi_e(H)/\chi_e(L)$ is changed from 0.52 to 0.78 inboard but only a little outboard, as shown in Fig. 4, much more reduced outboard than inboard, indicating that the confinement outboard is enhanced more than that inboard and the confinement mainly is enhanced in outboard side.

At the same time, the confinement is also improved at the plasma edge. In the range of r=23-

25cm($r/a=\sim-0.88$-0.95), the density fluctuations are reduced $\sim$10-50%, the toroidal Mach number M increases $\sim$20-50%, the poloidal rotation speed V_p measured by the Mach probes varies from $\sim$2km/s in co-diamagnetic direction in L-mode to $\sim$8.5km/s in counter-direction in H-mode, corresponding to $E_r\sim$20kV/m towards the outward direction[7], similar to the results on TEXTOR.

By injection Al impurity into the L- and H-mode plasmas with laser blow-off and measuring central chord AlXI intensities with VUV spectrometer, the particle confinement has been studied, resulting that $\tau_p\approx$20ms in the L-mode and $\tau_p\approx$30ms in the H-mode, estimated from the decay times of the AlXI lines. The impurity transport investigation by the transport code "STARTAHL"[8] shows that the particle diffusion coefficient D outside the surface of q=1 is reduced from 1.2m^2/s in L-mode to 0.6m^2/s in H-mode and a transport barrier exists in r$\approx$20-24cm($r/a\approx$0.8-0.9) in which D$\approx$0.2m^2/s, much smaller than the one outside this barrier[9]. The radial position of this calculated transport barrier is roughly consistent with the measurement of the poloidal rotation speed at the plasma edge measured by the Mach probes.

III. CONCLUSION

The enhanced confinement has been observed in the internal and edge regions of the H-mode plasma with wall boronizaton, fast ramp-up of bias voltage and fast ramp-down of the plasma current on the HL-1M tokamak. Experiments and simulation have shown that the central electron temperature is ramp up, the temperature profile $T_e(r)$ becomes steepend, the electron heat conductivity χ_e is reduced and an internal transport barrier probably exists in the internal region of $r/a\approx$0.2-0.6. The investigation of the impurity transport with laser blow-off and simulation show that the particle confinement is enhanced by a factor of 1.5 and an edge transport barrier exists at $r/a\approx$0.8-0.9, roughly consistent with the measurements of the Mach probes.

References

[1] TAYLOR R. J. et al., Phys. Rev. Lett. 63, 2365(1989).

[2] WEYNANTS R. R., et al., Nucl. Fusion 30, 045(1990).

[3] RAN L. B., et al., Proc. 1992 ICPP(Insbruck), VOL. 16C, I-213.

[4] RAN L. B., et al., Proc. 21st EPS Conf. on Contr. Fusion and Plasma Phys. (Montpellier,

1994), VOL. 18B, I-342.

[5] RAN L. B., et al., Proc. 22nd EPS Conf. on Contr. Fusion and Plasma Phys. (Bournemouth, 1995), VOL. 19C, I-273.

[6] WANG E. Y., IAEA-CN-64/AP1-14 (Montreal, 1996).

[7] HONG W. Y., et al, Joural of Nucl. Material 3201(1996)

[8] BEHRINGER K., JET-R(87)08.

[9] FENG X. Y., et al, 7th Int. Toki Conf. on Plasma Phys. and Contr. Nucl. Fusion Nov. 28-Dec. 1, 1996, Toki-city Japan.
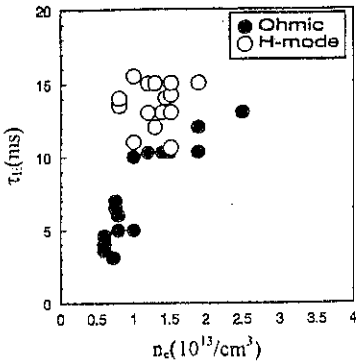
Fig. 1 Dependence of τ_E on n_e
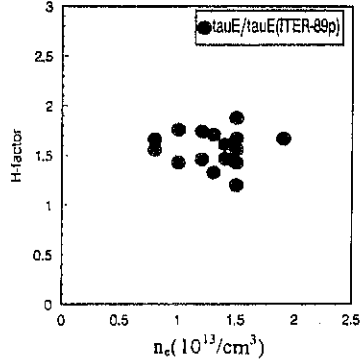
Fig.2 Dependence of H-factor on n_e
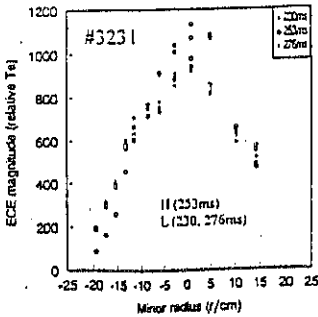
Fig. 3 Tc(r) in L-mode and H-mode with fast rising-up V_l
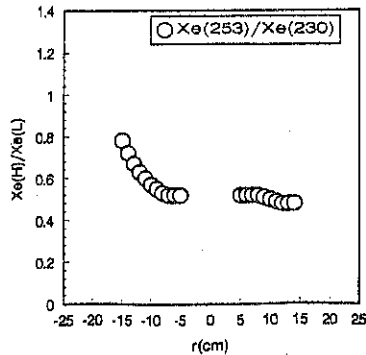
Fig. 4 Radial dependence of $\chi_e(H)/\chi_e(L)$ inboard and outboard

Suppression of Central MHD Instabilities and Snake Perturbations During LHCD in the HL-1M Tokamak

G.C.Guo, Yi.Liu, Y.Z.Zhong, B.Z.Fu, J.F.Dong, Z.Y.Cui, Y.Liu, L.Y.Chen
E.Y.Wang
Southwestern Institute of Physics, Chengdu,Sichuan, 610041, China

Suppression of instabilities

Lower-Hybrid Current Drive(LHCD) experiments were carried out in the HL-1M hydrogen plasmas. The effect of LHCD on central MHD activities[sawtooth(m=0), m=1 mode] were studied with the fluctuations observation of the soft X-ray (SXR) emission. The suppression of these instabilities by LHCD has been observed in the sawtoothing discharges(electron density $\overline{n_e} = 1 - 3 \times 10^{13} cm^{-3}$). As RF-power(P_{rf}) launched into plasmas increases to the power threshold, which depend on the electron density, the instabilities were suppressed by RF-pulse and the suppression threshold values for m=0 and m=1 modes are different(Fig.1). Generally, at lower P $_{rf}$ the residual or saturated m=1 modes were often found during RF-pulse in which the sawteeth were suppressed .The existence of residual or saturated m=1 oscillations during the sawteeth suppression suggests that the current profile may be barely stable and that a slight change in the imposed RF current profile may be sufficient to cause central MHD instability. Similar m=1 mode oscillations were frequent observed superimposed on sawteeth, and the duration of oscillations increase at the RF-power levels below the sawteeth suppression threshold. In Fig.1, the RF-power dependence of the amplitudes of sawtooth and the m=1 mode is distinct observed. Around this power threshold, the m=1 mode is destabilized and suppressed by further increase in RF-power. The typical time evolution pictures of the central MHD activities during LHCD are shown in Fig.2 and 3. Fig.2 gives the histories of the significant variation and partial suppression of sawtooth activities. Fig.3 shows the complete suppression of the central MHD instabilities by RF-power pulse at the higher power range in which there is no return of the sawtooth and m=1 mode is observed. In present experiments, the recurrence of sawteeth and/or m=1 mode was found as RF-power increase to certain value as shows in Fig.1, it seems to have an optimal RF-power levels for the suppression of sawtooth and m=1 mode 'as Alcator-C[1], it may be that the power deposition profile and the fast electron current profile vary with RF-power as the plasma parameters evolve during the RF-pulse. The sawtooth period increases with P_{rf} , the increase of threefold to fourfold its initial valve has been observed at RF-power level just below the threshold power for the discharges with electron density $\overline{n_e} = 1.5 - 1.8 \times 10^{13} cm^{-3}$.

The MHD instabilities related to the current profile, and the change in internal inductance(l_i) is consistent with the change in the current profile . So most probable explanation of instabilities suppression is the modification of plasma current profile by LHCD. The modification of l_i , which is detected with diamagnetic method, by applying LHCD has been observed during sawteeth and m=1 mode suppression in LHCD discharges, but the modification observed using diamagnetic method during LHCD is frequent no significant

even is nearly same with the that one before RF-pulse. A small decrease in l_i during sawteeth and m=1 mode suppression by LHCD has been detected (as shown in Fig. 2,3), it suggests that the disappearance of the q=1 surface in the plasma and the current profile has flattened. In some discharges, however, it has been also observed that the sawteeth and m=1 mode were suppressed by LHCD with accompanying the increase in l_i. Sometimes the measured value l_i without difference was observed in the stabilized and unstabilized portions of the RF-pulse, so we cannot invoke a significant change in l_i to explain the recurrence of MHD instabilities.

Snake-like perturbations

Snake perturbations have been already studied in detail in pellet injection experiments and sawtoothing discharges on the JET Tokamak[2]. Snake-like perturbations are observed in LHCD plasmas of HL-1M before the onset of sawteeth recurrence. They are only found to occur at the end or later phase of the suppression of sawteeth(or m=1 mode) by LHCD as shown in Fig.4, it implies that the formation of snakes-like is related to the instabilities suppression. In these LHCD discharges, after instabilities suppression a peaked soft X-ray(SXR) has been observed, and the increase of impurities radiation detected is distinct. The accumulation of impurities at plasma center during stabilization leads to the formation of the snakes-like. The electron density obtained shows a slight increase but no significant peaking during LHCD. The snakes-like obtained in HL-1M LHCD discharges are different from those of the pellet induced and spontaneous snakes in JET. The pellet produced or spontaneous snakes in JET are frequent long lived, surviving many sawtooth crash, but the present snakes-like in HL-1M are with very shout lifetime($t_l \leq 5ms$). They are always produced in sawteeth and/or m=1 mode stabilization discharges. In general, the snakes-like onset is preceded by normal m=1 activity which starts at the very small region of plasma center(r=3cm, minor radio of plasma a=26cm) and the central oscillations are frequency-doubled, and ended just before the first sawtooth crash (in Fig.4). Sometimes the generation of snakes-like during the sawtooth stabilization by LHCD are owing to the modification of RF-power value with the plasma parameters. Ultra-Violet(VUV) spectrometer and centrally radiated power measurement with Bolometers indicate that the impurities were enhanced and their accumulation in plasma center is also confirmed by the radial profile peaking of SXR emission because the electron density shows no significant peaking during central MHD activities stabilization and there are minor temperature increase. In addition, we have found that the m=1 oscillations must be frequency-doubled before the snakes-like formation. We have noticed that the central MHD activities(m=0 and/or m=1mode) superimposed on the SXR signals were completely suppressed accompany a relative enhancement outside of the q=1 surface(no m=2, it may be a turbulence), but the enhancement of turbulence does not seems to affect confinements, the increase of plasma energy w_p during stabilization of central MHD activities by LHCD is notable. Snakes-like found in HL-1M always rotates in the direction of the electron drift.

Conclusion

Central MHD instabilities has been successful suppressed by LHCD in HL-1M hydrogen plasmas as RF-power increases to the threshold, and an optimal RF-power range seems to exist for the complete suppression of the central MHD instabilities. The changes of internal inductance have detected by diamagnetic method, so the modification of current profile by LHCD was confirmed. Snakes-like observed in LHCD discharges are a magnetic island behavior, it was evolved by normal m=1 MHD activity due to impurity accumulation, they are different from the snakes induced by pellet and spontaneously snakes in JET. Owing to the lake of detailed measurements, the perturbations of electron temperature and electron density during the snake-like perturbations in the HL-1M plasma have no obtained. The mechanism of snake-like perturbations will be further studied.

Reference

[1] S.KNOWLTON, M.PORKOLAB, Y.TAKASE., Nucl. Fusion. Vol.28,No.1(1988)99.
[2] R.D.GILL, A.W.EDWARDS, D.PASINI, A.WELLER., Nucl. Fusion. Vol.32, No.5(1992)723.
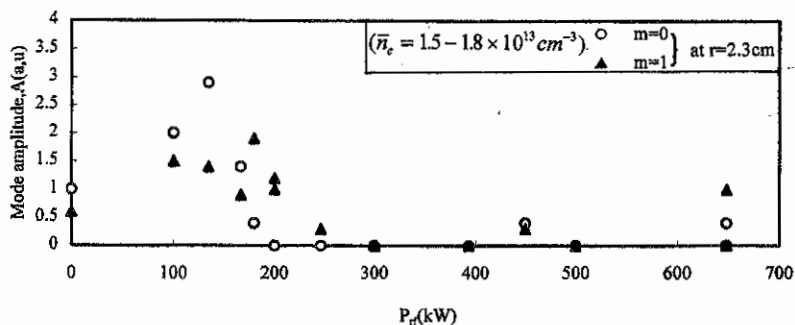
Fig. 1   Dependence of amplitudes of central MHD activities on LH-power
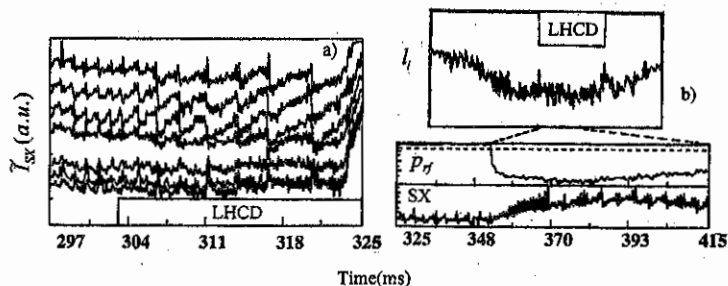
Fig.2. Temporal evolution of central MHD activities during LHCD.
a) Enhancement of sawteeth activities. b) Partial suppression of sawteeth.
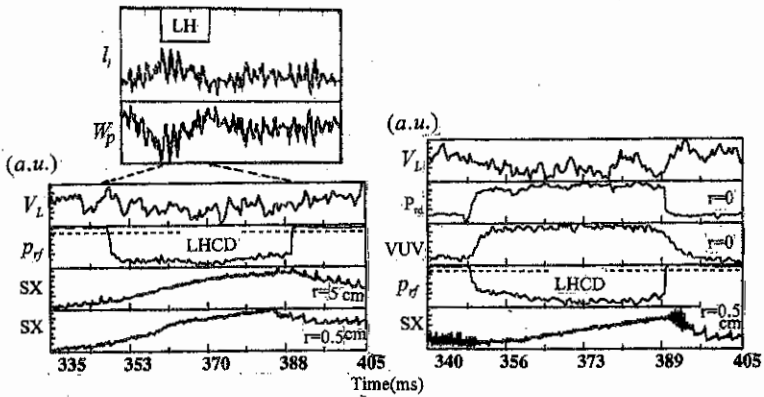
Fig.3.Complete suppression of central MHD instabilities during LHCD.
a) Suppression of sawteeth.   b) Suppression of m=1 mode.

Time(ms)
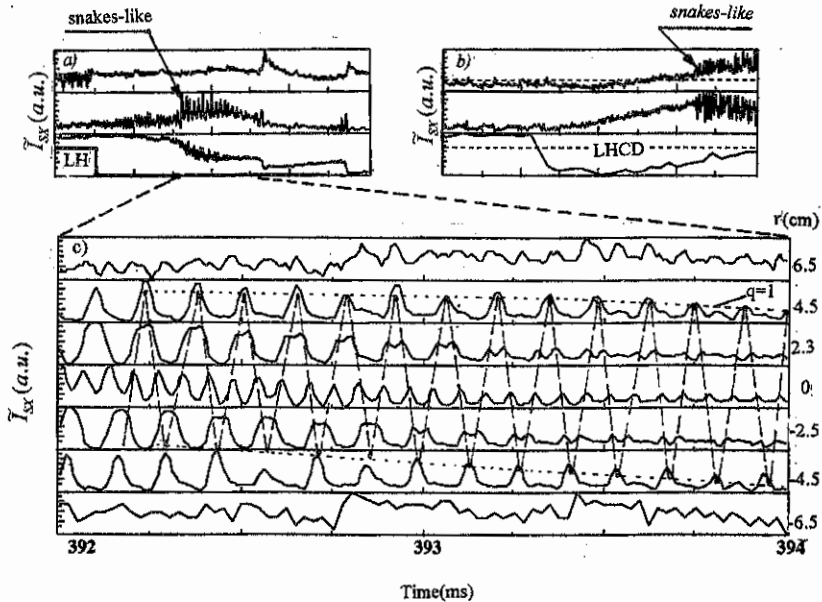
Fig.4. The snake-like perturbations.
a),b) MHD activities on the SXR signals of center region shows the formation of the snakes-like.
c) Expended time-scale show the snakes-like.

Injected impurity transport and confinement during improved confinement discharge induced by lower hybrid current drive[*]

J.CHEN   X.Y.FENG   Z.H.WANG   R.BURHENN**   E.Y.WANG

J.L.LUO   J.F.DONG   Y.Z.ZHONG   S.J.QIAN   J.C.YAN

Southwestern Institute of Physics, P.O.Box 432, Chengdu, Sichuan, P.R.China

**IPP in Germany

Lower hybrid power was injected into a medium density Ohmic(OH) plasma. The impurity transport and confinement in lower hybrid current driven (LHCD) plasmas in HL-1M tokamak were studied. The impurity transport coefficients (diffusion coefficient D and inward convect velocity V) were calculated by simulating different impurity ionized lines obtained using VUV spectrometer. The outside transport D decreases to $0.5 m^2/s$ in LHCD discharge from $1.0 m^2/s$ in OH discharge. In both cases D inside ($r/a < 0.3$) is found to be smaller close to neoclassical predictions. The impurity confinement time τ_{imp} is estimated from the characteristic decay time of the line intensity of the injected metal impurity. During OH plasmas τ_{imp} is about 17ms, while in LHCD period τ_{imp} goes up to 30ms. The improvement of impurity transport and confinement is related to the change of edge plasma electric potential profile Vp(r) which is induced by LHCD and detected by Mach probes.

1. INTRODUCTION

The main goal of LHCD on HL-1M tokamak is to achieve steady state tokamak operation. So it is important to study the impurity behavior in LHCD plasma either for controlling them or as a diagnostic for plasma characters [1]. In HL-1M experiment it is found that the particle confinement is improved by LHCD as in other devices [2]. The improved impurity transport and confinement have also been obtained. This was also found in JIPP T-IIU device [1]. The physical mechanism is partly explained as the change of edge plasma electric potential profile. Other reasons are not clear.

2. EXPERIMENT CONDITION

The experiments were carried out in hydrogen discharges. The main plasma parameters were: R=1.02 m, a=0.26m, I_P~100 k A, $\overline{N}_e$~ 1.3 × 10^{19}/m^3, Bt~ 2T, Te(0)~ 0.6-1.0keV. An RF wave with a frequency of 2.45 G Hz, a pulse length of 80ms and a power of 160-400 kW was injected into plasma. The metal impurities were injected into plasma by Laser Blow-Off system [3]. The time and amount of injection can be controlled easily. In experiment the brightness of spectral line emission of impurity ions were obtained by VUV spectrometer, the electron density by laser interferometer, T_e by the laser scattering system as barrier as ECE, H_α by monochrometer and Vp(r) by Mach probes.

3. EXPERIMENT RESULTS

When LH power is injected into a medium density ($\overline{N}_e$~ 1.5 × 10^{13}cm^{-3}) OH plasma, LH driven current is generated: the loop voltage V_L decreases sharply and the plasma current Ip increases slightly. The ion saturation current I_i measured by a double probe decreases and $\overline{N}_e$ of central chord increases. That means the central electron density Ne(0) increases. The H_α decreases as shown in Fig. 1. All these shows that the particle confinement is improved.

Figure 2 shows the brightness of four VUV lines (Al XI 55.00 nm, Al X 33.27nm Al IX 28.24nm Al VIII 38.11nm) detected in LHCD discharge and the simulation results of each line. The dash lines represent the results of simulation. Comparing the peaks of Fig. 2 (d), (c), (b),(a), one can easily see the process of impurity Al developing and ionizating from the outside to the central plasma. Using a impurity transport code to solve the transport eqation and calculate the line brightness, the diffusion coeficient D and convect velocity V were obtained [4].

The values of D and V which best reproduce the temperal evolution of the VUV lines in Fig. 2 are shown in Fig. 3. The D and V during OH discharge are also shown in Fig. 3. From Fig. 3 one can see that in OH and LHCD discharges the D(r) and V(r) (D~ 0.05 m^2/s, V~ 0.1m/s) close to neoclassical predictions in the central region of plasma are smaller than that in the outer region where the transport is abnormal. During LHCD plasma **D** (~0.5m^2/s) outside is smaller than that without LHCD (D~ 1.0m^2/s). That means LHCD helps to slow down the impurity transport in the anomalous transport region.

We detected the change of edge plasma electric potential profile $V_P(r)$ by Mach probes shown in Fig.4, which causes a barrier of D in the region (in Fig. 3) to deter the impurity development to the center.

Figure 5 is the comparison of Al XI lines in OH and LHCD discharges. Because the characteristic decay time of the line intensity is a measure of the confinement time τ_{imp} of the injected impurity [5], from Fig. 5 one can see that the impurity confinement time τ_{imp} during LHCD is about 30ms, improved from 17ms in OH discharge.

The physical mechanism of improved impurity confinement during LHCD is not yet known clearly. One certain mechanism is the change of $V_P(r)$ in edge plasma which causes a barrier of D to arrest impurity ions in that region, as discussed as above; One possible mechanism is the reduction of electrostatic turbulence in the outer region which causes abnormal transport; Another possible mechanism is the pinch effect.

Figure 6 shows the confinement time of injected impurity τ_{imp} versus the LH power during the same condition ($\bar{N}_e = 1.3 \times 10^{19}/m^3$, $I_p \sim 96$ k A, Te (0) ~ 600 e V, Bt = 1.9T). From this figure one can see that τ_{imp} can get the maxium value when the LH power is about less than 160kW under this condition, then decrease with the increase of LH power.

4. CONCLUSION

In LHCD discharge, with the particle confinement improved the injected impurity transport   coefficient decreases and impurity confinement time goes up.

5. ACKNOWLEDGEMENTS

REFERENCE:

[1]   S.MORITA, E. KAWATOH, K.OHKUBO et al., Nucl. Fusion Vol.30(5) 938 (1990).

[2]   M.NAKAMURA, T.MINAMI, K.HANADA et al., Nucl. Fusion Vol.31(8) 1485 (1991).

[3]   X.Y.FENG, Z.H.WANG et al., ITC-7   Toki-city, Japan, 1995.

[4]   D.PASINI, M.MATTIOLI, R.GIANNELLA et al., JET-P (90) 01.

[5]   D.PASINI, R.GIANNELLA et al, Plasma Physics and Controlled Fusion, 34(5) 677, (1992).
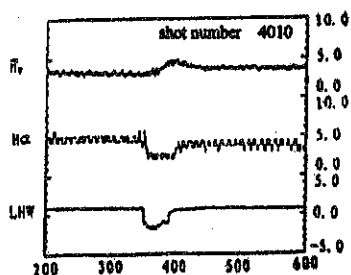
Fig. 1 Time evolution of the plasma parameters during LHCD.
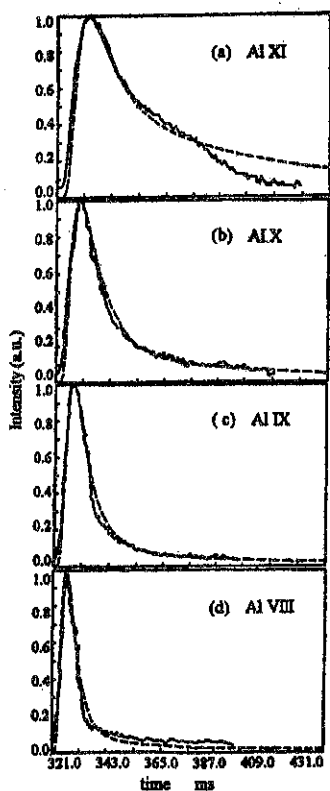
Fig. 2 The brightness of four VUV lines (Al XI 55.00nm, Al X 33.27nm, Al IX 28.24nm, Al VIII 38.11nm) around the time of Al injection (321.0ms) with the background emission subtracted. The dash lines represent the results of simulation.
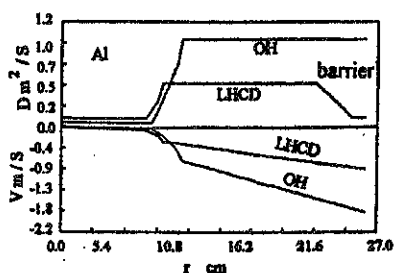
Fig. 3 Radial profile of D and of V used to simulate the injection on Al into an Ohmic plasma and LHCD plasma.
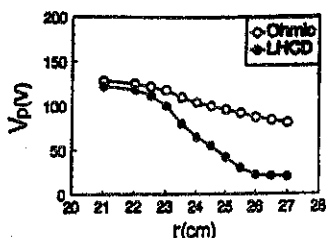
Fig. 4 Radial profile of plasma electric potential during Ohmic and LHCD plasma.
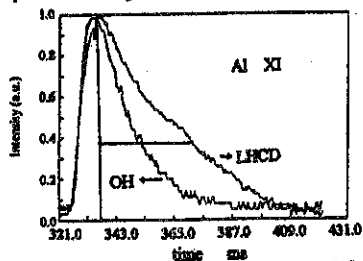
Fig. 5 The comparison of Al XI lines in OH and LHCD discharges.
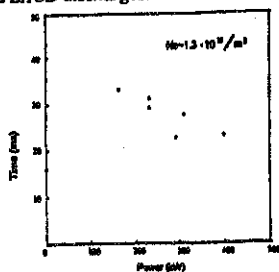
Fig. 6 The impurity confinement time versus the LH power under the same condition.

Measurements of Boundary Plasma Flow on The HL-1M Tokamak

W.Y.Hong, E.Y.Wang, Y.D.Pan and X.Q.Xu

Southwestern Institute of Physics, P.O.Box 432,
Chengdu, Sichuan 610041, China

Abstract

The results of the boundary plasma flow measurements are described in this paper. The radial profiles of plasma parallel flow Mach number M and poloidal flow velocity V_{pol} have been obtained during Lower Hybrid Current Drive (LHCD) and Pellet Injection respectively. In LHCD experiments, it was found that the direction of the poloidal flow velocity reverses as the toroidal magnetic field B_T reverses, which suggests that the poloidal flow velocity can be clarified as the effect of $E \times B$. So the confinement improvement seems to be related with the production of radial electric field during LHCD.

1. Introduction

The determination of flow velocity in Scrape-off layer(SOL) and the boundary of tokamak plasma has become of prime importance due to its possible role in confinement and the L-H mode transition[1-3]. The instability driven by the cross-field gradient(shear) of the plasma mass flow velocity parallel to the magnetic field in an inhomogeneous plasma has been investigated extensively since the early 1970's[4]. Recently, the L-mode to H-mode (L-H) transition in tokamak plasma confinement was modeled to be related to the presence of the poloidal flow shear near the plasma edge[4,5].

A Mach Probe Array with four pins is used to measure plasma flows in the HL-1M edge plasma[6]. It can measure not only parallel flows but the flow perpendicular to the magnetic field as well. Measurements of plasma flow velocities are carried out on HL-1M with this probe array for Ohmic, LHCD and Pellet injection.

2. Experimental conditions

HL-1M is circular cross-section tokamak, with R=1.02m, a=0.26m and two full poloidal graphite limiters located at 180° from each other toroidally. A simple chamber wall boronization and siliconization techniques were employed in HL-1M[7].

Experiments reported here were performed with the following parameters : B_t =1.8—2.5 T, I_p = 90 — 150 kA, $\bar{n}_e$ =1 — 3 × 10^{19} m^{-3}, $T_e(0)$ =0.5 — 1 keV.

In recent experiments of HL-1M, Pellet injection (with up to 8 pellets) and LHCD (with power up to 0.85 MW, 2.45MHz) were used to study confinement and current drive.

3. Experimental Results and Discussions

(a) LH wave injection

The HL-1 and HL-1M experiments showed significant density increase (up to factor of 2) during combined Ohmic and LHCD discharges[7].These results have commonly indicated a significant decrease in edge density fluctuations in improved confinement mode with LH wave injection. It also shows that the suppressions of the density fluctuations are accompanied by a higher poloidal rotation induced by LH wave injection[6].

The radial profiles of the poloidal rotation velocities measured by a Mach Probe Array during Ohmic and LHCD with B_t and B_t direction changed to opposite are shown in Fig.1. It was found that the direction of poloidal flow velocity reverses as the toloidal B_t changed to opposite direction. The altered edge electric field by LH wave injection leads to noticeable changes in the plasma poloidal and toroidal rotation velocities. Changes in the poloidal rotation velocities during LH wave injection can be explained by the modification of the radial profiles of E_r. It appears that the poloidal velocity is mainly determined by the E × B drift. The observed changes in the poloidal B flow velocity direction with B change in direction suggests that the effect of the radial electric field induced by LH wave injection dominates the poloidal rotation.

(b) Pellet injection

The pellet injection in the tokamak plasma is one of the most important methods for fueling, controlling the density profile and improving the confinement of a tokamak plasma. The improvement of the plasma energy confinement time τ_E was obtained. In the pellet injection experiment of the HL-1M tokamak, both the toroidal flow and the poloidal flow in the plasma boundary was changed. A large and reverse velocity variation of the poloidal flow is observed (see Fig.2). In the experiment of JIPP T-IIU tokamak, a large and rapid change in the local plasma potential is found to be induced by off-axis hydrogen pellet injection into a tokamak plasma. This change can be interpreted as being due to the gradient-B drift of particles in the high-density plasma of the pellet cloud, before the increase of the plasma density due to the

ablation becomes uniform on the magnetic surface[8]. The rate of potential change at the magnetic surface inside the pellet ablation region is

$$\frac{d\Phi}{dt} = \frac{2L_{pl}}{R_{pl}} \cdot \frac{kT_p}{e} \cdot \omega_{ci} Sin(Q_p)$$
(1)

where L_{pl} - a depth of the pellet cloud across the magnetic surface, R_{pl} - the major radius of the dominant ablation point in the plasma, T_p - an average temperature of the pellet cloud, it is a few eV, Q_p - the poloidal angle of the pellet cloud at the dominant ablation point, ω_{ci} - the cyclotron frequency of ion. The gradient-B drift can explain the polarity of the potential charge for off-axis injection through the dependence an $Sin(Q_p)$.

References

[1] R. J. Groebner, K. H. Burrell and R. P. Seraydarian, Phys. Rev. Lett. 64, 3015(1990).

[2] S. -I. Itoh and K. Itoh, Phys. Rev. Lett. 60, 2276(1988).

[3] K. C. Shaing and E. C. Crume, Jr., Phys. Rev. Lett. 63, 2396(1989).

[4] P. J. Cacto et al., Phys. Fluids. 16, 1719(1973).

[5] J. Q. Dong and W. Horton, Phys. Plasma, 1(10), 3250(1994).

[6] W. Y. Hong, E. Y. Wang and L. B. Ran, et al., J. Nuc. Mater., 3201(1996).

[7] E. Y. Wang, "Recent Experiments and Confinement Studies in the HL-1M Tokamak", Sixteenth IAEA Fusion Energy Conference, Motreal, Canada, 7-11 October 1996.

[8] Y. Hamada, et al., "Large potential change induced by pellet injection in JIPP T-IIU Tokamak Plasma." NIFS-357, May 1995.
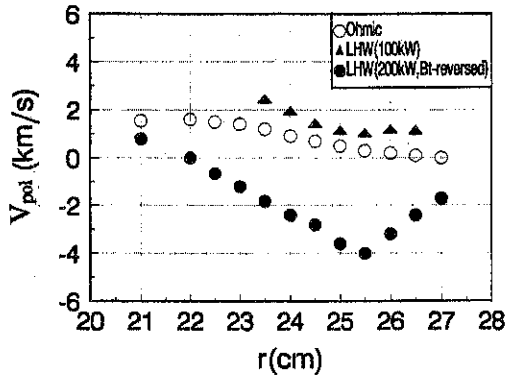
Fig.1. The radial profiles of poloidal flow velocities
during Ohmic, LHCD and LHCD with reversed B_t.
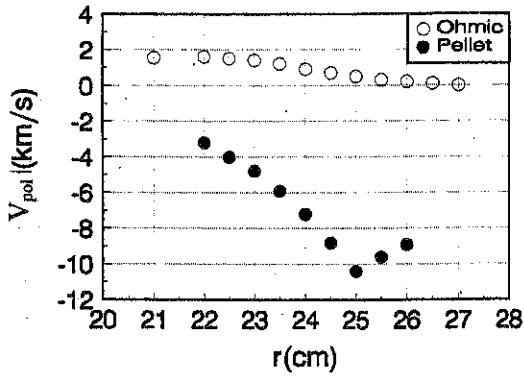
Fig.2. The radial profiles of poloidal flow velocities
during Ohmic and Pellet injection.

LASER BLOW-OFF EXPERIMENT AND STUDY OF IMPURITY TRANSPORT ON HL-IM TOKAMAK*

X.Y.Feng, Z.H.Wang, **E.Y.Wang**, J.Chen, J.L.Luo,Z.R.Yu,Y.Z.Zhong

J.F.Dong, K.H.Li, G.C.Guo, Z.C.Deng, M.L.Shi, J.C.Yan, Y.J.Zhen

(Southwestern Institute of Physics, P.O.Box 432, 61004 Chengdu, Sichuan, P.R. China).

Rainer Burhenn (IPP Garching, Germany)

Abstract : the Laser Blow-off technique has been used to HL-IM tokamak. Small quantities of metal impurities ,Al, Fe, Li etc., have been injected into the plasma. Their characteristics of the transports and the confinements were studied during the Ohmic, L-mode, Bias limiter and LHCD discharges. The diffusion coefficients, D (r), inward convection velocities ,V (r), and confinement times τ_{imp} were obtained.

1. Introduction

The Laser Blow-off technique is the right transient   perturbation method[1]. It has been used to several tokamaks[1,2,3].The injected time and the amount of the impurity can be controlled exactly and it is the minimum perturbation for the plasma. The data analysis is based on the measured curve of the line emission of injected impurity and the numerical simulation of the line brightness using an impurity transport code. We carried out the experiments of injecting various metals, Ni, Fe,Cr, Al , Li etc. on HL-1M device. We studied the transport and confinement characteristics of Al impurity. The results show that the diffusion coefficients and convection velocities are much small in the r/a~0.3 inside region of plasma with values for D~ 0.01-0.1m²/s, V~0-0.1m/s.They are closed to neoclassical calculation. But in the r/a > 0.4 outside region D and V reach great values for D~0.5 - 1.3m²/s ,V~0.4 -2.6m/s. They are greater than the neoclassical prediction. In the this region the transport is anomalous. The confinement times are given by the characteristic decay times of the spectral line emission brightness of injected impurities.

2. Experimental conditions and diagnostics

The experiment arrangement is shown in figure 1. HL-1M is a circular cross section tokamak, its main parameters are : major radius R=1.02m, minor radius a=0.26m, toroidal field B_T~2-2.8 T, plasma current I_p~100-320 kA, n_e~2-8x10¹⁹/m³, T_e~0.6-1.2 keV. The source is a single pulse ruby laser with output energy 1-3J, pulse duration 20-30ns.The laser beam is focused on the surface of target film by a lens. It can produce a spot of diameter 1-3 mm on the target film,

the metal element in the spot is evaporated to produce a burst of metal atoms, it contains a few 10^{18} atoms with energy of the order of a few eV . They move towards the plasma, but only a fraction of them can reach to center of plasma. The amount of injected impurity is kept sufficiently low to avoid perturbing parameters of plasma apart from radiation. This corresponds to concentration of 0.01-0.05% of the electron density[1,3]. These atoms reach to the plasma boundary and are ionized, These ions spread out rapidly along the toroidal field lines . At the same time, due to collision or turbulence, the ions move slowly radially inwards.

The penetration progression of the impurities into plasma is observed using four soft x-ray cameras(total 68 channels),the smallest spatial and temporal resolutions are 2cm and 10μs respectively. The intensities of line emission from injected impurity are measured with the VUV spectrometer and visible multichannel optical fiber sensors. The electron density and temperature are also measured by HCN laser interferometer ,laser Thomson scattered system and ECE system. The general energy radiation loss is given using multichannel bolometers.

3. Experimental results

The metals ,Al, Fe, Li etc. were injected successfully into HL-1M device during OH,L-mode, Bias limiter and LHCD discharges. The transport, confinement and penetration of the injected impurity were observed and studied .

Figure 1 shows the central channel soft X-ray signal , the central chord electron line average density n_e , the central chord VUV emission signal, the central channel bolometer signal and plasma current I_p when Al was injected in 2691 shot. We can see that there are additive pulse signals on the soft X-ray, VUV and bolometer signals around the time of Al injection. But n_e and I_p are not varied obviously. It means that the perturbations of plasma parameter were avoided.

Figure 2 shows the central chord X-ray emission signal around time of Al injection with the background emission subtracted during L-mode discharge in 2696 shot. It represents the contribution of soft X-ray emission from injected Al alone. As the impurity ions propagate inwards, they enter region of higher electron density and temperature, and the intensity of soft X-ray signal grows. When the intensity of X-ray reaches its maximum, the impurity concentration is also near its maximum in the center of plasma, and then the signal of x-ray starts to decay, as the impurity ions continuously escape due to the transport. During the rising phase of soft X-ray, We observed that the sawtooth was inverted for two times. It implies an inward flow of the impurity ions into the central region at the time of each sawtooth crash.

During the decay phase of the signal of soft X-ray, it is inversely progression , the impurity ions flow outwardly from central region at the time of each sawtooth crash[3].

Figure 3 gives the radial spatial distributions of the diffusion coefficients $D(r)$ and inward convection velocities $V(r)$ in the cases of Ohmic, L-mode, Bias limiter and LHCD discharges.

These distributions are obtained by the numerical simulation using an impurity transport code(selecting 2-4 spectral lines of the different ionized state to carry out simulating and fitting with the experiment data for each discharge state), assuming that the ion flux of injected impurity is in a form:

$$\Gamma_{imp} = -D\,\partial n_{imp}/\partial r - n_{imp}V \qquad (1)$$

where Γ_{imp} is the flux , D is diffusion coefficient , n_{imp} is the density, V is convection velocity of injected impurity.

We can see that from figure 4, the diffusion coefficients and convection velocities are much small close to neoclassical   calculation in the $r/a = 0.3$ inside region of plasma with values for $D \sim 0.01$-0.1 m^2/s, $V \sim 0$-0.1m/s. It means that in this region of HL-1M the transport is normal. But in the outside region, $r/a \geq 0.4$, of plasma the transports of impurity are much faster than neoclassical prediction with values for $D \sim 1.0$ m^2/s, $V \sim 0.05$-1.9m/s, $\tau_{imp} = 16.6$ms in OH plasma, $D \sim 1.3$ m^2/s, $V \sim 0.08$-2.6m/s, $\tau_{imp} = 17$ms in   L-mode, $D \sim 0.8$ m^2/s, $V \sim 0.05$-1.4m/s, $\tau_{imp} = 24$ms in bias limiter discharge, $D \sim 0.5$ m^2/s, $V \sim 0.05$-0.85 m/s, $\tau_{imp} = 33$ms in LHCD. So the transports are anomalous in all above states. there is barrier at 22-25 cm of HL-1M plasma, because there is the pulse electric field in this region from bias limiter. We also found that in LHCD discharge the confinement time is longer than that in the cases of   OH, L-mode and Bias limiter. The confinement characteristic is improved in the case of LHCD.

Figure 4 shows the distribution of Al XI(55.0nm) line brightness at the central chord in the OH,L-mode and LHCD, their characteristic decay times of line brightness are a measure of the confinement time of injected impurity.Above confinement times are given from figure 4.

References

[1] D.Pasini,   M. Mattioli ,et al., Nuclear Fusion,   Vol.30 ,No.7 pp. 2094 , 1990.

[2] A. Compatine La fontine, et al.,Plasma physics and controlled fusion, Vol.27, No.3 pp. 229, 1985 .

[3] D. Pasini   Plasma physics and controlled fusion , Vol. 34, No. 5 pp.677 ,1992.

- - IAEA TC project CPR/4/013
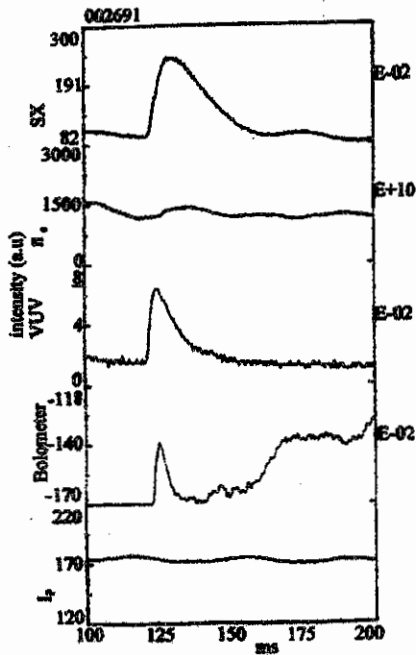
Fig. 1 Central chord soft x-ray signal, n_e, VUV signal, Bolometer signal and Ip diagrams in the case of injected Al.

Fig.3 The radial spatial distributions of the diffusion coefficients $D(r)$ and inward convection velocities $V(r)$ in the cases of Ohmic, L-mode, Bias limiter and LHCD discharges.
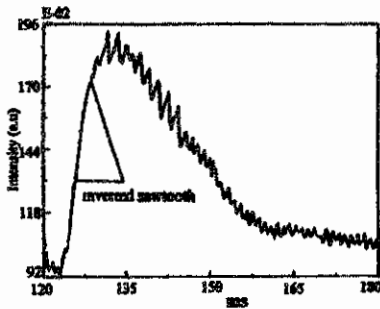
Fig.2 The central chord X-ray emission signal around time of Al injection with the background emission subtracted during L-mode
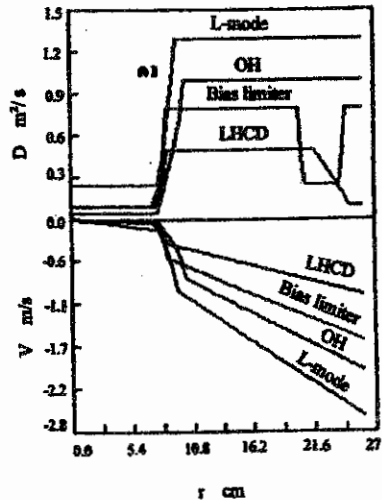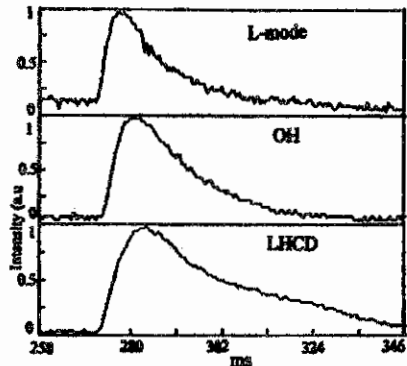
Fig.4 VUV spectral emission AL XI(55.0nm) diagrams.

Instability Driven by Ion Temperature Gradient and Parallel Velocity Shear in Plasma with Reversed Magnetic Shear

X.D.Peng, J.H.Zhang, Q.D.Gao, L.B.Ran

(Southwestern Institute of Physics, P.O.Box 432, Chengdu, 610041, P.R.China)

The confinement of plasmas plays a key role in the magnetic thermal nuclear fusion in tokamaks. Recently, the enhanced confinement with reversed magnetic shear(ERS mode) has been discovered in many tokamaks such as TFTR, DIII-D, JT-60U, and *et al.*.[1, 2] One characteristic is that the safety factor q is a nonmonotonic function of r (r is the coordinate in the direction of the minor radius). In ERS mode, the particle transport is reduced to roughly the neoclassical level, and the ion thermal diffusivity is well bellow predictions from conventional neoclassical theory. In addition, a high fraction of bootstrap was found in this plasma. In order to explain this new phenomenon, two approaches must be taken into account. The first is instabilities of plasmas in the presence of reversed magnetic shear, which is related to the suppression of anomalous transport. The second is the invalidity of conventional neoclassical theory in the presence of reversed magnetic shear.

In this paper, we only study instabilities driven by the ion temperature gradient (ITG) in the presence of reversed magnetic shear. The drift-like instability driven by ITG is currently the most plausible candidate for explaining the anomalous ion energy transport in tokamak plasmas.[3] Numerous studies on this mode have been carried out theoretically and experimentally in the last decade. But most of these investigations, however, have been confined to plasmas with positive magnetic shear. On DIII-D tokamak, the high toroidal velocity shear was observed in the region where the confinement is improved with the reversed magnetic shear.[2] So the effect of toroidal velocity shear must be taken into account.

The instabilities driven by ITG in the presence of the parallel velocity shear are described by the ion continuity equation, ion parallel velocity and ion pressure evolution equations, respectively.[4] In cylindrical geometry, the linearized equations are

$$\frac{\partial}{\partial t}(1-\nabla_\perp^2)\phi + v_D\left[1+\left(\frac{1+\eta_i}{\tau}\right)\nabla_\perp^2\right]\frac{\partial}{r\partial\theta}\phi + \nabla_\parallel v_i = 0, \tag{1}$$

$$\frac{\partial}{\partial t}v_\parallel + v_*\frac{\partial}{r\partial\theta}\phi = -\nabla_\parallel\phi - \nabla_\parallel p, \tag{2}$$

$$\frac{\partial}{\partial t} p + v_{\mathit{D}}\left(\frac{1+\eta_{i}}{\tau}\right)\frac{\partial}{r\partial\theta}\phi = -\frac{\Gamma}{\tau}\nabla_{\mathbf{I}}v_{\mathbf{I}}, \tag{3}$$

where $v_{*} = -(T_{c}/eBc_{s})dv_{x0}/dx$, $v_{D} = -(T_{c}/eBc_{s})d\ln n_{0}/dx$, $\tau = T_{c}/T_{i}$, $\eta_{i} = d\ln T_{i}/d\ln n_{0}$, and ϕ, v_{I}, and p are, respectively, normalized by T_{c}/e, c_{s} and $n_{0}T_{c}$, and spatial scales are normalized by ρ_{s}. Here, Γ is the ratio of parallel specific heat. The other symbols have their usual meanings. The perturbation quantities are assumed to be of the form

$$f(x,\theta,\zeta,t) = f_{k}(x)\exp[-i\omega t + i(m\theta - n\zeta)], \tag{4}$$

where θ and ζ are poloidal and toroidal angles, respectively. $\bar{k}$ represents the poloidal and toroidal mode number (m,n). $x = r - r_{k}$, with such that $q(r_{k}) = m/n$. Then, we obtain operators as follows:

$$\nabla_{\mathbf{I}} = iB^{-1}\left(m\frac{B_{\theta}}{r} - n\frac{B_{\zeta}}{R}\right) = ik_{y}\frac{r}{Rq(r_{k})}\left(\frac{q(r_{k})}{q(r)} - 1\right). \tag{5}$$

Because the safety factor is a nonmonotonic function, we assumed that the safety factor is expanded as

$$q(r) = q(r_{k}) + q'(r_{k})x + q''(r_{k})x^{2}/2 + \cdots. \tag{6}$$

Usually, we only consider the first order term of x. In the case of low magnetic shear, i.e., $q'(r_{k}) \approx 0$, the second order term of x^{2} must been taken into account. So, we obtain the operator

$$\nabla_{\mathbf{I}} \approx -ik_{y}\frac{r}{Rq(r_{k})}\left[\frac{q'(r_{k})}{q(r_{k})}x + \left(\frac{q''(r_{k})}{2q(r_{k})} - \frac{q'^{2}(r_{k})}{q^{2}(r_{k})}\right)x^{2}\right]. \tag{7}$$

Linearizing Eqs.(1) ~ (3), we obtain the following mode equation

$$\frac{d^{2}}{dx^{2}}\phi_{k} + V(x,\omega)\phi_{k} = 0, \tag{8}$$

where the "potential" function is given by

$$V(x,\hat{\omega}) = -k_{y}^{2} + \frac{1-\hat{\omega}}{\hat{\omega}+K} + \frac{\hat{k}_{1}'^{2}(r_{k})x^{2}}{\hat{\omega}^{2} - (\Gamma/\tau)\hat{k}_{1}'^{2}(r_{k})x^{2}} - \frac{\hat{\omega}_{*}\hat{\omega}[\hat{k}_{1}'(r_{k})x + \hat{k}_{1}''(r_{k})x^{2}\,2]}{(\hat{\omega}+K)[\hat{\omega}^{2} - (\Gamma/\tau)\hat{k}_{1}'^{2}(r_{k})x^{2}]}, \tag{9}$$

with

$$\hat{k}_{1}'(r_{k}) = -\frac{rq'(r_{k})}{v_{D}Rq^{2}(r_{k})}, \qquad \hat{k}_{1}''(r_{k}) = -\frac{r}{v_{D}Rq^{2}(r_{k})}\left(q''(r_{k}) - \frac{2q'^{2}(r_{k})}{q(r_{k})}\right), \qquad \hat{\omega} = \omega/k_{y}v_{D},$$

$\hat{\omega}_{*} = \omega_{*}/k_{y}v_{D}$, $K = (1+\eta_{i})/\tau$.

When $\hat{k}_1'(r_k)$ is small, further, assuming Γ/τ is small, or, simply, taking $\Gamma = 0$, the "potential" function is written as

$$V(x,\hat{\omega}) = \left[\frac{\hat{k}_1'^2(r_k)}{\hat{\omega}^2} + \frac{\hat{\omega}.\hat{k}_1''(r_k)/2}{\hat{\omega}(\hat{\omega}+K)} \right] x^2 + \frac{\hat{\omega}.\hat{k}_1'(r_k)}{\hat{\omega}(\hat{\omega}+K)} x - k_y^2 + \frac{1-\hat{\omega}}{\hat{\omega}+K}. \tag{10}$$

When $\hat{\omega}_* = 0$, this "potential" function is the usual one of ITG mode. Equation (8) with "potential" function (10) is a Weber equation. So, we can obtain the dispersion equation

$$-k_y^2 + \frac{1-\hat{\omega}}{\hat{\omega}+K} - \frac{\left[\hat{\omega}.\hat{k}_1'(r_k).\hat{\omega}(\hat{\omega}+K) \right]^2}{4\left[\frac{\hat{k}_1'^2(r_k)}{\hat{\omega}^2} + \frac{\hat{\omega}.\hat{k}_1''(r_k)}{2\hat{\omega}(\hat{\omega}+K)} \right]} = i(2l+1)\sqrt{ \frac{\hat{k}_1'^2(r_k)}{\hat{\omega}^2} + \frac{\hat{\omega}.\hat{k}_1''(r_k)}{2\hat{\omega}(\hat{\omega}+K)} }. \tag{11}$$

In the case of $\hat{\omega}_* = 0$, we obtain the eigenvalues of the standard ITG mode. In the bottom of the profile of safety factor, $\hat{k}'(r_k) = 0$. Then, Eq.(11) is written as

$$-k_y^2 + \frac{1-\hat{\omega}}{\hat{\omega}+K} = i(2l+1)\sqrt{ \frac{\hat{\omega}.\hat{k}_1''(r_k)}{2\hat{\omega}(\hat{\omega}+K)} }. \tag{12}$$

For the low k_y mode, i.e., $k_y^2 \approx 0$, Eq.(13) can be changed into

$$\hat{\omega}^3 - 2\hat{\omega}^2 + \left[1 + \frac{(2l+1)^2}{2} \hat{\omega}.\hat{k}_1''(r_k) \right]\hat{\omega} + \frac{(2l+1)^2 K}{2}\hat{\omega}.\hat{k}_1'(r_k) = 0. \tag{14}$$

Eq.(14) is a cubic equation. After a trivial calculation, we can find a kind of new instability will be driven.

Using WKB method, Eq.(8) can be solved numerically. Figure 1 shows the mode growth rate as function of $\hat{k}_1''(r_k)$. We may see that the mode is unstable in the region of moderate low $\hat{k}_1''(r_k)$, i.e., $\hat{k}_{lc}'' < \hat{k}_1''(r_k) < 0$, where $\hat{k}_{lc}''$ is the lowest critical value. Meanwhile, we may see also that if the shear of parallel velocity increases the lowest critical value $\hat{k}_{lc}''$ will move to left. And the calculation indicates that the high l mode is stable.

In a conclusion, we have studied the instability driven by ITG in the presence of the reversed
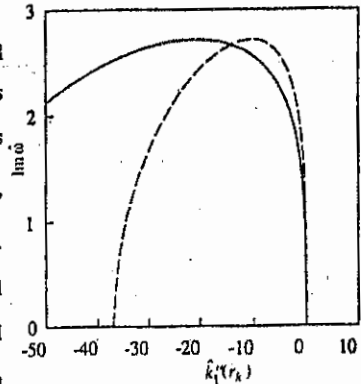
Fig.1. Mode growth rate as function of $\hat{k}_1''(r_k)$ for i) $\hat{\omega}_* = 4$ (solid line), and ii) $\hat{\omega}_* = 8$. The other parameters are $k_y^2 = 0.01$, $\hat{k}_1' = 0$, $\tau = 1$, $\eta_i = 3$, and $\Gamma = 0$.

magnetic shear. A new dispersion relation is obtained. It shows that the instability can be driven by $\hat{k}_1''(r_k)$. If we raised the shear of parallel velocity the region of instability can be changed more narrow. So, although the new instability occurs we can avoid it by raising the shear of parallel velocity.

[1] F.M.Levinton et al., Phys. Rev. Lett. 75, 4417(1995)

[2] E.J.Strait et al., Phys. Rev. Lett. 75, 4421(1995)

[3] J.Q.Dong et al., Phys. Plasmas 3, 3065(1996)

[4] N.Mattor et al., Phys. Fluids 31, 1180(1988)

Variation of small scale density fluctuations characteristics in discharges with different confinement in T-10 tokamak

Vershkov V.A., Soldatov S.V., Shelukhin D.A.

Nuclear Fusion Institute, RRC "Kurchatov Institute", Moscow, 123182, Kurchatov Sq. 1, Russia.

The experimental values of heat conductivity, particles diffusion and pinch velocities in tokamaks are usually significantly greater neoclassical predictions. It may be explained by the turbulence. Unfortunately its physics is still unclear. This report presents new results of turbulence investigations in T-10 and its variation in different regimes.

The T-10 parameters were described in [1]. Diagnostics arrangement is shown in Fig. 1. Density fluctuations in the core plasma were measured with the T-10 three wave heterodyne ordinary mode reflectometer [2]. This reflectometer is capable to measure simultaneously the radial and poloidal correlation lengths of the turbulence. High and low field side launchers were installed in the top port for the first time as it is shown in Fig. 1. The turbulent density fluctuations were investigated in T-10 SOL with multipin Langmuir probe situated in the bottom port. The high and low field side probe positions are shown.

Previous turbulence investigations [1], [2], [3], [4], [5], [6].make possible to distinguish six different turbulence types in the whole plasma column. Four of them were observed in the core plasma. **"Broad band" turbulence** exists over the whole plasma column, having the maximal amplitude at the rail limiter [3]. It is characterized by very broad amplitude and low and flat coherence spectra. The measured values of the poloidal and radial correlation lengths in the core [3] are about 0.5 cm. The values of $k \times \rho_i$ for the cold and hot parts of the SOL and for core plasma are in the range of $0.5 \div 1$ [4]. **"HF quasi-coherent" turbulence** has maximal amplitude in the core plasma [3]. It looks like bursts of quasi-monochromatic oscillations with 3 - 15 periods. The values of frequencies vary from 100 to 300 kHz. The poloidal wavelength is about $1 \div 3$ cm and poloidal number is $m \approx 45$. The measured radial correlation length is $2 \div 3$ cm [3]. **"LF quasi-coherent" turbulence** is observed in frequency range of 20 - 50 kHz and also looks as the bursts of several quasi-monochromatic oscillations. The interesting property of these fluctuations is the absence of poloidal rotation in core plasma. This makes difficult estimation of their poloidal wavelength. **"LF stochastic" turbulence** have a smooth spectrum which peaks near the zero frequency. It is produced by the stochastic density jumps with the rise time of 2 - 5 μs.

The T-10 reflectometer is able to make radial correlation measurements by means of the splitting launched frequency by an amplitude modulation [2]. The radial correlation lengths for turbulence phase fluctuation is about 0.5 cm for "broad band" and 2-3 cm for the quasi-coherent turbulence. The experimental data show that significant fast variation of turbulence amplitude in time is typical for the density fluctuations. A long radial correlation length of the turbulence amplitude bursts is predicted by the theories considering toroidal modes coupling or mechanism of "self criticality". Figure 2 a,b presents the results of the radial correlation measurements for discharges with plasma current 200 (Fig. 2 a) and 340 kA (Fig. 2 b) with cut off radii at 18 and 25 cm correspondingly. The dashed lines with circles present the data for the signals correlation itself in frequency range $180 \div 500$ kHz. The "broad band" is dominant in that frequency range. The solid lines with triangles show the radial correlation of the turbulence amplitude bursts in the same frequency range. All data were normalized to unity at small radial separations. One can see that in both cases the radial correlation lengths practically coincides. This evidenced against existing of long correlation lengths. The time delay of the bursts at different radial separation was absent, indicating that the bursts don't moves radially. Poloidal correlation analysis shows that turbulence bursts moves poloidally with the same velocities as the signals.

The installation of the high field side launch make possible for the first time to see the poloidal asymmetry of the core turbulence amplitude and compare it with the existing [4] probes data in the SOL. The local amplitude of "broad band" density fluctuations at different radii are shown in Fig. 3 for the OH discharge with rail limiter at 22 cm. Triangles present probe and squares reflectometry data. Full symbols correspond to the low field side and open to high field side probing. Due to the uncertainty in interpretation of reflectometry data the measured amplitudes of frequency fluctuations are plotted. Reflectometry data are normalized on probe data at $R=24$ cm. Strong poloidal asymmetry of "broad band" fluctuations is apparent. It is also seen, that the maximum of fluctuation amplitude is at the rail limiter for high field side. But it is shifted 3 cm in core direction for low field side. Thus the asymmetry value varies along the radius from 1.7 to 5. The bifurcation of the approximation curves at $R=15$ shows the influence of sawteeth activity. It decreases asymmetry even more in the central region of discharge. The solid line presents the estimation of maximal density fluctuations from the condition: $\delta n/n = \delta r/L_n$, where δr is a radial correlation length δr is taken from the condition $k \times \rho_i = 1$, and L_n is experimental density decay length. It shows that fluctuations are at maximal saturated level at the low field side plasma edge, while at high field side and in core region fluctuation amplitude much lower than saturation value.

The working gas influx rate was found to be the main parameter, which strongly influences the turbulence characteristics. Figures 4 and 5 compare turbulence properties during and after gas puffing cut off for three cases. Figure 4 presents Fourier spectra of auto-correlation functions for the tip rail limiter probe during (Fig. 4a) and after (Fig. 4b) gas puff. Figure 5a and b show the same characteristics for the phase fluctuations of the wave, reflected from half radius. Figure 5 c,d,e show the amplitude spectra (Fig. 5c), cross phases between two poloidal reflectometry channels (Fig. 5d) and the coherency spectra (Fig. 5e) during gas puff (solid line), 70 ms. and 150 ms after gas cut off with dotted and thin line correspondingly. The common feature is clearly seen which is the increase of low frequencies and "broad band" during gas puff and increase of high quasi-coherent turbulence after it. Thus "low frequency stochastic" and "broad band" turbulencies may be responsible for the confinement degradation under gas puff. Such behavior may also suggest the common physical origin of these turbulence types.

A radial particle turbulent flux may be calculated directly in SOL region as $G(r) = <\delta n \times \delta E>/B$ from the ion saturation current δI and poloidal electric field fluctuations δE which were measured simultaneously with multipin Langmuir probe. The brackets denotes the averaging over time sequence. Figure 6 compare turbulence characteristics measured with two poloidally separated Langmuir probes at high MHD level during gas puff (solid line) and after its cut off (dashed line). One can clearly see that after gas cut off only one "broad band" turbulence is dominant, which may be concluded from flat amplitude spectrum (Fig. 6a), unique cross-phase slope (Fig. 6b), flat coherence (Fig. 6c) and one narrow peak of cross-correlation function (Fig 6d). Figure 6e shows the cross-flux function obtained as $G(\tau) = <\delta n(t) \times \delta E(t-\tau)>/B$ by the averaging of density and electric field product with varied time delay. The value of the turbulent flux, obtained at zero shift agree with the experimental one and narrow width of the peak shows that it is explained only by "broad band". In contrary, during gas puff low frequency stochastic turbulence exited and the total flux decreases to zero. Thus it may be supposed, that this turbulence produces the inward particles pinch.

REFERENCES

[1] Vershkov V.A et al, 15th IAEA Conf, Plasma Phys and Contr Nucl Fus(1995)V 2, p.65

[2] Vershkov V.A,et al, 21th EPS Conf.,Montpellier (1994) V 18B, part 3 p.1192

[3] Vershkov V.A., 22th EPS Conf., Bournemouth (1995), V 19C, part IV, p. 5.

[4] Vershkov V.A, et al, be publ in Proc of 12th PSI Conf, Saint Raphael, France, 1996.

[5] Soldatov S.V., et al, 23th EPS, Kiev, 1996, V 1, p. 251.

[6] Vershkov V.A.,et al, to be publ. in Proc. of 16th IAEA Conference, Montreal, 1996.
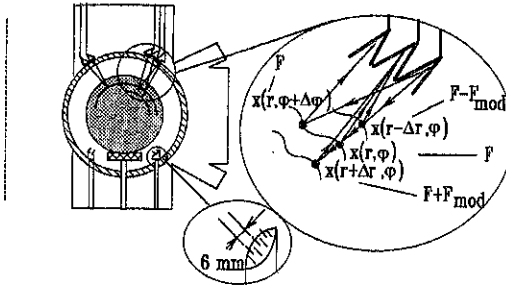
Fig. 1
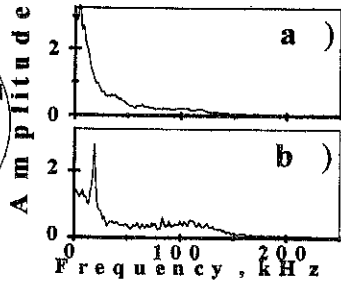
Fig. 4
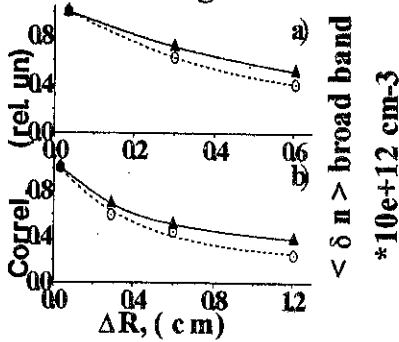
Fig. 2
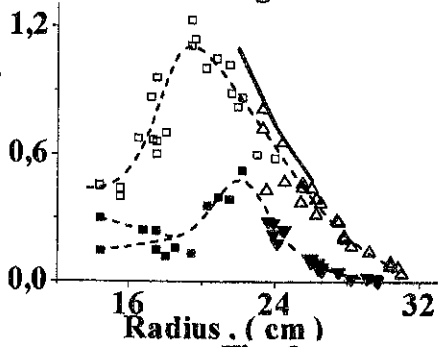
Fig. 3
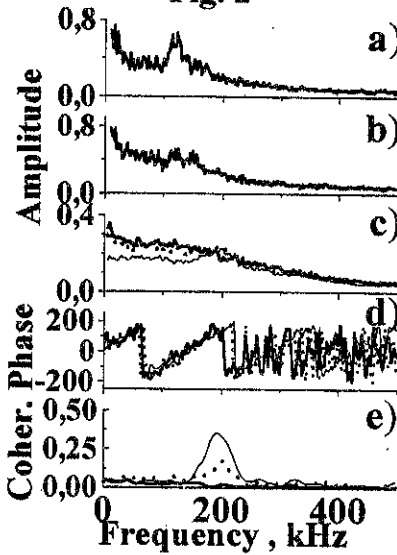
Fig. 5
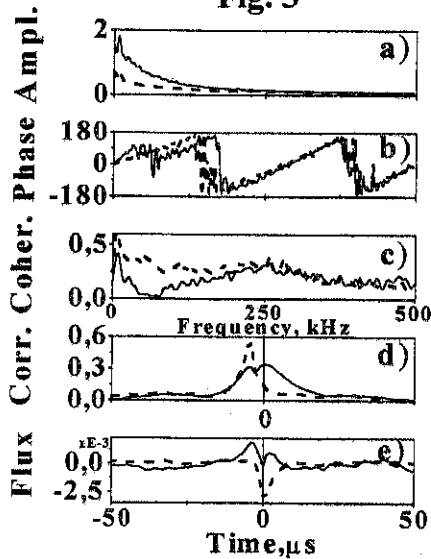
Fig. 6

Improved Core Confinement Study under Fast Current Ramp Up in the LHH Experiment at FT-2 Tokamak

S.I. Lashkul, V.N. Budnikov, V.V. Bulanin[1],V.V. Dyachenko, L.A. Esipov, N.A Joubr[1],
E.R. Its, M. Yu. Kantor, D. V. Kouprienko, A.D. Lebedev, A.V. Petrov[1], A.Yu. Popov,
A. Yu. Stepanov, I. E. Sacharov[1], A.Yu. Tukachinsky, A.V. Vers[1], V.B.Yermolaev[1].

A.F Ioffe Physico-Technical Institute, 194021, St.Petersburg, RUSSIA
[1] *State Technical University of St.Petersburg, St.Petersburg, RUSSIA*

In FT-2 tokamak experiments the transition into the improved confinement H-mode has been found during lower hybrid heating (LHH) [1]. The observed phenomena allowed us to identify this regime as H-mode with a heat transport barrier on the discharge periphery [1]. Thereby, in spite of small dimensions of the installation (a = 8 cm, R = 55 cm, B_T = 2.2 T, I_p = 22–40 kA) plasma exhibits the same properties in bifurcation as the large size plasma experiments. This fact as well as the goal of effective LH core heating has stimulated the new experiments to obtain the Improved Core Confinement (ICC) similar to "super shot" or VH mode. For this purpose at FT-2 tokamak during LHH (P_{LH} < 150 kW, f = 920 MHz) the Current Ramp Up (CRU) pulse (Δt_{CRU} = 0.5 msec) from 22kA up to 30kA has

Fig.1

been used. The following conclusions have been made from the first experiments: (1) considerable (by a factor of 1.5-2) decrease of the high energy charge-exchange neutral fluxes during CRU while the neutral fluxes by plasma bulk heated ions are kept about the same or increased. For both cases the neutral fluxes with E = 1900 eV, 1300eV and 650 eV are compared in Fig. 1, when only LHH is applied and simultaneously CRU+LHH is used. Here the oscilloscope traces of I_{pl}, and U_{pl} are shown also.

(2) Substantial (by factor of 3) increase in ion energy confinement time which became comparable with the particle confinement time (about 6 ms). In Fig 2 changes of the central ion temperature are shown for different discharge
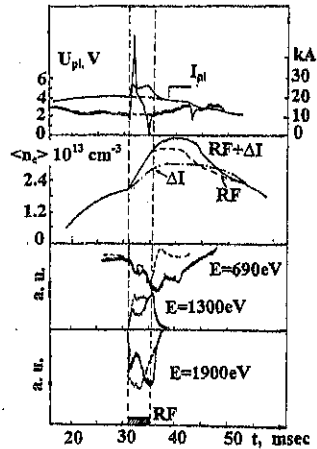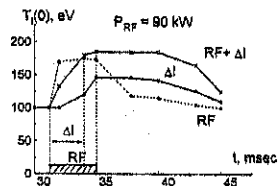
Fig. 2.
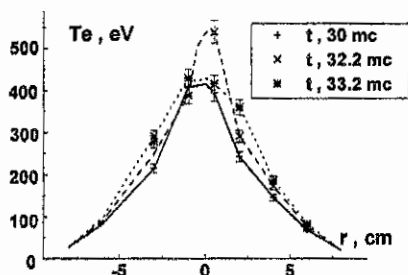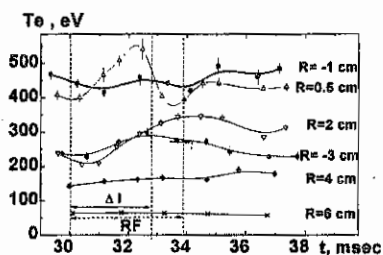
Fig. 3a

Fig. 3b

scenarios: (a) only fast CRU, (b) only RF heating and (c) combined additional heating (RF + ΔI) is applied.

(3) Sharp rise of the central electron temperature and picking profile followed by broadening its to RF pulse end. In the Fig. 3 (a and b) the profiles and temporal behavior of the electron temperature measured by photon recycling Thomson scattering system [2] are illustrated.

(4) The central density rises substantially due to the increase of the particle confinement. Plasma core with high density remained for more than 5 msec in post-heating stage. Plasma density profiles $n_e(r)$ for 4 moments are illustrated in Fig.4 (OH-marked by "1", end of LHH-"2", and 5 msec-"3" and 10 msec-"4" after switch off of additional heating). Besides, the average central density change for different discharge scenarios is shown in Fig. 1. In all cases H_β-line radiation has remained approximately constant. (5) The cross-correlation processing of the MHD-signals points to the increase of the rotational velocity by factor of 2-3

Microturbulenc observation. The collective CO_2-laser near forward scattering has been exploited to study small-scale fluctuations during the CRU, LHH and CRU+LHH. The diagnostic was able to investigate electron density fluctuations with wave numbers $k_\perp$ in a region from 12 to 30 cm^{-1} and in frequency band from 60 to 800 kHz . The scattered radiation has been detected for the both central and peripheral position of the vertical incident laser beam. In the Fig. 5 the scattering power P_s normalized to the squared plasma density for the both OH and CRU plasmas is compared. It is remarkable that the suppression has been observed even after the auxiliary current switching off. Such effect is
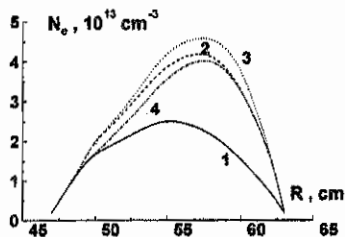
Fig. 4

correlated with the particle confinement increasing (see Fig.1 and 4). The fluctuation suppression under combined heating (CRU + LHH) was less pronounced. However the suppression is observed after additional current switching off. It is consisted with ion temperature behavior (see Fig.2). The comparison of scattering power data
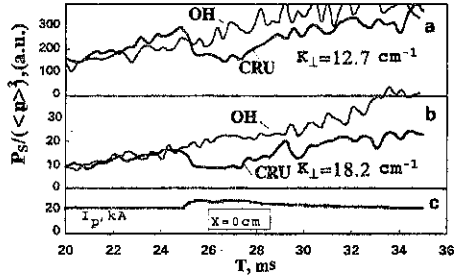
Fig. 5

obtained under the central and peripheral probing shows that the ICC is accompanied by the suppression microturbulence mainly in plasma core. The temporal evolution of scattering signal spectra during CRU for three $k_\perp$-values is illustrated at the maps shown in the Fig. 6.

Here dark gradations mark more intensive fluctuations. One can see, that just after CRU (strait line marks) the fluctuations are suppressed in broad frequency band, which is evidently shifted towards upper region with $k_\perp$ increasing. The frequency band of suppression becomes to be narrowed in 3 ms after the CRU start. The suppression after current pulse switching off as a hysteresis effect is correlated with the improvement of the particle and ion temperature confinement. One can assume, that each F - component processed as a Doppler frequency shift is related to the scattering from plasma radial layer where plasma poloidal velocity $V_\theta = 2\pi F / k_\perp$. The V_θ-scales are shown on Fig. 6 as well as F-one. In this assumption the suppression appears in the vast radial interval with poloidal velocity being from $5 \cdot 10^4$ cm/sec to $2 \cdot 10^5$ cm/sec. In the course of time this velocity interval is narrowed to value near of 10^5 cm/sec.
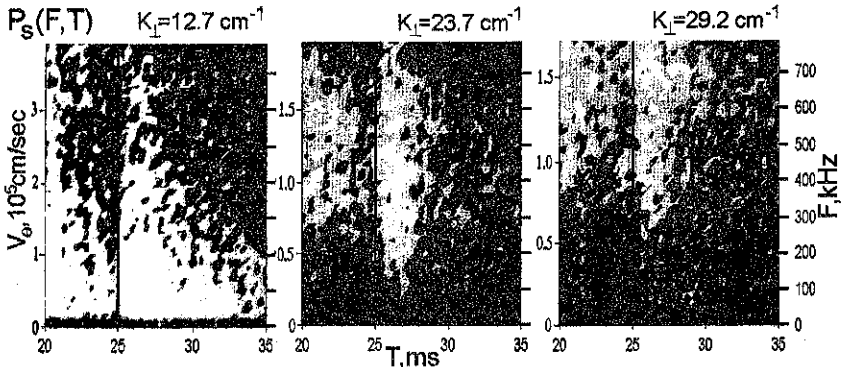
Fig. 6.

Discussion. So, main evidences of ICC transition observed in our experiment at fast CRU were the same as at large tokamaks, such as TFTR, DIII-D and "Tore Supra" [3, 4]. In all registered cases the ICC was observed as additional heating applied during the current rise phase. The data shows that, the decrease of the thermoconduction could be explained there by the formation of the Reversed Magnetic Shear. We do not have direct measurements of q-profile in our experiment, but modeling by the " ASTRA" code shows, that in FT-2 the current profile in the center can be broadened during LHH combined with CRU through ~1.5 - 2 msec after additional heating start. In this case the low value of shear $s = (r / q)(dq / dr) \approx 0$ calculated for plasma region $r \leq 2$ cm. can be formed. Thereby one can connect the observed phenomena, namely, suppression of microfluctuations, increase of the central particle and energy confinement with the plasma current profile reconstruction. At the same time, one can draw attention to the fact, that decreasing of the high energy neutral charge-exchange fluxes, suppression of microfluctuations and electron temperature rise begin earlier than core low flat shear is formed, just at the start of the CRU. So one can suppose, that during the CRU the processes in plasma are connected not only with diffusion of the longitudinal electrical fields $E_{\parallel}$ and current profile change, but with processes caused by abrupt radial changing of the electrical field distribution. At least for the high energy neutral charge-exchange fluxes we assume, that the Ware pinch should play an important role [5]. In particular, at the start of the CRU the value of $E_{\parallel}$ at the plasma periphery is several times higher than at the plasma center. In this case the inward directed flux of trapped particles $\sim n \sqrt{\varepsilon} \, cE_{\parallel} / B_p$ can compensate and even overcome their diffusion losses. The parallel velocity of trapped ions should increase simultaneously. The pinch enhancement and the increase of parallel ion velocity can lead to a remarkable change of the trapped ion rate, which in turn can explain the drop in high energy CX fluxes in the LHH + CRU experiments. The pinch processes can influence upon the radial electric field distribution and thereby result in energy and particle confinement. In conclusion, one can note that the plasma processes during the CRU are rather complicated and they need more accurate theoretical and experimental data processing.

References

[1] Budnikov V.N. et al., Tech. Phys. Lett, v. 23, (1), 32 - 34, 1997

[2] Kantor M.Yu. and Kouprienko D.V., Tech. Phys. Lett, v. 23, (4), 331-333, 1997

[3]. Batha S.H et al. Phys. Plasma. 3 (4), , 1348–1354, 1996

[4]. Strait E.J et al. Physical Review Letters. 1995, v. 75, No 24, 4421–4424

[5] Rojanskii V., Tendler M. Rev. Plasma Phys. ed. by B.B. Kadomtsev. Consultants Bureau, N. Y., 1996, v. 19, p. 147

Investigation of plasma oscillations in regimes with m=2,3 instabilities in T-10 Tokamak

S.V.Soldatov, A.A.Bagdasarov, V.V. Chistiakov, Yu.N.Dnestrovskii, N.V.Ivanov,

A.M. Kakurin, D.A.Martynov, V.V.Piterskii, V.I.Poznyak, S.V.Soldatov, S.V.Tsaun,

A.N.Yakovets, V.A. Vershkov, V.V.Volkov.

Russian Research Center "Kurchatov Institute", Nuclear Fusion Institute, 123182 Moscow,

123182, Kurchatov sq. 1, Russia

The goals of investigations of high frequency (0.5-10GHz) oblique Langmuir plasma oscillations are checking of different aspects of collective phenomena hypothesis [1,2] and application of them for analysis of total plasma dynamics in tokamak. Potential waves can be most important reason of transport phenomena up to development of any current instabilities due to their ability to transfer the longitudinal momentum across the magnetic field. Potential oscillations are excited on anomalous Doppler resonance. The main source of them generation *in nonuniform plasma* are superthermal electrons [3]. Important possibilities for understanding of plasma processes nature can be realised in discharges with ELM-like (m=3) instabilities (n_e=0.7-1.5*10^{13} cm^{-3}, I_p=250-320kA, B_z=23-26kGs, dI/dt up to 1MA/s). The peculiarities of such regimes are wide radial distribution of ECE with high T_e in the central region (1.4-1.7 keV, by SXR) and sharp downfall inside 2-3cm near limiter. Some discharge parameters are showed in Fig. 1. ECE drops in instability on 5-10% for the central zone and on 30-90% for the periphery. Boundary EC-emission is practically determined by superthermal electron population. HXR-signal and other diagnostics illustrate the loss of such electrons to limiter. It should mark there is a good correlation between total disruption and decreasing of "hot" electron population (monotonous or jump-like) to amount less then 0.1 from its maximal value at the beginning of the current plateau. Any instabilities are absent under relatively slow current ramp-up. The moment of the first ELM-like breakdown depends on dI/dt in the initial discharge stage. More fast growth of current corresponds to more earlier appearance of it. Fig. 2 illustrates the dynamics of plasma noises on the current ramp-up stage. HF components of spectrum increase and are saturated in the first turn in stable discharge. But LF components enhance very fast just before each acts of instability while HF one change on the contrary. Sawtooth modulation of ECE and plasma oscillations with period closed to duration of breakdown precede often to instability. Saturation of plasma noise level coincides in time with ECE profile expansion and exponential rise of the superthermal electron

flux on the plasma periphery. The comparison of behaviour of "hot" electrons and plasma noise dynamics shows that just superthermal electrons are main "generator" of oscillations. The curves of boundary EC-emission in Fig.3 were obtained with fixed receivers frequencies by means of change of main magnetic field. Essential exceeding of 64GHz ECE (first O-mode depends on $v_\parallel$ and $v_\perp$) above 128GHz ECE (second X-mode depends on $v_\perp$ only) manifests the appearance of peculiarity in current density near limiter. Evaluation of longitudinal electron energy due to relativistic shift of boundary ECE to limiter cyclotron frequencies (inside and outside torus) gives 20-30keV. Perpendicular (radiative) temperature of electron beam is smaller several times than central T_e. The dependencies of noise level (4GHz) and moment of the first ELM-like breakdown (as in Fig.1) are presented in Fig.4. It can see that fluctuations (oscillogrames on the left and rising curve on the right) enhance exponentially with current rise rate up to saturation. Moment of ELM-like instability (downfall curve) versus current rate is shown on the right. Any instabilities are absent in "A"-region, in "B" ELM's are present only, "C" is characterised by very high probability of global disruptive instability and discharge unstable always in "D". The obtained peculiarities in superthermal electron dynamics and generated by them plasma fluctuations correspond with hypothesis about driving role of high frequency plasma oscillations in plasma dynamic including development of different form of current instability. As we think, its reason consists of appearance in certain areas (inside q= 1, 2, 3... surfaces) of critical electric field when plasma electric conductivity from runaway phase turn into anomalous one. Under this condition, current density and electric field are connected by positive feedback that secures development of instability (downfall of the current density inside the excitation region).

Investigations of MHD modes radial location, amplitude, island width and identification of mode numbers were carried out with a specially developed set of diagnostics. Local density perturbations were measured with T-10 O-mode heterodyne reflectometer [4], the radial position of critical density was obtained with the help of 8-channels 1mm interferometer. The m=2 magnetic field oscillations were measured by MHD-analyzer [5]. The reflectometer and MHD-analyzer signals were recorded with ADC with sampling rate of 800kHz. The plasma density (m=2) oscillations were obtained by means of cross-correlation analysis [6] for reflectometer and MHD-analyzer signals. For identification of poloidal mode number, m, two antenna arrays were installed in the top port of tokamak at poloidal angles of 45° (at low field side) and of -35° (at high field side) from the vertical direction [7]. The experimental data were compared with the results of 1D full-wave computer modeling of the wave reflection.

The experiments were carried out for such regimes: I_p=300kA, B_z=2.3T, r_l=30cm, n_e=$1.5\div3.7\cdot10^{13}$ cm^{-3}. The reflectometer frequency was 39.6GHz. The radial position of reflection layer was changed during the tokamak discharge by slow plasma density variation. The phase shift between the reflectometer signal and MHD-analyzer signal, experimental density m=2 perturbation amplitude and absolute amplitude from 1D modeling are presented in Fig.5a,b,c. The condition for density gradient in the model was Vn'/Vn=0.5 in range r=[21.85;24.35]cm. The experimental amplitude (Fig.5b) shows a minimum at r=21.3cm and maximum at r=25cm in accordance with calculated data (Fig.5c). The difference in phases between minimum and maximum of the experimental curve in Fig.5a is much less than 180° as in the modeling results. The phase shift between MHD-coherent signals of inner and outer reflectometer channels ~105° which is also less then expected. These discrepancies can be explained by the presence of a component in the reflectometer signal which is correlated with the m=2 MHD-analyzer signal and do not depend strongly on the plasma minor radius. The second new feature is the observation of higher frequency modes in the region 20÷26kHz near island region (Fig.5d,e,f). A small phase shift between inner and outer reflectometry channels in the range +/- 30° is not informative if the distance may be more then one wavelength. In order to solve this problem the group time delay of the turbulence envelopes between inner and outer reflectometer channels was measured with the cross-correlation technique. Fig.6b shows that 20kHz oscillations doesn't propagate, while there is 50μs delay for 23kHz. It is seen that the average number of oscillations in bursts ~5. It is important that frequencies of those modes are near but not equal to the third m=2 harmonic. The work was carried out under support of Russian Academy Grant 96-02-18807.

References

1.V.I.Poznyak,et al,Proc. of Int. Conf. on Plas. Phys., Seville,1994,IAEA,Vienna,1995, 2,169.

2.V.I.Poznyak, et al. Proc. in 23rd EPS Conf., 1996, Kiev, a078.

3.V.I.Poznyak, et al. Proc. of the Ninth Joint Workshop on ECE and ECH, Borrego Springs, California, 1995, World Scientific Publishing Co. Pte., 137.

4. Vershkov V.A., et al, 21th EPS Conf.,Montpellier (1994) V18B, part 3, p. 1192.

5. Gvozdkov Yu.V., et al. Preprint KIAE-3618/7, Moscow, 1982.

6. Vasin N.L, et al. Plasma Physics (Moscow, 1986) v.12, p.259.

7. Vershkov V.A., et al, this Conference.

ECE
5cm

ECE
29cm

HXR

0   t,ms   800
Fig.1

GHz
1

4

8

MHD2

ECE,1
12cm

ECE,
29cm

10   t,ms   300
Fig.2

P   dI/dt,kA/s
10   986
      973
      960
      917
5   850

0   200   400 t, ms

P   t, ms
10   700

A

5   500

B

C   300
D   dI/dt,
800   1000 kA/s

Fig.4

ECE
15

—— 84 GHZ
-- - 128 GHZ

10

5

0
25   27   29 KG_s

Fig.3

DEGREES

ΔΦ   a)
50

Ampl.   b)
200
100

Ampl. (model)   c)
200
100

DEGREES

20 kHz   d)
50
25

23 kHz   e)
50
25

26 kHz   f)
50
25

20,0   22,5   25,0   27,5   30,0
r, cm

Fig.5

cross-correlation

20 kHz   a)
0,4
0,2
0,0
-0,2
-0,4

23 kHz   b)
0,4
0,2
0,0
-0,2
-0,4

-0,50 -0,25 0,00 0,25 0,50
t, ms

Fig.6

Observation of Electron Heat Transport Close to the Neoclassical One inside a Zone with Flattened q-Profile in Experiment on the Magnetic Plasma Compression in Tokamak.

S.G. Kalmykov, **S.V. Lebedev**

A.F.Ioffe Physical-Technical Institute, St.-Petersburg, Russia

1. Introduction. Results of old experiments on compression of the plasma by toroidal magnetic field, B_t, in the TUMAN-2A tokamak [1,2] are reconsidered here. In those experiments, in late discharge phase of magnetic decompression a flat radial q-profile arose due to joint action of the poloidal magnetic field, B_p, diffusion and the decompression. Along with this process the electron heat conductivity was deduced to decrease surprisingly down to the neoclassical limit. That time the phenomenon was not explained properly. At present, new reconsidering those data seems to be appropriate in scope of relation of the transport coefficients to the magnetic shear recently established [3].

2. Tokamak and diagnostics. In the discussed experiments on TUMAN-2A ($R_0 = 40$cm, $a = 8$cm, the whole discharge time was $\tau_d = 10$ms) several discharge phases could be distinguished: current ramp-up for approximately 1ms, then quasi-stationary ohmic heating period for 1.5ms (OH), fast twofold compression (C), postcompression phase at quasi-constant B_t (PC) and, finally, decompression when B_t went down to its initial value (DC). Time behaviour of main discharge parameters can be seen in Fig. 1. The experimental campaign was preceded by baking and dischage cleaning the vacuum chamber thus reducing the effective ionic charge down to a value as low as $Z_{eff} = 1.3$.

Evolution in time of $T_e(r)$ and $n_e(r)$ profiles [4] was measured with the Thomson scattering diagnostics at 6 radial positions and with 5-channel microwave interferometer. Scanning over the radius absolutely calibrated bolometer and VUV monochromator, and soft X-ray detector (SXR) were used for radiation loss profile measurements and for observing impurity behaviour. Rogovsky and voltage loops and set of local and resonant external magnetic probes completed the diagnostics family on TUMAN-2A.

3. Calculation methods. The plasma current density distribution, $j_{pl}(r,t)$, in all of the non-stationary discharge periods was found through a numerical solution of the one-dimensional equation for the classical transport of B_p in the plasma moving with the compressional velocity, $V_{r,C} = -0.5r\dot{B_t}/B_t$:

$$\partial B_p/\partial t + \partial(V_{r,C}B_p)/\partial r = \partial[(D_m/r)\partial(rB_p)/\partial r]/\partial r \qquad (1)$$

Here $D_m = c^2/4\pi\sigma_{pl}$ is the poloidal magnetic field diffusion coefficient. The parallel plasma conductivity, σ_{pl}, was deduced from measured experimentally T_e and n_e and

assumed Z_{eff} with the toroidal correction [5]. The $j_{pl}(r)$ profile for the quasi-stationary OH phase was used as the initial condition providing the initial value of $Z_{eff} = 1.3$. Such a low magnitude of Z_{eff} precluded any suggestion about substantial anomaly in σ_{pl} and also ruled out an error in the determination of $j_{pl}(r)$ due to a possible non-uniformity of $Z_{eff}(r)$ (in the calculations it was assumed to be constant over the radius).

Using the obtained data on the $B_p(r,t)$ evolution, the loop voltage, $U_l(t)$, was simulated as well (dots in Fig. 1) and then was compared with the experimental value (solid line) to verify the assumption about the classical nature of the B_p diffusion.

To determine the electron thermal conductivity at a radius r, the heat balance equation in the integral form was solved:

$$P_{e,tr}(r) = P_J(r) + P_{e,m}(r) - P_{rad} - P_{ei}(r) - dW_e(r)/dt \qquad (2)$$

In the right side of the equation $P_J(r) = 2\pi \int_0^r (j_{pl}^2/\sigma_{pl})r dr$ is the Joule heating, P_{rad} and P_{ei} are radiation loss and electron-ion heat exchange rates respectively, $dW_e(r)/dt = d/dt(2\pi \int_0^r w_e(r)r dr) = d/dt(2\pi \int_0^r 1.5n_e(r)T_e(r)r dr)$ is the rate of heat storage variations in the electron component. $P_{e,m}(r) = \dot{B_t}/B_t[2W_e(r)/3 + \pi r^2 w_e(r)]$ is due to the B_t time variations and describes the compression heating or the decompression cooling. It consists of two parts which correspond to terms in the heat balance equation, given in [6]: $nTdivV + div(1.5nTV)$, with V being the compressional velocity $V_{r,C}$. The rest in the left side of Eq.(2), $P_{e,tr}$, correct to the $nTdivV$, where V is the transport plasma flux velocity, is the electron heat flux through the lateral surface of a cylinder of unit length and radius r due to the heat conductivity and the heat flux carried by the transport flux of particles.

In accordance with this, an effective thermal conductivity coefficient was defined as

$$\kappa_{e,eff} = P_{e,tr}/(2\pi r|\nabla T_e|) \qquad (3)$$

4. Transport evolution in the discharge. The evolution of $\kappa_{e,eff}(r)$ profiles throughout all of the discharge phases is shown in Fig. 2. In OH (Fig.2a) an expressed increase in $\kappa_{e,eff}$ can be seen at the middle of the minor radius. In [1,2] it was attributed to existence of magnetic islands near resonant magnetic surfaces $q = 2$ and $q = 3$. Stability calculations showed that both modes 2/1 and 3/1 were unstable. The local magnetic probe signal, $\dot{B}_p$, demonstrated a strong noise during this discharge phase (Fig. 1).

The compression supressed the MHD instabilities and eliminated the increase in $\kappa_{e,eff}$ (Fig.2b). The $\dot{B}_p$ signal dropped dramatically and lasted at the low level till the end of the discharge. In comparison with the OH period, the heat conductivity decreased, with its average value $\overline{\kappa_{e,eff}} = (5-7) \times 10^{17} cm^{-1}s^{-1}$ being typical for the anomalous transport in tokamaks. The quiet state with quasi-flat $\kappa_{e,eff}(r)$ profile and with only weak variations of $\overline{\kappa_{e,eff}}$ within 30% kept for the whole PC phase (Fig.2c). Thus, the improvement of the confinement during the compression was explained with the trivial reasons.

The loop voltage, simulated at constant $Z_{eff} = 1.3$, perfectly coincided with the experimental one during the fast C period (Fig.1). In the PC phase one needed to increase Z_{eff} by 1.5 to 2 times to match the simulated U_l. It implied an accumulation of impurities during this quiet stage, the fact was confirmed by SXR and VUV measurements.

The accumulation terminated at the beginning of the DC phase and Z_{eff} went down to its initial value, $Z_{eff} \geq 1$.

An odd phenomenon had been observed in the decompression phase: the electron temperature in a central zone $0 < r/a < 0.5$ did not go down and kept approximately constant during whole the phase (Fig. 1) though the energy contribution to the zone decreased because of expansion of the current channel and the magnetic adiabatic cooling. Even when B_t became equal to the initial value, $T_e(0)$ was still significantly higher than at the start of the compression. It directly implied an improvement in the confinement (Fig. 1 - τ_{eE}^{tr} behaviour, Fig. 2d). The experimental $\kappa_{e,eff}(r)$ and $P_{e,tr}(r)$ for the late DC phase are presented in Fig. 3, together with their neoclassical analogues calculated with use of the simple Galeev & Sagdeev formalism [7]. One can see the thermal conductivity in the central zone to attain the neoclassical value.

5. Discussion.   In attempts to find the reason for the appearance of such a low heat conductivity, in [1,2] the attention was paid to rather flat profile of the safety factor, $q(r)$, which arose at the same time due to joint action of the diffusion expansion of $j_{pl}(r)$ profile during both the PC and DC phases and of the magnetic decompression.

In scope of the modern studies, this relation gains a new meaning. In 1995 a precipitous drop in both the diffusion coefficient and the ion heat coductivity was discovered in an internal part of the plasma column where the q-profile was reversed and the magnetic shear, $s = (r/q)dq/dr$, was negative [8]. More recent study [9] showed that the similar drop occurs not only in the zone with $s < 0$ but at the flat $q(r)$, i.e. $s \approx 0$, as well. Finally, in [3] the local electron thermal diffusivity was also found to decrease dramatically for weak or reversed magnetic shear configurations.

In the experiments on TUMAN-2A the most dramatical changes both in $q(r)$ and in $\kappa_{e,eff}$ occured during the first half of the DC phase. In Fig. 4 the radial profiles of $q(r)$ and $\kappa_{e,eff}/\kappa_{e,eff}^{neo}$ are shown for two moments, $t = 4.6ms$ and $t = 5.3ms$. One can see that, as well as in the quoted papers, flattening $q(r)$ profile seems to correlate with the drop in the relative value of $\kappa_{e,eff}$. According to the data obtained and in agreement with the results of [3], one can assume that the change in the heat conductivity does not have a threshold behaviour when κ_e would drop abruptly at the transition of s through zero; the dependence κ_e vs s is likely to be smoother.

References

[1] Goncharov, S.G., et al., in Plasma Phys. and Contr. Nucl. Fusion Res. 1984 (Proc. 10th Int. Conf., London, 1984), IAEA, Vienna, 1985, v.1, p.155.

[2] Kalmykov, S.G., et al., Sov. JETP Lett. **40** (1984) 1133.

[3] X.Litaudon & Equipe Tore Supra, Plasma Phys. Control. Fusion **38** (1996) A251.

[4] Goncharov, S.G., et al., Controlled Fusion and Plasma Phys. (Proc. 10th European Conf., Moscow, 1981), Vol.II, (Moscow, 1982), p.172.

[5] Hirshman, S.P., et al., Nucl. Fusion **17** (1977) 611.

[6] Braginskii, S.I., 1965, in: Reviews of Plasma Physics, edited by M.A.Leontovich, Consultants Bureau, NY, Vol.1.

[7] Galeev, A.A., and Sagdeev, R.Z., in: Reviews of Plasma Physics, edited by M.A.Leontovich, Consultants Bureau, NY, Vol.7.

[8] Levinton, F.M., et al., Phys. Rev. Lett. **75** (1995) 4417.

[9] Forest, C.B., et al., Controlled Fusion and Plasma Phys. (Proc. 22nd EPS Conf., Kiev, 1996), Vol.20C, Part II (EPS, Geneva, 1996), II-e025, p.910.
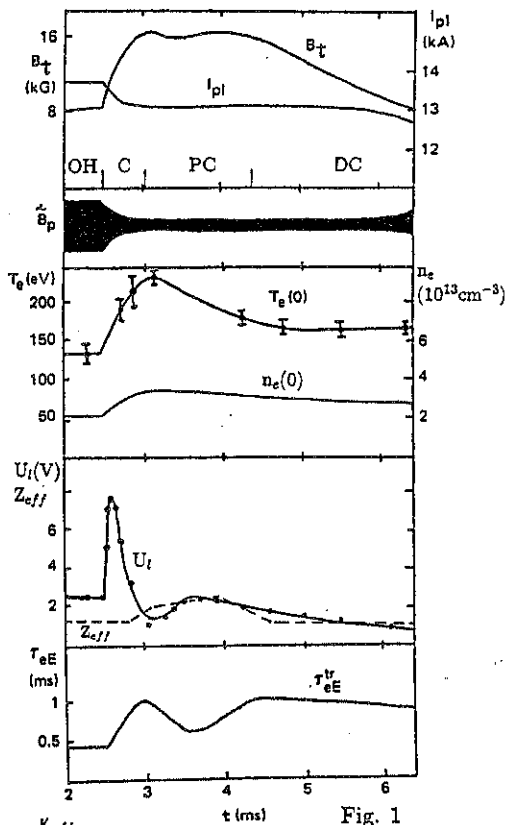
Fig. 1
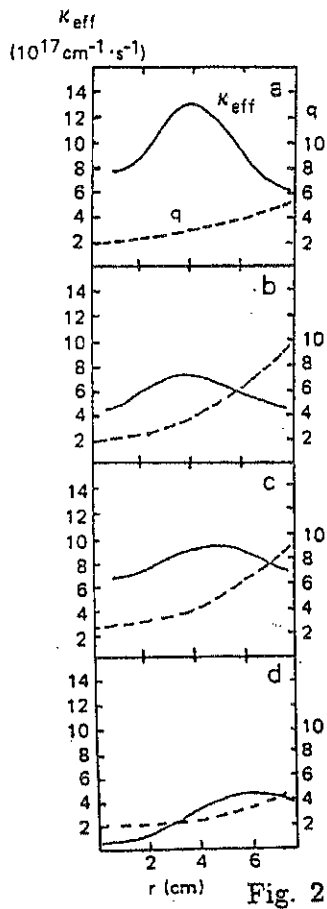
Fig. 2
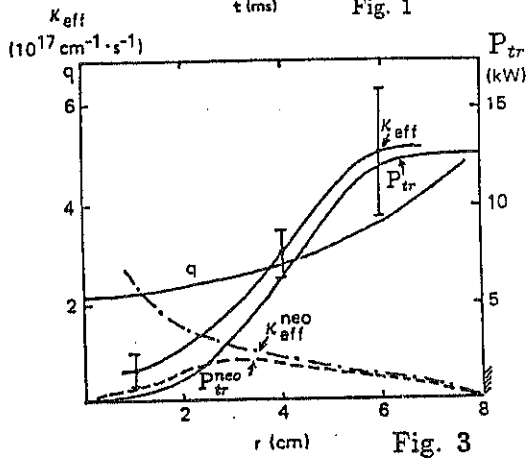
Fig. 3
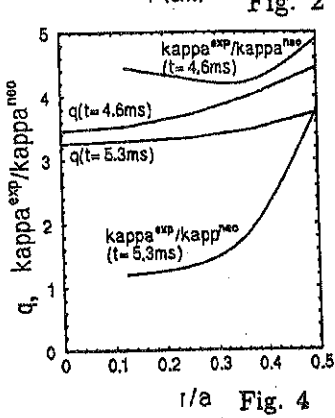
Fig. 4

THE EFFECT OF PLASMA BOUNDARY
ON ABSORPTION OF LOWER HYBRID WAVES AND
PLASMA IMPROVED CONFINEMENT IN FT-2 TOKAMAK.

V.N.Budnikov, V.V.Dyachenko, L.A.Esipov, M.A.Irzak, E.R.Its, S.I.Lashkul, M.Yu.Kantor,

D.V.Kouprienko, I.E.Sackharov[†], C.V.Shatalin[†], O.N.Scherbinin, V.B.Yermolaev[†], V.M.Zavadsky.

Ioffe Institute, Saint-Petersburg, Russia

[†] *Technical University, Saint-Petersburg, Russia*

1. INTRODUCTION.

Effects of plasma column positions on lower hybrid heating efficiency were investigated in FT-2 tokamak [1]. Higher LHH efficiency and ion energy confinement were found when plasma shifted outward along major radius. There observed higher electron temperature and density in the shadow of tokamak limiter in Ohmic discharge at this position. At inward plasma position LHH efficiency was lower. Ohmic edge electron temperature and density were lower too. But strong raise of edge plasma density occurs during RF pulse. Two mechanisms are considered for the explanation of these effects. First of them is parametric decay of LH wave in plasma boundary at lower electron temperature [2]. The following stochastic absorption of daughter slow-down wave in plasma periphery prevents effective ion heating at inward position of plasma column. The growth of parametric decay threshold with the increase of edge electron temperature allows pump LH wave to penetrate in plasma center and to be absorbed stochastically there. The second mechanism is associated with essential influence on LHH efficiency of different plasma confinement at these regimes.

It is clear that electron component is of great importance in these mechanisms. To distinguish their role in the processes under study electron temperature and density must be measured accurately and detaily. The study of the processes requires the measurements of evolution of electron temperature and density during RF pulse. This makes it possible to follow the variation of plasma confinement and RF absorption conditions. At LHH conditions temperature measured with SXR or ECE could be substantially distorted. Under these conditions Thomson scattering remains the only reliable way for electron temperature measurements.

2. ELECTRON TEMPERATURE MEASUREMENTS.

High precision multipulse Thomson scattering diagnostics based on laser photon recycling plasma probing was developed in FT-2 tokamak [3]. At these experiments the system operated at multipulse mode (8-10 pulses, 8 kHz repetition rate) with total probing energy up to 800J. The duration of laser oscillation determined by flash lamp discharge was shorter than RF pulse. Therefore the dynamic of electron temperature has to be measured in successive tokamak pulses. The example of electron temperature evolution measured in 8 tokasmak discharges are shown in **Fig. 1**. The statistical errors in a single laser pulse is about
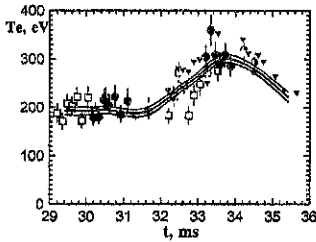
Fig.1.
Evolution of electron temperature

7%. To minimise the influence of irreproducibility of tokamak discharges and improve the statistical errors the measurements were smoothed. Smoothed temperature was determined from the sum of scattered signal within a given temporal gate. The result of smoothing of electron temperature evolution with temporal moving of 0.6 ms gate is shown in **Fig. 1** by thick line. Thin lines show the accuracy of smoothed measurements. Such procedure was performed for all the presented data. Temperature spatial profile was measured by shifting spectrometer along the laser probing axis shot by shot. Spatial resolution of the measurements was 1cm.

3. OHMIC HEATING REGIMES.

In this work *outward* (1) and *inward* (2) plasma column positions are investigated. Electron density profiles measured with 7-channel 2 mm interferometer show the shift of discharge axis along major radius from the center of chamber to be 2.5 cm and -0.7 cm at regime (1) and (2) correspondingly (**Fig. 2**). Laser probing was performed through the center of chamber (R=55 cm) in vertical direction. Threfore the axis of the discharge was not available for Thomson scattering. Electron temperature profiles plotted versus the distance from the axis of the discharge are shown in **Fig. 3**. The electron energy content of outward shifted plasma is no less than 22 J, that is twice more than in regime (2). Electron energy lifetime at these regimes are 0.6 and 0.2 ms taking into account power transfer to ions (~12 kW) and radiation losses (~20 and 30% correspondingly). Here ion temperature at the center of plasma column is 90 eV. H_β emission at regime (1) is twice less. Better energy confinement at regime (1) could be consequence of plasma edge heating that leads to suppression of resistive ballooning modes.[1]
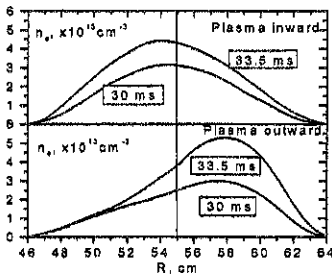
Fig. 2
Electron density profiles at
Ohmic (30 ms) and LH (33.5 ms) heating.
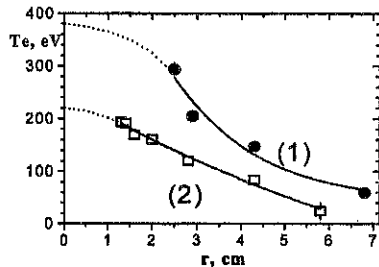
Fig.3
Ohmic heating profiles at regimes (1) and (2)

4. HEATING OF ELECTRONS.

The parameters of launched LH wave in FT-2 tokamak are as follows: 100 kW, 920 MHz, $N_\parallel$ =2.5. Under the experimental conditions RF power is not directly absorbed by electrons with stochastic mechanism. Nevertheless, electron temperature varies during RF pulse as is seen in **Fig. 4** and **Fig. 5**. There are substantial differences in the behaviour of electron temperature at these regimes. At outward shift there are weak changes of electron temperature and density measured with Thomson scattering from plasma periphery to the half of minor radius. Microwave interferometry shows more than twice picking of density profile in central region of 2-3 cm in radius. The central ion temperature increased up to 300 eV at the completion of RF heating. These facts points on substantial increase of plasma energy content at the central plasma region. At the same time there are about no differences in electrons outside this region. This could sign the absorption of RF power in plasma center and high energy confinement in this region.
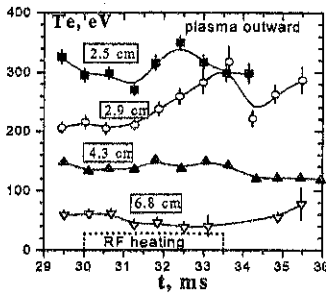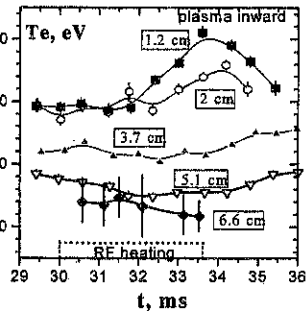
Fig. 4   *fig.5.*

Evolution of electron temperature during LH heating

At inward shift electron temperature and density evaluate over all the plasma column. The most raise of density is observed with Thomson scattering in plasma periphery. This could

be associated with ionisation of impurities caused by additional power deposition in this region. There are no picking electron temperature and density profiles at this regime.

4. LOWER HYBRID HEATING OF IONS.

Ion temperature was measured by scanning of 5-channel CX analyser. To decrease the influence of local-trapped ions the energy spectra were picked up at electron drift half of torus and horizontal scanning were used as well. **Fig. 6** and **Fig. 7** present ion temperature profiles for both regimes at OH, LHH and post LHH stages. Appropriate CX energy spectra are shown in **Fig. 8** and **Fig. 9**. Heating of ions is more effective in outward plasma. In this case ion temperature is increased by 3.5 times. Energy balance shows central RF power deposition in outward shifted plasma whereas absorption of RF power at inward plasma appears to be in
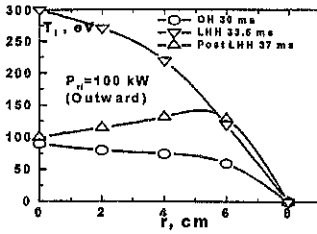
Fig. 6
Ion temperaure profiles of
outword shifted plasma
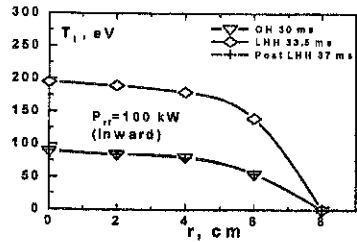
Fig. 7
Ion temperaure profiles of
inword shifted plasma

periphery. It is likely the evidence of parametric decay of LH wave. Its threshold is $\sim T_e^{\alpha}/n_e^{\beta}$ [2]. Lower edge electron temperature of inward shifted plasma could forward parametric decay at plasma edge. This is the reason of differences in fast ion spectra observed at horizontal scanning. RF power absorbed in plasma edge produces fast local trapped ions which dissipate rapidly in toroidal field ripples. The horizontal tilt of CX analyser decreases
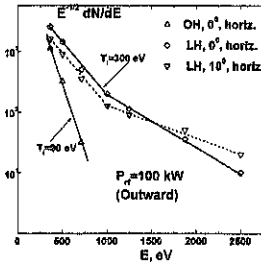
Fig. 8
CX spectra of outward plasma
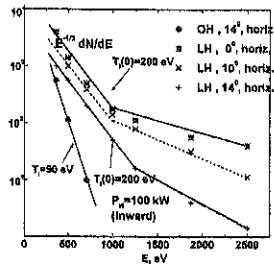
Fig. 9
CX spectra of inward plasma

the contribution of fast ions in measurements.

Parametric decay of LH wave may determine the absorption of LH wave in the center of the discharge of FT-2 tokamak. Thomson scattering confirmed improved confinement in outward shifted plasma [1]. These consequences are based both on precise electron temperature measurements and on developed analysis of CX data. The following investigation require electron temperature measurements on the axis region of the discharge and involving in the experiments additional diagnostics such as reflectometry and enchanced scattering.

LITERATURE

1. Budnikov V.N. et al., Tech. Phys. Lett, v. 23, (1), 32, 1997
2. Budnikov V.N., Irzak M.A., Plasma Phys. and Contr. Fusion, v. 38, (12A), 135, 1996,
3. Kantor M.Yu. Kouprienko D.V. Tech. Phys. Lett, v. 23, (4), 331, 1997

Investigation of plasma turbulence by microwave backscattering techniques in LH-heating experiments on the FT-2 tokamak

V.N.Budnikov, V.V.Bulanin*, A.D.Gurchenko, **E.Z.Gusakov**, V.V.Dyachenko,

L.A.Esipov, E.R.Its, V.Yu.Shorikov, A.Yu.Stepanov

Ioffe Physico-Techical Institute, St.Petersburg, Russia

*State Technical University; St.Petersburg, Russia

Introduction

The lower hybrid heating experiments on the FT-2 tokamak during the last decade were devoted to detailed investigation of the mechanisms of the wave interaction with ions and electrons. It was demonstrated that the density limit for the LH current drive as well as the threshold density for the fast ion tails production are correlated with the excitation of the parametric decay instability in the central part of the tokamak discharge [1]. This instability results in the generation of the slowed down wave at the local lower hybrid frequency and thus in the anomalous absorption of RF power, which could be responsible for the termination of the current drive and strong wave-ion interaction. It was shown recently [2], that the anomalous absorption of the LH wave at the threshold density is accompanied by the drastic enhancement of the low frequency turbulence level. The CO_2 laser scattering measurements used in [2] have shown that the enhancement is observed only in the small scale region typically for wave numbers higher than 15 cm^{-1}. The turbulence level in this wave number region was more than an order of magnitude higher, compared to the ohmic heating regime. Unfortunately the spatial localization of the turbulence perturbation was only roughly studied in [2], because of poor spatial resolution. This gap is covered in the present paper, where the behaviour of the small scale low frequency tokamak turbulence during the LH power incidence is studied using the microwave backscattering diagnostics. These diagnostics utilize the X-mode backscattering in the vicinity of upper hybrid resonance (so called Enhanced Scattering, ES) and reflectometric scattering, between the antenna and cut off of both, extraordinary X-RFL and ordinary O-RFL modes.

Experimental setup

The experiment was carried out on the FT-2 tokamak with standard parameters R= 55 cm, a= 8 cm, I_p < 40 kA, B_t < 2.4 T. The typical plasma parameters in the ohmic discharge were: n_e (0) = (1.0-5.5).10^{13} cm^{-3}, T_i = 100 eV, T_e = 500-600 eV. The RF power 20-140 kW was launched into the plasma at frequency 920 MHz by the two wave guide grill situated at the low magnetic field side. The wave interaction with the electron component was controlled

in the present experiment by the loop voltage, where as the information on wave-ion interaction was provided by the charge exchange diagnostics situated in the poloidal cross-section shifted by +90° from LH grill in toroidal direction. A pair of horn antennae standing in the same cross-section at the high magnetic field side was used as incident and receiving antennae for both ES and X-RFL diagnostics. The frequency of the incident microwave was varied from 54 up to 70 GHz at power level 10 mW. Two vertically directed horn antennae situated in the -90° toroidal cross-section were used for O-mode reflectometry. The frequency of O-RFL was varied in the range 26-35 GHz at the power of 10 mW. The ES diagnostics utilized the super heterodyne detection scheme, where as both reflectometry methods were based on the direct detection schemes. The microwave scattering diagnostics signals were fed to the data acquisition system with a sampling frequency up to 4 MHz. The consequent treatment of the stored data provided information on the frequency spectrum of the scattered signals and their time evolution. The spatial localization of measurements was determined by the position of upper hybrid resonance point for ES diagnostics and by cut off position for X-RFL and O-RFL. The spatial scan was provided by selection of the probing frequency before the discharge and by time variation of magnetic field and plasma density.

Experimental results

The typical transition of LH wave interaction from electron to ion component is shown in Fig.1. The RF power launching is as usual accompanied by the density growth. At the beginning of the RF pulse at small plasma density n_e (0) < 2.10^{13} cm^{-3}, a well pronounced decrease of the loop voltage is observed, which is explained by both LHCD and electron heating . At higher plasma density this decrease saturates and then is followed by growth of the loop voltage. Simultaneously the growth of the high energy 1 keV neutral flux is seen. As it is shown in Fig.2a this growth is accompanied by the factor of 3 increase of the ES signal picked up from the radial position r = 5 cm. At a larger starting density (Fig.2b) the growth of both signals take place from the very beginning of the RF pulse and the growth of the ES signal is much smaller. The spatial distributions of the ES signal in the ohmic discharge and its increase during the RF pulse are shown in Fig.3 for the case of plasma density $n_e(0) = 2.10^{13}$ cm^{-3}. As it is seen the ES signal is maximal for the upper hybrid resonance position 4 cm < r_{UHR} < 6 cm. The maximal enhancement of the low frequency turbulence is also observed in this region. In the high density case $n_e(0) = 3.5.10^{13}$ cm^{-3} the excess of ES signal is localized in the same region, however its magnitude is 5 times smaller. It is worth to mention that the ES signal is not sensitive to the application of RF power in the LHCD regime.

The time evolution of X-RFL signal is less correlated to the fast neutral flux behaviour. As it is seen from Fig.4a for the cut off position r_{co} = -6.5 cm the two signals are similar, where as at the plasma edge, for r_{co} = -7.5 cm, the X-RFL signal is suppressed simultaneously with the fast ion generation beginning (Fig.4b).

The observations with O-mode reflectometry have shown no correlation of the scattered signal and the fast ion generation. The correlation with the MHD probe signal was observed instead (Fig.5).

Discussion and summary

The results obtained by the microwave backscattering diagnostics are in agreement with the observation with CO_2 laser scattering technique [2]. The well pronounced correlation with the density threshold for fast neutrals production and CO_2 scattering enhancement is observed only by ES diagnostics. This diagnostics is only sensitive to small scale fluctuations with wavelength λ < 0.2-0.3 cm, which are enhanced at the density threshold according to [2]. The difference in the enhancement factor, which is 10-15 for CO_2 laser scattering and only 3 for ES diagnostics is probably explained by the fact that ES signal is integral in wave numbers and provides information not only about fluctuations enhanced by parametric instability excitation and/or fast ion acceleration. The weak correlation observed for X-RFL and absence of correlation with the CO_2 laser data for O-RFL is quite natural, because X-RFL is sensitive only to fluctuations with wavelength λ > 0.2- 0.3 cm and O-RFL - λ > 0.4-0.6 cm, for which the enhancement is much smaller [2]. The difference in the domain of sensitivity of these diagnostics is confirmed by the frequency width of scattering spectra shown in Fig.6, which is the most wide for ES.

The spatial localization of the turbulence enhancement effect according to ES diagnostics is 4 cm < r < 6 cm.

Coming to the possible reasons of the low frequency density turbulence enhancement one can mention two possible mechanisms. The first is associated with the trapped particle instability which could be influenced by the increased number of fast trapped ions produced by the LH wave. The second could be related to the secondary decay instabilities of the daughter lower hybrid wave leading to the excitation of small scale drift waves [3]. The last mechanism seems to be preferable for explanation of unusual enhancement of the small scale part of the turbulence spectrum only.

Acknowledgements

References

1. Budnikov V.N. Nuclear Fusion, vol.31, p.611-629, (1991).

2. Bulanin V.V. et al. In: Proc. 23 EPS Conf. Control.Fusion and Plasma Phys., v.20C, p.855, (1996).

3. Takase Y. et al. Phys.Fluids, vol.28, p.983, (1985).
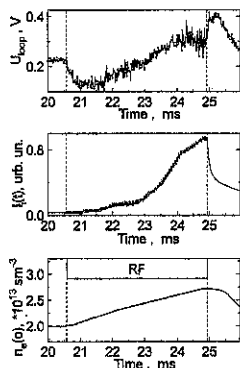
Fig.1. Oscillograms of the loop voltage U_l, high energy ion flux I_i ($E_i = 1$ keV) and electron density $n_e(0)$ during the RF-pulse on the FT-2 tokamak.
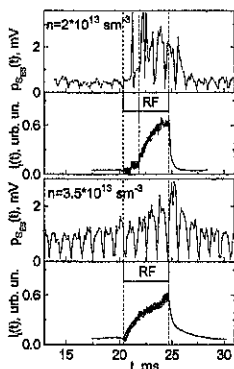
Fig.2. Evolution of the ES signal and high energy ion flux: (a) in the transition regime ($r_{UHR} \cong$ 5-6 cm); (b) in the regime when the ion generation starts at the very begining of the RF-pulse ($r_{UHR} \cong$ 5.5-6.5 cm).
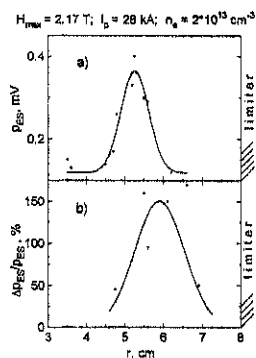
Fig.3. Radial profiles: (a) the enhanced scattering signal p_{ES} in the ohmic regime; (b) growth factor of the p_{ES} signal in the LH power regime.
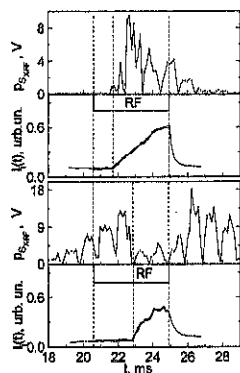
Fig.4. Evolution of the X-reflectometry signal and high energy ion flux: (a) cuttoff minor radius $r_{CO} = -6.5$ cm; (b) $r_{CO} = -7.5$ cm (on the plasma periphery).
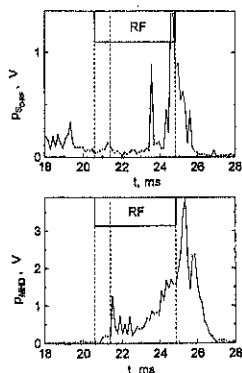
Fig.5. Evolution of the O-reflectometry and magnetic Mirnov's coil signals.
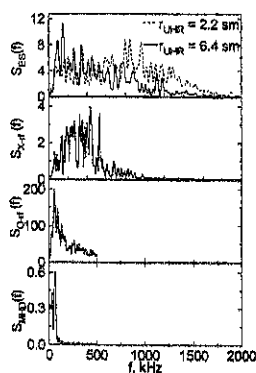
Fig.6. Frequency spectra of ES, X- and O- reflectometry and magnetic Mirnov's coil signals in the ohmic regime.

Investigation of plasma oscillations on resonant magnetic flux surfaces by the correlation reflectometry on FT-2 tokamak

Budnikov V.N., Gurchenko A.D., Gusakov E.Z., Esipov L.A., Its E.R., Shorikov V.Yu., Stepanov A.Yu.

Ioffe Physico-Technical Institute, St.Petesburg, Russia

Introduction

It was shown recently [1], that the cross correlation analyses of the signal of two poloidally separated reflectometers provides the possibility of identification of global MHD modes localized at the cut off of the incident microwave. This information can be used, in principle, for the determination of the position of resonant magnetic surfaces and thus for reconstruction of the safety factor profile. In the present paper this studies are continued. The experimental results are presented demonstrating that the usual one channel reflectometer operating in the direct detection scheme can provide such an information as well.

Experimental setup

The MHD density perturbations were investigated by two simultaneously operating reflectometers at frequency in the range 27-35 GHz. The ordinary mode probing was used, for which the cut off density varies in the interval $0.9 \cdot 10^{13} < n_c < 1.5 \cdot 10^{13}$. The scheme of the experiment is shown in Fig.1. The reflectometers are situated in the same poloidal cross-section and share the emitting antenna A_2 and the microwave generator with the output power of 10 mW. Their receiving antennae A_1 and A_3 are separated by 36°. The direct detection scheme is used providing information about reflected signal amplitude modulation. The signal is amplified in the 500 kHz band and stored by the data acquisition with a sampling time of $1 \mu s$. The experiment was carried out in the FT-2 tokamak ($R_0 = 55$ cm, $a = 8$ cm) at the following discharge parameters: $I_p < 30$ kA, $B_t = 2$ T, $<n_e> < 3 \cdot 10^{13}$ cm^{-3}. The time variation of plasma current and magnetic field during the discharge determined the evolution of the q-profile and thus the radial drift of resonant surfaces, where the global MHD modes are nested. The time changes of plasma density provided the cut

off spatial scan. These two factors and the change of probing frequency from discharge to discharge have given the opportunity of intersecting the probing wave cut off with magnetic surfaces with q = (1.5-4.0) at plasma maximal currents I_p = 20 and 30 kA.

Experimental results

The high level (P_s / P_0 ~ 10^{-4}) reflectometry or scattering signal is observed in the experiment when the plasma density is large enough and the cut off exists in the discharge. The time evolution of reflectometry signal picked up by A_1 and A_3 antennae and integrated in the frequency band 5-500 kHz is shown in Fig.2. The behaviour of these signals is similar in details and the strong amplitude modulation is typical for it. The bursts of signals occur when according to calculation based on the parabolic safety factor profile assumption the rational magnetic surfaces are situated in the cut off vicinity. The strong scattered signal was observed for q = 2.5, 3.0 and 4.0 both on the stage of growing and decreasing plasma density, when the cut off moved first to the plasma periphery and then back to the center of the discharge. It should be mentioned that the behaviour of the reflectometry signals depends on the tokamak discharge conditions. Namely on the major radius equilibrium and vacuum conditions, which could influence the burst amplitude and similarity of the two channel scattering data. The correlation analyses of two reflectometer signals has shown the high coherence level for some frequencies during these bursts see Fig.3). In the case when only a single separate line was seen in the coherence spectra the crossphase spectrum provided the possibility to determine the poloidal number of the MHD mode. It appears to be m^i = 6 for q = 3 in Fig.3, in agreement with peculiarities of the direct detection scheme mentioned in [1]. In the case when several near by standing high coherence lines were observed in the spectrum no mode identification was possible. It should be underlined that such a high coherence lines were observed only in the bursts of scattering signal and were not seen in between.

The behaviour of the scattering signal in A_3 reflectometer channel for discharges with different maximal densities $n_e(0)_{max}$ = (2.25, 2.85, 3.0)10^{13} cm^{-3} is shown in Fig.4. The change of the signal burst time with the varying discharge density is seen in Fig.4. These changes could be easily explained by the variation of the

overlapping time of the resonant surface and cut off. The clear interpretation of above effect seems to give an evidence of diagnostic potential of reflectometry scattering as a q-profile diagnostics.

In the experiment using asymmetric probing scheme where antenna A_1 was emitting the probing power and A_2, A_3 were receiving the signal. The bursts of the scattering data were observed as well (see Fig.5). However the dependencies for two channels were less similar (compare to Fig.2). Namely bursts in the signal of A_2 antenna were initiated slightly later compared to A_3 at the stage of increasing density. This effect could be probably explained by different position of cut off for ray trajectories of two reflectometers. The cut off density in the case of oblique propagation is given by $n_{co} = n_c (1 - \sin^2\alpha)$, where n_c is the critical density and α is a starting propagation angle of the ray trajectory.

The above effects could be applied to the multichannel cross correlative reflectometry diagnostics, the scheme of which is shown in Fig.6. The diagnostics utilize single emitting antenna with a wide diagram and several pairs of poloidally separated receiving antennae. The cut off position for each pair is different, thus providing the possibility of spatial resolution in the single frequency experiment.

Acknowledgements

References

1. A.*Yu.Stepanov, V.N.Budnikov, E.Z.Gusakov* e.a. Plasma Current Profile Diagnostics on FT-2 Based on the Correlation Reflectometry Measurements of MHD Modes. 23rd EPS Conf. on Controlled Fusion and Plasma Physics, Kiev, Ukraine, 1996, Contr. Papers.
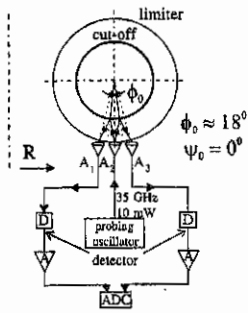
Fig.1. *Scheme of FT-2 Poloidal Correlation Reflectometer. (A - low pass filter and amplifier).*
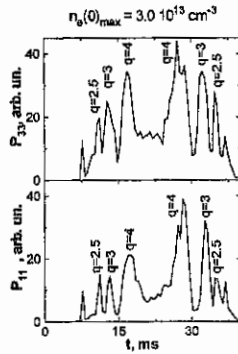
Fig.2. *Time evolution of the reflectometry signals from the receiving antennas 3 and 1 in the frequency range (5-500) kHz.*
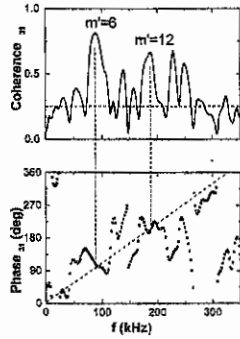
Fig.3. *Coherence and crossphase spectra for q=3. Dashed line in the phase plot is the calculated curve for $\phi_0 = 18^0$.*
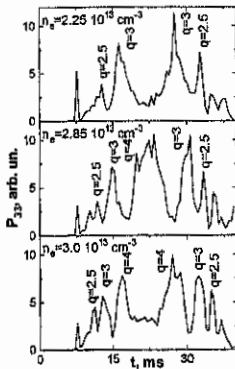
Fig.4 *Time evolution of the reflectometry signals P_{33} at different densities $n_e(0)_{max}$.*
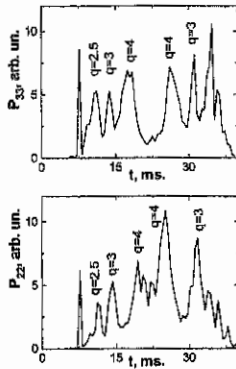
Fig.5. *Time evolution of the reflectometry signals from the receiving antennas 3 and 2. Angles between grad n_e and antenna beams are different.*
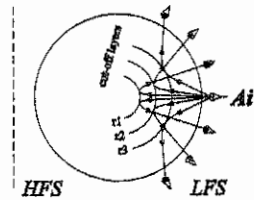
Fig.6. *Multy-channel correlation reflectometry scheme using only one probing frequency.*

β studies in TUMAN-3M tokamak.

M.V. Andrejko, L.G. Askinazi, V.E. Golant, V.A. Kornev, S.V. Krikunov,

S.V. Lebedev, L.S. Levin, G.T. Razdobarin, V.V. Rozhdestvensky, V.M. Sharapov*,

A.S. Tukachinsky, S.P. Yaroshevich and A.P. Zakharov*

A.F.Ioffe Physico-Technical Institute, Russian Academy of Sciences
194021, St.Petersburg, RUSSIA
* Institute for Physical Chemistry, Russian Academy of Sciences, Moscow, RUSSIA

1 INTRODUCTION

The ratio of the plasma kinetic pressure to the magnetic field pressure – β determines efficiency of plasma confinement in a magnetic configuration. Values of β_T in a tokamak are restricted by the ideal MHD limit (Troyon limit) [1]. The limit establishes correlation between maximum values of β_T (expressed in %) and parameter I/aB (MA, m, T). The maximum values of $\beta_N=\beta_T/(I/(aB_T))$ are close to 3.5 in a tokamak with conventional geometry. In the experiments with strong crossection shaping and powerful auxiliary heating β_N close to 5 have been obtained [2].

In this paper the results of experimental study of a possibility to increase β_T and β_N in a circular crossection tokamak without auxiliary heating are presented. The experiments were performed in the TUMAN-3M tokamak. The device has following parameters: R_0=0.53 m, a_l=0.22 m (circular limiter configuration), $B_T \leq 1.2$ T, $I_p \leq 175$ kA, $\overline{n_e} \leq 6.2 \cdot 10^{19}$ m^{-3}. Stored energy quantities were measured using diamagnetic loops and compared with calculated from kinetic data obtained by Thomson scattering and microwave interferometry. Measurements of the stored energy and of the β were performed in ordinary Ohmic regime [3], in Ohmic H-mode [4] and in the scenario with fast Current Ramp-Down [5] in Ohmic H-mode. The β values in boronized vessel [6] were compared with that ones obtained before boronization.

2 β MEASUREMENTS IN OHMIC H-MODE

Ohmic H-mode observed in TUMAN-3 and later in TUMAN-3M tokamaks reveals good energy confinement [7,8]. Further increase of the energy content could be expected during density ramp-up, if confinement does not degrade at high density.

In the recent experimental run attempts to achieve high β_T and β_N were undertaken using density ramp-up. Without boronization highest plasma current attainable in TUMAN-3M is 150 kA at $q^{cyl} = 2.4$. In this regime the maximum achieved density was 4.2 10^{19} m^{-3}. Corresponding toroidal beta is 1.3 % and normalized beta is 1.5.

Boronization of the vessel has been performed using $C_2B_{10}H_{12}$ evaporation into He glow [6]. After boronization q^{cyl} was reduced to 2.1 allowing to increase plasma current up to 175 kA. In the conditions of low impurity contamination and increased density range (provided by boronization) the energy content W was increased substantially. An example of the shot in which β_T was measured by diamagnetic loops and calculated using kinetic data is shown on Fig.1. Transition into Ohmic H-mode takes place on 52 ms. Starting from this time density was ramped-up. β_T as well as β_N rise simultaneously with density until the 78 ms. Figures 2a&2b show temperature and density profiles at 68.5 and 77 ms. Diamagnetic data agree within 15 % with kinetic calculations based on above profiles. Moderate decrease of the central temperature during density rise stage could be mentioned indicating some saturation of confinement.
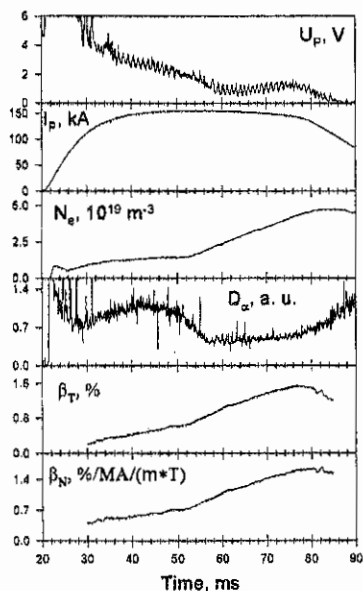
Fig.1 Temporal evolution of loop voltage, plasma current averaged density, D_α radiation and toroidal and normalized betas in the shot after boronization.

Diamagnetic data obtained before and after boronization are collected on the diagram displaying β_T as a function of parameter I/aB - Fig.3. Here open triangles correspond to the shots produced before and filled ones to the shots after boronization. Data shown on the diagram indicate substantial increase in the β_T as a result of boronization. At similar I/aB maximum toroidal beta is by a factor of 1.5 higher in boronized vessel compared to unboronized. Highest achieved β_T was 2.0 % at n_e=6 10^{19}m^{-3}. Temporal evolution of some plasma parameters in the record shot are presented on Fig.4.

Fig.2a Electron temperature profiles used in calcula-- tions of β at different times of the shot shown on Fig.1
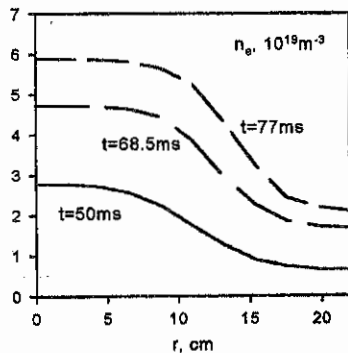
Fig.2b Electron density profiles during OH and Ohmic H-mode used in calculations of β at different times of the shot shown on Fig.1.

β_N was increased from 1.6 to 2.0 after boronization. These values are far from MHD limit. Nevertheless further increase of the energy content was impossible because of confinement degradation. The degradation reveals itself as saturation of β_T appearing before density saturation (see Fig.4) and as saturation of density despite of continuous gas puffing. No significant MHD activity was found in the shots with highest attainable β_N. Also should be mentioned that only few shots were ended with major disruptions. All above circumstances allow to conclude that restriction in the beta in our experiments is connected with "soft" (transport) saturation but not with MHD phenomena. Further analysis is necessary to clarify

Fig.3 β_T as a function of parameter I/(aB)
before and after boronization in TUMAN-3M.
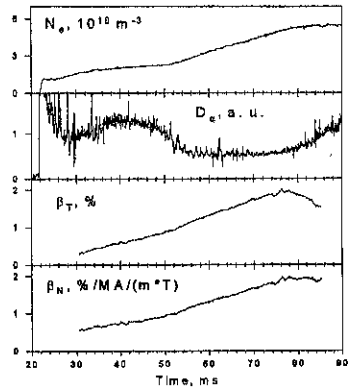
Fig.4 Temporal behavior of averaged
density, D_α radiation, and toroidal and
normalized betas in the shot with highest
achieved beta.

the actual cause for transport enhancement at high densities. Low input power in the conditions of pure ohmic heating might be the main explanation for observed limit. Experiments on other ohmically heated tokamaks also indicate lower level of beta limit compared to auxiliary heated devices. In T-11 maximum β_T was 1.7 % and β_N was 1.5 without NB heating [9]. Similar limitations were found in ohmic regime of START [10].

3 CURRENT RAMP-DOWN SCENARIO
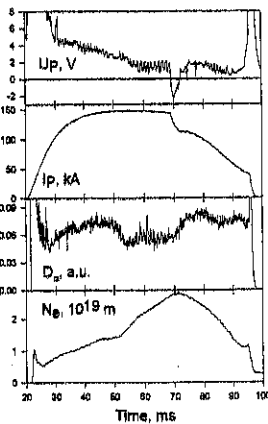
Fig.5 Temporal evolution of some plasma
parameters in the shot with fast Current
Ramp-Down.

Possibility to increase β_N in the experiments with fast Current Ramp-Down was investigated in TUMAN-3 in ordinary ohmic regime [5]. Because of low energy content of the target plasma the β_N values after CRD was very low. Described experiments were performed while target plasma was in Ohmic H-mode stage.

CRD was performed by applying negative voltage in the transformer primary. As a result current decay with rate up to 25 MA/s was obtained. Feedback position control provided plasma equilibrium during CRD. Waveforms of loop voltage, plasma current, D_α radiation and averaged density in the shot with CRD in Ohmic H-mode are shown on Fig.5. Although density in this regime was far from limit and puffing was not changed the n_e increase ceased just after CRD.

The drop in the energy content is less pronounced and this allow to increase or at least not lose β_N. Figure 6 shows temporal evolution of plasma current stored energy, β_T and β_N in expanded time scale. The figure evidences that during first 2-3 ms after CRD β_N
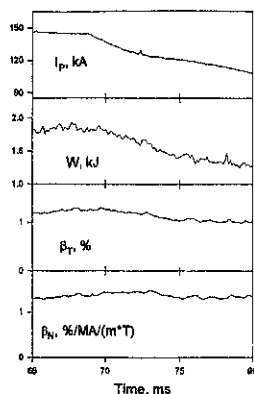
Fig.6 Behavior of the plasma current, stored energy, β_T and β_T in the CRD.

increases. This result is shown on Fig.3 by arrow originating from triangle corresponding to Ohmic H-mode and directed to diamond displaying CRD. In the CRD scenario decrease of the energy content was slow and this allow to increase slightly both β_N and β_T.

The decrease in the stored energy and in the density during CRD is not connected with MHD phenomena and has a character of transport enhancement. It is clearly seen on Fig.5 that CRD lead to termination of H-mode (D_α increase and density decay). H-L Transition can be considered as a reason of β_T reduction in this scenario. In order to check this assumption experiments with CRD in auxiliary heated H-mode plasma should be performed. Such experiments are planned in TUMAN-3M with ICR heating.

4 CONCLUSIONS

The experiments have shown that maximum value of β_T 2.0 % can be achieved without auxiliary heating. This value of beta-toroidal corresponds to the β_N value 2.0. Achieved β_N limit reveals itself as "soft" (nondisruptive) limit. Stored energy saturates during density rise or slowly decays after Current Ramp-Down. Possible explanation for β_T and β_N restrictions is enhanced transport near density limit or (in the case of CRD) resulting from H-L transition. No correlation was found between beta restriction and MHD phenomena.

β studies will be continued in near future under the conditions of the Ion Cyclotron auxiliary heating.

REFERENCES
[1] Troyon F., et al, Plas. Phys. Control. Fusion, v.26, p.209, 1984
[2] Chan V.S., et al XVI IAEA Fusion Energy Conf. (Montreal), IAEA-CN-64/O1-6, 1996
[3] Vorob'ev G.M., et al, Sov. J. Plas. Phys., v.9, p.65, 1983
[4] Arbuzov A.N., et al, Proc. 17th EPS Conf. on Contr. Fusion and Plas. Heat., v.14B, prt.I, p.299, 1990
[5] Sakharov N.V., et al, Plas. Phys. Control. Fusion, v.35, p.411, 1993
[6] Sharapov V.M., et al, J. Nucl. Mat., v220-222, p.730, 1995
[7] Lebedev S.V., et al, Plas. Phys. Control. Fusion, v.36, p.B289, 1994
[8] Lebedev S.V., et al, Plas. Phys. Control. Fusion, v.38, p.1103, 1996
[9] Barsukov A.G., et al, Proc. IX Int. Conf. on Plas. Phys. and Contr. Nucl. Fusion Res., v.1, p.83, 1982
[10] Akers R., et al XVI IAEA Fusion Energy Conf. (Montreal), IAEA-CN-64/C2-1, 1996

Modelling of the L-H transition on TUMAN-3 tokamak

V Rozhansky, M Tendler*, S Voskoboynikov

St.Petersburg State Technical University, 195251, St. Petersburg, Russia

*Alfven Lab., Euroatom NFR Association, Royal Institute of Technology, Stockholm, Sweden

1. Introduction

The model for the density evolution is employed for the TUMAN-3 tokamak accounting for the reduction of transport coefficients due to the enhanced shear of the $\vec{E} \times \vec{B}$ drift [1]-[3]. The evolution of the electric field profile is addressed consistently with transport equations. Modelling yields the dynamics of the L-H transition, including the formation of transport barrier at the edge and the density rise in the core of the TUMAN-3. Triggering of the L-H transition by gas puffing, demonstrated on TUMAN-3, [4] is adequately described by the model. The evolution of the particle source is taken directly from measurements carried out on TUMAN-3. The rise of the density in the core fits experimental measurements. In general, the model appears to be consistent with many features of L-H transitions observed on the TUMAN-3 tokamak.

2. Model

The particle continuity equation has the form

$$\frac{\partial n}{\partial t} - \frac{1}{r}\frac{\partial}{\partial r}[r(D(\omega_s)\frac{\partial n}{\partial r} - V(\omega_s)n)] = S. \tag{1}$$

Here the transport coefficients are supposed to be dependent on the shear of the $\vec{E} \times \vec{B}$ drift

$$\omega_s = \left| r \frac{\partial(v_o / r)}{\partial r} \right| = \left| r \frac{\partial(E_r / Br)}{\partial r} \right| = \left| r \frac{\partial(v_\vartheta - u_{pi})/r}{\partial r} \right|, \tag{2}$$

where the poloidal velocity is $v_\vartheta = v_0 + u_{pi}$ with u_{pi} being the ion diamagnetic drift velocity. In the Ohmic regime the toroidal rotation is damped by the anomalous viscosity [5-6]. The equation for the poloidal rotation velocity is [5-6]

$$n\frac{\partial v_\vartheta}{\partial t} + \Gamma\frac{\partial v_\vartheta}{\partial r} - \frac{1}{r}\frac{\partial}{\partial r}(r n\mu\frac{\partial v_\vartheta}{\partial r}) = -v_i n(v_\vartheta - v_\vartheta^{(NEO)}), \tag{3}$$

where $\Gamma = -D\partial n / \partial r + Vn$, $v_\vartheta^{(NEO)} = k(\partial T_i / \partial r) / eB$ is the neoclassical poloidal velocity, k is the numerical coefficient, dependent on collisionality [6], for calculation we chose $\mu = D$. The

last term of Eq. (3) describes the magnetic pumping, the second and the third terms corresponds to the radial transport of the poloidal rotation by the anomalous inertia and viscosity. The diffusion coefficient is $D=D_0 f(r)$, $(f(r=0)=1)$, the convective velocity $V=-(D_0/a)\psi(r)$ - is negative, a is the LCFS radius. The dependence of D_0 on the parameter ω_s is shown in Fig.1. The radial dependencies of the coefficients D and V were chosen to obtain the stationary profile before the transition, Fig. 2, 3. The particle source S in Eq.(1) was measured in the experiments both in L and H regimes, the experimental profiles were used for calculations. Since the ion temperature profile was not measured, it was taken in the form $T_i(r)=T_i(0)(1-r^2/a^2)$.
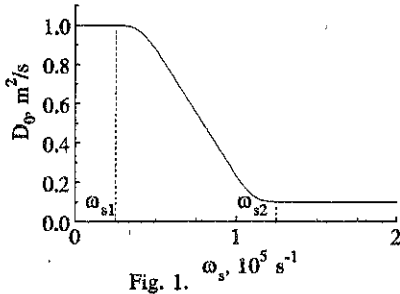
Fig. 1.

The model similar to ours was developed in [7], however our model differs from [7] by the account of the high derivatives in Eq.(1), and by including important convective term.

3. Results of the simulation

We considered two different scenaria of the L-H transition. In the first scenario the neoclassical value is chosen for the poloidal rotation, with the corresponding electric field

$$E_r^{(NEO)} = \frac{T_i}{e} [\frac{\partial \ln n}{\partial r} + (1-k)\frac{\partial \ln T_i}{\partial r}]. \qquad (4)$$

The Eq.(3) is thus excluded. The stationary profile before the transition is assumed to correspond to the marginal stability. In other words, the shear parameter ω_s at the edge is close to ω_1. Then, due to the small increase of the source, the edge shear becomes larger than the critical value, and the transition starts. The results are rather insensitive to the second parameter ω_2. The subtle details of the transport barrier formation were investigated in [7] for the Eq.(1) in the absence of the convective velocity V. Since for short distances of the order of few centimeters the diffusion is much more important than the convection, the results at small times coincide with [7]. At first the small positive density perturbation arises near the edge, and the transport coefficients decrease here. The transport barrier then propagates towards the core much faster than the diffusive signal, Fig. 4. The density gradient start to increase simultaneously, Figs. 6,7. The variation of the neoclassical electric field is shown in Fig. 5. The steady-state width of the barrier is of the order of 3cm, and is rather insensitive to the variation

of the chosen temperature profile and the values of ω_1, ω_2. This fact is explained by the sharp decrease of the shear ω_s with density, and thus its decrease towards the core.

Owing to the formation of the barrier in the edge region, the density in the core start to increase, Figs. 6,7. The density evolution here is to large extent controlled by the convective term. The characteristic time of the evolution and the absolute values of the density profiles in H-regime are in good agreement with the experimentally profiles, Figs. 6,7. However, the region where the transport coefficients are suppressed, in the calculations is smaller than in the experiment. Therefore, additional mechanism of the transport suppression should exist in the core. To investigate the effect of the ion temperature profile on the results, the calculations with the constant ion temperature were performed, Fig. 8. The width of the transport barrier and the absolute values of the density are smaller in this case, but the main features of the density evolution remains the same. Such rather insensitive behavior is explained by the fact that only the temperature variation inside the barrier is important.

In the second scenario the coupled Eqs. (1)-(2) have been solved. The density profile in L-regime corresponds to the $\omega_s < \omega_1$ at the edge. At t=0 a boundary condition was imposed on the poloidal rotation at LCFS: $v_\vartheta (r = a) = \Theta c_s$, where Θc_s is the poloidal sound speed, and L-H transition started. The evolution pattern in this case is very similar to the first scenario. The reason consists in the fact that the region where the poloidal rotation considerably exceeds the neoclassical value is smaller than the barrier width. The steady state poloidal velocity profile is shown in Fig. 9 for T_i=const (the neoclassical poloidal rotation is zero in this case). We see that the poloidal rotation vanishes towards the core, thus the situation resembles the first scenario.

References

[1]   Biglari H, Diamond PH & Terry PW, *Phys. Fluids* **B2** 11 (1990)
[2]   Groebner R J, *Phys. Fluids* **B5** 2343 (1993)
[3]   Moyer R A et al, Phys, Plasmas **2** 2397 (1995)
[4]   Andrejko M V et al, Plasma Phys. Contr. Fus. Res. 1992 (Proc. 14 Int. Conf. Plasma Phys. Contr. Fus., Wurzburg 1992) **1** 485 (1993)
[5]   Rozhansky V, Tendler M, Phys. Fluids **B4** 1877 (1992)
[6]   Rozhansky V, Tendler M, in Reviews of Plasma Phys., Ed. by B.B. Kadomtsev, Consultants Bureau N.Y.-London **19** 147 (1996)
[7]   Staebler, G.M.,et al. Phys. Plasmas **1** 909 (1994); Nuclear Fusion, **37**, 287 (1997).
[8]   Rozhansky V, Tendler M, Voskoboynikov S, in Controlled. Fusion & Plasma Phys. (Proc. 23 EPS Conf. Kiev 1996) **20C** Part 1 444 (1996).
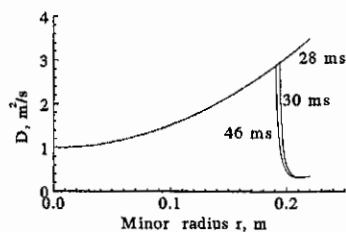
Fig. 2. Diffusion coefficient D.
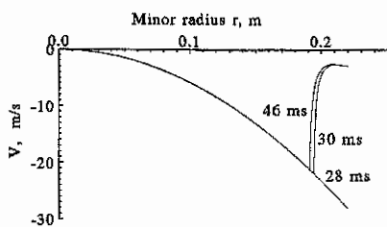
Fig. 3 Convective velocity V.
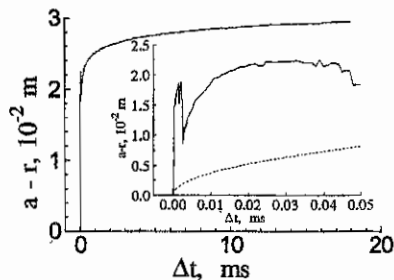
Fig. 4. Propagation of the transport barrier (solid line),
dashed line - a-r=(4Dt)$^{1/2}$, where D corresponds to L-regime.
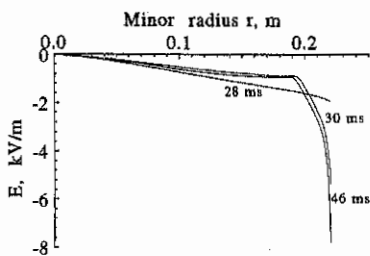
Fig.5 Neoclassical electric field.
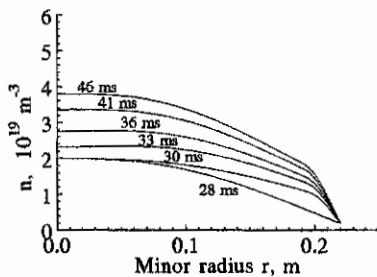
Fig. 6. Density evolution, calculations.
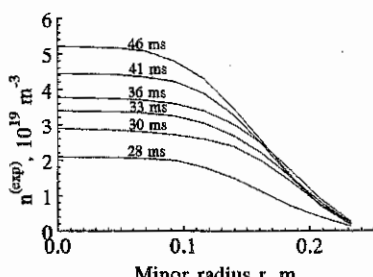
Fig. 7. Density evolution, experiment.
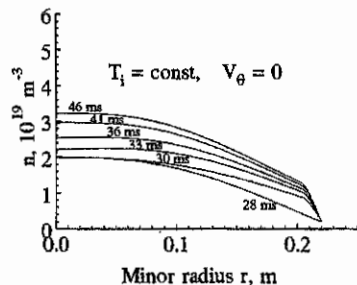
Fig. 8. Density evolution for T_i=const.
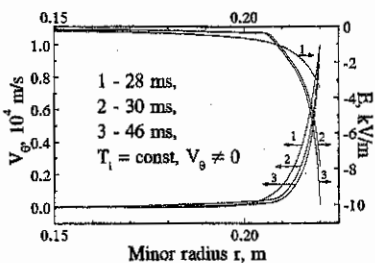
Fig. 9. Poloidal rotation and electric field in the second scenario.

Control of Edge Plasma Turbulence via Ergodic Magnetic Limiter in Tokamak TF-2

V.P. Budaev

Institute for High Temperatures of the Russian Academy of Sciences,
Scientific Station. 720049, IVTAN, Bishkek, Kyrgyzstan, CIS

1. Introduction

To control confinement in tokamak, the mechanisms that induce turbulent transport in edge should be identified. There are conceptions [see,f.e.,1] that consider the tokamak turbulence to consist of a few types of turbulences having got different physical nature, frequency and wave number spectra. The types react differently on dynamic changes of the discharge condition. Edge turbulence drives poloidally non-uniform anomalous particle transport. There is a need for improvements in producing of uniform power and particle load to the wall and in the avoidance of locked modes [2]. That may be assisted by producing of ergodic magnetic limiter (EML) in edge that was tested in TEXT[3], Hybtok-II[4], TEXTOR[5] and TORE SUPRA [6]. The aim of this study is to analyze the experimental data of small-scale tokamak TF-2 edge turbulence with respect to identifying the types of edge plasma fluctuations observed and how small-scale electrostatic turbulence and cross-field transport are modified by setting up EML in edge plasma.

2. Experimental Results

The experiments were performed with ohmically heated limiter discharges in small-scale tokamak TF-2, R=0.23 m, r=0.04 m , $B_{(r=0)}$=0.85T, I_{pl}=5-6 kA, n_e=2-3 10^{19} m^{-3} , T_{e0}=0.2-0.3 keV. The EML consist of a set of perturbation coils installed on the vacuum vessel. The perturbation current is resonant to the magnetic field near the q=3 surface at r/a=0.95. The characteristic Chiricov parameter (island width/island separation) is about. Changes in edge plasma parameters into outerboard and innerboard Scrape-Off-Layer (SOL) and inside Last Closed Field Surface (LCFS) were measured making use movable probe array that allows measure the edge plasma time-averaged parameters and fluctuations (with bandwidth 1<f<500 kHz) of density, floating potentials , electron temperature and particle transport. The poloidal phase velocity of the fluctuations has been obtained from the phase difference between I_{sat} signals measured in the same poloidal section and 2-4.5 mm apart.

With the EML relatively low temperature and high density of edge plasma was observed in shear layer whereas in SOL density is dropped by 30-50% (fig.1). Fluctuation level n_{rms}/n is reduced by 30% with the EML in SOL and shear region. Fluctuation-induced particle flux $F \sim <n\upsilon_\perp>$ is also reduced by 2 times in the SOL and growths in the shear region. In the SOL fluctuations propagate in the ion diamagnetic direction and inside LCFS (Last Closed Flux Surface) they propagate as a whole in the electron one (fig.2). The inversion of the poloidal velocity of the fluctuations is observed near LCFS (shear region) at r/a=0.95. The EML did not affected the location of the shear layer. Changes in k-ω spectra were detected with the EML in the region of destroyed magnetic surfaces (r/a~0.95-0.97).

In the outerboard SOL in floating phase (without EML) as a whole two different parts of the dispersion relation can be distinguished in the two point estimation of the conditional spectrum $S(k_\theta, \omega)$: (1) with frequency below ~30 kHz the fluctuations propagate in the ion drift direction, (denoted as "i"-mode); (2) turbulence of higher frequency (~100 kHz) propagates in the electron drift direction (denoted as "e"-mode). Like this bimodal structure was observed in different tokamaks and stellarator [7]. The EML resulted in no significant changes in "i"-modes in SOL.

In the shear region near LCFS the mentioned above multimodal structure is also observed without EML, with higher intensity of "e"-mode (fig.2). The EML leads to the enhancement of "e"-mode both into innerboard also outerboard and no significant changes in "i"-mode. The width of poloidal k-spectra in shear region (r/a~0.95) came to be narrower and w-spectra to be broader with EML. Both in float and the EML phase poloidal propagation velocity of the fluctuations reverses over a layer extended ~0.3 cm (fig.1d). Poloidal correlation length is about 4-5 mm without and with the EML (fig.3). Also into innerboard and outerboard without EML probability density function (PDF) of the density fluctuations departs from Gaussian PDF. It could be associated with nonlinear wave or mode coupling , or presence of coherent structure (fig.4). The EML leads to the PDF are nearly Gaussian in the shear layer. Quasi-coherent mode observed in the shear region without EML is destroyed by the EML (fig.5). In this region fractal dimensionality of the turbulence growths with EML as into outerboard also innerboard.

Inside the LCFS r/a<0.85 "e"-modes are mainly present with poloidal correlation length ~4 mm and ~20 mm. The oscillations have poloidal number m≤10 , they propagates in electron drift direction and its velocity the order of magnitude as local ExB drift velocity both into

outerboard also innerboard (where the curvature of toroidal magnetic field is unfavorable for driving of ballooning instability).

In conclusions, in edge of TF-2 the crucial processes in turbulence structure and driven transport in shear layer of boundary plasmas are detected with the EML. The EML effects on the formation of a layer in the shear region with higher plasma density and less correlative properties. The EML modifies the turbulence dispersion relation in this layer. Multimodal structure is observed both into outboard also innerboard of edge plasma.

References

[1]. V Vershkov e a.22nd EPS Conf Contr Fus PlasmaPhys, Bornemouth,IV19C,005(1995),

[2]. A.W. Morris et al. Phys. Rev. Letters 64, 1254 (1990).

[3]. Mc Cool S.C. at al Nucl Fus. 29 , 547, (1989)

[4]. Y.Shen et al. J. Nucl. Mat. 168 , 295-303, (1989)

[5]. TEXTOR team, ALT-I group. J.Nucl.Mat. 145-147,162 (1987).

[6]. Equipe TORE SUPRA, 12th EPS Conf Contr Fus PlasmaPhys,Nice, I,9(1989).

[7]. M.A. Pedrosa et al. 22nd EPS Conf Contr Fus PlasmaPhys,V19C,I,305(1995)
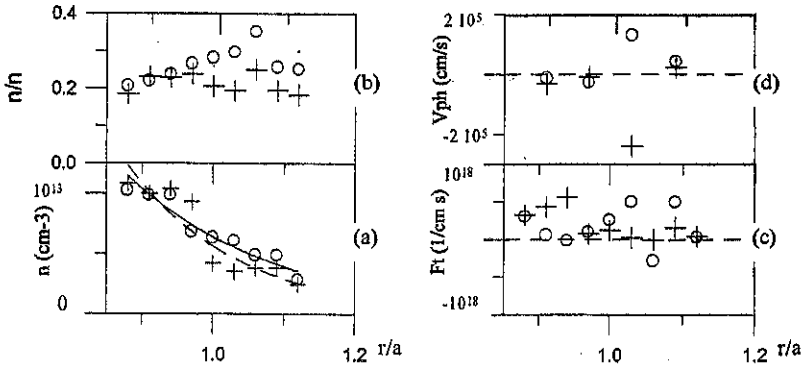
Fig. 1. Radial profiles of density $n(a)$, n_{rms}/n (b) turbulence induced flux $F=<n \, \upsilon_\perp>$ (c) and poloidal phase velocity of fluctuations (d) without (circles) and with the EML (crosses).Outerboard.
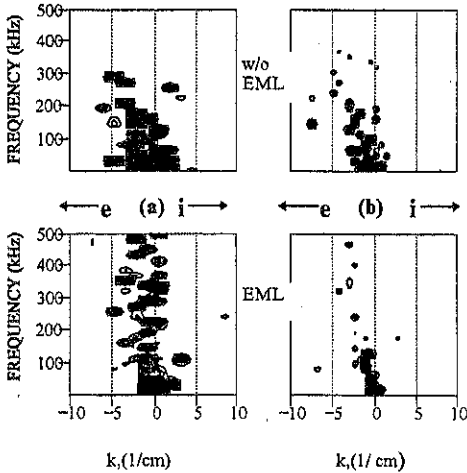
Fig. 2. Two-point estimate conditional spectrum $S(k_\theta\omega)$ at the innerboard (a) and outerboard (b) into shear region r/a=0.95 without and with the EML.
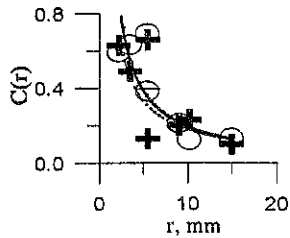
Fig. 3. Maximal cross-correlation coefficient Isat_Isat fluctuations vs. probe poloidal separation. In the shear layer r/a=0.95. Circles - without EML, crosses - with EML
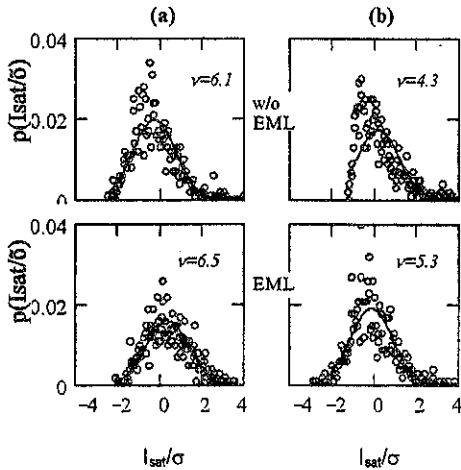
Fig. 4. Probability density function in the shear layer r/a=0.95. A Gaussian (solid lines) is plotted for reference. (a)- innerboard, (b) - outerboard without and with the EML. Fractal dimensionality ν growths with the EML.
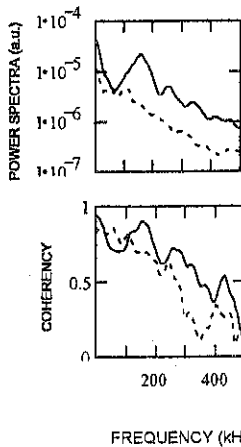
Fig.5. (a) I_{sat} spectra and (b) coherencies for I_{sat}-I_{sat} at r/a=0.95 outerboard. Solid lines - without, dashed - with th EML. The EML destroys quasi-coherent mode.

Study of dense and cold divertor with H-mode in the JFT-2M

H.Kawashima, S.Sengoku, T.Ogawa and H.Ogawa

Tokai Annex, Naka Fusion Research Establishment, JAERI, Ibaraki 319-11 Japan

1. Introduction

The coexistence of the good confinement (such as an H-mode) with high-density and low-temperature divertor becomes a significant issue in ITER[1] and fusion reactor. Remote radiative cooling by the neutral or impurity gas puff in the divertor chamber [2-4] is used for the dense and cold divertor. However, this coexistence was difficult with the open divertor because the neutral back flow from the divertor chamber increased the recycling in the main plasma which caused the degradation of the H factor or a termination of the H-mode[5,6].

The study of dense and cold divertor with H-mode has been carried out in the JFT-2M. The lower side of JFT-2M was modified the closed configuration in order to control the divertor plasmas independently with the core plasmas. This modification was proceeded in two stages, i.e. CD1 and CD2. CD1 is less closed configuration which baffling effect was not enough to achieve the purpose[7]. Therefore, the baffle structure was modified to the more closed configuration (CD2)[8]. This paper describes the experimental results on CD2, which are : 1)divertor characteristics related to the null point position (X_p), safety factor (q_s) and the electron density of main plasmas (n_e), 2)demonstration of the dense and cold divertor during H-mode by applying the gas puffing into divertor chamber, and 3)effect of the divertor gas puffing on the main plasma density. The divertor simulation by UEDA-code[9] is also presented for the divertor modeling. The dependence of closed divertor configuration on neutral gas pressure, electron density and temperature in the divertor chamber is shown to be qualitatively similar to the experimental results.

2. Closed divertor on JFT-2M

Figure 1 shows the schematic view of closed divertor in lower side of JFT-2M including both CD1 and CD2. The magnetic configuration of lower single null is used. The upper single null configuration is used for the open divertor (OD). Gas puffing is applied to each divertor chamber at lower or upper configuration, respectively. The advantage of closed divertor is to shield the back flow of the neutral particle from divertor chamber to main plasma region by the baffle plates. The divertor and baffle plates are made from the stainless steel. Some diagnostic systems are equipped for the divertor region. Thirty-two Langmuir probes are arrayed on the divertor and baffle plates
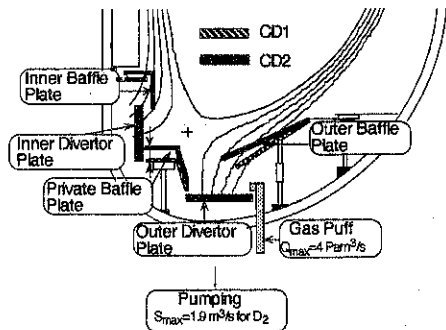
Fig. 1 Schematic view of closed divertor on JFT-2M

with high spatial resolution (5~20mm). The neutral gas pressure is measured by Penning gauges. The bolometer array and divertor spectroscope are viewing the outer divertor leg.

Plasma parameters at the experiments are : $R_0/a=1.3m/0.27m$, $\kappa=1.5$, $B_{T0}=1.3T$, $I_p=110$-250kA, $q_s=2.3$-4.4, $n_e^{ohmic}=1.5$-$3.5 \times 10^{19} m^{-3}$. The beam injection power (P_{NBI} ;H_0) is 0.4-0.8MW. Deutrium (D_2) is used as a working gas. Direction of the ion grad-B drift is toward the null point.

3. Experimental Results

The optimization of X_p, q_s and n_e is done so that heat and particle fluxes are concentrated into the divertor chamber. By a careful and rigid plasma control, the sharp distribution of ion saturation current (I_s) on the divertor plates is obtained and the neutral gas pressure in the divertor chamber becomes maximum. The peak saturation current is increased by making q_s small from 4.4 to 2.3. It is also enhanced with increasing n_e from 1.5 to $3.3 \times 10^{19} m^{-3}$ in the ohmic phase.

Under the optimum condition, the H-mode can be maintained for a long time and the remarkable dense and cold state in the divertor can be demonstrated by strong D_2 gas puffing into divertor chamber, even if the ohmic density is $2 \times 10^{19} m^{-3}$ which is lower limit of H-mode transition. Figure 2 shows the gas puff (Q_{div}) dependence of important parameters. The T_e^{div} decreases from 19 to 5 eV, n_e^{div} increases from 0.5 to 3×10^{19} m^{-3}, P_0^{div} also increases from 5 to 20mPa, and duration of H-mode (τ_H) is prolonged with increased Q_{div}. Though this tendency was also observed in the CD1 configuration, H-mode was returned to L-mode when Q_{div} is exceeded 3Pam^3/s[7]. At the open divertor, H-mode was shorten by

Fig.2 Parameter dependencies on gas puffing rate (Q_{div}) in H-mode.

n_e^{div} and T_e^{div} are peak values of electron density and temperature on the divertor plate. τ_H is H-mode duration time. n_e^{main}, P_0^{main} and P_{rad}^{main} are electron density, neutral gas pressure and radiation/CX loss power in the main plasma. P_0^{div} and P_{rad}^{div} are neutral gas pressure and radiation/CX loss power in the divertor chamber.

the gas puffing and the dense and cold divertor in H-mode could not be obtained.

The effect of divertor gas puffing on the main plasma density is investigated to elucidate the mechanism of H-mode prolonged by the gas puffing at CD2. This is carried out by the comparison between CD2 (lower single null discharge) and OD (upper single null discharge) with the L-mode plasmas which are relatively steady and bring the high heat and particle fluxes in the divertor. Figure 3(a) and 3(b) show the time dependence of important parameters for the cases of CD2 and OD. In the figures, the broken line shows the case without gas puff

case and the solid line shows the case with the gas puffing of 3Pam³/s. From Fig.3(a), there is a delay time of τ_d=47ms until density increment due to gas puffing is begun. Four different phases can be distinguished after gas puffing. It is considered that the time from t_0 to t_1 is a period until the gas reaches in the vacuum vessel since no parameter changes yet. From t_1, the fast gas comes out in the divertor chamber since D_α signal rises suddenly, and dense and cold state begins while n_e^{main} is not increased by gas puffing.

Fig.3 Density increment by gas puffing on (a):CD2 and (b):OD at L-mode discharges. I_x is soft x-ray intensity in the main plasma and D_α^{div} is deuterium α line intensity in the divertor chamber. Gas puff timing is shown in the bottom box.

From t_2, P_{rad}^{div} begins to increase, P_{rad}^{main} and I_{SX} begin to decrease. From t_3, n_e^{main} and P_0^{div} rise, and the dense and cold state is enhanced further as well as the case of H-mode. P_0^{main} does not change so much even if n_e^{main} and P_0^{div} increase. In contrast to this, for the open divertor of Fig.2(b), the density increment due to gas puffing begins earlier (which may come from a higher conductivity of the gas puff system used on the upper open divertor), P_0^{main} is increased by the gas puffing and the enhancement of dense and cold state in the divertor is less than that for CD2. These observations suggest that the less increase of P_0^{main} at CD2, while P_0^{div} increases drastically (well compressed), is solely due to baffle effect which can reduce the neutral back flow to the upstream. (Typically, gas compression ratios are ~90 for CD2 and ~5 for OD L-mode discharges.) This gas compression as well as dense and cold divertor and suppression in P_{rad}^{main} are considered to be responsible to prolong H-mode duration.

4. Divertor modeling by UEDA-code

UEDA-code, the two dimensional fluid code for divertor simulations coupled with Monte Carlo method for neutral gas behavior, is applied to JFT-2M closed divertor configurations both CD1 and CD2. Buildup of neutral particle, dense and cold divertor state are compared with their configurations. The simulation is modeled at the NBI heating plasma in which the

total loss power to SOL of 1MW and SOL density of $2 \times 10^{19} m^{-3}$ are assumed. For the particle diffusion coefficient (D) and the thermal diffusivity of electrons and ions ($\chi_{e,i}$), the following values are used : $D=2/3 m^2/s$, $\chi_e=2 m^2/s$ and $\chi_i=2/3 m^2/s$, which is based on the values obtained experimentally [10] and is consistent with the Bohm diffusion coefficient. Figure 4 shows the calculation result where the broken and solid lines correspond to cases of CD1 and CD2. The P_0^c is the value on the outer most SOL region, n_e^c and T_e^c are the peak values in the SOL. In front of the divertor plate, P_0^c, n_e^c and T_e^c of CD2 reach to 0.9Pa, $1.4 \times 10^{19} m^{-3}$ and 5.5eV which enhancement are larger than that of CD1. This result resembles qualitatively to the experimental observation. It can also represent that the enhancement of dense

Fig.4 Neutral pressure (P_0^c), density (n_e^c) and temperature (T_e^c) calculated by UEDA-code on poloidal direction from outer divertor plate to midplane.

and cold divertor is strong in more closed divertor configuration, CD2.

5. Conclusion

With the optimized plasma configuration at CD2, the dense and cold divertor with the prolonged H-mode can be demonstrated by a strong D_2 gas puffing into the divertor chamber. Such state has not been attained with OD or CD1 on JFT-2M. The prolongment of H-mode duration can be explained by the similar effects obtained with the gas puffing during L-mode discharges, which 1) radiation/CX loss power in main plasmas is suppressed by the gas puffing and 2)the neutral gas pressure of main plasma region is not increased. The calculation with UEDA-code shows the buildup of neutral particle, dense and cold divertor state on CD2 are enhanced stronger than that on CD1 as observed in the experiment.

References

[1] ITER Central Team, Plasma Phys. Controlled Fusion 35 Suppl. (12), B23 (1993).

[2] Shimada,M., et al., Nucl. Fusion 22 643 (1982).

[3] Itami, K., et al., 16th IAEA-CN-64/A-4-2 (1996).

[4] Gruber,O., et al., Phys. Lev. Lett. 74 4217 (1995).

[5] Sengoku.S.,et al., EPS 13B-Part III 959 (1989).

[6] Asakura,N., et al., submitted to Plasma Phys. Controlled Fusion.

[7] Sengoku,S., et al., Bull. Amer. Phys. Soc. 40 1675 (1995).

[8] Sengoku,S., et al., Bull. Amer. Phys. Soc. 41 1487 (1996).

[9] Ueda,N., et al., Nucl. Fusion 28 1183 (1988).

[10] Nagashima,K., et al., J.Nucl.Mater. 220-222 208 (1995).

Measurement of the plasma flow using the asymmetric double probe in the JFT-2M tokamak

M. Maeda, K. Uehara* and H. Amemiya**

Japan Science and Technology Corporation (JST), 4-1-8, Honmachi, Kawaguchi, Saitama,
*Tokai Annex, Naka Fusion Establishment, Japan Atomic Energy Research Institute (JAERI),
Tokai, Ibaraki,
**The Institute of Physical and Chemical Research (RIKEN), Wako, Saitama, Japan

1. Introduction

The ion temperature T_i and the plasma flow are important variables for the plasma transport in the boundary plasma in tokamaks[1-4]. The result of measurement of the boundary plasma of JFT-2M by an asymmetric double probe clarified that T_i exceeds the electron temperature T_e by a factor of about 10 [5-7]. In this method using the asymmetric double probe, the ion temperature can be evaluated from the ratio of ion saturation currents of two cylindrical electrodes with different lengths, when the axes are parallel to the magnetic field. Besides the ion temperature, the plasma flow for the edge plasma in tolamaks is also important. It has been indicated that the plasma flow of the edge plasma related to the occurrence of H mode [8]. However, only few experimental results on the edge plasma compared with the flow in the core plasma in tokamaks have been reported [9-12].

The objective of the present paper is to extend the above mentioned double probe method for the determination of not only T_i but also the plasma flow. This can be achieved by rotating of the probe and measuring the ion saturation current ratio C_R when the probe axes are oriented perpendicular to the magnetic field B and the longer pin is faced to up- or downstream of the flow. The method for obtaining the Mach number will be described below.

2. Experiment

The JFT-2M is medium size tokamak in JAERI. Figure 1 shows a schematic diagram of the cross section of the JFT-2M tokamak and the double probe measurement system. The asymmetrical double probe P is constructed by graphite cylindrical electrodes of 2 mm in radius, 6 and 14 mm in length.
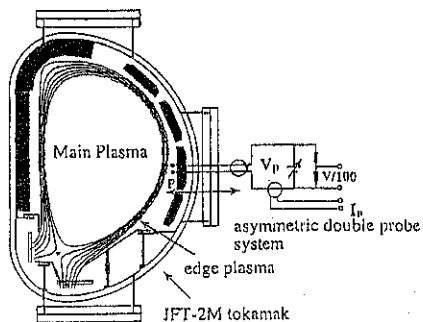
Figure 1. The cross section of the JFT-2M tokamak and the double probe measurement system.

Two cylinders are set parallel to each other. The experiment was performed in an ohmic plasma (H_2) where the toroidal magnetic field B_T on the axis was 1.3T, the discharge current was 220 kA, and the core plasma density was 2.4×10^{13} cm^{-3}. The ohmic heating (OH) was made and the flat top begun at $t = 300$ ms from the ignition and ended at about 780 ms. The double probe was located at about 2 cm in front of fixed limiter. The double probe was moved in the radial direction and rotated during the discharge with a frequency of 1-8Hz.

A triangle probe voltage V_p was given to the double probe with a frequency of 400Hz with an amplitude of 80 V. The probe current was measured by a current probe. The saturation current showed a minimum when the probe axes were oriented parallel to the magnetic filed B. The ion temperature could be determined from the ratio of ion currents to the electrodes.

3. Results and discussions

Figure 2 shows an example of the probe current I as a function of time T. Data are made smooth by averaging neighboring sample points to see the envelope of the saturated ion current more clearly. In this figure, (a), (b) and (c) indicate the spatial relation between the cross section of probe pins, the magnetic field B, and the flow vector u. The ion saturation current showed a minimum at (b) during the rotation as denoted by an arrow and this dip at (b) could be identified as the parallel alignment to B. The arrows at the (a), (c) indicate that the double probe was oriented perpendicular to B.

It was found that the current ratio C_R of the double probe pin was different at positions (a) and (c).This difference suggests the presence of a plasma flow because the one probe pin shields a part of the ion current to the other pin. In order to explain the result of this difference, some assumptions were made as follows.
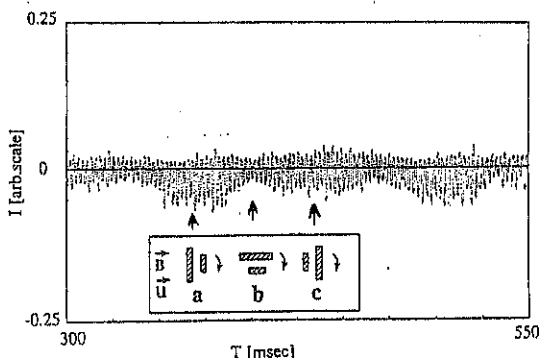
Figure 2. The probe current I as a function of Time T.

1) The effect of the plasma flow is parallel to the derection of magnetic field B.

2) The ion velocity distribution follows a drifting Maxwellian along B. When the plasma flow u exists, the velocity distribution f(v) is expressed to be

$$f(v) = (m_i / 2\pi\kappa T_i)^{1/2} \exp\{- m_i(v_z - u)^2/2\kappa T_i\} , \qquad (1)$$

where v_z is velocity, m_i: the ion mass, κ: the Boltzmann constant. The ion current to the surface of the cylindrical electrode oriented parallel to the magnetic filed B may be expressed as[4]

$$I_p = I_0 F(M) \; ; \; F(M) \equiv \{ \, (\exp(-M^2/2)) + (\pi/2)^{1/2} M(1 + \mathrm{erf}(M/2^{1/2})) \}, \quad (2)$$

where $I_0 = 2aLeN_e(\kappa Ti/2\pi m)^{1/2}$, a : probe radius, L : probe length, N_e : plasma density , M ($=u \cos\theta/C_s$) : Mach number, $\cos\theta = (M \cdot u)/Mu$. The ion acoustic velocity C_s is given by

$$C_s = (\kappa(T_i + T_e)/m_i)^{1/2}. \qquad (3)$$

3) When the cylindrical axes of the double probe are oriented perpendicular to B, only the projected area of the probe to B was taken into account for the current collection and the shadowed area between the probe pins does not collect current. This assumption is correct if the ion Larmor radius r_L is much smaller than the probe radius.

The value of M was estimated from the experimentally obtained current ratio C_R which is expressed by

case (a) : upstream

$$C_{Ra} = \{ S_1 F(M) + (S_1 - S_2)F(-M) \}/ S_2 F(-M), \qquad (4)$$

case (c) : downstream

$$C_{Rc} = \{ S_1 F(-M) + (S_1 - S_2)F(M) \}/ S_2 F(M), \qquad (5)$$

where $S_1 (=2aL_1)$, $S_2 (=2aL_2)$ are the projected probe areas, L_1 , L_2 : probe length ($L_1 > L_2$) . Eqs. (4) and (5) can be rewritten more concisely

$$C_R = S \, (1 + F(M)/ F(-M)) - 1, \qquad (6)$$

where $S = S_1/S_2$ and $+M$, $-M$ corresponds to the case when the longer pin faces up- and downstreams, respectively. The experimental result showed that it was more favorable and reliable to take M. T_i was estimated to be 100~120 eV and T_e was about 10 eV. The mach number is usually determined as a function of the electron temperature. However, due to $T_i \gg T_e$, we may say $C_s \cong (\kappa T_i/m_i)^{1/2}$.

Figure 3 shows the relation between C_R and M(>0) as described by eq. (6). M was determined and found to be 0.15~0.4 in OH plasma depending on the core plasma density. Here, it should be noted that the Mach number M determined above gives the lower limit value, because the ion currents that would be collected by the shadowed area of the cylindrical pins were neglected to be small.

If the double probe with two plainer electrodes are oriented to and against the flow, the expression of eq.(6) can be exactly applied to the current ratio to obtain a more accurate value of M. However, such a probe can measure only the plasma flow. On the other hand, the above probe technique has been able to make the simultaneous measurement of the ion temperature and plasma flow velocity.
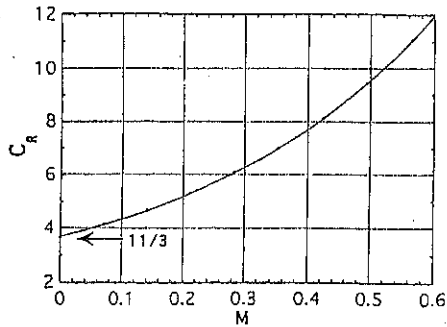
Figure 3. The relation between C_R and $M(>0)$ as described by eq. (6).

Acknowledgments

The authors would like to thank the members of the JFT-2M Group.

References

[1] P. C. Stangeby and G. M. McCracken , Nucl.Fusion 30, 1225 (1990).

[2] G. F. Matthews, Plasma Phys. Control. Fusion 36, 1595 (1994).

[3] K. Höthker, H.-J. Belitz, W. Bieger and H. Amemiya, Rev. Sci. Instrum. 61, 114 (1990).

[4] P. C. Stangeby and A.V. Chankin, Phys. Plasma 2, 707 (1995).

[5] K. Uehara, S. Sengoku and H. Amemiya, Jpn. J. Appl. Phys. 36, 2351 (1997).

[6] K. Uehara, A. Tsusima and H. Amemiya, Jpn. J. Phys. Soc. 66, 921 (1997).

[7] H. Amemiya and K. Uehara, Rev. Sci. Instrum. 65, 2607 (1994).

[8] K. H. Burrell et al., Phys. Fluids. B2, 1405 (1990).

[9] P. C. Stangeby, Phys. Fluids. 27, 2699 (1984).

[10] C. S. MacLatchy, C. Boucher, D. A. Poirier, and J. Gunn, Rev. Sci. Instrum. 63, 3923 (1992).

[11] B. M. Annaratone, T. Shoji, H. Maeda, S. Ohdachi, H. Tamai, Nucl. Fusion 34, 1453 (1994).

[12] K. Höthker, H.-J. Belitz, R. P. Schorn, W. Bieger, J. A. Boedo, Nucl. Fusion 34, 1461 (1994).

Optimized High Field Tokamak

Merezhkin V.G.

RRC "Kurchatov Institute", Institute of Nuclear Fusion, Moscow, Russia

A possibility to increase the β_N value up to 5 under ECH in the optimized high field and high-aspect-ratio device in the low-q regimes (q_a=2.2-2.5) is analyzed.

Introduction

The first T-6 and DIVA experiments have shown an essential effect of closed conducting shell on the macroscopic plasma stability in a tokamak in the low-q regimes, i.e. $1 \leq q_a \leq 3$. Scanning the plasma radius, $a = a_L$, T-6 experiments have found the relatively stable discharges with q_a = 1.2-1.3 and $1.5 < q_a < 3$ values, when the ratio of the conducting wall and plasma radii, a/a_w, was raised to O.8. With lower a/a_w ratio, ~ 0.6, the stable discharges in T-6 were found in the $q_a > 2$ region only. In DIVA experiments, no current disruption is observed in the low-q discharges with q_a ~ 1.7 and q_a ~ 1.3. These very-low-q regimes were found under strong sawtooth activity, but with a rather good energy confinement time (up to 20 ms between internal disruptions) at q_a=1.7 in a high plasma density case. At q_a=1.7 and mean plasma density nel ~10^{14}cm^{-3}, the averaged τ_E value reached 5.7 ms in a small-size plasma in DIVA tokamak (a=10cm, R=60cm).

Since 1978, the further study of plasma stability and confinement in low-q OH discharges was continues in T-11 tokamak (T-6 upgraded). Fig.1 shows the τ_E density dependence in a standard, q_a≈2.5, a_L=20cm, discharges in T-11, as well as, in q_a=1.65 and q_a=1.3 discharges running at increased a_L value to 21 - 22 cm (a/a_w = 0.85 - 0.9) [1]. Note, that the τ_E ~ q_a dependence, which was found first for the q=2.5 and q_a=4 regimes in T-11 at mean density of 1.5×10^{13} cm^{-3}, is in rough agreement with the data in the low-q regimes with q_a≈2.5, q_a≈1.65 and q_a=1.3 also, at low density. The conclusion is that the enhanced MHD stability, that gives the possibility to increase the plasma current and β_N values in the low-q regimes, should also essentially increase the plasma heat loss, as β_T / τ_E ~ $\beta_N I_p^2$, at constant B_o and n_e. Meanwhile, the τ_E rise with density can partially compensate this enhanced loss at increased β_N. If τ_E ~ n·q and n^{max} ~ β_T, the $(P_{loss})^{max}$ should rise as I_p ~1/q_a. In this case, and B_o=const., T =const.,

$$(n\tau_E)^{max} \propto \beta_T^2 \cdot q_a \propto \beta_N^2 / q_a. \qquad (1)$$

Note, that T-11 NBI experiments in the low-q regimes have reach the β_T^{max} value with β_N ~3, at q_a = 2.5 and β_N ~ 3.6 at q_a =1.8 [1]. The critical β_N in T-11 turn out to be higher than that

value, ~2.2-2.5, found in many tokamaks under NB-heating. This fact can be explained by the conducting wall stabilization effect [2] in T-11 case.

It is interesting to study experimentally the possibility for the essential rise of the β_N^{max} value in the quit q_a=2.2-2.5 low-q regimes first.

Fig. 1

The necessary plasma heating power in this regime could be markedly lower in a tokamak-device with a high plasma aspect ratio. Such possibility follows from the reduced electron transport ($\chi_e^{T-11} \sim \varepsilon^\alpha$, $\alpha \sim 1.5$-2), reduced plasma current and β_T in the high R/a range, 7-10.

To keep the low plasma collisionality, $\langle \nu^* \rangle < 1$ at $\beta_T \sim \beta_T^{cr}$, the high-aspect-ratio device should work with a rather high toroidal field of 6-8 T. Such results show the ν^* estimates, that follow from τ_{Ee} and τ_{Ei}^{neo} scaling-lows, as well as the modeling results at T-11 transport coefficients [3. Usually, the T-11 model fits the data found in improved confinement mode, as SS and VH-mode, and this model was used for testing the plasma confinement for a high field optimized tokamak (OT). Some parameters, R/a, B_o, nel, found as optimal for OT device are rather close to that found for the low-power D-T reactor concept - TEP tokamak [4]. A change of TEP characteristics in the $\beta_N \sim 5$ regime are also discussed in this paper.

Modeling results for OT and TEP tokamaks

The restricted parameters in OT-device are - the toroidal field strength, $B_o \leq 8$ T, a moderate plasma volume, $V_p \sim 2.5$ m^3, and moderate EC-heating power, $P_{ECH} \leq 4$ MW. The restriction for R/a ~ 8 in OT device was found from the condition $T_i /T_e \sim 1$ at $\langle \nu_i^* \rangle \sim 1$, which should be realized in the q_a=2.5, B_o=8 T case in OH regimes. The latter condition, which follows from τ_{Ee}^{T-11} and τ_{Ei}^{neo} scaling-lows and is typical for the moderate-size tokamaks, provides the possibility to keep low ions collisionality in the Ohmic-heated OT discharge as well.

Usually, the modeling results with T-11 transport coefficients give a higher averaged τ_E and β values and higher I_{boot} /I_p ratio for the EC-heated discharges relative to the NBI-heated one. That is because of the lack additional particles fuelling and the strong rise of the convective plasma loss, 5/2 $T_{ei}\Gamma_{ei}$, in the ECH case. In the central part of plasma in OT, the convective loss is negligible and ECH with peaked profile, $r_{ECH} \sim 0.2$ a, gives a rather high τ_E value, ~
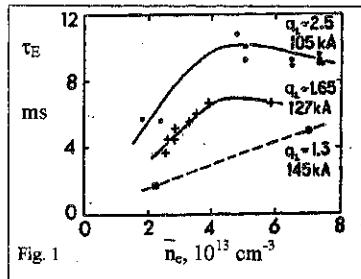
0.25 s, for the $\beta_N = 4.2$ regime at central electron temperature, T_{eo}, ~ 30 keV (Fig. 2a). The RS discharge scenario with $B_o = 8$ T, ECH-power of 3.5 MW and mean density ~2×10^{20} m^{-3} could have a maximal $n\tau_E T_e$ parameter in OT device. At lower field, $B_o = 6$ T, and at ECH power of 3 MW, the β_N and β_p can reach the maximal values ~ 5 in OT (Fig. 3b).
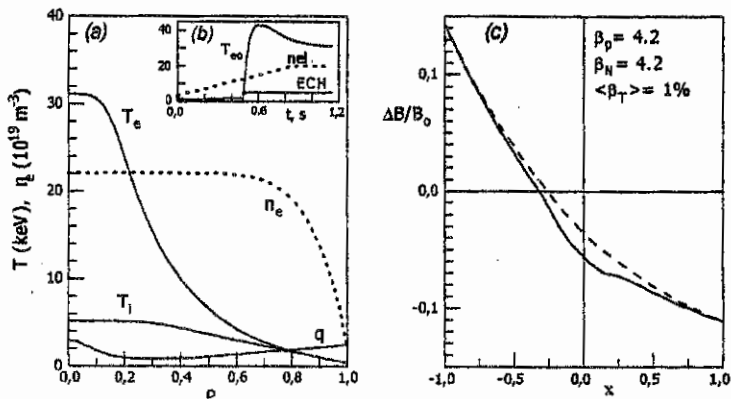
Fig. 2: (a), (b) – Modeling Te, Ti, ne and q-profiles in RS discharge with density rise during EC-heating in OT-tokamak ($B_o = 8$ T, $I_p = 0.5$ MA, $P_{ECH} = 3.5$ MW); (c) - Equilibrium toroidal field distribution in the torus medium plane: B (x), $x = (R-R_o)/a$. (R_o is plasma axis position.) Dashed line in (c) shows the B (x) associated with Shafranof shift of magnetic surfaces only.
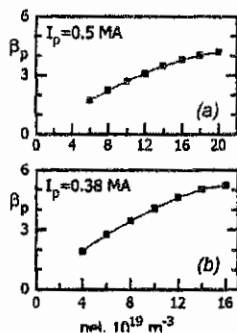
Fig. 3: Calculated β_p-values in OT at different field, density and EC-power, a) $B_o = 8T$, $P = 3.5MW$, b) $B_o = 6T$, $P = 3MW$.
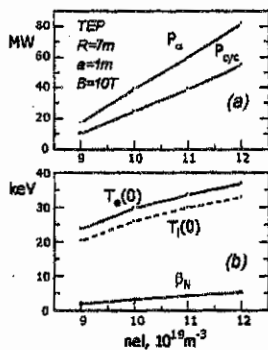
Fig. 4: Modeling P_α, P_{cyc} (a), the central T_e, T_i values and β_N (b) vs. mean plasma density in TEP

At $\tau_E \sim n$, we can rise of β and $n\tau_E T$ parameters in a tokamak by increasing the density at fixed ECH-power and it efficiency, as in OH regime. In ECH case, the restriction may come from the microwave cut-of at $W_{pe} > W_{oe}$. $W_{pe} \sim W_{be}$ condition gives the critical density as

high as 6×10^{20} m^{-3} in 8T regime, which is 3 times higher than transient density, 2×10^{20} m^{-3}, where the enhanced ion loss saturates the τ_E and β_p rise with density in OT (Fig. 3a). With peaked plasma pressure profiles at $\beta_N \sim 4.2$, the $B_T(x)$ profile in the plasma medium plane (Fig. 3c) is similar to that found in the modeling results for TFTR ERS-mode [5]. So, the OT experiments have a chance to test the neoclassical transport under significant change of $B_T \sim 1/R$ profile at r/a = 0.1-0.2 in the low $\beta_T \sim 1\%$ regime as well.

In 1991, The high aspect ratio, low current and low fusion power ($P_f \sim 100$-250 MW) reactor concept (tokamak for net electricity production -TEP) was analyzed first in [4]. It was shown that TEP tokamak should have $B_o \sim 10$ T, $I_p = 3$ MA, R=7-9 m. With optimized discharge scenario in the device with R~7 m, TEP could reach the ignition at $P_\alpha \sim 18$ MW, $P_{cyc} \sim 10$ MW, nel = 0.9×10^{20} m^{-3}, $\beta_p \sim 1.7$ and $\beta_N \sim 1.9$. Fig. 4 shows a significant change in the main TEP plasma characteristics when the β_N value is raised to ~ 5 by a little increase in the mean plasma density to 1.2×10^{20} m^{-3}. With the β_N increase from 1.9 to 5, the fusion power rises to ~ 400 MW and the neutron wall load rises to 1.2 MW/m^3. The bootstrap current fraction, I_{boot}/I_p, in TEP tokamak, as well as in OT, is found close to 1 at $\beta_N \sim 4$-5.

Conclusions:

The scaling-law $\tau_E \approx \tau_{Ee} \sim n \cdot q_a$, which describes, roughly, the data in the T-11 low-q ($q_a \sim 2.5$, 1.65, 1.3) and low density discharges, shows the possibility of $(n\tau_E)^{max}$ rise as β_N^2/q_a. The main mission of the proposed high-aspect-ratio tokamak-device is the experimental study of the β_N-limit and electron transport in the low-q ($q_a = 2.2$-2.5) regimes with the increased MHD plasma stability by conducting shell. In an optimized RS discharge scenario, the high field and high-aspect-ratio tokamak should reach the β_N value close to 5 at acceptable value of ECH power, ~3-4 MW.

References

[1] A. G. Barsukov, et al., proc. 11th EPS Conf., Aachen, Vol. 7D, Part 1, 35-37 (1983).

[2] A. Bondenson and D. J. Ward, Phys. Rev. Lett. 72, 2709 (1994).

[3] V. G. Merezhkin, V. S. Mukhovatov, A. R. Polevoj, Sov. J. Plasma Phys. 14, 63 (1988).

[4] B. B. Kadomtsev, V. G. Merezhkin, Comm. Plasma Phys. Contr. Fusion, 14, 99 (1991).

[5] V. G. Merezhkin, H. Shirai, IAEA Tech. Comm. Meeting on Advances in Computer Modeling of Fusion Plasmas, Los Angeles, 2-4 October 1996.

Ripple Losses of Fast Particles from Reversed Magnetic Shear Plasmas

K. Tobita, K. Hamamatsu, H. Harano [†], T. Nishitani,
K. Tani, Y. Kusama, T. Takizuka, S. Putvinski [‡]

Japan Atomic Energy Research Institute, Naka-machi, Naka-gun, Ibaraki, Japan
[†] University of Tokyo, Hongo, Bunkyo-ku, Tokyo, Japan
[‡] ITER JCT, La Jolla, San Diego, CA, U.S.A.

Abstract.
JT-60U experiments showed that reversed shear plasmas deplete a large fraction of MeV ions (fusion-produced tritons) compared with normal shear plasmas. The fraction of the particle depletion increases with ripple amplitude, indicating that ripple transport is responsible for the depletion. Computer simulations with an orbit following Monte Carlo code reasonably explain the experimental results. Using this code, α particle ripple loss is estimated for 12 MA ITER reversed shear plasmas. The estimated α particle ripple loss can reach 25% and then the resulting heat load on the first wall is as high as 3.7 MW/m^2 at the peak. Insertion of ferrite to the vacuum vessel reduces the peak heat load down to ~1 MW/m^2, satisfying the wall tolerance.

1. Introduction

Reversed magnetic shear research has come into the limelight in recent tokamak experiments, in that the plasma exhibits outstanding energy confinement and provides a bright prospect towards steady state tokamak operation with a large fraction of bootstrap current. However, low poloidal magnetic field and high q in the core can enhance ripple loss of fast ions, possibly causing a damage on the first wall. JT-60U reversed shear experiments actually showed an enhanced loss of fast tritons [1], and suggest that the enhanced loss of fast ions in reversed shear can be a real concern in a fusion reactor.

This paper consists of two parts. Section 2, experimental loss of fast tritons in JT-60U reversed shear plasma is presented. Section 3 describes computer simulations α particle ripple loss on ITER reversed shear operations.

2. Fast Triton Loss in JT-60U Reversed Shear Plasma

JT-60U is operated with deuterium gas, occasionally hydrogen. In such circumstances, a trace population of fusion-produced MeV ions has been utilized in several tokamaks to experimentally assess single particle behaviour of α particles in fusion plasmas. In our experiment, triton burnup measurement [2, 3, 4] was used for this purpose. The measurement is devoted to detecting 14 MeV neutrons which are produced by the subsequent reaction of DD-fusion-produced tritons, i.e. $t(d,n)^3He$. We expect a reduction in triton burnup when part of tritons are expelled from the plasma during their slowing down process.

Figure 1 shows time evolution of triton burnup in a reversed shear discharge. Here the triton burnup is measured with a scintillation fiber detector [6] covering the plasma core region ($r/a \leq 0.6$). As time evolves, the measured burnup increases. Yet, the yield is much

smaller than the burnup expected from a 1-D time-dependent calculation. Here, the calculation assumes classical slowing down of fast tritons at the location of their birth and no spatial diffusion. The difference between the measurement and the calculation is regarded as a loss of fast tritons from the plasma. The D-T reaction of tritiums recycled from the wall with the deuterium beam ions produces a background 14 MeV emission: as a result, the measured burnup happens to agree with the calculation early in time of NB injection. To determine the loss fraction of fast tritons, therefore, we should compare the both when 14 MeV neutron emission due to the D-T reaction of fast tritons with thermal deuterons builds up enough. In the case of Fig.1, about a half of fast tritons are expelled from the plasma.
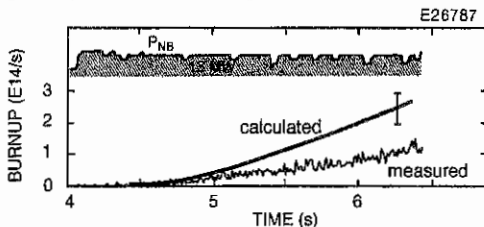
Figure 1
Time evolution of triton burnup in a 2.1 MA reversed shear discharge. A solid line is the burnup expected from a 1-D calculation assuming no fast triton losses.

By displacing the plasma position horizontally, the particle fraction of confined tritons was obtained as a function of TF ripple amplitude (Fig. 2). Here the TF ripple amplitude in the figure is averaged over the most-outer plasma surface. The fraction of confined tritons in particle decreases with ripple amplitude, both in normal and reversed shear plasmas, suggesting that ripple loss is responsible for the observed triton loss. What is the most important is that this fraction in reversed shear is lower than that in normal shear at any ripple amplitudes. We must note that triton burnup measurement determines the confined/lost fraction in particle number, which is less important than the fraction in power: the fraction of confined tritons in power is always larger than that in particle because a loss of slow tritons (~100 keV) contributes little to the power loss.

Computer simulations using the OFMC code [6] were done to help understanding the cause of the enhanced loss in the reversed shear. The code follows the guiding center orbits of test particles in rippled magnetic field and simulates Coulomb collisions (slowing down/pitch angle scattering) with Monte Carlo. When test particles drift near the wall, finite gyro-radius effects are taken into account. The result shown in Fig. 3 (a) almost matches the experimental data, indicating that ripple loss can explain the depletion of triton burnup. In fact, if TF ripple is ignored in the simulation, the loss is as low as 3%, too small to explain the experiment. The simulated result also indicates that the fractions confined in power are 88-95% in the normal shear and 53-72% in the reversed shear, respectively (Fig. 3 (b)): these values are never lower than the initial fraction of passing particles (60-70%). The reasons why the reversed shear plasmas exhibit such poor confinement for fast tritons are low poloidal magnetic field and high q in the core. Low poloidal magnetic field expands the banana width of fast ions, raising radial step sizes on fast ion transport processes,

Furthermore, at high q, fast ion orbits are affected by TF ripple more severely, so that the ripple transport of them is enhanced.
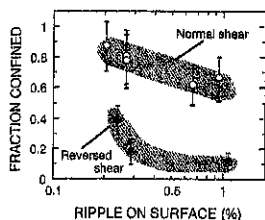
Figure 2 Experimental fraction of confined tritons.
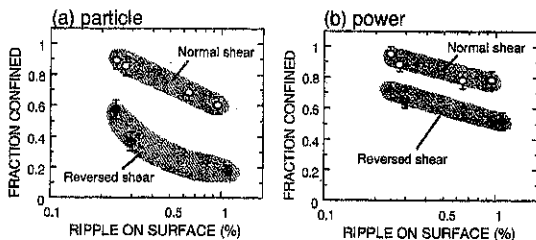
Figure 3 Simulated fraction of confined tritons: (a) in particle, and (b) in power.

3. Alpha Particle Loss in ITER Reversed Shear Plasma

With the OFMC code, α particle ripple loss in ITER reversed shear plasma and the resultant heat load on the first wall were evaluated.

The plasma conditions used in the calculations are basically the same as those used in the previous estimation [7]. The considered plasma has the plasma current I_p of 12 MA, a uniform electron density n_e of 10^{20} m^{-3}, a uniform effective ionic charge Z_{eff} of 1.5 (carbon impurity assumed) and electron and ion temperatures (T_e and T_i) with a trapezoid-like profile used in Ref. 7. Alpha particles are assumed to be created by the thermal D-T reaction only, so that the birth profile is implicitly determined by profiles of n_e, T_i and Z_{eff}. Profiles of q are assumed to be $q(0) = 5.7$ and $q_{min} = 3.2$ at $r/a = 0.7$ in a reversed shear plasma, and in a normal shear plasma $q(0) = 0.95$ and $q = 2.0$ at $r/a = 0.68$. The ripple at the outer plasma edge is about 1.0%.

Table I Ripple loss of α particles for ITER equilibria

	Normal shear	Reversed shear
Upward ion ∇B	6.3%	25.1%
Downward ion ∇B	6.2%	25.0%

Table I is the calculated ripple loss (power loss) in the normal and reversed shear plasmas. The loss is almost independent of the ion drift direction, and a significant α power loss is anticipated in the reversed shear operation. The previous assessment using a different code gives a 16.4-19.4% loss in a similar ITER equilibrium, comparable with our result. The other findings from our simulations are: 1) ripple loss is not sensitive to the Shafranov shift, in that ripple loss increases from 23% to 25% when β_p varies from 1.0 to 2.4, ; and 2) q profile is a key parameter of determining ripple loss because α ripple loss rises from 21% to 27% when $q(0)$ is changed from 4 to 11 without changing q_{min}.

Such a significant α loss gives rise to a concern whether the resulting heat deposition on the first wall will exceed an allowable heat load. Figure 4 shows the pattern of the heat deposition on the wall. When the ion ∇B direction points upward, escaping α particles concentrate on the upper outboard, producing a hot spot. Presumed $P_\alpha = 250$ MW, the peak heat load is expected to be 2.0 MW/m². When the ∇B direction points downward, lost α particles produce a smaller hot spot on the outboard near the midplane, raising the peak heat flux up to 3.7 MW/m². These heat fluxes are marginal in the light of tolerance.

To reduce ripple loss, insertion of ferro-magnetic material to the vacuum vessel is under consideration to lessen the ripple amplitude. According to our simulations, α ripple loss will be reduced down to 10% in the reversed shear and the peak heat load will be tolerably low (~1 MW/m²) by a 60% ripple reduction with the ferrite insertion.
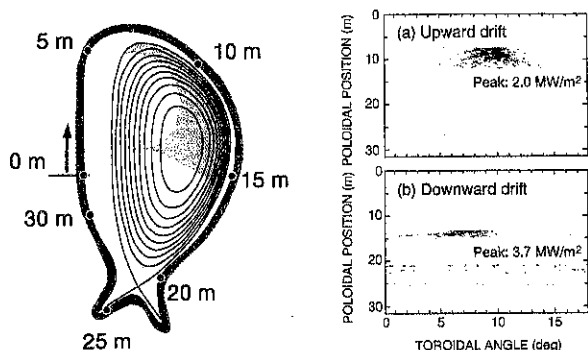
Figure 4 Calculated heat load due to ripple loss on the first wall due to ripple loss in an ITER reversed shear discharge: (a) upward ion ∇B drift, and (b) downward drift. Also shown is the poloidal cross section of the ITER plasma with the ripple well shaded.

Acknowledgments

References

[1] K. Tobita et al., in Fusion Energy Conference 1996 (to be published in Proc. 15th Int. Conf. Montréal, 1996), IAEA, Vienna.

[2] P. Colestock et al., Phys. Rev. Lett. **43** (1979) 768.

[3] C.W. Barnes, et al., in Controlled Fusion and Plasma Heating (Proc. 15th Eur. Conf. Dubrovnik, 1988) Vol. 12B, Part I, European Physical Society, Geneva (1988) 87.

[4] J.D. Strachan, et al., in Plasma Physics and Controlled Nuclear Fusion Research 1990 (Proc. 13th Int. Conf. Washington D.C., 1990), Vol. 1, IAEA, Vienna (1991) 257.

[5] G.A. Wurden et al., Rev. Sci. Instrum. **66** (1995) 901.

[6] K. Tani et al., J. Phys. Soc. Jpn. **50** (1981) 1726.

[7] Technical basis for the ITER detail design report, cost review and safety analysis (DDR), ITER (1996).

Particle Behavior after Vacuum Pumping and Gas-Feeding Termination during the Long LHCD Discharge in TRIAM-1M

M.Sakamoto, K.Kamiya, T.Yamagajo, E.Jotaki, K.Makino, K.Nakamura and S.Itoh

Advanced Fusion Research Center
Research Institute for Applied Mechanics, Kyushu University 87,
Kasuga, Fukuoka 816, Japan

Introduction

Understanding of particle behavior during the long duration discharge is one of the important issues for the fusion plasma research.[1] In TRIAM-1M, the ultra-long discharges have been demonstrated using lower hybrid current drive (LHCD) systems.[2,3] Two kinds of experiments have been performed in TRIAM-1M to study the particle behavior during the long 2.45 GHz LHCD discharge. In one experiment, vacuum pumping was stopped during the discharge by closing a gate valve to a pump unit. In the other experiment, both vacuum pumping and gas-feed were stopped during the discharge. In this paper, the particle behavior in the above two kinds of experiments is discussed.

Experiment of vacuum pumping termination

Figure 1 shows time evolution of the 2.45 GHz LHCD discharge in which the gate valve to the pump unit was closed at $t \sim 32$ s and the RF power was switched off on purpose at $t \sim 4$ min. The gas-feed controller was made working continuously after closing the gate valve. It controlled the applied voltage (Fig.1(d)) to the piezo valve so as to keep the Hα line intensity constant. No change can be seen in the plasma current and density at the timing of closing the gate valve.

The time evolution of the gas-feed rate through the piezo valve is shown in Fig.2. It should be noticed that the hydrogen gas continued to be supplied till the end of the discharge (t ~ 4 min). The averaged gas-feed rate and total number of hydrogen atoms supplied after closing the gate valve were about 4×10^{17} atoms/s and about 1×10^{20} atoms, respectively. The gas-feed rate after closing the gate valve is equivalent to the pumping rate by the wall because the plasma density was constant, and the neutral gas pressure inside the vacuum vessel increased from 1.4×10^{-4} Pa to 2.9×10^{-4} Pa just after closing the gate valve and stayed constant afterwards. It is found that the gas-feed rate (i.e. wall pumping rate) decreases with time. It is considered to be consistent with the result that the recycling ratio increases with time.[3]

Experiment of vacuum pumping and gas-feeding termination

Figure 3 shows time evolution of the 2.45 GHz LHCD discharge in which the gas-feed was stopped just after closing the gate valve to the pump unit at $t \sim 33$ s and the RF power was switched off on purpose at $t \sim 73$ s. The line-averaged electron density decreased from 1.5 ×

10^{18} m^{-3} to 1.0×10^{18} m^{-3} during 6 s after stopping the gas-feed and afterwards it became constant. The plasma current also decreased from 24 kA to 18 kA due to the density decrease. In the period that the density was constant without gas supply, the recycling ratio is considered to be one from the point of view of the particle balance. The wall did not pump in that period. The difference in the total number of hydrogen particles in the plasma was about 10^{17}. This is much less than the total number of hydrogen atoms which the wall pumped after closing the gate valve in the previous experiment of vacuum pumping termination. Therefore, it can not be concluded that the wall was saturated due to the density decrease.

Moreover, additional gas-puff was carried out four times (t ~ 50, 54.5, 61, 68 s) as shown in Fig.3(f) to investigate the particle balance between the plasma and the wall which was made of stainless steel. The electron density increased just after the gas-puff but it decreased to the former level within ~2 s. The neutral gas pressure inside the vacuum vessel also increased just after the gas-puff but it decreased to the former level within ~5 s as shown in Fig.4. This means that the particles supplied by the gas-puff were deposited in the wall. The particle flux from the plasma just after the gas-puff is considered to increase due to the density rise. This is supported by the experimental result that the particle confinement time measured in steady-state discharge has almost the same value in this density region.

The property of particle deposition in the wall seems to be quite different in plasmas with and without the gas-feed after closing the gate valve. The particle flux is considered to be one of causes of the different properties.

Conclusion

Two kinds of experiments were performed to investigate the particle behavior during the long LHCD discharge. Even after closing the gate valve to the pump unit, the hydrogen gas continued to be supplied to maintain the plasma density at constant level till the end of the discharge (t ~ 4 min). The supplied gas after closing the gate valve must be pumped by the wall and the averaged wall pumping rate was estimated to be about 4×10^{17} atoms/s. When the gas-feed was stopped just after closing the gate valve, the electron density and the plasma current decreased and afterwards they became again constant. In that period, the recycling ratio was one from the point of view of the particle balance. It became obvious that the recycling property was quite different in plasmas with and without the gas-feed after closing the gate valve.

Acknowledgement

References

[1] P.K.Mioduszewski et al., J. Nucl. Mater. **220-222**, 91 (1995)

[2] S.Itoh et al., Plasma Phys. and Contr. Nucl. Fus. Res. 1990 (Proc. 13th Int. Conf., Washington, D.C., 1990) Vol.1, IAEA, Vienna, 733 (1991)

[3] S.Itoh et al., 16th IAEA Fusion Energy Conference, Montréal, IAEA-CN-64/EP-6 (1996)
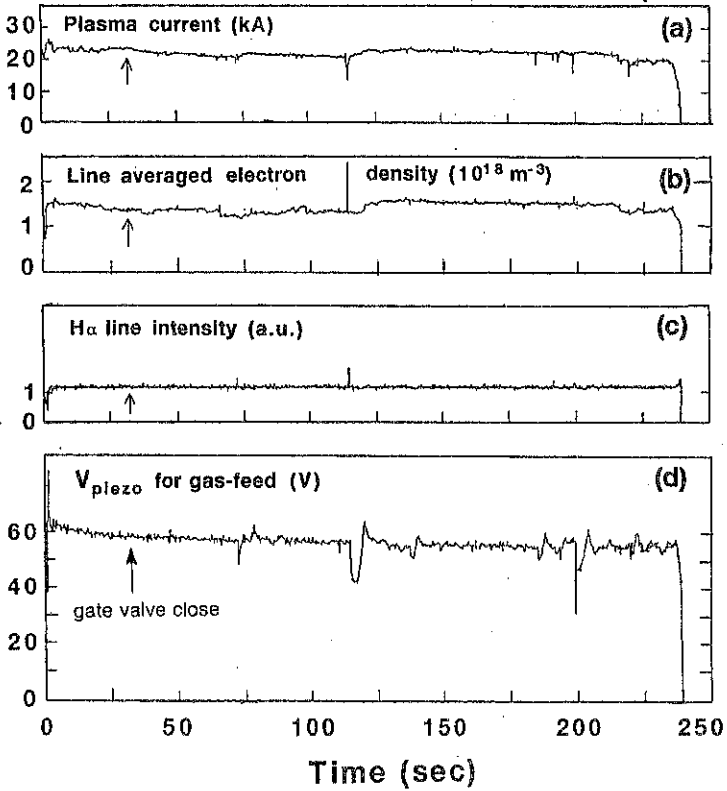
Fig. 1 Time evolution of 2.45 GHz LHCD discharge (RF power ~18kW). The gate valve to the pump unit was closed at $t \sim 32$ s.
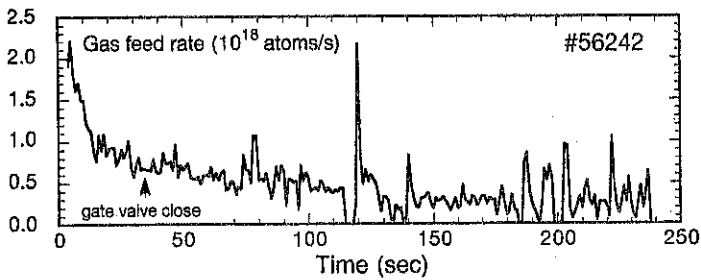
Fig. 2 Time evolution of the gas-feed rate.
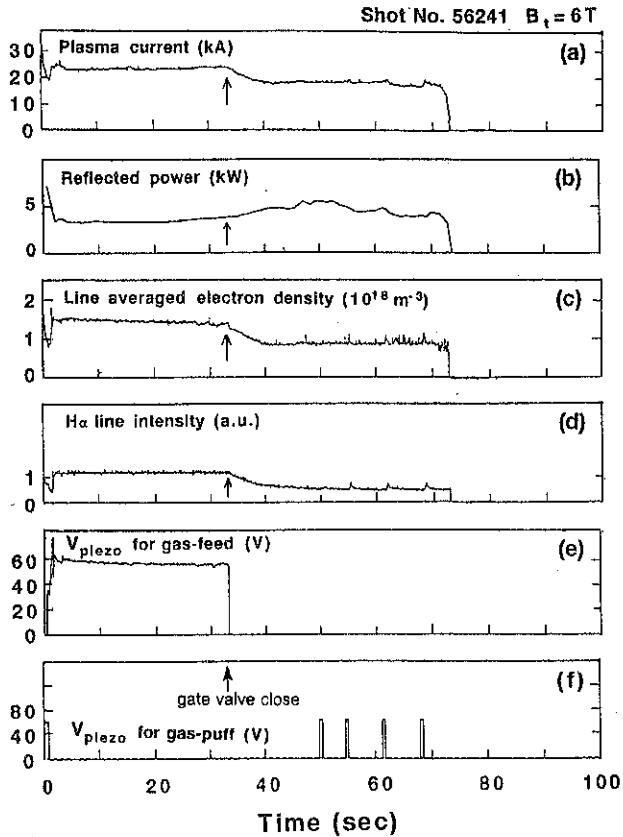
Fig. 3 Time evolution of 2.45 GHz LHCD discharge (RF power ~18kW). The gas-feed was stopped just after closing the gate valve to the pump unit at t ~ 33 s.
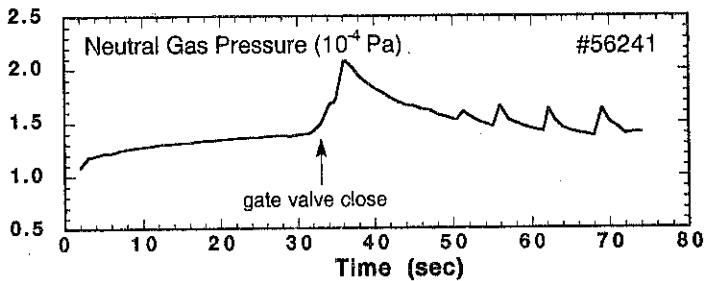
Fig. 4 Time evolution of the neutral gas pressure inside the vacuum vessel.

Full AC Tokamak Discharge in A Small Research Device CSTN-AC

S. Takamura, K. Hayashi, Y. Marushita, K. Tashiro, Y. Uesugi*, N. Ohno, K. Sakurai**,
M. Kobayashi, M. Takagi, O. Mitarai***

Department of Energy Engineering and Science, Graduate School of Engineering
* Center for Integrated Research in Science and Engineering
Nagoya University, Nagoya 464-01, Japan
**General Education, Literature, Aichi Prefectural University, Nagoya 467, Japan
***Department of Electrical Engineering, Kyushu Tokai University, Kumamoto 862, Japan

Introduction

A long pulse tokamak discharge is one of our concerns in recent fusion studies. Particle and heat control at the tokamak edge is quite important in this point of view as well as quasi-steady state sustainment of good core plasma confinement. A continuous alternating current (AC) tokamak discharge or a high duty high repetition tokamak discharge gives a chance to study a hydrogen particle balance, in terms of fueling, core confinement, retention in the wall and pumping in a similar way as in the steady-state discharges. In addition, we have some important possibilities to investigate phenomena of basic tokamak physics, for example, behavior of plasma current penetration during the current reversal phase by using such an AC tokamak.

In this context, a full AC operation of tokamak discharge is quite attractive. There have been some studies about AC operation, for example, the experiments in the STOR-1M and the STOR-M tokamaks [1,2] and a single cycle AC operation with a reactor relevant current(±2MA) demonstrated in JET [3]. AC operation with multi-cycles but for not long duration has been studied recently in CT-6B [4]. In these studies, there have been no reports on the experiments on the full AC operation for a long duration more than the PSI-related hydrogen recycling characteristic times.
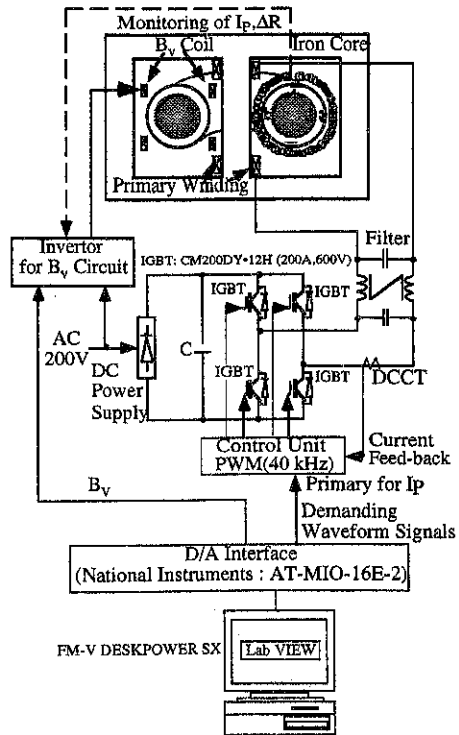
Fig.1 Invertor power supply system for Joule primary circuit and vertical magnetic field.

A full AC tokamak operation with a plasma current of $\pm 600A$ and a frequency of 60-100Hz was achieved for **one minute** in the small tokamak device CSTN-AC by employing a new invertor power supply system for ohmic and vertical field circuits under steady-state toroidal magnetic field of about 0.1T [5]. More than 1kA discharge with full AC operation could be possible if the heat load would be removed from the wall of toroidal vacuum vessel.

CSTN-AC Tokamak

The vacuum chamber of CSTN-AC tokamak has a major radius of 40cm, and a minor radius of 10.3cm. It is the same as that of CSTN series [6]. With a piezoelectric valve, the neutral gas flow rate is kept constant around 5×10^{-2} Toll $\cdot 1/s$. The steady state toroidal magnetic field is up to 0.12T. Typical hydrogen discharge parameters are as follows: B_t (toroidal magnetic field) $\sim$ 0.1T, I_p (plasma current) $\lesssim$ 1kA, V_L (loop voltage) $\lesssim$ 10V, n_e (electron density at the center of the chamber) $\lesssim$ 1.5 x $10^{18}m^{-3}$, and T_e (central electron temperature) $\lesssim$ 15eV.

To achieve AC operation, we employed an invertor power supply system for the Joule primary circuit and the vertical magnetic field coils, as shown in Fig.1. This system consists of two invertor power supplies which are controllable independently. IGBT(Insulated Gate Bipolar Transistor)'s are used for switching devices, and PWM(Pulse Width Modulation) feedback control operated at 40kHz is employed there. The outstanding feature of the power supply system is to have a feedback function so that the output current waveform may be almost similar to that of the input current signal given by an arbitrary waveform generator. Thus, it is possible to control the plasma displacement by adjusting the vertical field. In the case of continuous AC operation with the duty factor of 100%, a high heat load on the vacuum vessel due to the long AC operation should be handled. For this, a pair of water cooled limiters are installed.

Fig.2 Temporal evolutions for discharge and plasma parameters in AC tokamak operation. B_t= 0.091 T. Initial hydrogen gas pressure is 1.2×10^{-4} Torr.

Experiments

AC discharge at a period of 16.7ms with two cycles every second is performed as shown in Fig.2, where the discharge and plasma parameters are traced using a triple probe located at the

center of vacuum chamber without any thermal damage on the probe because of a small duty of 3% here. After a first cycle we obtain a stable AC tokamak discharge owing to preionization effect of the previous half cycle of discharge. A careful adjustment of vertical field waveform and compensation of error field coming from B_t coil current imperfection with external horizontal field makes such a stable discharge. At the current reversal phase the plasma current seems to change very smoothly across the zero with almost no dwell time. Detailed traces of characteristic parameters at these phases are shown in Fig.3 where the plasma density was found to become minimum at 0.2-0.3ms after the time of $I_p=0$ although the electron temperature quickly drops just after $I_p=0$. We note that the minimum plasma density is still substantial, $\sim 1 \times 10^{17} m^{-3}$.

A stable full AC tokamak discharge with 60Hz is successfully obtained with almost the same conditions as those in Figs.2 and 3. Figure 4 gives the initial one fifth of the whole discharge length of 60 seconds. The duration is limited by the temperature increase on the wall of vacuum vessel as shown in Fig.5 because we do not have any cooling system for the wall. In this case the primary input power of 3.3kW on the average is dissipated as follows: Hysteresys dissipation of the iron core is 0.3kW, and the power to the limiter is only 0.23kW estimated with calorimetric way. The power to the wall through the radiation or the plasma heat flow amounts to 2.4kW obtained by the increase in the wall temperature, and the unidentified part is 0.37kW.

We found completely different traces for gas pressure depending on the wall conditioning before starting full AC operation although they do not give any effects on the
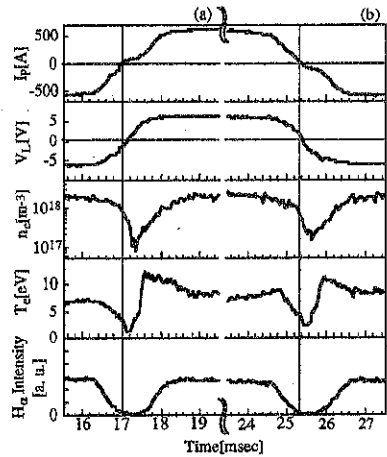
Fig.3 Detailed traces of characteristic parameters at the current reversal phases.
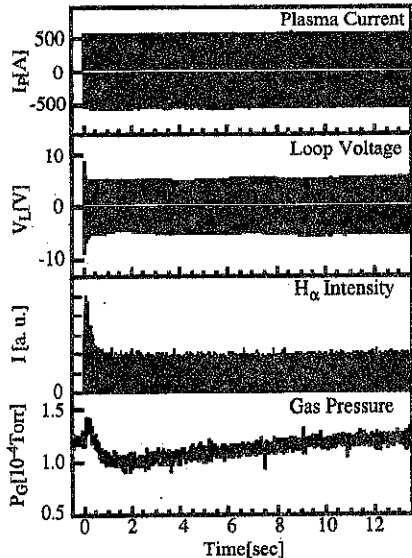
Fig.4 Traces of plasma current, loop voltage, H_α intensity and gas pressure for the initial one fifth of the whole one minute discharge.

macroscopic discharge and plasma parameters at least well after the initiation of the discharge. In the discharge shown in Fig.4, the surface of vacuum chamber was exposed to hydrogen gas for one minute between the start of full AC tokamak discharge and the termination of conditioning AC discharge with 20 cycles every second during ten minutes. First pressure increase seems to come from desorption of large amount of hydrogen molecules on the wall surface. On the other hand, the very short gas exposure time of about 4 seconds gives the trace of gas pressure shown in Fig.5, indicating a strong decrease of hydrogen gas

Fig.5 Trace of gas pressure for the whole discharge duration with a different wall conditioning from the discharge shown in Fig.4. Increase in temperature of the wall surface usually observed in these long discharges is also shown.

pressure at the initial phase of full AC operation, which comes from the effect of wall pumping.

Summary

By employing a new invertor power supply system, we achieved full AC tokamak operation with one minute in CSTN-AC device. The plasma current with a few milliseconds flat top is $\pm$ 600A, with $V_L \sim \pm 6V$, and the plasma parameters: $n_e \sim 1 \times 10^{18}m^{-3}$, $T_e \sim 10eV$. Quite different histories of gas pressure have been observed, depending on the quantity of adsorbed hydrogen on the wall surface. It will make possible fundamental studies on hydrogen recycling in the discharge longer than the surface-related characteristic time which is difficult to be covered by the current big tokamaks.

Acknowledgment

References

[1] O. Mitarai et al., Nucl. Fusion 27(1987)604.

[2] O. Mitarai et al., Nucl. Fusion 36(1996)1335.

[3] B.J.D. Tubbing et al., Nucl. Fusion 32(1992)967.

[4] X. Yang et al., Nucl. Fusion 36(1996)1669.

[5] K. Hayashi et al., Proc. ICPP96, Nagoya 2(1996)1246.

[6] K. Ushigusa et al., Rev. Sci. Instrum. 54(1983)1624.

POLOIDAL ROTATION STUDIES IN THE TJ-I U TORSATRON

B. Zurro, K.J. McCarthy, C. Burgos, A. Baciero, E. Ascasibar, T. Estrada
and E. de la Luna. Asociación **EURATOM/CIEMAT** para Fusión, Avd. Complutense 22, E-28040 Madrid, Spain

Introduction. The main motivation in obtaining poloidal rotation measurements in present fusion devices is to obtain information about the radial electric field. Neoclassical theory suggests that in stellarators the electric field reduces helical ripple loss, consequently improving plasma confinement. Poloidal rotation measurements have been reported in ECR heated plasmas in stellarator devices, but because these were made using passive emission spectroscopy of ions emitting in the visible, most of the results obtained are from the plasma periphery. For example, in the Heliotron-E device, the radial electric field at $r \approx 0.7\text{-}0.9 <a>$ was found to be positive (the electron root) in low density plasmas ($n_e < 1 \times 10^{13}$ cm^{-3}) and negative (the ion root) in high density plasmas ($n_e > 2 \times 10^{13}$ cm^{-3}) [1]. In electron cyclotron heated (ECH) plasmas ($n_e \approx 5 \times 10^{13}$ cm^{-3}) in the Weldelstein VII-A stellarator, the negative electric field observed was consistent with theoretical predictions [2]. In the Advanced Toroidal Facility, a positive electric field was observed in ECH low density plasmas ($n_e \approx 5 \times 10^{12}$ cm^{-3}), in this case measured by the heavy-ion beam probe method [3].

Here, we report measurements of poloidal rotation of impurity ions in the TJ-I U torsatron, and from these we estimate the sign and magnitude of radial electric field. In addition, we describe the experimental set up used and we discuss the results obtained in the context of other stellarator results.

Experimental. The TJ-I U is a torsatron device with a pole number $l = 1$, a toroidal period number $m = 6$, and an aspect ratio of 6. It has major radius $R = 60$ cm and an averaged minor radius $<a> = 10$ cm. The plasma is created and heated using 200 kW of ECR power (37.5 GHz) tuned to the second electron cyclotron harmonic. The discharge electron density is tailored by programming three piezoelectric gas valves. Hydrogen is used as the standard gas. A more detailed description of the machine is given in Ref. [4].

We have investigated the plasma poloidal rotation using measurements of the line shift of selected impurity lines (C V 2271 Å and O V 2781 Å) made using a shot to shot technique with high spatial resolution. A sequence of shots with good reproducible shots were used. The lineshapes were recorded using a 1 m monochromator having an intensified detector with 700 active pixels mounted at the focal plane. The input slit is rotated by 90° when is imaged into the

plasma to maximise the spatial resolution, the pivotal point of the optical scanning system is located on the plasma equatorial plane. From this position, the entire plasma cross-section can be observed through a large laterally positioned rectangular quartz window (70 x 240 mm^2). Because of the low density of TJ-I U plasmas, and in order to achieve significant statistics, it is necessary to integrate the detected spectral emission along the entire discharge plateau (10 - 15 ms). In addition, a correction is needed to compensate any thermal spectrometer drift during the sequence of 10 - 15 discharges needed to obtain a profile.

Results and discussion. Typical chord-averaged poloidal rotation profiles, for two line-averaged electron densities, are shown in Fig. 1, together with the corresponding chord-averaged line intensity for the higher density case. The radius (r_p) used in the plotting is measured along a vertical chord passing through the magnetic axis. Several features can be highlighted from the data obtained: 1) the bulk plasma ions rotate in the ion diamagnetic direction (chosen to be positive); 2) a sheared rotation is evident from the figure; 3) the peak rotation is higher in the lower density case and 4) the deep observed about 2 cm might be caused by the pressure gradient term which changes sign around that position. We have observed that discharges starting with a significant level of runaway electrons can behave differently of the general trend we try to present here.
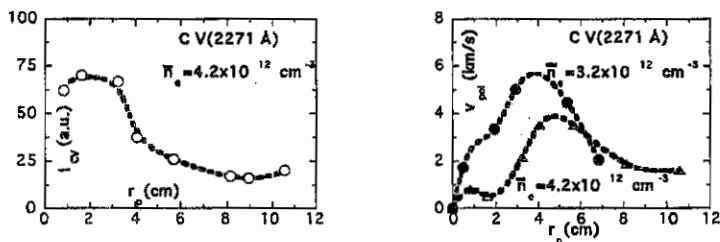
Fig. 1. Symmetrized profiles of line integrated emission (left) and poloidal rotation (right) for C V.

The poloidal rotation seen implies positive radial electric field values of between 25 and 40 V/cm for the maximum rotation chords in fig. 1. At lower densities E_r can reach values of about 60-70 V/cm. Because of the higher line intensities and better plasma sequences obtained when performing O V emission measurements at 2781 Å we have been able to separate, for some discharges, the upper and lower scan profiles. These results are shown in fig. 2 for two different densities. In the figures up/down poloidal rotation asymmetries can be discerned. The most obvious interpretation for this is that these effects are caused by asymmetries in the radial electric field. The impurity emission asymmetry (not shown) does not seem to be enough asymmetric to explain this behaviour. As yet, we have not been able to identifying the underlying operational cause for this interesting observation.
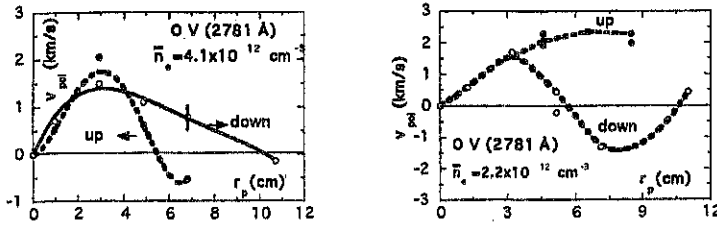
Fig. 2. *Chord averaged poloidal rotation (right) for O V at two densities. Up/down rotation asymmetries are evident in the raw data.*

In fig. 3, we show O V (2781 Å) and C V (2271 Å) chord-averaged data, for a range of plasma densities, taken along a fixed chord close to maximum rotation. The line-averaged density in this plot was that at 20 ms. Using this data for our study of poloidal rotation behaviour as a function of plasma density, we typically find that the velocity ranges from 6 to 10×10^5 cm/s, when the density is between 2 and 3×10^{12} cm^{-3}, to about 10^5 cm/s when densities are highest and close to ECRH cut-off. These results are consistent with those obtained in the Heliotron device for chords with effective radius ≈ 0.75. In both cases, the plasma is found to rotate in the ion diamagnetic direction at low densities. However, in the TJ-I U we do not reach densities that are high enough to clearly observe the change in direction to the electron diamagnetic direction, as seen in the Heliotron device. However, in some cases some of peripheral O V data obtained does exhibit rotation in the electron diamagnetic direction, see Fig. 2, and also some C V data at the lowest density.
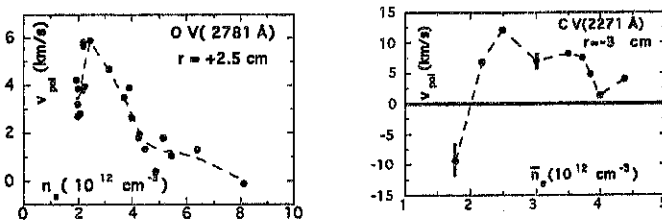
Fig. 3. *Chord-averaged poloidal rotation as a function of electron density, O V left and C V right.*

Finally, we should point out that the raw data values of poloidal rotation measured using O V data are generally lower than those obtained using C V data. The principal reasons for this are that the O V emissions are more weighted towards the plasma periphery and towards earlier

times along the discharge while the C V emission emerge later in the discharge. This point is being investigated in more detail.

We show in fig. 4 the detailed analysis of the higher density profile of C V presented in fig. 1. We present on the left the fitting of the chord-averaged emission and line shift profiles using a data analysis code explained in Ref. [5]. The obtained coefficients of the simple functions, used to fit the experimental data, are depicted on the top of this figure. The radial electric field profile obtained from these data, solving the radial momentum equilibrium equation, is presented on the right of the last figure as a dashed line. We have plotted in full line the E_r obtained directly from the fit of smoothed chord-averaged rotation data, neglecting the pressure gradient term. The toroidal velocity has been neglected due to its expected damping due to the ripple and because of the low shear of the TJ-I U device.
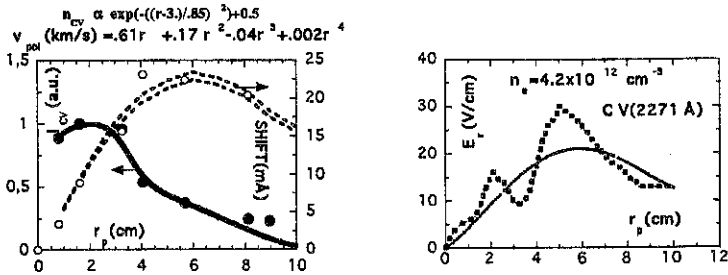
Fig. 4. *Simulation by a code of chord-averaged experimental data (on the left) and radial electric field profile deduced from the equilibrium equation (dashed line on the right); full line was obtained from chord-averaged poloidal velocity data neglecting the pressure gradient term.*

References
[1] K. Kondo et al., Rev. Sci. Instrum. **59**, 1533 (1988).

[2] H. Wobig, H. Massberg, H. Renner, The WVII-a Team, Plasma Physics and Controlled Fusion Research, 1986, Kyoto (IAEA, Vienna), Vol. II, 369 (1987).

[3] S.C. Aceto et al., in Proceedings of International Conference on Plasma Physics, Innsbruck, Vol. 16C, Pt. I, 529 (1992).

[4] E. Ascasibar et al., Trans. Fusion Technology **27**, 198 (1995).

[5] B. Zurro and C. Burgos, Rev. Sci. Instrum. **63**, 5196 (1992).

BEHAVIOUR OF SUPERTHERMAL ELECTRONS IN TJ-IUpgrade TORSATRON

L. Rodríguez-Rodrigo, F. Medina, F. Castejón, M. A. Ochando and TJ-IU Team.

Asociación Euratom-Ciemat para Fusión

Av. Complutense 22, 28040 Madrid.

Abstract

The behaviour of superthermal electrons has been studied in the TI-IU torsatron as a function of the magnetic configuration. The mean energies reached by the superthermal electron populations have been found to be consistent with the occurrence of EC off-axis absorption for the different radial ripple profiles. The interpretation of the experimental observations has been simply based in the facts that both, trapping factors at the axis and electron density profiles substantially change with magnetic configuration.

Introduction

In previous works [1, 2], the generation of high energy electrons in TJ-I Upgrade torsatron ($l = 1$, m=6, R=0.6 m, <a>= 0.1 m, B = 0.5÷0.7 T; ECRH at 37.5 GHz - X-mode, 2nd harmonic [3]) was investigated and several fast electron populations were characterised using Si(Li) (1 to 30 keV) and NaI(Tl) detectors (over 20 keV).

Here we are presenting the study of the behaviour of superthermal electrons in TJ-IU plasmas with line average electron densities, n_e, in the interval 0.2 to 0.6 x 10^{19} m^{-3} and electron temperatures, T_e, ranging between 100 and 200 eV. Also input power (100÷200 kW) and magnetic configuration scans (($0.15 \le \textit{t}$ (0) ≤ 0.29) were performed in order to try to determine the effect of magnetic ripple on characteristic energies and densities of uncoupled electrons, as well as the possible influence that the presence of these particles may have on plasma performance.

Experimental results and discussion

The specific diagnostic set-up used for the experiments presented here consits of: a 10 channel diode array at an equivalent toroidal angle $\Phi = 30°$ and a Si(Li) detector viewing a plasma radial chord through a beryllium filter of 105 μm also at $\Phi = 30°$, for the soft X ray region; two NaI(Tl) detectors observing the plasma through glass windows, either almost tangential or near perpendicular at $\Phi = 30°$ and an NaI(Tl) detector working in current mode for monitoring the average total hard X-ray (HXR) flux.

The HXR fluxes due to the bremsstrahlung of the runaway electrons generated during the rump up and down of the magnetic fields were supressed when adequate gas puffing was applied. For the present study only discharges emitting HXR during the ECRH phase have been considered, in order to try to investigate separately the characteristics of highly energetic electrons generated during the pulse.
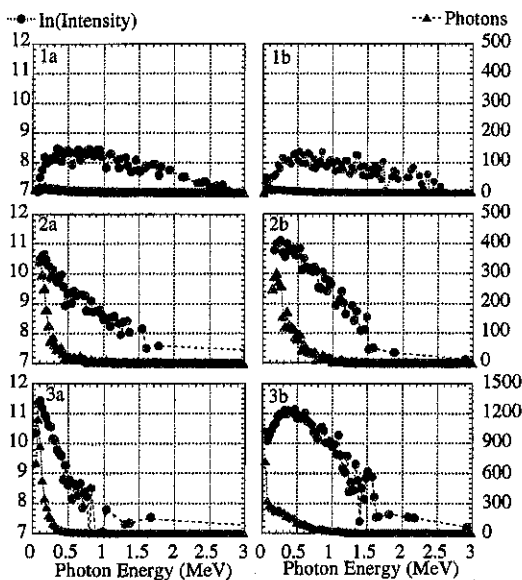
Figure 1. Hard X-ray intensity spectra for 3 different magnetic configurations: 1)τ (0)=0.29 2)τ (0)=0.2, 3)τ (0)=0.15. a) and b) are two different toroidal positions 120° and 0° from ECRH injection window.
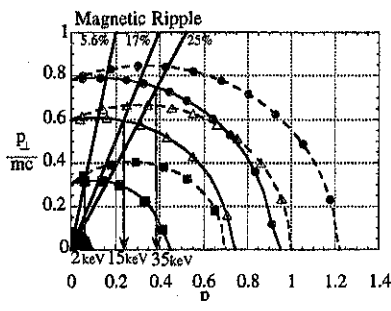
Figure 2. Resonance energy for superthermal electrons for different values of B field and parallel refraction index. Doted lines: $N_{||}$=0.25, full lines: $N_{||}$=0.1; ■ : B=0.7 T, ▲ : B=0.78 T and ● B=0.85 T. Also shown the trapping cones for three values of ripple.

To obtain high energy electrons spectra we have accumulated data from series of repetitive discharges for each configuration. Fig. 1 shows typical emission spectra from superthermal electrons in plasmas with the indicated magnetic configurations. As can be seen, the characteristic energy of superthermal electrons escaping from the plasma changes from one configuration to another and, in somes cases, fast electron losses are toroidally non symmetric. The low intensity and high energy spectra from the configuration with τ (0)=0.29 is characteristic of the remaining runaway electron population generated during the fields ramp up and that this spectrum is present in all configurations.

The differences in energy of the superthermal tails can be explained taking into account: a) the shape of the radial profile of the magnetic field ripple. Its value at the axis ranges from 25% to 5.6% as τ (0) changes from 0.29 to 0.15, being about 40% at the edge for all of the studied plasmas; b) the low first pass absorption, estimated of about 20%, and multireflection of the beam, confirmed through the detection of an important amount of the microwave power 180° away from the injection port; and c) the radial profile.
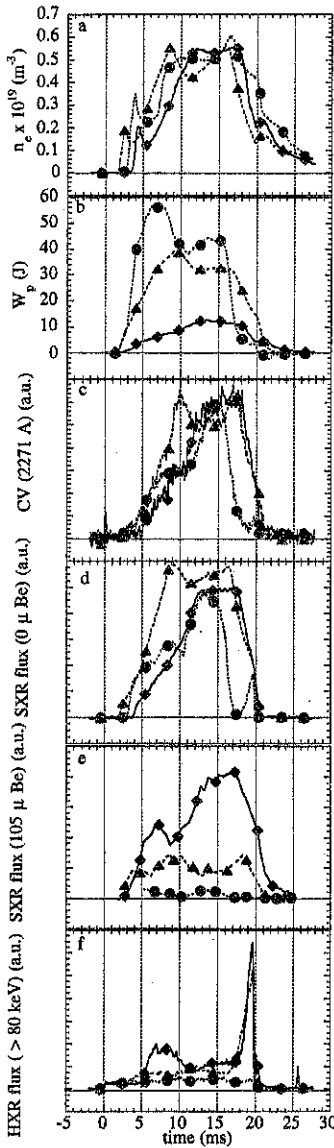
of electron density, which is flatter for lower central rotational transform plasmas.

The diagram of Fig. 2 shows the different trapping borders and the maximum resonant electron energies at the axis, for two values of $N_{||}$ and for three configurations. Electrons with the highest parallel velocities have the highest probability to become superthermal, specially for low ripple configurations. This, toghether with the more effective parallel diffusion in the momenta space as perpendicular velocity increases, would lead to the high observed energies of the superthermal tails. When $N_{||}$ is non zero, as occurs in the second pass of the microvawe front or when the density decreases, this effect would be more pronounced.

$$\vec{S} = \frac{B(r)}{B_0}\hat{s}_\perp + N_{||}\frac{p_\perp}{mc}\hat{s}_{||}$$

where $B_0 = 0.67$ T for TJ-IUpgrade torsatron.

The strong dependence of superthermal electron tails with the magnetic configuration observed in TJI-U can be understood via the increase of the minimum parallel momentum $p_{||}/mc$ necessary to produce passing superthermal electrons as ripple increases (corresponding to energies from 2 keV to 32 keV, see Fig. 2).

To illustrate this fact, Fig. 3 (a to f) shows a comparison of three shots belonging to the series used to obtain the HXR spectra of Fig.1. It can be seen that while line impurity (227.1 nm CV) and soft (400 eV to 1 keV) X ray emissions are of the same level, notable differences are found in the intermediate to high energy X ray signals and in the plasma stored energy. An inverse correlation between the signals from uncoupled electrons and density is observed, more pronounced as the ripple diminishes.

It is also important to try to establish whether or not fast electrons are affecting

Figure 3. Thermal and non-thermal signals for different magnetic configurations ● t (0)=0.3, ▲ t (0)=0.2, ◆ t (0)=0.15
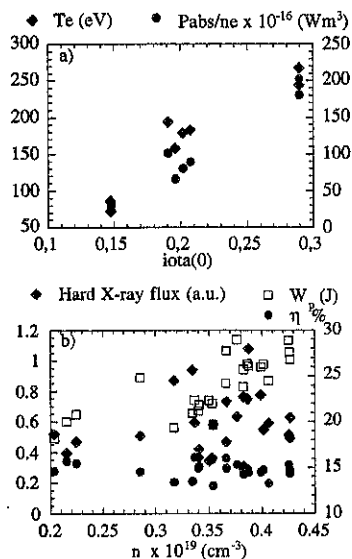
Figure 4. a) Power density and electron temperature versus ι (0) b) Energy content, fraction of absorbed power and hard X-ray flux versus linear electron density.

thermal plasma absorption, so that we have estimated the absorbed power in the stable phase of the discharges. In Fig. 4a, the absorbed power per particle is ploted against the value of the rotational transform at the axis. This result would indicate that there is a notable degradement in absorption when iota decreases. This fact has also been observed in other low shear devices but, appart from low order rational values at the plasma edge, the detrimental effect of decreasing iota was much less pronounced [4, 5]. In the present case the sharp decrease of the energy content in the lower iota plasmas studied could be better understood if superthermal electrons were considered as an important sink of energy.

To evaluate the influence of the low plasma optical thickness we have performed scans in electron density and input power for a fixed magnetic configuration (ι (0) ≈ 0.20) (see Fig. 4b) finding that there is not a clear relationship between the energy gained by fast electrons and the quality of thermal plasmas. So that, the most important effect seems to be trapping particles at the axis, which prevents the high loss of energy by the generation of fast passing electrons which may absorbe a relevant amount of the input power.

The present studies in TJ-I Upgrade torsatron are of relevance for TJ-II when exploring plasma properties in the lowest density region of its operational domain. In particular, the generation of high energy tails as a function of the magnetic field ripple must be taken into account.

References

1-Medina F., et al, Proceedings of the 23rd EPS Conf. on Controlled Fusion and Plasma Physics in Kiev (June 1996)

2-Ascasíbar E. et al, Proceedings of the 16th IAEA Conf. on Plasma Physics and Controlled Nuclear Fusion Research in Montreal (October 1996).

3- Ascasíbar E. et al, Transactions of Fusion Technology 27, 198, (1995).

4. Greiger G. et al, Plasma Phys and Controlled Fusion 28, 42 (1986)

5. Renner H. et al, Plasma Phys and Controlled Fusion 31, 1579 (1989)

ATOMIC BEAM CHARACTERISATION OF THE PLASMA EDGE IN THE TJ-I UP TORSATRON.

F.L. Tabarés, D. Tafalla and B. Brañas.
ASSOCIATION EURATOM/CIEMAT. Av. Complutense, 22. 28040 MADRID, SPAIN

1. Introduction.

Atomic beam diagnostics (1) are presently being applied to the SOL and edge characterisation of tokamaks and stellarators. Due to the relatively low penetration of the beams formed from thermal sources, the use of such diagnostics is generally restricted to the SOL region. As a general feature, reconstruction of the relevant plasma profiles from thermal beams is more accurately performed than from more energetic ones, due to the relatively simple collisional model describing the interaction of thermal atoms with plasma particles. Such interaction is restricted in that case only to electron collisions (1). In this work, the application of atomic beams produced from thermal sources to the characterisation of the plasma edge region of the TJ-IU torsatron $(0.4<r/a<1.1)$ is presented. The data are analysed in terms of transport characteristics and their dependence on plasma parameters, such as total density, heating power and magnetic configuration. Preliminary results of perturbative experiments (Ar injection) are also presented.

2. Experimental.

The TJ-I U has been previously described (2). Briefly, the device is a $l=1$, $m=6$ torsatron with plasma dimensions $R=0.6m$ and $<a>=0.1m$. Plasmas are generated and heated by ECRH (X-mode, 2nd harmonic, P=90 to 250kW) at 37.5 GHz. Average plasma densities range from 2 to 6×10^{18} m^{-3}, and typical central temperatures are in the range of 100-200 eV. Unless explicitly stated, experiments were performed at the standard configuration, corresponding to $\pm(0)=0.23$ Two types of atomic beams have been systematically used in the present experiments. First, a thermal Li beam has been used for the determination of edge density profiles. It is produced from an oven containing metallic lithium, at typical temperatures of 600 °C, and a set of collimators yielding a beam diameter at the detection region of ≈15 mm. Differential pumping is applied between the collimators. Detection of the fluorescence signal at 671 nm is performed either through a 38 pixel photodiode array or a 16 channel multianode phomomultiplier, with a typical radial resolution of 5 mm. The absolute electron density profile is reconstructed from the emission profile under complete attenuation conditions (1). Figure 1a shows a typical Li emission profile recorded by the photodiode array, once the background is subtracted. Secondly a newly developed, supersonic He beam (3), showing low divergence and good penetration into the plasma has been used for electron density and temperature determination. It is formed from the supersonic expansion of a He pulse (typical duration 0.5-2 ms) produced by a fast piezoelectric valve, and its diameter at the detection point is ≈10 mm. The emission lines from excited He atoms at 728 nm and 668 nm are recorded for the reconstruction of the electron density profile, and those at 706 and 728 nm for the electron

temperature values. Data are taken in a shot to shot basis. The line ratios are correlated to local plasma parameters by using the same collisional-radiative model as used in the Textor tokamak (1). Figure 1b shows the time evolution of the emission line intensities used for the electron temperature determination. As it is seen, the sharp peak taking place at the injection of the He pulse is followed by a much lower background corresponding to the effusion of the gas produced in the expansion chamber.

3. Results.

Figure 2 shows the reconstructed electron density profile at normalised radius $\rho = r_{eff}/a$ from 0.3 to 1.1, by using the Li and He atomic beam diagnostics. Density values from Langmuir probes are also included, their absolute value being normalised to those deduced from the Li beam emission profile. This normalization implies an effective probe area of 1.6 times the geometrical estimation (4). The range of application of the He beam diagnostic was limited by geometrical constraints in the observation optics. As it can be seen, a general good agreement is found between different density diagnostics, in spite of their sensitivity to possible deviations from thermal EED in the plasma edge is markedly different and the intrinsic uncertainties of the collisional-radiative model used in the reconstruction of the profile from the He beam data. Due to the different spatial ranges where these beam diagnostics show the best accuracy, they were used in a complementary way through the reported experiments.

The response of the edge ($\rho > 0.65$) electron density to the evolution of the plasma average value, <ne>, is shown in figure 3 for a typical example of pre-programmed gas injection. In this case, puffing was turned off at t=24 ms and the ECRH heating at t=28 ms. As it is seen, a fast formation of the edge density profile takes place, with almost negligible evolution as the average density is increased in a factor of 1.5. Significant variations at the edge region are only observed upon turning off the gas source. As expected, a drastic change is apparent in the afterglow phase. The relative insensitivity of the edge density profile to the average value was also seen under steady state conditions. Thus, for example, a change of the average density from 6 to 2.3 (10^{12} cm^{-3} units) is followed by a decrease of only 1.4 times at $\rho = 0.7$ to 1.1. These results are in very good agreement with Langmuir probe data (4). Temperature profiles from $\rho = 0.5$ to 1 were found to scale with the inverse of average density in that range, with typical values at the LCFS from 20 to <10 eV, again confirming the probe data. A simple analysis of the particle balance in the decay phase of figure 3 was performed, under the assumption of purely diffusive particle flow (5). Under this assumption, the results are consistent with a systematic increase of D vs. minor radius and a fairly broad neutral density profile. Density and temperature profiles were also recorded at different heating powers, and constant average density. A strong dependence of the electron temperature is generally seen, the effect of increased heating power being more pronounced at inner radii. Typical values at a constant line density of 2.5×10^{12} cm^{-3} are : 60, 40 and 35 eV, at $\rho = 0.5$ and 20, 17 and 15 eV at $\rho = 1.0$, for heating powers of 200,130 and 90 kW, respectively. Previous estimates of central temperatures by ECE (6) indicate values of 150-250 eV at 200 kW and similar scaling with

injected power, thus implying fairly peaked profiles. Although no detailed study of the power dependence of the electron density profiles has been possible, a slight steepening of that profiles is seen as the power is increased from 90 to 200 kW, at constant average electron density. Modelling of the results shown above with the PROCTR code is presently underway.

The magnetic configuration of the TJ-IU allows for central iota scans in the range $0.13 < \iota(0) < 0.4$, corresponding to magnetic axis displacements of ± 3 cm around the centre of the vacuum vessel. Electron density and temperature scans at the edge region were also performed. Due to fixed location of the observation region, the spatial profiles so obtained for different configurations only partially overlapped. In experiments at constant line average density, broader density profiles were systemetically observed at lower iota values, thus implying a lower central density. A sharp decay of edge parameters at $r \approx 8.5$ cm for $\iota(0)$ =0.32 was measured, even when calculations and magnetic surface mapping give a value of a=11.5 cm. This can be attributed to the presence of the 1/3 rational surface inside the confined region. These results are in good agreement with the change in HXR fluxes due to supra thermal electron absorption at the high field side as the configuration is changed (6).

Finally, the fast response of the atomic beam diagnostics was used for the monitoring of temperature perturbations at the edge region. For that purpose, a fast piezo valve, delivering 0.25 ms pulses of Ar, was closely coupled to the TJ-I U plasmas. The Ar puffing rate was set low enough to allow for constant electron density and global plasma energy content during the injection. The simultaneous injection of 2 ms He beam pulses allowed for the fast recording of the electron temperature evolution at several minor radius values. The results are displayed in figure 5. As shown, a constant characteristic decay time, $\tau = (d\ln Te/dt)^{-1}$ of ≈ 0.8- 1 ms is obtained for all positions under the conditions reported. An estimate of 0.8 ms for τ_E is predicted from the LHD scaling for TJ-IU . More details and modelling of the perturbative experiment will be presented elsewhere.

Acknowledgements. The authors are indebted to M.Pedrosa and R. Balbin for the Langmuir probe data and to B.van Miligen for his help with the C-R model. Clarifying discussions with M.A. Ochando and F. Castejón have also been extremely helpful.

References

[1] E.Hintz and B.Schweer. Plasma Phys. Control. Fusion **37** (1995) 87

[2] Ascasfbar E. et al, Transactions of Fusion Technology **27** (1995) 198.

[3] F.L. Tabares et al. J.Nucl. Mater (1996) in press. Proc. 12th Int. Conf. on Plasma Surface Interactions.

[4] M.A. Pedrosa. Privated comunication

[5] H. Maassberg et al. Plasma Phys. Control. Fusion **35** (1993) B319-B332

[6] Ascasibar et al. Proceedings of the 16th IAEA Conf. on Plasma Physics and Controlled Nuclear Fusion Research in Montreal (October 1996) F1-CN-64/CP-9
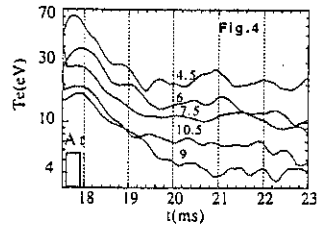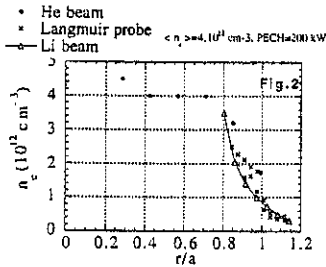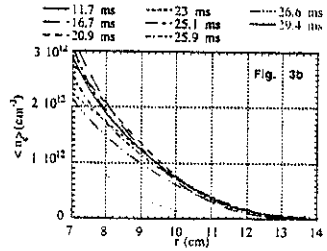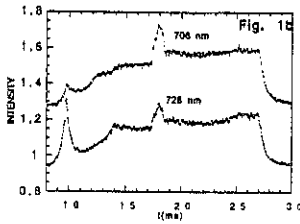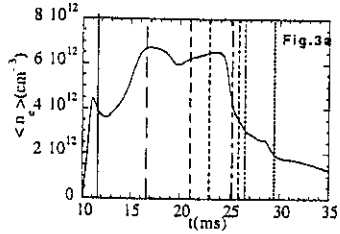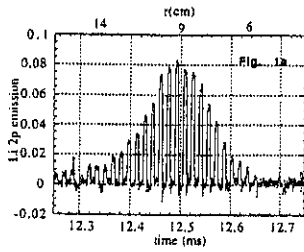
FIGURE CAPTIONS

Figure 1. a) Li beam: Typical signal from P.D. array. Also shown are the corresponding radial positions b) Typical traces of the He beam diagnostic. 1 ms He pulse is injected at 17 ms.

Figure 2. Density profile reconstructed from the beam diagnostics. Also shown are the normalized data from the Langmuir probe.

Figure 3. Time evolution of line average (a) and edge profile (b) densities. Gas turned off at 24 ms, ECR heating turned off at 28 ms.

Figure 4. Time evolution of the electron temperature at different minor radii after the injection of a short (0.25 ms) Ar pulse.

First Experimental Results in TJ-II Flexible Heliac: Magnetic surface mapping

The TJ-II Team* presented by **C. Alejaldre**

Asociación Euratom-Ciemat para Fusión, Ciemat. Madrid, Spain

Abstract

In December 1996 a short campaign of magnetic surface measurements were carried out in TJ-II. A limited number of configurations were studied with the main goal of checking that the high accuracy required in positioning of the coils and the vacuum vessel had been achieved. The existence of closed and nested magnetic surfaces, in good agreement with the calculated ones, demonstrated this issue.In this work the results obtained are discussed.
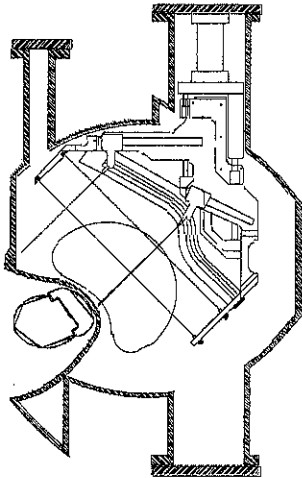
Fig. 1: Schematic view of the fluorescent detector

Description of the device

The flexible Heliac TJ-II is a medium size device (R=1.5 m, <a>=0.2 m, $\bar{B}(0)$=1.0 T) located at CIEMAT, Madrid, and about to start plasma operation [1]. TJ-II coil configuration consists of 32 toroidal field (TF) coils centred around a four periods toroidal helix. Two additional coils provide its unique flexibility ($0.96 \leq$ ι_0 ≤ 2.5, $-1\% \leq$ magnetic well $\leq 6\%$), a circular coil located at the major axis, 1.5 m, and a helical winding wrapped around the circular one, following the same winding law as the toroidal coils. Two poloidal field coils (2.25 m radius) complete the coil configuration.

Experimental results

First measurements of the magnetic surfaces in the device were performed in December 1996, using a directed electron beam in combination with a movable fluorescent rod array [2-6]. At that time, the final adjustment of the TF coils was still not finished, so that the maximum deviation of some of them respect to the nominal position (2.9 mm, in radial direction) exceeded the design tolerance (1 mm). The magnetic field was steady state, $B_0 \leq 0.05$ T (5% of the nominal field), with 50 s pulse length. The technique

* C. Alejaldre, J. Alonso, L. Almoguera, E. Ascasíbar, R. Balbín, M. Blaumoser, J. Botija, B. Brañas, A. Cappa, R. Carrasco, F. Castejón, J. R. Cepero, J. Doncel, T. Estrada, A. Fernández, M. Francés, C. Fuentes, A. García, I. García, M. García, J. Guasp, J. Herranz, C. Hidalgo, J.A. Jiménez, I. Kirpitchev, J.R. Knaster, V. Krivenski, I. Labrador, F. Lapayese, M. Liniers, A. López-Fraguas, A. López-Sánchez, E. de la Luna, R. Martín, A. Martínez, l. Martínez, M. Medrano, P. Méndez, A. Montoro, K. McCarthy, F. Medina, B.van Milligen, M. Ochando, L. Pacios, L. Pallás, I. Pastor, M.A. Pedrosa, A. de la Peña, J. Qin, L. Rodríguez, A. Salas, E. Sánchez, J. Sánchez, F. Tabarés, D. Tafalla, V. Tribaldos, J. Vega, V. Zhuravlev, B. Zurro.

used is based on imaging the spots produced by the impact of an electron beam, launched in the vacuum vessel along the magnetic field lines, when intersecting an array of four fluorescent rods (1.5 mm diameter each, coated with P24, ZnO:Zn powder), sketched in Fig. 1, that sweeps the vessel cross section.
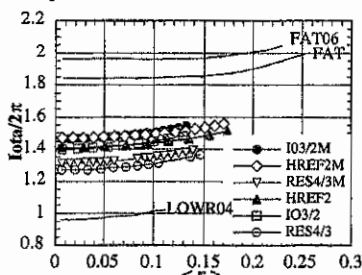
Fig. 2: Theoretical rotational transform profiles of the measured configurations

The electron beam (0.5 mm diameter at the gun exit; energy 150 eV) is launched with the main velocity component, $v_{||}$, parallel to the magnetic field of the device. The gun head is driven over a rectangular region (147 mm in radial direction, 328 mm in vertical direction) by means of a PLC controlled manipulator installed in a top port; the magnetic surfaces are measured about 199° away in toroidal direction. Three LEDs located inside the vacuum vessel, at the same cross-section where the image is formed, are used as a reference system for measuring distances. The images are acquired with an intensified CCD camera looking perpendicularly to the image plane through a tangential NBI port and processed by means of an image integrator. The spatial resolution of the experimental system is estimated to be about 2 mm (fluorescent rod, 1.5 mm thick, plus the space charge broadening of the electron beam cross section as it travels around the torus).
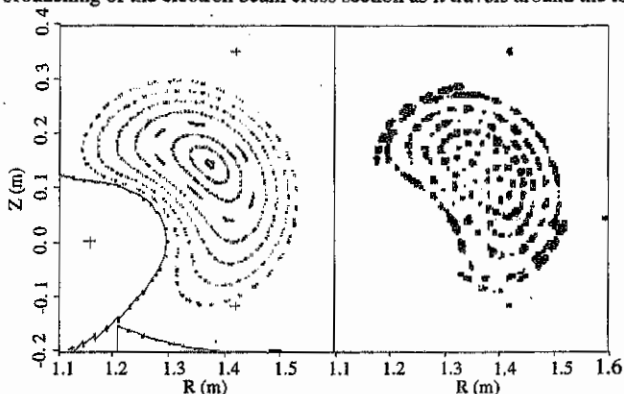
Fig.3: Calculated and experimental surfaces for the standard (HREF2)configuration

TJ-II configurations are low shear. Nine of them have been measured, covering the iota range $0.96 \leq t_0 \leq 1.97$. Their iota profiles are shown in Fig.2. In all the studied configurations closed and nested magnetic surfaces are found, provided that the low order resonances ($t = 1, 3/2$ and 2, in our case) are kept away from the corresponding rotational transform profile. Size and shape of the magnetic surfaces, as well as the coil current values needed for all the configurations, fully agree with the design parameters. Figure 3 shows that the calculated and experimental surfaces for the standard configuration, named HREF2 ($t \leq 3/2$), are in very good agreement. If the $t = 3/2$ value is allowed inside this low shear configuration, islands are measured, probably due to the above mentioned non corrected internal field error, in good qualitative agreement with the theoretical model. After final

positioning of the TF coils, within the design tolerances, additional experiments will be done to further investigate this point.
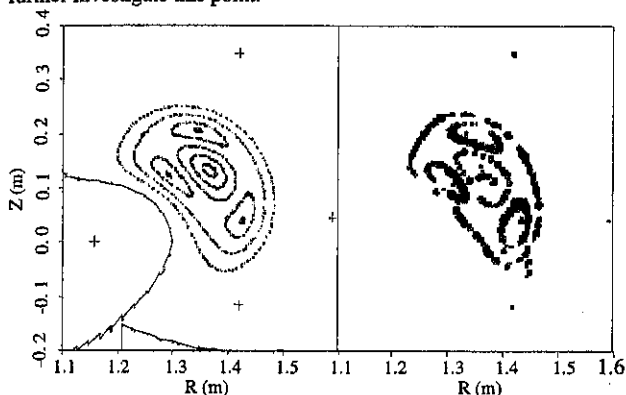
Fig.4: Calculated and experimental surfaces for the RES4/3M configuration

The ideal vacuum field contains field components, associated with the four-fold toroidal symmetry, that lead to the appearance of natural islands on magnetic surfaces with $t = (n=4)/m$. This has been experimentally confirmed for the $t = 4/3$ case, named RES4/3M, where the agreement with the theoretical model is remarkable, as shown in Fig. 4. In the experimental image only individual points are found for the two most external surfaces because the second transit of the electron beam is intercepted by the vacuum vessel, whose finite thickness is not taken into account in the calculation. It should be noted that the apparent displacement of the secondary magnetic axis of the islands, in the experimental image, is due to the finite size of the electron gun head (9 mm diameter).
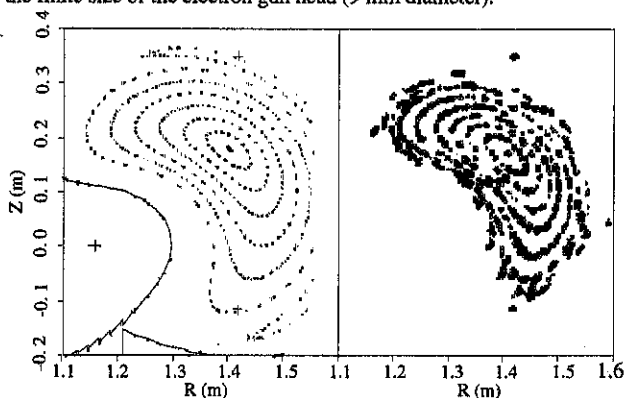
Fig.5: Calculated and experimental surfaces for the FAT configuration

Fig. 5 shows the good agreement between the experimental and calculated magnetic surfaces corresponding to one of the configurations with largest plasma volume, named FAT (0.25 m effective plasma radius; t ranging between 1.84 and 1.99). In the external part of the theoretical image part of an island corresponding to $t = 2$ is clearly visible. It couldn't be resolved in the experiment because it would be partially intersected by the vessel wall, but, probably, this is the reason why the last experimental contour appears to be not clearly closed.
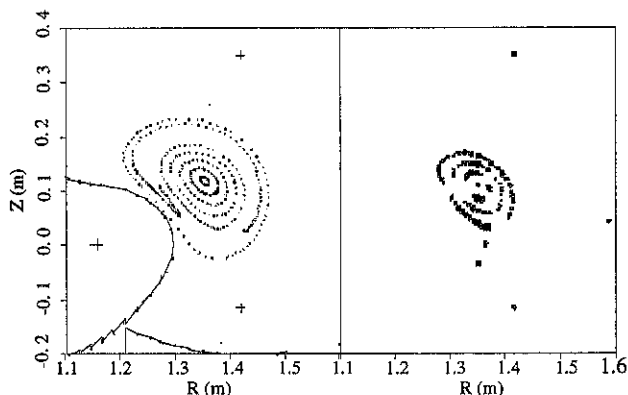
Fig.6: Calculated and experimental surfaces for the LOWRO4 configuration

In Fig. 6 another comparison between theory and experiment is presented. It corresponds to one of the smallest configurations in terms of plasma radius, named LOWRO4 (0.11 m effective plasma radius; ι ranging between 0.96 and 1.02). Again the similarity between theory and experiment is clear. In the region close to the external $\iota = 1$ island only the first transit of the electron beam can be found because subsequent transits are intercepted by the electron gun head.
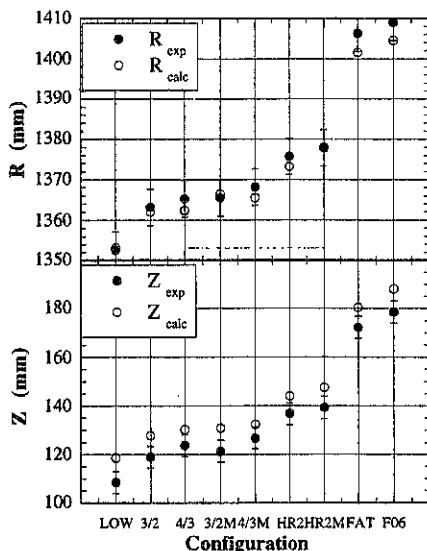
Fig.7: Experimental and calculated values of R and Z coordinates of the magnetic axis

Fig. 7 shows the comparison between experimental and calculated positions of R and Z coordinates of the magnetic axis at the detection plane, for all the measured configurations. As regards R coordinate, the agreement is quite good, but for the Z coordinate, a systematic discrepancy of 7 mm, in average, between experimental and calculated values is observed. The origin of this deviation is still being investigated.

References

[1] C. Alejaldre et al., Fusion Technol. **17**,(1990) 131.
[2] Hailer, H., et al., in Controlled Fusion and Plasma Physics (Proc. 14th Eur. Conf. Madrid, 1987), Vol. 11D, Part I, European Physical Society (1987) 423.
[3] Jaenicke, R., et al., Nucl. Fusion **33** (1993) 687.
[4] Lesnyakov, G.G., et al., Nucl. Fusion **32** (1992) 2157.
[5] Lin, H., et al., Rev. Sci. Instrum. **66** (1995) 464
[6] Shats, et al., Nucl. Fusion **34** (1994) 1653.
[7] Ascasíbar. E., et al., Nucl. Fusion **37** (1997).

FLUCTUATIONS AND TURBULENT TRANSPORT IN THE TJ-IU TORSATRON

M.A. Pedrosa, C. Hidalgo, G. Fiksel[+], E. Sánchez, B. van Milligen, R. Balbín,
I. García-Cortés, E. Ascasibar, F. Medina, M.A. Ochando, L. Rodríguez-Rodrigo
and the TJ-IU team
Asociación Euratom-Ciemat Madrid, Spain
[+]*Department of Physics, University of Wisconsin, Madison, USA*

INTRODUCTION

The statistical properties of the time resolved turbulent flux and fluctuations have been investigated in the plasma edge region of tokamak and stellarator devices [1, 2]. Further studies have been done to quantify the frequency resolved radial coherence of fluctuations and turbulent transport in the scrape off layer (SOL) and in the edge plasma region of the TJ-IU torsatron.

In the framework of theoretical models based on the idea of critical gradients (such as SOC models [3]), the probability distribution function (PDF) of fluctuations in pressure/density gradients is expected to be non symmetric (non-gaussian). An experimental effort has been made to quantify the statistical properties of pressure/density gradients.

Finally, to improve the understanding of edge plasma turbulent transport, measurements of electrostatic and magnetic fluctuation-induced transport have been carried out in the plasma boundary region of the TJ-IU torsatron.

EXPERIMENTAL SET UP

Measurements of fluctuations and turbulent flux have been carried out in the electron cyclotron resonance heated TJ-IU torsatron ($\ell=1$, $m=6$, $P_{ECRH}=200$ kW, $f_{ECRH}=37.5$ GHz, $\iota \approx 0.23$, R=0.6 m, $\bar{a} \approx 0.1$ m, $\bar{n}_e \approx (1-5) \times 10^{18}$ m^{-3}, $B_t=0.67$ T) [4] by means of Langmuir probes. The experimental set up is composed of three arrays of Langmuir probes (three tips each) mounted together and radially separated (2 - 20 mm). One tip of each array is used to measure ion saturation current (I_s) and two tips, aligned perpendicular to the magnetic field and poloidally separated $\Delta \approx 2$ mm, are used to deduce the poloidal electric field ($E_\theta \approx [V_f(\theta_1) - V_f(\theta_2)]/\Delta$) from the measured floating potential (V_f). Probes were oriented with respect to the magnetic field direction in such a way that shadows between them were avoided [5].

A pyrobolometer and an array of small pick-up coils located inside it, have been used to measure the magnetic fluctuations induced heat flux and fluctuations in the magnetic field.

The statistical analysis of the signals has been done using wavelet cross-correlation techniques [6].

TURBULENCE RADIAL STRUCTURE

Figure 1 shows the radial profiles of the ion saturation current and the normalized level of fluctuations, measured simultaneously by two probes 0.8 cm radially apart, together with the
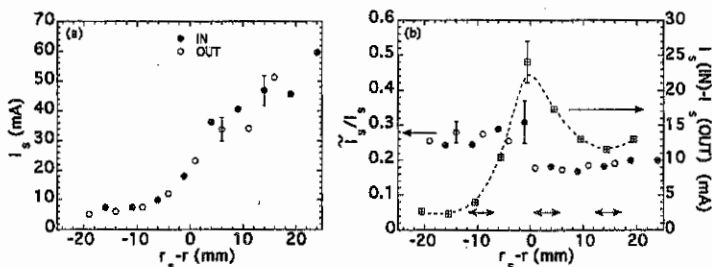
Fig. 1.- Ion saturation current profile (a) and fluctuations and radial gradient of ion saturation current (b) measured by probes 0.8 cm radially apart.

gradient in the ion saturation current. The velocity shear layer location (r_S) has been taken as a radial point of reference.

To study the detailed behavior of fluctuations and turbulent particle flux, $\Gamma_T = \tilde{n}_e \tilde{E}_\theta / B_t$ (being $\tilde{n}_e$ and $\tilde{E}_\theta$ the fluctuating density and poloidal electric field respectively), three regions of the profile have been selected: the SOL ($r > r_S$), the region close to the maximum gradient ($r \approx r_S$) and the plasma edge, well inside the plasma ($r < r_S$) (see Fig. 1).

Moving radially inwards the power spectra of fluctuation become narrower in TJ-IU (Fig. 2a). The mean frequency of fluctuations changes from about 60 kHz in the SOL region to approximately 20 kHz at the innermost radial position [7].

The radial cross-coherence between I_S signals, calculated in the three above-mentioned regions of the plasma, is shown in Figure 2b. For these measurements, probes were radially separated by 0.6 cm and the cross-correlation was computed during a 5 ms time window. In spite of the decrease in the power of fluctuations for frequencies above 100 kHz in the plasma edge, the radial cross-coherence increases in the upper frequency range when crossing the velocity shear layer location from the SOL to the edge plasma region. This result is more evident for the I_S signals than for the V_f signals and does not depend on the probe radial distance (6 - 15 mm).
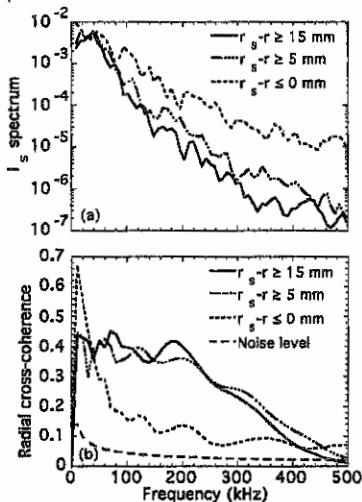
Fig. 2.- Ion saturation current spectra (a) and radial cross-coherence of ion saturation current signals measured by probes 0.6 cm radially apart (b).

Although the spectral behavior of the cross-coherence is independent of the radial separation of the probes, the level of the cross-coherence decreases as the distance between probes
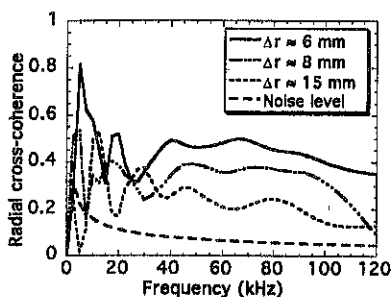
Fig. 3.- *Cross-coherence between two ion saturation signals measured by probes 0.6, 0.8 and 1.5 cm apart.*

increases. Figure 3 shows the cross-coherence between two ion saturation current signals for different radial separations between probes in the edge plasma region ($r_s-r \geq 10$ mm). A decrease of the cross-coherence, mainly for frequencies above 30 kHz, is observed as the distance between probes is increased. This behavior is similar for I_s and V_f, but the level of the cross-coherence is higher for I_s signals than for V_f ones.

In agreement with previous experiments [5] the radial cross-coherence associated with fluctuations is higher than the one associated with the turbulent flux. The systematic comparison of those magnitudes shows that this result is independent of the radial location of the probes and also of the radial distance between them, in the range investigated in this work.

To study the influence of global plasma parameters on edge turbulence, the line average density has been modified in a wide range. The mean frequency of the cross-coherence spectra increases with increasing plasma density. For very low values of mean plasma density, ($\bar{n}_e < 0.5 \times 10^{18}$ m^{-3}) very high radial cross-coherence (close to one) between potential fluctuations has been observed, as can be seen in Figure 4. This effect is less notable for ion saturation current fluctuations and may be related to an enhancement in the population of superthermal electrons. Actually an increase in the hard X-ray flux, due to absorption by fast resonant electrons as plasma transparency increases, has been observed [8].

Fig. 4.- *Radial correlation for V_f and I_s fluctuations signals (b) for a very low plasma density (a).*

CRITICAL GRADIENTS

The statistical properties of the probability distribution function (PDF) of density gradients have been investigated in the plasma boundary region of the TJ-IU torsatron. The PDF has been computed for ion saturation current gradient fluctuations in the radial and poloidal directions. In the presence of critical gradients the PDF of fluctuations of pressure gradients
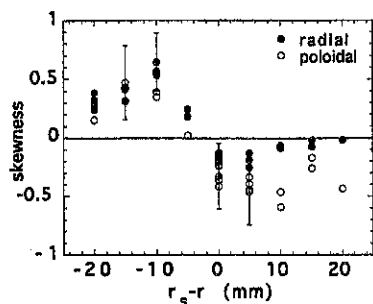
Fig. 5.- Skewness of the probability distribution function of the ion saturation current radial gradient compared to the corresponding poloidal gradient.

(in the radial direction) is expected to be non symmetric (non-gaussian), unlike to the behavior of the poloidal gradient.

Although the skewness of the PDF for pressure fluctuations deviates significantly from zero, no significative differences in the skewness of the distribution function between radial and poloidal pressure plasma gradient fluctuations have been observed (Fig. 5).

MAGNETIC ENERGY TRANSPORT

The local electron energy flux produced by magnetic fluctuations has been measured directly in the edge plasma ($r/r_s>0.7$) of the TJ-IU. This flux is obtained from the correlation between fluctuations in the electron heat flux parallel to the equilibrium magnetic field and fluctuations in the radial magnetic field [9]. The measurements reveal that the amplitude of the magnetic field fluctuations is very small $\tilde{B}_r/B_t \approx (1\text{-}3)\times10^{-5}$ and the corresponding heat transport is also very small, less than 1% of the expected total energy transport.

SUMMARY

The radial cross-coherence of fluctuations and turbulent transport has been studied using a multiple array of Langmuir probes in the plasma boundary region of the TJ-IU torsatron. The measured radial coherence decreases with increasing the radial distance between probes, and is higher for fluctuations than for turbulent fluxes both in the SOL and in edge plasma regions. In the SOL region the radial coherence is dominated by low frequencies (lower than 100 kHz) whereas in the plasma edge high frequencies (> 100 kHz) are significantly correlated. The statistical properties of fluctuations in gradients have been investigated. No evidence of critical gradients (i.e., non-gaussian distributions in the PDF of gradient) has been found.

The magnetic fluctuation-induced electron energy flux measured in the plasma edge of the TJ-IU torsatron cannot account for the observed total energy flux.

[1] HIDALGO, C., Plasma Phys. Controll. Fusion 37, A53 (1995).
[2] CARRERAS, B. A., HIDALGO, C., et al., Plasma Physics 3, 2664 (1996).
[3] MEDVEDEV, M. V., DIAMOND, P. H., CARRERAS, B. A., Phys. Plasmas 3, 3745 (1996).
[4] ASCASIBAR, E. et. al., in Plasma Physics and Controlled Nuclear Fusion Research (Proc. 15th Int. Conf. Seville, 1994) Vol. 1, IAEA, Vienna (1995) 749.
[5] PEDROSA, M. A., HIDALGO, C., et al., in Controlled Fusion and Plasma Physics (Proc. 23th Eur. Conf. Kiev). Vol. 20C, Part II, European Physical Society (1996) 827.
[6] VAN MILLIGEN, B. Ph., HIDALGO, C., et al., Phys. Rev. Lett. 74, 395 (1995).
[7] PEDROSA, M. A., OCHANDO, M. A., et al., Plasma Phys. Control. Fusion 38, 365 (1996).
[8] RODRIGUEZ-RODRIGO, L., MEDINA, F., et al., This Conference.
[9] FIKSEL, G., PRAGER, S. C., SHEN, W. and STONEKING, M., Phys. Rev. Lett. 72, 1028 (1994).

DIAMAGNETIC DRIFT AND FINITE ION LARMOR RADIUS EFFECTS ON BALLOONING STABILITY OF THE TJ-II FLEXIBLE HELIAC

R. SANCHEZ, J.A. JIMENEZ[†] and L. GARCIA

Universidad CARLOS III, Madrid, SPAIN

[†] Asociación EURATOM-CIEMAT, Madrid, SPAIN

1. Abstract

The collisionless kinetic ballooning equation in the intermediate frequency regime is rederived in Boozer coordinates and numerically solved for the most unstable MHD ballooning surfaces of the TJ-II flexible heliac. Ideal modes are found to stabilize for wave numbers over a threshold m_u, which can be roughly estimated as $m_u \simeq (2a/\delta L_n)\bar{\gamma}_{MHD}$, where $\bar{\gamma}_{MHD}$ is the normalized MHD growth rate of the mode and δ is a kinetic parameter which vanishes in the MHD limit. The critical β_c for the onset of ballooning instabilities is weakly modified. The parameter regions where TJ-II is scheduled to operate are examined and dominant ballooning wave numbers identified.

2. Kinetic ballooning equation

In a previous work [1] the most unstable MHD ballooning modes were found in the unfavourable curvature regions which appear at the outer surfaces of the TJ-II heliac device [2] with growth rates $\bar{\gamma} \equiv \gamma\tau_A \sim 0.1$, where τ_A is the Alfvén time. Since the poloidal wave number m did not enter the equations at first order, the dominant modes could not be identified. Furthermore, for $m \gg 1$ the size of the modes becomes of the same order that ρ_L^i implying that FLR corrections should be retained.

For TJ-II parameters, neglecting collisions, the relevant kinetic regime corresponds to the intermediate frequency regime [3], where the growth rate of the modes lies between the ion and electron bounce frequencies and, therefore, only trapped electrons need to be considered. Since the trapped electron contribution can be shown to be much smaller than the rest of the kinetic corrections, it will be neglected [3]. In Boozer coordinates (s, θ, ξ), the collisionless kinetic ballooning equation in this regime is then:

$$\frac{d}{dy}\left(k_\perp^2 \frac{dF}{dy}\right) = \alpha_{1i}a_1 k_\perp^2 \bar{\gamma}^2 F - a_2\bar{p}'KF + G(\bar{\gamma},\eta_i,\eta_e,\tau)a_2\bar{p}K^2F \tag{1}$$

where all quantities have the same meaning that in [1] except $K \equiv \kappa_s + \iota'(y - y_0)\kappa_\theta$, $\tau \equiv T_e/T_i$ and $\eta_s \equiv dlnT_s/dlnn_s$. The function G is defined as:

$$G(\bar{\gamma},\eta_e,\eta_i,\tau) \equiv \frac{1}{2(1+\tau)}\left(7\alpha_{2i} + 4\tau\frac{\alpha_{1i}\alpha_{1e}}{\alpha_{0e}}\right) \tag{2}$$
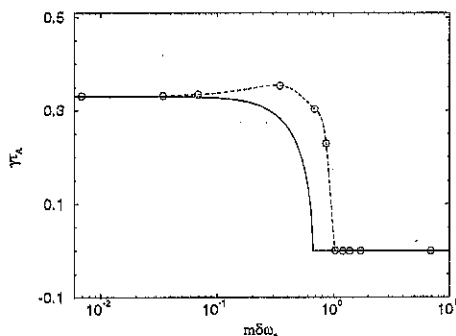
Figure 1: Growth rate $\gamma \tau_A$ vs. $m\delta\omega_*$, using Eq. 4 (black line) and Eq. 1 (circles) ($\tau = 1$ and $\eta_i = \eta_e = 0$).

where $\alpha_{li} \equiv 1 - im\delta\omega_* \bar{\gamma}^{-1} (1 + l\eta_i)$ and $\alpha_{le} \equiv 1 + im\delta\tau\omega_* \bar{\gamma}^{-1} (1 + l\eta_e)$, being l an integer. The ion and electron diamagnetic frequencies have been redefined as $\omega_*^i \equiv -m\delta\omega_* \tau_A^{-1}$ and $\omega_*^e \equiv -m\delta\tau\omega_* \tau_A^{-1}$, where $\omega_* \equiv -n_0'/n_0$ and $\delta \equiv (1/2) \left(\rho_L^i/a\right)^2 (\Omega_i \tau_A)$.

In the MHD limit $\delta \to 0, \tau \to 1, \eta_i, \eta_e \to 0$ and Eq. 1 reduces to:

$$\frac{d}{dy}\left(k_\perp^2 \frac{dF}{dy}\right) = a_1 k_\perp^2 \bar{\gamma}^2 F - a_2 \bar{p}' KF + \frac{11}{4} a_2 \bar{p} K^2 F \qquad (3)$$

which has an extra term (the K^2 term) in comparison with the MHD ballooning equation solved in [1]. This term is not a truly diamagnetic effect, though, since it can be derived from the whole MHD ballooning equations taking the excitation of parallel sound waves into account. As shown in [1] it has a weakly stabilizing effect.

3. Diamagnetic stabilization of MHD modes

We have solved Eq. 1 on a surface with effective radius $\rho/a \simeq 0.9$ of an ideally unstable equilibrium with $<\beta> \simeq 1.5\%$ of the standard configuration of TJ-II. The obtained growth rates are plotted vs. $m\delta\omega_*$ in Fig. 1. In the same figure, it has also been plotted the growth rate obtained from Eq. 1 when the K^2 term is neglected, given by the dispersion relation:

$$\bar{\gamma} = i\frac{m\delta\omega_*(1+\eta_i)}{2} \pm \sqrt{\bar{\gamma}_{MHD}^2 - \left(\frac{m\delta\,\omega_*(1+\eta_i)}{2}\right)^2} \qquad (4)$$

which predicts stabilization for modes with $m \geq m_u \equiv 2\bar{\gamma}_{MHD}/\delta\omega_*(1+\eta_i)$. The K^2 term has no effect on the growth rate except near m_u, where the function $G(\bar{\gamma}, \eta_i, \eta_e, \tau)$ can be approximated as:

$$G \simeq -\frac{1}{2(1+\tau)}\left(7\left(1 + \frac{2\eta_i}{1+\eta_i}\right) + 4\tau\frac{1+\eta_i+2\tau(1+\eta_e)}{1+\eta_i+2\tau}\right) \qquad (5)$$

which is negative for any value of τ, η_i and η_e and therefore destabilizing.
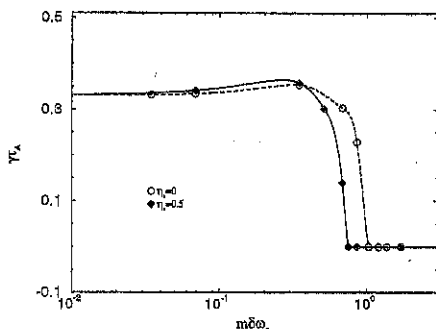
Figure 2: *Comparison between solutions of Eq. 1 for $\eta_i = 0$ (white circles) and $\eta_i = 0.5$ (black diamonds) ($\tau = 1$ and $\eta_e = 0$).*

For modes with $m \gg m_u$, $G(\bar{\gamma}, \eta_i, \eta_e, \tau)$ can be written as:

$$G \simeq -\frac{7}{2(1+\tau)}\left(\frac{\eta_i}{1+\eta_i}\right) \qquad (6)$$

implying that further desestabilization is only expected for $\eta_i \neq 0$. But when $\eta_i \neq 0$ the inertia term in Eq.1 is also enhanced and quickly dominates as m increases leading to a reduction of m_u (see Fig. 2), whilst modes with $m \lesssim m_u$ are further destabilized. If $m \ll m_u$, the function $G(\bar{\gamma}, \eta_i, \eta_e, \tau)$ reduces to:

$$G \simeq \frac{7+4\tau}{2(1+\tau)} \qquad (7)$$

and we recover the MHD parallel sound wave excitation stabilizing effect obtained in [1]. The effect of $\tau > 1$ is weakly stabilizing, whilst $\eta_e > 0$ enforces destabilization near m_u.

4. Critical β_c

To study the possible reduction or enhancement of β_c we follow [4] and assume that at marginal stability, the K^2 term can still be considered a small correction, so that $\bar{\gamma} \simeq im\delta\omega_*(1+\eta_i)$. In this case, the marginal stability equation reduces to:

$$\frac{d}{dy}\left(k_\perp^2 \frac{dF}{dy}\right) = \epsilon_c^2(1+\eta_i)^2 a_1 k_\perp^2 F - a_2\Delta_c\bar{p}'KF - \frac{1}{2(1+\tau)}\frac{\eta_i}{1+\eta_i}a_2\Delta_c pK^2F \qquad (8)$$

where $\epsilon_c \equiv \delta\omega_*/2$. Since $\epsilon_c \ll 1$, we have introduced a multiplying factor Δ_c in the equations which accounts for the pressure gradient variation. This formulation of the problem is only valid for $\Delta_c \simeq 1$, since we assume that the magnetic surfaces do not change when the pressure profile does. Solving Eq. 8 as an eigenvalue problem for Δ_c using an equilibrium with $\beta \simeq \beta_c$, we have evaluated the relative change of β_c as a function of η_i for two different values of ϵ_c (see Fig. 3). If ϵ_c is sufficiently large, the inertia enhancement caused by $\eta_i > 0$ dominates and β_c increases.
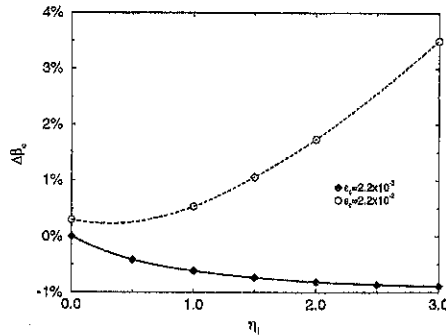
Figure 3: $\Delta\beta_c \equiv (\beta_c^{kin} - \beta_c)/\beta_c$ vs. η_i for two different values of ϵ_c.

5. Kinetic stabilization in TJ-II

We have estimated the main kinetic parameters for TJ-II plasmas heated with ECRH or NBI on the surface of interest (Table 1) [5]. Kinetic effects are expected to be larger in NBI plasmas, since the ion inertia and pressure are higher. ϵ_c is then sufficiently large to provide a relative enhancement of β_c of approximately 1%. Most unstable modes are found previous to $m_u \simeq 40 - 70$, since for $m \gg m_u$ modes are stabilized by ion inertia and for $m \ll m_u$ by the excitation of parallel sound waves. This situation can nevertheless be changed if collisions are included, specially in NBI plasmas. An study to validate these results in the presence of collisions is under way.

	ECRH	NBI (2MW)	NBI (4MW)
$\delta\omega_*$	$1.3 \cdot 10^{-3}$	$8.6 \cdot 10^{-3}$	$1.5 \cdot 10^{-2}$
τ	4	1	1
η_i	0.69	0.59	0.52
η_e	0.87	0.59	0.52
m_u	500	70	40

Table 1: Kinetic parameters relevant to the outer surfaces of TJ-II

References

[1] Sánchez, R. et al (accepted for publ. in **Nuclear Fusion**, 1997)

[2] Alejaldre, C. et al, Fus.Tech. **17** (1990) 31

[3] Tang, W.M. et al, Nucl.Fus. **20** (1980) 1439

[4] Chu, M.S. et al, Phys.Rev.Lett. **41** (1978) 247

[5] Guasp, J., et al, EUR-CIEMAT 30 (Proc.10th Int.Conf.Stell., Madrid), (1995) 322

Solving Threedimensional Plasma Equilibria with a Neural Network Technique

B.Ph. van Milligen, J.A. Jiménez and V. Tribaldos
Asociación EURATOM-CIEMAT para Fusión,
Avda. Complutense 22, 28040 Madrid, Spain

Abstract

A new method to solve differential equations, based on neural networks, has been developed recently. The method is generally applicable to n^{th} order partial differential equations on a finite domain with boundary conditions [1]. The method avoids the use of finite differences since all derivatives are programmed explicitly. The use of a neural network guarantees a compact representation of any type of multivariate continuous solution [2, 3]. Due to this compact representation (using a low number of free parameters), and due to the fact that the minimizing process involved can be entirely formulated using analytic derivatives and these can be evaluated using a highly parallel algorithm, the technique is potentially fast, especially for problems that have to be solved repeatedly with similar boundary conditions.

In the present work, the technique is applied to the solution of the 3-D ideal magnetohydrodynamic (MHD) plasma equilibrium problem. A torsatron has been chosen for the first 3-D equilibria computed.

1. Introduction

We apply a recently introduced method for the solution of differential equations [1], based on MLP-1 type neural networks, to the solution of stellarator equilibria [4]. The method consists in representing the solution to the differential equation (i.e. some spatial potentials whose derivatives give the magnetic field) by a neural network mapping. The differential equation is solved in real space. All derivatives required are taken analytically, and the learning algorithm is intrinsically parallel. Therefore the method shows potential for the development of fast equilibrium codes.

2. Magnetic field representation

We will solve the ideal magnetohydrodynamic equilibrium problem, given by $\vec{j} \times \vec{B} = \vec{\nabla} p$. The often used representation of the magnetic field (Clebsch-Gordon):

$$\vec{B} = \vec{\nabla}\psi \times \vec{\nabla}\chi \tag{1}$$

is not directly applicable when we wish to solve magnetic equilibria by means of a neural network representation of the scalar potentials, because one of the potentials is multivalued. Neural networks cannot handle such quantities, since they are one-to-one mappings.

Therefore, we return to Helmholtz's theorem which states that any vector field can be split in a divergence-free and a rotation-free part:

$$\vec{B} = \vec{\nabla}\psi \times \vec{\nabla}\chi + \vec{\nabla}\xi \tag{2}$$

where $\nabla^2\xi = 0$ since the field is divergence-free.

The choice $\xi = $ const. that leads to the Clebsch-Gordon representation is only one of an infinity of possible "gauges". We may therefore choose another "gauge" that allows us to eliminate the multivaluedness of the potentials in the plasma region. We select precisely the potential ξ that reproduces the magnetic field on the axis (i.e. $\vec{B}\big|_{ax} = \vec{\nabla}\xi$). Additionally, we require that ψ be a flux function, or: $\vec{\nabla}\psi \cdot \vec{\nabla}\xi = 0$.

3. Programmatic details

The scalar potentials are represented by a MLP-1 neural network: its inputs are the spatial coordinates (R,ϕ,Z); its outputs are the three scalar potentials $\{\psi, \chi, \xi\}$ of Section 2.

The deviation from zero of the differential equation, at a number of points in the plasma interior, as well as the deviation of the boundary conditions, at some points on the boundary, are used to define a penalty functional, E, which is minimized using an advanced gradient-descent algorithm by varying the neural network weights. This procedure is described in [1, 4]. Here we only wish to stress that the algorithm for calculating the penalty functional and its gradients is *highly parallel* (more than 97%), and important speedups are expected on massively parallel computers.

4. An equilibrium of the TJ-IU torsatron

In this section, we describe the results obtained for a low-β equilibrium of the Spanish TJ-IU torsatron ($l = 1$, m = 6, major radius $R_0 = 0.6$ m, average minor radius $<a> = 0.1$ m, toroidal field $B_T = 0.5$ - 0.67 T).

First, we wished to ascertain that the representation we use is capable of reproducing the magnetic field and pressure corresponding to this equilibrium. In previous publications, we have already shown how the magnetic flux of such equilibria can be fitted [5, 6]. The equilibrium code VMEC [7] was used to produce a data file containing the magnetic field and plasma pressure for a given equilibrium on a regular grid ($N = 8500$ data points over one period; $0 \le \phi < \pi/3$). We then trained the network to reproduce the magnetic field and the pressure, p. The penalty functional E to be minimized consists of two terms:

$$E = \gamma_1 \sum_{n=1}^{N}\left[\vec{B} - \vec{B}_{exact}\right]^2 + \gamma_2 \sum_{n=1}^{N}\left[p - p_{exact}\right]^2, \tag{3}$$

which are evaluated in the plasma region, Ω. The two weighting factors γ_i are chosen such that both terms contribute in about the same amount to E. To relate the pressure to the scalar potentials, we used the expression

$$p = p(\psi) = 1.5 \cdot 10^{-2}(10^{-2} - \psi). \tag{4}$$

Table I gives the result of the training procedure for each of the field components and the pressure for networks with $K = 63$, 127 and 255 hidden nodes, respectively.

The errors in the magnetic field and the pressure are reasonable (of the order of or below 1%). We conclude that it is possible to represent the field of a typical torsatron equilibrium with a neural network.

Table I

Quantity	Average	Spread	Error (K=63)	Error (K=127)	Error (K=255)
Iterations			5000	7000	13000
B_R	0.000362	0.103	0.00159	0.000851	0.000651
B_ϕ	0.521	0.108	0.00136	0.000713	0.000494
B_Z	0.00857	0.118	0.00188	0.000864	0.000620
p	$7.44 \cdot 10^{-5}$	$4.34 \cdot 10^{-5}$	$0.119 \cdot 10^{-5}$	$0.0639 \cdot 10^{-5}$	$0.0508 \cdot 10^{-5}$
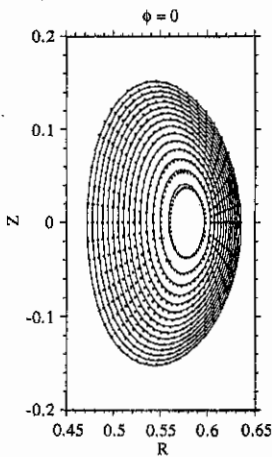
Fig. 1 - The ψ-surfaces of a low-β equilibrium of the TJ-IU stellarator at $\phi = 0°$. Dots indicate the position of the flux surfaces as calculated by VMEC, and lines indicate the flux surfaces calculated by a neural network differential equation solver.

We then solved the equilibrium by the method described in [1, 4]. Initial network weights were taken randomly. The boundary surface ($\partial\Omega$) was specified on a 48×12 equidistant (in VMEC co-ordinates) grid in the toroidal angle ϕ and the poloidal angle θ ($N_{bound} = 576$). The internal points of the region Ω were selected with ϕ again in the range $0 \leq \phi \leq \pi/3$, their total number being $N = 4250$. Finally, the pressure was specified on a chord of 150 points at $\phi = 0$ and again at $\phi = \pi/3$ due to stellarator symmetry. The pressure profile was the one given in Eq. (4). The total toroidal flux was set at $\Phi_0 = 1.99 \cdot 10^{-2}$ T m^2 and the net toroidal current was kept equal to zero. The network we used had $K = 127$ hidden nodes.

The calculations converged to a solution with an average RMS force balance error $\sqrt{\langle |\varepsilon|^2 \rangle}$ of 8.5% (where $|\varepsilon| = |\vec{j} \times \vec{B} - \vec{\nabla}p| / |\vec{\nabla}p|$). Fig. 1 shows the ψ-surfaces of the equilibrium at $\phi = 0°$, compared with results from VMEC. There is a significant difference with the VMEC results, which is not surprising at error levels as high as this. Fig. 2 shows the spatial distribution of the force balance error $|\varepsilon|$, while Fig. 3 shows its numerator. Observe that the force balance (i.e. $|\vec{j} \times \vec{B} - \vec{\nabla}p|$) does not show a maximum at the magnetic axis, due to the fact that the chosen magnetic field representation does not have a singularity there.

5   Conclusions

In this paper we have shown that the three-dimensional plasma equilibrium problem can in principle be solved by the method of solving differential equations with the aid of a neural network. To do so, we first introduced a new representation for the magnetic field, which differs from the usual Clebsch-Gordon representation by a choice of gauge, and in which the scalar potentials are not multivalued. The magnetic field is represented by three instead of two scalar potentials.
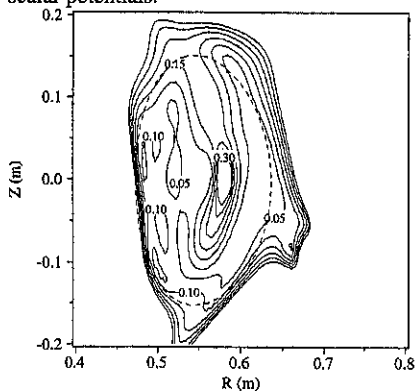
Fig. 2 - *The force balance error* $|\varepsilon|$ *at* $\phi = 0°$.   Fig. 3 - *The force balance at* $\phi = 0°$.
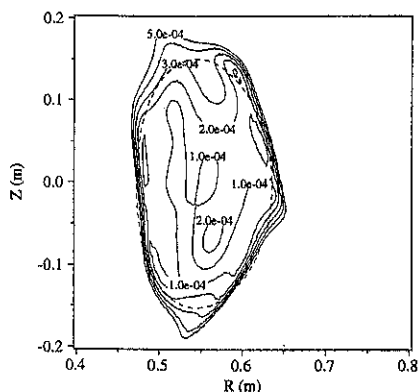
The use of a neural network to represent the scalar potentials is shown to provide reasonable accuracy in both the magnetic field and the pressure. That is to say, reasonable for the purposes of e.g. experimental data interpretation; for the purposes of the calculation of Poincaré sections (by following field lines) or stability limits, the accuracy achieved here is in general not sufficient. However, there is no limit *in principle* on the accuracy that can be reached - only a practical limit in terms of calculation time.

Finally we emphasize that, independently of the actual representation used, equilibrium solvers based on this neural network technique are by nature parallel, and large acceleration factors are to be expected on highly parallel computers.

References

[1]   B.Ph. van Milligen, V. Tribaldos, J.A. Jiménez, Phys. Rev. Lett. **75**, 3594 (1995)

[2]   K. Hornick, Neural Networks **4**, 251 (1991)

[3]   K. Funahashi, Neural Networks **2** (3), 183 (1989)

[4]   B.Ph. van Milligen, J.A. Jiménez and V. Tribaldos, *Solving differential equations using a neural network: Application to three-dimensional plasma equilibria*, Submitted to J. Comput. Physics (1997)

[5]   V. Tribaldos, B.Ph. van Milligen, Nucl. Fusion **36**, 283 (1996)

[6]   V. Tribaldos and B.Ph. van Milligen, Rev. Sci. Instrum. **68**, 931 (1997)

[7]   S. P. Hirshman and D.K. Lee, Comp. Phys. Comm. **39**, 161 (1986)

ECRH PLASMA BREAKDOWN STUDIES IN TJI-U TORSATRON

A.Cappa and F.Castejón

Asociación EURATOM/CIEMAT para fusión.

Av. Complutense, 22 - 28040 Madrid.Spain

It is well known that microwaves at twice the electron cyclotron frequency can produce neutral gas ionization if appropiate initial conditions are fulfilled. This process can be understood considering the nonlinear interaction between the wave and the electrons trapped in local magnetic minima where resonance has been tuned. If there are no external decorrelation mechanisms, as collisions with other particles, electrons can undergo perpendicular energy excursions with amplitude E_{exc} and frequency f_{exc} [1,2] where:

$$E_{exc} \cong 0.3 \frac{|E_-|}{f} \quad eV \tag{1a}$$

$$f_{exc} \cong 75 |E_-| \quad s^{-1} \tag{1b}$$

$|E_-|$ is the modulus of the right-hand circularly polarized electric field in V/m [3] and f is the wave frequency in GHz. The electrons accelerated by the wave will produce new electrons when colliding with neutrals and breakdown is therefore possible. In this study four different species - H_2, H_2^+, H, H^+- and six processes involving them are considered:

$$e + H_2 \longrightarrow H_2^+ + 2e \tag{1}$$
$$e + H_2 \longrightarrow 2H + e \tag{2}$$
$$e + H_2 \longrightarrow H + H^+ + 2e \tag{3}$$

$$e + H_2^+ \longrightarrow 2H \tag{4}$$
$$e + H_2^+ \longrightarrow H + H^+ + e \tag{5}$$
$$e + H \longrightarrow H^+ + 2e \tag{6}$$

A polynomial fit for $ln < \sigma v >$, which only depends on electron energy, can be find for each case in ref.[4]. This energy is computed using a simplified kinetic model that divides electron momentum space into three separate regions [2] as shown in Fig.1. A highly non linear system of first order ordinary differential equations can be raised and solved by numerical integration. The solution provides the time evolution of density for the different plasma species and for the different electron groups.

Region 1 contains magnetically trapped electrons strongly interacting with the wave with high perpendicular energy. This energy can be estimated as [2] :

$$E_1 \cong \frac{E_{exc}}{2} \left(\frac{f_{exc}^2}{f_c^2 + f_{exc}^2} \right) \tag{7}$$

The frequency f_c is the sum of the different electron-particle (H_2, H_2^+, H, H^+) collision frequencies. The products $\sigma_T V$ are nearly constant in the energy range given by (1a)

$$f_c = \sigma_{T(e+H_2)}Vn_{H_2} + \sigma_{T(e+H_2^+)}Vn_{H_2^+} + \sigma_{T(e+H)}Vn_H + \sigma_{T(e+H^+)}Vn_{H^+} \tag{8}$$

The cold group-3-electrons existing in the vacuum vessel before the ECRH discharge act as a seed. Once the microwaves are injected they become trapped (enter region 1) in a time roughly equal to $1/f_{trap}$ [2] and start to gain energy by its interaction with the wave. When a collision occurs, interaction is stopped. For all processes with energy E_1, except (1.4), the original electron appears in region 2 with energy E_2 and can collide again many times until it lefts region 2 and appears in region 3. In this model we consider that only one collision is necessary to move the electron from region 2 to 3. Through processes (1.1), (2.1), (1.3), (2.3), and (1.6), (2.6) group-1 and group-2-electrons may produce new electrons. Those appear in region 3 due to their low energy. Then the cycle repeats.

Due to the low value of E_3 only reaction (4) is taken into account. Also a group-1-electron can leave region 1 by elastic collision with a proton, only the components of momentum will change. Process (1.0) considers this fact.

The whole set of processes is:

with energy E_1 :		with energy E_2 :	
$e_1 + H_2 \rightarrow H_2^+ + e_2 + e_3$	(1.1)	$e_2 + H_2 \rightarrow H_2^+ + e_3 + e_3$	(2.1)
$e_1 + H_2 \rightarrow 2H + e_2$	(1.2)	$e_2 + H_2 \rightarrow 2H + e_3$	(2.2)
$e_1 + H_2 \rightarrow H + H^+ + e_2 + e_3$	(1.3)	$e_2 + H_2 \rightarrow H + H^+ + e_3 + e_3$	(2.3)
$e_1 + H_2^+ \rightarrow 2H$	(1.4)	$e_2 + H_2^+ \rightarrow 2H$	(2.4)
$e_1 + H_2^+ \rightarrow H + H^+ + e_2$	(1.5)	$e_2 + H_2^+ \rightarrow H + H^+ + e_3$	(2.5)
$e_1 + H \rightarrow H^+ + e_2 + e_3$	(1.6)	$e_2 + H \rightarrow H^+ + e_3 + e_3$	(2.6)
$e_1 + H^+ \rightarrow e_2 + H^+$	(1.0)		

with energy E_3 :

$$e_3 + H_2^+ \rightarrow 2H \tag{3.4} \qquad\qquad \text{and } e_3 \longrightarrow e_1 \tag{9}$$
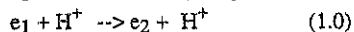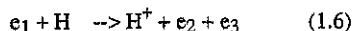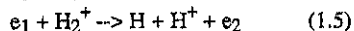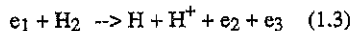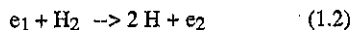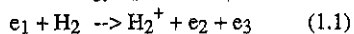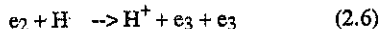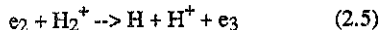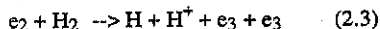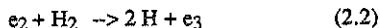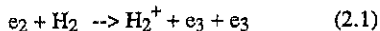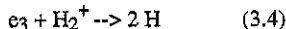
Process (i.j) will occur at a rate c_{ij} ($c_{ij} = <\sigma v>_j$ cm^3 . s^{-1} for a given energy E_i). Electron transport losses from the system can also be considered (an electron e_k will be lost in a time $1/fl_k$). The energy E_2 necessary to calculate the c_{2j} coefficients can be found by averaging the threshold energy plus the energy of reaction products for each particular process and substracting it from the original group 1 electron energy:

$$E_2 = E_1 - <E_l> \quad ; \qquad <E_l> = \frac{(E_{l(1)}c_{11} + E_{l(2)}c_{12} + E_{l(3)}c_{13})n_{H_2} + E_{l(5)}n_{H_2^+} + E_{l(6)}n_H}{(c_{11} + c_{12} + c_{13})n_{H_2} + c_{15}n_{H_2^+} + c_{16}n_H + c_{10}n_{H^+}}$$

(10)

$E_{l(j)}$ is the energy lost in the process j. From ref [4] we find:

$$E_{l(1)} = (15.4 + E_3) \text{ eV} \qquad E_{l(2)} = 16 \text{ eV} \qquad E_{l(3)} = 1.5 \text{ eV}$$
$$E_{l(5)} = 11 \text{ eV} \qquad E_{l(6)} = (13.6 + E_3) \text{ eV} \qquad 0 \text{ eV} < E_3 < 4 \text{ eV}$$

(11)

and

$$\ln c_{ij} = \sum_{k=1}^{9} b_{kj}[\ln(E_i)]^{k-1} \qquad ; \qquad \ln c_{34} = \sum_{k=1}^{9} b_{k4}[\ln(E_3)]^{k-1}$$

(12)

The coefficients b_{kj} used in (12) are listed in ref.[4]. The system of ordinary differential equations that governs the population of the several species is :

$$\dot{n}_{e_1} = f_{trap}n_{e_3} - [(c_{11} + c_{12} + c_{13})n_{H_2} + (c_{14} + c_{15})n_{H_2^+} + c_{16}n_H + c_{10}n_{H^+}]n_{e_1} - fl_1 n_{e_1}$$

$$\dot{n}_{e_2} = [(c_{11} + c_{12} + c_{13})n_{H_2} + c_{15}n_{H_2^+} + c_{16}n_H + c_{10}n_{H^+}]n_{e_1} - fl_2 n_{e_2}$$
$$\quad - [(c_{21} + c_{22} + c_{23})n_{H_2} + (c_{24} + c_{25})n_{H_2^+} + c_{26}n_H]n_{e_2}$$

$$\dot{n}_{e_3} = [(c_{11} + c_{13})n_{H_2} + c_{16}n_H]n_{e_1} + [(2c_{21} + 2c_{23} + c_{22})n_{H_2} + c_{25}n_{H_2^+} + 2c_{26}n_H]n_{e_2}$$
$$\quad - c_{34}n_{H_2^+}n_{e_3} - f_{trap}n_{e_3} - fl_3 n_{e_3}$$

$$\dot{n}_{H_2} = -[(c_{11} + c_{12} + c_{13})n_{e_1} + (c_{21} + c_{22} + c_{23})n_{e_2}]n_{H_2}$$

$$\dot{n}_{H_2^+} = (c_{11}n_{e_1} + c_{21}n_{e_2})n_{H_2} - [(c_{14} + c_{15})n_{e_1} + (c_{24} + c_{25})n_{e_2} + c_{34}n_{e_3}]n_{H_2^+}$$

$$\dot{n}_H = [(2c_{12} + c_{13})n_{e_1} + (2c_{22} + c_{23})n_{e_2}]n_{H_2} + [(2c_{14} + c_{15})n_{e_1} + (2c_{24} + c_{25})n_{e_2}]n_{H_2^+}$$
$$\quad + 2c_{34}n_{H_2^+}n_{e_3} - [c_{16}n_{e_1} + c_{26}n_{e_2}]n_H$$

$$\dot{n}_{H^+} = (c_{13}n_{e_1} + c_{23}n_{e_2})n_{H_2} + (c_{15}n_{e_1} + c_{25}n_{e_2})n_{H_2^+} + [c_{16}n_{e_1} + c_{26}n_{e_2}]n_H$$

(14)

the initial values are:

$$n_{e_1} = n_{e_2} = n_{H_2^+} = n_H = n_{H^+} = 0 \quad ; \quad n_{e_3} = n_{SEED} \quad ; \quad n_{H_2} = n_i$$

(15)

For the calculations we approximate E_3 by a constant value E_{trap} defined in [2]. These calculations have been done for TJI-U [5] parameters (P=200 kW, f=37.5 GHz, R=0.6 m, M=6, l=1, $A_T = 0.2$ m^2, $A_C = 5$ m^2). A_T is the area through which microwaves can leak out of the chamber and A_C is the internal chamber area. Fig.2 shows the time evolution of total electron density for $n_i = 2.5 \times 10^{12}$ cm^{-3} and $n_{SEED} = 100/V$ where V is the plasma volume. Fig.3 shows the H_2, H_2^+, H, H^+ densities for the same initial conditions.

The computed breakdown time for these initial values is $t_{bkd} \cong 2$ ms, which agrees fully with experiments performed at the same conditions. The dependence of this time on initial neutral gas pressure is illustrated in Fig.4 for two different frequencies, 28 and 37.5 GHz.
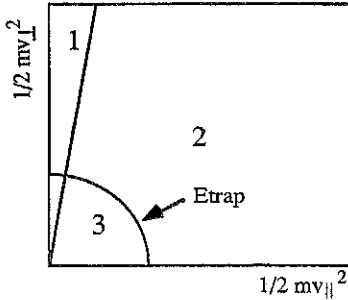
Fig.1. Three group model
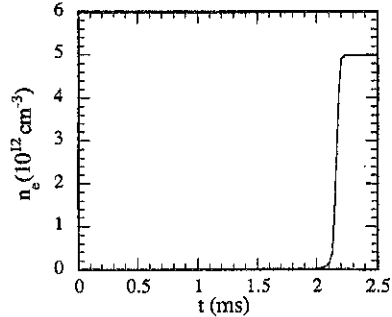
Fig.2. Total electron density
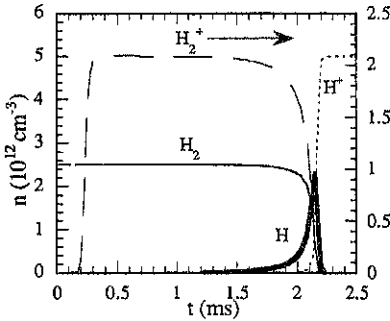
Fig.3. H_2, H_2^+, H, and H^+ densities
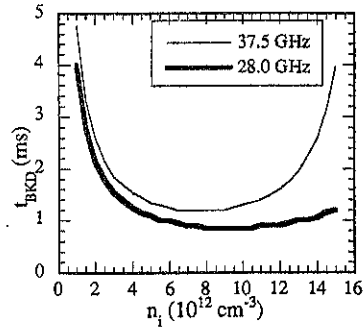
Fig.4. Breakdown time for 37.5 and 28 GHz

As we can see from Fig.4 higher values of n_i can improve breakdown ($t_{bkd} \cong 1.2$ ms for 37.5 GHz) but cut-off density in TJU-I is reached with $n_i \cong 4*10^{12}$ cm^{-3} and makes difficult the comparison with experimental data. Validation of this model in other confinement devices is planned in the near future.

[1] M.D.Carter, J.D.Callen, D.B.Batchelor, R.C.Goldfinger, Phys.Fluids **29**, (1986)100
[2] M.D.Carter, D.B.Batchelor, A.C.England, Nucl.Fusion **27**, (1987) 985
[3] T.L.White, Analysis of Mixed Mode Microwave Distribution Manifolds, Rep.ORNL-TM--8127, (1982)
[4] R.K.Janev, Elementary Processes in Hydrogen-Helium Plasmas, Springer-Verlag, 1987
[5] E.Ascasíbar, et al,Transactions of Fusion Technology **27**, (1995) 198

Kinetic Global Alfvén Modes and Kinetic Flute Modes in a Stellarator with Trapped Energetic Ions

Zh.N.Andrushchenko*, O.K.Cheremnykh*, J.W.Edenstrasser**

*Institute for Nuclear Research, Kiev, Ukraine,

**Institute for Theoretical Physics, Innsbruck, Austria

Introduction   The presence of a non-thermal ion component in both tokamak and stellarator plasmas can give rise to Alfvén-type instabilities. There is a large number of theoretical and experimental studies [1-3] on different Alfvén Eigenmodes in tokamaks. In a stellarator energetic ions can also drive a variety of discrete shear Alfvén Eigenmodes. For low shear stellarators the Global Alfvén Eigenmodes (GAE) appear most likely and have been observed experimentally [4]. The characteristic frequencies of GAE´s are below the minimum of the Alfvén continuum: $\omega < \omega_{A\min}$, where $\omega_A = k_1 v_A$, $k_1 = (m\mu - n) / R$, m and n are the poloidal and toroidal wave numbers, $\mu = 1/q$ is the rotational transform, R is the major radius. The influence of trapped energetic ions on the GAE´s can lead to a new type - Kinetic Global Alfvén Modes (KGAM).

The MHD stability in stellarators is mainly determined by pressure driven modes, which are localized around low order rational magnetic surfaces with the rotational transform $\mu = n/m$, where $k_\| = 0$. In this paper we are primarily interested in flute perturbations, which may occur in low-pressure stellarators. Moreover, in such devices trapped energetic ions can also generate Kinetic Flute Modes (KFM).

Basic equations   The calculations are performed in a „quasi-toroidal" coordinate system with „straightened magnetic field lines"[5]. The equation for small oscillations then reads [1]:

$$\hat{L}X = 0, \tag{1}$$

$$\hat{L} \equiv \frac{1}{a^2}\frac{d}{da}\left(a^3\left(\frac{\omega^2}{v_A^2} - k_\|^2\right)\frac{d}{da}\right) - \frac{m^2}{a}\left(\frac{\omega^2}{v_A^2} - k_1^2\right) + \omega^2\frac{d}{da}\left(\frac{1}{v_A^2}\right), \tag{2}$$

where X is a radial plasma displacement, a is a radial coordinate. The last term is important for the existence of GAE´s. By taking into account the magnetic well in such a stellarator, the application of a multiple space scale approach for the description of low-scale perturbations, then leads to the following modification of Eq.(1):

$$\hat{L}X - WX = 0, \tag{3}$$

$$W \equiv \frac{2P'm^2}{R^2 B_0^2}\left(1 + \mu^2(1 + S) - \frac{\mu J'}{2\pi B_0}\frac{R}{a} - \frac{RB_0^2 V_0''}{2} - \frac{a\mu_\nu'' + 3\mu_\nu'}{2}\frac{R\Delta}{a}\right), \tag{4}$$

where P is the plasma pressure, B_0 and J are the toroidal magnetic field and the toroidal current, V_0'' is the vacuum magnetic well, μ_v is the vacuum rotational transform, $S = a\mu'/\mu$ is the shear, and Δ is the Shafranov shift, where the prime denotes the derivative with respect to the radial coordinate.

In our model the contribution of energetic ions is described by the equation:

$$\hat{L}X - WX - Q = 0, \tag{5}$$

$$Q \equiv \frac{2im}{aRB_0^2}\left(\frac{\partial \delta P}{\partial \theta}\cos\theta + a\frac{\partial \delta P}{\partial a}\sin\theta\right), \tag{6}$$

where $\delta P = \delta P(X)$ is the perturbed particle pressure, obtained by the application of a multiple time-scale approach, and θ is a poloidal angle.

Spectrum of GAE´s and Kinetic Global Alfvén Modes. First we omit for simplicity the influence of energetic particles and investigate the spectrum of the GAE´s. We start with Eq.(3) and expand ω_A^2 around the surface $a = a_0$, on which ω_A^2 attains its minimum value. With the help of the notations:

$$x = a - a_0, \quad L^2 = 2\omega_A^2/(\omega_A^2)'', \quad \Delta^2 = 2(\omega_A^2 - \omega^2)/(\omega_A^2)'', \quad \xi = x/\Delta, \quad \varphi = X, \tag{7}$$

we can represent Eq.(3) in the form:

$$\frac{d}{d\xi}\left((1+\xi^2)\frac{d\varphi}{d\xi}\right) + G\varphi - \Gamma^2(1+\xi^2)\varphi = 0, \tag{8}$$

together with the boundary condition $\varphi(\xi \to \pm\infty) = 0$ and where G and Γ are defined by

$$G \equiv L^2\left(-\frac{2Sm}{a_0^2 k_1 R} + \frac{1}{a_0 k_1^2}W\right), \quad \Gamma \equiv \frac{m\Delta}{a_0}. \tag{9}$$

The condition for the existence of GAE´s is then given by the inequality

$$E \equiv G - 1/4 > 0. \tag{10}$$

Following [6], the frequencies in the vicinity of the continuous spectrum are found to be:

$$\omega_1^2 = \omega_A^2\left(1 - \frac{a_0^2}{m^2 L^2}E^2 f_1\right), \quad f_1 = \frac{2^4}{e^2}\exp\left(-\frac{(n+1/2)\pi}{\sqrt{E}} - \frac{1}{2E}\right), \tag{11}$$

if $\quad \dfrac{2Sm}{k_\parallel R} > \dfrac{a_0^2}{k_\parallel^2}W - \dfrac{a_0^2}{2L^2} - \dfrac{m^2\Delta^2}{L^2}, \quad$ and

$$\omega_2^2 = \omega_A^2\left(1 - \frac{a_0^2}{m^2 L^2}Ef_2\right), \quad f_2 = \frac{2^6}{e^4}\exp\left(-\frac{(2n+1)\pi}{\sqrt{E}}\right), \tag{12}$$

if $\quad \dfrac{2Sm}{k_\parallel R} > \dfrac{a_0^2}{k_\parallel^2}W - \dfrac{a_0^2}{4L^2} - \dfrac{m\Delta a_0}{L^2}.$

Let us now consider the influence of energetic ions on GAE´s in a stellarator. The accurate calculations of the contribution of trapped particles leads us to the equations:

$$\frac{d}{d\xi}\left(\left(1+\xi^2\right)\frac{d\varphi}{d\xi}\right)+\left(G-\Delta_t\right)\!\varphi-\Gamma^2\!\left(1+\xi^2\right)\!\varphi=0, \tag{13}$$

$$\Delta_t = \Delta_t^0 + \Delta_t^\omega, \tag{14}$$

$$\Delta_t^0 = -A\int_{1-\varepsilon}^{1+\varepsilon}d(\alpha B)\int_0^\infty\frac{m}{a\omega_b\omega_D}\frac{\partial F}{\partial a}\frac{K_2^2}{K_b}E^{5/2}dE, \tag{15}$$

$$\Delta_t^\omega = A\int_{1-\varepsilon}^{1+\varepsilon}d(\alpha B)\int_0^\infty\frac{\omega}{\omega-\omega_b}\left(\frac{\partial F}{\partial E}+\frac{m}{a\omega_b\omega_D}\frac{\partial F}{\partial a}\right)\frac{K_2^2}{K_b}E^{5/2}dE. \tag{16}$$

Here F and E are the equilibrium distribution function of the energetic particles and their energy per unit mass, K_2 and K_b are the full elliptical integrals of I and II kinds, $\varepsilon = a/R, \alpha = \eta/E$, η is the magnetic moment, ω_b is the ion cyclotron frequency, ω_D is the averaged bounce frequency of the energetic particles,

$$\omega_D = \frac{Em}{a\omega_b R}\overline{\cos\theta}, \quad \overline{(...)} = \oint(...)d\theta/v_1\Big/\oint d\theta/v_1, \quad A = \frac{Mm^2L^2\pi\sqrt{2}}{a_0^2R^2k^2B_0^2}, \tag{17}$$

M is the mass of an energetic particle and $v_\|$ its parallel velocity. Thus, the inclusion of the trapped particles mainly results in a renormalization of the magnetic well: $G \to G - \Delta_t^0$. Consequently, the requirement for the existence of GAE's is written as $G - \Delta_t^0 - 1/4 > 0$. For energetic ions with a distribution function close to a Maxwellian one, the following expressions for the growth rates of GAE's are obtained:

$$\frac{\gamma_1}{\omega_1} = \frac{\beta_\alpha}{4R^2k^2}\left(\frac{\omega}{\omega_D}\right)^{5/2}\left(\frac{\omega}{\omega_D}+R\!\left(\kappa-\frac{1}{2a}\right)\right)\exp\!\left(-\frac{\omega}{\omega_D}\right)\frac{\pi}{\gamma(3/2,1)}Ef_1, \tag{18}$$

$$\frac{\gamma_2}{\omega_2} = \frac{\beta_\alpha}{4R^2k^2}\left(\frac{\omega}{\omega_D}\right)^{5/2}\left(\frac{\omega}{\omega_D}+R\!\left(\kappa-\frac{1}{2a}\right)\right)\exp\!\left(-\frac{\omega}{\omega_D}\right)\frac{\pi}{\gamma(3/2,1)}f_2, \tag{19}$$

where $\beta_\alpha = 8\pi n_\alpha T_\alpha/B_0^2$, $\kappa = -d\ln P/da$, $\gamma(3/2,1) = \int_0^1 x^{1/2}\exp(-x)dx$, and where ω_1, f_1 and ω_2, f_2 are given by Eqs.(11)-(12). Thus, in a stellarator trapped energetic ions can either stabilize or destabilize GAE modes, depending on the plasma and device parameters, in other words, can generate Kinetic Global Alfvén Modes.

Kinetic Flute Modes. It is well known, that the unstable flute modes change into stable drift flute modes, if the stabilizing effect of the finite ion Larmor radius is taken into account. In order to include also drift effects in our equation for small oscillations (3) we replace ω^2 by

$$-\gamma_{MHD}^2 = \omega\!\left(\omega-\omega_{*i}\right), \tag{20}$$

where ω_{*i} is the ion drift frequency. If we expand Eq.(3) into a series around the resonance surface $a = a_0$, then formally Eq.(8) is recovered, if ξ, G and Γ are identified as:

$$\xi \equiv \frac{k_s a_0}{m}, \quad G \equiv \frac{R^2}{a_0 m^2 \mu'^2} W, \quad \Gamma \equiv \frac{\gamma_{MHD} R}{a_0 \mu' v_A}. \tag{21}$$

The actual calculations of the contribution of toroidally trapped energetic ions to Eq.(8) formally result in Eqs.(13)-(16), if we replace A by $A = 2^{5/2} M(\pi q/B_0 S)^2$. We now conclude that the inclusion of trapped particles leads to a deeping of the magnetic well, thus improving the stability. If for a given set of plasma parameters the inequality $\gamma_{MHD} \leq \omega_{*i}/2$ is satisfied, then a Kinetic Flute Mode exists (Fig.1), where the characteristic growth rate is given by:

$$\gamma \approx \frac{\rho_h}{\rho_0} \frac{v_{Ti}^2}{R^2 \omega_D}, \tag{22}$$

ρ_h and ρ_0 are the dencities of the energetic particles and of the main plasma component.
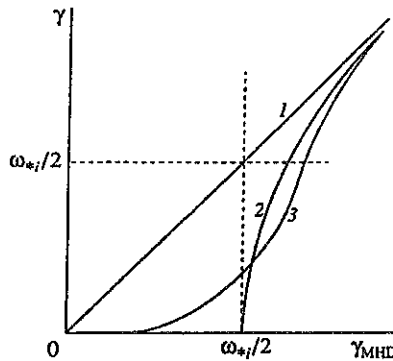
Fig.1. A dependence of the growth rate (γ) on parameters of both the plasma and a confinement system:
(1) $\omega_{*i} = \Delta_t = 0$; (2) $\omega_{*i} \neq 0, \Delta_t = 0$; (3) $\omega_{*i} \neq 0, \Delta_t \neq 0$.

References
1. Y.M.Li, S.M.Mahajan, D.W.Ross, *Phys.Fluids*, **30**, 1466 (1987).
2. G.F.Fu, J.W.Van Dam, *Phys.Fluids* **B1**, 1949 (1989).
3. K.L.Wong, R.J.Fonck, S.F.Paul *et al.*, *Phys.Rev.Lett.*, **66**, 1874 (1991).
4. A.Weller, D.A.Spong, R.Jaenicke *et al.*, *Phys.Rev.Lett.*, **72**, 1220 (1994).
5. V.D.Pustovitov, B.D.Shafranov, Reviews of Plasma Physics, B.B.Kadomtsev, Ed., Moscow, Energoatomizdat, 1987, No. 15, p. 146.
6. O.K.Cheremnykh, S.M.Revenchuk, *Plasma Phys. and Contr. Fusion*, **34**, 55 (1992).

Two Problems of the Plasma Confinement in Stellarators

M.I. Mikhailov, V.D. Shafranov, A.A. Subbotin, D. Sunder*

Russian Research Centre "Kurchatov Institute", 123182, Moscow, Russia
* Max-Plank-Institut für Plasmaphysik, Bereich Berlin, Germany

Introduction

Two questions are considered in present paper. 1. A new approach to improve the plasma confinement in stellarators is discussed. We analyze here an idea to eliminate the locally-trapped particles by excluding the local extremes of the magnetic field strength B on the magnetic surfaces. In such stellarators there exists straight field line flux coordinate system a, θ, ζ in which $B = B(a, \theta)$ or $B = B(a, \zeta)$. 2. An attempt is done to elucidate the reason of the "local ballooning mode" instability, which restricts strongly the β limit in stellarators. Considering the conventional stellarators in the frame of the stellarator expansion we show that such instability can be explained by the effect of $3D$ geometry of the magnetic surfaces without taking into account three dimensional helical secondary currents.

1. Symmetric-like topology of $B = $ const lines on magnetic surfaces

Dependence of the magnetic field strength B on magnetic surface on two angle variables strongly effects on the drift trajectories of charged particles and the neoclassical transport. In the symmetric systems the lines $B = $ const on magnetic surfaces coincide with the direction of symmetry. In 3D closed systems toroidal effect leads to appearance of the additional inhomogeneity of B, so that in general case the part of the lines $B = $ const form islands on the magnetic surfaces. This leads to appearance of locally-trapped particles with orbits having large radial excursion which increase the neoclassical transport. Some different ways to eliminate such orbits were considered in [1-3]. Here we propose in some aspects more clear requirement similar to the quasisymmetry (QS) condition, but less restrictive one.

The QS condition $B = B(a, \theta_B)$, where a, θ_B, ζ_B are the Boozer flux coordinates, restores the $B = $ const lines behavior like that of the symmetric systems, and excludes the transport enhancement due to symmetry violation. It is known however, that the QS condition can't be satisfied in the whole plasma volume. To obtain reliable system one can try to use more weaker condition which nevertheless will remain the plasma transport coefficients significantly smaller then in conventional stellarators. One can see that the condition of locally-trapped orbits elimination is almost equivalent to the condition of elimination of the islands of lines $B = $ const on magnetic surfaces and can be formulated as

$$B = B(a, \theta), \tag{1}$$

where a, θ, ζ is the straight magnetic field lines flux coordinate system. We call such systems as "normal" ones [4].

To clear up the additional freedom in the parameters choice of the normal systems in comparison with the QS ones let's use the method of expansion on the distance from the magnetic axis. The expression for B in Boozer coordinates can be written as [5]

$$B = B_0(1 + a(C_{11c}\cos\theta_B + C_{11s}\sin\theta_B) + a^2(C_{20} + C_{22c}\cos 2\theta_B + C_{22s}\sin 2\theta_B) + ...) . \tag{2}$$

Here in general case all the coefficients C are the functions of longitudinal coordinate. As the QS condition requires all the coefficients to be const, the number of conditions grows faster then the number of available free parameters. This is the reason of the

impossibility to fulfill the QS condition in all powers of expansion. The transition to new poloidal variable

$$\theta_B = \theta + \eta_{00} + a(\eta_{11c}\cos\theta + \eta_{11s}\sin\theta) + a^2(\eta_{20} + \eta_{22c}\cos 2\theta + \eta_{22s}\sin 2\theta) + ... \quad (3)$$

leaves the structure of the expression (2) for B just the same, while the additional free parameters η_{ik} appear. The number of free parameters is now not smaller then the number of the conditions following from Eq. (1) and equilibrium condition. This situation is conserved in higher power terms. So, at least formally the existing of the normal configurations is not forbidden.

To demonstrate the difference in the freedom of the parameters choice in QS and normal configurations let's consider these conditions in first approximation on a. The linear term in B is proportional to the curvature and can be written as $aB_0(C_1\cos\theta_B + C_2\sin\theta_B)$, where $C_{1,2}$ are explicit functions on elongation and orientation of the near-axis elliptical cross-sections [6]. The QS condition requires $C_{1,2} = $ const while the condition of normality requires $C_1^2 + C_2^2 = $ const only. Thus, an additional freedom arises which may be used to increase the plasma stability pressure limit.

Another kind of normal systems, when B is independent on poloidal angle,

$$B = B(a, \zeta), \quad (4)$$

could be considered too. Corresponding condition of QS, $B = B(a, \zeta_B)$, can be fulfilled in straight unclosed systems only. Such a systems are called "isodynamic" ones [7]. In contrast to the QS condition, the condition of normality (4) can be satisfied in closed systems. It can be easily demonstrated in linear on a approximation, when $B = B_0(\zeta_B)(1 + akC\cos\theta_B)$. Here C is a known function of ζ_B. Transition to new toroidal variable $\zeta_B = \zeta + a\gamma\cos\theta_B$ allows to eliminate term with $\cos\theta_B$ at $kCB_0(\zeta) + \gamma\,\partial B_0/\partial\zeta = 0$. This means that curvature should be zero at B-extreme cuts. In some special case, $B_0 = B_{00}(1 + \delta B\cos N\zeta)$, $k = k_0(1 - \cos 2N\zeta)$ we get $\gamma = 2k_0C(\zeta)\sin N\zeta/(NB_{00}\delta B)$, so that $\gamma = 0$ (no difference between ζ and ζ_B) in cuts of B-extremes, like in "quasi-isodynamic" systems [2].

2. Ballooning modes in high-β conventional stellarators

Numerical calculations of the ballooning modes stability show that very localized in the extended poloidal angle domain disturbances [8] can restrict the plasma pressure. As these modes was not found in $2D$ approximation for conventional stellarator and for tokamak, one can believe that two causes of instability are possible: one is the $3D$ helical currents which are not taken into account in $2D$ approach and another one is the $3D$ geometry of the magnetic surfaces itself.

Two dimensional description of equilibrium in "stellarator approximation" gives a possibility to study the effect of $3D$ geometry of the magnetic surfaces without taking into account the helical secondary currents.

We have used an analytical description for vacuum magnetic configuration and simple Sigmar-Clark model for $2D$ relations between the vacuum and the plasma flux coordinates. Three-dimensional metric coefficients of the flux coordinate system of configuration with plasma were used then in the ballooning modes equation. The results show that the localized modes are found to be unstable in the used approximation. It means that the geometrical effect plays an important role in the local ballooning instability.

Two typical cases of unstable modes are demonstrated in Figs. 1,2. Here, the functions A_0, A_1, and f are presented for two different values of plasma radius and initial values of longitudinal coordinate. The initial value of poloidal coordinate is taken equal to

zero (outwards part of the column). The functions A_0 and A_1 are the coefficients of the ballooning modes equation $\partial(A_0\partial f/\partial\theta)/\partial\theta + A_1 f = 0$, and the function $U(\theta)$ is the potential in corresponding Schrödinger-type equation. Calculations were fulfilled with the parameters that roughly approximate ATF stellarator ($\epsilon = 0.33$, $A = 7.78$, $N = 12$) by single helical harmonic. The relative plasma pressure profile is given by $p = p_0 + p_1 a^2 + p_2 a^4 + p_3 a^6$ with $p_0 = 0.03$, $p_1 = 0$, $p_2 = -0.09$, $p_3 = 0.06$. The value of the magnetic axis shift equals to $\Delta(0) = 0.484$, and the maximum value of $\Delta'(a)$ is equal to -0.78.

One can give the next interpretation of the results. Two effects became important when plasma pressure increases. Both of them are connected with the increase of $\Delta'(a)$. Due to this effect the slope of the magnetic field line increases locally in the outer part of the column, especially in the vertically elongated cross-sections. The increase of the magnetic field line slope leads to increasing of the poloidal coordinate θ interval which correspond to one period on ζ. The sign of the magnetic field line curvature in the outer part ($\theta = 0$) of the column becomes negative for all values of ζ in opposite to the vacuum or small plasma pressure cases. The presence of the regions with large values of $|\nabla a|^2$ (small value of A_0) in every period gives a possibility to decrease the value of the disturbance abrupt without large increase of the energy variation. If the regions with large negative curvature take place in configuration too, the possibility arises for instability of modes which are localized in this regions and are diminishing in the regions of large $|\nabla a|^2$, if the local shear is not very large.

Conclusions. 1) The new approach is suggested for stellarator improvement by elimination of local extremes of magnetic field strength (the lines $B = $ const do not form the islands) on magnetic surfaces. The existing of such "normal" 3D magnetic configurations have been demonstrated.

The condition of normality is weaker then that of the quasisymmetry, and one can hope that the additional freedom in the parameters choice will permit to increase the plasma pressure limit on stability.

2) An appearance of the very localized along magnetic field lines ballooning modes in conventional stellarator is elucidated. It is shown that the geometrical effects play the important role in such modes of instability.

[1] Mynick H.E., Chu T.K., and Boozer A.H. Phys. Rev. Lett. 48 (1982) 322.

[2] Gori S., Lotz W., Nührenberg J. Theory of Fusion Plasmas, SIF, Bologna, 1996, Ed. by J.W. Connor, E. Sindoni and J. Vaclavik, p. 335.

[3] Carry J.R., Shasharina S.G. Phys. Rev. Lett. (1997)

[4] Shafranov V.D., Skovoroda A.A. Plasma Phys. Reports 21 (1995) 937., Isaev M.Yu., Mikhailov M.I., Shafranov V.D. Plasma Phys. Reports 20 (1994) 319.

[5] Garren D.A., Boozer A.H. Phys. Fluids B 3 (1991) 2805.

[6] Isaev M.Yu., Shafranov V.D. Sov. Journ. of Plasma Phys 16 (1990) 419.

[7] Palumbo D. Nuov. Cimento B 53 (1968) 507.

[8] W. Cooper, S. Hirshman, D Lee, Nucl. Fusion 29 (1989) 617.
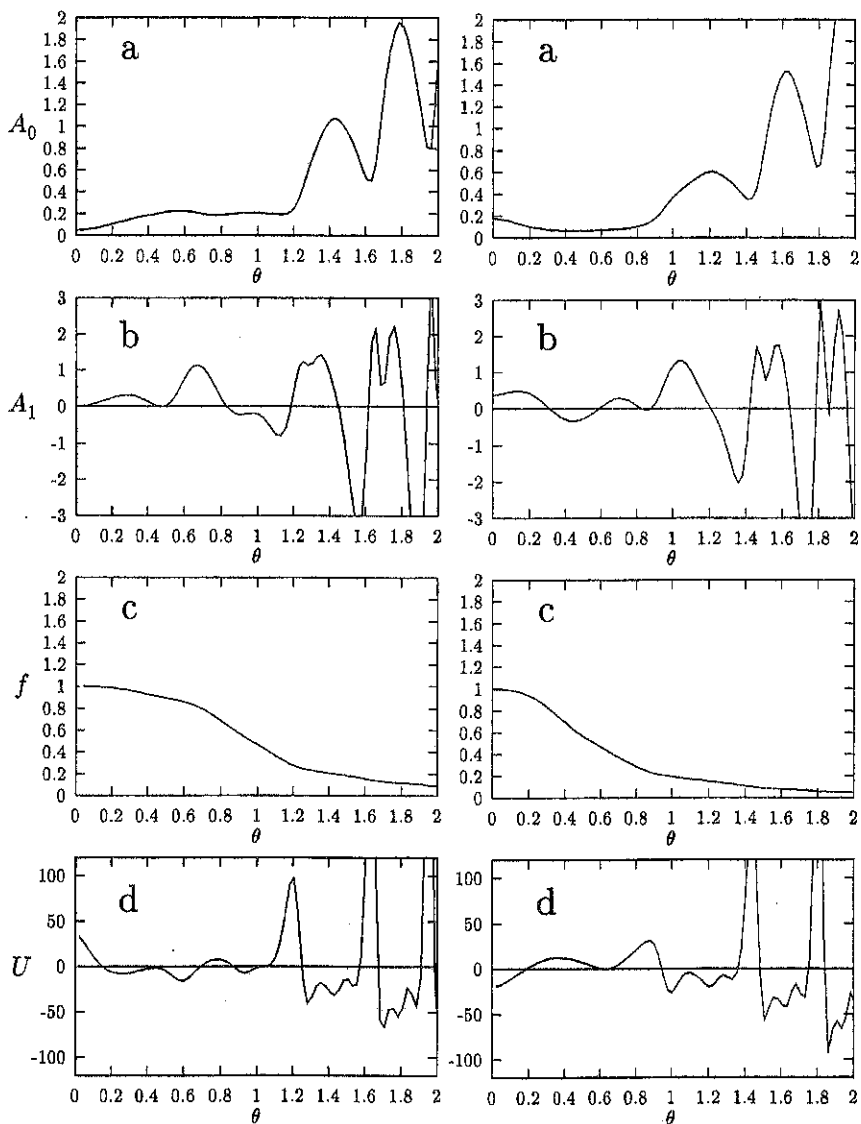
Fig. 1. The coefficients A_0 and A_1 of the ballooning mode equation and the eigenfunction f for plasma radius $a = 0.95$, and for initial point on outwards part of vertically oriented ellipse. The dependence of potential U on poloidal coordinate θ along the magnetic field line is shown also. The mode is unstable.

Fig. 2. The same as in Fig. 1, but for $a = 0.9$, and for initial point on outwards part of horizontally oriented ellipse. The mode is unstable.

Few Period Quasisymmetric Stellarators

M.Yu. Isaev, W.A. Cooper*, S.Yu. Medvedev+, M.I. Mikhailov,
V.D. Shafranov, **A.A. Subbotin**

Russian Research Centre "Kurchatov Institute", 123182, Moscow, Russia
* Centre de Recherches en Physique des Plasmas, Association Euratom-Confederation Suisse,
Ecole Polytechnique Federale de Lausanne
+ Keldysh Institute of Applied Mathematics, Russian Academy of Sciences, Moscow

1. Introduction

The results of plasma equilibrium and local stability investigations in two and four-period quasisymmetric stellarators are presented. A near-axis approximation is used for 2-period systems and the 3D codes VMEC and TERPSICHORE are used for four-periods devices to optimise the configurations.

2. Four-period Heliac-like configurations

In this Section, the results of the partial optimisation of four-period Heliac-like magnetic configurations by plasma boundary control are presented. We use the term "Heliac-like" configuration for systems in which the magnetic surface cross-section rotates in phase with the principal normal with respect to the magnetic axis, $n_1 = 0$. Here n_1 constitutes the number of elliptical near-axis magnetic surfaces cross-sections turns relative the principal normal to the magnetic axis in one field period. Helias-like configuration such as the well-known WVII-X have $n_1 = -1/2$.

We look for the shape of the plasma boundary for which the Mercier $< \beta >$ limit is maximal and the accuracy of fulfilling the quasisymmetry (QS) condition is moderate, $X \approx 3$. Here X is the ratio of dominant helical Fourier component of the magnetic field strength in Boozer coordinates to the maximal Fourier component that violates the symmetry evaluated at the plasma boundary.

The plasma boundary surface obtained from the QS condition in the near-axis approximation, Ref. [1], was used here as the initial guess. After optimisation of the plasma boundary with the VMEC and TERPSICHORE codes to increase the $< \beta >$ limit with respect to Mercier mode stability, we have found the configuration with the following boundary Fourier spectrum:

MB	NB	RBC	ZBS
0	0	9.9520E-00	0.0000E+00
0	1	2.3600E-00	-2.1200E-00
0	2	1.5000E-01	-1.5000E-01
1	0	6.5000E-01	7.3000E-01
1	1	-7.0000E-02	7.0000E-02
1	2	-2.9300E-01	2.6500E-01
1	3	6.1000E-02	-6.1000E-02
1	4	1.0000E-02	-1.0000E-02
2	0	-6.0000E-02	-6.0000E-02
2	1	7.0000E-02	7.0000E-02
2	2	-1.2500E-01	-1.5000E-02
2	3	7.1000E-02	-7.1000E-02
2	4	-1.0000E-03	1.0000E-03

The equilibrium $< \beta >_{eq}$ limit in this configuration equals 9.8%. Magnetic surface cross-sections are shown in Fig. 1. For $< \beta >= 3.5\%$, the Fourier spectrum of the magnetic field strength in Boozer coordinates is shown in Fig. 2. The dependencies of the Mercier criterion and the ballooning eigenvalues on the radial variable s that labels the magnetic surfaces (s is proportional to plasma volume enclosed) are shown in Fig. 3. It is seen that the $< \beta >_M$ limit is about 4% and the ballooning $< \beta >$ limit is $< \beta >_B= 1.4\%$. The plasma pressure was considered as parabolic ($p'(s)$ is const).

One can see that there exists a rather large difference between $< \beta >_M$ and $< \beta >_B$. Since this configuration was found by optimization of the Mercier criterion, it is worth to try to modify the plasma boundary to get larger a $< \beta >_B$. Retaining the accuracy of the QS condition fulfillment to X=3, the result of such an attempt was the sharp diminishing of the $< \beta >_M$ with only a modest increase of $< \beta >_B \approx 1.6\%$.

In the Heliac-like systems considered as well as in Helias-like QS stellarators, Ref. [2,3], the very localised ballooning modes along the magnetic field lines are the most dangerous. The optimisation carried out here cannot be considered as exhaustive. We have not changed the plasma pressure profile and did not use higher harmonics in the boundary representation (see Table). As mentioned in Ref. [4], these harmonics can be used to improve the quasisymmetry. The availability of a large number of free parameters makes it reasonable to further continue the optimization procedure.

3. Two-period quasisymmetric configurations

Recently the most compact two-period quasisymmetrical stellarator systems of the figure-eight type were found numerically. They became the basis for a project MHH-2, Ref. [3,5] under development in the USA, and a corresponding project under development in Japan, Ref. [4]. In these systems, the principal normal with respect to the magnetic axis does not rotate relative the "torus hole" (quasiaxial symmetry), while the magnetic surfaces make one-half turn per period.

In this Section, a search of two-period quasisymmetric systems in a wide range of the configuration parameters is undertaken. Calculations were made in the paraxial approximation with the application of a semianalytic method previously developed, Ref. [6]. We have estimated the equilibrium $< \beta >$ limit and the possibility of stabilising the Mercier modes. The elongation and triangularity of the magnetic surfaces at the beginning of a period, the aspect ratio and the ellipticity of the reference torus on which the trajectory of the magnetic axis lies have been optimised. In Fig. 4, the dependencies of the equilibrium $< \beta >$ limit on the toroidicity r_1/R_0 of the magnetic axis reference torus are shown. As is seen, three types of two-period quasisymmetric stellarators exist. They are characterised by the number of magnetic surface cross-section turns in one system period, n_1, with respect to the magnetic axis principal normal.

For small values of r_1/R (cases A and A_1), the principal normal of the magnetic axis does not rotate. Thus, quasiaxial symmetry (QAS) is realized here. The case A corresponds to $n_1 = 1/2$. The magnetic surface cross-sections make one-half turn of rotation per system period with respect to the magnetic axis principal normal. This situation corresponds to those proposed in Ref. [3-5]. In this case we have not found Mercier stable systems. The case A_1 corresponds to $n_1 = 0$. The magnetic surface cross-sections here do not rotate (they only oscillate) with respect to the torus hole. This is a tokamak-like situation with small rotational transform which is Mercier unstable.

When the aspect ratio of the reference torus on which the magnetic axis lies decreases, case B, the principal normal of the magnetic axis rotates, thus quasihelical symmetry (QHS) is realized. When the QS conditions are satisfied, the magnetic surface cross-section rotates in phase with the principal normal, $n_1 = 0$. These systems are Mercier stable up to $< \beta > = 4.5\%$ at $r_1/R \approx 0.45$.

It is worth to emphasize that here we have used the *precise* conditions of QS in the approximation to second order. In this approximation, the shear of the rotational transform is considered to be zero and the precise conditions allow to satisfy the Mercier criterion only for configurations with $n_1 = 0$, whereas the numerical 3D calculations have shown that stabilisation of local modes in two-period QAS configurations with $n_1 \neq 0$ is also possible at the expense of some violation of QS conditions, Ref. [3].

4. Conclusions

The four-period Heliac-like QS configurations studied earlier in the near-axis approximation have been considered here with 3D codes. It is shown that with moderate accuracy of QS, the configurations of such type have $< \beta >$ limits comparable to the widely investigated Helias-like QS configurations.

The possibility of the existence of two-period QS configurations have been studied also. Only the near-axis approximation was used. It is shown that Mercier stable Heliac-like configurations of the figure-eight type do exist. As reported in Sec. 2 of the present paper, the ballooning mode stability condition can decrease the $< \beta >$ limit significantly. 3D ballooning stability results for two-period $n_1 = 0$ configurations are being examined.

To find stellarator systems with better properties, including higher β and moderate transport, weakening slightly the QS condition could be reasonable, Ref. [7,8].

Acknowledgements

References

[1] Isaev M.Yu., Mikhailov M.I., Shafranov V.D., Subbotin A.A.// Proc. of 10th Int. Conf. on Stellarators, **27**, 186(1995). Madrid, 1995, p.278.

[2] Matthews P.G., et al.// in Proc., 10th Int. Conf. on Stellarators, (Int. Atomic Energy Agency Technical Committee Meeting), Madrid, 1995 (IEAE, Vienna, 1995). p.167.

[3] Reiman A.H., Ku L.P., Monticello D.A., Nührenberg C., Cooper W.A. // Plasma Physics Reports **23**, 472 (1997).

[4] Nakajima N., Yokoyama M., Okamoto M., Nührenberg J.// Plasma Phys. Reports **23**, (1997) to be published.

[5] Garabedian P.// Phys. Plasmas **3**(7), 1996, 2483.

[6] Isaev M.Yu., Mikhailov M.I.// Plasma Phys. Reports **22**, 43 (1996).

[7] Gori S., Lotz W., Nührenberg J.// Theory of Fusion Plasmas, SIF, Bologna, 1996, Ed. by J.W. Connor, E. Sindoni and J. Vaclavik, p. 335.

[8] Mikhailov M.I., Shafranov V.D., Subbotin A.A., Sunder D.// This conference.
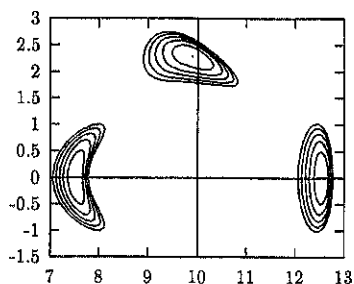
Fig. 1. Magnetic surfaces cross-sections for $< \beta > = 3.5\%$.
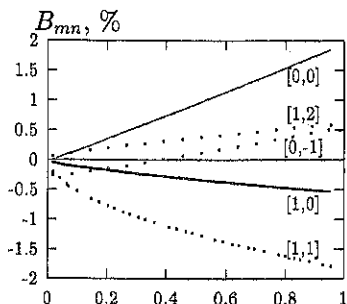
Fig. 2. Fourier spectrum of magnetic field strength in Boozer coordinates for $< \beta > = 3.5\%$ in dependence on radial coordinate.
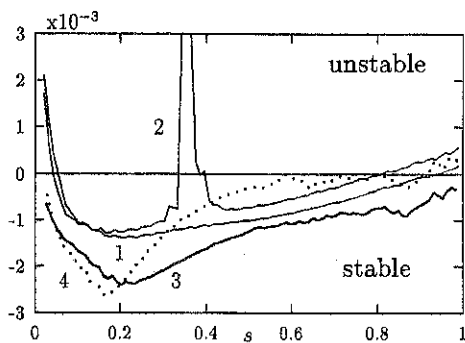
Fig. 3. The dependencies of Mercier criterion and ballooning eigenvalues on s, labeling the magnetic surfaces (s is proportional to plasma volume enclosed).

1 - Mercier criterion for
   $< \beta > = 3.73\%$
2 - Mercier criterion for
   $< \beta > = 4.06\%$
3 - Ballooning eigenvalues for
   $< \beta > = 1.07\%$
4 - Ballooning eigenvalues for
   $< \beta > = 1.4\%$
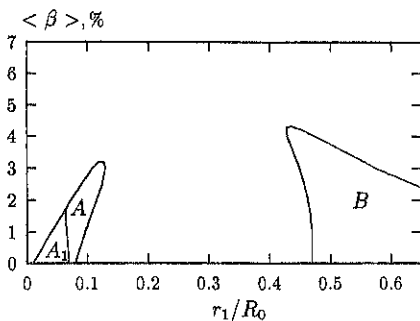
Fig. 4. The dependencies of equilibrium $< \beta >$ limit on the thickness of magnetic axis reference torus. All other parameters are optimal.

$A: \quad n_1 = 1/2 \; ; \qquad A_1: \quad n_1 = 0 \; ;$
$B: \quad n_1 = 0 \; .$

PLASMA EQUILIBRIUM WITHOUT PFIRSCH–SCHLÜTER CURRENT IN CONVENTIONAL STELLARATORS

Pustovitov V.D.

Russian Research Center "Kurchatov Institute", Moscow, Russia

In recent experiments in helical device Heliotron E it was observed [1] that dependence of plasma column shift on β changed dramatically when external vertical field was applied to control the position of vacuum magnetic axis. When magnetic axis was moved inward, into the region of stronger toroidal field, pressure-induced plasma shift became weak. In one case with the largest inward shift, magnetic configuration became almost insensitive to β.

The reason of weaker dependence of plasma column shift on β was quite clear: the reduction of Pfirsch-Schlüter (PS) current. However, at that time the existing theory gave only qualitative explanation of this phenomenon and could not answer the general questions

- Whether it is possible or not to get plasma equilibrium without PS current in conventional stellarators
- If possible, at what conditions
- If impossible, how and to what extent can be reduced the influence of PS current on equilibrium configuration?

To answer these questions, let us turn to the general expression for PS current in conventional stellarators [2,3]:

$$j_\zeta = 2\pi R p'(\psi)\Big[\Omega - <\Omega> \Big] \qquad (1)$$

Here, R is the major radius, p is the plasma pressure, ψ is the poloidal flux, Ω is a quantity characterizing the inhomogeneity of the magnetic field:

$$\Omega = \Omega^0 + 1 - \frac{R^2}{r^2} \cong \Omega^0 - \frac{2\rho}{R}\cos u , \qquad (2)$$

$\Omega^0 \equiv \widetilde{\mathbf{B}}^2{}_\zeta / B_0^2$, $\widetilde{\mathbf{B}}$ is the helical field, B_0 is the toroidal field at the geometrical axis, ρ, u, ζ are quasi-cylindrical

co-ordinates related to this axis axis so that $r = R - \rho \, cosu$, $<...>$ denotes volume averaging and $<...>_\zeta$ stands for averaging over the toroidal angle ζ.

The right hand side of Eq. *(1)* is identically zero if

$$\Omega = <\Omega> = \Omega(\psi) . \qquad (3)$$

We must solve this equation together with equilibrium equation

$$\Delta \left[\psi - \psi_V \right] = - 2\pi R j_\zeta , \qquad (4)$$

where ψ_V is the poloidal flux of the helical field. Assumption $j_\zeta = 0$ turns out Eq. *(4)* into a "vacuum" equation. Finally, equilibrium without PS current would be possible if Eq. *(3)* could be satisfied with vacuum ψ:

$$\psi = \psi_V + \sum_{n=1}^{\infty} C_n \rho^n \cos nu \qquad (5)$$

where C_n are constant to be found from Eq. *(3)*. To find C_n means to find external poloidal field necessary for PS current suppression (if it is possible).

To start operations with Eq. *(3)* we must specify two functions: Ω^0 and ψ_V. They are determined by vacuum helical field $\tilde{B} = \nabla\varphi$, which is known for any device. In the simplest case the potential φ can be approximated by a single helical harmonic: $\varphi \propto \sin (\ell u - m\zeta)$. Then $\psi_V = \psi_V(\rho)$,

$$R\Omega^0 = - \frac{1}{2\pi R B_0} \frac{m}{\ell} \left[2\psi_V + \rho\psi_V' \right] , \qquad (6)$$

and the problem can be treated analytically.

In analytical calculations it is convenient to replace Eq. *(3)* by equivalent differential formulation

$$\nabla\Omega \times \nabla\psi = 0 . \qquad (7)$$

Using *(2)* and *(3)* one can get from Eq. *(7)*

$$2 \frac{d\psi_V}{d\rho} + RC_1 \frac{d\Omega^0}{d\rho} - 4\rho C_2 = 0 \qquad (8)$$

and for $n \geq 2$

$$RnC_n \frac{d\Omega^0}{d\rho} - 2\rho(n+1)C_{n+1} = 0 . \qquad (9)$$

In a general case $\Omega^0 \neq C\rho^2$, and Eq. *(9)* can be satisfied by $C_n = 0$ only (for all $n \geq 2$). Then Eq. *(8)* gives

$$2\psi_V = -RC_1\Omega^0 . \qquad (10)$$

This equality is compatible with Eq. *(6)* at $m\rho/R \ll 1$ only, when $\psi_V \propto \rho^{2\ell-2}$. Then we get C_1 from Eq. *(10)* and corresponding value of the external vertical field:

$$B_\perp = -B_0/m . \qquad (11)$$

We can answer now the questions stated above: plasma equilibrium without PS current is possible in large-aspect-ratio stellarators with $mb/R \ll 1$. Vertical field *(11)* must be applied to get such equilibrium.

Approximation $\psi_V \propto \rho^{2\ell-2}$ is valid near the geometrical axis $\rho = 0$. But we need it in a rather wide region, which must include the new position of the plasma shifted under the action of the vertical field *(11)*. This requirement is *not* satisfied at typical parameters of conventional stellarators. This can be easily seen from the expression

$$\frac{\Delta_\perp}{b} = \frac{R}{mb\mu_b} \qquad (12)$$

which gives the value of the inward shift $\Delta_\perp$ of the plasma produced by the field *(11)*. Rotational transform μ_b at the plasma boundary is usually of the order of unity, but it must be very large to make smaller $\Delta_\perp$ in *(12)*.

In other words, vertical field *(11)* is too large, and the state without PS current is too far from the ordinary operational regimes. That is why strong suppression of PS current was neither observed in experiments before recently, nor seen in calculations. Only once it was shown numerically [4] that it is possible to get equilibrium insensitive to β in some $\ell = 3$ stellarator. Given analytics explains now this result, which remained unexplained for more than 35 years. It shows also that the effect demonstrated in [4] is not related

with a special choice of a pressure profile in [4], but reflects the general propertis of a vacuum configuration.

From many viewpoints the most interesting are $\ell = 2$ stellarators. For $\ell = 2$ stellarator the restriction $m\rho/R \ll 1$ means that there should be no shear. Also, as already mentioned, rotational transform must be very large for getting zero PS current. Such combination of parameters is unusual.

It must be noted that in $\ell = 2$ stellarators $\Omega^0 = C\rho^2$, when $m\rho/R \ll 1$. It allows to get another solution in addition to *(11)*, because at $\Omega^0 = C\rho^2$ Eq. *(9)* can be satisfied by nonzero C_n. It can be shown that this additional solution corresponds to combination of the vertical field *(11)* and magnetic field of a ring filament current of radius $R - R/(m\mu_b)$, lying in equatorial plane. One can see from *(12)* that this position is exactly the position of the magnetic axis shifted by the field *(11)*. So, the second solution for shear-free stellarators represents an exotic configuration with an internal conductor.

For all cases described above the initial assumption was that PS current vanished everywhere in the plasma. Conventional $\ell = 2$ stellarators with a shear, which are typical devices at present, do not satisfy the restrictions expressed as Eqs *(8)* and *(9)*. It means that it is impossible to get $j_\zeta \neq 0$ in such systems. However, Heliotron E with a large shear seems to be close to $\ell = 3$ stellarator. Also, it has large m and μ_b, which makes the value *(12)* reasonable. It explains [6,7] why strong PS current reduction was observed in Heliotron E [1].

REFERENCES

[1] Besshou S., Ogata K., et al, Nucl. Fusion **35** 173 (1995).
[2] Anania G., Johnson J.L., Weimer K.E., Phys. Fluids **26** 2210 (1983).
[3] Pustovitov V.D., Sov. J. Plasma Phys **14** 305 (1988).
[4] Greene J.M., Johnson J.L., Phys. Fluids **4** 875 (1961).
[5] Greene J.M., Johnson J.L., Weimer K.E., Plasma Phys. **8** 145 (1966).
[6] Pustovitov V.D., Nucl. Fusion **36** 583 (1996).
[7] Pustovitov V.D., Nucl. Fusion **36** 1281 (1996).

Fast Pressure Measurements of the Local Island Divertor on the Compact Helical System

J. F. Lyon, C. C. Klepper, A. C. England

Oak Ridge National Laboratory, Oak Ridge, Tennessee, 37831 U.S.A.

A. Komori, N. Ohyabu, S. Masuzaki, T. Morisaki, S. Morita, H. Suzuki, K. Tanaka,
O. Motojima, *National Institute for Fusion Studies, Oroshi, Toki 509-52, Japan*

Development of an effective divertor is critical for the viability of the stellarator (helical system) concept. Figure 1 shows the local island divertor (LID) concept [1] in which particle and heat fluxes are channeled to the back of the LID head by the magnetic field structure of an
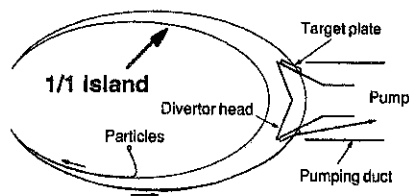
Fig. 1. The 1/1 magnetic island geometry and its relation to the LID chamber for O-point operation. The outer edge of the island intersects target plates on the back of the LID head.

externally produced $m = 1$, $n = 1$ island that is outside the last closed flux surface. The leading edge of the LID head is protected from the outward heat flux from the plasma because it is located inside the 1/1 island and the particles that strike the target plates on the back of the LID head in the throat of the LID pump module are then pumped efficiently.

A set of 16 coils was used to create a 1/1 island in the Compact Helical System (CHS). The current (I_{LID}) in the LID coils was chosen to position either the O-point or the X-point of the external 1/1 magnetic island at the location of the LID head. The principal diagnostic in this study [2] was an ASDEX-style ionization gauge [3] that allowed fast (~1-ms) measurements of the neutral pressure buildup behind the divertor head in the LID module.

1/1 Island Effect on Particle Pumping

A typical O-point island case is shown in Fig. 2. Ion Bernstein wave (IBW) heating was used for plasma initiation and neutral beam injection (NBI) was used for plasma heating. The on-axis field was 0.92 T and P_{NBI} was 0.82 MW in these experiments. The pressure p in the LID chamber and the electron density n_e peak just after the end of the gas puff. The second rise in the LID pressure (at $\approx$170 ms) after the plasma terminates is due to a second gas puff used to suppress runaway electrons during the magnetic field
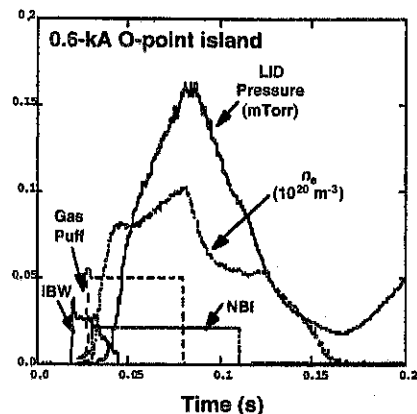
Fig. 2. An O-point island shot with $I_{LID} = 0.6$ kA.

The relation of the 1/1 island to the LID head can also be changed by moving the head through a fixed island. Figure 4 shows the variation of the LID pressure at gas puff turn-off as the LID head is moved inward with I_{LID} = 0 or 0.6 kA (O-point and X-point operation). The LID pressure increases exponentially with distance into the 1/1 island. The e-folding lengths of 2.2 cm (O-point), 2 cm (no LID) and 1.8 cm (X-point) are similar to the 1.6-cm to 2-cm decay lengths for the ion saturation current measured on the back of the LID head during the same radial scan [4].

Fig. 4. *The LID pressure falls exponentially as the LID head is retracted from the plasma edge. The 0.6-kA O-point values are larger than the no-LID and 0.6-kA X-point values.*

The LID head was biased to determine if $E \times B$ drifts could be imposed on the plasma edge to affect the flow of particles into the LID chamber. Figure 5 shows that the pressure in the LID chamber is ~50% higher when ~150 V is applied to the LID head for a short period (80 ms < t < 100 ms) during 0.6-kA O-point operation [5]. Although biasing the head improved the pumping efficiency, it did not affect the bulk plasma properties: the plasma density and the stored energy were unchanged. Biasing the LID head also led to a

Fig. 5. *Biasing the LID head improves the pumping efficiency for 0.6-kA O-point operation.*

pressure increase in the LID chamber with I_{LID} = 0 and with 0.6-kA X-point operation. A similar observation was made by Evans et al. [6] when a small scoop limiter was inserted in the O-point of a small $m = 7$, $n = 2$ island on the TEXT tokamak. A large $E \times B$ island circulation velocity was postulated to compensate the effect of the large radial diffusion and to explain the larger than expected increase in the scoop pumping efficiency that was observed.

With no LID island, the particle exhaust is limited by the conductances to the vacuum vessel and LID chamber pumps. With an O-point island, additional particle flux is channeled into the LID pump chamber. The value for the particle flux Γ into the LID chamber from Fig. 2 is ≈3 torr·l/s, compared to ≈10 torr·l/s from the CHS gas puff. From the I_{LID} scan in Fig. 3, the ratio of particle fluxes into the LID chamber for optimized O-point operation vs X-point or with no 1/1 island is ≈3.6.

A value of $S + C$ = 16,000-20,000 l/s is obtained by requiring $\Gamma = 0$ when the ion satura-

rampdown. The LID pressure p lags the gas puff, the rise in n_e and the total particle flux into the LID chamber, $\Gamma = (S + C)p + Vdp/dt$, because of the LID chamber pumpout time. Here V, S and C are the volume, pumping speed and conductance for the LID chamber.

The LID pressure is higher with O-point operation than with no island or X-point operation for a constant gas puff. The density is lowest and falls fastest after gas puff turnoff with O-point operation, as expected if particles exit the vacuum vessel faster, thus reducing the gas that can recycle to the plasma. With no 1/1 island, the density remains high until NBI turnoff. X-point operation gives intermediate behavior. The increase in p and the decrease in n_e demonstrate that the island is effective in moving particles from the plasma edge to the LID chamber.

The pressure in the LID chamber should increase as the 1/1 island size grows to encompass the LID head. However, too large an island could lead to the island intercepting the vacuum vessel wall or to ergodization of the island, and hence less effective diversion of particles into the LID chamber. With X-point operation, the amount of particles entering the LID chamber should not change

Fig. 3. The LID pressure and the plasma density depend on the island size and orientation. The normalized value p/n_e peaks at the design value for the O-point island size. The symbols "o" and "x" refer to O-point and X-point operation.

with I_{LID} unless some particles are intercepted by the wall, or the balance between flow along field lines and diffusion across the field changes with I_{LID}. Lithium beam measurements of n_e in the plasma edge are consistent with a 1/1 island at the plasma edge [4].

Figure 3 shows peak values for p and n_e (at gas puff turnoff) as I_{LID} is varied from 0 (no island) to 1.1 kA for a constant gas puff with O-point and X-point operation. The LID pressure for O-point operation peaks at $I_{LID} \approx 0.5$ kA whereas the X-point p falls monotonically with I_{LID} in approximately the same way as n_e falls as the island size is increased. Comparing the O-point and X-point pressures for the same n_e values shows that O-point operation has a much higher exhaust efficiency. The ratio p/n_e peaks at $I_{LID} \approx 0.6$-0.7 kA at a value >3 times the no-LID value while the X-point values remain roughly constant at the no-LID value.

tion current and n_e decay to zero after gas puff turnoff. This in reasonable agreement with the values $C \sim 9000$ l/s and $S \sim 9000$ l/s obtained by comparing the time behavior of the pressure in the LID chamber (with and without the LID chamber cryopump) with the calculated time dependence of the pressure for a gas puff without plasma. The approximate agreement of the $S + C$ values with and without plasma suggests that the plasma flux into the LID pump chamber does not affect the flow of neutrals back into the CHS vacuum chamber (no plasma blocking occurs in the relatively wide channel into the LID pump chamber).

These experiments indicate that a local island divertor can be effective for particle control on a stellarator with a helical separatrix (a heliotron/torsatron). The next application will be on the Large Helical Device. The improvement in the particle exhaust efficiency using the LID head in combination with an O-point island is related to the change (as a result of the 1/1 island) in the density gradient at the plasma edge and the wall recycling [4]. The 1/1 island also has a significant effect on the main plasma properties, as seen by the similar variation of n_e with I_{LID} for the LID head fully retracted and the LID head inserted. The global plasma properties (stored energy, radiated power P_{rad}, density decay time) also change with I_{LID} and insertion or retraction of the LID head in a way that correlates with n_e. The value of P_{rad} is a sensitive indicator of the effect of the island on the plasma; it varies a factor of 5 as I_{LID} varies. However, Fig. 6

shows that $P_{rad} \propto n_e^2$, which implies that Z_{eff} is constant, for O-point and X-point operation independent of I_{LID}. Also W/n_e, which is proportional to the average plasma temperature and the energy confinement time τ_E, is the same for O-point and X-point operation and improves with island size for both cases.
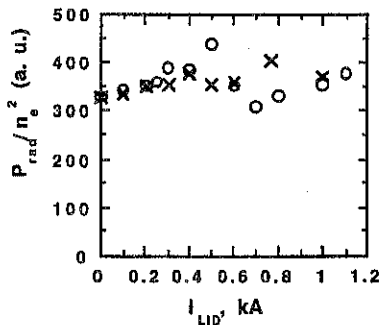
Fig. 6. P_{rad}/n_e^2 is independent of O-point (o) or X-point (×) operation with the LID head in.

References

[1] N. Ohyabu, et al., *J. Nucl. Mater.* **145-147**, 844 (1987).

[2] A. Komori, et al., *Proc. Plasma Physics and Controlled Nuclear Fusion Research*, Montreal, 1996, IAEA-CN-64/C1-2.

[3] G. Haas, et al., *J. Nucl. Mater.* **121**, 151 (1984).

[4] S. Masuzaki et al., "Edge plasma control using an LID configuration on CHS," *this conf.*

[5] A. Komori, et al., *Annual Report of National Institute for Fusion Science April 1995-March 1996*, ISSN 0917-1185, 218 (1996).

[6] T. E. Evans, et al., *Controlled Fusion and Plasma Physics* (Proc. 15th Eur. Conf. Madrid, 1987), Vol. 11D, Part II, 770 (1987).

Fast Reconstruction of H-1NF Heliac Electron Density Profiles from Multi-View Far-infrared Interferometer Signals

John Waller, Xuehua Shi
Department of Applied Physics.
Central Queensland University. Rockhampton. QLD 4702. Australia
John Howard, Boyd D. Blackwell, George B. Warr
Plasma Research Laboratory, Research School of Physical Sciences and Engineering.
Australian National University. Canberra. ACT 0200. Australia

Introduction

A three-view, 40-beam Michelson configuration interferometer has been installed and operated on the H-1NF heliac[1]. A rapidly rotating disk grating is used in the interferometer to time-multiplex the laser beams which are scanning across a bean-shaped plasma poloidal cross section. The tomographic density reconstructions from the multi-beam interferometer were reported for a large plasma instability during the discharge[2]. In this paper, we present a fast reconstruction of plasma density profiles by a transputer system with the phase data only from the top view scanning laser beam (see figure 1(a)). The reconstructed density profiles are displayed immediately after each plasma discharge.

Reconstruction of density profiles

For the low β plasmas considered in this experiment, an analytically invertible transformation between the real-space nested bean-shaped flux surfaces and simple circular surfaces allows reconstruction of the density profile in the latter space (flux space) using Fourier-Bessel basis functions,

$$n_e(r,\theta,t) = \sum_{ls} A_{ls}(t) J_l(\alpha_{l,s} r) \exp[il(\theta - \phi_{ls})] \qquad (1)$$

where l is the poloidal mode number and s is the radial mode number, A_{ls} and ϕ_{ls} are the basis function amplitude and phase respectively, and r, θ are the coordinates in the flux space. For the fast reconstruction of global density profiles, only the two lowest radial modes are being considered, and equation (1) may be re-written as

$$n_e(r,t) = \sum_{s=1,2} A_{0s}(t) J_0(\alpha_{0,s} r) \qquad (2)$$

The amplitude of the Bessel function $A_{0s}(t)$ can be determined from the tomographic inversion of the eleven density line integrals L_j, $j=0, 1,\dots 10$, derived from the top view scanning laser beam phase data:

$$A_{0s}(t) = \sum_j R_{js}^{-1} L_j(t) \qquad (3)$$

where the matrix elements R_{js} are the line integrals of the basis modes along each of the eleven plasma probing beam in the flux space:

$$R_{js} = \int J_0(\alpha_0, sr) ds_j(r, \theta) \qquad (4)$$

The matrix R was pre-calculated for the standard H-1NF magnetic configuration[3] before the experiment.

The interface and the transputer system

The eleven scanning laser beams from the top view, each of which is executing a double pass of the plasma, are doubly Doppler shifted by the rotating grating. After mixing with the local oscillator the line integral phase information is phase modulated on the detector output signals which have a frequency range from 143 to 176 kHz. The interface includes one programmable control card and three ADC cards with fast 12 bit ADC's and Digital Signal Processors (ADSP-2101's) for real time pre-filtering. Signals are taken from the top view laser beam detector, from a reference laser beam detector, and from a light diode which gives the pulses indicating the start and the stop time of each scanning path (see figure 2). By using the quadrature demodulation technique[4][5] the sampled signals are made to be proportaional to either $\sin\theta$ or $\cos\theta$, where θ is the phase data of each scanning laser beam.

Five transputer modules are used in the main processing unit, each has on module memory and a 25 MHz T800 with four bi-directional serial communication links (2.4 Mbytes/second) for parallel processing purposes. A block diagram of the transputer system and the interface are shown in figure 2. The three input signals are taken in via interface cards through three transputer links, and the phase information of the top view laser beam and of the reference laser beam is extracted simultaneously by the T3 and T4 transputers, the phase information is then passed to appropriate transputers for further processing or display. The tomographic inversion is performed by T2 and the density profiles are saved on the PC hard disk via T1 and displayed on a monitor connected to the graphics transputer module. This system can be programmed to either display and save the final results, or display and save the intermediate results during the adjusting and debugging stage.

Results and Discussions

Measurements were made in the rf-heated argon plasma under the standard H-1NF magnetic configuration. The results obtained from a typical shot (1.21×10^{-4} Torr filling pressure and 0.072 T magnetic fields) is shown in figure 1 (b) to (d). Three scans were made by the top view laser beam in an 80 *ms* discharge. The averaged phase data on each path for the three scans is shown in figure1 (b), and the reconstructed density profiles from the second and the third scan data are shown in figure 1 (c) and (d) respectively. Density profiles are assumed not to vary during the second and the third scans, and the two solution sets of $[A_{01}, A_{02}]$ for the two scans were used to reconstruct the density profiles using equation (2). The least square error is checked by calculating the residual r_e of each solution set using the following equation:

$$r_e = |R \cdot A - L| \qquad (5)$$

where matrix R, A, L were defined in equation (3) above. The residual for the solution set of the second scan is 0.40, which is about 9% of the length of the measured line integral vector L. For the residual of the third scan, it is about 12% of the length of the measured line integral vector L.

The time needed for the transputer system to reconstruct a density profile depends mainly on the quadrature sampling rate. At an 18 kHz sampling rate, which was used in this experiment, a density profile was constructed within about 80 ms with most of the time spent on extracting the phase information from the raw data and subtracting the phase baseline from the extracted phase data. Further experiment will be carried out with higher radial modes also being considered in the tomographic reconstruction process in order to minimize the error in the reconstructed profiles.

References

[1] Hamberger, S.M., Blackwell, B.D., Sharp, L.E., Shenton, D.B. *Fusion Tech.*, **17** 123-30, 1990.

[2] Warr, G.B., Howard, J. 21st AINSE Plasma Science & Tech. Conf., Paper 39, Sydney, Australia. 1997.

[3] Shats, M.G., Rudakov, D.L., Blackwell, B.D., Sharp, L.E., Tumlos, R.. Hamberger, S.M. Fedyanin, O.I. *Nuclear Fusion.* 34 No.12 1654-1661, 1994.

[4] Howard, J., and Landgraf, H., *Rev. Sci. Instrum.*, 65, 2130-2133, 1994.

[5] Waller, J.W., Shi, X.H., Altoveros, N.C., Howard, J., Blackwell, B.D., Warr, G.B. *Rev. Sci. Instrum.*, 66, 1171-1174, 1995.
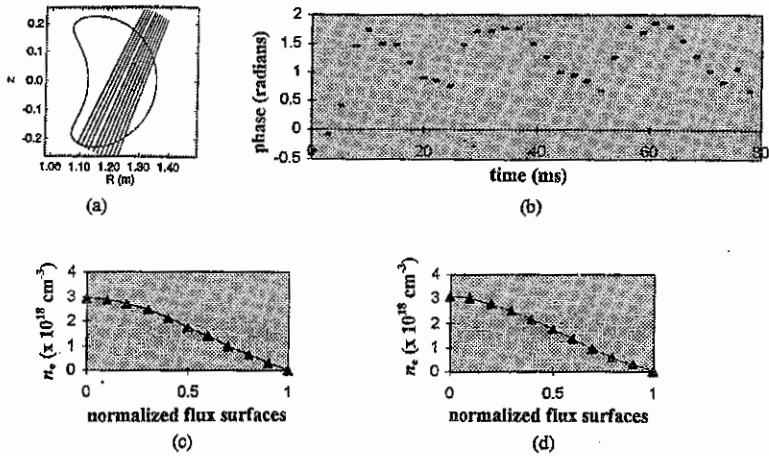
Figure1. (a) the top view laser beam geometry. (b) phase data from the three scans of the top view beam during plasma shot 23893. (c) and (d): the reconstructed density profiles from the second and the third scan data.
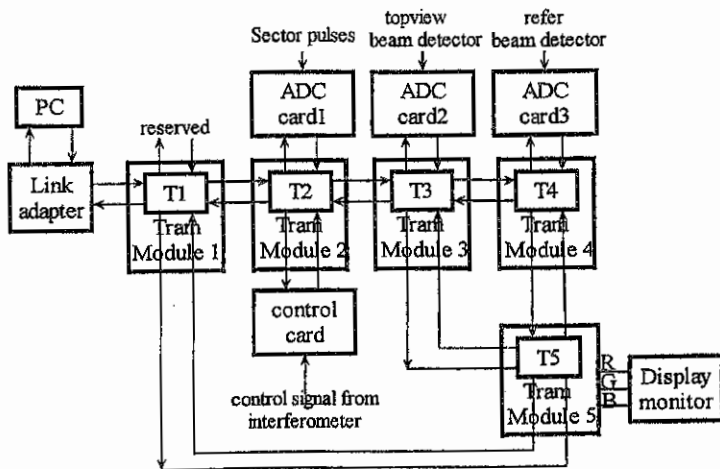
Figure2. Block diagram of the interface and transputer system

SUPPRESSION OF PFIRSCH-SCHLÜTER CURRENT IN INWARD SHIFTED STELLARATOR PLASMA IN HELIOTRON E

S. Besshou, V.D. Pustovitov*, N. Fujita[†], K. Kondo, T. Mizuuchi,[†]
K. Nagasaki[†], M. Nakasuga, T. Obiki[†], H. Okada[†], F. Sano[†], H. Zushi

Graduate School of Energy Science, Kyoto University, Gokasho, Uji, Kyoto, 611, Japan
[†]*Institute of Advanced Energy, Kyoto University, Gokasho, Uji, Kyoto, 611, Japan*
* Russian Research Centre "Kurchatov Institute", Moscow, 123182, Russian Federation

Abstract
    Observation of the complete suppression of integral effect of Pfirsch-Schlüter current in Heliotron E plasmas is reported. Poloidal magnetic field was measured to control the plasma boundary position. We found that pressure-induced plasma shift, an observable characteristic of Pfirsch-Schlüter current, depends strongly on the initial position of magnetic axis. When it was moved by the vertical field inside the torus, finite-β shift became smaller. Complete suppression of finite-β shift was achieved in a deeply inward shifted configuration: 7 cm from the standard position R_{axis} = 2.20 m.

1. Introduction

    The main goal of these experiments was studying the effects of finite plasma pressure on currentless equilibrium configuration in a helical device. In toroidal magnetic systems, such as tokamaks and stellarators, magnetic field is inevitably inhomogeneous. When plasma is maintained in equilibrium in such a field, a dipole current appears to compensate the toroidal drift of charged particles. This pressure-induced current, flowing along the whole system, is called Pfirsch-Schlüter (PS) current. It becomes larger with increasing plasma pressure, which finally puts the upper limit for β, which is the volume-averaged ratio of thermal plasma pressure to the magnetic field pressure. This limit, β_{eq}, is related with a strong shift of magnetic axis (known as Shafranov shift) produced by the vertical field of PS current. Being a fundamental phenomenon, Shafranov shift always attracts attention in a theory from the very beginning of stellarator research, see [1]. Progress in operation with a finite-β plasma allowed to study it in stellarator experiments also [2,3].
    Recently it was claimed [4] that conventional stellarators also need shift control system if they are oriented to β close to β_{eq}. This conclusion followed from the analysis of free-boundary plasma equilibrium. It was experimentally confirmed later: 1 cm pressure-induced plasma shift was observed by VUV spectroscopy in CHS [5]. It proved the necessity to study this phenomenon.
    In tokamaks the standard method to measure the plasma shift is based on magnetic diagnostics . It was logical to apply the same technique in stellarators. Necessary theory was developed in Ref. [6], and then method of Ref. [6] was successfully realized in Heliotron E [7]. Our first results also confirmed the predictions of Ref. [4]. At the same time we found unexpected strong dependence of the finite-β plasma column shift Δ_β on the geometry of initial vacuum configuration.
    Obviously, this experimental observation was an evidence of PS current suppression in inward shifted configurations. There were theoretical indications that such suppression might be possible in conventional stellarators [8, 9]. But existing theory was insufficient to explain our first results. The knowledge was rather limited: two numerical examples [1, 8] and model analytical expression for PS current [8, 9]

$$j_{PS} = \frac{2p'(\rho)}{\iota(\rho)B}\left(1 + B^2V''(\Phi)\frac{\Delta(\rho)}{2}\right)\cos\theta, \tag{1}$$

where p is the plasma pressure, B is the magnetic field at the axis, $V''(\Phi)$ is the vacuum magnetic hill value, $\Delta(\rho)$ is the shift of a magnetic surface of minor radius ρ, and θ is the poloidal angle. This expression is good for shearless systems, but it is not justified for stellarators with large shear like Heliotron E. Finally, it contradicts to numerically shown possibility [1] to make configuration completely insensitive to plasma pressure in some $\ell = 3$ stellarator. Till recently [10,11] these results of [1, 8] were neither confirmed, nor refuted. It was known that proper shaping of magnetic surfaces could provide a considerable reduction of PS current in stellarators [12,13]. But it was shown for configurations evidently different from those produced in Heliotron E.

Recent theory [10,11] explained our first results and also predicted that strong suppression of PS current and even the unusual reversal of its phase are possible in a deeply inward shifted configurations in Heliotron E. This prediction is the motivation of these physics experiments. The present paper describes the first experimental observation of strong suppression and reversal of PS current in Heliotron E plasma.

2. Experiment on Complete Integral Suppression of Pfirsch-Schlüter current

Heliotron E device is a stellarator/torsatron toroidal device with a large shear of the vacuum rotational transform: $\iota_0 = 0.5$, $\iota_b = 2.8$. The major radius is $R_0 = 2.20$ m and typical minor radius is $b = 0.21$ m. An $l = 2$ helical coil with $m = 19$ helical field periods can produce a toroidal magnetic field B up to 2 T at the axis. We can control the vacuum configuration by changing the total vertical field B_v produced by poloidal coils in the range $-0.2227 < \beta^* < -0.15189$, where $\beta^* = B_v/B$ [14]. Then we get configurations with magnetic axis positions 2.10 m $< R_{axis} < 2.28$ m at $B = 1.9$ T. Figure 2 shows the poloidal cross section of vacuum magnetic surfaces of strongly inward shifted configuration with $R_{axis} = 2.13$ m.

The experiments were performed at $B = 1.9$ T. Currentless target deuterium plasmas were produced with the second-harmonic electron cyclotron resonance heating (ECRH) by 300 to 400 kW of rf power from 106 GHz gyrotron, without ohmic transformer. The line averaged density $\bar{n}_e$ rose to $(1.5\text{-}2.0)\times10^{13}$ cm^{-3}, then 28^0 and 11^0 co-injecting neutral beam injectors were turned on. Up to 2 MW of hydrogen neutral beam power at energy of 24-26 keV was thus injected almost perpendicularly into the torus. Deuterium gas puffing was used to raise the density further during injection to reduce shine through loss. The typical plasma parameters during the discharge were: $\bar{n}_e = (3\text{-}7)\times10^{13}$ cm^{-3}, $T_{e0} = (400\text{-}800)$ eV, $T_{i0} = (400\text{-}700)$ eV, the stored energy $W_{dia} = (4\text{-}13)$ kJ, the volume averaged $\beta = (0.1\text{-}0.2)$ %, the thermonuclear fusion neutron yield rate Y_n in the range 10^8 n/s, the radiative loss power $P_{bol} = (200\text{-}800)$ kW.

Finite-β plasma boundary shift Δ_β, the part of Δ due to plasma-generated magnetic field, was measured magnetically as described in [6,7]. We have used one pair of poloidal magnetic flux loops (ψ-loops) which are set in the equatorial plane and form a saddle loop to determine the "ribbon" averaged vertical field. One pair of cosine coils, separated by a half helical period, was also used. These two signals and the measured net toroidal current allow to derive the shift Δ_β, which was nearly proportional to the dipole moment of PS current [15]. Diamagnetic volume averaged β was used as a measure of plasma pressure.

Figure 2 shows the measured values Δ_β, β, plasma current and poloidal magnetic diagnostic signals in the discharge in strongly inward shifted configuration ($R_{axis} = 2.13$ m, $\Delta R_{axis} = R_{axis} - R_0 = -7$ cm, see Fig. 1). The diamagnetic β, as well as the stored energy, increased during neutral beam injection to 0.21% and 13 kJ. The net toroidal plasma current increased from zero to 3 kA in the direction of co-injection mainly due to the neutral beam driven current. The line averaged density increased to 7×10^{13} cm^{-3}. The radiative loss, measured by a bolometer, increased up to 800 kW and did not indicate the radiative collapse during neutral beam heating. We observed the finite amplitude signals in the cosine coils and

the ψ-loops, although Pfirsch-Schlüter current was integrally completely suppressed as indicated by almost zero plasma shift, Fig. 2(a).

On the other hand, in initially outward shifted Heliotron E configurations we could detect "normal" finite-amplitude fields due to Pfirsch-Schlüter current. The finite-β plasma shift and diamagnetic β are shown in Fig. 3(ΔR_{axis} = +3cm)in configuration with R_{axis} = 2.23m . In this case, as in other typical regimes with a small $|\Delta R_{axis}|$, we observed relatively large "natural" outward pressure-induced plasma shift during the neutral beam heating (2 MW).

Our final goal was to verify the prediction of MHD theory [10,11] that in Heliotron E we can realize an exotic regime with overcompensation, when increasing plasma pressure moves plasma inward. And, indeed, when the magnetic axis was shifted deeply toward the major axis (R_{axis} = 2.12 m, ΔR_{axis} = -8 cm), we observed this "anomalous" behavior of plasma column during neutral beam heating, Fig. 3. Figure 3 summarizes magnetically determined finite-β plasma shift as a function of diamagnetic β in the magnetic axis scan (R_{axis} scan) experiments.

The measured equilibrium plasma shift was strongly dependent on the initial magnetic axis position R_{axis}. It is unusual for conventional stellarators, however it can be explained from the first principles of MHD equilibrium theory. In stellarators there are two sources of inhomogeneity of the magnetic field: toroidicity and helical field. Accordingly

$$j_{PS} = j_t - j_h. \tag{2}$$

In l = 2 stellarator with a shear [10], where $B_\perp$ is the external vertical field shifting magnetic axis from the standard position, we can control this ratio, but rather strong vertical field $B_\perp$ is necessary to get substantial effect. At the same time, in a real device the acceptable range of $B_\perp$ is determined by the natural geometrical constraints: being shifted by $B_\perp$, plasma should not touch the wall. This restriction leads to the conclusion [10] that experimental efficiency of PS current reduction must be characterized by the value $\omega^0 = \iota_b mb / R$. The larger this value, the stronger suppression can be achieved by inward shifting of the vacuum magnetic axis. Heliotron E with ω^0 = 4.3 turns out to be a unique device: in other stellarators ω^0 = 1.6 (ATF), 1.5 (LHD), 1.3 (CHS) or smaller. Such a pronounced difference is the reason why the effect shown in Fig. 3 could not be seen in other stellarators or in calculations with a typical choice of parameters.

3. Conclusions

We have made the unique observation of the complete integral suppression of Pfirsch-Schlüter current with magnetic diagnostics in a finite-β stellarator plasma in Heliotron E and even more exotic "reversed" pressure-induced plasma shift. These effects are generally explained by MHD equilibrium theory for stellarator toroidal plasma with a strong magnetic hill and deep inward shift.

[1] J.M. Greene, J.L. Johnson, Phys. Fluids 4, 875 (1961).
[2] B.A. Carreras, G. Grieger, J.H. Harris et al., Nuclear Fusion 28, 1613 (1988).
[3] H. Yamada, K. Ida, H. Iguchi et al., Nuclear Fusion 32, 25 (1992).
[4] V.D. Pustovitov, Sov. J. Plasma Physics 14, 840 (1988).
[5] K. Matsuoka, S. Okamura,et al., Fusion Engineering and Design 26, 135 (1995).
[6] V.D. Pustovitov, Nuclear Fusion 30, 1523 (1990).
[7] S. Besshou, K. Ogata, K. Kondo et al., Nuclear Fusion 35, 173 (1995).
[8] J.M. Greene, J.L. Johnson, K.E. Weimer, Plasma Phys. 8, 145 (1966).
[9] M.I. Mikhailov, V.D. Shafranov, Plasma Phys. 24, 233 (1982).
[10] V.D. Pustovitov, Nucl. Fusion 36, 583 (1996).
[11] V.D. Pustovitov, Nucl. Fusion 36, 1281 (1996).
[12] J. Nührenberg, R. Zille, Phys. Lett. A 129, 113 (1988).
[13] G. Grieger, W. Lotz, P. Merkel et al., Phys. Fluids B 4, 2081 (1992).
[14] T. Obiki, M. Wakatani, M. Sato, S. Sudo et al., Fusion Technology 17, 101 (1990).
[15] S. Besshou, N. Fujita, K. Ogata et al., Nucl. Fusion 37, 13 (1997).

Fig. 1

Vacuum magnetic surfaces of Heliotron E configuration with inward shifted magnetic axis (R_{axis} = 2.13 m, ΔR_{axis} = -7 cm), where complete suppression of Pfirsch-Schlüter current was observed. The surfaces are produced by the helical coil (l = 2, m = 19), main vertical coils and auxiliary vertical (AV) coils. Magnetic surfaces rotate helically along the toroidal direction.
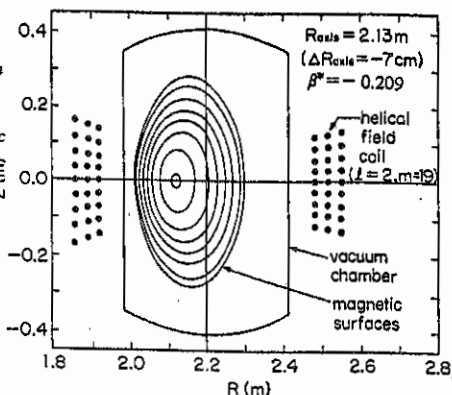
Fig. 2

The wave forms of plasma parameters of the discharge with the complete suppression of Pfirsch-Schlüter current (R_{axis} = 2.13 m): (a) finite-β plasma boundary shift, (b) volume averaged β measured by diamagnetic loop, (c) net toroidal plasma current, (d) first Fourier harmonic of the poloidal magnetic field measured by the cosine coil, (e) magnetic flux signal of y-loops.

R_{axis} = 2.13 m
(ΔR_{axis} = -7 cm)
β^* = - 0.209

helical field coil (l = 2, m=19)

vacuum chamber

magnetic surfaces

● : R_{axis} = 2.23 m, β^* = - 0.174, #74916
▲ : R_{axis} = 2.18 m, β^* = - 0.192, #74219
□ : R_{axis} = 2.13 m, β^* = - 0.209, #74862
— : R_{axis} = 2.12 m, β^* = - 0.213, #71231

B = 1.9 T, R_{axis} = 2.13 m (ΔR_{axis} = -7cm), #74862
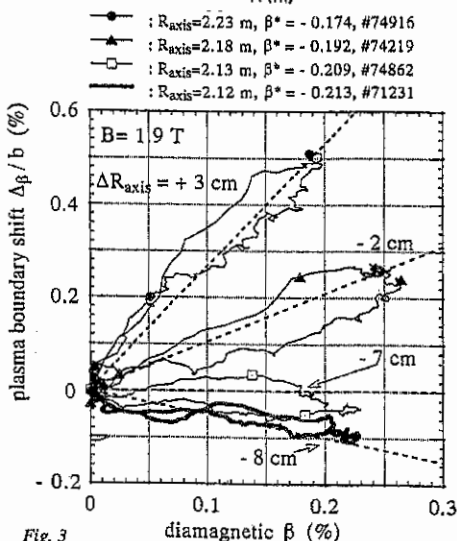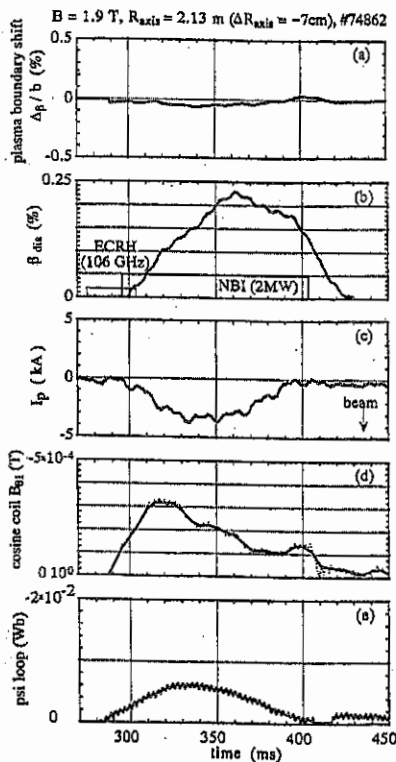
Fig. 3

Measured finite-β plasma shift at various initial positions of the magnetic axis. Each curve represents one plasma shot. Shown is dependence of Δ_β on diamagnetic β in outside shifted configuration with R_{axis} = 2.23 m, in slightly inside shifted configuration with R_{axis} = 2.18 m, in configuration with R_{axis} = 2.13 m, where almost complete compensation of Pfirsch-Schlüter current was observed, (plasma boundary was insensitive to plasma pressure), and in another deeply inward shifted configuration with R_{axis} = 2.12 m, where pressure-induced shift was "reversed". Dotted lines show average behavior of Δ_β as function of β.

Plasma Confinement Analysis
for Large Helical Device and Modular Heliotron Reactor

K.Yamazaki, T. Amano, K.Y.Watanabe, O.Motojima and M.Fujiwara

National Institute for Fusion Science,

322-6 Oroshi-cho, Toki-shi, Gifu-ken 509-52, Japan

1. Introduction

Helical systems have remarkable advantages in steady-state operations of fusion reactors. To demonstrate this, the Large Helical Device (LHD) with helical divertor (Fig.1a)[1] is now under construction, and the Modular Heliotron Reactor (MHR) concept with sectored helical coil system without poloidal coils (Fig.1b) [2] is under design based on this LHD physics concept. Here, special emphasis is put on the plasma transport analysis for the LHD experimental planning and for the MHR design studies.

(a) (b)

LHD   MHR
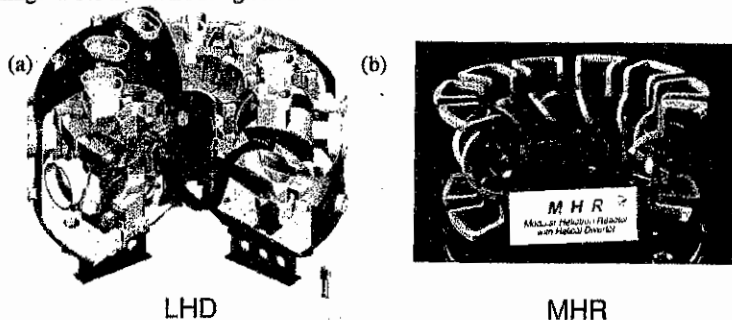
Fig. 1   (a) Schematic drawing of the Large Helical Device (LHD) and
(b) Model of the Modular Heliotron Reactors (MHR).

2. Physics Design for the Large Helical Device (LHD)

The physics properties of the LHD configuration have been widely investigated, and the beta achievement (~5%) and the plasma transport performance have already been clarified. Especially, the detailed transport analysis using 3-dimensional equilibrium / 1-dimensional transport code[3] has been performed for the LHD projection using anomalous transport (empirical or drift turbulence theory) combined with neo-classical transport. The flow chart of this analysis are shown in Fig. 2. This analysis is applicable to both tokamak and helical systems . Typical results on LHD plasmas have been obtained and reported in Ref.[3].
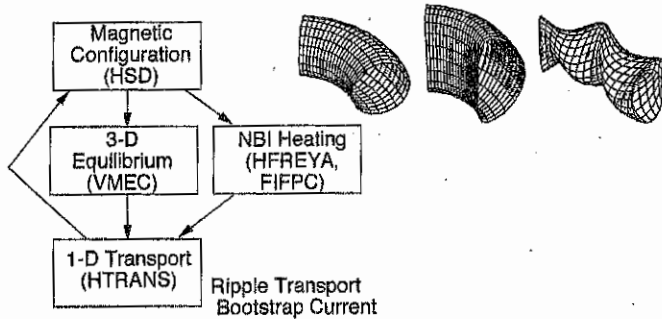
Fig. 2 Flow-chart for 1-dimensional transport / 3-dimensional equilibrium analysis applicable to both tokamak and helical systems

The simple zero-dimensional analysis with radial profile correction and impurity radiation is also used for the estimation of the LHD plasma performance. The initial plasma will be produced at the end of March in 1998, with 1.5 T magnetic field strength and 1 MW ECH heating power. Figure 2 shows the fusion triple product as a function of plasma pulse duration. The LHD target area for 3 T magnetic field / 20 MW heating power and the long pulsed operation regime with 3-10 MW heating power are shown. The shaded circles are initial trial experiment with half field and smaller heating power. The experiment will be built up from the initial stage ((1),(2)) to the higher performance (3a) and the longer pulse (3b).
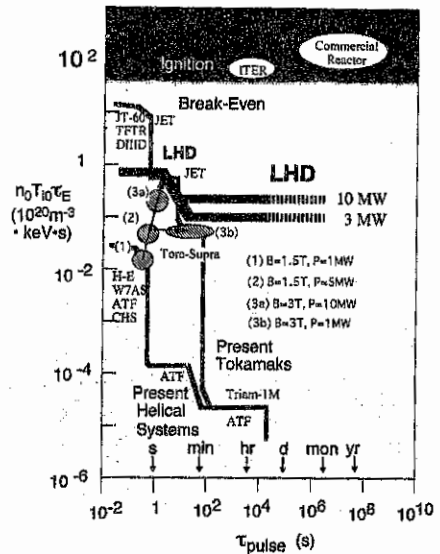
Fig. 3 Final target and initial parameter regimes for LHD experiment.

3. System Design for the Modular Heliotron Reactor (MHR)

The Modular Heliotron Reactor (MHR) had been proposed for the requirement of the compatibility between the clean helical divertor configuration and the modularized helical coil

system. The physics design of MHR is based on the physics advantage of the LHD concept. The equilibrium, stability and transport properties have been clarified in Ref.[4,5]. The system analysis for this reactor system have been carried out in Ref.[2,6]. The typical reactor design parameters for the standard and the compact reactors are given in Table 1.

Table 1

MHR parameters

	MHR-C (Compact Design)	MHR-S (Standard Design)
Major Radius (m)	10.5	16.5
Average Plasma Radius (m)	1.5	2.4
Toroidal Field on Axis (T)	6.5	5
Maximum Field on Coils (T)	14.7	14.9
Averege Plasma Density (10^{20}m^{-3})	3.4	2.0
Average Plasma Temperature (keV)	7.8	7.8
Volume Average Beta (%)	5	5
Energy Confinement Time (s)	1.53	2.67
LHD Scaling	2.64	4.01
NeoClassical Confinement	3.66	7.61
LHD Confinement Multiplier	2	2
Average Effective Helical Ripple	0.05	0.05

The ignition conditions of D-T burning plasmas in MHR are studied firstly using zero-dimensional power balance equations with profile corrections based on several empirical confinement scalings (LHD, gyro-reduced Bohm, Lackner-Gottardi or International Stellarator scalings) combined with one-point neo-classical ripple loss model (combined model of $1/\nu$, $\nu^{1/2}$ and ν regimes). For compact reactors confinement improvement factor of 2 is required with respect to the anomalous transport, and 1.5 times larger density limit is required. Figure 4 shows the typical examples of the effect of the density limit scaling.
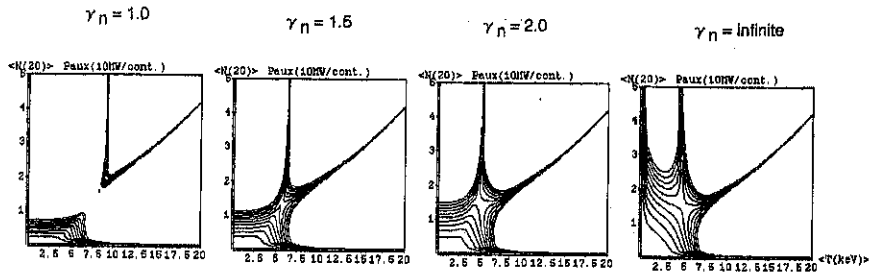
Fig. 4   POPCON diagram for MHR showing the effect of

density limit ($n < 0.25\gamma_n(PB/a^2R)^{0.5}$).

In addition to the simplified one-point model, detailed transport analyses using 3-dimensional

equilibrium / 1-dimensional transport code have been performed, and the achievement of the D-T ignition has been confirmed for MHR. The plasma density and the external heating power (less than 200 MW) are feedback-controlled to produce and sustain 500 MW alpha heating power. Ripple ion transport is dominant in the central region and the self-consistent negative radial electric filed reduces ion heat loss in the outer region.

Figure 5(a) shows the typical time history of the MHR start-up with external heating power of 100MW, and its radial profiles are given in Fig. 5(b).
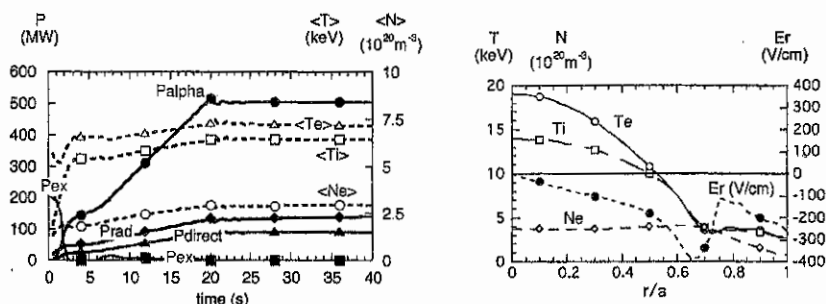
Fig. 5 (a) Time evolution and (b) radial profile of MHR plasma parameters

4. Summary

The transport analysis for the Large Helical Device (LHD) and the Modular Helical Reactor (MHR) is done with both one-point model including profile effect and the 1-dimensional transport / 3-dimensional equilibrium model. For the LHD initial start-up experiment, a kev plasma even in 1.5T / 1MW ECH heating is confirmed. For MHR, it is clarified that the standard design (major radius = 16.5m / field strength = 5T) can be ignited when the confinement enhancement factor of 2.

References:

[1] A Iiyoshi and K.Yamazaki, Phys. Plasma 2 (1995) 2349.

[2] K. Yamazaki et al., 16th IAEA Conference on Fusion Energy Conference, Montreal, Canada, 7-11 October 1996, IAEA-CN-64/G1-5.

[3] K.Yamazaki and T. Amano, Nucl. Fusion 32 (1992) 633.

[4] K. Yamazaki and K.Y.Watanabe, Nucl. Fusion 35(1995)1289.

[5] K.Y.Watanabe, K.Yamazaki and O.Motojima, Controlled Fusion and Plasma Physics (23rd EPS Conference)(Kiev, 24-28 June, 1996) Part II p. 567-570.

[6] K. Yamazaki et al., Trans. Fusion Tech., 27(1995)260.

Study of Ion Cyclotron Heating Experiment in LHD by Code Calculation

T. Seki, T. Watari, T. Mutoh, R. Kumazawa, E. F. Jaeger*, D. B. Batchelor*

National Institute for Fusion Science, Oroshi, Toki, Gifu 509-52, Japan
*Oak Ridge National Laboratory, Oak Ridge, TN 37831, USA

Introduction

In the National Institute for Fusion Science (NIFS), the Large Helical Device (LHD), which is the biggest superconducting helical system is under construction and the experiment is scheduled to start in 1998 [1]. Ion cyclotron range of frequency (ICRF) heating is planned as one of additional heating for LHD and the amplifier and rf components for long pulse operation have been developed in these several years. The frequency is variable from 25 MHz to 100 MHz and output power of 3 MW for steady state operation and 12 MW for pulse operation is expected. At the start, we intend to install two different type antennas. One is an innovative folded waveguide antenna (FWGA) and the other is conventional half turn loop antenna. FWGA produces the wave electric field parallel to the line of helical magnetic force and will be used for plasma production and ion Bernstein wave heating. The loop antenna launches fast wave and is thought as a main antenna for ICRF heating.

It is very difficult to get the good heating result in ICRF heating regime in helical plasma, since the high energy ions which are produced by waves escape from plasma. In compact helical system (CHS) in NIFS, the good heating result by fast wave was acquired by electron heating [2]. As seen from this result, it is important to prepare the many heating scenarios and understand the wave behavior in helical plasma. In this paper, ICRF heating using fast wave is studied by code calculation.

ORION Code

We used ORION code to analyze the fast wave heating in helical system. This code was developed by Dr. Jaeger in Oak Ridge National Laboratory [3,4] and introduced to NIFS by US-Japan collaboration activity. This code is global wave code and reduced-order-wave equation is solved in two-dimensional helical symmetry magnetic field configuration. The upshift of wave number parallel to the line of magnetic force and heating by mode-converted ion Bernstein wave are not included. This code was used to analyze the experiment of ATF and Alcator C-mod, and so on.

Calculation Results and Discussion

Electron Heating Scheme

Figure 1 shows the dependence of power absorption on rf frequency. Amplitude of magnetic field is 3 tesla and cyclotron resonance layer is located on the plasma center at the frequency of about 45 MHz. Plasma density is 1×10^{20} m^{-3} and the temperature is 2 KeV. Fast wave is launched from high field side. The ion cyclotron resonance layer is out of plasma at the frequency lower than 35 MHz and higher than 53 MHz. Deuterium plasma including 30 % hydrogen ion is used in this calculation. Electron heating is dominant in a frequency lower than 43 MHz and higher than 47 MHz. In these frequency range, the cyclotron layer is located on the outside from a half of the plasma radius. The range which electron heating is dominant moves inside of plasma as the fraction of minority ion increases. This result is reasonable to mode-conversion theory. Figure 2 shows the power deposition profile on flux surface in 40 MHz case. The main electron absorption is caused at the plasma center region through Landau damping/transit time magnetic pumping. In other frequency, electron absorption also occurs at the two ion hybrid resonance, which is located on slightly high field side of the cyclotron resonance. In this case, deposition profile of electron becomes peak at off-center position. Since ion absorption mechanism and electron absorption mechanism are competitive, ion heating becomes predominant when the cyclotron resonance layer goes into plasma center region even in this electron heating scheme. In a helical devices, it is predicted and observed [2] that the high energy ions which is produced by fast wave heating escape from inside of plasma. Then, the ion heating had some limit in achieving the best performance plasma in CHS experiment. To obtained the good heating efficiency comparable to NBI heating in LHD, strong electron heating may have to be accomplished by fast wave.

Ion Heating Scheme

Figure 3 shows the dependence of power absorption on rf frequency in ion heating case. Most of plasma parameters are same as electron heating scheme. However, fraction of minority ion is relatively small and 3 % of hydrogen is assumed in this calculation. Power absorption by minority ion becomes strong as the cyclotron layer moves into the plasma core region. Figure 4 shows the deposition profile on flux surface at the frequency of 44 MHz. Dotted line shows the normalized total absorption. In this case, the cyclotron layer is located near the plasma core and ion heating concentrates on plasma center region. At the frequency of 46 MHz, one cyclotron layer faces the antenna. Ion heating is stronger in this resonance layer than the other one. The peak of deposition profile moves to off-center position accompanied with the movement of resonance layer. Increase of minority absorption at the higher frequency side in Fig. 3 attributes to the cyclotron layer which exists in front of antenna. In the high field launch case, most of fast waves mode-convert to ion Bernstein waves and strong electron heating occurs in the tokamak plasma. However, this calculation shows that ion heating is

predominant in the wide position range of cyclotron layer.

For ion heating, the method that utilizes the "heavy" minority isotope ion (Li^7, C^{13}, Ne^{21}) was proposed by Dr. Vdovin et al. [5]. Figure 5 is schematic drawing of the dispersion relation in this case. It is expected that the fast wave launched at high field side converts into ion Bernstein wave at two-ion hybrid resonance layer ($\omega=\omega_{i-i}$) and it is absorbed at the second harmonic resonance layer of added isotope ion ($\omega=2\omega'_i$). This absorption is distinguished from another ion heating since the resonance layer does not degenerate into those of hydrogen and deuterium. Figure 6 shows the power absorption as function of fraction of minority ion. As a "heavy" minority, 10 % of lithium isotope ion (Li^7) is used in this calculation. Absorption by lithium increases slowly with the fraction of minority ion and reached maximum at 20 % of minority fraction. Two-ion hybrid resonance layer moves toward the second harmonic resonance layer of lithium ion with the increase of minority ion concentration and is located very closely in 20 % fraction of minority ion.

Summary

Using the global wave code, ORION, the calculation about fast wave heating in LHD has been carried out. Two heating schemes are distinguished from survey of the plasma parameters. Electron heating is dominant when the fraction of minority ion is relatively high and ion cyclotron resonance layer is located on plasma peripheral region. Ion heating is dominant when the minority ion concentration is small and ion cyclotron resonance layer is located on the plasma core region. For ion heating, the method using a "heavy" minority is tested. Scan of fraction of minority ion shows that some suitable condition seems to exist for effective "heavy" ion absorption.

As for future work, following matters are listed: proceed the analysis in comparison with the result from the other calculation code; include toroidal effect and consider the mode-converted ion Bernstein wave; develop the three-dimension code.

References

[1] M. Fujiwara, et al., Journal of Fusion Energy **15**, Nos. 1/2, (1996) 7.

[2] S. Masuda, et al., Nuclear Fusion **37** (1997) 53.

[3] E.F. Jaeger, et al., Rep. ORNL/TM-10223, Oak Ridge National Laboratory (1987).

[4] E.F. Jaeger, et al. Nuclear Fusion **30** (1990) 505.

[5] V. Vdovin, et al., submitted to NIFS report, National Institute for Fusion Science.
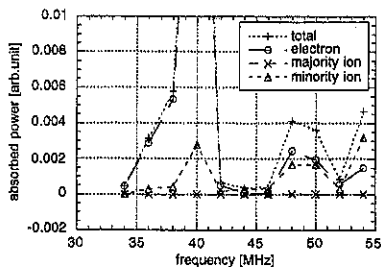
Fig.1. Power absorption dependence on rf frequency in electron heating scheme.
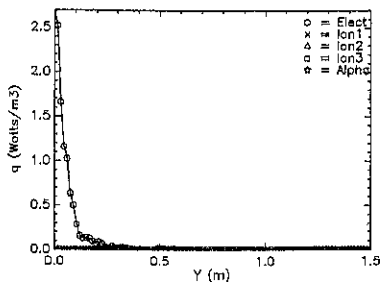
Fig.2. Power deposition profile on flux surface in electron heating scheme.
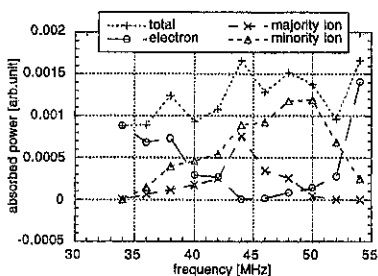
Fig.3. Power absorption dependence on rf frequency in ion heating scheme.
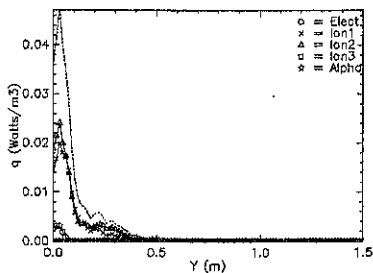
Fig.4. Power deposition profile on flux surface in ion heating scheme.
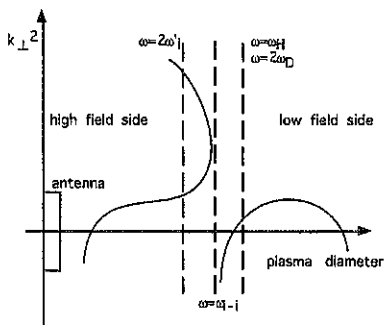
Fig.5. Dispersion relation in "heavy" minority scenario.
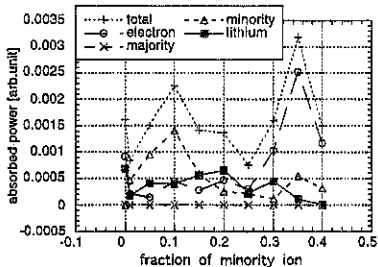
Fig.6. Power absorption as function of fraction of minority ion in addition of lithium isotope.

Preparative Study of Simulated Magnetic Measurements in Large Helical Device

S. Sakakibara, H. Yamada, K.Y. Watanabe, K. Yamazaki, K.Nishimura and O.Motojima

National Institute for Fusion Science
Oroshi-cho 322-6, Toki -shi, Gifu 509-52, Japan
e-mail address: sakakis@LHD.nifs.ac.jp

1. Introduction

For an experimental study on MHD equilibrium in helical devices, measurements of magnetic field and flux due to local currents which arise to satisfy ideal MHD equilibrium condition $J \times B = \nabla P$ are main subjects. In particular, the poloidal magnetic field and flux due to Pfirsch-Schlüter currents (P.S. currents) along magnetic field line causes the outward shift of magnetic axis (Shafranov shift), and this shift decides equilibrium β-limit and affects MHD characteristics such as rotational transform, magnetic shear and magnetic well/hill. Also, there is some possibility that it destroys the peripheral magnetic surfaces.

The magnetic measurements are valid to monitor the above-mentioned MHD characteristics, while they may give us information on pressure profile, current profile, beta value and so on. Since a currentless operation is possible in helical devices, the accurate measurement of magnetic field due to local currents is easy as compared with tokamaks. In real experiments of several helical devices, pressure profile and P.S. currents were discussed from comparison between poloidal loop signals and analytical calculation[1].

Measured magnetic field and flux should be interpreted by a careful comparison with the results from numerical analysis. The definition of plasma boundary given as initial condition for the numerical analyses on plasma equilibrium is very important for precise interpretation of signals from magnetic measurements. Nevertheless, the last closed flux surface (LCFS) in helical devices is not clear and the peripheral region is ergodic.[2] We should make the dependence of the plasma boundary position on calculated signals clear before real measurements.

At present, the measurement systems for magnetic flux and magnetic field are being developed in Large Helical Device (LHD). To optimize the specification of the measurement systems, peripheral magnetic structure in finite-β plasmas with various parameters has been investigated using the 3-D magnetic field analysis code DIAGNO[3,4], which calculates the response from finite-β-equilibria constructed by the 3-D equilibrium code VMEC.[5] In this study, the dependence of size of the LCFS and pressure profile on signals from diamagnetic loop and magnetic probes are mainly investigated. This analysis is also applicable to preparation for the database which is used for controlling magnetic configuration.

2. Magnetic Measurement Systems in LHD

The LHD is heliotron device which has the toroidal field period number of $m = 10$ with $l = 2$ helical coil, the plasma major radius $R = 3.9$ m and the plasma minor radius $\bar{a} \sim 0.6$ m.[6] The rotational transform in vacuum condition monotonically increases from 0.4 at magnetic axis to around 1.3 at the LCFS. Since the LHD has three pairs of poloidal coils, the operation with various magnetic configuration is available. This enables flexible operation such as real-time control of magnetic configuration in steady-state operation oriented superconductive coils.

In LHD, Rogowski coils, one-turn loops, diamagnetic loops, magnetic probes, hall probes and saddle loops are planned to be installed as basic systems (in detail, see Ref.[7]). Figure 1 shows magnetic surface in vacuum condition and location of poloidal array of magnetic probes. Three-type magnetic probes are installed to measure poloidal, radial and toroidal component of magnetic field, B_θ, B_r and B_ϕ, respectively. These probes are arranged by turns right under helical coils at inner wall of vacuum vessel as shown in this figure. Each magnetic surface indicated as A, B, C and D is the plasma boundary given for this calculation. It should be noted that ergodic region is not shown here. These surfaces have averaged minor radius of 55.2, 57.6, 61.4 and 65.2cm, respectively, and the radius of surface B is close to that of the outermost flux surface in vacuum configuration calculated by KMAG code.[8]
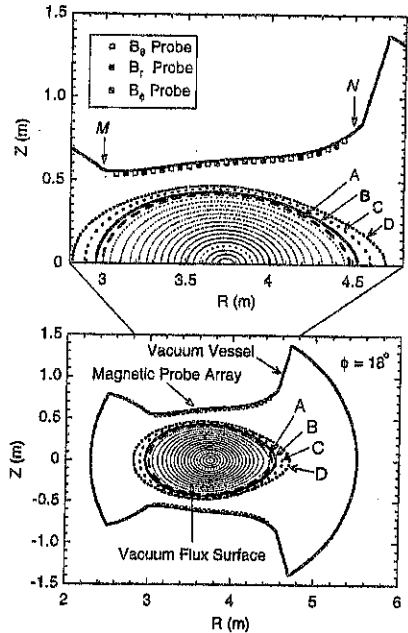
Fig.1 Vacuum flux surface and locations of magnetic probes
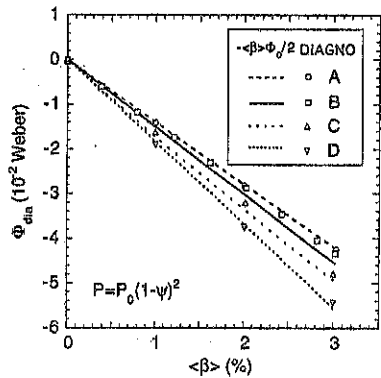
Fig.2 Changes in diamagnetic loop signals in different LCFS cases as a function of $\langle \beta \rangle$.

Signals from diamagnetic loops and magnetic probes are used as a subject of this analysis

3. Magnetic Field and Flux Analyses in finite-β plasmas

Measured magnetic flux as well as local magnetic field has been estimated using the 3-D magnetic field analysis code DIAGNO, which calculates the response from finite-β-equilibria constructed by the 3-D equilibrium code VMEC (In detail, see Ref[3]). Figure 2 shows changes in diamagnetic loop signals in plasmas with different LCFS as a function of $<\beta>$. The pressure profile is assumed as $P = P_0(1-\psi)^\alpha$, where ψ is the toroidal flux function which is normalized by the value at the LCFS. The diamagnetic loop signals linearly increase as a function of $<\beta>$ and are able to fit the diamagnetic flux estimated in cylinder plasmas, $\Delta\Phi_{dia}/\Phi_0 = -<\beta>/2$ within the limits of 6 %. This estimation is valid regardless of size of LCFS, and it suggests that toroidal effects are almost negligible and the diamagnetic flux depends on the only toroidal flux Φ_0. An identification of LCFS is a key issure for an accurate estimation of diamagnetic flux.

Figure 3 shows profiles of B_θ and B_r probe signals when the $<\beta>$ is 3 %. The horizontal axis means a distance from point M in Fig.1, and black and white arrows point to locations of B_θ and B_r probes, respectively. In practice, the measurement of parallel and perpendicular components, δB_1 and $\delta B_\perp$, to inside wall of vacuum vessel is easier than that of poloidal and radial component, and therefore these components are analyzed here. The dipole structure is gradually formed by increasing P.S. currents as a function of $<\beta>$, although the profiles are distorted because these components are decided by the complex shape of vacuum vessel. The ratio of parallel and perpendicular field to vacuum magnetic field is the order of 10^{-3}. Fig.3(a) shows the dependence of size of the LCFS on probe signals. All of magnetic components increase with the size of LCFS, and the profile is eventually deformed in the D case. In particular, the signals from probe
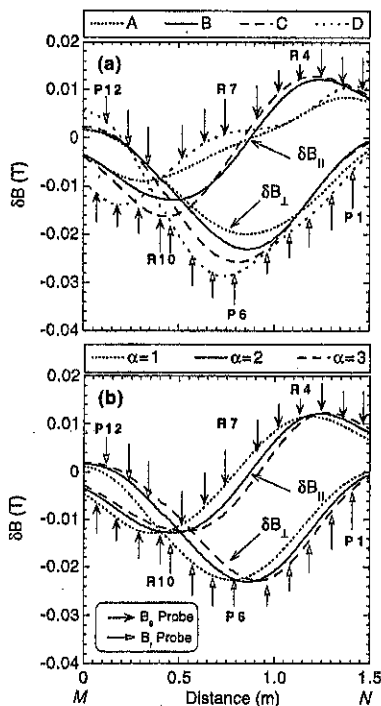
Fig.3 Profiles of δB_1 and δB_θ component on inner wall of vacuum vessel when $<\beta> = 3\%$. (a): different LCFS case and (b) different pressure profile case.

P6 increases by 50% as the radius of LCFS expands by 0.1 m. One of the reasons is the distanse between probes and the LCFS. The profile of probe signals in different pressure profile case is shown in Fig.3(b). The outward shift of peak of the profile in $\alpha=3$ (peaked) case is larger than that in $\alpha=1$ (broaden) case. This is reasonable for the dependence of pressure gradient on Shafranov shift. For example, the amplitude of R7 signal in the peaked case is about four times as large as that in the broaden case (Fig.4).

4. SUMMARY

The error included in the probe signals is estimated as about 3% when the averaged minor radius changes by 1%, even in currentless plasmas. This estimation cannot be bypassed from a view point of identification of pressure and current profiles. In addition, the peak shift of the profile of probe signals is caused in both cases (LCFS and pressure profile scan), and this trend is also impediment to physical interpretation of probe signals. On the other hand, the accurate diamagnetic flux may be estimeted by improving the precision of the measurement of the LCFS if net toroidal current is zero. The precise measurement of the LCFS with useful tools such as Li beam probe may make physical interpretation of magnetic measurements clear.

Fig.4 Changes in signals from (a): B_θ and (b): B_r probes as a function of $<\beta>$.

Acknowledgement

Reference

1) S. Morimoto et al., Nucl. Fusion 28 (1990) 1491.

2) N. Ohyabu, T. Watanabe et al., Nucl. Fusion, vol.34 (1994) 387.

3) H.J. Gardner, Nucl. Fusion 30 (1990) 1417.

4) R.N. Morris et al., Nucl. Fusion 29 (1989) 2115.

5) S. P. Hirshman and W. I. van Rij: Comput. Phys. Commun. 43 (1986) 143.

6) O. Motojima et al., Plasma Physics and Controlled Nuclear Fusion Research 3 (1990) 513.

7) S. Sakakibara et al., Proc. International Conf. on Plasma Phys. vol.2 (1996) 1430.

8) Y. Nakamura et al., J. Plasma Fusion Research 69 (1993) 41.

Introduction and Role of Effective Toroidal Curvature in L=1 Torsatron

S.Shiina, M.Aizawa and K.H.Saito

Atomic Energy Research Institute, College of Science and Technology, Nihon University, Tokyo, Japan

1 Introduction

This paper is concerning with the attractive transport features of negatively pitch-modulated L=1 torsatron, which leads to a nearly complete collisionless particle confinement[1]. We intend to explain these observed attractive transport features by introducing the effective toroidal curvature term (proportional to $\cos\theta$) for the localized trapped particles, ϵ_T, in the singular solutions of the equations of charged particle motion[2]. Here ϵ_T is given by the combination of usual toroidal curvature term ϵ_t and one of the nearest satellite harmonics of L=1 main helical field ϵ_0, $\epsilon_t - \epsilon_0$. The smallness of ϵ_T makes the field configuration quasi-helically symmetric in a sense that helically trapped particles are completely confined. This result indicates that, in a practical sense, small ϵ_T form a larger class than quasi-helical[3] systems.

2 Implications of effective toroidal curvature

The magnetic field B is given by a Fourier series along the magnetic line:

$$B(\psi,\theta,\phi)/B_0 = 1 + 2\sum_{n,m}' A_{n,m}(\psi)/A_{0,0}\cos(m\theta - n\phi)$$
$$\sim 1 - \epsilon_t(\psi)\cos\theta + \sum_i \epsilon_{L+i}(\psi)\cos((L+i)\theta - N\phi),$$

where B_0 is the magnetic field on the axis, θ is the poloidal angle, ϕ is the toroidal angle, L is the multi-polarity of helical windings, N is the number of helical field periods over the length of the machine, and ϵ_t is the coefficient of toroidal inhomogeneity, $\epsilon_t(= -2A_{0,1}/A_{0,0}) = r/R$. The amplitude of the helical ripple is given by the fundamental harmonic $\epsilon_L(= -2A_{N,L}/A_{0,0}, i = 0)$ and the satellite harmonics $\epsilon_{L+i}(= -2A_{N,L+i}/A_{0,0})$. For present L=1 torsatron, the relatively large Fourier components are ϵ_L, $\epsilon_0(= -2A_{N,0}/A_{0,0}, i = -1)$ and ϵ_t. In helical magnetic axis configurations as L=1 torsatron, the rotational transform N associated with the twisting of the surface about the major axis must be added to the usual rotational transform in stellarators with planar axes $\iota(\psi)$, so that $\theta \sim \iota(\psi)\phi + \omega$, $\omega = N\phi$. The relation of $\omega = N\phi$ is exact near the magnetic axis[4], but not always satisfied at distant position from the magnetic axis. However, the helically trapped particles localized in a limited narrow region of toroidal angle($\Delta\phi \sim 2\pi/N$) are considered to drift effectively in the magnetic field with the relation $\omega \sim N\phi$, then $\theta \sim N\phi$, at any magnetic surface ψ. With $\iota << N$ and $\theta \sim N\phi$, the term ϵ_0 being one of the nearest satellites is represented with the expression $\epsilon_0\cos N\phi \sim \epsilon_0\cos\theta$. In this circumstance, the effective toroidal curvature term (proportional to $\cos\theta$) for the trapped particles is given by the combination of two terms ϵ_t and ϵ_0, $\epsilon_t - \epsilon_0(\equiv \epsilon_T)$.

3   Singular Solutions of Charged Particle Drift Equations

The singular solutions of the charged particle drift equations in the magnetic coordinates(ψ, θ_0, χ) can be obtained by setting $d\theta_0/dt, d\psi/dt, d\chi/dt$ and $d\rho_\parallel/dt$ equal to zero[2], where ψ is the magnetic surface label, θ_0 is the field line label and χ is the scalar potential[5], $\rho_\parallel = m_i v_\parallel/eB$, m_i is the particle mass. Then, the obtained singular curves combine the minima, maxima and saddle points of B with the particle turning points. Thus, to consider the dependence of the particle confinement properties of a given device on its parameters, it is necessary to analyze the topology of singular curves. For this purpose it is convenient to use the longitudinal adiabatic invariant $J_\parallel = \oint v_\parallel d\ell$ of a particle trapped in a helical ripple well[6,7]. The form of the invariant $J_\parallel$ is expressed as follows

$$J_\parallel = (16R/N)\sqrt{\mu B_0 \bar{\epsilon}_L/m_i}[E(q^2) - (1-q^2)K(q^2)],$$

where E and K are the complete elliptic integrals of the first and second kind; q^2 is the modulus of elliptic integrals of the form $q^2 = [\lambda^2 + \epsilon_t \cos\theta + \bar{\epsilon}_L]/2\bar{\epsilon}_L$, where $\bar{\epsilon}_L = \epsilon_L\bar{\epsilon}$ and $\bar{\epsilon} = \sqrt{A^2 + D^2}$, $A = -\sum \bar{\epsilon}_{L+i}\sin(i\theta)$, $D = \sum \bar{\epsilon}_{L+i}\cos(i\theta)$, $\lambda = v_\parallel/v_\perp$ and $\bar{\epsilon}_{L+i} = \epsilon_{L+i}/\epsilon_L$. When $J_\parallel$ is conserved, it is convenient to consider the particle confinement conditions on a plane, $r\cos\theta$, $r\sin\theta$, where r is the radius of a given magnetic surface, $r = \sqrt{2\psi}$. Expression $J_\parallel$ is valid when $0 \leqq q^2 < 1$. Using $q^2 = 1$ and $q^2 = 0$, one can obtain two kinds of curves(transition curves and forbidden curves). For a fixed value of $\lambda = \lambda_0$, the equation for the transition curve has the form $\bar{f}_t \equiv \lambda_0^2 + \epsilon_t \cos\theta - \bar{\epsilon}_L = 0$. A particle starting inside the region given by eq. $\bar{f}_t = 0$ is helically untrapped (passing) until the velocity pitch angle obeys the condition $|v_\parallel(t)/v_\perp(t)| \geqq \lambda_0$. For an L=1 torsatron with a single harmonic field $(i = 0, \bar{\epsilon}_L = \epsilon_L, \bar{f}_t = f_t)$, the transition curves are the circles with radius $R_t \sim \sqrt{(\lambda_0^2/\epsilon_L) + (\epsilon_t/2\epsilon_L)^2}$, which are displaced to the outside of the torus by the value $\Delta r_t = \epsilon_t/2\epsilon_L$ if it is positive. Thus, the fraction of a given pitch having transitional orbits as well as the fraction of particles with absolutely passing particles are proportional to the ratio ϵ_t/ϵ_L. Both functions of $f_t(r, \theta)$ and $\bar{f}_t(r, \theta)$ have its minimum on θ for a fixed value of r when $\theta = \pi$, and it is obvious that, if $\bar{f}_t(r, \theta = \pi) > f_t(r, \theta = \pi)$ or $\sum(\bar{\epsilon}_{L+i} + \bar{\epsilon}_{L-i})(-1)^{i+1} > 0$, then the fraction of passing particles increases owing to the satellite effect. The equation for the forbidden curve, which gives the confinement conditions for trapped particles, can be obtained from eq. for q^2, under the assumptions $\lambda = 0$ and $q^2 = q_0^2 =$const., $\bar{f}_f \equiv \epsilon_t \cos\theta - \bar{\epsilon}_L(2q_0^2 - 1) = 0$. All turning points($v_\parallel = 0$) of helically trapped particles with a given value of the trapping parameter q_0^2 are concentrated on curves $\bar{f}_f = 0$. For an L=1 torsatron with a single harmonic field, the forbidden curves are the circles with radius $R_f \sim \epsilon_t/[2\epsilon_L(2q_0^2 - 1)]$, which are shifted from the axis by the value R_f. For the most-deeply-trapped particles($q_0^2 \sim 0$) the contours of forbidden curves are close to the contours of constant-B_{min} curves. Since the orbits of the trapped particles with $q_0^2 < 1$ are far from the B_{min} contours, the confinement conditions for trapped particles in this case are determined by the forms of the forbidden curves and the degree of their being closed in the confinement region. The radius R_f of the forbidden circle is proportional to the ratio ϵ_t/ϵ_L. Therefore, the confinement conditions for trapped particles in the $\epsilon_t > \epsilon_L$ configuration are worse than those in the $\epsilon_L >> \epsilon_t$ configuration. The improvement of trapped particle confinement under the satellite effect takes place if the contours of the $\bar{f}_f$ curves are encompassed by the contours of the f_f curves inside the torus, $\bar{f}_f < f_f$ or $\sum(\bar{\epsilon}_{L+i} + \bar{\epsilon}_{L-i})(-1)^{i+1} < 0$. This condition is incompatible with an increase of the fraction of passing particles owing to the satellite effect.

4 Role of ϵ_T on Collisionless Particle Confinement

The transitional curves $f_t = 0$ predict that the fraction of the passing particles becomes the largest in the L=1 torsatron with the coil pitch modulation parameter of $\alpha^* = -0.4$ because the ratio of $|\epsilon_t/\epsilon_L|$ is the largest for $\alpha^* = -0.4$[1]. This prediction is consistent with the observation of the fraction of passing particles to total particles, averaged over the particles starting at four different θ positions on the magnetic surface of $\psi = 0.5$ with the energy of E_K=25keV and random values in the velocity pitch angle $v_{||}/v$ ($v_{||}$ is velocity parallel to B): the fraction is 98/164(60%) for $\alpha^* = +0.4$, 104/164(63%) for $\alpha^* = +0.2$, 111/164(68%) for $\alpha^* = 0$, 116/164(71%) for $\alpha^* = -0.2$ and 123/164(75%) for $\alpha^* = -0.4$, indicating the largest fraction for $\alpha^* = -0.4$ even though the perturbation of the main satellite $\bar{\epsilon}_0$ has an effect of rather decreasing the passing particle fraction since it is negative for $\alpha^* = -0.4$. The forbidden curves for the deeply-trapped-particles having the trapping parameter of $0 < q_0^2 < 0.5$ predicts that the confinement conditions for these trapped particles become the best in the L=1 torsatron configuration with $\alpha^* = +0.4$, since the ratio $|\epsilon_t/\epsilon_L|$ is the smallest or the radius of the forbidden curves R_f becomes the smallest for $\alpha^* = +0.4$[1]. This prediction is inconsistent with the observation that the averaged fraction of lost particles to trapped particles is 26/66($\sim$39%) for $\alpha^* = +0.4$ and 8/48($\sim$17%) for $\alpha^* = -0.2$, indicating the worst confinement of the trapped particles in the $\alpha^* = +0.4$ configuration and the best one in the $\alpha^* = -0.2$ configuration where the ratio $|\epsilon_t/\epsilon_L|$ is relatively large, then the radius R_f is predicted to be relatively large. This inconsistency would be explained by considering the perturbation of the main satellite $\bar{\epsilon}_0(= A_{N,0}/A_{N,1})$, which has an effect of rather deteriorating the confinement condition for $\alpha^* = +0.4$ since it is positive, and improving it for $\alpha^* = -0.2$ since it is negative. The effect of $\bar{\epsilon}_0$ can be understood physically by the playing role of the effective toroidal curvature term for trapped particles, ϵ_T, which is the largest($\sim$0.2) for $\alpha^* = +0.4$ and the smallest($\sim$0) for $\alpha^* = -0.2$. Introducing ϵ_T instead of ϵ_t on evaluating R_f gives the largest and the smallest($\sim$0) forbidden radius, for $\alpha^* = +0.4$ and for $\alpha^* = -0.2$, respectively. Therefore, the smallness of ϵ_T results in the good confinement of trapped particles. For the most-deeply trapped particles the contours of forbidden curves are close to the contours of const-B_{min} curves. So, in this case, the unclosure of the B_{min} contours reveals bad confinement of the most-deeply trapped particles. Indeed, the largest area of closed B_{min} contours within the last closed flux surface is observed in $\alpha^* = -0.2$ configuration [1]. Furthermore, the forbidden curves for the moderately-deeply-trapped particles having the trapping parameter $0.5 < q_0^2 < 1$ predicts, if ϵ_T is introduced instead of ϵ_t, that the confinement conditions of these trapped particles becomes the best in the $\alpha^* = -0.2$ configuration because $\epsilon_T \sim 0$ or $R_f \sim 0$, and relatively worse in the $\alpha^* = +0.4$ configuration because the ratio ϵ_T/ϵ_L is negative, then the forbidden region becomes wider. These predictions are also consistent with the observations. The velocity pitch angle of the loss particles in the $\alpha^* = -0.2$ configuration is within the region of $0.6 < \lambda < 1.2$, which corresponds to transitional and/or toroidally (toroidal field) trapped particles [1]. The lower boundary $\lambda \sim$ 0.6 corresponds to the upper limit of pitch angle of helically trapped particles and the upper boundary $\lambda \sim 1.2$ to the lower limit of pitch angle of passing particles. Noticeable results is that the helically trapped particles are completely collisionlessly confined in the configuration with $\alpha^* = -0.2$ because of the significant reduction of ϵ_T. The fraction of the loss particles (averaged over different starting θ positions and velocity pitch angle) is smaller $\sim$2.5% for the 100keV protons starting at $\psi = 0.3$($r = 0.55a$, aspect ratio $A = 15$, where ϵ_T is minimum) than $\sim$6.0% for those starting at $\psi = 0.5$($r = 0.7a, A = 12$)[1]. The 100keV proton orbits calculation was

made with $a/\rho = 32$ (a is plasma radius, ρ is gyro radius, $a = 0.25m$, magnetic field strength on axis $B_0 = 4.4T$) value of which gives the same collisionless loss times as that for α-particles in a reactor with $a = 1.6m, B_0 = 5.3T$. Two characteristic loss times can be distinguished; the larger loss rate in the time range of 10^{-4}sec and the smaller loss rate in relation of 10^{-3}sec. The faster loss depends strongly on ϵ_T through α^* and the slower loss is nearly independent of ϵ_T. Last, we intend to explain the effect of ϵ_T on the drift width of trapped particles[1]. The drift width observed is the smallest in the $\alpha^* = -0.2$ configuration with the smallest ϵ_T, suggesting that ϵ_T plays role of determining the drift width. The other small satellites excluding ϵ_0 makes the drift width larger by a factor of ~ 3 in maximum (for the 25keV proton started at $\psi = 0.5$, $\theta = \phi = 0$ with $v_\parallel/v = 0$) compared with that($\sim$1cm)in the presence of the nearest satellite harmonic ϵ_0 only. However, these small satellites have little effect on the fraction of loss particles so that they change to loss particle from passing particle for a limited pitch angle of $v_\parallel/v \sim \pm 0.76$ only. The drift width of trapped particles is weakly dependent of particle energy, as the result, the loss rate is nearly constant in the range of observed 25keV to 100keV.

5   Conclusion

In the L=1 torsatron with $N >> \iota$, the effective toroidal curvature term, which is given by the combination of usual toroidal curvature and one of the nearest satellites of L=1 main helical field, plays an important role on collisionless particle confinement. The fraction of passing particles is determined by the usual toroidal curvature term ϵ_t, on the other hand, the confinement conditions of trapped particles by the effective toroidal curvature term ϵ_T. There is an optimum coil pitch modulation parameter which leads to nearly complete collisionless particle confinement. The smallness of ϵ_T makes L=1 torsatron quasi-helically symmetric in a sense that helically trapped particles are completely confined, and the loss particles are transitional particles and/or toroidally trapped particles. This result indicates that, in a practical sense, small ϵ_T systems form a larger class than quasi-helical systems.

References

[1] M.Aizawa,K.H.Saito,K.N.Saito,I.Kawakami,S.Shiina; Extended Synopses IAEA-CN-64 of 16th IAEA Fusion Energy Conference CP-8(PartB) 307 (1996).

[2] M.S.Smirnova,A.A.Shishkin; Nucl. Fusion 32(No.7), 1147 (1992).

[3] J. Nuhrenberg, R. Zille; Phys. Lett. A.129 113 (1988).

[4] A.H.Reiman, A.H.Boozer; Phys. Fluids 27, 2446 (1984).

[5] A.H.Boozer; Phys. Fluids 23, 904 (1980); A.H.Boozer,G.KUO-PETRAVIC; Phys. Fluids 24, 851 (1981).

[6] K.C.Shaing,S.A.Hokin; Phys. Fluids 26 (No.8), 2136 (1983).

[7] V.E.Bykov,H.V.Georgievskij,V.G.Peletminskaya,A.V.Khodyachikh,A.A. Shishkin; Nucl. Fusion 24, 1195 (1984).

A model equation for high-n ballooning and TAE modes in an $L = 2$ heliotron/torsatron system

N. Nakajima

National Institute for Fusion Science, 322-6, Oroshi-cho, Toki, 509-52, Japan

1. Introduction

Recently, characteristics of high-n ballooning modes and the relation with low-n ballooning modes are examined in a planar axis $L = 2/M = 10$ heliotron/torsatron system with a large Shafranov shift, where L and M are the polarity and the toroidal pitch number of helical coils, respectively [1, 2]. On the basis of the intensive investigation of the properties of the local and global quantities of finite-β equilibria relevant to ballooning modes, destabilization mechanism of the high-n ballooning modes in the region with stellarator-like global magnetic shear is clarified, i.e., high-n ballooning modes are destabilized due to the disappearance of the local magnetic shear. This disappearance comes from a large Shafranov shift corresponding to the high-β ordering and a model expression of the local magnetic shear is obtained. In this paper, a simple model equation for high-n ballooning and Toroidicity-induced shear Alfvén Eigenmodes (TAE) modes is derived in a planar axis $L = 2$ heliotron/torsatron system with a large Shafranov shift by using the model expression of the local magnetic shear. By using this model equation, the 2nd stability of the high-n ballooning modes in the stellarator-like global magnetic shear region could be investigated. The dispersion relation of high-n TAE modes is also obtained analytically.

2. Model Equation

Essential characteristics of finite-β equilibria of a planar axis $L = 2$ heliotron/torsatron system are described by nearly axisymmetric large Shafranov shift (Δ) due to toroidal force balance under the non-axisymmetric distribution of the magnetic field strength inherent in the vacuum configuration. The Shafranov shift is so large ($\Delta' \equiv d\Delta/dr \sim O(1)$) that the equilibria correspond to high-β ordering of tokamaks and that both the poloidal field and flux surfaces are axisymmetrically compressed on the outside of the torus as β increases, leading to nearly axisymmetric deformation of the local magnetic shear with β value. An effect of the helicity due to the helical coils, i.e., the three dimensional property appears only in the local magnetic curvature in the lowest order as well as the toroidicity through the distribution of the magnetic field strength inherent in the three dimensional vacuum magnetic field.

In order to obtain a model expression for the local magnetic shear, the equation of a current-less equilibrium based on the stellarator expansion (high-β ordering) is approximately solved with the use of the Shafranov coordinate system (r, θ, φ) [3]. Then, Shafranov coordinate system (r, θ, φ) is treated as a uni-arc magnetic coordinate system $(\psi, \theta_u, \zeta_B)$ associated with the Boozer magnetic coordinate system $(\psi, \theta_B, \zeta_B)$ [4], where ψ is the toroidal flux divided by 2π, θ_B and ζ_B are the Boozer poloidal and toroidal angles, respectively. θ_u is the poloidal angle proportional to the arc length defined on planes of constant ψ and ζ_B, which is related to the Boozer poloidal angle as $\theta_B = \theta_u + \lambda_u(\psi, \theta_u, \zeta_B)$ with a periodic function λ_u with respect to θ_u and ζ_B. Since the Boozer poloidal angle θ_B in a vacuum configuration is very similar to the uni-arc poloidal angle and since the dominant part of the change in the local magnetic

structure due to the Shafranov shift is axisymmetric, the function λ_u in a finite-β equilibrium may be approximated by axisymmetric components only. Note that the Boozer toroidal angle ζ_B is very similar to the geometrical toroidal angle of the Shafranov coordinates φ and that the poloidal angles in the Shafranov coordinate system θ is proportional to the arc length as well as θ_u in uni-arc magnetic coordinates. As a result of it, the periodic function λ_u is written in terms of the Shafranov shift Δ as $\lambda_u = \Delta'(r)\sin\theta$ where Δ has the properties: $\Delta'(r) = R_0\beta'/(4\iota^2) (\leq 0) \sim O(1)$, $\Delta(r) \geq 0$, $\Delta(a) = 0$ with the major radius R_0, the magnetic field strength at $R = R_0$ B_0, $\beta = 2P/B_0^2$. Note that $\Delta' \sim O(1)$ for the high-β ordering $\beta \sim O(\varepsilon_t)$. Thus, the integrated local magnetic shear along a field line and the perpendicular wave number are given by [1]

$$
\int_0^\theta \hat{s}\,d\theta = s(\theta - \theta_k) - \overline{\alpha}\left[1 - \overline{\alpha}\cos\theta + 3s + \frac{r\beta''}{\beta'}\right]\sin\theta,
$$

$$
|\vec{k}_\perp|^2 = (1 - \overline{\alpha}\cos\theta)^2 \left[1 + \Lambda^2\right], \quad \Lambda = \frac{\displaystyle\int_0^\theta \hat{s}\,d\theta}{(1 - \overline{\alpha}\cos\theta)^2},
$$

where

$$
\overline{\alpha} \equiv -\Delta' = -\frac{R_0}{4\iota^2}\beta' (\geq 0) \sim O(1), \quad s = \frac{r}{q}\frac{dq}{dr},
$$

By using above quantities, the model equation for high-n ballooning and TAE modes is expressed as follows:

$$
\frac{1}{1 - \overline{\alpha}\cos\theta}\frac{\partial}{\partial\theta}\left\{(1 - \overline{\alpha}\cos\theta)\left[1 + \Lambda^2\right]\frac{\partial\xi}{\partial\theta}\right\}
$$
$$
+ \; \Omega^2\left\{1 + 4\varepsilon_t\cos\theta + 4\varepsilon_h\cos\left[(L - qM)\theta + Mq\overline{\alpha}\sin\theta - M\alpha\right]\right\}(1 - \overline{\alpha}\cos\theta)^2\left[1 + \Lambda^2\right]\xi
$$
$$
+ \; 4\overline{\alpha}\left\{\delta + \cos\theta + r\frac{\varepsilon_h'}{\varepsilon_t}\cos\left[(L - qM)\theta + Mq\overline{\alpha}\sin\theta - M\alpha\right]\right.
$$
$$
\left. + \left[\sin\theta + L\frac{\varepsilon_h}{\varepsilon_t}\sin\left[(L - qM)\theta + Mq\overline{\alpha}\sin\theta - M\alpha\right]\right]\left[\overline{\alpha}\sin\theta + (1 - \overline{\alpha}\cos\theta)\Lambda\right]\right\}\xi = 0 \;(1)
$$

where α and δ indicate the label of the magnetic field line and the averaged magnetic well ($\delta < 0$) or hill ($\delta > 0$), respectively. ε_t and ε_h correspond to toroidicity and helicity of helical coils, respectively. Note that the influence of the helicity of the helical coils, i.e., the three dimensional property denoted by the label of the field line α is included only in the normal and geodesic magnetic curvature terms through the magnetic field strength except for the small correction in the inertia term.

More simplified model equation with essential parts of the finite-β effect (Shafranov shift) is obtained by neglecting the effect of Shafranov shift ($\overline{\alpha}$) except for the local magnetic shear:

$$
\underbrace{\frac{\partial}{\partial\theta}\left\{\left[1 + \Lambda^2\right]\frac{\partial\xi}{\partial\theta}\right\}}_{\text{field line bending term}} + \underbrace{\Omega^2\left\{1 + 4\varepsilon_t\cos\theta + 4\varepsilon_h\cos\left[(L - qM)\theta - M\alpha\right]\right\}\left[1 + \Lambda^2\right]\xi}_{\text{inertia term}}
$$
$$
+ \; \underbrace{4\overline{\alpha}\left\{\delta + \cos\theta + r\frac{\varepsilon_h'}{\varepsilon_t}\cos\left[(L - qM)\theta - M\alpha\right]\left[\sin\theta + L\frac{\varepsilon_h}{\varepsilon_t}\sin\left[(L - qM)\theta - M\alpha\right]\right]\Lambda\right\}\xi}_{\text{curvature term}} = 0\,(2)
$$

where

$$\overline{\alpha} \equiv -\frac{R_0\beta'}{4\ell^2} \ (> 0) \ \sim O(1), \tag{3}$$

$$\Lambda \equiv \int_0^\theta \delta d\theta = s(\theta - \theta_k) - \overline{\alpha}\left[1 + 3s + \frac{r\beta''}{\beta'}\right]\sin\theta \tag{4}$$

3. The 2nd stability of high-n ballooning modes

From the model equation given by Eq. (2), we can discuss the possibility of the 2nd stability of the high-n ballooning modes in the stellarator-like global magnetic shear region, $s < 0$, by using the energy principle. Creating the quadratic form of Eq. (2) in terms of an appropriate Gaussian type test function, we can see

$$\Omega^2 = \frac{\delta W_s - \delta W_c}{\delta W_i}, \tag{5}$$

where three terms in the right-hand side have the quadratic form with respect to $\overline{\alpha}$. $\delta W_s(> 0)$ and $\delta W_i(> 0)$ are stabilizing term due to the field line bending and inertia term, respectively. The coefficients of $\overline{\alpha}^2$ in both terms are positive definite. δW_c is the destabilizing term due to pressure gradient in the locally bad magnetic curvature, which has the following form:

$$\begin{aligned}\delta W_c &= -4\overline{\alpha}^2\left[1 + 3s + \frac{r\beta''}{\beta'}\right]a_c' + 4\overline{\alpha}b_c' \\ &\sim -4\overline{\alpha}^2\left[1 + 3s\right]a_c' + 4\overline{\alpha}b_c'\end{aligned} \tag{6}$$

where $a_c' \ (> 0)$ comes from the integration of geodesic curvature and a part of Λ given by Eq. (4) and the second similarity holds around the flux surface with the maximum pressure gradient. Note that the sign of the coefficient of $\overline{\alpha}^2$ depends on the sign of $1 + 3s + r\beta''/\beta'$ or $1 + 3s$. When $s > 0$ as tokamak-like shear, the sign of the coefficient of $\overline{\alpha}^2$ is negative, leading to the 2nd stability. When $s < 0$ as stellarator-like shear, however, the sign of the coefficient of $\overline{\alpha}^2$ becomes positive if the condition of $1 + 3s + r_s\beta''/\beta' < 0$ or $1 + 3s < 0$ is satisfied, which leads to the expectation that once high-n ballooning modes become unstable in the region with strong stellarator-like global magnetic shear, the 2nd stability is unlikely to occur. More precise investigation will be done elsewhere.

4. Dispersion Relation of high-n TAE

By using the asymptotic matching method[5], the dispersion relation of the high-n TAE modes is obtained from Eq. (1) by putting $\varepsilon_h = 0$. In the limit of $|s| \ll 1$, the lower and upper boundaries of the 1st spectral gap are given by

$$\Omega^2_{lower} = \frac{1}{4}\frac{1 - 3\overline{\alpha}}{1 + 2\varepsilon_t - \overline{\alpha}} < \frac{1}{4}, \quad \Omega^2_{upper} = \frac{1}{4}\frac{1 + 3\overline{\alpha}}{1 - 2\varepsilon_t + \overline{\alpha}} > \frac{1}{4}. \tag{7}$$

As β increases, the eigenvalue corresponding to the lower (upper) boundary decreases (increases), namely, the 1st spectral gap becomes wide. The eigenvalue of the high-n even TAE mode is given by

$$\Omega^2 = \frac{1}{4}\left\{1 + \frac{2(\varepsilon_t + \overline{\alpha})}{\frac{1 + \Xi}{1 - \Xi} - 3\overline{\alpha}}\right\}^{-1}, \quad \Xi = \frac{\pi^2 s^2}{16}\left[1 - \frac{\overline{\alpha}}{\overline{\alpha_c}}\right]^2, \quad \overline{\alpha_c} = \frac{s^2}{2(1 + 4\delta) + s(1 + 5s + \frac{r\beta''}{\beta'})}. \tag{8}$$

As β increases, Ω^2 decreases. When β reaches a value which satisfies $\overline{\alpha} = \overline{\alpha_c}$, high-$n$ even TAE modes hit the lower boundary and disappear. Since the eigenvalue corresponding to the lower boundary decreases as β increases, the high-n ballooning modes appear immediately after disappearance of the high-n even TAE modes.

In the same limit, the eigenvalue of the high-n odd TAE mode is given by

$$\Omega^2 = \frac{1}{4}\left\{1 - \frac{2(\varepsilon_t + \overline{\alpha})}{\frac{1 + \Xi^{-1}}{1 - \Xi^{-1}} + 3\overline{\alpha}}\right\}^{-1}, \quad \Xi = \frac{\pi^2 s^2}{16}\left[1 - \frac{\overline{\alpha}}{\overline{\alpha_c}}\right]^2, \quad \overline{\alpha_c} = \frac{s^2}{2(4\delta - 1) - s(1 + 5s + \frac{r\beta''}{\beta'})} \quad (9)$$

when the condition $\overline{\alpha} > \overline{\alpha_c} > 0$ is satisfied. Thus, the magnetic hill, $\delta > 0$, and the stellarator-like global magnetic shear, $s < 0$, are favorable to the appearance of the high-n odd TAE modes. When $\alpha \gtrsim \alpha_c$, the eigenvalue exists near the upper boundary. By hitting the upper boundary, the high-n odd TAE modes disappear. The analysis in the opposite limit, $|s| \gg 1$, will be done elsewhere.

5. Discussion

In the case of $L = 2$ heliotron/torsatron with a large Shafranov shift, there is a possibility that the local magnetic shear disappears in the region with the stellarator-like strong global magnetic shear, which leads to the destabilization of the high-n ballooning modes. The integrated local magnetic shear appearing in the high-n ballooning equation consists of the secular term due to global magnetic shear and the oscillatory correction term due to the Shafranov shift as seen in Eq. (4). Between tokamaks and heliotron/torsatron with strong stellarator-like global magnetic shear around the flux surface with the maximum pressure gradient, both coefficients of the secular term and the oscillatory correction term, namely, s and $-\overline{\alpha}[1 + 3s]$ have opposite sign. Thus, after disappearance of the integrated local magnetic shear, the restoration of the stabilizing force due to field line bending occurs in both devices. However, the difference of the sign of $-\overline{\alpha}[1 + 3s]$ between both devices changes the contribution of the geodesic curvature. Thus, although in the case of tokamaks there is the 2nd stability for high-n ballooning modes, in the case of heliotron/torsatron the 2nd stability is unlikely to occur, once high-n ballooning modes occur.

References

[1] N. Nakajima, Phys. Plasmas **3** (1996) 4545.

[2] N. Nakajima, Phys. Plasmas **3** (1996) 4556.

[3] V. D. Shafranov, in *Reviews of Plasma Physics*, ed. M. A. Leontovich (Consultants Bureau, New York, 1966), Vol.2, p103.

[4] A. H. Boozer, Phys. Fluids **23** (1980) 904.

[5] G. Y. Fu and C. Z. Cheng, Phys. Fluids B **1** (1990) 985.

Electron temperature and density determination in combination of hydrogen spectroscopy and collisional-radiative model in plasma decay phase of CHS

M. Goto, S. Morita, T. Ozaki, Y. Shirai, H. Idei, N. Inoue, S. Kubo,
K. Matsuoka, T. Minami, S. Okamura, M. Osakabe, R. Sakamoto, K. Tanaka
and torus experiment group
National Institute for Fusion Science, Toki 509-52, Japan

Abstract

Spectra of neutral hydrogen atoms have been observed from NBI plasmas in CHS. In the plasma decay phase after turning off the NBI pulse, a typical recombining plasma was identified. Assuming the Saha-Boltzmann equilibrium for the highly excited levels, the electron temperature of 0.1 eV was determined and found to be constant for several tens of millisecond. From the comparison between experimentally determined population density distribution and the collisional-radiative model calculation, the electron density was successfully obtained. The electron temperature and density determination using hydrogen spectroscopy in the plasma decay phase are demonstrated with well agreement between the experimental results and the model calculation.

1   Introduction

After turning off the NBI pulse in compact helical system (CHS, $R = 1$ m, $<a> = 0.2$ m, $B_t = 2$ T, $l/m = 2/8$), the plasmas are typically maintained for several tens of millisecond. Since the magnetic surface for the confinement is steadily formed, the electron density slowly decays rather than the electron temperature. In this plasma decay phase, line radiations from neutral hydrogen atoms are strongly emitted. The obtained spectra indicate the typical recombining plasma.

In the fusion research the importance of the study on low-temperature and high density plasma, which is normally indicated as a recombining plasma, is increasing in connection with understanding of the divertor plasma. Spectroscopy is a powerful method for studying such a plasma. The hydrogen population densities of the excited levels are followed by the collisional and radiative atomic processes which depend on the plasma parameters such as the electron temperature T_e and density n_e. Since the population densities can be measured from the line intensity, the parameters of T_e and n_e are determined by comparing with the collisional-radiative (CR) model calculation.

Several spectroscopic methods are proposed for the measurement of the plasma parameters [1, 2]. However, they are applicable only for ionizing plasmas. The method which can treat such a recombining plasma has not been established. In this report we demonstrate a possibility of the visible hydrogen spectroscopy for determination of T_e and n_e in low-temperature recombining plasma which can be seen in the divertor plasmas. A newly constructed CR model code by Sawada [3] is adopted for the analysis.

2 Experiment

The experiment was made with NBI plasma in CHS as shown in Fig. 1. The NBI ($\sim$ 1 MW) was injected into the ECH (53GHz) target plasma, and continued during 100 ms until $t = 160$ ms. The hydrogen gas puffing was turned off at $t = 150$ ms. The electron density is measured with HCN interferometer. The H_α line is observed at an opposite
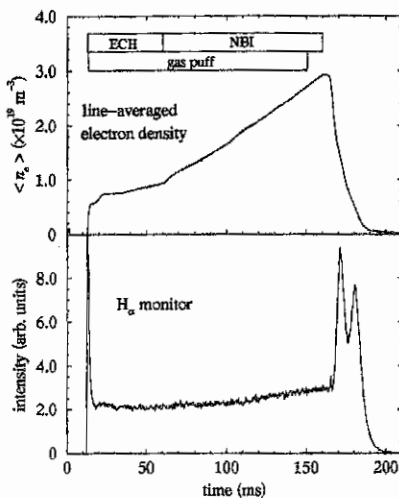
Fig. 1. Electron density and H_α behaviors during the discharge.
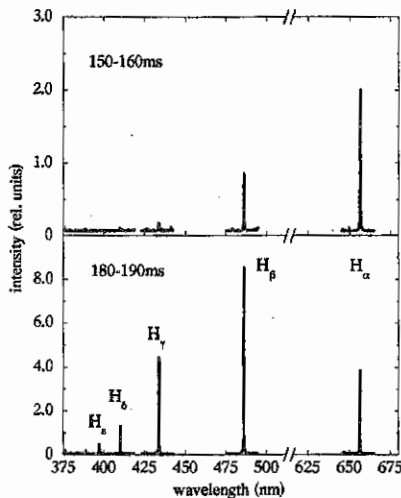
Fig. 2. Time-integrated spectra during $t = 150$–160 ms and 180–190 ms.

toroidal location from the gas puffing position.

The Balmer series lines of neutral hydrogen atoms were observed at the same position with as the H_α monitor. Each line is measured shot by shot using a 1 m visible spectrometer with multichannel detector. The time interval for signal accumulation is 10 ms. The spectra obtained during $t = 150$–160 ms and 180–190 ms are shown in Fig. 2, which correspond to the heating phase and decay phase, respectively. In the decay phase, the line intensities are reversed between H_α and H_β. This is a peculiar feature for the low-temperature recombining plasma.

3 Analysis and Discussion

The T_e and n_e dependences of the excited level population densities were calculated using the CR model. The results are shown in Figs. 3 and 4. Since the distributions are sensitive to the both parameters, simultaneous measurement becomes possible.

The experimentally obtained three sequential spectra from $t = 180$ ms were analyzed and the population density of the excited levels was determined from the line intensities. They are plotted in Fig. 5 with the solid circles. The population distributions in the highly
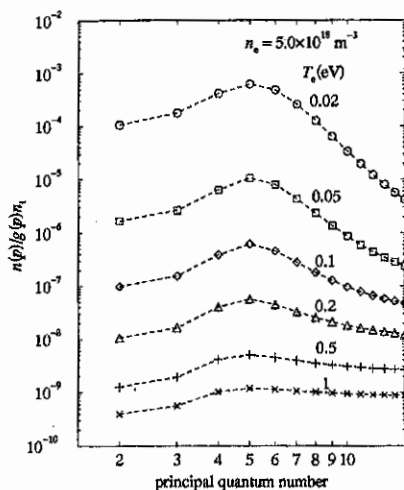
Fig. 3. Electron temperature dependence of the population distribution profile.
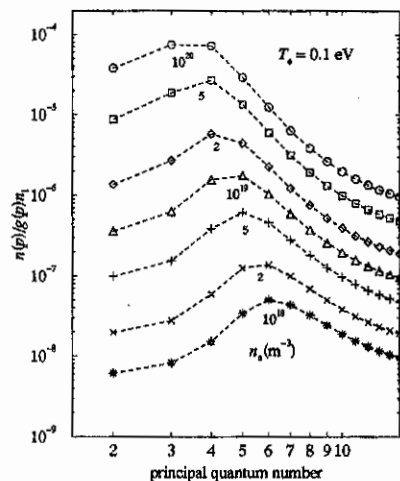
Fig. 4. Electron density dependence of the population distribution profile.

excited levels ($n \geq 7$) clearly indicate that those levels are in partial local thermodynamic equilibrium (LTE). Here, the definition of LTE is that the population density of level p is described by the Saha-Boltzmann equation [4],

$$n(p) = n_i n_e \frac{g(p)}{2} \left(\frac{h^2}{2\pi m k T_e} \right)^{3/2} \exp \left[\frac{\chi(p)}{kT_e} \right], \tag{1}$$

where $g(p)$ and $\chi(p)$ are the statistical weight and the ionization potential of level p, respectively. And the other symbols show their usual meanings. From the figure $T_e = 0.1$ eV is determined in a manner of the best fitting with the experimental data. The curve of the Saha-Boltzmann equation of $T_e = 0.1$ eV is also shown in Fig. 5.

The electron density is determined from the peak position of the population distribution. From the comparison between the CR model calculation (open circles) and the experimental result (solid circles) in Fig. 5 the densities of 4.0×10^{18}, 1.4×10^{18} and 8.0×10^{17} m^{-3} are obtained for time intervals of $t = 180$–190 ms, 190–200 ms and 200–210 ms, respectively. In the calculations the radiation trapping effect is also considered, which depends on the hydrogen ground state density $n(1)$ and the hydrogen temperature T_H. We assumed $T_H = T_e$. The $n(1)$ is determined as 1.0×10^{18} m^{-3} of which the density gives the best fit against the experimental result of 180–190 ms. For other time intervals it is assumed that $n(1)$ increases according to the decreasing n_e. The discrepancy between the two distribution at $n \leq 4$ during 190–200 ms is attributed to the inadequate treatment of this effect. The obtained electron densities are shown in Fig. 6 with the electron density measured by HCN interferometer.

The time behavior of the density decay was also simulated using only the recombining rate obtained from the CR model calculation and the experimentally obtained n_e during
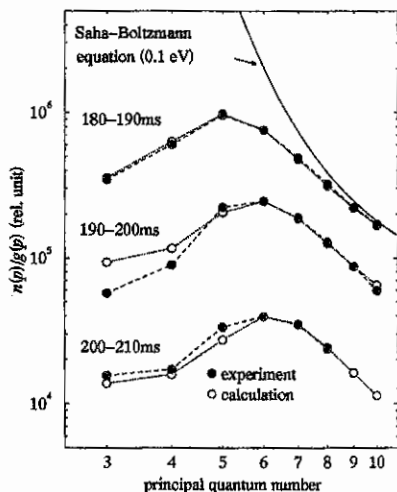
Fig. 5. Excited level populations in time intervals during $t = 180$–190 ms, 190–200 ms and 200–210 ms (solid circles). The calculated results are also shown with the open circles.
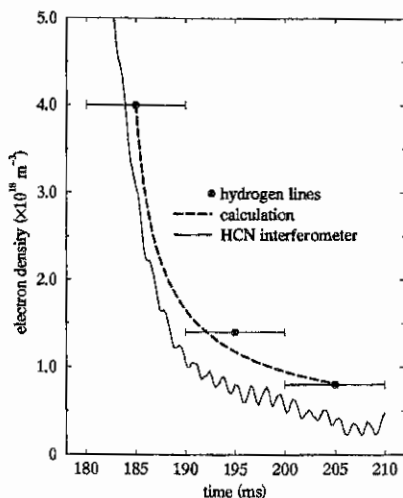
Fig. 6. Electron density decay curve after turning off the NBI input power.

180–190 ms and 200–210 ms. The result is shown in the figure with the dashed line. We can see the calculation shows the good agreement with the HCN data. This agreement means the recombination is the quite dominant process for the density decay.

In the transient phase ($160 < t < 180$ ms) just after turning off the NBI pulse the distribution could not be explained with pure ionizing or the pure recombining plasma. Both of them have to be taken into account for further analysis. No significant results are obtained so far for this phase. However, if the data are obtained with higher time resolution in such a transient phase, the understanding will much progress.

References

[1] B. Schweer, G. Mank, A. Pospieszczyk, B. Brosda and B. Pohlmeyer, J. Nucl. Mater. **196–198**, 174(1992).

[2] K. Sawada, T. Fujimoto, Phys. Rev. E **49**, 5565(1994).

[3] K. Sawada, thesis, Kyoto University(1994).

[4] T. Fujimoto and R. W. P. McWhirter, Phys. Rev. A **42**, 6588(1990).

MHD Instability Study with Soft X-Ray Detector Array System on CHS Heliotron/Torsatron

S.Ohdachi, S.Takagi[1], M.Takechi[1], K. Toi, R. Akiyama, H. Idei, N. Inoue, M. Kojima,
S. Kubo, T. Minami, S. Morita, S. Nishimura, M. Osakabe, R. Sakamoto, C. Takahashi,
K. Tanaka, Y. Yoshimura, S. Okamura, K. Matsuoka and CHS group
National Institute for Fusion Science, Oroshi-machi 322-6, Toki 509-52, Japan
[1]Dep. of Energy Eng. Science, Nagoya Univ., Nagoya 464-01, Japan

1.Introduction

MHD instabilities observed in helical systems have attracted interests as well as those in tokamaks. Though helical systems with no net toroidal currents are free from the disruptive instabilities, the pressure driven instabilities such as interchange or ballooning modes probably determine the β limit of the system[1]. Compact Helical System(CHS) is a Heliotron/Torsatron type device with a small aspect ratio(R=1 m, $<a>$= 0.2 m). Two types of global MHD modes, those are, so called 'burst mode' and 'TAE–like mode' have been found in CHS. Here, the characteristics of the burst mode, especially its radial structure, with a newly installed soft X-ray detector array system is reported

The burst mode is a global mode observed in a low β plasma ($\beta \leq 0.5$ %) with co-injected NBI beam heating[2-4]. Bursts of magnetic fluctuations with an interval of several ms is the distinctive feature of burst mode as is shown in Fig. 1(b). From magnetic probe measurements, it has been found that this is m/n=2/1 mode and that the dependence of fluctuations levels on the β, magnetic axis position R_{ax} and the plasma current I_p suggests that this is the ideal/resistive interchange mode[2,3]. The potential fluctuations, which correlate with the magnetic fluctuations in the growing phase(phase I in Fig. 1(E).), is consistent with this picture[4]. However the radial structure of the mode and the relation between the growing phase and the decaying phase, that is to say, the nonlinear evolution of fluctuations, has not been understood well.

2.Experimental Setup

Recently, linear array of high-speed PIN photodiode without a glass cover has been installed on CHS device as a soft X-ray detector. Important merit of this device is its homogeneous sensitivity. Our detector was originally developed for WT-3 Tokamak by a group in Kyoto University and Hamamatsu Photonics K. K. The array contains 20 detectors, each 12 mm × 1.5mm, with a center-to-center spacing of 2.25mm. Calibration using synchrotron radiation light form a storage ring shows that the sensitivity has no characteristic peaks and dips between 100eV-1keV range. The dispersion of the sensitivity of each detector is less than 5% The crosstalk between the two adjacent detector is less than 7%. Maximum frequency response is about 200kHz in our experimental setup.

The array is installed on a top port at the vertically elongated section of CHS with a pinhole covered by Be film(8 μ m in thickness). Spatial resolution across the minor radius is about 15mm. [1]

---

[1]To determine the measuring position in plasma is not straightforward. Shafranov shift is not negligible even in these low β discharges. Comparing the measured peak of soft X ray radiation with the center position of the equilibrium flux surface using the value of averaged β obtained by the diamagnetic loop, the shift of SXR peak is outer in NBI plasma. This discrepancy was explained by the parallel component of the pressure of the fast ions from

3. Results

Time evolution of plasma parameters with burst modes is shown in Fig.1(a)-(d). As was studied previously[2-4], a burst mode consists of two stages. At first, the magnetic fluctuations with relatively high frequency($\sim$30kHz) grows(Phase I in Fig. 1(e)). Shortly after the saturation of amplitude, sawtooth-like crash occurs, and the modes amplitude and the frequency change into another stage(phase II). The radial structure of mode in each phase is found to be different significantly. The observations of bursts modes by our SX array system are listed up in the following. That will complete the mode analysis based study using the magnetic probes.

- The comparison of the SXR profile, before and the after sawtooth-like crash, is shown in Fig. 2(a). The inversion radius is about 0.5. However, by considering the line integral effect of this measurement, inversion position is $\rho \sim 0.6$ where $\iota = 1/2$.

- The fluctuation part of the SXR exhibits a very complex phase relation(Fig. 2(c),(e));all channels detect the coherent wave, but the cross phase of each channel changes its sign almost everywhere. Line integrated signal simulated with a rotating hot spot (m=2) around the $\iota =1/2$ surface give similar result of the phase profile. Observed fluctuation in the Phase II can be explained by island formation near $\iota =1/2$.

- In the Phase I, measured peak of fluctuations is well inside the $\iota =1/2$ surface(Fig.2(b)). This is important to understand the nature of the burst mode; the evolution of this mode trigger the breaking of the magnetic surface. There are also fluctuations at the $\iota =1/2$ surface, mode number is even m(the SXR on inboard side and the outboard side are in-phase.). Combined with the mode analysis by the probes the main component is probably m/n=2/1. However the radial dependence of the mode amplitude is completely different from the case of phase II. The profile is not symmetric along the major radius. The peak of amplitude is localized on outboard side(ρ=0.2 in Fig. 2(b)) The pressure gradient at this position is also large when the mode is growing (See. Fig. 1(c) and Fig. 2(a)). Therefore, Ballooning-like mode driven by pressure gradient is one of the candidate. The badness of curvature is, however, enhanced at the horizontally(not vertically) elongated positions. Measurement at another toroidal section should be important. troidally Present status of database for this mode is very poor. Further accumulation of data to study the parameter dependence of the mode should be needed.

In summary, a new detector array system for soft X-ray is successfully introduced to the CHS system. The observed characteristics of the burst modes is consistent with the picture of the past studies in the Phase II. The fluctuations with high frequency in Phase I spread inside the $\iota =1/2$ surface.

NBI beam[5]. After the effects are included using the numerical simulation described in ref. [5], there remains small difference ($0 \sim 10$ mm). We assume value of β from profile of SXR itself in this paper when we examine the measuring position of each lines of sight. From the uncertainty in beta, resultant error in the determination of ρ is about $\pm 0.1\rho$.
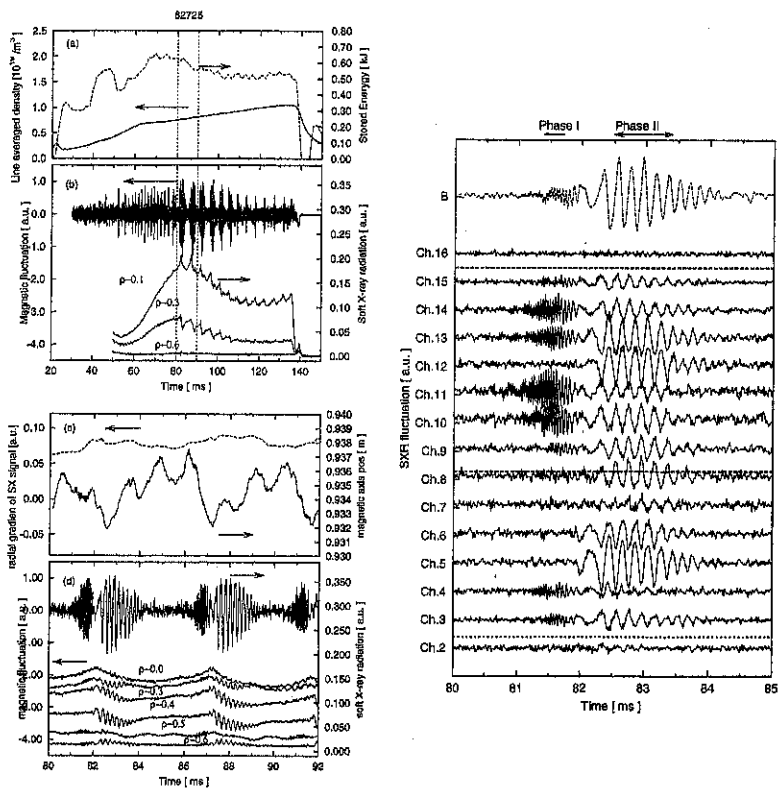
Fig.1 Typical time evolution of fluctuations measured by SX-detector array system are shown in these group of figures. Plasma was started up by ECH heating(53GHz, 20-50ms) and co-injected NBI beam heats the plasma untill 140ms. Discharge conditions are: Toroidal magnetic field $B_t = 0.89$ T, magnetic axis for vacuum magnetic field :0.921m, $\beta_{dia} \sim 0.2\%$ from the diamagnetic loop measurement, the Electron/Ion temperature at the center $T_{e0}/T_{i0} = 0.3/0.2$keV, respectively. The line averaged electron density and the stored energy are shown in Fig.1(a). Time evolution of magnetic fluctuation measured by a pick-up coil and the soft X-ray radiation(SXR) signals are shown in Fig. 1(b). Fig.1(d) is a extended view(82–92ms) of a burst mode. Time evolution of the position of the magnetic axis, which is estimated from the peak of the SXR are also shown in Fig.1(c). Fluctuating components of the SXR(2-40kHz) are shown in Fig.1(e). Channels with smaller number views inboard part of plasma(smaller major radius). Dashed horizontal lines roughly indicates the magnetic axis position and the rotational transform $\iota =1/2$ surface.

References

[1] M. Wakatani, *et al.* , Fusion Enginnering and Design **15** (1992) 395

[2] S. Sakakibara, *et al.* , J. Phys. Soc. Japan, **63** (1994) 4406

[3] S. Sakakibara, *et al.* , Jpn. J. Appl. PHys. **34** (1995) 252

[4] A. Fujisawa *et al.* , *in Plasma Physics and Controlled Nuclear Fusion Research (Proc. 16th Int. Conf. Montreal, 1996)* IAEA-CN-64/C1-5(1996)

[5] H. Yamada, K.Ida, *et al.* , Nucl. Fusion, **32** (1992) 1
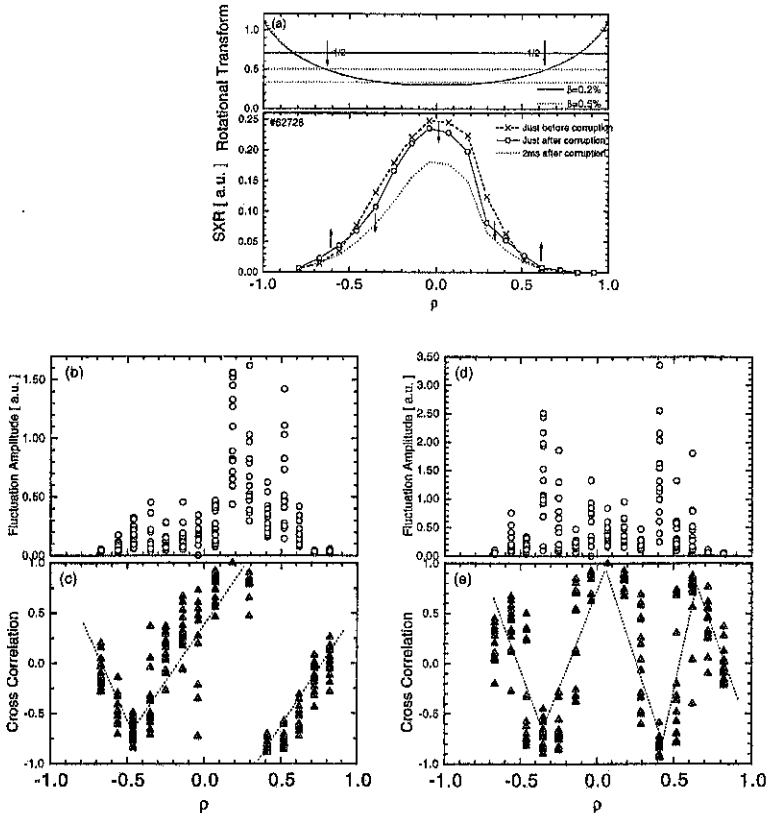
Fig.2. Line integrated radiation of soft X-ray as a function of averaged minor radius ρ are shown in Fig. 2(a);The value of ρ is labeled such way that value of ρ is the minimum on a certain line of sight. Profile of ι is also shown for convenience. Magnitude of fluctuation measured by each line of sight and the cross correlation coefficient with a certain reference signal is shown in Fig. 2(b)(c) (phase I) and Fig. 2(d)(e) (phase II). The reference signal is Ch. 9 in Fig3(c) and Ch.8 in Fig.3(e),respectively.

Sawtooth Oscillations Observed in CHS Heliotron/Torsatron and Their Effects on Edge Plasma

K. Toi, S. Ohdachi, K. Ohkuni[1], T. Morisaki, M. Takechi[1], S. Takagi[1],

S. Morita, S. Sakakibara, H. Yamada, R. Akiyama, H. Idei, N. Inoue,

M. Isobe, M. Kojima, T. Kondoh, S. Kubo, K. Matsuoka, T. Minami,

S. Okamura, M. Osakabe, R. Sakamoto, M. Sasao, A. Shimizu[1]

K. Tanaka, C. Takahashi, Y. Yoshimura and CHS Group

National Institute for Fusion Science, Nagoya 464-01, Japan

1) Dep. Energy Eng. Science, Nagoya Univ., Nagoya 464-01, Japan

Abstract

Sawtooth oscillations are observed in neutral beam heated plasmas of the CHS heliotron/torsatron. The oscillations having $m=2/n=1$ mode structure are strongly enhanced after the sawtooth crash, while precursor oscillations are observed for only a few cycles. Both core and annular crashes are observed. It is often observed that a density pulse generated by a large sawtooth crash arrives at the last closed flux surface(LCFS) faster than a heat pulse.

1. Introduction

Sawtooth oscillation is one of the most typical magnetohydro-dynamic(MHD) phenomena observed in a tokamak plasma[1]. This oscillation attracts much attention because it has a strong impact on plasma confinement near the plasma center and also provides a good example to test various MHD theories. When the safety factor (q) in the plasma center goes down to less than unity, $m=1/n=1$ internal kink mode becomes unstable and then induces the sawtooth oscillations through magnetic reconnection process. The electron cyclotron emission (ECE) or soft X-ray (SX-) signals inside q=1 surface suddenly drop after the sawtooth crash, which is called as "core crash". Recently, off-axis sawteeth are observed in negative magnetic shear configuration of the TFTR tokamak, where the $m=2/n=1$ mode appears before and after the crash[2]. The sawteeth are produced through double-tearing magnetic reconnection process. In the off-axis sawteeth, both "core crash" and "annular crash" are observed. Moreover, a heat or density pulse produced by a sawtooth crash plays an important role in perturbative heat and particle transport studies[3]. For these reasons the sawteeth are paid much attention also in helical plasmas[4,5]. In this paper, we report sawtooth oscillations induced by burst-like magnetic fluctuations with $m=2/n=1$ mode structure in the CHS heliotron/torsatron[6,7], where the rotational transform profile is similar to that in negative magnetic shear($q'<0$) configuration of a tokamak.

2. Sawtooth Oscillations Observed in Neutral Beam Heated Plasmas

So far, sawtooth oscillations are observed only on low density plasmas ($<2.5 \times 10^{19} m^{-3}$) with small net plasma current induced by co-injected neutral beams or small ohmic field at lower toroidal field($Bt < 1.2$ T). Figure 1 shows large sawteeth which lead to "core crash", that is, the soft X-ray emission coming from the core region inside the relevant rational surface q=2 suddenly drops and recovers slowly until the following crash. In this discharge co- and counter-neutral beams are injected, and a small amount of net current ($Ip \sim 8$ kA) is induced by a small ohmic field to increase the rotational transform . As shown in Fig.1 the sawtooth oscillations are observed accompanying burst like magnetic fluctuations with m=2/n=1 mode structure[8]. The location of sawtooth inversion in line integrated soft X-ray signals is estimated to be $\rho \sim 0.3$. The location of q=2 surface is predicted to be slightly larger than the sawtooth inversion radius. The different type of crash is observed in a discharge shown in Fig.2, where the location of sawtooth inversion is $\rho \sim 0.4$. The second crash shown in Fig.2 exhibits a character of "annular crash", because the soft X-ray signals near the rational surface(that is, q=2 surface) are depressed considerably but the signal near the magnetic axis is kept almost constant across the sawtooth crash. As seen from Figs 1 and 2 successor oscillations of 3-5 kHz are considerably enhanced after the crash, and precursor oscillations are observed for a
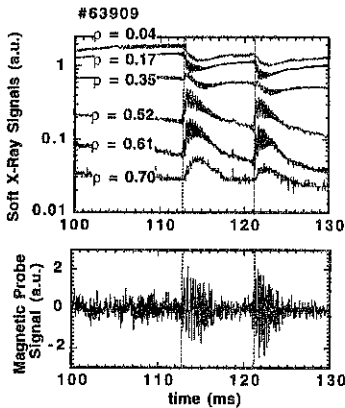
Fig.2 *Time evolution of soft X-ray signals in an NBI heated plasma where the sawtooth crash is fairly slow and the second sawtooth crash at t~113.5 ms exhibits "annular crash."*

Fig.1 *Time evolution of of soft X-ray signals along various chord radii normalized by averaged minor radius together with magnetic fluctuations in a sawtoothing hydrogen plasma heated by co- and counter-NBI, where Bt=1.2 T and line averaged density is 2.5×10^{19} m^{-3}.*

few cycles just prior to the crash. The observed sawteeth accompanying successor are similar to "compound sawtooth" [9] or "partial sawtooth"[10] reported from several tokamaks, but the driving mechanisms of the sawteeth in CHS is not clarified yet.

3. Propagation of Heat and Density Pulses Generated by Sawtooth Crash

A large sawtooth as shown in Fig.1 considerably modify edge plasma by launching heat and density pulses towards LCFS. Figure 3 shows time evolution of ion saturation current measured at two radial positions just outside LCFS by a set of single Langmuir probes (LP). The heat pulse monitored through a Be-foil of 8 μ thickness by a soft X-ray detector array arrives at the radial position of $\rho \sim 0.7$ in ~1.5 ms after the crash. Moreover, the time delay of the peak of SX-pulse at $\rho \sim 0.8$ is estimated to be ~2.2 ms, although the signal-to-noise ratio of the signal is not sufficiently large. This time delay is in the order of global energy confinement time. However, the pulse of ion saturation current measured by single Langmuir probes arrives at the location just out side LCFS (i.e., $\rho \sim 1.02$) in ~1.2 ms. The density pulse measured at just outside LCFS by a thermal lithium beam probe(LIBP) also shows similar time delay to the LP-data. The density pulse produced by the sawtooth crash propagates rapidly from the core region towards LCFS much faster than the heat pulse. This phenomenon suggests that the density pulse has no contribution to heat transfer even if the pulse is launched from the plasma core. The rapid increase in floating potential is also observed just outside LCFS, suggesting enhanced ion loss(Fig.4).
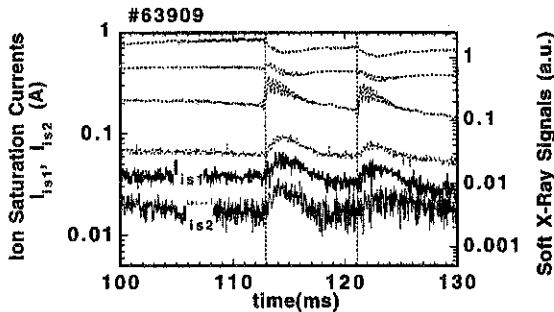
Fig.3 *Comparison of soft X-ray pulse (heat pulse) propagation with ion saturation current pulse(approximately density pulse) in NBI heated plasma shown in Fig.1. Solid curves denote ion saturation currents, where Iis1 and Iis2 are measured outside LCFS(i.e., at $\rho=1.02$, and 1.03 respectively). Dotted curves denote soft X-ray signals at various chord radii($\rho=0.04$, 0.35, 0.52 and 0.70 from upper traces).*
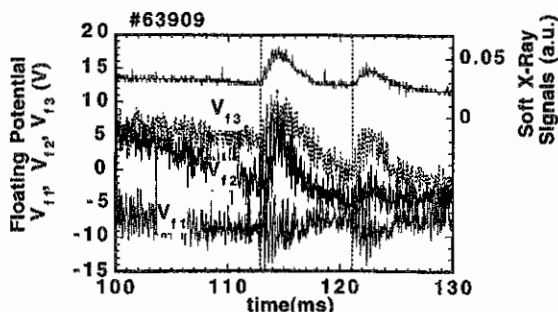
Fig.4 *Time evolution of floating potential outside LCFS in a sawtoothing plasma, where Vf1, Vf2 and Vf3 are measured at ρ= 1.02, 1.03, and 1.04, respectively. Upper solid curve shows the soft X-ray signal measured at ρ=0.70.*

Three possibilities to explain this peculiar phenomenon may be speculated: (1) propagation of the electron heat pulse differs from that of the density pulse, (2) a different type of sawtooth crash is induced near the LCFS by the sawtooth crash which takes place near the plasma center, and (3) prompt loss of injected fast ions enhanced by a large sawtooth crash may considerably modify the density pulse observed near the edge. If the particle source of the density pulse is the bulk plasma near the plasma center, enhanced particle transport due to large off-diagonal transport contribution is required for the first possibility. So far, any sawteeth are not observed near the edge, synchronizing with the sawteeth appear in the plasma core. The second possibility is unlikely. The last possibility seems to be plausible, because promptly lost energetic ions will not affect heat transport of a bulk plasma. The rapid increase of floating potential shown in Fig.4 also may support the last idea. Further study is necessary to elucidate this peculiar heat and particle transport, paying attention to complex magnetic field structure near the edge of a heliotron/torsatron plasma.

References
[1] S. von Goeler et al., Phys. Rev. Lett. **33**, 1201 (1974).
[2] Z. Chang et al., Phys. Rev. Lett. **77**, 3553 (1996).
[3] J. D. Callen and G.L.Jahns, Phys. Rev. Lett.**38**, 491 (1977).
[4] M. Wakatani et al., Nucl. Fusion **23**, 1669 (1983).
[5] Y. Suzuki et al., in Proc of the 21th EPS on Controlled Fusion and Plasma Physics, Vol.18B, 424(1994).
[6] S. Sakakibara et al., J. Phys. Soc. Jpn. **63**, 4406(1994).
[7] S. Sakakibara et al., Transactions of Fusion Technology **27**, 231(1995).
[8] S. Ohdachi et al., this conference.
[9] W. Pfeiffer, Nucl. Fusion **25**, 673 (1985).
[10] R.D. Gill et al., in Proc of the 13th EPS on Controlled Fusion and Plasma Heating, Vol.1, 21 (1986).

Edge plasma control using an LID configuration on CHS

S. Masuzaki, A. Komori, T. Morisaki, N. Ohyabu, H. Suzuki, C. Takahashi,
S. Sakakibara, K. Watanabe, T. Minami, S. Morita, K. Tanaka, S. Ohdachi, S. Kubo,
N. Inoue, H. Yamada, K. Nishimura, S. Okamura, K. Matsuoka, O. Motojima
National Institute for Fusion Science, Oroshi, Toki 509-52, Japan
C.C. Klepper, J.F. Lyon, A.C. England
Oak Ridge National Laboratory, Oak Ridge, Tennessee 37831, U.S.A.

1. Introduction

A Local Island Divertor (LID) has been proposed to enhance energy confinement through neutral particle control [1]. For the case of the Large Helical Device (LHD), the separatrix of an $m/n=1/1$ magnetic island, formed at the edge region, will be utilized as a divertor configuration. The divertor head is inserted in the island, and the island separatrix provides connection between the edge plasma region surrounding the core plasma and the back plate of the divertor head through the field lines. The particle flux and associated heat flux from the core plasma strike the back plate of the divertor head, and thus particle recycling is localized in this region. A pumping duct covers the divertor head to form a closed divertor system for efficient particle exhaust. The advantages of the LID are ease of hydrogen pumping because of the localized particle recycling and avoidance of the high heat load that would be localized on the leading edge of the divertor head. With efficient pumping, the neutral pressure in the edge plasma region will be reduced, and hence the edge plasma temperature will be higher, hopefully leading to a better core confinement region. An LID configuration experiment was done on the Compact Helical System (CHS) to confirm the effect of the LID[2,3]. The typical effects of the LID configuration on the core plasma are reduction of the line averaged density to a half, and small or no reduction of the stored energy. In this contribution, the experimental results which were obtained in edge plasma control experiments with the LID configuration in the CHS are presented.

2. Experiment

The CHS is a heliotron/torsatron type device whose major radius is 1.0m and average plasma minor radius is 0.2m, respectively. The toroidal magnetic field is 0.9T, and the magnetic axis is fixed at $R = 99.5$ cm in this experiment. Plasma was produced with ECH or ion Bernstein heating, and was heated by neutral beam injection (0.82MW, 38kV). The separatrix of the $m/n=1/1$ magnetic island formed by 8 pairs of additional coils was utilized for the LID configuration. A cryogenic pump (21,000L/sec) was installed behind the divertor head for particle exhaust. Fueling was done by gas puffing. Edge plasma modifications by the LID configuration were measured using Langmuir probes, a Lithium beam probe and $H\alpha$ detectors, as shown in Fig.1. There are two types of Langmuir probes, one movable (#1-#3) and the other attached to the back of the LID

Fig.1 Schematic view of experimental setup

head. The Li beam probe is located 135° (CCW direction) from the LID port, and the beam line comes into the plasma from the bottom port [4].

The edge plasma was controlled with the $m/n = 1/1$ magnetic island and insertion of the LID head. The island's phase can be changed as follows; O-point of the magnetic island is formed at the position of the LID insertion port (normal case) and at the opposite side of the torus

Fig. 2 Time development of line integrated density,
upper: center(z=0) chord, middle: z= 63.9 chord,
bottom: z=-116 chord.

(opposite case) , and the island width can be
changed by controlling the coil current (I_{LID}).
The LID head can be moved from outside the
vacuum chamber to inside the magnetic island.

3. Experimental results
3-1 Edge density profile

Scince one of the typical LID effects is the
decay of the line-integrated center-chord density,
the change of the density profiles with the island
is very important for understanding the LID
experimental results. Figure 2 shows the time
developments of the line-integrated density for 3
chords [z = 0 (center chord), z = 63.9 mm, z = -
116 mm, z: vertical axis]. The density reduction
caused by the island occurs in not only the
center chord but in the other chords as well. The
reduction rate is almost the same in all the
chords except in the 'normal case' without LID
head. In this case, the reduction rate is larger in
the outer chord(z = -116 mm) than the other
chords.

Figure 3 shows the edge density profiles

Fig. 3 Edge electron density profiles obtained by
Li beam probe; (a) and (b) are normal and opposite
case, respectively, without insertion of LID head.
(c) and (d) are normal and opposite casse,
respectively, with insertion of LID head.

obtained using a Li beam [4]. The horizontal axis (Z_{Li}) is the position on the Li beam line
whose origin is on the equatorial plane. Figures 3(a) and (b) show the density profiles without
insertion of the LID head, and Figs. 3(c) and (d) are with insertion of the head. In the 'normal
case', the O-point of the island is opposite the Li beam probe port, and is on the Li beam side in
the 'opposite case'. In Fig. 3(a), the density profile shrinks with increasing I_{LID}. This is
considered to be due to a change in magnetic structure, that is, the ergodic region surrounding
the last closed magnetic surface (LCFS) is broader near the X-point of the island. On the
contrary, in Fig. 3(b), the density profile is slightly spread outward with increasing I_{LID} until
I_{LID} reaches 0.6 kA due to the existence of the island separatrix farther out the LCFS without
the island. The tail density ($Z_{Li}>15cm$) also increases with I_{LID} until 0.6 kA, and decreases at
larger I_{LID} values. This result suggests that too large a value of I_{LID} destroys the closed

Fig. 4 Toroidal distributions of normalized Hα intensity. All signals are normalized by the corresponding values for the case of no I_{LID} and LID head. (a) for normal case, (b) for opposite casse. (c) At the position of toroidal angle of 135∞ (Li beam probe position)

magnetic surface in the edge region, and spreads the ergodic layer. This is clearly indicated in the case of $I_{LID} = 1$ kA in Fig. 3(b).

In Figs. 3(c) and (d), the position on the Z_{Li} axis corresponding to the edge of the LID head is $Z_{Li} = 13.3$ cm. The edge plasma is scraped off by the LID head, and the density profiles reflect that [4]. The effects of the island are qualitatively similar without insertion of the LID head qualitatively, though a discrepancy occurs for the 'normal case' with the LID head inserted.

3-2 Particle Recycling

Hα intensities were measured for various I_{LID} values to make the effect of the LID configuration on particle recycling clear. Figures 4(a) and (b) show the toroidal distributions of the normalized Hα intensity for different I_{LID} values for the 'normal' and the 'opposite' cases, respectively. The toroidal angle is defined CCW from the LID position. It is very clear that the Hα intensity decreases when the LID head is inserted except in the region near the LID head. In this case, the LID head plays the role of a normal limiter. In Fig. 4(a), near the LID position (0°) where the island has its maximum width, the Hα intensity increases even without insertion of the LID head. On the other hand, in Fig. 4(b) for the opposite case, the Hα intensity decreases near the LID position where the X-point of the island is located. In the case of $I_{LID} = 1$ kA, the ergodic region spreads outward, and the particle recycling increases. At the toroidal angle of 135°, the Hα intensity change for various I_{LID} values can be compared with the edge electron density profiles measured by the Li beam probe. In Fig. 4(c), normalized Hα intensities at this point for various cases are shown. For the opposite case, the Hα intensity increases with increasing I_{LID} up to 0.6 kA, and decreases at larger I_{LID} values. This change is similar to the change in the tail density mentioned in the previous section. On the contrary, the 'normal case' is not so simple. In this case, the Hα intensity depends not only on the tail density but also on the density profile near the LCFS. It is reasonable for the case with the LID head inserted that the Hα intensity decreases because the LID head scrapes the edge density as shown Fig. 3(c), (d). These results suggest that particle recycling closely depends on the magnetic field structure, so that moderate I_{LID} values and insertion of the LID head can be used for particle recycling control.

3-3 Distribution of the Particle flux on the LID head

The amount of the particle flux to LID head, and its distribution on the head, are important in determining the LID pumping efficiency. They are estimated using Langmuir probes attached on the up and down sides of the LID head, respectively. Figure 5 shows the distribution of the particle flux on the LID head for various NBI cases. The toroidal field direction corresponding to the NBI direction is CW for NBI(#1) counter and NBI(#2) co injection, CCW for NBI(#1) co and NBI(#2) counter injection. The horizontal axis is the LID head position, and the origin of this axis is the normal position of the LID head where the edge of the head is at the center of the island. A negative sign means that the head is retracted outward from its normal position. This figure is for the 'normal case', that is, the outer separatrix of the island strikes the LID

824

head. All distributions have a peak at the position corresponding to the outer separatrix striking point. Though the up and down side probes were set symmetrically, the striking point is asymmetrical. The down side striking points are 1-2 cm farther in than that of the upper side. The reason for this asymmetry is not clear. One possibility is that the phase of the island is moved due to an error field. A small error field was shown to exist in the CHS by magnetic surface mapping and its strength and direction estimated [5], but it is not enough in this case. The decay length of the particle flux on the LID head is estimated with the assumption that the particle flux decreases exponentially. The results are also shown in Fig.5. The decay length for the particle flux distribution on the upper side is larger than that on the down side, though the decay length for the case of NBI(#2) co-injection is relatively short. So this asymmetry does not depend on the direction of NB injection (co or counter), but rather on the toroidal field direction.

4. Summary

To understand the mechanism of improved confinement, edge plasma control experiment using this configuration was done.

Line integrated densities for 3 chords mainly inside the LCFS and edge density profiles were measured by an interferometer and a Li beam probe, respectively. Former results suggest that the density profile in the core region is not changed that much by the island. The edge density profiles clearly

Fig. 5 Distributions of normalized particle flux for various NBI directions, and decay length of them.

show the effect of the LID configuration. The density profiles which reflect the broadened ergodic region due to destruction of closed magnetic surface were observed in the case of relatively large I_{LID} values.

Measurement of the toroidal distribution of the Hα intensity was done for various I_{LID} values to understand the effect of the LID configuration on particle recycling. Insertion of the LID head decreases the Hα intensity except near the head. For the case without LID head, the distribution depends on I_{LID}. Due to a broadened ergodic region, the Hα intensity increased significantly in the case of a relatively large I_{LID} value. This is consistent with results from Li beam probe measurements.

Measurement of the particle flux on the LID head was done using Langmuir probes attached to the LID head. The particle flux distribution on the LID head has a peak at the position corresponding to the outer separatrix of the island for the 'normal case'. Two types of up and down particle flux distribution asymmetry were observed. One is the peak position, and the other is the decay length. The latter is considered to be related to the toroidal field direction.

References

[1] N. Ohyabu, et al., J. Nucl. Mater. 145-147 844 (1987).
[2] A. Komori, et al., Proc. 12th International conference on plasma surface interactions in controlled fusion devices (1996). (to be published in J. Nucl. Mater.)
[3] A. Komori, et al., Proc. Plasma Physics and Controlled Nuclear Fusion Research, Montreal, 1996, IAEA-CN-64/C1-2.
[4] T. Morisaki, et al., Proc. 12th International conference on plasma surface interactions in controlled fusion devices (1996). (to be published in J. Nucl. Mater.)
[5] H. Yamada, et al., Rev. Sci. Instrum., 61, No.2 (1990).

DEVELOPMENT OF A PULSED RADAR REFLECTOMETER FOR CHS PLASMAS

R.Pavlichenko [§], *S. Ohdachi, A.Ejiri, K.Kawahata, K.Matsuoka*

National Institute for Fusion Science, Toki-shi, Gifu-ken 509-52, Japan
[§] *Graduate University for Advanced Studies, School of Mathematical and Physical Science, Department of Fusion Science, 240-01 Hayama, Japan*

Introduction

Reflectometry is a diagnostic to determine the position of the critical density layer (CDL) at which microwaves are reflected [1, 2]. In the case of pulsed radar reflectometry, short (~1ns) microwave pulses are launched into plasmas. From the time delay between the launched and received pulses, information on the positions of CDL can be determined. By use of multiple frequencies pulsed radar reflectometry has the potential to reconstruct electron density profiles. Since each short microwave pulse measurement is independent, temporary loss of the reflected pulse does not deteriorate the measurements significantly. Furthermore, false reflections from microwave components or vacuum window can be easily distinguished in the time domain. Plasma fluctuations don't influence the measurements because they are almost frozen during the propagation time of the pulse through the plasma.

This paper describes the pulsed radar system that is under development for CHS plasma experiments. Firstly, the distinctive features of our system and the performance of main system components are described. Then we present some results of the free space propagation test. Finally, preliminary results of the experiments with CHS plasmas are shown.

Description of system components and free space propagation test

A multiple frequency (51, 54, 57GHz) pulsed radar system has been designed for CHS. Figure1 shows the block diagram of this system. The difference from the existing systems (in RTP [3] and TEXTOR) is that we multiplex three frequencies into single `mixed` pulse and split the received pulses with band-pass filters at IF stage. In this scheme, we can launch three different frequencies simultaneously, and we need only one local oscillator. As a result, we can improve the time resolution and simplify the system.

Gunn oscillators with the output power of 50-100mW have been used as a microwave source. Two types of switches are used to make a short pulse. One is a broad band (54±3GHz) PIN switch (Millitech) and the other is a narrow band (51±0.25GHz, 57±0.25GHz) varactor diode modulator (developed in Kharkov Institute of Radiophysics and Electronics, Ukraine). In order to reduce the power losses and pulse broadening, X-band oversized waveguides are used. The loss in the waveguides is 5.2dB for one way transmission.

A heterodyne technique is used to detect the reflected pulses. Although signal to noise ratio (SNR) for the reflected pulses from the CHS inner wall is around 100, SNR of the reflected pulse from CDL is around 5. We use band pass filters to split and to detect pulses of different frequencies.

Large amplitude modulation due to the refraction of wave and density fluctuation could happen. Thus, we use a Constant-Fraction-Discriminator (CFD), which yields the pulse timing independent of amplitude. However, CFD is affected by the pulse shape deformation, which arises from the dispersion in plasmas. A numerical simulation has been done to estimate the CFD timing errors. The pulse deformation is more serious for shorter pulse width, and the deformation leads to a larger error in the timing. We found that the errors are negligible for the pulse width longer than 0.5ns. Time to Amplitude Converter (TAC) module is used to measure the timing from the output of CFD. TAC yields a square pulse, of which amplitude is proportional to the time delay. And the amplitude is measured by an ADC.

Free space propagation test measurements are done to estimate the timing errors in the system. A movable aluminum mirror is used to simulate pulse reflection from CDL. Figure 2 shows the dependence of the time delay versus distance from the antenna to the mirror. The time delay measurements were done for the different powers at the mixer. For the case of 5 and 10µW at the mixer, the slope of the time delay is the same as the velocity of light and the spatial resolution of 0.2-0.3cm is achieved. However, for the case of 1µW the errors become slightly larger. One of the possible reasons is nonlinearity of the IF components of the system.

Preliminary results of the pulsed radar reflectometry in CHS

51GHz 1-channel pulsed radar reflectometer has been installed in CHS. The waves are launched into the plasma in the ordinary mode. The critical density is 3.2×10^{13} cm^{-3}. The transmitter is placed at the distance of about 5m from CHS. Detection part is placed close to the device (~1 m). A conical horn with a Teflon lens has been used for launching and receiving microwave pulses. The plasmas were initiated by IBW and heated by NBI. The

maximum density is about 6.2×10^{13} cm^{-3}. Without plasma we clearly observe reflected pulse from the inner wall of the device. In these experiments we measured reflected pulses by a sampling oscilloscope, for which 10000 pulses are required to get a pulse shape. Figure 3 shows the comparison of the measured and calculated time delays as a function of maximum density. During the discharge time, at the low-density stage where $n_{e\ max} \leq 0.5 \times n_{critical}$, we could observe the reflected pulse from the inner wall. In this case, the system is operated as an interferometer. When the plasma density becomes $0.5 \times n_{critical} \leq n_{e\ max} \leq n_{critical}$ the amplitude of the reflected pulse became very small, because of the refraction of the wave. When the density becomes higher that the critical density $n_{e\ max} \geq n_{critical}$ we observed the reflected pulse from CDL. In this case the system is operate as a reflectometer. The measured data follow the calculated curve, but error bars are large. This comes from the strong amplitude modulation of the reflected signals and using of a sampling oscilloscope.

Summary

A pulsed radar reflectometer for CHS experiments has been constructed and tested with/without plasma. For short microwave pulse production, two kinds of fast switches (Millitech, IRE) were tested. These can produce pulses with the width of 0.8 and 1.7ns, respectively. To estimate the CFD timing errors, a numerical simulation has been done. The pulse deformation is more serious for shorter pulse width, and leads to a larger error in the timing. We found that the errors are negligible for pulse width longer than about 0.5 ns. The laboratory tests of free space propagation showed that the present spatial resolution is ±0.3 cm. During plasma experiments the reflections from the plasma and the CHS inner wall were observed. Measured time delay has large errors. This should be because of the using of the sampling oscilloscope.

REFERENCES

[1]   F.Simonet, Rev.Sci.Instrum. **56**, 664 (1985)

[2]   A.E.Costley, Diagnostics of fusion plasma using reflectometry, in International School of Plasma Physics "PERO CALDIROLA", pp.379-396, Bologna, 1986.

[3]   C.A.J.Hugengoltz, S.H.Heijnen, Rev.Sci.Instrum. **62**, 1100 (1991)
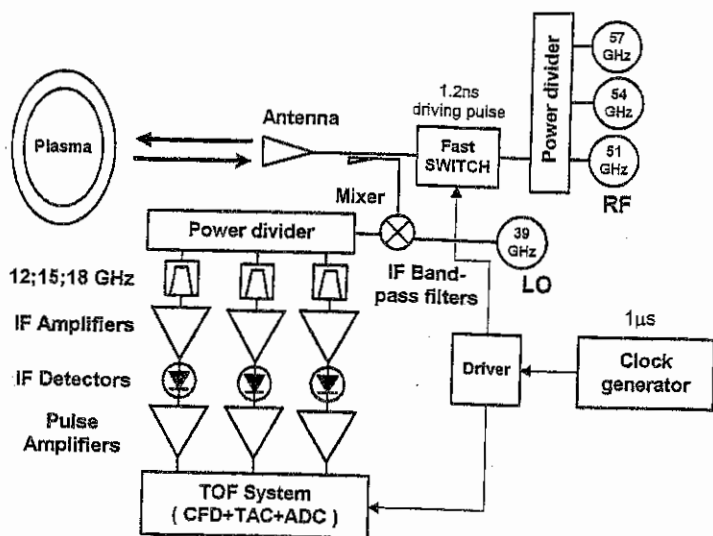
Fig. 1. Block diagram of the CHS pulsed radar reflectometer
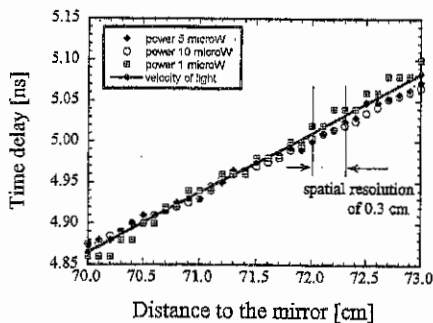
Fig. 2: Time delay for free space propagation as a function of distance between the antenna and the mirror. Different symbols are used for the different power at the mixer
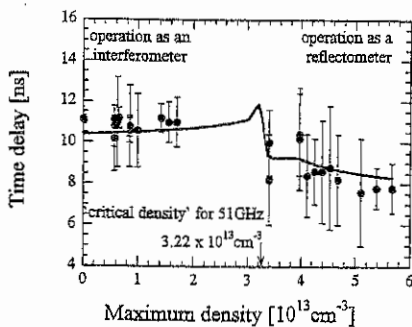
Fig. 3: Comparison of measured (circles) and calculated (line) time delay as a fuction of maximum density. Parabolic profiles are assumed.

Li Pellet Injection Experiments and Extension to Advanced Particle Transport Diagnostics with Tracer-Encapsulated Pellet

S. Sudo, K.V. Khlopenkov[†], H. Itoh[*], K. Kondo[**], H. Zushi[**], F. Sano[***], T. Mizuuchi[***], H. Okada[***], S. Besshou[**], K. Nagasaki[***], K. Sakamoto[***], T. Obiki[***]

National Institute for Fusion Science, 322-6 Oroshi-cho, Toki, Gifu, 509-52 Japan,
[†]Graduate Univ. for Advanced Studies, Hayama, Kanagawa, 240-01 Japan,
[*]Nippon Sanso Corp., 6-2 Kojima-cho, Kawasaki-ku, Kawasaki-city, 210 Japan,
[**]Graduate Scool of Energy Science, Kyoto University, Uji, Kyoto, 611 Japan,
[***]Institute of Advanced Energy, Kyoto University, Uji, Kyoto, 611 Japan

1. INTRODUCTION

In order to study particle transport, a series of experiments are planned. The first one is to inject a pure Li pellet into a plasma to observe a feature of Li pellet ablation and behavior of Li ions. This is carried out on Heliotron E. The second one is to inject a tracer-encapsulated pellet as a new method for studying transport characteristics more accurately. The method for producing a tracer-encapsulated pellet is recently established, and the injection experiments are planned on CHS and later on LHD [1]. In this article, the essential results of transport characteristics on pure-Li-pellet injection experiments and the preparation of a tracer-encapsulated pellet injection are described.

For Li pellet injection experiments, a new design of the Li pellet injector is developed. Its main part is a disk with 30 holes containing pellets. The clearance between the disk and the housing is kept small enough by using precise rollers so that the available pellet size can range from 0.3 mm$\varnothing$ in sphere form up to 1 mm$\varnothing \times$ 1 mmL in cylinder form.

The Li pellets of 1 mm$\varnothing \times$ 1 mmL in cylinder form were injected into the Heliotron E plasma. The transport property after pellet injection in cases of ECH and NBI was investigated using several spectroscopic methods including Charge eXchange Recombination Spectroscopy (CXRS) which showed temporal change of the spatial profile of the Li ion density. The behavior of Li ions is simulated with a transport code.

For further extension of more accurate impurity transport analysis, the new method [2] using a tracer-encapsulated pellet has been developed. The essential point of this diagnostic is based upon the poloidally and toroidally localized particle source as a tracer within a small volume of about 1 cm^3 in the plasma. The tracer-encapsulated pellet consists of a small core as a tracer of light atom such as Li and the outer layer made of the different material from that of the core.

2. LI PELLET INJECTION EXPERIMENTS

As Li can easily react with air and water, we set up a glove box filled with helium gas during the process of Li pellet setting for maintaining Li pellet purity. The detail technique of the preparation and loading of the lithium pellets are described in the separate paper [3]. The pellet speed is 400~600 m/s, and the pellet trajectory distributes within 1 degrees in full angles. Pellets are injected horizontally and crosses the plasma column nearly perpendicularly.

The ablating pellet was observed by the optical system which includes two light filters for Li I and Li II lines (wave lengths $\lambda_1 = 670.6$ nm and $\lambda_2 = 548.5$ nm, respectively) and two independent photo-multipliers and data acquisition system. The image of the emission from the ablating pellet was recorded by a CCD camera having filters of Li I (λ_1) and Li II (λ_2).

A multi-channel vacuum ultraviolet spectrometer, which is available from 4.5 nm to 40.0 nm, is used to measure Li line emission [4]. The neutral Li I (λ_1) emitted near the wall is measured by a visible spectrometer, which is separated by 132 degrees in the toroidal direction from the port of the pellet injector. A 1.26 m visible spectrometer with a 2-dimensional detector [5] is employed to analyze the spectral profiles of the charge exchange recombination line of Li^{3+} ion with time resolution of 20 ms.

Figure 1 shows the typical response of the main plasma parameters by Li pellet injection during (a) ECH and (b) NBI. The drastic change of density and temperature is seen due to the relatively large pellet size compared to the total number of the bulk plasma particles of Heliotron E. The injected Li pellet is not completely ablated but about 60% of the pellet is deposited in the plasma.

The prominent line observed by the VUV spectrometer is Li III (13.5 nm), while the emission of Li II (19.93 nm) is not observed. Figure 2 shows the time evolution of the Li III obtained by VUV (open circles) and CXRS (closed circles). Immediately after Li pellet injection emission of Li III peaks and decreases with a decay time of about 60 ms. The transition ($\lambda_3 = 449.9$ nm) from n=5 (2G) to n=4 (2F) is selected for CXRS, which is only available to our diagnostic system. The decay time of Li^{3+} estimated on the magnetic axis is 90 ms which is comparable to the decay time of 60 ms for the behavior of the above Li III intensity observed by the VUV spectrometer. The behavior of Li ions is simulated rather well as shown in Fig. 2 with a transport code combined with the data of atomic processes. The fitting parameters in simulation are shown with $D = 0.1$ m^2/s (dash-dot line), 0.15 m^2/s (solid line), 0.2 m^2/s (dashed line), and $V = 1.0$ m / s (fixed), where D is diffusion coefficient and V is velocity of inward pinch. In this simulation, recycling of Li particles is

given as negligibly small. These D and V values will be examined locally in detail by experiments in near future with the tracer-encapsulated diagnostic pellet described below.

3. TRACER-ENCAPSULATED PELLET

A device for producing a Tracer-Encapsulated Cryogenic PELlet (TECPEL) is constructed for an accurate transport diagnostic system to measure particle transport both in parallel and in perpendicular to the magnetic field lines on magnetic confinement devices. The concept is illustrated in Fig. 3. For the purpose of making the unique feature of the method clear, the expected advantage of TECPEL is shown with overlapped on the experimental data with pure Li pellet injection.

As a typical configuration of TECPEL, a carbon sphere with a diameter of 240 μm is encapsulated in the center of a 3 mm diameter cylindrical form of solid hydrogen. There are a pile of tracer spheres in the storage device to be loaded. The typical number of the stored spheres is 20. One core tracer pellet is supplied automatically by the tungsten wire.

Such a TECPEL is accelerated by a light gas gun to velocities of 400 - 800 m/s. The pellet has been photographed simultaneously from two directions, and a 3D image is reconstructed from two 2D images. The 3D image shows the existence of the carbon sphere in the adequate location inside the hydrogen pellet. Thus, the proof-of-principle of device operation has been demonstrated.

The scheme to encapsulate the other light atoms such as Li, Be, B, and so on as a tracer is also proposed for the variety of experiments. The above materials can be made in a spherical form in principle, but such process is not always practical. So, the better scheme to handle the even irregular shape and/or easily reacting materials is invented. The concept is based essentially on the technique to cover these non-sphere material with polymer such as polystyrene. This method is now being tested experimentally.

ACKNOWLEDGMENTS

REFERENCES

[1] A. Iiyoshi, M. Fujiwara, O. Motojima, et al., Fusion Technology 17 (1990) 169.

[2] S. Sudo, J. Plasma and Fusion Research, 69 (1993) 1349.

[3] K.V. Khlopenkov, S. Sudo, et al., NIFS Report NIFS-TECH-4, Nagoya, Japan, 1996.

[4] K. Kondo, et al., 12th Int. Conf. Plasma Surface Interaction, France, 1996.

[5] K. Ida and S. Hidekuma, Rev. Sci. Instrum., 60 (1989) 867.
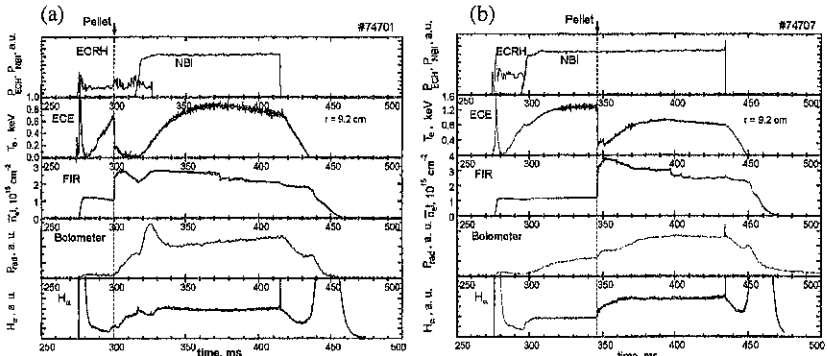
Fig. 1 Typical response of the main plasma parameters by Li pellet injection during (a) ECH and (b) NBI.
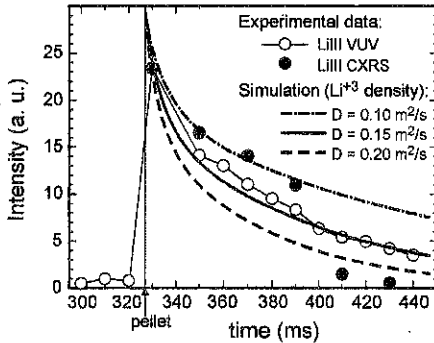
Fig. 2 Time evolution of Li III CXRS (closed circle) and VUV (open circle) intensity observed experimentally, and the simulated results are also shown. Three different values of D and fixed value of V (= 1.0 m / s) are given.
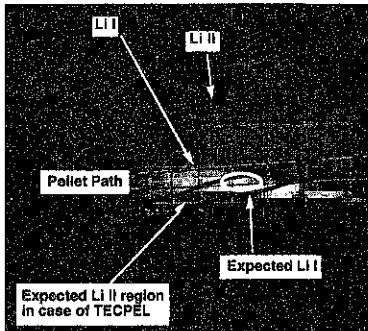
Fig. 3 (a) Concept of diagnostics with locally deposited Li of TECPEL. Li I and II will be limited in the region between the solid lines. These are overlapped on the experimental data obtained by the conventional pure Li pellet injection.
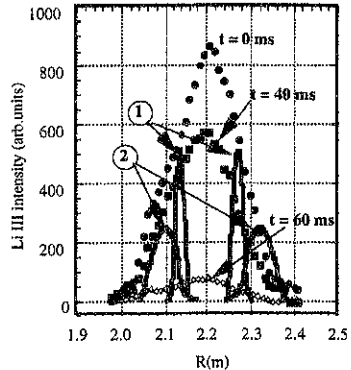
Fig. 3 (b) Concept of diagnostics with TECPEL. The continuous lines of 1 and 2 indicate the expected temporal developments of the spatial profiles of the locally deposited Li ions. The discrete points indicate experimental data from pure Li pellet injection.

Analysis of Neo-Classical Double Tearing Mode

Qingquan Yu[1] and Hong Feng[2]

Max-Planck-Institut für Plasmaphysik, Euratom Association, D-85748, Garching, Germany

[1]Present address: Institute of Plasma Physics, Academia Sinica, Hefei, 230031, P.R. China.

[2]Hefei Union University, Hefei, 230022, P. R. China

I.   INTRODUCTION

It is well known that double tearing modes (DTM) can exist in a tokamak plasma with a nonmonotonic q-profile. DTM was proposed as a possible mechanism for the observed Mirnov oscillations of the tokamak plasma during the first few milliseconds of discharge[1, 2]. The linear and nonlinear theory and numerical calculations of the resistive DTM have already been developed [3, 4 and reference therein].

Large tokamak plasmas are essentially in the banana regime, and it is known that the neoclassical effect is important for the tearing mode and leads to the neoclassical tearing mode[5, 6]. It is therefore necessary to have an understanding of the DTM in the banana regime, and we will call it the neoclassical double tearing mode hereafter.

In the present work a theory for the nonlinear neoclassical DTM is presented.

2 .   Island evolution equations of neoclassical DTM

Large aspect-ratio tokamak approximation is used here. We define ψ as the helical flux function, $\mathbf{B}=B_{0z}\mathbf{e_z}-(kr/m)B_{0z}\mathbf{e_\theta}+ \nabla\psi\times\mathbf{e_z}$, and $\mathbf{B}$ denotes the magnetic field, m/r and k being the wave vector in $\mathbf{e_\theta}$ (poloidal) and $\mathbf{e_z}$ (toroidal) direction, respectively, and the subscript 0 denoting an equilibrium quantity.

For the case of nonmonotonic q-profile we take $\psi_0'=0$ at locations r_1 and r_2 of the rational surfaces, with $r_1<r_2$, where the prime denote $\partial/\partial r$. The magnetic flux perturbation $\tilde{\psi}$ of the DTM can then be expressed as[3, 4]

$$\tilde{\psi} = \tilde{\psi}_1 + \tilde{\psi}_2, \tag{1}$$

where $\tilde{\psi}_1$ is bounded in $0 \leq r \leq r_2$ and satisfies the boundary conditions

$$\tilde{\psi}_1(0)= \tilde{\psi}_1(r_2)=0, \tag{2}$$

and $\tilde{\psi}_2$ is bounded in $r_1 \leq r \leq b$ (b is the conducting wall radius) satisfying

$$\tilde{\psi}_2(r_1)= \tilde{\psi}_2(b)=0. \tag{3}$$

Outside the islands inertia can be neglected. For a given equilibrium $\mathbf{B}$, it can be found from the equation of motion the four outer matching parameters defined by[4, 7]

$$\Delta_{11}=\frac{\tilde{\psi}_{1(s1+)}' - \tilde{\psi}_{1(s1-)}'}{\tilde{\psi}_{1(r_1)}}, \quad \Delta_{22}=\frac{\tilde{\psi}_{2(s2+)}' - \tilde{\psi}_{2(s2-)}'}{\tilde{\psi}_{2(r_2)}},$$

$$\Delta_{12}=\frac{\tilde{\psi}_{2(s1+)}'}{\tilde{\psi}_{2(r_2)}}, \qquad \Delta_{21}=\frac{-\tilde{\psi}_{1(s2-)}'}{\tilde{\psi}_{1(r_1)}}, \tag{4}$$

where the subscripts s1+(s2+) and s1-(s2-) denote the two sides of the inner (outer) island separatrix around r_1 (r_2) respectively.

Assuming $(r_2-r_1)>>w_1$, w_2, where w_1 (w_2) is the inner (outer) island width, we find the matching parameters from the island regions, Δ_1 and Δ_2,

$$\Delta_1=\frac{dw_1}{\eta_1 dt} + \frac{\Delta_{b1}w_1}{w_1^2 + w_{d1}^2} + \frac{iw_1}{2\eta_1}(\omega_1 + kv_{z1} + t\frac{d\omega_1}{dt}), \tag{5}$$

$$\Delta_2=\frac{dw_2}{\eta_2 dt} + \frac{\Delta_{b2}w_2}{w_2^2 + w_{d2}^2} + \frac{iw_2}{2\eta_2}(\omega_2 + kv_{z2} + t\frac{d\omega_2}{dt}), \tag{6}$$

where η_1 and η_2 are neoclassical resistivity at r_1 and r_2, $\Delta_{b1}=(k_1\sqrt{\varepsilon}\beta_{pe}L_s / L_p)_{r=r_1}$, $\Delta_{b2}=(k_2\sqrt{\varepsilon}\beta_{pe}L_s / L_p)_{r=r_2}$, $L_s=q/q'$, q being the safety factor, $L_p=p_e/p'_e$, p_e being electron pressure, β_{pe} is the ratio between the local electron pressure and poloidal magnetic field pressure, $\varepsilon=r/R$ is the inverse aspect ratio, k_1 and k_2 are parameters depending on the equilibrium and are of the order of unity[5, 6], w_{d1} and w_{d2} are of the order of one percent of the minor radius for large tokamak plasmas[8], ω_1 (ω_2) is the oscillating frequency of $\tilde{\psi}_1$ ($\tilde{\psi}_2$), v_{z1} (v_{z2}) is the toroidal plasma rotation velocity at r_1 (r_2).

Matching the inner and outer solution it is found that[7]

$$\Delta_1=\Delta_{11}+\Delta_{12}e^{-i\omega t}\,\tilde{\psi}_2(r_2)/\tilde{\psi}_1(r_1), \tag{7}$$

$$\Delta_2=\Delta_{22}+\Delta_{21}\,e^{i\omega t}\,\tilde{\psi}_1(r_1)/\tilde{\psi}_2(r_2), \tag{8}$$

where $\omega=\omega_1-\omega_2$.

Using Eqs. (4) - (6), the imaginary parts of Eqs. (7) and (8) becomes

$$t\frac{d\omega}{dt} + (\omega + kv_z) = -2(\,\eta_1|c|\Delta_{12}\frac{w_2^2}{w_1^3}+ \eta_1|c|^{-1}\Delta_{21}\frac{w_1^2}{w_2^3})\sin(\omega t), \tag{9}$$

where $v_z=v_{z1}-v_{z2}$. If kv_z is assumed to be much larger than the coupling terms on the right hand side of Eq. (9), the asymptotic solution of Eq. (9) is $\omega =- kv_z$.

The real parts of Eqs. (7) and (8) are

$$\frac{dw_1}{\eta_1 dt} =\Delta_{11}(w_1) + |c|\Delta_{12}\frac{w_2^2}{w_1^2}\cos(\omega t) - \frac{\Delta_{b1}w_1}{w_1^2 + w_{d1}^2}, \tag{10}$$

$$\frac{dw_2}{\eta_2 dt} =\Delta_{22}(w_2) + |c|^{-1}\Delta_{21}\frac{w_1^2}{w_2^2}\cos(\omega t) - \frac{\Delta_{b2}w_2}{w_2^2 + w_{d2}^2}, \tag{11}$$

where $c=\psi_0''(r_2)/\psi_0''(r_1)$. Equations (9)-(11) describe the nonlinear evolution of the magnetic islands with different rotation frequencies. The first terms on the right hand side of Eqs.(10) and (11) are the conventional Δ' term resulting from plasma current gradient, the second terms result from the coupling between the two islands, and the third terms result from the perturbed bootstrap current. Since $L_s/L_p>0$ ($L_s/L_p<0$) at r_1 (r_2), the perturbed bootstrap current has a stabilizing (destabilizing) effect on the inner (outer) island.

When the poloidal electromagnetic torque between the two islands is larger than plasma viscous torque, the relative phase between the two island will be locked. The phase locking condition is found to be[7]

$$w_1^2 \, w_2^2 (w_1 + Q w_2) > 16^2 R^2 \mu_1 \frac{r_1^2}{r_2} \frac{L_{s1} L_{s2} \omega}{n r_1 \Delta_{12} v_{A1}^2}, \tag{12}$$

where $v_{A1} = B_{0z}/(\mu_0 \rho_1)^{1/2}$ being the local Alfven velocity at r_1, $\omega = (v_{z1} - v_{z2})/R$, $Q = r_1^3 \mu_1 \rho_1/(r_2^3 \mu_2 \rho_2)$, μ is plasma viscosity, ρ is plasma mass density, and the subscripts 1 and 2 denote taking values at r_1 and r_2 respectively. It is seen that the island width is the key parameter in determining the island phase locking.

3. Magnetic island width

3.1 Outer island width

For most circumstances, the approximation $\Delta_{22}(w_2) w_2^2 >> c^{-1} \Delta_{21} w_1^2$ is valid, and it is found from Eq. (11) that

$$\Delta_{22}(w_2) \approx \frac{\Delta_{b2} w_2}{w_2^2 + w_{d2}^2}. \tag{13}$$

The saturation of the outer island is due to the balance of the destabilizing effect from the perturbed bootstrap current and the stabilising effect from the negative $\Delta_{22}(w_2)$.

3.2 Inner island width

The inner island could have a variety of behavior depending on plasma parameters as it can be seen from Eq. (10) and (11). Following are three typical cases.

For the rotating island with $\omega >> \kappa$, where $\kappa = 3a^2 \Delta_{b1}/(w_{d1}^2 \tau_R)$, it is found that

$$w_1 \approx [A_1 \sin(\omega t)]^{1/3} \tag{14}$$

when $\Delta_{11} w_{d1}^2/\Delta_{b1} << w_1 << w_{d1}$, where $A_1 \approx |c| \Delta_{12} \omega_{2s}^2 3a^2/(\tau_R \omega)$. It is seen that $w_1 \sim \omega^{-1/3}$.

When the relative phase between the two island is locked, for a high-β_{pe} plasma with $\Delta_{11} w_{d1}^2/\Delta_{b1} << w_1 << w_{d1}$, we have

$$w_{1s} = \left[\frac{c \Delta_{12} w_{2s}^2 w_{d1}^2}{\Delta_{b1}} \right]^{1/3}. \tag{15}$$

For a low-β_{pe} plasma with $w_1 >> w_{d1}$, when

$$w_c = 4c \Delta_{11} \Delta_{12} w_{2s}^2/\Delta_{b1}^2 > 1, \tag{16}$$

w_1 will continues its growth without saturation, and the hollow current profile will be destroyed.

The island width of the $m/n = 3/1$ mode is calculated for two examples using the safety factor profile $q = q_0 r^2 / \int_0^{r^2} (1-t)^{g_1} (1 + \alpha t)^{g_2} dt$.

One q-profile is obtained with $q_0 = 4.0$, $g_1 = 4.0$, $g_2 = 0.4$ and $\alpha = 150$. This q-profile is close to that achieved on TFTR shown on Fig. 2 of Ref. [9]. The $q = 3$ surfaces are at $r_1 = 0.13a$ and $r_2 = 0.68a$. With the experimental and calculated values of $a\Delta_{11} = -25$, $a\Delta_{22} = -2.0$, $a\Delta_{12} = 0.71$, $a\Delta_{21} = 0.14$, $\Delta_{b1} = 12$, $\Delta_{b2} = -0.11$, $c = 3.5$, and $w_{d1} = w_{d2} = 0.02a$[7, 9], it is found that $w_{2s} \approx 4.8 \times 10^{-2}a$ and $w_{1s} \approx 5.7 \times 10^{-3}a$.

Another q-profile is obtained with $q_0=4.0$, $g_1=4.0$, $g_2=1.0$ and $\alpha=22$. For $r<0.9a$ this q-profile is close to that achieved on DIII-D shown on Fig. 3 of Ref. [10]. The q=3 surfaces are at $r_1=0.20a$ and $r_2=0.82a$. With the experimental and calculated values of $a\Delta_{11}=-12$, $a\Delta_{22}=-2.6$, $a\Delta_{12}=0.85$, $a\Delta_{21}=0.21$, $\Delta_{b1}=5.2$, $\Delta_{b2}=-0.16$, $c=8.2$, and $w_{d1}=w_{d2}=0.02a[7, 10]$, it is found that $w_{2s} \approx 5.3\times 10^{-2}a$ and $w_1 \approx A_1^{1/3} \approx 6.9\times 10^{-3}a$.

The calculated inner island width for both examples is small than $10^{-2}a$, which agrees with the experimental results that no coherent MHD activity was observed in the reversed shear region[9, 10]. More detailed analysis of Eq. (9)-(11) are given in Ref. [7].

4. Summary

(1) For a high β_{pe} plasma, the inner magnetic island width will be greatly reduced by the perturbed bootstrap current. This makes the island coupling not important for the outer island, and the outer island behaves like a single tearing mode with the inner rational surface acting as a conducting wall.

(2) The relative rotation between the two islands mainly has a stabilising effect on the inner island, while the outer island is essentially not affected. Periodical burst of the inner island can be excited by the outer island via the coupling effect when there is a differential rotation.

(3) The island width is the key parameter in determining the phase locking.

(4) For the locked islands, when $w_c=4c\Delta_{11}\Delta_{12}(w_{2s}^2/\Delta_{b1}^2>1$, the inner island will continue its growth, and this will eventually destroy the nonmonotonic q-profile.

References

[1] H. P. Furth, P. H. Rutherford, and H. Selberg, Phys. Fluids **16**, 1054(1973).

[2] D. H. J. Goodall and J. A. Wesson, Plasma Phys. and Controlled Fusion **26**, 789 (1984).

[3] R. L. Dewar and M. Persson, Phys. Fluids **B 5**, 4273 (1993).

[4] Qingquan Yu, Phys. Plasmas **3**, 2898 (1996).

[5] J. D. Callen, W. X. Xu, and et al., in Plasma Physics and Controlled Nuclear Fusion Research 1986, Kyoto (IAEA, Vienna, 1987), Vol. 2, p. 157.

[6] R. Carrear, R. D. Hazeltine, and M.Kotschenreuther, Phys. Fluids **29**, 899 (1986).

[7] Qingquan Yu, Phys. Plasmas **4**, 1047 (1997).

[8] Richard Fitzpatrick, Phys. Plasmas **2**, 825(1995).

[9] F. M. Levinton, M. C. Zarnstorff, and et al., Phys. Rev. Letts **75**, 4417(1995).

[10] E. J. Strait, L. L. Lao, M. E. Mauel, and et al., Phys. Rev. Letts **75**, 4421(1995).

Extension of lattice Boltzmann techniques to flows with arbitrary Prandtl number

M. Soe, G. Vahala, **P. Pavlo**[a], L. Vahala[b] and H. Chen[c]

Department of Physics, College of William & Mary, Williamsburg, VA 23187, USA

[a]Institute of Plasma Physics, Acad. Sci. Czech Rep., Prague 8, Czech Republic

[b]Dept. of Electrical & Computer Engineering, ODU, Norfolk, VA 23529, USA

[c]EXA corporation, Cambridge, MA 02140, USA

Introduction

Turbulence simulations, because of the inherent complexity of the governing equations, are very difficult for complex flows. This has forced most computational schemes into Reynolds averaged Navier-Stokes (RANS) modelling. Direct numerical simulations (DNS) for simple flows are found to be an important tool to refine RANS modeling so as to allow computations for realistic geometries. Thermal lattice Boltzmann equation (TLBE) method is a new form of DNS. With the advent of massively parallel processor machine architectures, TLBE methods become important new tools to solving turbulence problems. A steady increase of interest in TLBE simulation techniques is witnessed in the past few years due to their major advantages over conventional computational methods. These include, for example, massive parallelism, complex fluids modeling capability, and easy implementation of boundary conditions. In standard TLBE (and incompressible LBE), one replaces the nonlinear macroscopic equations with a linearized Boltzmann equation with the simple scalar BGK collision operator and solves on a discrete lattice.

The use of this BGK collision operator is sufficient to recover the desired nonlinear transport equations under Chapman-Enskog expansions, and is computationally more efficient. However, most of the TLBE models which utilize the BGK collision operator, use only one relaxation time scale so that the shear viscosity μ and thermal conductivity κ transport coefficients are intrinsically linked. Therefore these models allow only for fixed Prandtl number flows, where $Pr = \frac{\mu}{\kappa} = \frac{1}{2}$.

In this paper, we propose an extended tensor collision operator for TLBE methods that will allow variable Prandtl number flows. Incorporation of an additional free parameter in the off diagonal components of the proposed matrix collision operator will lead to a multi-relaxation scheme. The relaxation parameters will be generalized so that transport coefficients become density independent, a result well known from classical kinetic theory of dilute gases. All previous LB models have suffered from density dependent transport coefficients. Even though this poses no problem for incompressible flows, it is critical and must be handled for compressible fluid simulations.

Generalized collisional operator

The governing equation of TLBE, in local microscopic units of length and time, takes the generic form

$$N_{pi}(\mathbf{x} + \mathbf{e}_{pi}, t + 1) - N_{pi}(\mathbf{x}, t) = \Delta_{pi} \qquad i = 1, ...b_p \tag{1}$$

This describes the evolution of the mean particle population N_{pi} in the discrete phase space. The indices p and i are for sub-lattice and lattice links respectively. $\mathbf{e}_{pi}$ is the lattice vector giving the velocity of moving particles in the system. The speed in each sub-lattice is $\mid \mathbf{e}_{pi} \mid = p$. Δ_{pi} is the collision matrix whose eigenvalues control the transport coefficients. To allow for variable Prandtl number flows, we generalize the scalar BGK collision operator into a circulant matrix with the inclusion of another free parameter θ in the off-diagonal components

$$\Delta_{pi} = -\frac{1}{\tau}(N_{pi} - N_{pi}^{eq}) - \frac{\theta}{b_p c_p^2} \sum_j e_{pi\alpha} e_{pj\alpha}(N_{pj} - N_{pj}^{eq}) \equiv -\frac{1}{\tau} \sum_j A_{ij}(N_{pj} - N_{pj}^{eq}) \tag{2}$$

Here, we do not define Δpi by the scattering rules as in LGA, but enforce certain symmetry requirements. As a result, A_{ij} is symmetric, cyclic with non-zero eigenvalues $\lambda_1 = 1$, $\lambda_2 = (1 + \frac{\theta \tau}{2})$ of multiplicity 4 and 2 respectively, for hexagonal lattice. The equilibrium distribution is assumed to be a truncated power series in the mean velocity

$$N_{pi}^{eq} = A_p + B_p(\mathbf{e}_{pi}.\mathbf{v}) + C_{pi}(\mathbf{e}_{pi}.(\mathbf{v}) + D_p v^2 + E_p(\mathbf{e}_{pi}.\mathbf{v})^3 + F_p(\mathbf{e}_{pi}.\mathbf{v})\mathbf{v}^2 \tag{3}$$

The coefficients $A_p, B_p, ..., F_p$ are functions of the mean density n and mean temperature ε, where $n = \sum_{pi} N_{pi}$, $n\mathbf{v} = \sum_{pi} N_{pi}\mathbf{e}_{pi}$ and $n\varepsilon = \frac{1}{2}\sum_{pi} N_{pi}(\mathbf{e}_{pi} - \mathbf{v})^2$. Constraints imposed on N_{pi}^{eq} and the collision matrix Δ_{pi} are such that the local collisional invariants $\sum_{pi} \Delta_{pi} = 0$, $\sum_{pi} \Delta_{pi}\mathbf{e}_{pi} = 0$ and $\sum_{pi} \Delta_{pi}\mathbf{e}_{pi}^2$ are satisfied. Further physical constraints are also imposed, in particular, one must impose Galilean invariance and requires that the pressure be independent of the mean macroscopic velocity. If once's choice of lattice is symmetric enough to ensure isotropy for macroscopic flux tensors, a perturbative multi-scale procedure would lead to the desired macro-dynamic equations in the compressible Navier-Stokes from with the transport coefficients $\mu = n\varepsilon(\frac{\tau}{\lambda_1} - \frac{1}{2})$ and $\kappa = 2n\varepsilon(\frac{\tau}{\lambda_2} - \frac{1}{2})$. On choosing the relaxation times $\tau = (\frac{\mu_0}{n} + \frac{1}{2})$ and $\theta = (\frac{4n}{\kappa_0 + n} - \frac{2}{\tau})$, we obtain the final transport coefficients

$$\mu = \mu_0 \varepsilon; \quad \kappa = \kappa_0 \varepsilon \tag{4}$$

where $\kappa_0(\varepsilon)$ is an arbitrary function of temperature, while $\mu_0(\varepsilon) = \alpha\kappa_0(\varepsilon)$ with $\alpha = const$. The Prandtl number is then

$$Pr = \frac{\mu_0(\varepsilon)}{\kappa_0(\varepsilon)} = \alpha = \text{arbitrary} \tag{5}$$

Note that the transport coefficients μ and κ are independent of density but are functions of temperature, in agreement with the standard kinetic theory.

For the linear stability analysis of TLBE with extended collision operator, we have used the method developed in [1]. Numerical results show a moderate improvement of stability for $Pr < 1/2$ and moderate deterioration for $Pr > 1/2$ [2]. However, we can conclude that varying Pr does not *adversely* affect the limited stability in TLBE models.

Numerical results

To see the role of variable Prandtl number on 2D free-decaying turbulence induced by a double velocity shear layer, we have performed simulations on a 512×512 hexagonal grid for the Reynolds number $Re \simeq 1655$ with various Prandtl numbers; the results presented here are for $Pr = 0.9$ and $Pr = 15$. We used a code based on the model by Alexander et al. [3]. For simplicity, periodic boundary conditions were imposed. Not unexpectedly, we can see some effect of Prandtl number variation on the geometry of the dominant vortex structures but no significant magnitude variations in the size of these structures. A detailed description of these results will be given in [2].

As another example, we present the results of simulations of 2D Rayleigh-Bernard flow. In this case, the code used was based on a special modification of a 17 bit composed rectangular model, with the same modulae of base (speed) vectors for the axial and diagonal directions ("octagonal model"). A detailed description of the model, especially the handling of the off-grid distributions, will be presented elsewhere [4]. In Fig. 1, the spatial distribution of temperature and the corresponding vorticity patterns are shown for $Pr = 0.1$, 0.5 and 5 (Figs. a, b and c, respectively), at time $t = 40,000$. All other parameters are the same (grid size 120x120, bottom (heated) and top (cooled) plate temperatures 0.4 and 0.5, respectively, $\tau = 0.51$, i.e., the Reynolds number is about 1200). The typical quiescent smooth convection and temperature patterns, seen for $Pr = 0.1$ (enhanced thermal conductivity), are established at time about $t = 8,000$ and persist till later times; $Pr = 0.5$ case exhibits already a strong perturbation of these patterns while in the last case (reduced conductivity, $Pr = 5$), the flow is fully turbulent.

[1] P. Pavlo, G. Vahala, L. Vahala, M .Soe: Stability Analysis of TLBE Models. *Submitted to J. Comput. Phys.*

[2] F. J. Alexander, S. Chen and J. D. Sterling, Phys. Review E 47 (1993) R2249.

[3] M. Soe, G. Vahala, P. Pavlo, H. Chen, L. Vahala: Thermal Lattice Boltzmann Simulations of Variable Prandtl Number Turbulent Flows. *Submitted to Phys. Fluids.*

[4] P. Pavlo, G. Vahala, L. Vahala, M. Soe: A High Reynolds Number TLBE Model, *18th Symposium on Plasma Phys. and Tech., June 1997, Prague, to be presented.*
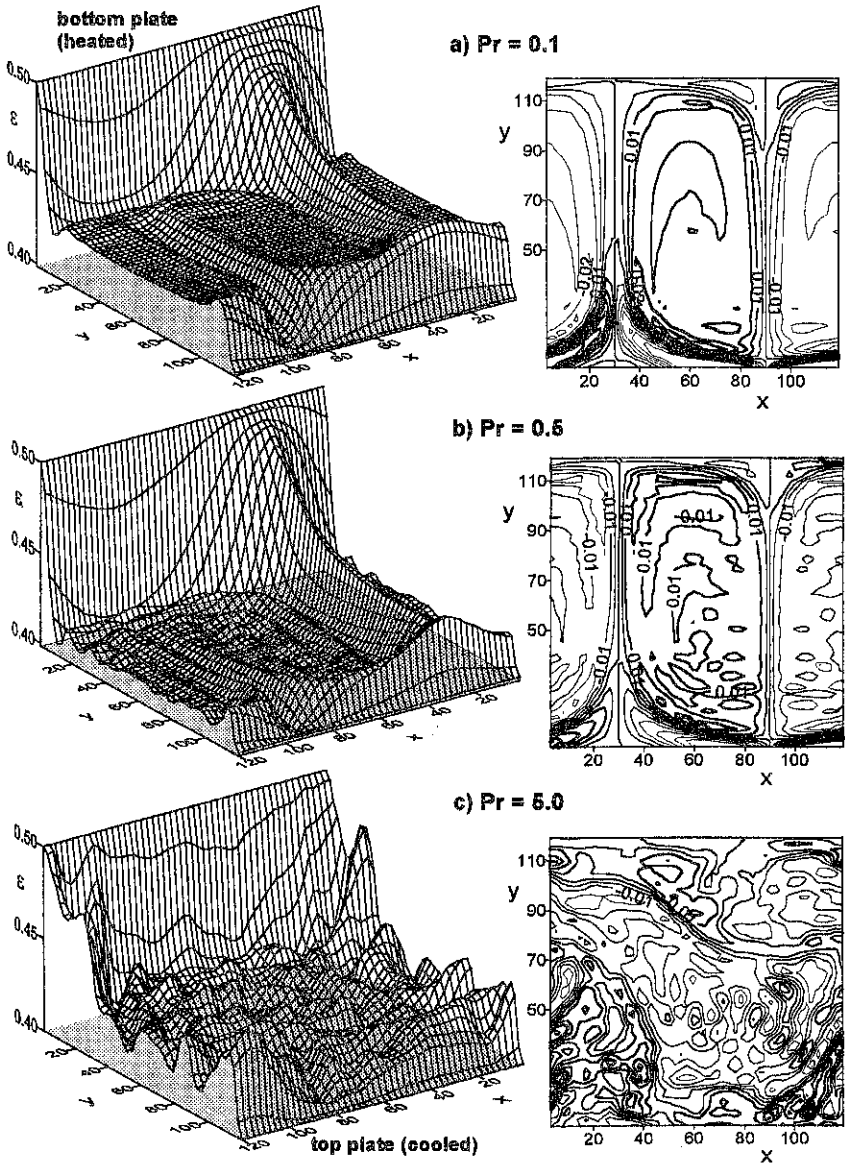
Fig. 1. Temperature distribution (left) and vorticity contours (right), at time t=40K, for 2D Rayleigh
-Bernard instability and Prandtl number Pr = 0.1 (a), 0.5 (b) and 5.0 (c). The corresponding
Rayleigh number Ra = 200K, 1M and 10M, respectively; the Reynolds number is about 1200.

Improved Regimes in the Tokamak Core

S. Sen

Dept. of Physics, Flinders University of South Australia, GPO Box 2100, Adelaide 5001, Australia

A popular and arguably most successsful picture of the high (H) mode is that some mechanism(s) (ion orbit loss, poloidal asymmetry in the transport and/or Reynold stress) creates an equilibrium radial electric field ($\mathbf{E}$) which gives rise to a *perpendicular* $\mathbf{E} \times \mathbf{B}$ drift which in turn stabilises microinstabilises and as a result fluctuation is suppressed and confinement is improved, the so-called H-mode. The same hypothesis is also believed to be the best possible explanation for the *core* confinement improvement during the very high (VH) modes in the DIII-D plasma. However, unlike the edge where the radial force balance equation relates $\mathbf{E}$ to the main ion pressure gradient and the poloidal rotation, in the core $\mathbf{E}$ is primarily related to the toroidal flow. In other words, a sheared toroidal velocity in the core is believed to give rise to a sheared $\mathbf{E}$ which in turn can stabilise (through the $\mathbf{E} \times \mathbf{B}$ shear) the turbulence to improve the core confinement.

However, while this $\mathbf{E} \times \mathbf{B}$ shear stabilising mechanism *alone* can satisfactorily explain the confinement improvement in the edge, its role in the *core* confinement improvement does not seem so ubiquitous. For example, the expansion of the ideal ballooning second stability region and of the region with drift reversal stabilisation of trapped particle modes were *also* (apart from the $\mathbf{E} \times \mathbf{B}$ shear stabilisation) considered as possible explanations for the core confinement improvement in the DIII-D. Similarly, in the so-called "two-stage" turbulence suppression in DIII-D, a second reduction phase in the plasma *interior* (contrary to the initial rapid suppression phase which is observed at the plasma *edge*, the conventional H-mode), it was not decided whether the turbulence suppression is because of the sheared $\mathbf{E} \times \mathbf{B}$ flow or due to the flattening of the pressure profile. However, the magnetic braking experiments performed by La Haye *et al.* [1] in which the plasma toroidal rotation (and its shear) is controlled externally made one to conclude that it is the $\mathbf{E} \times \mathbf{B}$ shear which leads to the confinement improvement in the plasma core.

In this article, we first investigate into why the $\mathbf{E} \times \mathbf{B}$ shear stabilisation mechanism may not be sufficient to account for the confinement improvement in the core. We then propose for the first time a plausible explanation of this core confinement improvement in terms of stabilisation of microinstabilities by the parallel flow curvature. We argue that the *main* stabilising role of the toroidal flow in the improved confinement regimes in the tokamak core (unlike the usual belief) is *not* through its weak perpendicular $\mathbf{E} \times \mathbf{B}$ component (although we do not deny its stabilising contributions), but through its strong parallel component. This picture satisfactorily explains the internal transport barrier formation in the Japan Torus-60U (JT-60U) [2] where the transport barrier is always accompanied by a sharp change in the toroidal velocity at $r/a = 0.6 - 0.8$ during the time 5.35 to 5.63 sec. (e.g., in shot 17129), whereas $\mathbf{E}$ (and the poloidal velocity) measured at $r/a = 0.8$ during the same time (5.35 to 5.63 sec.) does not show any appreciable change (fig. 6(b) in [2]). The same mechanism might also be responsible for the negative central magnetic

shear (NCS) discharges observed in the DIII-D plasma where a big jump in the toroidal velocity is always found in the region of the transport barrier formation.

Before we show the stabilising role of the parallel component of flow, let us discuss why the $\mathbf{E} \times \mathbf{B}$ shear stabilising mechanism *alone* is unlikely to explain the confinement improvement in the core. For this we start with the radial force balance equation:

$$v_\perp \approx E/B_\phi = \frac{v_\phi B_\theta}{B_\phi} - v_\theta + \frac{\partial P_i/\partial r}{nZeB_\phi}$$

where all the symbols have their usual meaning. It is obvious that with $B_\phi \gg B_\theta$, v_ϕ can contribute only weakly to $v_\perp$. As $v_\theta \approx 0$ in the core (the value of the pressure gradient is also much less in the core than in the edge during the improved regimes of confinement) this clearly shows that $v_\perp$ (and/or its spacial variation) is indeed weak in the core (note, this is contrary to the edge where $v_\perp \sim v_\theta$). More quantitatively, as evident from the radial force balance equation, to produce the same change in E, v_ϕ should change by $\frac{B_\phi}{B_\theta}(\gg 1)$ times that of v_θ. Experiments however indicate otherwise. This weak $\mathbf{E} \times \mathbf{B}$ shear *alone* is therefore unlikely to account for the improved confinement in the core. Apart from the magnitude, the $\mathbf{E} \times \mathbf{B}$ shear stabilisation hypothesis in the core has another serious drawback. This is because it is well known that the shear in the parallel flow has destabilising influence on the drift-type microinstabilities [3]. Now, since the toroidal flow shear is accompanied by a large amount of parallel flow shear which is known to destabilise the drift-like microinstabilities, an obvious next question is - can the stabilising effect of the weak $v_\perp$ shear, the $\mathbf{E} \times \mathbf{B}$ shear (coming from the toroidal flow), supersede the destabilising effect of the strong $v_\parallel$ shear (coming from the toroidal flow) so that the plasma can enter the the improved regimes (VH modes, say)? Needless to say that it seems highly unlikely (for example, note that the confinement improvement in the VH mode is a factor of 2 higher than the H-mode scaling)! So, a complete theory of the confinement improvement in the core *must* explain what happens to this destabilising effect of the parallel flow shear.

We will now show that the usual belief that the shear $(V_\parallel'(\rho))$ in the parallel flow is destabilising for drift-type mode can be changed altogether if the flow curvature $(V_\parallel''(\rho))$ effect is taken into account. To show this we start with the simple fluid description of the toroidal drift-wave model in the presence of parallel flow. The leading order eigenvalue equation after the ballooning transformation can be written as [4]

$$[\frac{\omega_e^{*2}}{\omega^2}(\frac{\epsilon_c}{k_\theta \rho_s})^2 \frac{\partial^2}{\partial \chi^2} - (\omega_e^* - \omega)/\omega + 2\epsilon_n \frac{\omega_e^*}{\omega}(cos\chi + \hat{s}(\chi + \chi_o)sin\chi) + \frac{1}{4}(\frac{dV_{\parallel o}}{d\rho} \frac{k_\theta \rho_s C_s}{\omega^2 qR})^2 / \frac{\omega_e^{*2}}{\omega^2}(\frac{\epsilon_c}{k_\theta \rho_s})^2 +$$

$$(k_\theta \rho)^2(1 + \hat{s}^2(\chi + \chi_o)^2) - \frac{\rho^2 \omega_e^*}{L_*^2 \omega}]\xi = 0 \tag{1}$$

where $\rho_s^2 = \frac{C_s^2}{\omega_{ci}^2}, C_S^2 = \frac{T_e}{m_i}, \epsilon_n = q\epsilon_c = L_n/R, V_{\parallel o}(\rho)$ is the equilibrium parallel velocity, ρ the radial distance from the reference mode rational surface, $\omega_e^*(\rho)$ the diamagnetic drift frequency and L_* the density gradient variation scale length and typically of the order of

density scale length L_n, χ is the extended ballooning coordinate. Parallel flow has therefore two effects. First, it introduces a Doppler-shift, $k_\| V_{\|o}$, in all time derivatives and second, an extra term representing the radial convection of the ion momentum. It is the second term which makes the effect of parallel flow shear completely different from that of perpendicular flow shear. However, we notice that the radial variation in the Doppler shift, $k_\| V_{\|o}$, in the mode frequency due to the parallel flow is negligible for flute type modes ($k_\| \ll k_\perp$). We therefore eliminate the Doppler shift by performing a Galilean transformation in the $\hat{e}_\|$ direction. In fact, because of the Doppler shift in the mode frequency due to the parallel flow is negligible we are allowed to use the conventional ballooning formalism (this is because the ballooning formalism treats all rational surfaces to be equivalent, i.e., modes associated with different rational surfaces have degenerate eigenvalues. This degeneracy is destroyed in the presence of shear rotation). The effect of the parallel shear/curvature enters the problem through an extra term $V_E . \nabla V_{\|o}(x)$ representing the radial convection of the ion momentum. In fact, it is this term which makes the effect of the parallel flow shear completely different from that of the perpendicular flow shear. It is also important to note that in deriving Equation (1) we have removed the first derivative (with respect to χ) term by suitably changing the dependent variable (to ξ).

Now to explore the implication of the velocity profile on the radial structure and the stability of the modes one needs the higher order ballooning theory. In the higher order theory, the radial envelope function $A(x)$ satisfies

$$\frac{\partial^2 \Omega}{\partial \chi_o^2} \cdot \frac{d^2 A}{dx^2} + [2(\Omega - \Omega_0) - p_1 - 2p_2 x^2]A = 0, \tag{2}$$

where, $\Omega = \frac{1}{k_\theta^2 \rho_s^2 \hat{s}^2}[\frac{\omega_*^*}{\omega} - 1 - k_\theta^2 \rho_s^2]$, $\Omega_o(=i\sigma) = i\frac{\epsilon_o}{k_\theta^2 \rho_s^2 \hat{s}}$, $p_1 = \frac{1}{2}(\frac{C_s V_{\|o}}{\omega^2 q R \hat{s} L_{v1}})^2 / \frac{\omega_*^{*2}}{\omega^2}(\frac{\epsilon_o}{k_\theta \rho_s})^2$, $p_2 = \frac{1}{k_\theta^4 \rho_s^2 \hat{s}^4}(\frac{1}{L_n^2} - (\frac{V_{\|o}}{C_s}\frac{L_s^2}{L_{v2}^2}\frac{1}{L_s k_\theta \rho_s})^2/(\frac{L_n}{R q k_\theta \rho_s})^2)$, $x = k_\theta \rho \hat{s}$, $L_{v1} = (\frac{V_{\|o}'}{V_{\|o}})^{-1}$, $L_{v2} = (\frac{V_{\|o}''}{2V_{\|o}})^{-1}$ and χ_o is an arbitrary phase of the eikonal. Equation (2) is a simple Weber equation. When p_2 is positive and $\partial^2 \Omega / \partial \chi_o^2 > 0$ ($\partial^2 \Omega / \partial \chi_o^2 > 0$ is necessary in order that the mode be most unstable), $A(x)$ is a localised Gaussian function. However, an important change is introduced by the velocity term. Choosing representative values of plasma parameters $V_{\|o} \sim C_s$, $L_s \sim qR$, $k_\theta \rho_s \sim 1$, we find that p_2 is negative for $L_{v2} < L_n$. Now for example, during the internal transport barrier formation in the JT-60U [2], $L_n \sim 15cm$, while $L_{v2} \sim L_{v1} \sim 12.5cm$. $A(x)$ is then given by

$$A(x) = exp[-i\frac{1}{2}(\mid p_2 \mid / \mid \frac{\partial^2 \Omega}{\partial \chi_0^2} \mid)^{1/2} x^2]$$

So, the mode envelope is now radially outgoing which is reminiscent of the equivalent slab problem. Velocity curvature in the toroidal problem like the magnetic shear in the corresponding slab problem creates an *antiwell* in the radial direction (instead of the well formed by the diamagnetic frequency). The wave energy is therefore convected outward. The eigenvalue is given by

$$\Omega = \Omega_0 + \frac{p_1}{2} - i\frac{1}{2}(p_2 \mid \frac{\partial^2 \Omega}{\partial \chi_0^2} \mid)^{1/2}$$

This also shows damping contribution in the global eigenvalue. Thus, both the radially outgoing nature and the damping contribution in the global eigenvalue unambiguously show that the parallel flow profile might *stabilise* toroidal drift-like waves which otherwise escape magnetic shear damping! It is important to notice that the toroidal drift wave model we are considering does not have any dissipation and is therefore marginally stable. Hence, even though the negative imaginary contribution in the global eigenvalue might be small in compared to Ω_o, it can be crucial in determining stablity. The presence of dissipation (e.g., inverse electron Landau damping, trapped particle and/or collision) however can make the mode unstable. In this case, the shift in the real frequency due to flow (represented by p_1) can play an indirect but important role in stability. This is because the driving term in both inverse electron Landau damping and trapped particle case is proportional to $\mid \omega_r - \omega_e^* \mid$ and any shift in the direction of the diamagnetic drift (which is the case in this problem) will therefore reduce the driving term. That the shift in the real frequency reduces the driving term has indeed been demonstrated numerically by Sidikman it et al. in the case of trapped particle driven drift mode in a sheared slab geometry. Concerning the collisional drive, we have shown elsewhere that the stabilising role of velocity profile persists in this case also [5] . It is interesting to note that the sign and the magnitude of the first derivative of the velocity field has no direct effect on the stability. The main stabilising effect comes from the quadratic term which forms an additional *antiwell* which pushes the wave function away from $\rho = 0$, thus incresing the shear stabilising effect and weaking the driving term simultaneously. It is also interesting to notice that this stabilisation by the flow curvature is achieved irrespective of the sign of the curvature. In this respect the effect of the flow curvature is entirely different than that of its perpendicular counterpart [6].

In summary, the stabilisation of the toroidal drift-ballooning type microinstabilities by the parallel flow profile might have a crucial role in explaining the confinement improvement in the core of tokamaks. We have argued that the $\mathbf{E} \times \mathbf{B}$ (shear) coming from the toroidal velocity (shear) is weak and may not be an obvious explanation of the core confinement improvement. We believe that the major stabilising contribution of the toroidal flow comes through its strong parallel component. This picture seems more realistic and is a plausible explanation of the internal transport barrier formation in the JT-60U [2] where the transport barrier is always accompanied by a sharp change in the toroidal velocity at $r/a = 0.6 - 0.8$ during the time 5.35 to 5.63 sec. (e.g., in shot 17129), whereas $\mathbf{E}$ (and the poloidal velocity) measured at $r/a = 0.8$ during the same time (5.35 to 5.63 sec.) does not show any appreciable change (fig. 6(b) in [2]). We have endeavoured to focuss on the experimental data relevant to the internal transport barier in the JT-60U and have come to this conclusion.

References

[1] R. J. La Haye et al., Phys. Plasma, **1**, 373 (1994)

[2] Y. Koide et al., Phys. Rev. Lett., **72**, 3662 (1994)

[3] N. Mattor and P. H. Diamond, Phys. of Fluids, **31**, 1180 (1988)

[4] S. Sen and J. Weiland, Phys. Plasma, **2**, 777 (1995)

[5] S. Sen, Plasma Phys. Cont. Fus. **37** 95, (1995)

[6] S. Sen, M. G. Rusbridge and R. J. Hastie, Nuc. Fus., **34**, 87 (1994).

Beta Limits Against External Kink Modes in Tokamaks Taking into Account Plasma Outside Separatrix

L. Degtyarev, A. Martynov, S. Medvedev

Keldysh Institute of Applied Mathematics

Russian Academy of Sciences, Moscow

L. Villard

Centre de Recherches en Physique des Plasmas

Association Euratom - Confédération Suisse

Ecole Polytechnique Fédérale de Lausanne

1 **Introduction** Pressure driven external kink modes are believed to set an upper limit for the values of β in tokamaks [1]. Extensive investigations of the β limit dependence on plasma geometry and profiles were performed for single axis plasmas. However self consistent modeling of divertor plasma configurations with separatrix at the boundary requires taking into account plasma outside the separatrix. This is evident in the case of typical H-mode profiles with current density and pressure gradients non vanishing at the separatrix. The same question holds for doublet configurations. The codes CAXE and KINX were developed [2] to compute equilibrium and stability of the axisymmetric plasma configurations with separatrix.

. The first question to answer is related to a simple case of pressureless and currentless mantle plasma outside the separatrix. Such a case can be readily treated with conventional equilibrium and stability codes for single axis plasma: the equilibrium outside the separatrix was just the same as vacuum. However the current perturbations in a conducting mantle plasma can make the stability of such a configuration different from the traditional approach with vacuum instead of mantle. The difference does take place for axisymmetric $n = 0$ stability. The surface current perturbations play stabilizing role for vertical plasma instability in the case of up-down non symmetric plasma cross section [3]. The mantle plasma outside the separatrix does not considerably change external kink β limits in doublets [4].

For the equilibria with a current density pedestal at the plasma boundary the self consistent modeling of separatrix plasma demonstrates more specific features even still in the frame of ideal MHD approach. Finite current density at the plasma edge brings a question of peeling mode stability. As the peeling mode stability is extremely sensitive to the proximity of vacuum rational magnetic surface to the plasma boundary, the questions arise: what is the plasma boundary and whether it is satisfactory to stay with its conventional ψ_{95} definition. Including the plasma outside the separatrix into the model gives more consistent answer to these questions [5].

Finite pressure gradient in plasma outside the separatrix affects not only localized peeling modes but also global external kink mode stability limits.

2 **External kink mode limits in doublets** External kink modes in doublet configurations are not restricted to the inside of the separatrix: the perturbations in the outside plasma are as high as inside (Fig.1). Therefore the overall β limit depends on the pressure gradient in the plasma outside separatrix too. Several examples of doublet equilibria with different current density values at the separatrix, different outside plasma layer thickness and several types of pressure gradient profiles outside the separatrix are considered below.

Doublet equilibria with the up-down symmetric boundary (aspect ratio $A = 3.8$, elongation $\kappa = 3.2$) [3] fitted into the TCV vacuum chamber were used in the computations.

The "H-mode" type plasma profiles, with pressure gradient having a maximum at the separatrix and finite separatrix current density, were prescribed by

$$I^* = 1 - (1 - I_s)\bar{\psi}^{in}, \quad p' = p_s\bar{\psi}^{in}, \quad \text{inside separatrix} \tag{1}$$
$$I^* = I_s(1 - \bar{\psi}^{out}), \quad p' = p_s(1 - \bar{\psi}^{out})^{\alpha_p}, \quad \text{outside separatrix}$$

where $0 < \bar{\psi}^{in,out} < 1$ are the normalized poloidal fluxes inside and outside the separatrix, respectively, I_s is the value of the current density at the separatrix, p_s is the maximal

value of the pressure gradient at the separatrix; I^* is the surface averaged toroidal current density. The plasma profiles of a typical equilibrium are given in Fig.2.

In the first series the current density pedestal value is fixed: $I_s = 0.1$. The limiting values of $g = 2\beta/(I_p/aB) \times 100$ for doublet plasmas are computed against the $n = 1$ external mode stability with a conducting wall sufficiently far from plasma. The factor 2 in the definition the g value is used for easier comparison with the corresponding values in single axis configurations. The value of safety factor at the magnetic axis is $q_0 = 1.05$. Fig.3a presents the results of the stability limit calculations for different values of normalized flux outside separatrix ψ_s (different outside plasma layer thickness): the value of $\psi_s = 1$ corresponds to initial doublet configuration with the ratio of the outside poloidal flux to the total flux inside the plasma 0.19, $\psi_s = 0$ corresponds to a doublet with all plasma outside separatrix removed.

The limiting value g for the single axis plasmas inside the separatrix is $g = 3.65$. The doublet limiting value $g_{\lim} \simeq 3.5$ at $\psi_s \to 0$ (when the mantle plasma is very thin) is not far from the single axis plasma value. The limit is getting lower when the plasma outside the separatrix with finite pressure gradient is building up. The decrease in the g value limit is bigger when the exponent α_p is lower in outside pressure gradient profile (1) which corresponds to higher values of pressure at the separatrix.

The difference between the values of $g_{\lim}$ at $\psi_s = 0$ and $\psi_s = 1$ is about the same for toroidal wave number $n = 2$: $g_{\lim} = 3.84$ and $g_{\lim} = 3.14$ respectively ($\alpha_p = 1$).

Localized ballooning mode criterion gives instability at $g \simeq 2.2$ ($\alpha_p = 1$) for the plasma near the separatrix from inside: marginally stable values of p' are shown in Fig.2 with dashed line. The plasma outside the separatrix is stable against localized ballooning modes for all considered equilibria and seems to be in the second stability region.

In the next two series the value of the current density at the separatrix changes ($\alpha_p = 1$). The value of the safety factor at magnetic axis is either fixed $q_0 = 1.05$ (Fig.4a) or adjusted to give total normalized current in doublet $I_N = I_p/(aB) \simeq 1.1$ (Fig.4b). The difference between the single axis and doublet limits in g is about the same versus the value of current density at the separatrix I_s when the normalized current is not too high (Fig.4a for $I_s < 0.2$ and Fig.4b).

Keeping the values of q_0 fixed and raising the value of I_s leads to an increase in the value of normalized current. The values of q_{95} in the plasma inside the separatrix are less than 2 for $I_s > 0.3$ and the current limit corresponds to $I_s = 0.34, I_N = 1.8/2$ for single axis plasma. The current limit in doublets with increasing I_s is higher: $I_s = 0.67, I_N = 2.4$. Still the limiting g values are very low: $g_{\lim} < 1$ at $I_s > 0.4$. However the decrease in the limiting g values for single axis as well as doublet plasmas also takes place at relatively low value of normalized current $I_N = 1.1$ (Fig.4b). It is connected with higher values of q_0 and lower global shear.

Pressure gradient profiles with a maximum at the separatrix is close to optimal concerning the external kink mode stability of single axis plasma. The last series of stability computations confirms the above results for another class of pressure gradient profiles still close to the "H-mode" profiles but with $p' = 0$ at the separatrix. They are produced from the initial profiles (1) by multiplication by $(1 - \psi_{in})^{0.5}$ inside the separatrix and by $\psi_{out}^{0.5}$, ψ_{out} and 0 outside the separatrix (Fig.5abc). The value of g limit for single axis plasmas is very close to the result with the initial profile $g = 3.65$. The limiting value for the doublets is quite unexpectedly goes down despite of lower values of pressure gradient: from $g_{\lim} = 2.9$ to $g_{\lim} = 2.5$ (compare Fig.2 and Fig.5a). At the same time the plasma outside the separatrix is not in the second stability region of ballooning modes. Still lower values of pressure gradient (Fig.5b) give again an increase in doublet limiting value $g_{\lim} = 3.15$. Finally the doublet limit is practically the same as for single axis plasma in the case of force free outside plasma $g_{\lim} = 3.65$ (Fig.5c).

3 Stability of divertor configurations The divertor equilibria with plasma outside the separatrix can be treated with the divertor versions of the CAXE and KINX codes. A characteristic feature of a divertor configuration is a presence of open magnetic field lines penetrating the end plates. The boundary conditions at the end plates are discussed in [5].

The choice of vanishing displacement condition at the end plates (fixed plates) leads

to a strong stabilizing effect of the plasma outside separatrix. Fig.3b present the results of stability calculations analogous to that of Fig.3a for doublets. The dashed curves show a growth of the limiting g values with a thickness of the plasma outside the separatrix independently of the pressure gradient profile.

Another choice is to use natural boundary conditions at the end plates following from the variational formulation of the stability problem and leave the boundary conditions for vacuum solution the same as in the fixed plates case. The resulting model does not include the stabilizing vacuum potential energy perturbations corresponding to the non zero perturbations at the end plates and omits the additional surface term in the potential energy [5] and therefore is not self-consistent. However the g limits according to that model behave in the same way as the limits in doublets with increasing pressure gradient in the outside plasma (Fig.3b, solid lines). The decrease in g_{lim} with higher pressure at the separatrix is less pronounced in the divertor case than in the case of doublets.

One of possible extensions of the model is the inclusion of positive vacuum energy contribution due to the plasma displacements at the end plates.

4 Conclusions The pressure profile variation in relatively thin plasma layer outside the separatrix can influence global external kink mode stability and considerably change the β limit in doublet configurations.

The conclusions for divertor configurations strongly depend on the choice of boundary conditions at the open field lines. Fixed boundary conditions at the divertor end plates result in stabilizing effect of the plasma outside separatrix independent of pressure gradient there. More realistic choice of boundary conditions gives a behavior similar to the doublet case.

References

[1] Troyon F. *et al.* Plasma Phys. and Contr. Fusion **26** (1984) 209

[2] Degtyarev L., Martynov A., Medvedev S., Troyon F., Villard L., Gruber R. The KINX ideal MHD stability code for axisymmetric plasmas with separatrix. Comput. Phys. Commun. (1997) to appear

[3] Degtyarev L., Martynov A., Medvedev S., Troyon F., Villard L. Influence of plasma near separatrix on ideal MHD stability in tokamaks. 22th EPS Conf. on Controlled Fusion and Plasma Phys., Bournemouth, Proc. Contrib. Papers Vol.19C, Part I (1995) 217

[4] Degtyarev L., Martynov A., Medvedev S., Troyon F., Villard L. MHD limits and axisymmetric stability of doublets. 21th EPS Conf. on Controlled Fusion and Plasma Phys., Montpellier, Proc. Contrib. Papers Vol.18B, Part II (1994) 556

[5] Degtyarev L., Martynov A., Medvedev S., Troyon F., Villard L. External kink mode stability of tokamaks with finite edge current density in plasma outside separatrix. 23th EPS Conf. on Controlled Fusion and Plasma Phys., Kiev, Proc. Contrib. Papers Vol.20C, Part III (1996) 1191
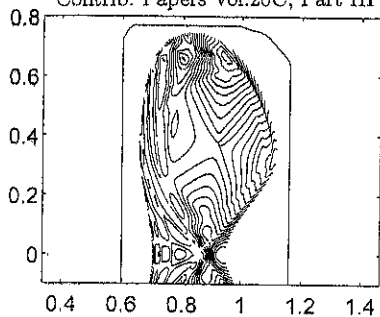
Fig.1. External pressure driven kink mode structure in doublet equilibrium, $g = 4.3$. Normal displacement level lines. $\omega^2/\omega_A^2 = -1.5 \cdot 10^{-3}$
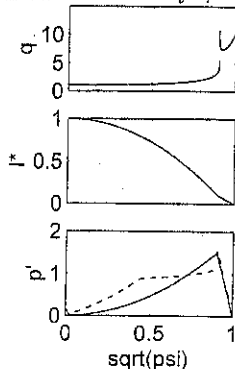
Fig.2. Plasma parameter profiles for doublet equilibrium, $g = 4.3$.
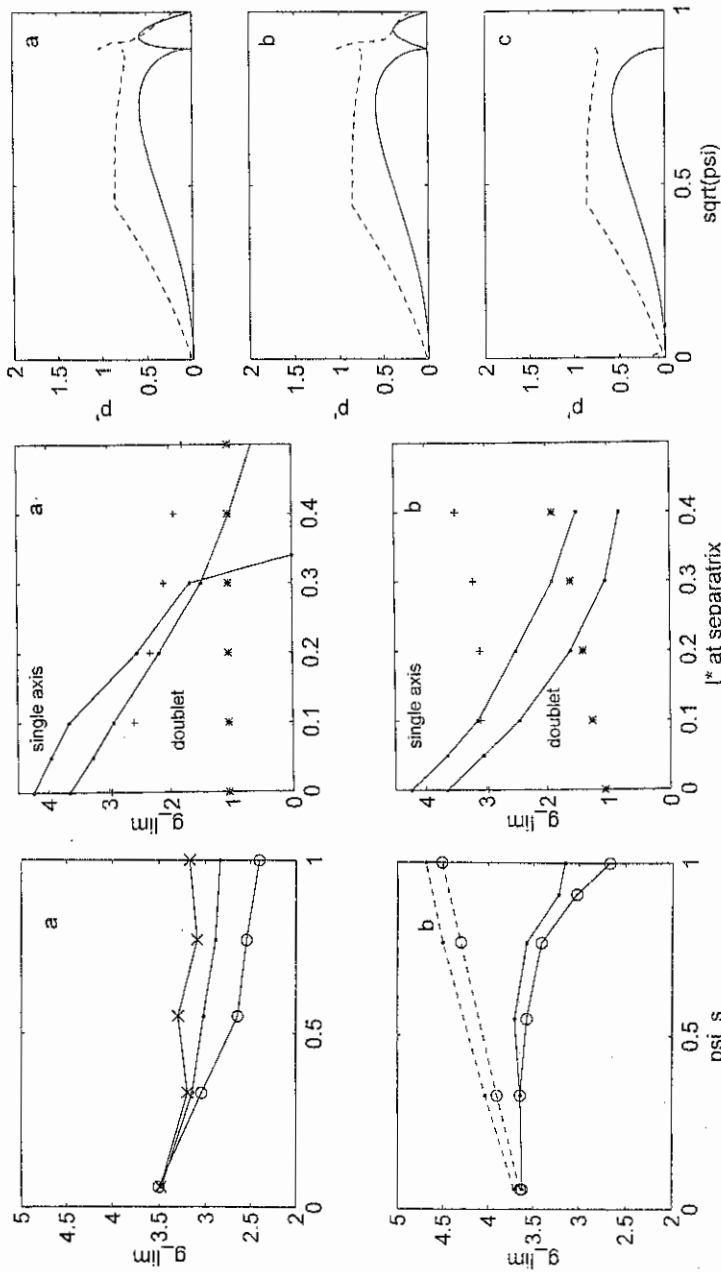
Fig.3. Limiting g values against external n = 1 kink mode versus normalized flux in outside plasma, points - $\alpha_p = 1.0$, circles - $\alpha_p = 0.5$, crosses - $\alpha_p = 2.0$. a) doublet b) divertor, solid lines - free plates, dashed lines - fixed plates.
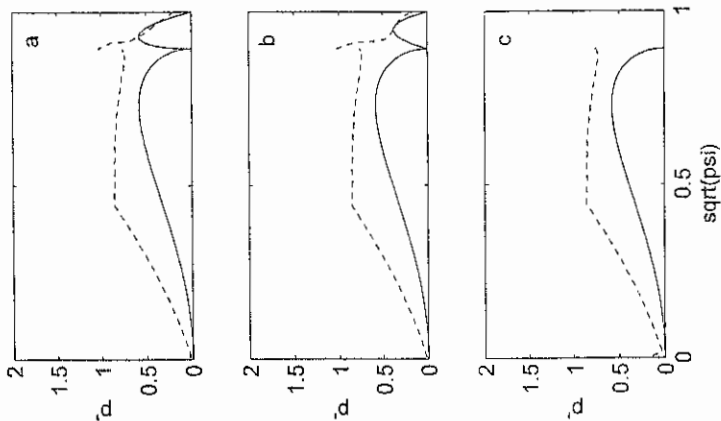
Fig.4. Limiting g values against external n = 1 kink mode for doublets versus current density separatrix for doublet equilibria at separatrix, crosses - q_{95} values, stars - q_0 values. a) $q_0 = 1.05$ b) normalized current $I_N = 1.1$
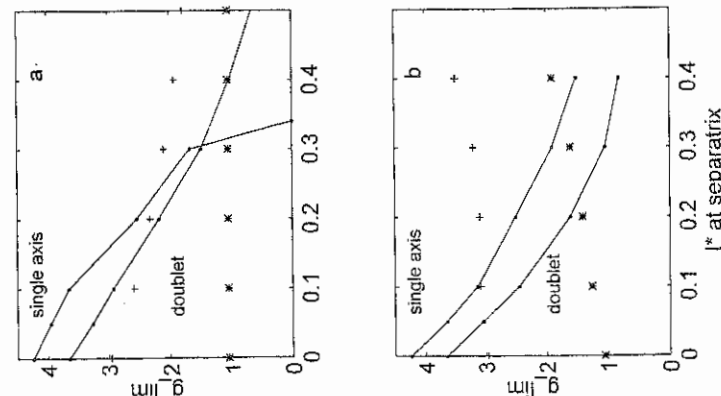
Fig.5. Pressure gradient profiles with $p' = 0$ at separatrix for doublet equilibria

Integral Equation Approach to Modelling of the Observed Phenomena of Fast Nonlocal Heat Transport in a Tokamak

A.B.Kukushkin

INF RRC "Kurchatov Institute", 123182 Moscow, Russia

I. Introduction. Interpretation of anomalous cross-field energy transport (ACFET) is known to be based on an assumption of "local" transport which is described by the diffusion-type differential equation. Within the frame of such a formalism, fast changes of absolute values of the temperature, which don't influence appreciably temperature profile, should be interpreted as a sharp change of transport coefficients in a large part of plasma volume, not only in a narrow layer, e.g., near plasma edge. This is the case for a number of recent experiments on major large tokamaks, see [1-6], which did manage to resolve evolution of temperature profile either during L-H transition or in the case of fast localized temperature perturbations. Here, the faster and more localized the perturbations, the stronger are the instant (within diffusion time scale) "jumps" of transport coefficients.

On the other hand, there is a possibility to treat the ACFET problem in the frame of energy transport by the energy carriers of *long free path* (LFP), of the order and even much larger than plasma characteristic size L. Mathematically, such an approach corresponds to an integral equation in space variables, irreducable to a diffusion-type differential equation. Here, dominant contribution of the LFP energy carriers makes the corresponding thermal diffusivities explicitly dependent on L (and tending to infinity with $L \Rightarrow \infty$) that makes the very concept of thermal diffusivities irrelevant to this mechanism of transport.

The latter is the case for the ACFET by a wide class of EM waves in magnetically confined plasmas. The dominance of the LFP waves' contribution to energy transport by EM waves has been shown, for the first time, for longitudinal waves by Rosenbluth and Liu [7] (the ACFET by the electron/ion Bernstein waves) and, for transverse waves, by Tamor [8] (electron cyclotron radiation (ECR) transport in a tokamak).

II. Integral equation approach and formulation of inverse problem. The approach developed for interpreting the observed phenomena of fast nonlocal transport, includes the following three parts.

(1) Derivation of the *integral equation* formalism for the ACFET. Here, the approaches [7-10] are extended to the case of describing the *local* energy balance of the ACFET by the LFP waves, under conditions of the applicability of *geometrical optics*, in the regime of *multiple* reflections of the waves from/at plasma boundary/periphery. The following non-linear (in T_e and n_e) term is obtained for the power density $Q_{wave} \equiv dE/dVdt$, acquired by the plasma due to emission/absorption of the LFP waves,:

$$Q_{wave} = \sum_{\xi} \int d\Omega_n \, d\omega \left[\kappa(\Phi, \vec{r}) J_{esc}(\omega) - q(\Phi, \vec{r}) \right], \Phi \in \left\{ \int_{\vec{r}_b}^{\vec{r}} \kappa(\Phi, \vec{r})(\vec{n}, d\vec{r}) \le 1 \right\} (1)$$

$$J_{esc} = \frac{\int dV \int d\Omega_n \, q(\Phi, \vec{r})}{\int d\Omega_n \int (\vec{n}, d\vec{S}_s)(1 - R(\Phi, S_s)) + \int dV \int d\Omega_n \, \kappa(\Phi, \vec{r})}, \quad V = V_{esc}(\omega), \quad (2)$$

where $J_{esc}(\omega, \xi)$ is the intensity of the LFP waves, differential in $\Phi \equiv \{\omega, \vec{n}, \xi\}$; κ is absorption coefficient (with allowing for stimulated emission processes) and q is source function; $\vec{n} \equiv \vec{k}/k$; and ω and $\vec{k}$ are the frequency and wave vector, respectively; and ξ stands for polarization; $V_{esc}(\omega)$ is the projection of phase space Φ_{esc}, defined by the inequalty of Eq.(1) with angle-averaged κ, onto coordinate space; S is plasma surface; R is the coefficient of wave reflection from/at plasma boundary/periphery (cf. [10]). Equation (1),(2) gives approximate analytic solution of the LFP waves transport problem, for fixed T_e and n_e profiles, under condition *(1-R)<<1*. Here, the intensity of LFP waves substantially deviates from LTE (Planck) distribution, at least due to almost free propagation of waves in an inhomogeneous medium. In the first order approximation the integration space in Eq.(1) is reduced to allowing for the outer layer of the unit optical thickness. Equation (1),(2) neglects *diffusion* component of the transport (e.g short free path waves in residual (opaque) part of plasma) and thus extracts *nonlocal* component of transport.

The term Q_{wave} , Eq.(1), is to be added, as a sourse term, to commonly used particle energy transport equation. The validity of the approach [10] is proved by the results of its application to energy transport by the ECR waves in a tokamak (see [10]).

(2) Formulation [11] of the *inverse problem* of reconstructing the major parameters of the integral term, Eq.(1). To this end, a model is proposed which is based at phenomenological description of (i) dispersion and emission/absorption characteristics of LFP waves in *non-equilibrium* magnetically confined plasmas (i.e. κ and q functions); (ii) coefficient R of reflection of a wave from/at plasma boundary/periphery.

(3) *Modelling,* with few phenomenological parameters, of the initial stage of the following recently observed phenomena of fast nonlocal energy transport: **(i)** net inward flux of electron energy during *off-axis heating* (similarly to ECRH experiments on D-III-D [1]); **(ii)** prompt rise/drop of temperature in the core caused by the fast cooling/heating of the periphery on TEXT [4] and TFTR [5]. This class of nonlocal phenomena comprises fast response of the core in *cold pulse* experiments on JET [6]; **(iii)** fast "volumetric" response of energy transport to plasma edge behavior during L-H transitions (see [2], for JET, and [3], for JT-60U).

The program outlined is implemented in the frame of the following physics model. The nonlocal component of electron energy transport stems from the emission/absorption of longitudinal waves by a fast electron population of relative concentration $\delta \ll 1$ and effective temperature $T_e^{(f)}(r)$, related to background plasma temperature $T_e(r)$ as follows: $\alpha = T_e^{(f)}(r)/T_e(r) \geq$ several units. The nonlocal exchange of energy between fast electrons population by means of the LFP wave transport is converted, due to (anomalous) collisional energy exchange between fast electrons and background plasma, into nonlocal energy exchange in background plasma. Here, the plasma energy is still accumulated in background plasma particles whereas significant contribution to energy flux (namely, its nonlocal component) stems from the LFP longitudinal waves emitted by fast electrons. To test the model, we assume that the spectral distribution for the emission/absorption of these hypothetical LFP longitudinal waves is close to that of the ECR (transverse) waves. Here, the smallness of relative concentration δ is compensated by the well-known dominance of the intensity of emitting/absorbing the longitudinal waves by a (fast) electron in a plasma over that for the transverse waves, by a factor $\varepsilon \gg 1$, with the net enhancement factor $A \sim \delta\varepsilon \gg 1$ for sink/source functions, with respect to ECR case.

The modelling has been carried out for solving the inverse problem in terms of the introduced above phenomenological parameters A, α, and R. To extract the nonlocal component of energy transport, it is most appropriate to analyze fast (within diffusion time scale) transport, i.e. initial stage of propagation of perturbations from a heat source, localized in space and time, at the background of the "frozen" all other, diffusion-type components.

Within the physics model outlined, the L-H transitions can be interpreted as a sudden drop of reflectivity R [10]. However, it appears that the reconstruction of the major characteristics of L-H transitions (e.g., energy confinement time increase) is compatible with a broad band of solutions of such an inverse problem. On the contrary, in the case of localized fast

perturbations the allowable space for the inverse problem solutions shrinks dramatically. Thus, the present approach gives simple model for the mechanism of nonlocal inward energy flux which is lost in diffusion-like approaches. For instance, the most intriguing manifestation of nonlocality, namely the prompt rise of $T_e(r)$ in the core caused by the fast cooling of the periphery, results from the following chain of energy exchange between the core, which is always a net emitter of wave energy, and the periphery, which is a net absorber of wave energy in the regime of nonlocal energy transport (cf. [10]): (a) "narrowing" of the absorption spectrum at the periphery, due to temperature drop; (b) "enlightenment" of the periphery at respective frequencies of the intensity J_{esc} due to a decrease of absorption by the periphery; (c) enhancement of the inward flux of LFP waves, due to the reflection of the flux formerly absorbed by the periphery (if there is no simultaneous appreciable drop of the reflectivity R); (d) prompt volumetric rise of $T_e(r)$ in the core. Interestingly, the latter model, being inverted in sign of the peripheral source (from cooling to heating), gives "symmetric" scenario for the instant cooling of the core in experiments on fast heating of the periphery (via current ramp).

III. Conclusions. (i) The results of the modelling in the frame of the present approach suggest a necessity to *append* existing numerical codes with the nonlocal transport term, an integral in space variables, of Eqs.(1),(2) type and to try it for various fast LFP waves. **(ii)** Detailed diagnostics of nonlocal inward energy flux in experiments on fast localised cooling or heating of the periphery can give significant information on the nature of the ACFET in a tokamak.

REFERENCES

[1] Luce T.C., Petty C.C., de Haas J.C.M., Phys.Rev.Lett. **68** (1992) 52.
[2] Neudatchin S.V., et al, Proc. 20th EPS Conf., Lisbon, 1993, v.17C, part 1, p.83;
Cordey J.G., et al, Plasma Phys. and Contr. Fusion, 36 Suppl. 7A (1994) A267;
Parail V.V., et al, Proc. 21th EPS Conf., Seville, 1994, v.1, p.106;
Cordey J.G., et al, Nucl. Fusion, **35** (1995) 101.
[3] Neudatchin S.V., Shirai H., Takizuka T., et al, Proc. 22nd EPS Conf., Bornemouth, 1995,v.19C, p.III-029.
[4] Gentle K.W., et al, Plasma Phys., **2** (1995) 2292; Phys. Rev. Lett. **74** (1995) 3620.
[5] Kissick M.W., et al, Nuclear Fusion, **36** (1996) 1691.
[6] De Angelis R., et al, Proc. 22nd EPS Conf., Bornemouth, 1995, v.19C, p.I-053.
[7] Rosenbluth M.N., Liu C.S., Phys. Fluids, **19** (1976) 815.
[8] Tamor S., Fusion Technol., **3** (1983) 293; Nucl. Instr. and Meth. Phys. Res., **A271** (1988) 37.
[9] Kukushkin A.B., Lisitsa V.S., Saveliev Yu.A., JETP Lett. **46** (1987) 448.
[10] Kukushkin A.B., JETP Lett. **56** (1992) 487; Proc. 14th IAEA Conf. on Plasma Phys. Contr. Fusion, Wuerzburg, 1992, v.2, p.35; Proc. 20th EPS Conf., Lisbon, 1993, p.IV-1391.
[11] Kukushkin A.B., Rep. 4th ITER Confinement Data Base and Modelling Expert Group Workshop, Moscow, 15-17 April, 1996; Bulletin of Am.Phys.Soc., Program of 38th Annual Meeting of the Division of Plasma Physics, 11-15 November 1996, Vol.41, No.7, 6F11, p.1506.

AUTOMODEL DYNAMICS OF CURRENT "COALESCENCE"
IN A THIN CURRENT LAYER

Zhdanov S.K., Vlasov V.P.[*]

Moscow Engineering Physics Institute, 115409, Moscow, Russia
* Institute of Nuclear Fusion, RRC "Kurchatov Institute",
123182, Moscow, Russia

Dynamic processes in the layers of a current are of interest in a connection with their manifestations in both laboratory and astrophysical plasmas. The dynamics of current filamentation in a thin current layer, in vacuo, is discussed in this paper. The dynamic model under zero pressure - proposed in [1] in connection with the problem of generating the cosmic rays - is used. This model also represents the splitting of a current-free thin flat substance layer into filaments under an effect of intrinsic gravitational forces.

It is shown that the dynamic set under consideration is a Hamiltonian one, and some isolated current filaments capturing a finite current are being formed in it. In that case, the collapse of filaments occurs: their thickness tends to zero; their dencity, to infinity. Automodel solutions representing the collapse of an isolated current filament in the case of "selfcompression", as well as under taking account of an effect by all other filaments into which a current layer is being splitted, have been built.

In the model [1], it is assumed that 1) a flat current layer is in vacuo; 2) currents pass along the z-axis; 3) the layer has a constant thickness (h) along the y-axis, and it is not changed in the process of the layer evolution. Then, the dynamics of long wavelength perturbations in the set - occuring along the x-axis - is represented by the equations:

$$\sigma_t^{'} + (\sigma v)_x^{'} = 0, \qquad v_t^{'} + v v_x^{'} = g_0 \hat{H} \sigma, \qquad (1)$$

where $v(t,x)$ is the velocity of a medium along the x-coordinate, $\sigma(t,x)$ is the volumetric medium density normalized to the density of a uniform layer, ρ_s; $g_0 = 2\pi h \rho_s [I/(Mc)]^2$, where I is a total current passing through the

layer, M is the mass of current layer strip oriented along the x-axis and having a unit length along the y-axis (dimensionality of M is equal mass/length). The Ampere force (divided by the density σ) is $g_o \hat{H} \sigma$. It is expressed via the Gilbert operator $\hat{H}$,

$$g_o \hat{H} \sigma = g_o \pi^{-1} [v.p. \int \sigma(y,t)(y-x)^{-1} dy]. \qquad (2)$$

Note that the splitting of a current-free flat thin substance layer under an effect of intrinsic gravitational forces is also represented by Eq.(1). In that case, $g_o = 2\pi h \rho_s G$, where G is the gravitational const. It is related with the fact that the gravitational field of straight filament is changed with distance, according to the same law as that for the magnetic field of a straight-directed current.

A perturbation in an initially-uniform current distribution turns out to be unstable with the increment $(g_o |k|)^{1/2}$, where k is the wave number. The perturbation quickly rises and results in the splitting of a layer into separate fragments. Later on, at the non-linear stage, the fragments are singled-out and their collapse starts to take place, as seen from the following precise automodel solution:

$$v = x(dL/dt)/L, \quad \sigma = (L_o/L)f(\xi), \quad \xi=x/L, \quad |x| \leqslant L, \quad (3)$$

$$L\ d^2L/dt^2 = -g_o L_o, \qquad (4)$$

where $L = L(t)$ is the filament halfwidth ($\sigma \equiv 0$, when $|x| \geqslant L$), L_o is its initial value. The function $f(\xi)$ has the form $f(\xi) = (1 - \xi^2)^{1/2}$, and the function $L(t)$ is determined by the relationship

$$t/\tau = \Phi(r), \quad r = \left(\ln(L_o/L) \right)^{1/2}, \quad \tau^{-1} = \left(2g_o/(\pi L_o) \right)^{1/2}, \quad (5)$$

where

$$\Phi(r) = (2/\pi^{1/2}) \int_0^r \exp(-x^2) dx \quad \text{is the integral of errors.}$$

By the instant of time, $t=\tau$, the singled-out fragment collapses.

A given solution, (2) – (4), is referred to an

essentially-isolated current filament. If some other current filaments are present on the right and on the left from the singled-out fragment, it is evident that they make its selfcompression hard. This effect is approximately taken into account by the following way. Let the filamentation attain a rather deep stage, and the current filaments size, L, is much less then the distances, L_0, between them: $L \ll L_0$. For a periodic set of similar current filaments an effect of all other filaments onto one - singled out - can be taken into account, having written the right-hand side of the second equation (1) in the form of two components, $g_0 \hat{H}\sigma = F_1 + F_2$, one of which $(F_1 \sim X)$ represents the current filament "selfcompression" considered above, another, (F_2) represents an effect of all other filaments. When $L \ll L_0$, F_2 can be easely found. In that case, the "correction" F_2 is proportional to X. Therefore an automodel solution of the type (3) is possible again, with the previous function $f(\xi)$. However, the function $L(t)$ - instead of (4) - is determined by an equation:

$$d^2 L/dt^2 = - g_0 \left[(L_0/L) - \varepsilon(L/L_0) \right], \quad \varepsilon = \pi^2/24 < 1, \quad (6)$$

having the integral of motion

$$u^2 + \ln(Z^2) - \varepsilon Z^2 = -\varepsilon, \quad (7)$$

where $Z = L/L_0$, $u = dZ/d\tilde{t}$, $\tilde{t} = t/t_*$, $t_* = (L_0/g_0)^{1/2}$; it is assumed that, at $t=0$ "coordinate" $Z=1$, and the "velocity", $u=0$. From (7) one can see that the correction decelerates the collapse, but it is not able to stop it.

In conclusion note that the set (1) can be written in the Hamiltonian form:

$$\delta H/\delta \sigma = - \Psi_t', \quad \delta H/\delta \Psi = \sigma_t', \quad (8)$$

where $v = \Psi_x'$, **H** is the Hamiltonian

$$\mathbf{H} = \int dx \left[\frac{\sigma(\Psi_x')^2}{2} - \frac{1}{2} g_0 \sigma[\hat{K}\sigma] \right] \quad (9)$$

and the operator $\hat{K}$ is determined by the relationship $\hat{H}\sigma \equiv \partial(\hat{K}\sigma)/\partial x$. Along with $\mathbf{H}$, the set (1) retains the "momentum" and the "number of particles": $P = \int \sigma\Psi'_x dx$, $N = \int \sigma dx$. This representation shows the presence of a collapse with its necessity. Indeed, let us make a scale transformation, retaining the momentum, P, and the number of particles, N : $x \rightarrow bx$, $\sigma \rightarrow \sigma/b$, $\Psi \rightarrow b\Psi$. Then the Hamiltonian – with a scale reduction $(b \rightarrow 0)$ – can be only reduced:

$$\mathbf{H} \rightarrow \mathbf{H} - [g_0/(2\pi)]N^2 \ln(1/b). \qquad (10)$$

It is useful to note that the Hamiltonian can be written in the form:

$$\mathbf{H} = \int dx\left[\frac{\sigma v^2}{2} + \frac{\sigma g_0}{2\pi}\left(v.p.\int \sigma(y,t) \ln|y-x| \, dy\right)\right]. \qquad (11)$$

The first term in (11) can be interpreted as a kinetic energy of a set of the currents; the second one, as their potential energy, W_p. Such a representation also allows one to easely – show the presence of the automodel filament collapse. For this purpose, let us consider a symmetric filament of the form $\sigma = (L_0/L)f(\xi)$, $\xi=(x/L)^2$, when $|x| \leqslant L$ and $\sigma = 0$, when $|x| \geqslant L$, satisfying the condition of retaining the "number of particles", $N \subset L_0$ is the filament size at the initial instant of time, t_0). Then, even not specifying the form of the function $f(\xi)$, one finds that the potential energy of the filament is reduced under its compression $(L<L_0)$, according to the law:

$$W_p(t) = W_p(t_0) - \left[[g_0/(2\pi)] \, N^2 \ln(L_0/L)\right]. \qquad (12)$$

Since the total energy of the filament is retained, its kinetic energy, as a result, is increased all the time in the process of its compression. This results in the collapse of the filament.

References. [1] Trubnikov B. A. Uspekhi Phys. Nauk. /Russia/ V.160, N.12, P.167–186, 1990.

Subcritical Excitation of Plasma Turbulence

K. Itoh*, S.-I. Itoh†, M. Yagi† and A. Fukuyama††

* National Institute for Fusion Science, Nagoya 464-01, Japan
† Research Institute for Applied Mechanics, Kyushu University, Kasuga 816, Japan
†† Faculty of Engineering, Okayama University, Okayama 700, Japan

Abstract   Nonlinear excitation of the turbulence in inhomogeneous plasmas is analyzed. The fluctuation amplitude is expressed in terms of the global pressure gradient, and shows the feature of the subcritical excitation. Critical pressure gradient at which the transition from the collisional transport to the anomalous one occurs is obtained.

1. Renormalized Equation for Dressed-Test Mode

We study the nonuniform plasma with the magnetic inhomogeneity and the magnetic shear. The system is characterized by the pressure gradient, $-p_0'$, the curvature of the magnetic field, κ, the magnetic shear, s, and by the ratio of the collisionless skin depth δ to the minor radius a [1]. The reduced set of equations for the static potential, ϕ, the parallel current, J, and the pressure, p, is employed. The dynamical equation of the fluctuation mode in the turbulent plasma has been expressed by use of the method of the dressed test mode [1]. The nonlinear interaction of the test mode with the back-ground turbulence is renormalized in a form effective diffusivities, and we have

$$\left\{ \frac{\partial}{\partial t} \begin{pmatrix} -\nabla_\perp^2 \\ (1 - \xi\nabla_\perp^{-2}) \\ 1 \end{pmatrix} + \begin{pmatrix} \bar{\mu}\nabla_\perp^4 & \nabla_\| & (\vec{b}\times\kappa)\cdot\nabla \\ \xi\nabla_\| & \xi\eta_\| - \xi\bar{\lambda}\nabla_\perp^2 & 0 \\ -\frac{dp_0}{dx}\frac{\partial}{\partial y} & 0 & -\bar{\chi}\nabla_\perp^2 \end{pmatrix} \right\} \begin{pmatrix} \phi \\ J \\ p \end{pmatrix} = 0 \quad (1)$$

with $\bar{\mu} = \mu_N + \mu_c$, $\bar{\lambda} = \lambda_N + \lambda_c$ and $\bar{\chi} = \chi_N + \chi_c$. ($\mu$, λ, χ are the viscosity, current diffusivity and thermal diffusivity; suffix c and N denote collisional one and turbulent one, respectively.) $\eta_\|$ is the resistivity, which is neglected in the following for the simplicity, and $\xi = a^2\delta^{-2}$. Length and time are normalized to a and to the poloidal Alfven time τ_{Ap}, respectively.

The stationary turbulence is studied and the limit $\partial/\partial t \to 0$ is taken. For the stationary solution, the renormalized nonlinear coefficients satisfy the relations

$$\mu_N(\mu_N + \mu_c) = \hat{\phi}^2 \quad \mu_{e\,N}(\mu_{e\,N} + \mu_{e\,c}) = P^2\hat{\phi}^2 \text{ and } \chi_N(\chi_N + \chi_c) = Q^2\hat{\phi}^2 \quad (2)$$

where the averaged fluctuation amplitude $\hat{\phi}$ is defined as $\hat{\phi}^2 = \sum_k |\phi_k|^2 (2 + 2C)^{-1}$ and ϕ_k is the back-ground fluctuations. The coefficients C, P and Q, (P and Q being related to Prandtl numbers) are close to unity.

2. Turbulence in a System with Magnetic Hill

2.1 Nonlinear Marginal Stability Condition

For the plasmas with magnetic hill, the magnetic gradient is expressed in terms of the averaged (bad) curvature of the magnetic field, Ω'. The eigenmode equation (1) reduces to

$$k_{||} \frac{1}{\bar{\lambda} k_\perp^2} k_{||} \phi + \bar{\mu} k_\perp^4 \phi - \frac{k_\theta^2 G_0}{\bar{\chi} k_\perp^2} \phi = 0 \tag{3}$$

for the stationary condition ($G_0 = \Omega' p_0'$). Equation (3) was solved in the presence of the magnetic shear, and the nonlinear marginal stability condition was derived as [2]

$$\frac{G_0^{3/2}}{s^2} \frac{(\lambda_N + \lambda_c)}{(\chi_N + \chi_c)^{1.5} (\mu_N + \mu_c)^{0.5}} = \Im_c \tag{4}$$

where s is the shear parameter and $\Im_c$ is a critical Itoh-number and is of the order of unity. Equation (4) together with Eq.(2) determines the fluctuation level and turbulent transport coefficient as a function of the equilibrium pressure gradient.

2.2 Backward Bifurcation and Subcritical Turbulence

Equation (4) describes the subcritical excitation.

We first consider the neutral condition in the vicinity of the linear boundary. The linear stability condition is expressed as $G_0 \leq G_c$, where the *linear* critical pressure gradient G_c is obtained by taking the limit of $\hat{\phi} \to 0$. Imposing $\mu_N = \lambda_N = \chi_N = 0$ in Eq.(2), we have $G_c = \Im_c^{2/3} (sa\omega_p/c)^{4/3} \chi_c \mu_c^{1/3} \chi_{ec}^{-2/3}$. By expanding Eq.(4) near $G_0 \simeq G_c$, the amplitude $\hat{\phi}$ near the marginal condition is given. Relations $\mu_c \approx \chi_c$ and $\mu_{ec} << \chi_c$ are usually satisfied. For collisional diffusion, the relation $\mu_{e,c}/\chi_c \sim \sqrt{m_e/m_i}$ holds, where m_e/m_i is the mass ratio. Under this circumstance, we have

$$\hat{\phi}^2 = -\left(3\mu_{ec}^2/2P^2\right)\left(G_0/G_c - 1\right) \tag{5}$$

near $G_0 \simeq G_c$. This result shows the backward-bifurcation: turbulence develops below the critical pressure gradient, $G_0 < G_c$.

The transition from collisional transport to turbulent transport, is predicted to occur at the critical pressure gradient

$$G_0 = G_* \cong \Re_c^{2/3}(2s)^{4/3}\left(a\omega_p/c\right)^{4/3}\chi_c^{2/3} \tag{6}$$

which is lower than the linear stability criterion G_c. The critical gradient G_* is given in experimental variables as $a/L_p^* = \left(\varepsilon^2/2\Omega\right)\!\left(s^2 g m_i/m_e\right)^{2/3}(a\nu_i/\nu_{thi})^{2/3}$, where $1/L_p = -\beta'/\beta$, g is the numerical factor introduced as $\chi_c = g\nu_i\rho_i^2$, and ν_i, ρ_i and ν_{thi} are the collision frequency, the gyro radius and the thermal velocity of ions.

2.3 Direct Nonlinear Simulation

The analytic estimation is compared to the numerical simulation. Direct nonlinear simulation of the basic set of equations was performed [3]. The two-dimensional turbulence has been calculated in a system, for which the condition $G_c \simeq 0.4$ holds.. Figure 2 compares the theoretical result of the transport coefficient and that from the numerical simulation (black points). The theoretical formula (4) well reproduces the subcritical nature of the turbulence which is obtained by the nonlinear simulation.

3. Turbulence in a System with Magnetic Well

This subcritical nature of turbulence is widely observed in plasma turbulence. The analysis is extended to the ballooning mode turbulence in systems with the magnetic well, i.e., tokamaks and stellarators. We study the high-aspect-ratio tokamak with circular cross section. The normalized pressure gradient is represented by the parameter $\alpha = -q^2 R\beta'$. Equation (1) is solved, and the nonlinear marginal stability condition is obtained. When α and s are small, the nonlinear marginal stability condition is obtained analytically as ($\hat{s} = s - \alpha$)

$$\frac{\alpha_*^{3/2}\,\overline{\lambda}}{\overline{\chi}^{3/2}\overline{\mu}^{1/2}} = (1 - 2\hat{s})\sqrt{2 + \frac{6\hat{s}^2}{1 - 2\hat{s}}}\ . \tag{7}$$

Equations (2) and (7) have nontrivial solution if α exceeds the critical value

$$\alpha \ge \alpha_* \simeq 2^{1/3}\left(a\omega_p/c\right)^{4/3}\chi_c^{2/3} \tag{8}$$

At this critical gradient, the transition from the collisional transport to turbulent one takes place. The subcritical excitations of the fluctuations are predicted to occur in the parameter region of the linear instability. Turbulent transport appears at $\alpha > \alpha_*$, although the linear ideal high-n ballooning mode was found to be stable in the low s case (i.e., the first stability region and the second stability region are connected). The critical gradient for the transition of turbulent transport, α_*, has the same dependence on χ_c and a/δ as the one for the interchange mode turbulence, G_*.

4. Summary

In summary, the nonlinear theory of the current-diffusive mode turbulence in confined plasmas was developed. A nature of the subcritical turbulence was shown from the theoretical analysis as well as by the direct nonlinear simulation. The critical pressure gradient for the transition from collisional transport to turbulent transport, $G_0 \geq G_*$ or $\alpha \geq \alpha_*$, was obtained. The generic roles of the parameters $a\omega_p/c$ and χ_c for the critical gradients, G_* and α_*, are found, while the influences of geometry (e.g., magnetic shear or magnetic well) are clarified.

References
[1]   K. Itoh, et al., *Plasma Phys. Contr. Fusion* **36** (1994) 1501.
[2]   K. Itoh, et al., *J. Phys. Soc. Jpn.* **65** (1996) 2749.
[3]   M. Yagi, et al., *Phys. Plasmas* **2** (1995) 4140.
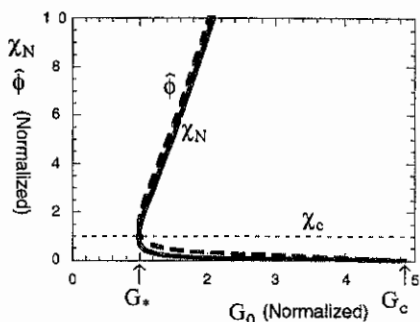
Fig.1 Pressure gradient G_0 vs. turbulent transport coefficient χ_N and turbulence level $\hat{\phi}$. Subcritical excitation is clearly demonstrated. (χ_N and $\hat{\phi}$ are normalized to χ_c, and G_0 is normalized to $\left(sa\omega_p/c\right)^{4/3}\chi_c^{2/3}$.)
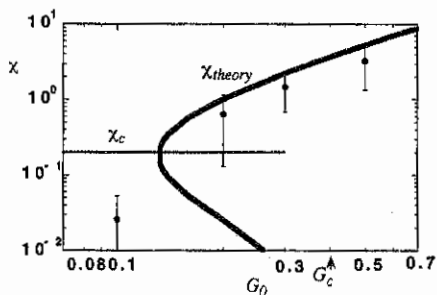
Fig.2 Result of nonlinear simulation (dots with error bar) is compared to the analytic result. Subcritical excitation is confirmed by the direct nonlinear simulation. χ is normalized to $\left(c/a\omega_p\right)^2$

SHEAR FLOW EFFECTS ON RESISTIVE
BALLOONING TURBULENCE

L. Garcia

Universidad Carlos III. 28911 Leganés, Madrid. SPAIN
B.A. Carreras and V.E. Lynch
Oak Ridge National Laboratory, Oak Ridge, USA

Resistive ballooning modes could be responsible for the turbulence and induced transport observed at the edge of present tokamaks [1]. Due to the mode structure, the geometry of the calculation is fully toroidal. The increase in computer capabilities allows now high resolution turbulence calculations. This is very important in the case of ballooning modes since the spectrum is very flat. Two main issues are addressed in this paper: 1) The validity of the mixing length approach for toroidal modes. It is especially important to identify the characteristic spatial and temporal scales in this approach, since these scales would be determinant of the induced transport. 2) The role and characterization of the Reynolds stress in toroidal geometry. Because of the intrinsic poloidal asymmetry of the ballooning modes, flows with $m \neq 0$ are generated. The effect of these flows will be analyzed.

The equations used to describe the resistive ballooning turbulence are the reduced equations in the electrostatic approximation with plasma compressibility effects included. For the nonlinear calculations, the $V_\parallel$-equation is replaced by a parallel diffusivity in the pressure equation. Viscosity and perpendicular transport are also included in the equations in order to provide the energy sink needed to get steady-state turbulence. The geometry is fully toroidal, and we use a flux coordinate system (ρ, θ, ζ) in which ρ is an equilibrium flux surface variable which behaves as a generalized minor radius, θ is a generalized poloidal angle variable, and ζ is the toroidal angle [2]. With these assumptions, the model is described by the perpendicular momentum balance equation:

$$\rho_m \frac{dU}{dt} = -\mathbf{B} \cdot \nabla\left(\frac{R^2}{\eta F^2}\mathbf{B} \cdot \nabla\Phi\right) + 2\frac{\mathbf{b} \times \boldsymbol{\kappa}}{B} \cdot \nabla p + \rho_m \mu \nabla_\perp^2 U, \tag{1}$$

and the equation of state

$$\frac{dp}{dt} + \Gamma p \nabla \cdot \mathbf{v}_\perp = D_\parallel \frac{R^2}{F}\mathbf{B} \cdot \nabla\left(\frac{R^2}{F}\mathbf{B} \cdot \nabla p\right) + D_\perp \nabla_\perp^2 p. \tag{2}$$

Here, p is the pressure, $\mathbf{v}_\perp$ is the perpendicular velocity, U is the ζ-component of the vorticity, η is the resistivity, $\boldsymbol{\kappa}$ is the magnetic field curvature, $F = RB$ is the toroidal flux function, and ρ_m is the mass density. The derivative along the magnetic field can be expressed as

$$\mathbf{B} \cdot \nabla = \frac{F}{R^2} \left(\frac{\partial}{\partial \zeta} - \frac{1}{q} \frac{\partial}{\partial \theta} \right). \tag{3}$$

The perpendicular velocity can be expressed in terms of the electrostatic potential, $\mathbf{V}_\perp = -\nabla \Phi \times \zeta / B$. Here, ζ is the unit vector in the toroidal direction. The ζ-component of the vorticity is defined as $U = \zeta \cdot \nabla \times \mathbf{v}_\perp / B$.

The parameters used in the nonlinear calculations correspond to a medium-size tokamak with circular cross section, major radius 1m, aspect ratio 4, and magnetic field 1 T. The equilibrium pressure and safety factor correspond to a flux-conserving sequence with $p(\rho) = p(0)\left(1 - \rho^2\right)^3$, and $q(\rho) = 0.9\left[1 - \left(\rho/0.6521\right)^4\right]^{1/2}$. The value of β_0 is varied from 0.01 up to 0.087. For the highest-β case, the Lundquist number $S = \tau_R / \tau_{Hp}$ is 10^5, and the viscosity for the equilibrium components is very close to the neoclassical value. Both S and μ are maintained constant in the β-scan.

The perpendicular diffusivities are chosen to stabilize all modes with the toroidal mode number $n > 35$, with no change in the growth rate for the ones with $n < 30$. With this choice, the linear spectrum peaks at n-values close to 30. The linear mode structure can be seen in Fig. 1 for the mode $n = 30$. The structure is the typical of a ballooning mode with two characteristic scales: The scale of each (m, n) Fourier component, and the scale of the envelop of the eigenfunction. The characteristic time scale is the inverse growth rate, and for the dominant modes in the high-β case is of the order of $10^{-4}\tau_R$.

The nonlinear convection terms in the poloidal momentum balance generate the nondiagonal $\rho\theta$ term of the Reynolds stress tensor. Purely growing modes lead to a poloidal asymmetric Reynolds stress. Since

$$\Phi(\rho,\theta,\zeta) = \sum_{m,n} \Phi_{m,n}(\rho) \sin(m\theta + n\zeta), \tag{4}$$

the toroidal angle average of the nondiagonal $\rho\theta$ term of the Reynolds stress tensor is:

$$\left\langle \tilde{V}^\rho \tilde{V}^\theta \right\rangle_\zeta = \frac{1}{2F^2\rho} \sum_\mu \sum_{m,n} m \Phi_{m,n} \frac{\partial \Phi_{m-\mu,n}}{\partial \rho} \sin(\mu\theta). \tag{5}$$

To study the effect of the shear flow, we have considered equilibrium flows with $m = 1$, $n = 0$. With this choice, the symmetry of purely growing modes (4) can be maintained. As radial profile of the poloidal velocity we take an hyperbolic tangent centered at the dominant poloidal component of the linear spectrum with radial width L_E. The efficiency of the shear stabilization depends on the radial width of the shear, and the mode is stabilized for a shearing rate of the order of the linear growth rate. The structure of the linear eigenfunctions is strongly modified with a reduction of the amplitude of the poloidal components in the region of high shear.

To begin the nonlinear calculations, we take a random amplitude for each Fourier component. The initial components are Gaussian functions of ρ and peak at the corresponding rational surface. The fastest growing modes dominate the initial phase of the calculation, in which the fluctuations growth at an approximately exponential rate. After this initial phase, the pressure and electrostatic potential fluctuations nonlinearly evolve to a saturated state in a time scale of 0.02 to 0.04 resistive times.

The structure of the turbulence has been analyzed by calculating correlation functions for the fluctuations at different poloidal positions. As can be seen in Fig. 2 for the high-β case, there is a significant reduction in the radial correlation length of the fluctuations from the linear phase to the nonlinear phase of the evolution. In the linear approximation, the coherence as a function of θ can be estimated analytically as $\gamma(\theta) = \cos\left(\Delta_\rho n q' \theta\right)$, where Δ_ρ is the radial separation. This yields a radial correlation length proportional to $1/\theta$. In the nonlinear phase, the poloidal dependence of the radial correlation length weakens considerably. These results imply a reduction of the characteristic scale of the fluctuations in the nonlinear phase.

For the high-β case, the spectrum at saturation is very flat. However, for low values of β ($\beta_0 = 0.01, 0.021$), the spectrum is dominated by a single mode. The coherence is then similar to that of a linear eigenfunction, and the characteristic scale of the fluctuations is given by the linear estimate.

The saturation level $\tilde{p}/p$ is of the order of the mixing length estimate Δ/L_p. Due to the flattening of the average pressure profile, the pressure scale length L_p is almost constant in the region where the fluctuations are located. To check the scaling with L_p, we maintain the average pressure profile frozen during the evolution. The comparison of the r.m.s. value of the pressure fluctuations normalized to the local equilibrium pressure and the mixing length estimate is shown in Fig. 3. We have taken for Δ the mean value of the radial correlation length at the poloidal angles $\theta = 0$ and $\theta = \pi$. As can be seen, the agreement is very good.

The nonlinear evolution with $m = 1$ shear flow shows a reduction of turbulence and induced transport. Comparing with the case without equilibrium flow, the radial correlation length decreases slightly, and the pressure profile steepens since the perturbation of the average pressure is negligible. The reduction of the induced transport can be seen in Fig. 4, where the diffusion coefficient for two different shear widths is compared with the diffusion coefficient in absence of an external flow. For the two cases shown, the linear growth rate is roughly one-half of the linear growth rate without flow.

References

[1] B.A. Carreras et al., Phys. Rev. Lett. **50**, 503 (1983)

[2] V.E. Lynch et al., Comp. Phys. Comm. **24**, 465 (1981)
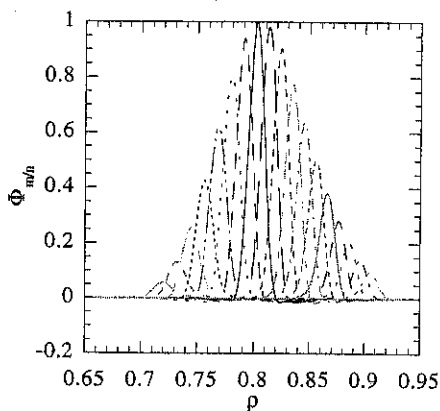
Fig. 1. Poloidal components of the linear eigenfunction with $n = 30$. The dominant component is $m = 49$.
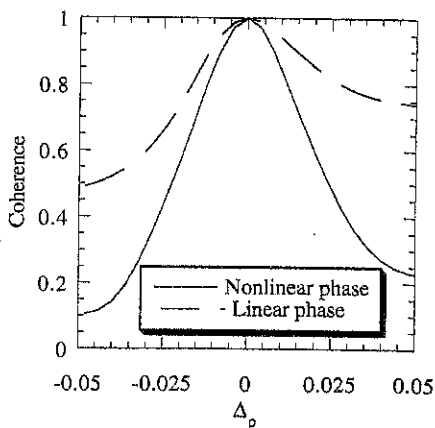
Fig. 2. Coherence vs radial separation at $\theta = 0$ in the linear and nonlinear phase of the evolution
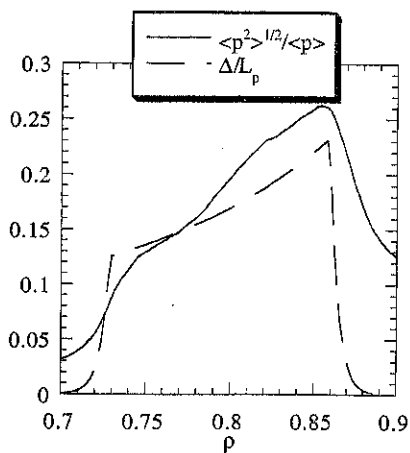
Fig. 3. Comparison of the pressure fluctuations r.m.s. value with the mixing length estimate for the $\beta_0 = 0.087$ case.
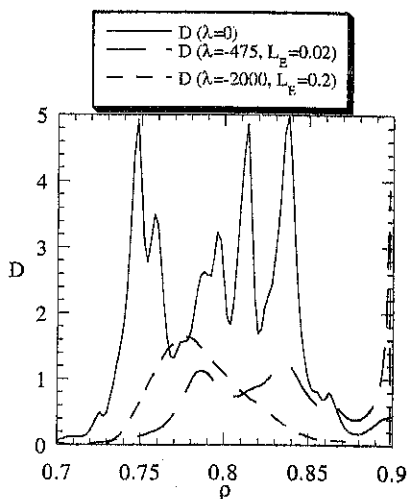
Fig. 4. Diffusion coefficient for two different shear flow profiles and without shear flow.

Energy Limits on Runaway Electrons in Tokamak Plasmas

R. Martin-Solis, J.D. Alvarez, R. Sanchez, B. Esposito [1]

Universidad Carlos III de Madrid, C/Butarque 15, Leganes, 28911-Madrid, Spain.
[1] Associazione Euratom-ENEA CRE, 00044-Frascati, Italy.

Abstract The dynamics of runaway electrons in tokamak plasmas is analysed using a test particle description that includes acceleration in the toroidal electric field, collisions with the plasma particles and deceleration due to synchrotron radiation losses. The trajectories of the test electrons in momentum-space show a stable equilibrium point which sets a limit on the energy that the runaway electrons can reach. Analytical expressions are given for this energy limit as function of the toroidal electric field and plasma parameters. The test electron equations are extended to include the effects of a resonance between gyromotion and magnetic field ripple of the tokamak, which can lead to enhanced radiation losses and therefore to lower the maximum energy that the runaway electrons can reach.

1. Test Electron Relaxation Equations The dynamics of relativistic runaway electrons in a tokamak plasma is described using the test particle equations:

$$\frac{dp_\parallel}{dt} = eE_\parallel - F_S\frac{p_\parallel}{p} - \frac{n_e e^4 \ln\Lambda m_e}{4\pi\varepsilon_0^2}\gamma(Z_{eff} + 1 + \gamma)\frac{p_\parallel}{p^3} \tag{1}$$

$$\frac{dp}{dt} = eE_\parallel\frac{p_\parallel}{p} - F_S - \frac{n_e e^4 \ln\Lambda m_e}{4\pi\varepsilon_0^2}\frac{\gamma^2}{p^2} \tag{2}$$

where $p_\parallel$ is the electron momentum parallel to the magnetic field, and p the total electron momentum; $E_\parallel$ is the toroidal electric field and γ the relativistic gamma factor. The first term in the above equations is the acceleration due the toroidal electric field, and the second term includes the effects of the synchrotron radiation with decelerating force:

$$F_S = \frac{2}{3}r_e m_e c^2 \left(\frac{v}{c}\right)^3 \gamma^4 \left\langle\frac{1}{R^2}\right\rangle, \tag{3}$$

(r_e is the classical electron radius) with the radius of curvature averaged over one gyrorotation [1],

$$\left\langle\frac{1}{R^2}\right\rangle = \frac{1}{R_0^2}\left[\cos^6\theta + \cos^2\theta\sin^4\theta + \cos^4\theta\sin^2\theta\left(\frac{5}{2} + \frac{r_g^2}{8R_0^2}\right)\right] + \frac{1}{r_g^2}\sin^4\theta, \tag{4}$$

(R_0 is the plasma major radius, θ the pitch angle, and r_g the gyroradius of the runaways); the third term in equations (1) and (2) includes the effect of the collisions with the plasma particles [2]. From (1) and (2) we obtain,

$$p_\perp\frac{dp_\perp}{dt} = -F_S\frac{p_\perp^2}{p} + \frac{n_e e^4 \ln\Lambda m_e}{4\pi\varepsilon_0^2 p}\left(\gamma(Z_{eff} + 1 + \gamma)\frac{p_\parallel^2}{p^2} - \gamma^2\right) \tag{5}$$

The system of equations (1) and (5) have in $(p_\parallel, p_\perp^2)$ space two singular points (a saddle point, P_1, and a stable focus, P_2) as it is shown in the phase-space plot of Fig.1. The

limiting particle trajectories passing through P_1 and P_2 are the separatrices S_r and S_a. The region outside S_r constitutes the runaway region: all the electrons initially in this region will eventually move towards the stable focus P_2, in which the collisional and synchrotron radiation losses balance the energy gain in the electric field. Since an electron outside S_r gain energy, while electrons inside S_r lose it, energy is conserved on trajectories near S_r [3], and therefore, the critical energy for runaway generation can be estimated as that of the saddle point P_1.

Thus, P_1 and P_2 will give, respectively, the critical energy E_c for runaway generation and the energy limit E_l for the runaway electrons. These energies, for a given electric field, can be obtained from Eqs. (1) - (5) setting $\dot{p}_\parallel = 0$, $\dot{p}_\perp = 0$ (or $\dot{p} = 0$). From $\dot{p} = 0$, we get,

$$D = \frac{\gamma^2}{\cos\theta(\gamma^2 - 1)}\left\{1 + F_{gy}\frac{(\gamma^2 - 1)^{3/2}}{\gamma}\sin^2\theta + F_{gc}\frac{(\gamma^2 - 1)^{5/2}}{\gamma}\right\}, \qquad (6)$$

with $\cos\theta$, from $\dot{p}_\perp = 0$, given by

$$\cos^2\theta = 1 + \frac{F_{gc}(\gamma^2 - 1)}{2F_{gy}} + \frac{\alpha + \gamma}{2F_{gy}(\gamma^2 - 1)^{3/2}}\left\{1 - \left[\frac{4\alpha F_{gy}(\gamma^2 - 1)^{3/2}}{(\alpha + \gamma)^2} + \left(1 + \frac{F_{gc}(\gamma^2 - 1)^{5/2}}{\alpha + \gamma}\right)^2\right]^{1/2}\right\} \qquad (7)$$

In these relations, γ is the relativistic gamma factor for the singular points; $D = E_\parallel/E_R$ is a normalized electric field, where $E_R = n_e e^3 \ln\Lambda/4\pi\varepsilon_0^2 m_e c^2$; $\alpha = 1 + Z_{eff}$, and F_{gc}, F_{gy} describe the two contributions to the radiation losses (the electron motion on toroidal paths and the electron gyromotion, respectively) given by: $F_{gc} = F_{gy}(m_e c/eB_0 R_0)^2$, $F_{gy} = 2\varepsilon_0 B_0^2/3n_e \ln\Lambda m_e$ (B_0 is the toroidal magnetic field).

Fig.2 shows, for given plasma parameters, the relation (6) between D and the energy of the singular points. For each value of D, there are two values of the energy, corresponding to the singular points P_1 and P_2: branch I in Fig.2 gives the critical energy E_c for runaway generation (P_1) while branch II gives the runaway energy limit E_l (P_2). When D decreases, E_c increases and E_l decreases until both of them coalesce for a given value of D (the minimum of D vs. energy) which sets the minimum electric field for runaway generation, below which no electrons run away.

In Fig.3, E_l is shown as function of D together with its estimated values in the two following cases:

(i) the radiation losses are assumed to be dominated by the electron gyromotion (the second term contributing to the radius of curvature in (4)); in this case, E_l can be obtained from

$$E_l = (\gamma_{gy} - 1)m_e c^2 \quad \text{with} \quad \gamma_{gy} = \frac{D(D-1)}{2\alpha F_{gy}}\left\{1 + \left[1 - \frac{2\alpha^2 F_{gy}}{D^3(D-1)^2}\right]^{1/2}\right\} \qquad (8)$$

(ii) the radiation losses are assumed to be dominated by the electron motion on toroidal paths ($\langle 1/R^2\rangle \sim 1/R_0^2$), and E_l is given by

$$E_l = (\gamma_t - 1)m_e c^2 \quad \text{with} \quad \gamma_t = \left[\frac{D-1}{F_{gc}}\right]^{1/4} \qquad (9)$$

For low values of D, the pitch angle scattering due to collisions is effective enough to let E_l be dominated by the contribution due to the electron gyromotion and obtained from (8); for high electric fields, the effects of the electron gyromotion are negligible and E_l can be calculated using (9).

2. Ripple Resonance An additional barrier to the increase in the runaway energy can appear due to a resonance between the electron gyromotion and the harmonics of the toroidal field ripple [4]. The resonant interaction between the electron gyromotion and the nth toroidal harmonic takes place at a parallel momentum $p_{\|n} = eB_0R_0/nN_c$, where N_c is the number of toroidal field coils. The dynamics of the interaction between the nth harmonic of the magnetic field ripple and the runaway electron motion has been included in the test relaxation equations given before by taking into account that:

(i) a pitch angle scattering process takes place at the resonance that, following [1], can be described by a momentum diffusion coefficient:

$$D_{ripple} = \frac{d<p_\perp^2>}{dt} = \frac{\pi}{32} \frac{eB_0}{\gamma m_e} \left(\frac{\delta B_n}{B_0}\right)^2 \frac{p_{\|n}^3}{\Delta p_\|}, \quad \text{if } |p_\| - p_{\|n}| < \Delta p_\| \quad (10)$$

where δB_n is the amplitude of the nth harmonic, and $\Delta p_\| = (\frac{\delta B_n}{B_0} p_\| p_\perp)^{1/2}$ is the resonance width.

(ii) the magnetic field does not change the electron energy, so that the energy equation (2) keeps the same form.

As the interaction with the ripple resonance does not change the electron energy, the runaway energy limit is still given by (6) (equation obtained from (2) setting $\dot{p} = 0$), but with a pitch angle $\cos\theta = p_{\|n}/p$. In Fig.4, this energy limit is shown as a function of D for a $n = 2$ toroidal harmonic together with the energy limit calculated without including the ripple resonance. In the same figure is also indicated the range of electric field values (D_{low}, D_{up}) for which the ripple interaction becomes effective:

• for $D < D_{low}$, the runaway electrons reach the equilibrium energy before there is any interaction with the ripple harmonic; thus, as shown in Fig.4, D_{low} is given approximately by the intersection of the two energy limit curves (with and without ripple). Fig.5 (a) shows D_{low} calculated for different values of the toroidal harmonic number n and for the same plasma parameters that in Fig.4.

• D_{up} is the minimum electric field to overcome the ripple harmonic; for $D > D_{up}$, the runaway electron crosses the ripple resonance $(dp_\|/dt > 0)$ before reaching the equilibrium energy; Fig.5 (b) shows D_{up} as function of $\delta B_n/B_0$ for $n = 2$ and plasma parameters as in Fig.4.

References

[1] B.Kurzan, K.-H.Steuer, and G.Fussmann, Phys. Rev. Lett. **75**, 4626 (1995).

[2] D.Mosher, Phys. Fluids **18**, 846 (1975).

[3] V.Fuchs, R.A.Cairns, and C.N.Lashmore-Davies, Phys. Fluids **29**, 2931 (1986).

[4] L.Laurent, J.M.Rax, Europhys.Lett. **11**, 219 (1990).
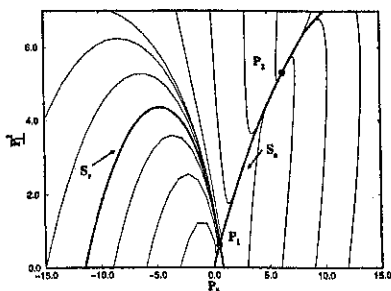
Fig.1: Phase-space plot of Eqs.(1) and (5); $p_\parallel$ and $p_\perp$ are normalized to $m_e c$. Plasma parameters: $E_\parallel \simeq 0.02\,V/m$, $B_0 = 3\,T$, $R_0 = 3\,m$, $n_e = 0.5 \times 10^{19}\,m^{-3}$, $T_e = 2\,keV$, $Z_{eff} = 3$.
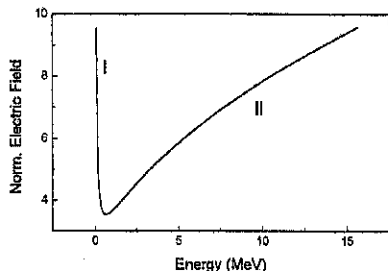
Fig.2: Normalized electric field vs. energy of the singular points: branch I gives the critical energy for runaway generation; branch II gives the runaway energy limit. Plasma parameters are the same that those in Fig.1 ($E_\parallel \simeq 0.02\,V/m$ in Fig.1 corresponds to $D \simeq 4.4$).
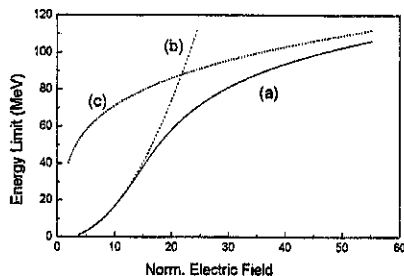
Fig.3: Runaway energy limit vs. normalized electric field (trace (a)) for the same plasma parameters that Figs.1 and 2. The energy limits calculated assuming that the radiation losses are dominated by the electron gyromotion (trace (b)), and by the motion on toroidal paths (trace (c)) are also shown.
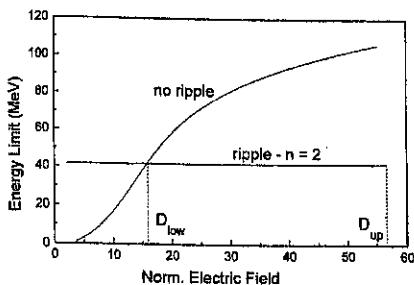
Fig.4: Runaway energy limit for a $n = 2$ ripple resonance ($\delta B_n/B_0 = 10^{-6}$) and plasma parameters as in previous figures. The energy limit calculated without including the ripple resonance is also shown. The range of normalized electric field values (D_{low}, D_{up}) for which the ripple interaction becomes effective is indicated.
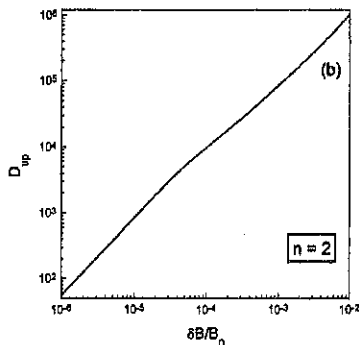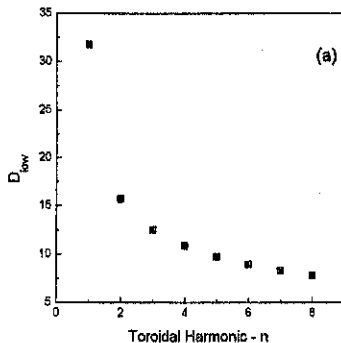
Fig.5: (a) Lower normalized electric field for effective ripple interaction vs. toroidal harmonic number; (b) Minimum normalized electric field for crossing a $n = 2$ ripple resonance as function of $\delta B_n/B_0$.

Non-Linear Saturation of Ion Temperature Gradient Modes

J.D.Alvarez and L.Garcia

Universidad CARLOS III, Madrid, SPAIN

1. Introduction

Ion temperature gradient (ITG) turbulence, also referred as η_i-mode, has been proposed as one of the dominant mechanisms determining the transport properties in the core of tokamak plasmas. In this work we intend to study the saturated ITG turbulence using a non-linear fluid description of the plasma, where compressibility and fluid viscosities are retained. As a previous step for this analysis, both an analytical and numerical study of the linear fluid equations has been carried out. The influence of different plasma parameters on the growth rate and frequency of linear modes has been analyzed. Single helicity non-linear calculations have been done and preliminary saturation levels obtained. The dominant saturation mechanism is investigated.

2. Basic model

The starting set of equations describing the η_i-mode behavior are obtained from Braginskii fluid equations assuming adiabatic electrons :

$$\frac{\partial}{\partial t}(\nabla_\perp{}^2\phi - \frac{\gamma\omega}{T_{eq}}(\phi - \phi_{00})) = \omega\nabla_\|\mathbf{v_{i\|}} + \omega\frac{nI_{eq}}{n_{eq}}\nabla_\theta\phi - \frac{1}{\gamma}\frac{(n_{eq}T_{eq})I}{n_{eq}}\nabla_\theta U - (\mathbf{z}\times\nabla\phi)\cdot\nabla_\perp{}^2\phi$$

$$\frac{\partial}{\partial t}\mathbf{v_{i\|}} = -\omega\epsilon^2(\nabla_\|\phi_\| - \frac{1}{\gamma n_{eq}}\nabla_\|P_\|) - (\mathbf{z}\times\nabla\phi)\cdot\mathbf{v_{i\|}}$$

$$\frac{\partial}{\partial t}P_i = (n_{eq}T_{eq})I\nabla_\theta\phi - \Gamma n_{eq}T_{eq}\nabla_\|\mathbf{v_{i\|}} - (\mathbf{z}\times\nabla\phi)\cdot P_i$$

We consider a cylinder with minor radius a and length $L_0 = 2\pi R_0$, and that the electron and ion temperatures are the same. We have used for the adimensionalisation $n_{eq}(0)$, $T_{eq}(0)$, τ_r, a, R_0, density and temperature at r=0, resistive time, minor and major radius respectively. The parameters which appear in these equations are: $\gamma = \frac{eB_0a^2}{T(0)\tau_r}$, $w = w_{ci}\tau_r$ and $\epsilon = \frac{a}{R_0}$

The term ϕ_{00} that appears in the ϕ-equation comes from using adiabatic electrons, $n^e = n_0\frac{|e|}{T_e}(\phi - <\phi>)$ This term reflects the fact that $n^e{}_{00}$, i.e., $<ne>$ should be zero. It plays an important role in the non linear calculation.

2. Linear analysis

As a first step, we introduce as possible solutions, functions of the form

$$\hat{f}(r,\theta,\zeta;t) = \hat{f}(r)e^{i\Omega t}e^{i(m\theta+n\zeta)}$$
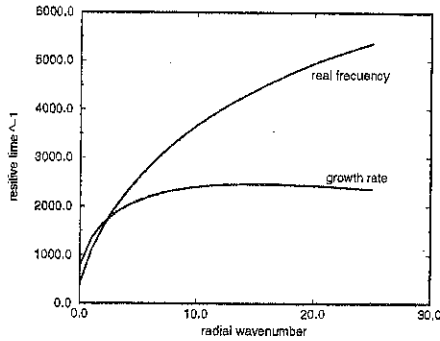
Figure 1: Analytical solution of the eigenvalue equation. We represent $|\Omega_{im}|$ and $|\Omega_{re}|$

and assuming that the linear modes are radially localized, we can use a slab approximation around a singular surface $q(r_s) = \frac{m}{n}$, obtaining the associated potential equation for the linear autofunctions (with $\Gamma = 0$ and in the range $k_\theta{}^2 = (\frac{m}{r_s})^2 \ll \frac{\omega\gamma}{T} \approx 10^5$)

$$\phi'' + \left(\frac{1-\Omega}{\Omega+(1+\eta)} + \frac{\hat{L}^2}{\Omega^2}X^2\right)\phi = 0$$

where $\Omega \mapsto \Omega \frac{1}{\gamma}\frac{n'}{n}Tk_\theta$, $X \mapsto (r-r_s)\sqrt{\frac{T}{\gamma\omega}}$, $\hat{L} = \epsilon\frac{L_n}{L_q}$ and $\eta = \epsilon\frac{L_n}{L_T}$. This eigenvalue problem admits as solutions Ω verifying

$$\frac{1-\Omega}{\Omega+(1+\eta)} = \pm i(2n+1)\hat{L} = i\hat{L}_n$$

or

$$\Omega^2 + (i\hat{L}-1)\Omega + i\hat{L}_n(1+\eta) = 0$$

where n is the radial wavenumber (the order of the Hermite polynomial associated to the solution). Therefore, all the linear properties of these modes depend only on η, and $\hat{L}_n$. Fixing $\eta(r_s)$, the dominant linear mode is obtained:

$$\frac{\partial}{\partial\hat{L}_n}\hat{\Omega}_{im}(\hat{L}_n, \eta) = 0$$

and their associated radial wavenumber $(n \geq 0)$

$$L(\hat{r}_s)(2n+1) = \hat{L}_n^{max}$$

Both scale linearly with η.

As shown in figure[1], we can have a radial number interval in which $|\Omega_{im}| < |\Omega_{re}|$, where the potential-well structure disappears and turns into a potential hill. Hence, the linear autofunction, could be an outgoing wave, that is not localized.
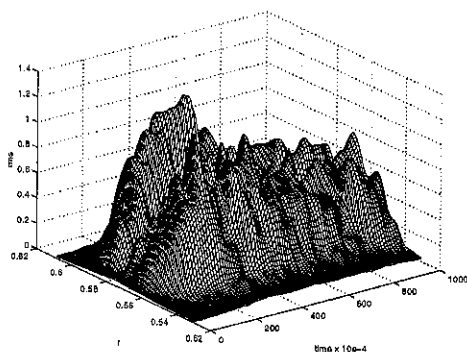
Figure 2: Radial-rms ϕ.

This effect disappears when we introduce compressibility ($\Gamma \neq 0$); the potential structure is now different flattens when we move further away from the singular surface (r_s), and suppresses those eigenmodes which do not stay at r_s. The introduction of compressibility has another effect on the linear behavior, as stabilizing term, decreasing the growth rate and the radial index of the most unstable eigenfuction.

3. Non linear calculation

In this section, we present some, preliminar, results about the numerical solution of η_h-mode equations, using a single helicity approach, and retaining the non linear terms. Note that the main non-linear term is associated with electric potential convection, as has been numerically tested, since retaining the ion parallel velocity convection does not change remarkably the saturation properties.

In this non linear calculation the compressiblity term ($\Gamma = 2$) has been retained. Thus we expect that the modes do not move from the singular surface. It must also be retained to account for the energy pressure and parallel velocity fluctuations.

Numerical viscosity is introduced to guarantee the existence of a stable, high-m dissipation range, which serves as an energy sink. The numerical calculations have been performed using typical equilibrium profiles of ion density and $q(r)$, withan equilibrium radially constant, $\eta = 4$. Our calculations have been done around $q(r_s) = \frac{3}{2}$, in a range $3 \leq m \leq 90$ (figure[4]).

As shown in figure[2], where we have represented the radial-rms of ϕ_{mn}, after a brief exponential increase, the level of turbulence is saturated. The compresibility does not permit that modes move from the singular surface, and the radial wavenumber is not zero. Therefore, the fluctuations have a valley in $r = r_s$.

We have also observed a flattening of the equilibrium pressure profile. The change $\eta(r)$ profile can be the main physical mecanism for the saturation. To test it, we have mantained
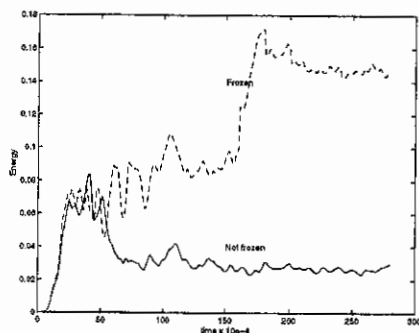
Figure 3: Different saturation levels between frozen and not frozen $\hat{P}_{00}$.
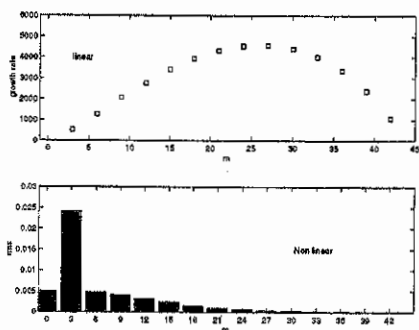
Figure 4: Linear and non linear spectrum with viscosity. In the non linear spectrum we represent $\int dr\phi_{mn}{}^2$.

$\hat{P}_{00} = 0$, obtaining higher fluctuation levels twice that in the previus case (figure[3]).

As shown in figure[4], the spectra are quite different in the linear and non linear cases. In the non linear case, the most unstable mode is the one with the lowest m. We have also done the calculation without substracting the ϕ_{00} term in the n^e expresion for the adiabatic electron resulting that the lowest m-mode is not the most unstable.

References

[1] G.S. Lee and Diamond, Physic Fluids **29**, 3291, (1985)

[2] Satoshi Hamaguchi and Wendell Horton, Physic Fluids B **2**, 3040, (1990)

Gyrokinetic Particle Simulation of Small-Scale Magnetic Islands in High Temperature Tokamak Plasmas

R.D. Sydora

Department of Physics and Astronomy
University of California, Los Angeles
Los Angeles, California, USA 90024-1547

1. Introduction

Small-scale drift magnetic islands have been advanced as a possible candidate for anomalous electron thermal transport in tokamak plasmas[1,2]. Anomalous transport from these islands has been investigated theoretically in the regimes where the islands interact radially[3] or remain isolated from each other[4,5]. However, a rigorous analytical analysis for the nonlinear evolution, including the self-consistent spectrum of fluctuations is a difficult problem, particularly in the high temperature regime where Landau resonance and finite gyroradius effects are important. Recent simulations using two-fluid equations have shown that it is possible to obtain self-sustaining islands under certain conditions[6]. The growth and nonlinear formation of the magnetic island structure is presented here using a nonlinear gyrokinetic particle-in-cell simulation model. We consider the regime where the islands remain isolated from each other and collisions are very weak. The island widths are considered to be smaller than the ion gyroradius.

2. Simulation Model

As a first step we consider magnetic islands in slab geometry and the equilibrium magnetic field is given by $\vec{B} = B_o\hat{z} + \nabla A_z \times \hat{z}$ where $A_z = B_o(x - x_o)^2/2L_s$ and x_o is the position of the rational surface. The equilibrium electron temperature and density profiles are taken to be linear.

The basic equations of the particle simulation model are based on the gyrokinetic Vlasov-Poisson-Ampere system[7]. The model is collisionless and electron-ion collisions corresponding to the Lorentz collision operator, for example, are easily incorporated by performing a pitch angle-scattering of the electron parallel and perpendicular velocities. The ions dynamics are evolved according to the gyrokinetic equation and the electron dynamics is described by the drift-kinetic equation. The canonical momentum formulation is used for computation of the self-consistent magnetic field pertubation.

The equation for the gyrophase-averaged distribution in a collisionless plasma can be put in a form that conserves phase space density along the characteristics. The equations for the characteristics, for each particle j, are

$$\frac{d\vec{R}_j}{dt} = v_{z_j}\hat{b} - \frac{c}{B}\left(\frac{\partial \bar{\Psi}}{\partial \bar{R}} \times \hat{b}\right)_j \tag{1a}$$

$$\frac{dp_{z_j}}{dt} = -\hat{b} \cdot [\frac{q}{m}\frac{\partial \bar{\Psi}}{\partial \vec{R}}]_j \qquad (1b)$$

where $\bar{\Psi} \equiv \bar{\phi} - v_z \bar{A}_z$ and $\bar{\phi}(\vec{R}) \equiv < \int \phi(\vec{r})\delta(\vec{r} - \vec{R} - \vec{\rho})dr >_\varphi$ and $<>_\varphi \equiv \oint d\varphi/2\pi$. The gyroradius is denoted by ρ, φ is the gyrophase angle, and $\delta()$ denotes the delta function. Also, $\vec{R} = \vec{r} - \vec{\rho} = \vec{r} + \vec{v}_\perp \times \hat{b}/\Omega$ with $\hat{b} = \vec{B}/B$, and $\Omega = qB/mc$. The Klimontovich microdensity, $F(\vec{R}, \mu, p_z, t) = \Sigma_i \delta(\vec{R} - \vec{R}_i)\delta(p_z - p_{z_i})\delta(\mu - \mu_i)$, where $\mu = v_\perp^2/2B$ and $p_z = v_z + \frac{q}{m}A_z$, is used to determine the gyrophase-independent distribution function and for the computation of the charge and current densities at each time step.

The self-consistent determination of the plasma evolution requires the electrostatic potential be determined from the macroscopic charge density accumulated from the charged particles. The Poisson relation for the low frequency gyrokinetic system in the particle coordinates is

$$\frac{\tau}{\lambda_D^2}(\phi - \bar{\phi}) = 4\pi \mid e \mid (\bar{n}_i - n_e) \qquad (2)$$

where $\tau = T_e/T_i$, $\lambda_D^2 = T_e/4\pi n_o e^2$, $\bar{\phi}(\vec{r}) = < \int \bar{\phi}(\vec{R})F_M\delta(\vec{R} - \vec{r} + \vec{\rho})dRd\mu dv_\parallel >_\varphi$ where F_M is assumed a Maxwellian in $v_\perp$ with weak spatial variation. The ion charge density is obtained from $\bar{n}(\vec{r}) = < \int F(R, \mu, v_\parallel)\delta(\vec{R} - \vec{r} + \vec{\rho})dRd\mu dv_\parallel >_\varphi$ where F is the discrete gyrocenter particle distribution. The self-consistent magnetic field perturbation is computed from Ampere's law and the vector potential in the canonical momentum formulation is obtained from[7]

$$(\nabla_\perp^2 - \frac{\omega_{pe}^2}{c^2})A_z = 4\pi \mid e \mid \Sigma_{e,i}[\Sigma_j p_{z_j}\delta(\vec{R} - \vec{R}_j) + \frac{\omega_p^2}{c^2}A_z(\frac{\Sigma_j(\vec{R} - \vec{R}_j)}{n_o} - 1)] \qquad (3)$$

3. Theoretical Results

We consider the low collisionality regime with a single mode rational surface with tearing mode parameter $\Delta' < 0$. An extension of the analysis by Drake and Lee[8] has show that, in this regime, saturated islands are possible for η_e sufficiently large (ratio of electron temperature gradient to density gradient)[4]. The characteristic size of the islands is on the order of the electron collisionless skin depth and the rotation frequency is on the order of $\omega \sim \omega_{*e}(1 + \eta_e/2)$. For very thin islands the Landau resonance, $\omega = k_\parallel v_\parallel$, is typically outside the island. The regime where the resonance is inside the island has been treated recently[5].

4. Simulation Results

In this section we present nonlinear computational results based on Eqs. 1-3 for the collisionless regime. The base parameters used for the simulations are as follows: $L_s/L_T = 30, L_x = 10c/\omega_{pe}, \rho_i = 2c/\omega_{pe}, T_e/T_i = 1, m_i/m_e = 1837, \omega_{ce}/\omega_{pe} = 1$, and $\omega_*/\omega_{ci} = 0.015m$. The number of particles used was 10^5 for each species and this corresponds to approximately 100 particles/cell. The value of η_e varied between 1 and ∞ and we present the results from the latter case.

Fig. 1a illustrates the time history of the various energies. A nearly exponential growth is observed for a very short time in the magnetic energy and then becomes nearly linear in time, which is characteristic of the Rutherford-type phase. Associated with the decrease in magnetic energy is an increase in the electron kinetic energy. There is also a slight increase in the electrostatic energy. Total energy is well conserved over the course of the simulations. Fig. 1b shows the contours of the vector potential, which corresponds to the magnetic surfaces(in 2D), and the appearance of a magnetic island is observed with a characteristic width of appromiately the collisionless skin depth. Fig. 1c reveals a flattening of the distribution function in the vicinity of the lowest energy electrons and this occurs due to the fact that the Landau resonance regions are in the vicinity of the island. Fig. 1e also indicates that the electron temperature is flattening over the island width as well. Finally, the rotation frequency of the island is determined from the power spectrum of the time series of the electrostatic potential data. The spectral peak is observed to maximize at the value corresponding to one-half the diamagnetic drift frequency using the temperature gradient value. Other peaks at lower amplitude are also observed and may correspond to local radial variations of the thermal relaxation region. More detailed studies are underway with extensive parameter variations and the addition of collisions.

5. Summary

In summary, we have presented nonlinear simulation results on the evolution of small-scale magnetic pertubations in the presence of diamagnetic drifts and negative tearing mode stability parameter, Δ'. The spontaneous formation of magnetic islands with characteristic size of the collisionless skin depth is found. In the weakly collisionless regime, flattening of the parallel electron distribution in the vicinity of low energy electron is observed as well as the electron temperature profile in the vicinity of the electron resonance region. Work is in progress to investigate the nonlinear behavior in the presence of electron-ion collisions as well as the 3D case with radial mode interactions.

References
[1] A. Samain, *Plasma Phys. Controlled Fusion* **26**, 731 (1984).
[2] B.B. Kadomtsev, *Nucl. Fusion* **31**, 1301 (1991).
[3] P.H. Rebut and M. Hugon, *Plasma Phys. Controlled Fusion* **33**, 1085 (1991).
[4] A.I. Smolyakov and A. Hirose, *Phys. Fluids B5*, 663 (1993).
[5] J.W. Connor and H.R. Wilson, *Phys. Plasmas* **2**, 4575 (1995).
[6] J.H. Chatenet, J.F. Luciani, and X. Garbet, *Phys. Plasmas* **3**, 4628 (1996).
[7] T.S. Hahm, W.W. Lee, and A. Brizard, *Phys. Fluids* **31**, 1940 (1988).
[8] J.F. Drake and Y.C. Lee, *Phys. Rev. Lett.* **39**, 453 (1977).
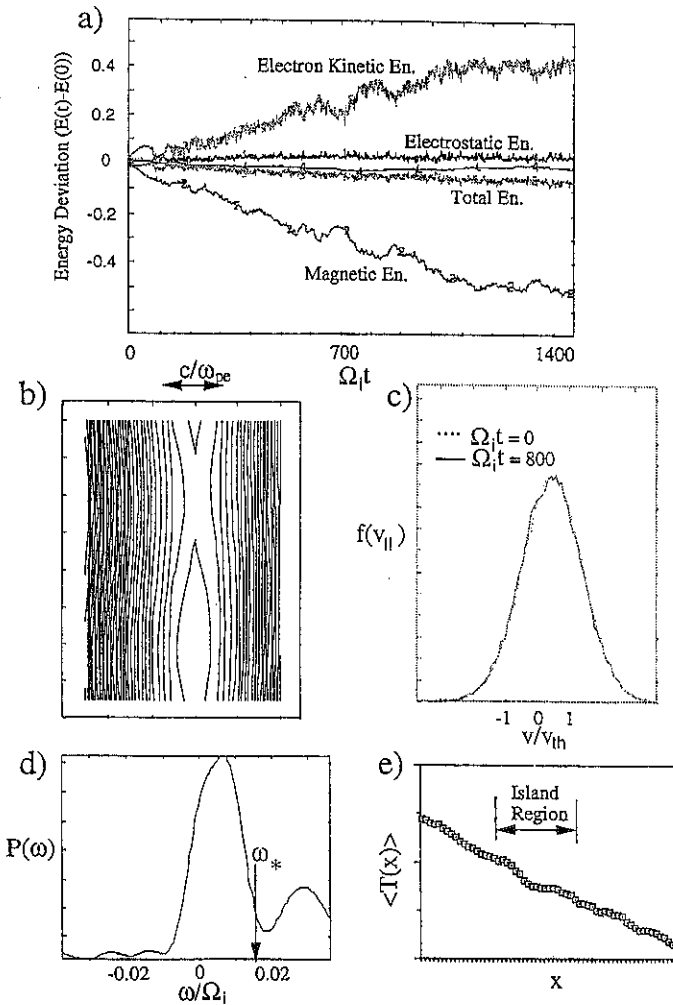
Fig.1: a) Time evolution of the electron kinetic, electrostatic and magnetic energies, b) contours of the vector poential, Az, at saturation, c) electron parallel velocity distribution taken initially and at saturation, d) power spectra of the electrostatic fluctuation corresponding to the unstable wavelength, ky, and e) electron temperature profile averaged over the y-direction.

LARGE TEMPERATURE GRADIENT TOROIDAL η_i MODES IN FLUID AND KINETIC DESCRIPTIONS

A. Jarmén

Institute for Electromagnetic Field Theory and Plasma Physics
EURATOM-NFR *Association, Chalmers University of Technology*
S-412 96 Göteborg, Sweden

Introduction

It is well known that the η_i mode [η_i=d(lnT$_i$)/d(lnn$_i$)=L$_n$/L$_T$, L$_n$=density scale length, L$_T$=temperature scale length] is stabilized at low temperature gradients [1-3]. It has also been noted using a fluid description that the η_i mode may be stabilized at larger temperature gradients [2]. This stabilization has recently been reported using a basic toroidal gyrokinetic ion model [4] assuming isotropic η_i and no collisions. The η_i modes are assumed to be an important driving source for drift wave turbulence causing anomalous particle and heat transport [5]. One may expect that an upper η_i stability threshold can give rise to enhanced confinement regimes. Equilibria with large η_i can occur e.g. in regions with negative shear in combination with high heating power [6].

In the present paper we study the toroidal η_i mode at large η_i values, $\eta_i\gg1$, comparing the results of a gyrokinetic model with those of a reactive two-fluid model [2] based on the Braginskii equations. The validity of the fluid model is limited to the regime $b_o=k_\perp^2\rho_i^2\ll1$ (k$_\perp$ =perpendicular wave number, $\rho_i=\sqrt{T_i/m_i}/\omega_{ci}$= ion Larmor radius). In this regime the fluid model is found to reproduce the results of the gyrokinetic model with a good accuracy whereas for larger b_o the fluid model gives a lower stability threshold than the gyrokinetic model.

Two-fluid model

We assume a perturbation of the form exp(jk$_\parallel$x$_\parallel$+jk$_\perp$x$_\perp$-jωt) where k$_\parallel$ and k$_\perp$ are along and perpendicular to the background magnetic field, respectively and an electrostatic electric field $\mathbf{E} = -\nabla\phi$ where ϕ is the electrostatic potential. For the ions we use a toroidal fluid model [2] based on the Braginskii equations. The model includes compressibility effects due to the

magnetic field curvature, finite Larmor radius (FLR) effects to first order and the divergence of the diamagnetic heat flow in the ion energy equation and is valid for arbitrary curvature, i.e. arbitrary values of $\varepsilon_n = 2L_n/L_B$ (L_B = magnetic field curvature and ∇B scale length). We neglect parallel ion motion (assuming $\omega/k_\parallel >> v_{thi}$), electron and ion trapping and collisions in order to concentrate on the main η_i mode characteristics. The model gives the ion density response

$$\frac{\delta n_i}{n_0} = Q_1 \frac{e\phi}{T_i} \tag{1}$$

where $Q_1 = T_1/N_1$ and

$$T_1 = \omega(\omega_{Di} - \omega_{*i}) + \left(\frac{7}{3} - \eta_i\right)\omega_{*i}\omega_{Di} - \frac{5}{3}\omega_{Di}^2 - b_0(\omega - \omega_{*iT})\left(\omega - \frac{5}{3}\omega_{Di}\right) \tag{2}$$

$$N_1 = \omega^2 - \frac{10}{3}\omega\omega_{Di} + \frac{5}{3}\omega_{Di}^2 \tag{3}$$

and $\omega_{*iT} = \omega_{*i}(1 + \eta_i)$, $\omega_{*i} = \mathbf{k} \cdot \mathbf{v}_{*i}$ is the ion diamagnetic frequency and $\omega_{Di} = \mathbf{k} \cdot \mathbf{v}_{Di}$ is the ion magnetic frequency (magnetic drift = curvature drift+∇B drift). In the regime under consideration $k_\parallel v_{thi} << \omega << k_\parallel v_{the}$ the electrons are assumed to be isothermal. We then obtain a Boltzmann distribution for the electron density, $\delta n_e/n_e = e\phi/T_e$. Using finally the quasineutrality condition, $\delta n_e = \delta n_i$, we obtain a dispersion relation in the form of a second order equation in ω.

Gyrokinetic model

In a gyrokinetic ion model the ion density response may be derived from the ion gyrokinetic equation. Assuming a Maxwellian ion velocity distribution one obtains

$$\frac{\delta n_i}{n_0} = Q_2 \frac{e\phi}{T_i} \equiv (-1 + I)\frac{e\phi}{T_i} \tag{4}$$

where

$$I = \int \frac{\omega + \omega_{*i}(v^2)}{\omega + \omega_{Di}(v)} J_0^2\left(\frac{k_\perp v_\perp}{\omega_{ci}}\right) f_{Mi} dv \tag{5}$$

and

$$\omega_{*i}(v^2) = \frac{cT_i}{eB_0^2}\left[1 + \eta_i\left(\frac{mv^2}{2T_i} - \frac{3}{2}\right)\right][\nabla(\ln n_0) \times \mathbf{B}_0] \cdot \mathbf{k}_\perp \tag{6}$$

$$\omega_{Di}(v) = \frac{cm}{eB_0^3}\left(\frac{1}{2}v_\perp^2 + v_\parallel^2\right)(\nabla B_0 \times \mathbf{B}_0) \cdot \mathbf{k}_\perp \tag{7}$$

As in the fluid model the electrons are assumed to be thermalized which gives a Boltzmann distribution for the electron density response, $\delta n_e/n_0 = e\phi/T_e$. Using the quasineutrality condition the dispersion relation may then be written $Q_2 = 1/\tau$ where $\tau = T_e/T_i$.

Results

Figs. 1a and 1b show the upper stability thresholds in the η_i-ε_n plane with b_0 between 0.1 and 0.5 as a parameter. The threshold is strongly reduced by smaller ε_n. The lowest values occur at $b_0 \approx 1$. For $b_0 \ll 1$ the agreement between the kinetic and fluid values are good, the fluid values being in general lower than the kinetic ones.

Figs. 2a and 2b show growthrate and frequency (normalized to the electron diamagnetic frequency) as a function of η_i for $\varepsilon_n = 0.15$ and three different b_0-values lower than one. We note that the mode propagation is in the ion drift direction (except at values close to the lower η_i stability threshold) and that the frequency increases linearly from low values at the lower η_i threshold to around $2\omega_{*i}$ at the upper η_i threshold. The level of the maximum growthrate is well reproduced by the fluid model and also the growthrate and frequency at lower b_0-values (as compared to the kinetic result).

In Figs. 3a and 3b the kinetic and fluid normalized growthrate and frequency have been plotted again as a function of η_i but now for $b_0 = 0.25$ and with ε_n between 0.01 and 0.4 as a parameter (the lower ε_n values unrealistically low but shown for comparison).
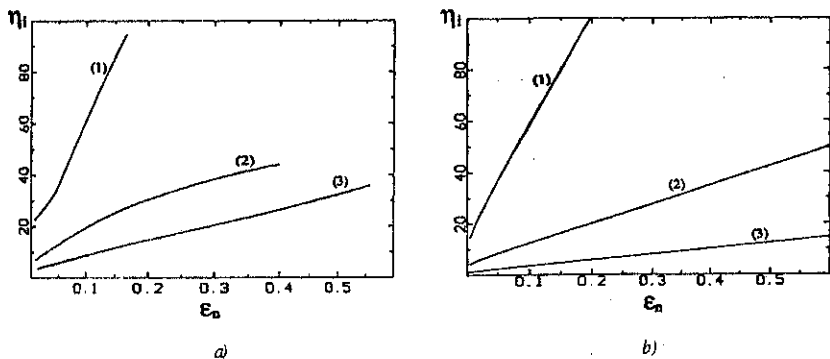
Figs. 1a and 1b. η_i upper stability threshold versus ε_n for $\tau=1$ and $b_0=0.1$ (1), $b_0=0.25$ (2), $b_0=0.5$ (3) from a) gyrokinetic model and b) two-fluid model.
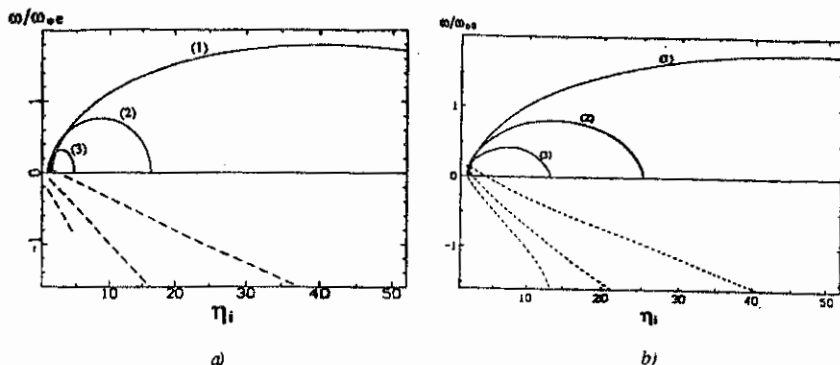
Figs. 2a and 2b. Normalized growthrate γ/ω_{*e} (full line) and real frequency ω_r/ω_{*e} (dashed line) as a function of η_i for $\tau=1$, $\varepsilon_n=0.15$ and $b_0\approx0.1$ (1), $b_0=0.25$ (2), $b_0=0.5$ (3) from a) gyrokinetic model and b) two-fluid model.
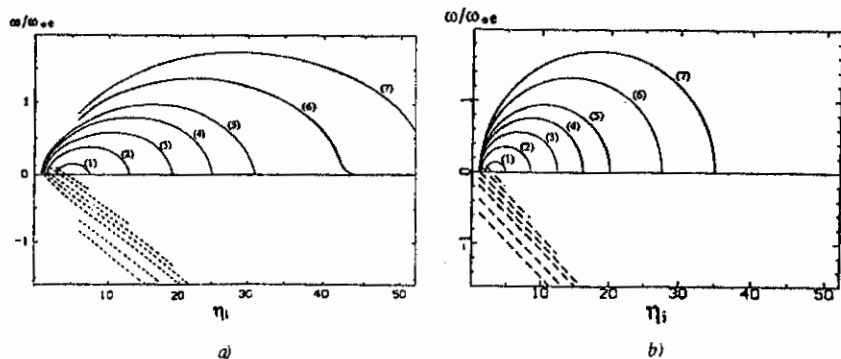
Fig. 3a and 3b. Normalized growthrate γ/ω_{*e} (full line) and real frequency ω_r/ω_{*e} (dashed line) as a function of η_i for $\tau=1$, $b_0=0.25$ and $\varepsilon_n=0.01$ (1), $\varepsilon_n=0.05$ (2), $\varepsilon_n=0.1$ (3), $\varepsilon_n=0.15$ (4), $\varepsilon_n=0.2$ (5), $\varepsilon_n=0.3$ (6), $\varepsilon_n=0.4$ (7) from a) gyrokinetic model and b) two-fluid model.

References

1. B. Coppi and F. Pegoraro, Nucl Fusion 17, 969 (1977).

2. A. Jarmén, P. Andersson and J. Weiland, Nucl. Fusion 27, 941 (1987).

3. F. Romanelli, Phys. Fluids B1, 1018 (1989).

4. A. Jarmén, Phys. Scr. (1997).

5. J. Weiland and H. Nordman, Nucl. Fusion 31, 390 (1991).

6. C. Kessel, J. Manickam, G. Rewoldt and W.M. Tang, Phys. Rev. Lett 72, 1212 (1994).

Stability of ideal and resistive modes in cylindrical plasmas with resistive walls and plasma rotation

A. Bondeson
Institute of Electromagnetic Field Theory, Euratom-NFR/Fusion Association,
Chalmers University of Technology, S-412 96 Göteborg, Sweden

H. X. Xie
Department of Technology, Euratom-NFR/Fusion Association,
Uppsala University, Box 534, S-751 21 Uppsala, Sweden

Advanced tokamaks, where the main part of the plasma current comes from the bootstrap effect, require conducting walls to stabilize external kink modes at high beta [1]. Also, reversed field pinches need conducting walls for stable operation [2]. In reality, a wall always has a finite conductivity, and this can destabilize resistive wall modes (RWM) [3,4], when the equilibrium is unstable in the absence of a wall. The resistive wall mode has rather different stability properties than modes stabilized by ideal walls. An ideal instability can be stabilized by a resistive wall, if the wall is sufficiently (but not too) far away from the plasma, and the plasma rotates with a few per cent of the Alfvén speed [4]. Recently, Finn found that a cylindrical equilibrium that is ideally unstable with the wall at infinity can be stabilized by a close-fitting resistive wall and plasma rotation frequencies of the order of *resistive* growth rates [5]. Here we study RWM stability by applying the "resistive kink" dispersion relation [6], that incorporates resistive and ideal instabilities as well as the correct damping from the Alfvén continuum. The analysis confirms that the stabilization found by Finn is possible in principle. However, the region in parameter space where such stabilization occurs is very small and appears to be too fragile to be relevant to experiments.

We study resistive MHD instabilities in cylindrical equilibria with a single mode rational surface at $r = r_s$ where $q = m/n$ in the finitely conducting plasma. We define two solutions of the "external" equation (ideal MHD force balance away from the resonant surface). The solutions are distinguished by their behavior in the vacuum: ψ_0 is the solution with no wall, normalized so that $\psi_0 = 1$ at the resistive shell, $r = d$, while ψ_∞ satisfies the external equation for $r < d$, and has $\psi_\infty(d) = 0$ and $\psi'_\infty(d) = -1/d$. (ψ_0 and ψ_∞ are solutions without a shell and with a perfectly conducting shell at the position of the resistive shell, respectively.)

Using the jump condition at the resistive shell, the jump in the logarithmic derivative of ψ at the rational surface can be expressed as $\Delta'_{\text{ext}} = (\delta_0 + \gamma\tau_w\delta_\infty)/(\psi_0 + \gamma\tau_w\psi_\infty)$ where γ is the growth rate, $\delta_0 = \psi'_0(r_{s+}) - \psi'_0(r_{s-})$ and $\delta_\infty = \psi'_\infty(r_{s+}) - \psi'_\infty(r_{s-})$ denote the jumps in the radial derivative at the rational surface of the two basis solutions. With an ideal wall, the stability properties depend on ψ_∞ and δ_∞ as follows:

- $\psi_\infty > 0, \delta_\infty < 0$, ideally and resistively stable,

- $\psi_\infty > 0, \delta_\infty > 0$, ideally stable, resistively unstable,

- $\psi_\infty < 0$, ideally unstable.

Figure 1 is a schematic stability diagram in terms of normalized wall radius d/a versus normalized pressure $\hat{\beta}$. In region I the plasma is resistively unstable without a wall and resistively stable with an ideal wall. In regions II and III, the plasma is ideally unstable without a wall. In region II it resistively unstable and in region III resistively stable with an ideal wall.

At the resonant surface, we use the resistive kink dispersion relation [6]. This dispersion relation was derived by several authors, and in Ref. 7 we show that it can be extended to all growthrates γ with $|\arg(\gamma)| < \pi$. We assume that the plasma near the resonant surface rotates with respect to the wall, so that there is a Doppler shift $\omega_0 = mv_\theta/r - nv_z/R$.
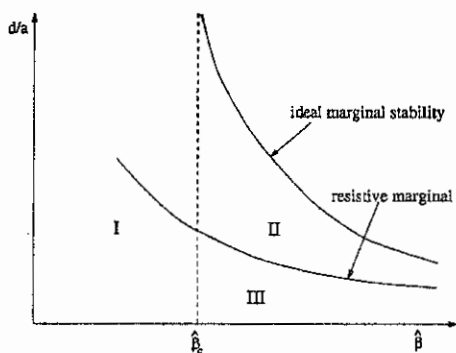
Fig. 1. Schematic stability diagram in wall radius and pressure.
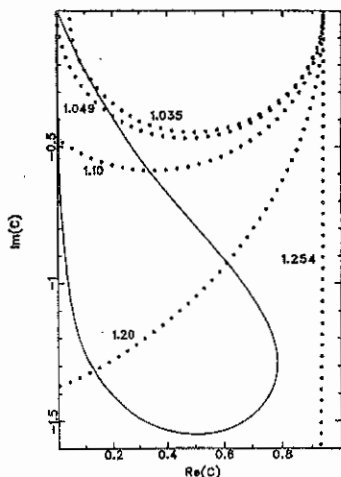
Fig. 2 Complex C-plane for a case that is ideally unstable without a wall.

The number of instabilities can be counted by examining the phase variation of $F(\gamma) = \Delta'_{\text{ext}}(\gamma) - \Delta'_{\text{in}}(\gamma)$ when γ traverses a contour encircling the unstable halfplane with a small indentation at the origin. It greatly simplifies to assume that the wall time is much longer than typical resistive growth rates. Then, the F contour can be constructed as the $-\Delta'_{\text{in}}$ contour shifted by Δ'_∞, with the Δ'_{ext} circle added onto it, at $\omega = \omega_0$. This amounts to setting $\gamma \approx i\omega_0$ in the internal Δ' for the resistive wall modes and assuming the wall is ideal whenever γ deviates from $i\omega_0$ by more than $O(\tau_w^{-1})$. For the RWM, the expression for the external Δ' then gives γ as an explicit function of ω_0:

$$\hat{\lambda} = i\hat{\omega}_0 - \alpha(\hat{\Delta}_0 + C)/\alpha(\hat{\Delta}_\infty + C), \tag{1}$$

where

$$C(i\hat{\omega}_0) \equiv -\hat{\Delta}_{\text{in}}(i\hat{\omega}_0) = (i\hat{\omega}_0)^{5/4} \frac{\pi}{8} \frac{\Gamma\{\frac{1}{4}[(i\hat{\omega}_0)^{3/2} - 1]\}}{\Gamma\{\frac{1}{4}[(i\hat{\omega}_0)^{3/2} + 5]\}}. \tag{2}$$

The normalized variables in (1-2) are defined as $\hat{\Delta} \equiv \Delta' S^{-1/3}$, $\hat{\lambda} = \gamma\tau_A S^{1/3}$, where $S = \tau_r/\tau_A$ is the Lundquist number. Marginal stability is found by letting $\text{Re}(\hat{\lambda}) = 0$ in

(1), which gives

$$|C|^2 + \left(\hat{\Delta}_0 + \hat{\Delta}_\infty\right)\mathrm{Re}(C) + \hat{\Delta}_0\hat{\Delta}_\infty = 0. \tag{3}$$

This represents a circle in the complex plane through $C = -\hat{\Delta}_0$ and $C = -\hat{\Delta}_\infty$. Figure 2 shows the $C(i\hat{\omega}_0)$ contour together with several circles $\mathrm{Re}(\lambda) = 0$ (3), corresponding to different wall positions, in the complex C-plane for an equilibrium that is ideally unstable with the wall at infinity.

When the rotation frequency is much larger than the resistive kink growth rate, $\hat{\omega}_0 \gg 1$, the ideal approximation $C \approx -i\pi/\hat{\omega}_0$ applies. When $\hat{\omega}_0 \ll 1$, the tearing approximation $C(i\hat{\omega}_0) \approx -(i\hat{\omega}_0)^{5/4}/h$ applies with $h = \Gamma(\frac{1}{4})/[2\pi\Gamma(\frac{3}{4})] \simeq 0.4709$. The regimes where the ideal and tearing approximations hold are the two straight sections of the $C(i\hat{\omega}_0)$ curve approaching the origin in Fig. 2.

Resistive instability with the wall at infinity, $\psi_0 > 0$, $\delta_0 > 0$. To stabilize this case, the wall must be placed inside the resistive stability boundary so that $\delta_\infty < 0$, that is, in **region I** in Fig. 1. A Nyquist plot based on the resistive dispersion relation shows one instability if ω_0 is below some threshold ω_R, and no instability if $\omega_0 > \omega_R$. This wall stabilization of resistive modes by slow rotation has been discussed by several authors. The limiting rotation frequency is

$$\hat{\omega}_R^{5/4}/h = -\frac{1}{2}\left(\hat{\Delta}_0 + \hat{\Delta}_\infty\right)\sin\frac{\pi}{8} + \left[\left(\hat{\Delta}_0 + \hat{\Delta}_\infty\right)^2\frac{1}{4}\sin^2\frac{\pi}{8} - \hat{\Delta}_0\hat{\Delta}_\infty\right]^{1/2} \tag{4}$$

The full dispersion relation has one pole, and the F curve encircles the origin 0 or 1 times in the positive sense. The naive conclusion, that there is either one or two instabilities, is, however, incorrect. A false root is created by the idealized behavior of $\hat{\Delta}_{\mathrm{in}}(\hat{\lambda})$ at large $|\hat{\lambda}|$. The spurious root corresponds to $|\hat{\lambda}|$ so large that the thin layer approximation breaks down. This extra root is not physical, and there is either 0 or 1 instability. The Nyquist diagram of the full dispersion relation does show that an "ideal" instability can be created if $\hat{\omega}_0$ is large enough [5].

We conclude that, the resistively unstable case can be stabilized by a resistive wall in region I, if the rotation speed is larger than the resistive threshold, ω_R (4), but less than an ideal critical speed ω_I.

$$\omega_I\tau_A = \pi\left(-\Delta_0'\Delta_\infty'\right)^{-1/2}. \tag{5}$$

Ideal instability with the wall at infinity. The equilibrium is ideally unstable without a wall if $\psi_0 < 0$, $\delta_0 > 0$. In **region II**, where $\psi_\infty > 0$, $\delta_\infty > 0$, an ideal wall gives ideal stability but resistive instability. The resistive dispersion relation shows that with a resistive wall there is one instability at zero rotation frequency ("tearing"), and one additional instability appears when the rotation velocity exceeds a resistive threshold (RWM). Thus, there is always one instability in region II. The full dispersion relation shows that the resistive wall mode is stabilized if ω_0 exceeds an *ideal* threshold. The RWM is unstable in the interval

$$\omega_R < \omega < \omega_I$$

where the limiting frequencies are given by Eqs. (4-5).

In **region III** in Fig. 1 the wall position is close enough so that an ideal wall makes the plasma resistively stable, $\psi_\infty > 0$, $\delta_\infty < 0$. A Nyquist plot based on the resistive approximation now reveals that there is one instability if $\omega_0 = 0$ (one pole in $\hat{\Delta}'_{ext}$ and the origin is not encircled). If the ratio Δ'_0/Δ'_∞ is sufficiently small, or sufficiently large, there is a small window of frequencies, where the origin is encircled once in the negative sense, and there is no instability. This confirms the result of Finn [5]. For complete stabilization, ω_0 must be between two limits, that are both of the order of a resistive growth rate:

$$\hat{\omega}_{R\pm}^{5/4}/h = -\frac{1}{2}\left(\hat{\Delta}_0 + \hat{\Delta}_\infty\right)\sin\frac{\pi}{8} \pm \left[(\hat{\Delta}_0 + \hat{\Delta}_\infty)^2\frac{1}{4}\sin^2\frac{\pi}{8} - \hat{\Delta}_0\hat{\Delta}_\infty\right]^{1/2} \tag{6}$$

In region III, both Δ'_0 and Δ'_∞ are positive, and in order for the frequencies (6) to be real, Δ'_0/Δ'_∞ has to be sufficiently large or sufficiently small. Equation (6) shows that stabilization is *not* possible when

$$\frac{1}{g} < \Delta'_\infty/\Delta'_0 < g \ , \quad g = \left(\frac{1 + \cos\pi/8}{\sin\pi/8}\right)^2 \simeq 25.3 \tag{7}$$

Thus, the condition for complete stability in region III is very restrictive. The condition is satisfied near the boundary to region II, where Δ'_∞/Δ'_0 is small ($1.035 < d/a <$ 1.049 for the model equilibrium in Fig. 2). Further into region III, $|\Delta'_\infty/\Delta'_0|$ increases and stabilization is lost (for $d/a < 1.035$). In addition, the rotation frequency is restricted to a window in the range of resistive growth rates. For reversed field pinches, such restrictive conditions would have to be satisfied for several different toroidal mode numbers, and the different conditions may be expected to be in conflict with one another. We conclude that this type of stabilization is difficult to achieve in practice.

If we use the complete dispersion relation, the number of times the origin is encircled does not change, but there is one more pole in $\hat{\Delta}'_{in}$. Therefore, the complete dispersion relation appears to predict another instability. However, for the same reason as discussed for region I, this is a spurious ideal mode that appears when $\delta_\infty < 0$ and $\psi_\infty > 0$. Consequently, in region III, there is typically one instability. Complete stabilization of the m/n mode occurs very near the boundary to region II, where $0 < \Delta'_\infty/\Delta'_0 \lesssim 0.04$.

Summary. Equilibria that are *resistively* unstable in the absence of a wall can be stabilized by a slow rotation provided the resistive wall is inside the marginal position of an ideal wall for resistive modes. Equilibria that are ideally unstable in the absence of a wall can be made *ideally* stable by an ideal rotation velocity if the resistive wall is inside the ideal marginal position. However, when the wall-at-infinity configuration is ideally unstable, it is very difficult to wall stabilize *resistive* modes in the cylindrical model.

REFERENCES

[1] C. Kessel, J. Manickam, G. Rewoldt, and W. M. Tang, Phys. Rev. Lett. **72**, 1212 (1994).

[2] D. C. Robinson, Nucl. Fusion **18**, 939 (1978).

[3] T. H. Jensen and M. S. Chu, J. Plasma Phys. **30**, 57 (1983).

[4] A. Bondeson and D. J. Ward, Phys. Rev. Lett. **72**, 2709 (1994).

[5] J. M. Finn, Phys. Plasmas **2**, 3782 (1995).

[6] B. Coppi, *et al*, Sov. J. Plasma Phys. **2**, 533 (1976) [Fiz. Plasmy **2**, 961 (1976)].

[7] A. Bondeson and H. X. Xie, Phys. Plasmas **4**, 1997 (June issue).

MHD OPERATIONAL LIMITS FOR TOKAMAKS WITH NEGATIVE CENTRAL SHEAR

A. Bondeson, M. Benda and M. Persson

Institute for Electromagnetic Field Theory, EURATOM-NFR/Fusion
Association, Chalmers University of Technology, Göteborg, Sweden

M. S. Chu

General Atomics, San Diego, California, U. S. A.

Equilibria with negative central shear (NCS) have many favorable properties [1–5]. In DIII-D and TFTR, NCS plasmas develop internal transport barriers [3,4] that produce good central confinement. In the region of negative shear, ideal magnetohydrodynamic (MHD) ballooning modes are unconditionally stable. Furthermore, NCS equilibria tend to have good alignment between the bootstrap and equilibrium currents. However, excessive peaking of the pressure leads to instability of low-n modes, typically $n = 1$, and many NCS discharges end disruptively at rather modest beta [6]. Thus, NCS discharges have significant advantages, but the operational space is more complicated than for conventional profiles. Here, we report an MHD beta limit study of the operational limits for NCS discharges concerning, in particular, the limits of $\beta^* = 2\mu_0 \langle p^2 \rangle^{1/2} / \langle B^2 \rangle$ and the bootstrap fraction $f = I_{\mathrm{bs}}/I$. We have taken into account the following conditions

1. The parallel current density from bootstrap must nowhere be larger than the total parallel current density, so that no negative current drive is needed: $\langle \vec{j}_{\mathrm{bs}} \cdot \vec{B} \rangle_\psi \leq \langle \vec{j} \cdot \vec{B} \rangle_\psi$, The bootstrap current is calculated at low collisionality assuming $T_e = T_i$ and $\eta = d(\log T)/d(\log n) = 1.5$.

2. Stability to ideal ballooning modes with toroidal mode number $n = \infty$.

3. Stability to resistive interchanges.

4. Stability to ideal $n = 1$, 2 and 3 external kink modes without a conducting wall.

The bootstrap condition (1) typically limits the pressure gradient in the outer part of the plasma. In the NCS region, the pressure gradients are effectively limited by the stability of low-n, external kink modes.

In the optimizations, we have specified the current profiles by giving the surface averaged toroidal current density I^*. NCS equilibria with different internal inductances have been constructed by varying the slope $dI^*/d\psi$ at the edge. The equilibrium code CHEASE [7] increases the pressure gradient on every flux surface (starting from a low value) until it becomes marginal to the most restrictive of the local conditions 1-3 listed above and an artificially imposed condition $-dp/d\psi < c$. c is ψ-independent parameter used to limit the pressure gradients in the NCS region. The stability code MARS [8] is then run to find the c for which the equilibrium is marginal to the most restrictive of the $n = 1$, 2 and 3 external modes. We have held the aspect ratio A fixed at 3, and studied two elongations, $\kappa = 1.6$ and 2.0, and two triangularities, $\delta = 0.3$ and 0.7. q_{min} has been

varied from 1.1 to 2.5.
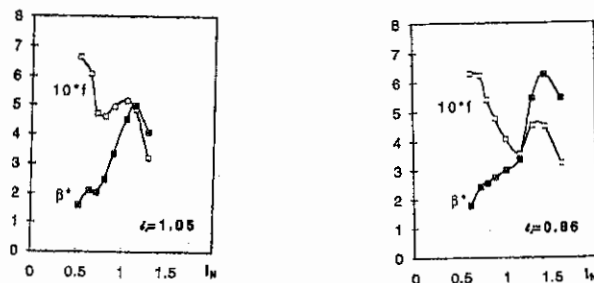
Fig. 1 β^* and bootstrap fraction versus normalized current for NCS current profiles
and JET cross section (a) $l_i = 1.05$ (b) $l_i = 0.86$.

Results for JET cross section. Four different I^* profiles were tested with internal inductances from 0.79 to 1.05. They have maximum I^* at $\rho \approx 0.38$ and q_{min} at $\rho \approx 0.47$. Results for the optimum β^* and bootstrap fraction f vs the normalized current I_N are shown in Fig. 1 for two current profiles with different inductances. The optimal pressure profiles are not very peaked, with peaking factors $p_0/\langle p \rangle$ generally between 2.5 and 3. The peaking of the pressure is in most cases limited by $n = 1$ stability. In all cases, the maximum β occurs for q_{min} slightly above unity, typically $q_{min} \simeq 1.2$. When q_{min} approaches unity, the beta limit drops sharply. The main reason for this is destabilization of the $n = 1$ external kink mode, which acquires a large non-resonant $m = 1$ component when q_{min} approaches unity.

Figure 1 shows that the maximum beta increases with decreasing inductance. One reason for this is that a broader profile gives more plasma current at fixed q_{min}. Therefore, according to the Troyon scaling $\beta_{max} \propto I_N$, one may expect a higher maximum beta at low inductance. However, in contrast to the empirical DIII-D scaling $\beta_N \leq 4l_i$ [9], also the maximum $\beta_N = \beta/I_N$ increases when l_i is decreased. The main reason for this is that the broader current profile can support larger pressure gradients at large radius without violating the bootstrap condition (1). Profiles conventionally used for high beta operation have broad pressure profiles and peaked current profiles, and the beta limit does increase with l_i when the current and pressure profiles are treated as independent. However, the highest beta limits are found for equilibria where the bootstrap current exceeds the equilibrium current near the edge, and such equilibria are not in steady state. With the assumption of steady state and no negative current drive, it is more advantageous to use a rather broad current profile. The broadening is limited by instability of mainly current driven external kinks, causing "ravines" in the beta limit when q_a is just below some rational number m/n, most notable for integers ($n = 1$). Optimizations made with somewhat different current profiles indicate that the beta limit is rather insensitive to details of the current profile (except q_{min}).

Two interesting regions of operation can be identified in Fig. 1 for $l_i = 0.86$. The first is at high current $q_{min} \simeq 1.2$. In this region, $\beta^* \simeq 6.2\%$ and $\beta_N \simeq 3.7$ is reached

with a bootstrap fraction of about 40%. This is a fairly conventional equilibrium. The other region, relevant for advanced tokamaks, is with q_{min} slightly above 2. Here, the $l_i = 0.86$ gives a bootstrap fraction of about 65%, $\beta^* \simeq 2.5\%$ and $\beta_N \simeq 2.8$.
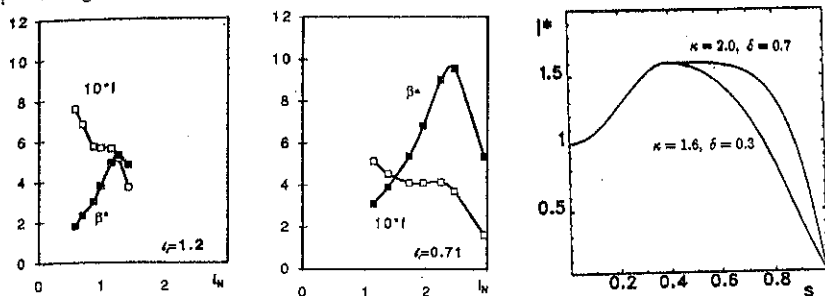
Fig 2. β^* and bootstrap fraction versus normalized current for NCS current profiles and $\kappa = 2$, $\delta = 0.7$. (a) $l_i = 1.2$ and (b) $l_i = 0.71$. (c) Optimized current profiles in different geometries

Strong shaping. Results for $\kappa = 2.0$ and triangularity $\delta = 0.7$ are shown in Fig. 2 for different inductances. The dependence on inductance is similar to that in the JET case: the beta limit increases with decreasing l_i until ravines appear. The optimized I^* profiles are shown in Fig. 2c, both for JET shape and for the strongly shaped case. For the stronger shaping, a much broader current profile is optimal than for the JET shaped cross section. The optimized current profile is flat over a large part of the cross section, where the shear is weak. Most remarkable in Fig. 2 is the strong improvement in the maximum β^* achieved by the increased shaping. The maximum β^* is now 9.8% with $\beta_N \simeq 4.4$. This comes from increases both in the maximum I_N and β_N. The values of β_N for the broad current profiles in this strongly shaped geometry exceed the DIII-D scaling $\beta_N \leq 4l_i$. Figure 4 shows the profiles for the optimized equilibrium with $q_{min} = 1.2$ and $\beta^* = 9.8\%$. This equilibrium is stable to ideal $n = 1, 2, 3$ and ∞ modes and resistive interchanges.
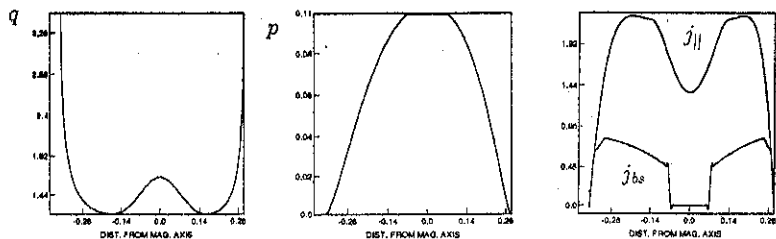
Fig 3. (a) q (b) p and (c) $I_{\parallel}$ and I_{bs} profiles for the optimized equilibrium with $\kappa = 2$, $\delta = 0.7$, $q_{min} = 1.2$, $l_i = 0.95$, $f = 38\%$ and $\beta^* = 9.8\%$.

Concerning the possibilities for a high bootstrap fraction, we note that profile with $l_i = 0.86$ gives $f = 68\%$ with $\beta^* = 3.3\%$, which is considerably better than with the JET shape. The profiles for this equilibrium are shown in Fig. 5.
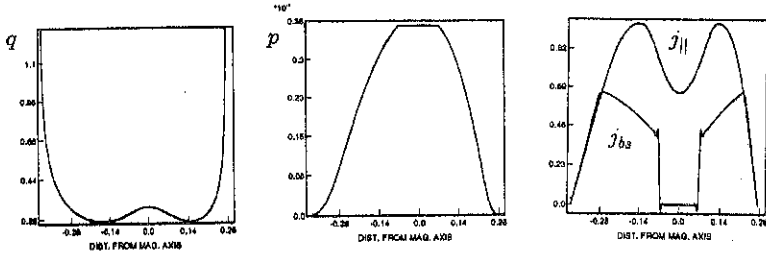
Fig 4. (a) q (b) p and (c) $I_\parallel$ and I_{bs} profiles for the optimized equilibrium with $\kappa = 2$, $\delta = 0.7$, $q_{min} = 2.5$, $l_i = 0.96$, $f = 68\%$ and $\beta^* = 3.3\%$.

To distinguish the effects of elongation from those of triangularity, we have also studied other geometries ($\kappa = 1.6$, $\delta = 0.7$ as well as $\kappa = 2.0$, $\delta = 0.3$). The maximum β^*, stable to ideal $n = 1, 2, 3, \infty$ modes and resistive interchanges for the four different cross section shapes are reported together with other equilibrium parameters in the table. The table shows that the combined effect if increasing ellipticity and triangularity is highly favorable.

κ	δ	$\beta^*_{max}[\%]$	$\beta_{N,max}$	I_N at max β^*	Optimum l_i
1.6	0.3	6.2	3.7	1.4	0.86
1.6	0.7	7.7	4.0	1.8	0.71
2.0	0.3	6.5	3.3	1.8	0.84
2.0	0.7	9.8	4.3	2.4	0.71

REFERENCES

[1] KESSEL, C., et al, Phys. Rev. Lett. **72** (1994) 1212.

[2] TAYLOR, T. S., et al, Plasma Phys. Controlled Fusion **36** B (1994) 229.

[3] LEVINTON, et al, Phys. Rev. Lett. **75** (1995) 4417.

[4] STRAIT, E. J., et al, Phys. Rev. Lett. **75** (1995) 4421.

[5] LAZARUS, E. A., et al, Phys. Rev. Lett. **77** (1996) 2714.

[6] CHU, M. S., et al, Phys. Rev. Lett. **77** (1996) 2710.

[7] LÜTJENS, H., BONDESON, A., SAUTER, O., Computer Phys. Comm. **97** (1996) 219.

[8] BONDESON, A., VLAD, G., LÜTJENS, H., Phys. Fluids **B4** (1992) 1889.

[9] TAYLOR, T.S., et al, in Proc. 13th IAEA Conf., Washington D.C. 1990 (IAEA, Vienna 1991), Vol. 1, p. 177.

Nonlinear stability analysis of external hydromagnetic modes in a tokamak

H.G. Eriksson* and C. Wahlberg

Department of Materials Science, Uppsala university, Box 534, S-751 21 Uppsala, Sweden.
*Permanent address: Mälardalens högskola, IKP, Box 325, S-631 05 Eskilstuna, Sweden.
(EURATOM / NFR Fusion Association)

Introduction

This study uses bifurcation analysis to investigate the nonlinear stability properties of external, ideal magnetohydrodynamic (MHD), $m \geq 2$ modes with helical symmetry in a straight tokamak [1]. The study is essentially analytical, based on an expansion in the amplitude of the helical displacement, and the calculations have been carried through by using computer algebra.

A systematic investigation of the dependence of the nonlinear effect on poloidal mode number, current profile and wall distance is performed. In particular, we include current profiles which are peaked off axis in order to model the bootstrap current in a high-performance tokamak [2]. Previous studies of the nonlinear properties of the $m \geq 2$ modes have dealt either with a uniform plasma current [3], or with the $m = 2$ mode exclusively and constant wall distance [4-5].

The nonlinear evolution equation of a non-resonant, nearly marginal, MHD mode in a cylindrical plasma column in general has the form [6-7]

$$\eta_{tt} + D_1\eta + D_3\eta^3 = 0 \tag{1}$$

where $\eta(t)$ represents the amplitude of the mode. D_1 is equal to the linear eigenvalue, ω^2, of the mode. D_3 determines the leading order nonlinear effect. To calculate D_3 it is sufficient to consider the time independent version of eq. 1, i.e. eq. 2. In this way, the nonlinear stability problem reduces to a problem of finding the bifurcated plasma equilibria, eq. 3.

$$D_1 \eta + D_3 \eta^3 = 0 \qquad ; \qquad \eta = \pm\sqrt{-\frac{D_1}{D_3}} \tag{2) ; (3}$$

Considering a slightly unstable mode ($D_1 < 0$), two different cases may be distinguished:
(i) $D_3 < 0$, and the nonlinear development of the mode is further destabilizing (subcritical bifurcation). (ii) $D_3 > 0$, and the nonlinear development is stabilizing (supercritical bifurcation).

Helical equilibrium

The present study is concerned with deriving an equilibrium equation of type (2), describing an equilibrium with helical structure, and analysing the properties of the coefficients D_1 and D_3. The equilibrium equation is obtained in the following way: We initially consider the plasma current to be flowing in a number, N, of infinitely thin, perfectly conducting, nested, helical

shells with constant pressure in between, and then take the continuous limit $N \to \infty$. Using this method, it is simple to take into account flux conservation and an equation of state, e.g. incompressibility [8].

Considering the requirement that the magnetic field is tangential to the shells on their outer as well as inner surfaces together with the pressure balance condition, three "internal" and two "external" equilibrium equations are derived.

An expansion up to third order is made of the amplitude of the helical deformation of the flux surfaces including, to second order, a term proportional to $\cos 2m\zeta$, and a third order term proportional to $\cos m\zeta$, where the angle $\zeta = \varphi - kz/m$.

To first order, considering a perfectly conducting wall with radius b, the equilibrium equations then give an expression for D_1. The coefficient D_1 depends on the derivative of the normalized eigenmode at the plasma boundary, f_1', and the functions $F = 1 - nq_a/m$, and $\beta_1 = -\{[(b/a)^{2m}+1]/[(b/a)^{2m} - 1]\}/m$, where a is the plasma radius. We point out that D_1 and D_3 obtained in this manner are undetermined with respect to a common factor. The system is hence linearly stable if $D_1 > 0$ and the points of marginal stability are found by letting $D_1 = 0$. As is well known, there are two marginal points, given by

$$nq_a = m \qquad \text{and} \qquad nq_a = m\,(f_1' - m^2\beta_1 - 1)\,/\,(f_1' - m^2\beta_1 + 1) \qquad (4)\ ;\ (5)$$

Proceeding to third order, we obtain a rather large expression for the D_3 coefficient which depends, in a complex way, on F, m, β_1 (and a similar quantity β_2), f_1', and the wall distance b/a. In addition, D_3 also depends on the derivatives of the higher order mode amplitudes at the plasma surface. The values of the mode amplitudes, including f_1', are obtained by numerically solving a system of three coupled, ordinary differential equations, obtained from the "internal" equilibrium equations.

In the special case of a uniform plasma current the equilibrium equations can be solved analytically. The method outlined above then yields the same result as has previously been obtained in [3].

We refer to paper [1] for details.

Results

The dependence of the nonlinear effect on the mode number, m, wall distance, b/a, and current profile is illustrated by plotting the value of D_3 at the marginal point. The amplitude of the helical state, given by eq. 3, is also shown. Two different kinds of current profiles have been used: "Ordinary" flat and peaked profiles and profiles which are peaked off axis.

As a function of the radial coordinate ρ ($\rho \le 1$), the first type of profiles is defined by

$$j(\rho) = (\nu + 1)(1 - \rho^2)^{\nu}, \ \ \nu \ge 1, \ \ j(\rho) = \frac{1 - \nu\rho^2}{1 - \nu/2}, \nu < 1 \qquad (6)$$
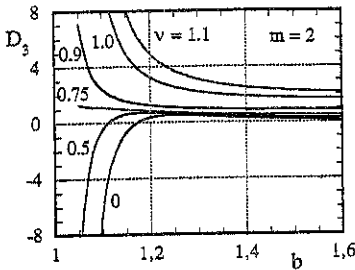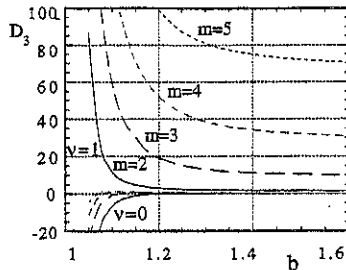
Figure 1

Figure 2

Figures 1 and 2 illustrate the value of D_3 at the marginal point, and it's dependence on the wall distance b/a and current profile, for different poloidal mode numbers $m = 2 - 5$.
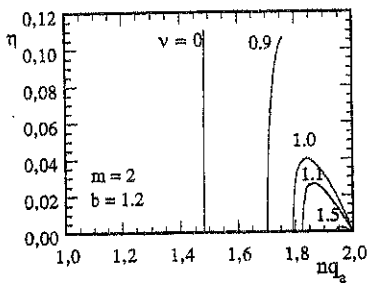
Figure 3
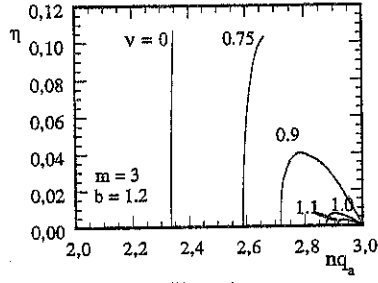
Figure 4

Figures 3 - 4 illustrate how the amplitude of the helical equilibrium, η, depends on nq_a in the region in between the two marginal points for different current profiles and mode numbers m, with $b/a = 1.2$. It is seen that helical states with reasonably small amplitudes are found only for sufficiently peaked profiles, with the most stringent limit determined by the $m = 2$ mode, which requires roughly $v \gtrsim 1$. The amplitudes of the helical equilibria with high m are very small.

The current profiles which are peaked off axis are shown in figure 5, and defined in [9].
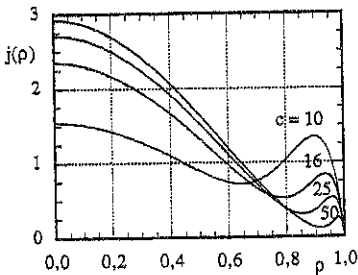
Figure 5
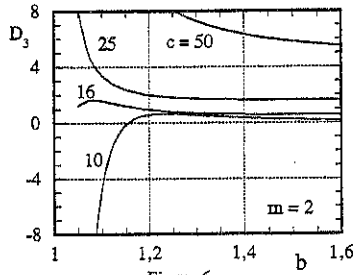
Figure 6

Figure 6 illustrates the dependence of D_3 on the wall distance and current profile for different poloidal mode numbers m = 2 - 5.
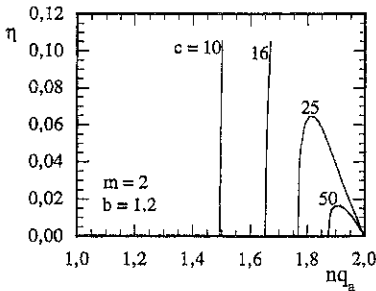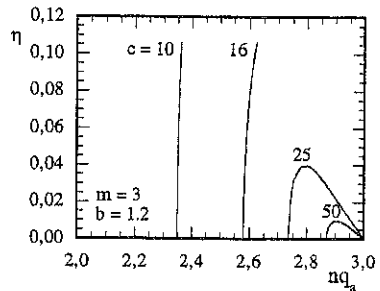
Figure 7   *Figure 8*

Figures 7 - 8: The dependence of the helical amplitude η on nq_a in the region in between the two marginal points for the different current profiles and mode numbers m, with b = 1.2.

The results show that helical modes with $m \geq 2$ with realistic wall distances ($b/a \geq 1.15$) are, in principle, nonlinearly stable, i.e. the bifurcation is supercritical, for all studied current profiles. The stabilizing effect increases with m and depends strongly on the mode number. For high m, the nonlinear effect is significant already at very small mode amplitude and, consequently, the amplitudes of helical states with high m are very small. Also, the stabilizing effect depends strongly on the current profile and increases when the profile is peaked. However, if too much current is flowing in a region near the plasma edge, the bifurcation is still supercritical but the amplitudes of the bifurcated equilibria are very large, thus indicating a situation where nonlinear stability would not be obtained in practice. This finding may be of interest in connection with high-performance tokamaks operating with a large fraction of bootstrap current.

References

[1] Eriksson H.G. and Wahlberg C. *Plasma Phys. Controlled Fusion* **39**, 1 (1997)

[2] Goldston R. J. *Phys. Plasmas* **3**, 1794 (1996)

[3] Rutherford P. H., Furth H. P., and Rosenbluth M. N., in *Plasma Physics and Controlled Nuclear Fusion Research*, Proceedings of the 4th International Conference, Madison, 1971 (IAEA, Vienna, 1971), Vol.2, p.553.

[4] Rosenbluth M. N., Monticello D. A., Strauss H. R., and White R. B. *Phys. Fluids* **19**, 1987 (1976)

[5] Dnestrovskii Yu. N., Kostomarov D. P., Pedorenko A. V., and Popov A. M. (1987) *Sov. J. Plasma Phys.* **13**(10), 683.[12] Pao Y. *Phys. Fluids* **21**, 765 (1978)

[6] Wahlberg C. *Phys. Fluids* **B4**, 1547 (1992)

[7] Pao Y. *Phys. Fluids* **21**, 765 (1978)

[8] Eriksson H.G. and Wahlberg C. *Plasma Phys. Controlled Fusion* **36**, 1269 (1994)

[9] Eriksson G. and Wahlberg C. *Phys. Rev. Lett.* **72**, 2713 (1994)

RELAXATION OF BANANA DRIFT ORBITS TOWARDS TURBULENT EQUIPARTITION

Hans Persson

Group of Theoretical Electrotechnics, Department of Materials Science, Uppsala University, Box 534, S - 751 21 Uppsala, Sweden.

The idea of canonical profiles in tokamaks was suggested long ago [1]. A number of suggestions to explain this have been made. Recently [2,3] it was suggested that turbulent transport drives a plasma towards a state of Turbulent Equipartition, a kind of attractor, in which Lagrangian invariants are uniformly distributed. Different invariants decay with different rates, and in tokamaks the frozen-in law of particles in the poloidal magnetic field survives longer than the corresponding law for the toroidal field, assuming that the trapped particles dominate the turbulent transport. Therefore, the plasma profile depends on the safety factor q(r), and the canonical profile becomes nq=const. This is supported by some experimentally determined profiles.

First results are reported from the work with a numerical model for the time development of the drift of the center of a banana orbit, with the driving force either formed by a random electrostatic field with varying properties (amplitude, distribution, bias, filtering, sampling rate), or a few incommensurable electrostatic waves. The model used is similar to that used by Isichenko and Petviashvili [4], but the physical situation is different, and extra complications are provided by the magnetic drift of the banana orbit and by the strongly inhomogeneous wave field.. This inhomogeneity is meant to represent the radial confinement.

The equations used are

$$\frac{d\phi}{dt} = \frac{V(r)}{R} + \frac{1}{RB_\theta} \frac{\partial \Phi}{\partial r}$$

$$\frac{dr}{dt} = -\frac{1}{RB_\theta} \frac{\partial \Phi}{\partial \phi}$$

Here, we assume $B_\theta = \dfrac{r}{1+4r^2}$; $\Phi = A h(r) G(r,\phi,t)$

The quantity R is assumed to be constant (10). The function V is a complicated, implicit function of r and the first two adiabatic invariants. So far, we have assumed that V=const. For

h(r) various functions have been tried. Usually, h contains a factor r^2, in order to give E_r, E_ϕ tend to zero when r tends to zero. The velocity component v_r also tends to zero, whereas v_ϕ tends to a nonzero value. Both these things appear natural.

The functional form of h that works best has, in addition to the factor r^2, a radial dependence given by $\dfrac{1}{1+e^{10(r-1)}}$.

This choice of h is depicted in Fig. 1.

In one series of runs harmonic waves are assumed :

$$\sum_i \sin(m_i\phi + k_i r - \omega_i t + \alpha_i)$$

The amplitudes of all the waves have been varied, as well as the initial phases. Many simulations have been based on equal amplitudes.

Runs have also been made with a completely stochastic or bandwidth limited time dependence:

$$G = f_1(t)\sin\phi + f_2(t)r$$

For the entering f functions normal and rectangularly distributed sequences have been taken, the former also bandwidth limited.
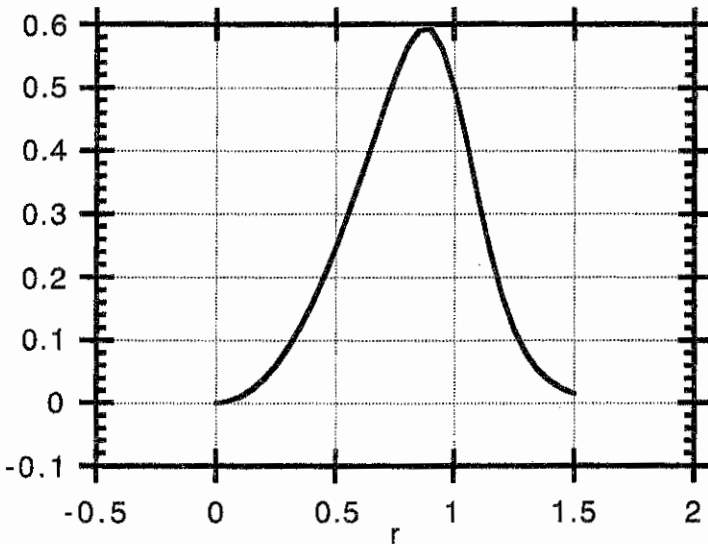
Fig. 1. Radial variation of the exciting electric potential.
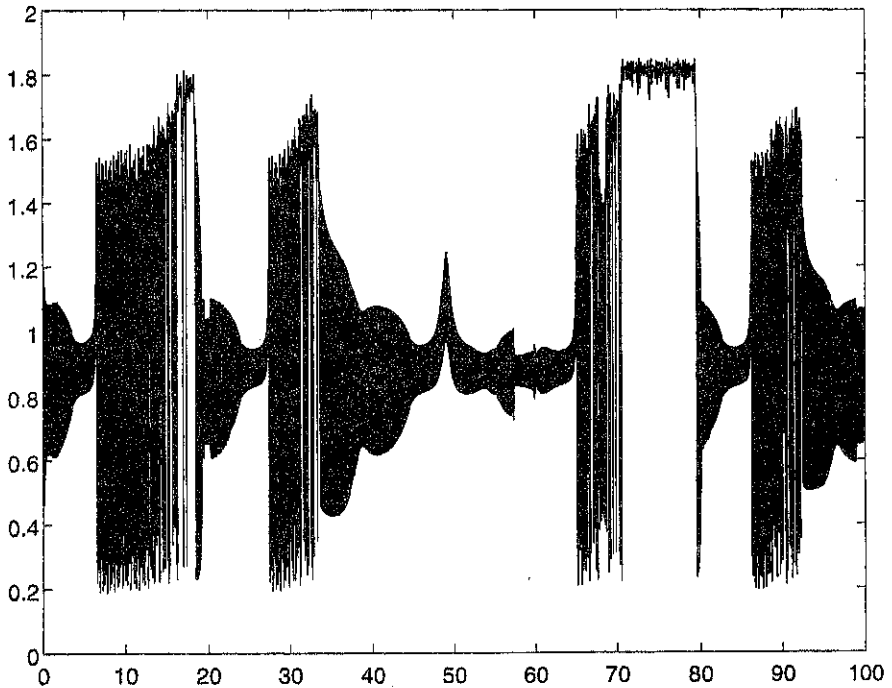
Fig. 2. Trace of radius versus time for three waves.

The trajectories are sometimes quite complicated. See for instance Fig. 2, which shows the radius as a function of time, when there are three waves. Apparently, the system jumps in an irregular fashion between large oscillations covering the available space and a focussing to a location near that of maximum field strength.

The integration method used so far is a modern Runge-Kutta algorithm, usable for non-stiff and moderately stiff problems. Under some circumstances, particularly when the system varies very little in time, a phenomenon suggestive of stiffness appears, which is somewhat remarkable for a Hamiltonian system. At least with the Hamiltonian structure apparent, the trace of the functional determinant is zero, which means that the eigenvalues are normally one positive and one negative, with the same modulus. It appears that the method of integration deserves increased attention.

In Fig. 3 the quantity nq, the product of density and safety factor, is plotted as a function of the radius. In this case, which corresponds to a stochastic time variation, nq is reasonably constant, but other cases also appear when this is not very well fulfilled.
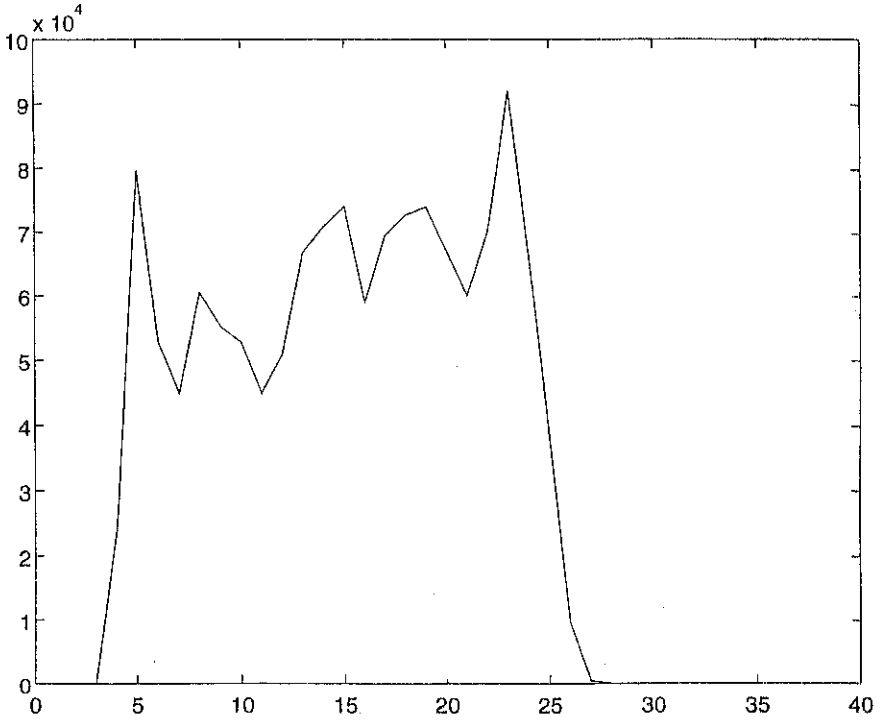
Fig.3. Product nq of density and safety factor for stochastic excitation.

References:

1. B. Coppi, Comments Plasma Phys. Cont. Fusion {\bf 5}, 261 (1980).

2. V. V. Yankov, JETP Letters {\bf 60}, 171 (1994).

3. J. Nycander and V. V. Yankov, Phys. Plasmas {\bf 2}, 2874 (1995).

4. M. B. Isichenko and N. V. Petviashvili, Phys. Plasmas {\bf 2}, 3650 (1995).

Plasma equilibrium with flow in axisymmetric toroidal magnetic traps

O.K. Cheremnykh*, J.W. Edenstrasser**, Zh.N. Andrushchenko*

* Institute for Nuclear Research, Kiev, Ukraine

** Institute for Theoretical Physics, University of Innsbruck, Austria

Introduction. A considerable amount of papers dealing with the investigation of the equilibrium and stability of plasmas with flow in magnetic traps and especially in tokamaks can be found in the literature. In the theoretical investigations of these stationary plasma equilibria in toroidal magnetic traps, one of the main questions is whether the centrifugal force, arising from a sufficiently fast plasma flow, possibly contributes to a favourable high pressure in a plasma column, a question we are particularly interested in. Unfortunately, no general statements on these questions can be drawn so far. The solution of the non-linear equations describing stationary plasma equilibria usually fails on account of the mathematical complexities [1]. This fact has motivated us to analyse these non-linear equations in the case of the relatively simple theoretical model of a stationary tokamak plasma equilibrium, where the toroidal effects have been taken into account by an expansion with respect to the inverse aspect ratio. Our investigation is thus concerned with the analysis of stationary non-linear toroidal plasma equilibria and has the two following aspects. First, we are interested on solutions of the non-linear vector MHD equations in general, and secondly on the investigation of the influence of the plasma flow on the equilibrium. In handling these problems we use the expansion scheme developed by Shafranov [2], which has already successfully been employed in the investigation of static toroidal equilibria.

The reduction of the vector equations. As starting point we consider the following set of stationary, non-linear single-fluid MHD equations, which describe the macroscopic dynamics of an incompressible and non-dissipative plasma

$$
\begin{aligned}
&\rho(\mathbf{v} \cdot \nabla)\mathbf{v} = -\nabla P + (1/c)\mathbf{j} \times \mathbf{B}, \\
&\nabla \times \mathbf{B} = (4\pi/c)\mathbf{j}, \quad \mathbf{E} + (1/c)\mathbf{v} \times \mathbf{B} = 0, \quad \mathbf{E} = -\nabla\Phi, \\
&\nabla \times \mathbf{E} = \nabla \cdot \mathbf{B} = \nabla \cdot \mathbf{v} = \mathbf{v} \cdot \nabla\rho = 0.
\end{aligned}
\tag{1}
$$

Here we have used the generally accepted notations for all physical quantities.

Axially symmetric solutions of the system of Eqs.(1) are considered in toroidal co-ordinates (a, θ, ϕ) [3]. According to our symmetry assumption we put $\partial/\partial\phi = 0$ and introduce the magnetic and velocity fields in the form

$$\mathbf{B} = \nabla\Psi \times \mathbf{e}_3 + B^3\mathbf{e}_3,$$
$$\mathbf{v} = \nabla\varphi \times \mathbf{e}_3 + v^3\mathbf{e}_3, \tag{2}$$

where the superscripts and subscripts indicate contravariant and covariant components of a vector, respectively.

By taking into account the representation (2), the system of Eqs.(1) can after some manipulations be reduced to the following scalar partial differential equations:

$$\{\varphi, \Psi\} = \{\Phi, \Psi\} = \{\rho, \Psi\} = 0,$$
$$\{P + \rho v^2 / 2 - \rho g_{33} v^3 c(d\Phi / d\Psi), \ \Psi\} = 0,$$
$$\{P + \rho v^2 / 2 - g_{33}B^3 c(d\Phi / d\Psi) / 4\pi(d\varphi / d\Psi), \ \Psi\} = 0, \tag{3}$$
$$\{g_{33}B^3 - 4\pi\rho g_{33}v^3(d\varphi / d\Psi), \ \Psi\} = 0,$$
$$v^3 = (d\varphi / d\Psi)B^3 + c(d\Phi / d\Psi),$$

$$\Delta\Psi\nabla\Psi - 4\pi\rho\Delta\varphi\nabla\varphi - 2\pi v^2\nabla\rho = -4\pi\nabla(P + \rho v^2 / 2) - B^3\nabla(g_{33}B^3) + 4\pi\rho v^3\nabla(g_{33}v^3),$$

where the following definitions have been employed

$$\{x, y\} \equiv \frac{1}{\sqrt{g}}\left(\frac{\partial x}{\partial a}\frac{\partial y}{\partial \theta} - \frac{\partial x}{\partial \theta}\frac{\partial y}{\partial a}\right),$$
$$\Delta x \equiv \frac{1}{\sqrt{g}}\frac{\partial}{\partial a}\left(\frac{g_{22}}{\sqrt{g}}\frac{\partial x}{\partial a} - \frac{g_{12}}{\sqrt{g}}\frac{\partial x}{\partial \theta}\right) + \frac{1}{\sqrt{g}}\frac{\partial}{\partial \theta}\left(\frac{g_{11}}{\sqrt{g}}\frac{\partial x}{\partial \theta} - \frac{g_{12}}{\sqrt{g}}\frac{\partial x}{\partial a}\right), \tag{4}$$

g_{ik} are the coefficients of the metric tensor, $g = \det g_{ik}$.

Eqs.(3) describe the general structure of the magnetic and the velocity fields, and of the pressure and density profiles for a toroidal plasma equilibrium with flow. Note that Eqs.(3) are obtained under the assumption that the velocity and magnetic fields are nonparallel.

The modified Grad-Shafranov equation. Based on quasi-toroidal co-ordinates, with the help of Eqs.(3) and (4) one may easily derive the following useful expressions

$$\Pi \equiv [P + \rho v^2 / 2 - \rho g_{33}c^2(d\Phi / d\Psi)^2] / [1 - 4\pi\rho(d\varphi / d\Psi)^2] = \Pi(\Psi),$$
$$B^3 = \left[I / g_{33} + 4\pi\rho c(d\varphi / d\Psi)(d\Phi / d\Psi)\right] / \left[1 - 4\pi\rho(d\varphi / d\Psi)^2\right], \tag{5}$$
$$v^3 = \left[(I / g_{33})(d\varphi / d\Psi) + c(d\Phi / d\Psi)\right] / \left[1 - 4\pi\rho(d\varphi / d\Psi)^2\right],$$

where the poloidal current $I = I(\Psi)$ is a surface function.

The last one of Eqs.(3) gives the modified Grad-Shafranov equation for an incompressible plasma equilibrium with flow in the form

$$g_{33}\Delta\Psi\left[1 - 4\pi\rho\left(\frac{d\varphi}{d\Psi}\right)^2\right] + g_{33}\frac{|\nabla\Psi|^2}{2}\frac{d}{d\Psi}\left[1 - 4\pi\rho\left(\frac{d\varphi}{d\Psi}\right)^2\right] + \frac{1}{2}\frac{d}{d\Psi}\left[\frac{I^2}{1 - 4\pi\rho(d\varphi / d\Psi)^2}\right] +$$

$$+ 4\pi g_{33} \frac{d\Pi}{d\Psi} + \frac{(g_{33})^2}{2} \frac{d}{d\Psi} \left[\frac{4\pi\rho c^2 (d\Phi / d\Psi)^2}{1 - 4\pi\rho(d\varphi / d\Psi)^2} \right] = 0, \tag{6}$$

where the differential operator $|\nabla\Psi|^2$, appearing in Eq.(6), is given in tensor notation by

$$|\nabla\Psi|^2 = \frac{g_{11}}{g} \left(\frac{\partial\Psi}{\partial\theta} \right)^2 + 2\frac{g_{12}}{g} \left(\frac{\partial\Psi}{\partial\theta} \right) \left(\frac{\partial\Psi}{\partial a} \right) + \frac{g_{22}}{g} \left(\frac{\partial\Psi}{\partial a} \right)^2 \tag{7}$$

In the static limit ($d\varphi / d\Psi = d\Phi / d\Psi = 0$) Eq.(6) reduces to the classical Grad-Shafranov equation for the potential Ψ.

Equilibrium with nested magnetic surfaces. Following Shafranov [2], we consider an equilibrium with nested-in circular magnetic surfaces wrapped around a single magnetic axis, which is shifted relatively to the geometric axis by an amount ξ. For such configurations a general magnetic field can suitably be represented in the form [3]

$$B^i = \frac{1}{2\pi\sqrt{g}} (0, \chi', \Theta'), \tag{8}$$

where χ and Θ are the poloidal and toroidal magnetic fluxes, $(\ldots)' = \partial(\ldots) / \partial a$.

Thus the representation (8) of the magnetic field is formally obtained from the one of Eq.(2) by the transformation

$$\begin{aligned} B^3(a,\theta) &\Rightarrow \left(1 / 2\pi\sqrt{g}\right)\Theta' \\ \Psi(a,\theta) &\Rightarrow \Psi(a) = -(1 / 2\pi)\chi(a). \end{aligned} \tag{9}$$

Now the potential Ψ only depends on the radial co-ordinate a, immediately leading to the following relations for the physical variables:

$$\varphi = \varphi(a), \ \rho = \rho(a), \ I = I(a), \ \Phi = \Phi(a), \ \Pi = \Pi(a), \ v^1 = B^1 = 0, \ v^2 = (d\varphi / d\Psi)B^2. \tag{10}$$

The equilibrium, described by Eq.(6), can be investigated by means of an expansion with respect to the inverse aspect ratio $\varepsilon = a / R$. Following [3], we obtain with the help of Eq.(5) by neglecting terms of the order $O(\varepsilon^3)$ the non-zero components of the metric tensor g_{ik} in the form:

$$\begin{aligned} g_{11} &= 1 + 2\xi'\cos\theta, \quad g_{12} = (a^2\lambda' - a\xi')\sin\theta, \quad g_{22} = a^2 + 2\lambda a\cos\theta, \\ g_{33} &= (R - \xi + a\lambda / 2 - a\cos\theta)^2, \quad \sqrt{g} = aR(1 + (\xi' + \lambda - ka\cos\theta)), \\ \lambda &= -\xi' - ka / (1 + 4\pi\rho cR^2 (d\varphi / d\Psi)(d\Phi / d\Psi) / I). \end{aligned} \tag{11}$$

Under the conventional tokamak ordering, Eq.(6) is solved by the formal ordering

$$B_\phi^0, q \approx 1; \quad B_\theta^0 / B_\phi^0, \Delta \approx \varepsilon; \quad P^0 / (B_\phi^0)^2, \rho(v_\phi^0)^2 / (B_\phi^0)^2, \rho(v_\theta^0)^2 / (B_\theta^0)^2 \approx \varepsilon^2, \tag{12}$$

where the superscript "0" denotes the cylindrical terms.

In the leading order $O(\varepsilon^2)$ Eq.(6) describes the stationary cylindrical equilibrium

$$\frac{d}{da}\left[P^0 + \frac{(B^0_\theta)^2 + (B^0_\phi)^2}{8\pi} \right] + \frac{1}{4\pi a}(B^0_\theta)^2 = 0, \tag{13}$$

where

$$B^0_\phi = I/R + E^0_a(v^0_\theta / c^0_{A\theta})(c / c^0_{A\theta}), \quad E^0_a = -d\Phi / da. \tag{14}$$

In the next order ($\approx \varepsilon^3$), Eq.(6) describes the first-order toroidal correction to the cylindrical equilibrium (13) leading to

$$\frac{1}{a}\frac{d}{da}\left(a\xi' B^{0\,2}_\theta \right) = \frac{B^{0\,2}_\theta}{R} - \frac{8\pi a}{R}\frac{d}{da}\left(P^0 + \rho v^{0\,2}_\phi / 2 \right), \tag{15}$$

with the relations

$$v^0_\phi = \frac{v^0_\theta}{B^0_\theta}\frac{I}{R} + \frac{cE^0_a}{B^0_\theta}, \quad v^0_\theta = \frac{d\varphi}{d\Psi}B^0_\theta \tag{16}$$

If the plasma is surrounded by a rigid wall at $a = a_0$, then we have $\xi(a = a_0) = 0$. With the help of this boundary condition, we obtain from Eq.(15) the following simple expression for the Shafranov shift ξ:

$$\xi = -\frac{1}{R}\int_a^{a_0} \frac{da'}{a'B^{0\,2}_\theta}\int_0^{a'} a''B^{0\,2}_\theta da'' + \frac{8\pi}{R}\int_a^{a_0}\frac{da'}{a'B^{0\,2}_\theta}\int_0^{a'} a''^2\frac{d}{da''}(P^0 + \frac{\rho v^{0\,2}_\phi}{2})da'' \tag{17}$$

In the case of $d\varphi / d\Psi = 0$, Eqs.(13) and (17) describe an equilibrium with purely toroidal and in the case $d\Phi / d\Psi = 0$ - one with purely parallel rotation.

On conclusion we note, that from the condition $\Pi = \Pi(a)$ it follows, that in the presence of flow the magnetic surfaces do not coincide with the one of constant pressure

$$P = P^0(a) + P^1(a)\cos\theta,$$
$$P^0(a) = \Pi(a) - \rho(v^0_\phi)^2 / 2 - \rho(v^0_\theta)^2 / 2 + \rho(cE^0_a / B^0_\theta)^2, \tag{18}$$
$$P^1(a) = -\rho(v^0_\theta)^2(ka - \xi') - \rho ka[(I/R)^2(v^0_\theta / B^0_\theta)^2 + (cE^0_a / B^0_\theta)^2 + (cE^0_a / B^0_\theta)(v^0_\theta / c^0_{A\theta})].$$

Now the pressure consist of two parts: the term $P^0(a)$, which is constant on the magnetic surfaces, and its deviation $P^1(a)\cos\theta$ arising from a finite plasma flow.

References.
[1]   W.Kerner, S.Tokuda. Z.Naturforsch., **42a**, 1154 (1987).
[2]   V.D.Shafranov. Nucl.Fusion, **4**, 213 (1964).
[3]   L.S.Solov'ev, V.D.Shafranov. Rev.Plasma Physics, v.5, p.1, Consultant Bureau, New York, 1970.

DISTRIBUTION OF DIVERTOR PLASMA FLUXES IN THE "HELIOTRON E" DEVICE

V.Voitsenya, V.Chechkin, T.Mizuuchi[1], H.Zushi[2], K.Nagasaki[1], M.Nakasuga[2],
H.Okada[1], **S.Masuzaki**[3], S.Besshou[2], A.Hayakawa[1], K.V.Khlopenkov[3], H.Funaba[1],
T.Hamada[1], K.Kondo[2], F.Sano[1], S.Sudo[3], O.Motojima[3], T.Obiki[1]

Institute of Plasma Physics, 310108, Kharkov, Ukraine
[1]*Institute of Advanced Energy, Kyoto University, Gokasho, Uji 611, Japan*
[2]*Graduate School of Energy Science, Kyoto University, Gokasho, Uji 611, Japan*
[3]*National Institute for Fusion Study, Nagoya 464-01, Japan*

1. Introduction

The Heliotron E device is characterized by a very "deep" insertion of the outermost magnetic surface (OMS) into the vacuum chamber: in any cross section both x-point-like area is located at a rather long distance, $\Delta r \cong 10$ cm, from the chamber wall. In this respect, Heliotron E differs from other stellarator-type devices that have the vacuum chamber inside the helical coils. Due to this feature, Heliotron E has a natural divertor configuration like U-3M and LHD. The divertor flows in Heliotron E hit some regions of rounded parts of the chamber which played the role of a divertor plate. Positions of maxima in the flow distributions agree well with the plots of the longest open field lines [1,2].

For the detailed investigation of divertor plasma flow distributions in Heliotron E, eight array of plane collectors (with 6-7 ones in each array) have been installed at four cross sections of a magnetic field period. The collectors of 5×0.8 cm^2 in size were placed at 1.5cm from the wall along the minor azimuth, Θ, with locations of the central ones in every set at $\Theta = 0°$, $45°$, $90°$, $135°$, $180°$, $225°$, $270°$ and $315°$. Practically, these Θ coordinates of the collectors were identical to positions of "x-points" in corresponding cross sections.

The collectors were biased to -120V to measure ion saturation currents (ISC). So, the plasma flow along the open magnetic field lines crossing collector's surfaces were measured. The poloidal distribution of ISC along probes in one array is measured per a discharge. To obtain the divertor flow (DF) distribution on the whole magnetic field period, it is necessary to have 8 reproducible discharges at least.

Using this probe system, a quite complete study of divertor flows was carried out for different experimental conditions of Heliotron E: various magnetic configurations, different methods of plasma maintaining and heating, various heating power, and with hydrogen or lithium pellet injection. This paper presents some results of this study.

2. Effects of magnetic configuration

The utilization of three groups of coils in Heliotron E for producing the $\ell = 2$ heliotron/ torsatron magnetic configuration allows to vary the magnetic surface characteristics in a wide range. An additional vertical field shifts the magnetic axis horizontally. This axis shift leads to the change of all parameters of the magnetic configuration [3]. An additional toroidal field results in changing the size of OMS and parameters of the magnetic, but almost does not change the magnetic axis position.

The scenario of discharges was similar to that described in [2]: plasma was built up in conditions of electron cyclotron resonance (ECH-1 phase) at fundamental frequency (f = 53 GHz) or at the second harmonic (f = 106 GHz). Close to the end of this phase, the neutral beam injection phase (NBI-1) started with several neutral beam injectors, leading to increase of the plasma pressure. Near the quasi-steady state phase of the discharge, the second group of

gyrotrons were pulsed in different combinations (ECH-2 phase): 53 GHz or 106 GHz section only, or both of them simultaneously. Finally, after finishing second ECH pulse, the rest of NB injectors were energized giving further change of plasma parameters (NBI-2 phase). In some cases lithium pellets were injected during the NBI-2 phase.

Figure 1 shows $\Gamma(\Theta)$ distributions obtained during the first ECH phase for two cases: with and without the magnetic axis shift ($\Delta R = -3$ or 0 cm), the former corresponds to the regime of optimal energy confinement in Heliotron E [3]. It follows from these data that DF distributions are very much inhomogeneous and the strongest asymmetry is in the vertical direction, which is a characteristic peculiarity of DF measurements in majority of regimes investigated. Comparing both Θ dependencies, one can conclude that the strongest effect of axis shift on $\Gamma(\Theta)$ distribution is observed for those probe sets that are located at the inner side of torus: $\Theta = 180°$ and 225°. It means that with horizontal axis shift the mostly changeable is the index of in/out asymmetry, i.e., the ratio of $\Gamma(180°)/\Gamma(0°)$, which increases from 0.27 for $\Delta R = 0$ cm to 1.8 for $\Delta R = -3$ cm.

The full in/out asymmetry of DF distributions can be characterized by the ratio of the total inward flow value, i.e., $\Gamma_{in} = \Gamma(135°) + \Gamma(180°) + \Gamma(225°)$, to the total outward flow, $\Gamma_{out} = \Gamma(315°) + \Gamma(0°) + \Gamma(45°)$. This ratio is almost linear function of ΔR as it is shown in Fig.2 for initial ECH-1 (a) and for the NBI-1 (b) phases of a discharge. Note that for the initial ECH discharge phase the inward flow exceeds the outward flow already with about -2 cm inward shift, and for the later NBI stages both flow values become to be close each other with magnetic axis ~ 4 cm inward shifted.

The additional toroidal magnetic field influences mostly on the up/down asymmetry of a DF distribution. Similar to in/out ratio, the up/down asymmetry of DF can be characterized by the ratios $\Gamma(90°)/\Gamma(270°)$ or $\Gamma_{up}/\Gamma_{down}$ where $\Gamma_{up} = \Gamma(135°) + \Gamma(90°) + \Gamma(45°)$ and $\Gamma_{down} = \Gamma(225°) + \Gamma(270°) + \Gamma(315°)$. For strongly shrunk magnetic surfaces, namely, with $B_{tor} = 0.18T$ in the counter direction to the main toroidal field produced by helical coils, the $\Gamma(90°)/\Gamma(270°)$ ratio was found to be close to unit. The equalization of fluxes "up" and "down" was obtained also in the original configuration, i.e., without additional toroidal field, after the main magnetic field direction was changed (from clockwise to counterclockwise). These facts can be explained by the influence of the limiter which "scrapes" some part of the divertor plasma subjected to a toroidal drift when moving along the open magnetic field lines.

3. Effects of heating conditions

In all experiments with fixed magnetic configuration the outward shift of magnetic surfaces due to plasma pressure is small enough [4] to be neglected from the view point of changing the locations of magnetic field line "footprints' on probe surfaces. Thus, for every given magnetic configuration any change of DF distribution observed during the discharge pulse has to be prescribed to peculiarities of changing the plasma diffusion across magnetic field (portion of trapped particles, density and temperature gradient and so on). The manifestation of these peculiarities at different phases of a discharge results in changing the DF distribution along every probe set and global $\Gamma(\Theta)$ distribution, as well as the in/out and up/down asymmetry. Besides, comparing time behaviour of the sum of all $\Gamma(\Theta)$ values we can make a qualitative conclusion concerning the plasma particle loss rate at different phases of a discharge.

In Table 1 for the $\Delta R = -2$cm case and for different discharge phases shown are: asymmetry indices Γ_{in}/Γ_{out} and $\Gamma_{up}/\Gamma_{down}$, and also the total flux $\Gamma_{total} = \Sigma\Gamma(\Theta_i)$ normalized to the mean plasma density, n_e, measured by FIR interferometer along the central vertical channel.

It is seen that all values shown in Table 1 are influenced by any variation of experimental conditions. The most significant differences were observed between cases when plasma was initiated at fundamental ECH (53GHz) or at the second harmonic ECH (106GHz). The increase of heating power reveals the increase of total particle loss, independently on the method of plasma heating in use, however, without so big change of Γ_{in}/Γ_{out} and $\Gamma_{up}/\Gamma_{down}$ ratios.

Experimental Conditions	$\Gamma_{total}/n_e,$ $mA/10^{11}cm^{-3}$	Γ_{in}/Γ_{out}	$\Gamma_{up}/\Gamma_{down}$
ECH-1 (53)	5.1	1.26	0.15
ECH-1 (106)	15.1	0.8	0.42
NBI-1	12.7	0.69	0.1
NBI-1+ECH-2 (53)	26.2	0.7	0.1
NBI-1+ECH-2 (53+106)	26.2	0.85	0.15
NBI-2	22	0.81	0.2
NBI-2+ECH-2 (53)	25	0.74	0.16
NBI-2+ECH-2 (53+106)	30	0.63	0.15

Table 1. Γ_{in}/Γ_{out} and $\Gamma_{up}/\Gamma_{down}$ and the total flux $\Gamma_{total}=\Sigma\Gamma(\Theta_i)$ normalized to the mean plasma density for different discharge phases ($\Delta R=-2cm$)

4. Effect of pellet injection

In several series of shots with injection of lithium pellets [5] the DF distribution were also measured. The injection of pellets was provided near the end of NBI-2 phase, however, no complete series of 8 identical shots was done successfully. Thus, we present here effects of pellet injection on the DF distribution inside the individual probe sets.

Fig. 3 shows data for probe sets located at $\Theta=180°$ (a) and 270° (b) for the original configuration ($\Delta R = 0$). Three series of points correspond to different time intervals through a discharge: 1- just before the pellet injection, 2- soon after pellet injection, 3- just before switching off the NBI power. One can see that after pellet was injected, the DF distribution inside both probe sets became to be wider. Such behaviour might be related with increase of collision frequency due to sudden plasma temperature decrease [5]. The pellet injection leads also to changing the in/out and up/down asymmetry indices.

Qualitatively similar results were obtained for the case with shifted magnetic axis ($\Delta R = -2$ cm). In this series of shots the $\Gamma(180°)/\Gamma(0°)$ ratio decreased from ~0.65 at the beginning of NBI-2 phase to ~0.47 after pellet injection. But at the same time, for the $\Gamma(90°)/\Gamma(270°)$ ratio some increase was observed, from ~0.04 to ~0.1.

5. Conclusive remarks

In conclusion, we can summarize the main results of this paper as follows.

- The inhomogeneity of the diverted plasma flow distribution was observed in Heliotron E in all cases when measurements of particle (or heat [1]) flows were carried out. We can say that, practically, the observation of a DF distribution with small homogeneity along a divertor slit is very exclusive event in this machine, like probably in any other ones.
- The degree of inhomogeneity of flow distribution depends strongly on characteristics of vacuum magnetic configuration, as well as on the details of an experiment that determines

the plasma parameters. Some of effects observed can be stipulated by generation of trapped particles with density and space location different for various stages of a discharge.

− Thus, the knowledge of mapping of vacuum magnetic field line traces in a divertor region is not enough to predict the real quantitative picture of divertor plasma distribution in the heliotron/torsatron type machines.

References

1. T.Mizuuchi, H.Matsuura, et al., In Proc. of 18th EPS Conf. on Contr. Fusion Plasma Phys., Berlin, 1991, vol.15C, Part 2, p.III-65.
2. V.V.Chechkin et al. Diverted plasma studies under NBI and ECH conditions in Heliotron E. - prepared for publication.
3. T. Obiki, S.Sudo, et al., Proceedings of 13th IAEA Conf., Washington, 1990, vol.2, p.425.
4. S.Besshou, K.Ogata, et al., Nucl. Fusion, vol. 35 (1995) 173.
5. V.Yu.Sergeev, K.V.Khlopenkov, et al., Research Report, NIFS-428, Nagoya, 1996.
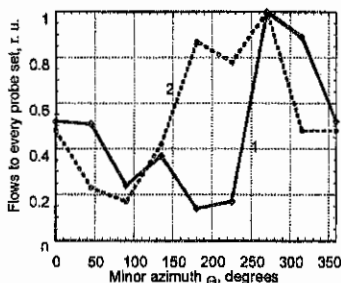
Fig.1. Divertor flow distribution vs minor azimuth Θ.
1 - no magnetic axis shift case,
2 - 3cm inward shift of magnetic axis.
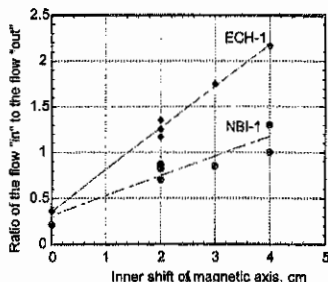
Fig. 2. Influence of the inward magnetic axis shift on the in/out asymmetry for the initial ECH and NBI phases of a discharge.
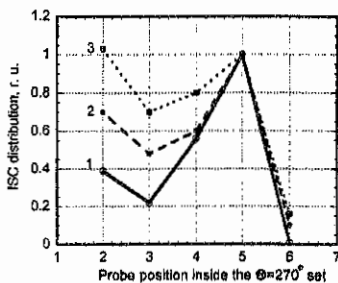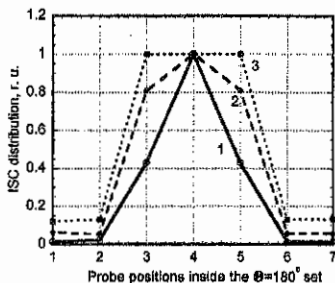
Fig.3. ISC distributions inside Θ=180° (a) and 270° (b) probe sets for the nonshifted magnetic axis case.

Theory of Ion and Impurity Transport in Edge Plasmas

P Helander[1], F Wising[2], Peter J Catto[3], and **R D Hazeltine**[4]

[1]UKAEA Fusion, Culham, Abingdon, Oxon, OX14 3DB, U.K.
(UKAEA/Euratom Association)

[2]Chalmers University of Technology, S-412 96 Göteborg, Sweden.

[3]PSFC, Massachusetts Institute of Technology, Cambridge, MA 02139, USA.

[4]Institute for Fusion Studies, The University of Texas at Austin, TX 78712, USA.

Abstract: The transport of ions impurities in an impure, partially ionized, edge plasma is examined. The presence of neutral atoms is found to enhance the thermal force between main ions and impurities, while not affecting the dynamical friction. An additional force on the impurities arises when the neutral viscosity is large enough to compete with the parallel ion flow. This force is parallel to the magnetic field and is caused by the rapid cross-field diffusion of neutrals.

1 Introduction

To avoid excessive heat and particle loads on the first wall, it appears necessary for large tokamaks to operate in a regime where the divertor plasma detaches. Detachment can be induced by introducing impurities into the plasma edge, which gives rise to radiative cooling of the divertor plasma and can lower the temperature to the range of 1 eV or less, where recombination occurs. The neutral atom density then rises in the divertor, and the plasma loses parallel momentum and energy when interacting with the recycling neutrals by charge exchange. The plasma detaches from the plates, and a self-sustained gas target is thus established. A key difficulty with this scenario is the problem of impurity transport. The burning core plasma must necessarily be quite pure to avoid Bremsstrahlung losses, while enough impurities should be present in the edge to facilitate detachment. In the present work, we examine the kinetic theory of impurity transport in a partially ionized plasma, and find that the presence of neutrals alters the transport properties of impurity ions.

2 Kinetic Theory

We consider an impure, partially ionized, edge plasma, where the (hydrogenic) bulk ions interact with neutral atoms by charge exchange, ionization and recombination. The kinetic equations for ions and neutrals are [1,2,3]

$$\mathbf{v} \cdot \nabla f + \frac{e}{m_i} \left(\mathbf{E} + \mathbf{v} \times \mathbf{B} \right) \cdot \frac{\partial f}{\partial \mathbf{v}} = C(f) - X(f,g) + \nu_z g - \nu_r f, \tag{1}$$

$$\mathbf{v} \cdot \nabla g = X(f,g) - \nu_z g + \nu_r f, \tag{2}$$

where f and g are the ion and neutral distribution functions, ν_z and ν_r the ionization and recombination rates, and the charge exchange operator is $X(f,g) = K_x \left(n_n f - n_i g \right)$ with n_i and n_n the ion and neutrals densities, respectively, and $K_x = \nu_x / n_i$ the charge exchange rate constant. We employ the ordering

$$\delta \sim \frac{v_T / L_\perp, \nu_z, \nu_r}{\Omega, \nu_{ii}, \nu_x} \sim \frac{L_\perp}{L_\parallel} \ll 1,$$

where $L_\parallel$ and $L_\perp$ are the parallel and perpendicular length scales, $\Omega \equiv eB/m_i$, $v_T \equiv (2T_i/m_i)^{1/2}$, and ν_{ii} is the ion collision frequency. Analysis of (1), (2) gives rise, in second order, to a "Spitzer problem"

$$C_{iz}(F) = u_\parallel \left[A_1 + \left(\frac{m_i u^2}{2T_i} - \frac{5}{2} \right) A_2 \right] f_0, \tag{3}$$

governing the transport of impurities (z) relative to the main ions (i). Here, f_0 is Maxwellian, $\mathbf{u} \equiv \mathbf{v} - \mathbf{V}$ is the velocity relative to that of the impurities, and F is the odd part (in $u_\parallel$) of f_2. The thermodynamic forces A_1 and A_2 driving the transport are

$$A_1 = a_1 + \frac{m_i u_\perp^2}{2T_i} a_3, \qquad A_2 = a_2 + \frac{m_i u_\perp^2}{2T_i} a_4,$$

where (if $\nu_{ii} \sim \nu_x \ll \Omega$)

$$
\begin{aligned}
a_1 &\equiv \frac{n}{n_i} \left(\nabla_\parallel \ln p + \frac{m_i \mathbf{V} \cdot \nabla V_\parallel}{T_i} \right) - \frac{eE_{\parallel *}}{T_i}, \\
a_2 &\equiv \frac{n}{n_i} \nabla_\parallel \ln T_i, \\
a_3 &\equiv -\frac{n_n}{n_i} \left[\nabla_\perp \cdot \left(\frac{\nabla_\perp V_\parallel}{\nu_x} \right) + \frac{2}{\nu_x} \nabla_\perp V_\parallel \cdot \nabla_\perp \ln n_n \right], \\
a_4 &\equiv -\frac{2n_n}{n_i \nu_x} \nabla_\perp V_\parallel \cdot \nabla_\perp \ln T_i,
\end{aligned}
$$

$n = n_i + n_n$, and $\mathbf{E}_* \equiv \mathbf{E} + \mathbf{R}_{ie}/e$, with $\mathbf{R}_{ie}/e$ the force between electrons and ions. Thus, a_1 and a_2 are the same thermodynamic forces as those appearing in the classical Spitzer

problem but enhanced by the factor n/n_i (except in the electric field term). The reason for this enhancement is that the neutrals, through charge exchange reactions, carry information about the ion kinetics, as explained in detail in Ref [3]. The appearance of the new thermodynaymic forces a_3 and a_4 is due to the diffusion of neutrals across the magnetic field, which competes on an equal footing with conventional parallel transport.

Solving this modified Spitzer problem in the Lorentz limit gives the particle and heat fluxes of the bulk ions relative to the impurities,

$$\Gamma_\parallel = -\frac{32}{3\pi}\frac{n_i T_i \tau_{iz}}{m_i}\left(a_1 + \frac{3}{2}a_2 + \frac{8}{5}a_3 + 4a_4\right),$$

$$q_\parallel = -\frac{32}{3\pi}\frac{n_i T_i \tau_{iz}}{m_i}\left(\frac{3}{2}a_1 + \frac{25}{4}a_2 + 4a_3 + 18a_4\right),$$

with $\tau_{iz} = 3(2\pi)^{3/2}\epsilon_0^2 m_i^{1/2}T_i^{3/2}/n_z Z^2 e^4 \ln\Lambda$ the ion-impurity collision time. Note that these parallel flows are driven not only by parallel gradients, but also by perpendicular gradients in a_3 and a_4. The force exerted upon the impurities by the main ions becomes

$$R_{zi} = \frac{3\pi}{32}\frac{m_i n_i\left(V_{i\parallel} - V_{z\parallel}\right)}{\tau_{iz}} + \frac{3}{2}n\nabla_\parallel T_i + R_n,$$

$$R_n = -\frac{3}{5}n_n T_i \nabla_\perp\cdot\left(\frac{\nabla_\perp V_\parallel}{\nu_x}\right) - \frac{6T_i}{5\nu_x}\nabla_\perp V_\parallel\cdot\nabla_\perp n_n - \frac{6n_n}{\nu_x}\nabla_\perp V_\parallel\cdot\nabla_\perp T_i.$$

The first term in R_{zi} is the usual friction force and is not modified by the presence of neutrals. The next term, which is the thermal force, is enhanced by a factor n/n_i over the classical expression, and the third term, R_n, is caused entirely by the neutrals. It arises because of the diffusion of neutrals across the magnetic field, but is, of course, brought about by ion-impurity collisions.

3   Numerical results

To assess the importance of the preceding results for impurity transport in the tokamak edge, we have carried out simulations of the Alcator C-Mod divertor using the UEDGE code [4]. We simulate only the main ion and neutral dynamics, assuming a fixed fraction of stationary impurities which affect the plasma only through radiative losses in the energy equation. We then evaluate what the various forces on the impurities would be in this situation. Detachment is induced by introducing a fraction of 0.5 % carbon impurities, and results in a substantial decrease of the heat and particle fluxes to the targets with a simultaneous drop in electron temperature and increased volume recombination.

Figure 1 shows the thermal force and the new force R_n acting on the impurities. A positive force is parallel and a negative force is antiparallel to the magnetic field, which encircles the plasma core clockwise. The thermal force, being positive on the left and negative on the right, is mostly directed up from the divertor toward the core. The force R_n caused by the presence of neutrals exceeds, or is comparable to, the thermal force in the lower parts of the divertor and in the private flux region, and could therefore play a significant role in the transport of the impurities. The direction of R_n is sometimes in the favourable and sometimes in the unfavourable direction. To determine its net effect would require more extensive simulations.

(a)   (b)
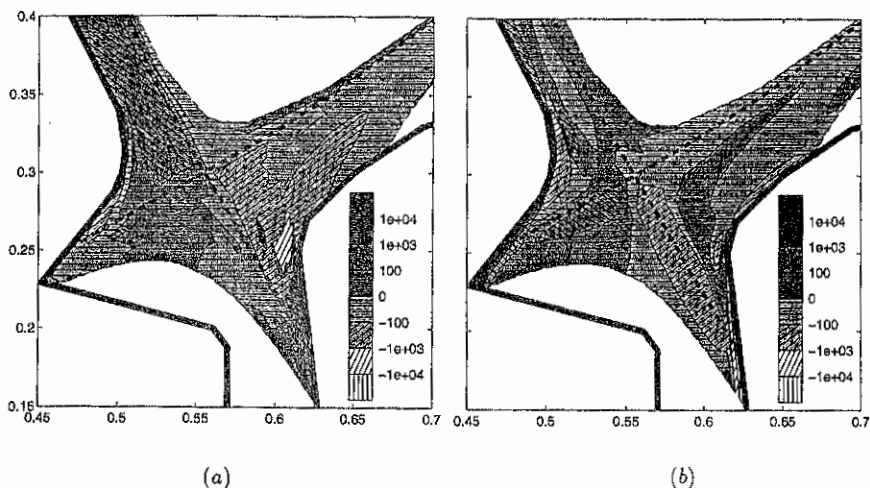
Fig 1. (a) The thermal force (in N/m^3), and (b) the force R_n between bulk ions and heavy impurities in Alcator C-Mod.

[1] R.D. Hazeltine et al., Nucl. Fusion **32**, 3 (1992).

[2] P.J. Catto, Phys. Plasmas **1**, 1936 (1994).

[3] P. Helander, S.I. Krasheninnikov, and P.J. Catto, Phys. Plasmas **1**, 3174 (1994).

[4] F. Wising et al., Contrib. Plasma Phys, **36** 136 (1996).

Divertor plasma flows affected by ExB drifts

A. Ödblom[1] and S.I. Krasheninnikov[2]

[1]Institute for Electromagnetic Field Theory, Chalmers University of Technology and
EURATOM-NFR Association, S-412 96 Göteborg, Sweden.
[2]Massachusetts Institute of Technology, Plasma Science and Fusion Center,
Cambridge, MA 02139, U.S.A.

Motivation: It is recognized that the peak heat load onto material surfaces leads to severe design constraints for the next generation of magnetic fusion experiments. Detachment is a promising operation scenario, and it is characterized by a significant drop in the plasma pressure along the field lines in the divertor volume, high radiation losses as well as a low temperature in front of the divertor plates. The strong variation of the plasma pressure along the magnetic field lines in the divertor can appear, not only due to plasma-neutral interactions and recombination [1], but also due to the presence of the electric fields and the associated sheared ExB drift velocity [2]. The electric field exists naturally in the scrape-off layer (SOL) plasma since it is generated by the inhomogeneous temperature and density distributions. It is therefore important to include the effects of electric fields in scrape-off layer models. We have in the present work analyzed a simplified edge model numerically and analytically in order to focus on the physical effects of the ExB driven flows in the divertor.

Model: We adopt the following model for the description of the dynamics of the plasma in the scrape-off layer and the divertor volume,

$$\frac{\partial n}{\partial t} + \nabla \cdot n\mathbf{v} = s \tag{1}$$

$$\frac{\partial Mnv_{\parallel}}{\partial t} + \nabla \cdot Mnv_{\parallel}\mathbf{v}_{\perp} + \nabla_{\parallel}Mnv_{\parallel}^2 = -\nabla_{\parallel}nkT \tag{2}$$

$$-\nabla_{\parallel}nkT - \alpha n\nabla_{\parallel}T + en\nabla_{\parallel}\phi + en\eta_{\parallel}j_{\parallel} = 0 \tag{3}$$

where n is the density, $v_{\parallel}$ is the ion velocity along the magnetic field, and ϕ is the electrostatic potential. M, k, α, $\eta_{\parallel}$ stand for the ion mass, the Boltzmann constant, the coefficient of the thermal force, and the Braginskii resistivity, respectively. The particle source is denoted with S, T is the electron temperature, whereas $T_i = 0$, and $j_{\parallel}$ is the parallel current. The magnetic field configuration is assumed constant and the field lines reach the sheaths in front of the target plates with a tilted angle, i.e. $\nabla_{\parallel}(...) \approx b \, \partial(...)/\partial y$, where $b = B_{pol}/B << 1$, and B_{pol} is the poloidal projection of the magnetic field strength B. The geometry is simplified to a closed Cartesian box

which poloidally (y-direction) is delimited by axisymmetric divertor target plates. The cross-field transport is due to the ExB-drift, which may lead to significant poloidal asymmetries which drives plasma currents. Here, cross-field currents are neglected and the parallel current density at the sheath reads,

$$j_{\scriptscriptstyle \parallel} = en(v_{\scriptscriptstyle \parallel} \pm c_s \sqrt{\frac{M}{2\pi m}} \exp(-\frac{e\varphi}{T}))$$ (4)

where the positive sign (negative sign) on the right hand side corresponds to the sheath where the magnetic field comes out from (goes into) the target, and $\varphi = \phi - \phi_t$, where ϕ_t is the potential of the target (in the present work is the effect of biasing not investigated). S and T are prescribed to model experimental observations of strong T variations along B in a high recycling case.

Results and discussions: Many features of stationary ExB driven flows of plasma and momentum in the divertor volume can be captured within a reduced 11/2D analytical model, where two dimensional effects are included into a one dimensional picture.
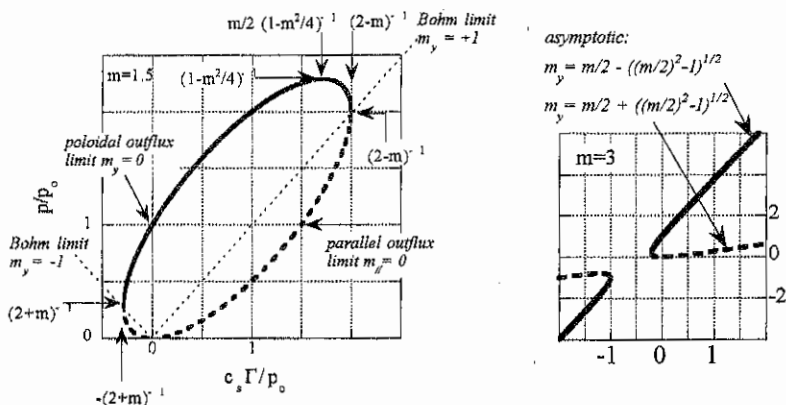
Fig. 1. Normalized plasma pressure p/p_o versus normalized poloidal flux $c_s\Gamma/p_o$ of ions when (a) $m \equiv v_{\scriptscriptstyle \parallel}/bc_s < 2$ in the left figure and (b) $m > 2$ in the right graph.

The model leads to a quadratic equation for the plasma pressure p, and the corresponding roots for the functional dependence of the pressure on the poloidal ion flux Γ is shown in Fig. 1 where $m_{\scriptscriptstyle \parallel} = v_{\scriptscriptstyle \parallel}/c_s$, $m_y = v_y/bc_s$, and p_o is the plasma pressure where m_y vanishes (c_s is the sound speed). Indicated in Fig. 1 is also the Bohm-Chodura sheath criteria in the presence of ExB drifts [3]. It could generally be expected that the integration constant can be determined by some constraints at the boundaries, for example the Bohm-Chodura sheath condition. It should

be noted, however, that the integration constants are entirely determined by the physical constraints introduced by the absorbing target plates instead of outer boundary conditions. Indeed, the outflow of plasma to the absorbing targets yields that the pressure within the plasma box is minimized which can be expressed in the following way,

$$\min_{g_o}[\max_{|y/y_{max}|\leq 1}[P^{\pm}(y,g_o)]] \equiv p_o \tag{5}$$

where $P^{\pm}$ is a function of the particle sources and includes the effect of poloidal and radial ExB-drift. The integration constants g_o and p_o are completely determined by eq. (5). As a result, various flow regimes are possible depending on the actual temperature profile and the strength of the drift-driven transport of plasma and momentum. An example in the case of strong drifts is shown in Fig. 2 which also illustrates that under certain conditions may two stationary solutions exist in the plasma interior. Note also the significant drop in total plasma pressure in front of the targets in Fig. 2. The temperature is low at the divertor plates compared to upstream values (4%) and high-recycling is considered.
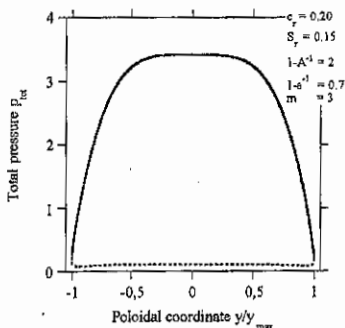
Fig. 2. The total plasma pressure profile in the case of strong ExB-drifts, which allows for two states in the inner plasma region (solid/dashed). Note also the significant variation in the total plasma pressure along the field lines.

The dynamical properties of the SOL plasma has been studied numerically by solving eqs.(1-4). In case of weak drifts the flow evolves towards a stationary state characterized by poloidal conservation of the radially integrated plasma momentum $\Pi(y) = \int dx(p+Mnv_{\parallel}v_y/b) =$ constant, and of particles, since there is no loss of plasma or momentum to the side-walls. The stationary state is reached within a few poloidal transit times (long time in the cold regions). The pressure gradient balances the ion inertia term for vanishing drifts and the total plasma pressure $p+Mnv_{\parallel}^2$ is constant along a field line cf Fig. 3a. A substantial drop in total pressure in front of the divertor plates is observed when the ExB drift is strong and associated with a non-vanishing divergence in the momentum equation as illustrated in Fig. 3b. Significant variation is obtained when $v_{\perp}/bc_r > 1$ i.e. $\Delta_r < \rho_p$, where Δ_r is the radial width of the temperature profile. Moreover, the flow in the divertor chamber does not reach a stationary state in the case of strong drifts. Nonlinear shockwave-like transients remain, but these structures are localized towards the radial edges of the SOL, and the main flow is stable. This dynamical behaviour is induced by the radial feed of plasma into the colder outer regions. Indeed, the radial convection becomes particularly important when the radial cross-over time is comparable to the poloidal transit time,

$\Delta_r/v_x < y_{max}/v_y$ which again yields $\Delta_r < \rho_p$. Thus, the flow pattern changes completely due to the ExB-drift. The calculations in Fig. 3 are based on high-recycling and temperature detachment; target temperature is 0.8 eV for a upstream temperature of 100 eV.
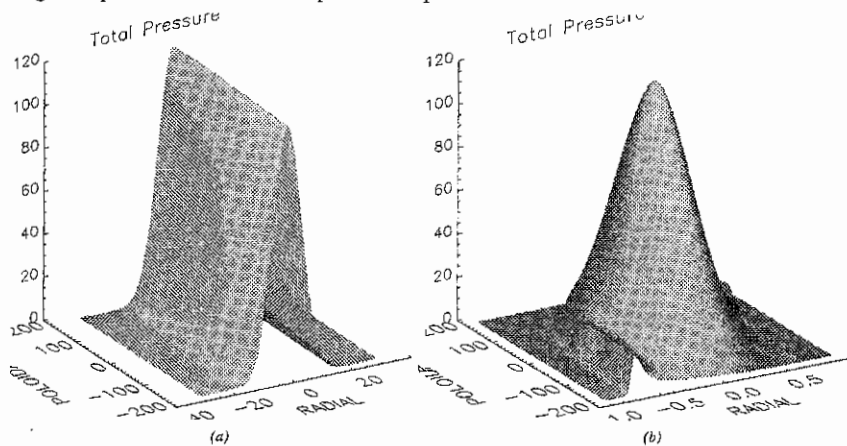
Fig. 3. The total plasma pressure profile in the case of (a) weak drifts, $\Delta_r/\rho_p=10$, and (b) strong drifts, $\Delta_r/\rho_p=0.3$, respectively. The coordinates are in units of the maximal poloidal ion gyro radius, $\rho_p=c/b\Omega$

Summary: It is shown numerically and analytically that the stationary total pressure in front of the divertor targets may, when ExB effects are important, be reduced several orders of magnitude compared to upstream values, which is a signature of detachment. At the same time the flow pattern is altered significantly due to the increased importance of the radial flow. Moreover, dynamical transients makes the flow locally unstable when ExB drifts are strong. Based on analytical modelling, two interior plasma solutions are under certain conditions found in the stationary flow of plasma and momentum.

References:

[1] F. Wising, S.I. Krasheninnikov, D.J. Sigmar, D.A. Knoll, T.D. Rognlien, B. LaBombard, B. Lipschutz, and G. McCracken, to appear in Jounal of Nuclear Materials.
[2] S.I. Krasheninnikov, D.J. Sigmar, and P.N. Yushmanov, Phys. Plasmas **2**, 1972 (1995).
[3] I.H. Hutchinson, Phys Plasmas **3**, 6 (1996).

Transport of intensive LHW pulses into the tokamak plasma and accompanying plasma biasing

L. Krlín, V. Petržílka, R. Klíma, P. Pavlo, J.A. Tataronis[a]

Institute of Plasma Physics, Acad. Sci., CR, 182 00, P.O. Box 17, Prague 8, CR

[a] University of Wisconsin, 1500 Engineering Dr., Madison, WI 53706, USA

1. Introduction

In a thermonuclear tokamak plasma, lower hybrid waves (LHW) are strongly absorbed at the plasma boundary (e.g. [1,2]), which prevents their penetration into the plasma core. To overcome this limitation, Cohen et al. [3] proposed the use of a train of intense short pulses instead of a continuous train of LHW. A pulse power as high as 10 GW for two pulse durations of 10^{-5} s and 10^{-8} s, with an averaged power of 100 MW, has been considered in [3]. Aspects of this approach were discussed in [4]. This proposed method opens a number of issues which should be studied more thoroughly. Among them, we mention the following: plasma biasing and nonlinear coupling of LHW (both caused by the effect of ponderomotive forces at the plasma boundary), possibilities of ponderomotive forces elimination, the scattering of LHW on low frequency density fluctuations, and the applicability of the quasilinear approximation. We address here these important issues.

2. Large variations of the plasma bias and plasma rotation induced by intense LH waves

A strong pulsed wave can also exert a strong poloidal ponderomotive force [5]. Our computations presented here show that, for intense LH wave pulses, this ponderomotive force may induce large stationary radial electric fields, up to about 10 kV/cm. This value is approximately two orders of magnitude higher than the electric field required for induction of enhanced confinement H modes by plasma biasing, see Fig. 1. Poloidal ponderomotive forces in front of LH grills would likely arise from wave propagation in the poloidal direction with respect to the toroidal magnetic field. Poloidal wave propagation is a possibility if the mutual phasing of the horizontal waveguide rows of the grill were of a suitable value. The appearance of strong radial electric fields produces poloidal and toroidal plasma rotation because of the ponderomotive force exerted by the LH wave.

3. Nonlinear wave coupling at very high LH powers

At large LH power levels, toroidal ponderomotive forces in front of the antenna structure may expel plasma from the space near grill mouth and thus reduce the plasma density, with consequent reduction in the wave coupling. This reduction in wave coupling could be weakened if local plasma heating occurs in front of the antenna grill. We assume that the boundary plasma temperature T_b grows with the growing launched LH power S, as observed on the ASDEX tokamak as $T_b = T_0(1 + S/S_T)$. We see that e.g. for $S = S_T$, the boundary temperature is twice that for zero LH power, $S = 0$. For $S >> S_T$, the boundary temperature is much higher with LH heating with the power density S, than for zero LH power. On the other hand, for $S << S_T$, the boundary temperature almost does not change, when the LH power grows. At ASDEX, the best fit of nonlinear reflection curves to experimental data was obtained for $S_T = 2$ kW/cm², for launched powers up to 4 kW/cm². As the typical launched LH powers in intense LH pulses would be much

higher, about 50 kW/cm², the corresponding S_T might be also higher. Because of the ponderomotive forces, the boundary plasma density n_b in front of the grill decreases as $n_b = n_0 \exp(-\delta)$, where $\delta = W/T_b$ and W is the ponderomotive potential of the LH wave $W = (e^2 E_0^2)/(4m\omega^2)$. The power in the the $5 - 10$ GW range corresponds to wave power densities of about 50 kW/cm² in front of the grill.

4. Conditions for good RF - plasma coupling

The potential W of the ponderomotive force is expressed in terms of radial RF power density S, $W_{max}[eV] \approx 8 \times 10^{11}(N_{\parallel}S)/(f_p f)$, where $f_p = \omega_{pe}/2\pi$, $f = \omega/2\pi$ and the reflection coefficient $R << 1$. For Cohen's et al. parameters with $f_p \geq f$, $W_{max} \leq 10 eV$. The deterioration of RF - plasma coupling in the Cohen's regime "B" with longer pulses ($\tau_p \approx 80\mu s$) can be avoided at boundary plasma temperature $T_b > 30 eV$ (collisional heating and/or parametric instabilities heating).

The characteristic time of plasma displacement is $\tau_i \approx (1/\omega N_{\parallel})(\varepsilon_{0i}/W_{max})^{1/2}$, where $\varepsilon_{0i} = m_i c^2$ is the ion rest energy. For Cohen's regime "A" ($\tau_p \approx 10^{-8} s$), $\tau_i \approx 10^{-7} s$ and, therefore, the ponderomotive effect is negligible.

5. Scattering on plasma fluctuations at the boundary

Scattering of lower hybrid waves on low frequency density fluctuations [6] can influence the pulse scheme. In the presence of the wave scattering from plasma density fluctuations at the plasma boundary, the spectrum of LH waves broadens.

As the density fluctuations have a very small wave vector $k_{\parallel}$ component along the magnetostatic field B, they do not change the lower hybrid $P(N_{\parallel})$ spectra directly, but only rotate in the scattering process the initially radial perpendicular component of the LH wave vector k, which leads to appearance of a nonzero poloidal k_θ component of the wave vector. Now, this nonzero poloidal k_θ component produced by the scattering can significantly contribute to the $k_{\parallel}$ at subsequent radial propagation of the LH wave in the sheared tokamak magnetostatic field (see Fig. 2). We find that the LH wave scattering on the boundary plasma fluctuations can significantly broaden $P(N_{\parallel})$ spectra, which results in enhanced LH wave absorption and in reflection of LH waves, before they reach the plasma center. This effect may be namely strong at low plasma boundary temperatures and high plasma densities.

6. Problem of applicability of the quasilinear approximation for the case of intensive wave pulses

The quasilinear approach is considered as an excellent tool for the description of LHW-plasma interaction. Nevertheless, the quasilinear approximation itself has been developed on the basis of the perturbative analysis, i.e., on assumption that the change of the particle velocities during the wave-particle interaction is small.

In case of large wave power fluxes, a possible change of particles energy during their single transit through the LHW cone can easily constitute a significant fraction of their original energy. This makes the reliability of the quasilinear approach questionable. Since the Cohen's model of the interaction of intensive pulses with the thermonuclear plasma largely depends on the quasilinear description (QLD), it is advisable to test the validity of QLD by means of direct numerical simulation (DNS) of this interaction.

The simulation is based on the equations of motion of particles in the tokamak geometry for a prescribed form of launched LHW spectrum. Our earlier numerical code, successfully used already for other waves in plasma [7], has been employed. The code is

based on the Hamiltonian formalism which enables to take into account all features of the particle dynamics.

The first numerical results already show some differencies from the quasilinear description. The most striking difference consists in a dramatic broadening of the diffusion coefficient with the potential $\phi > 1$ (cf. Fig. 3), which is accompanied by a slower increase of the coefficient within the resonant range (compared to the quasilinear scaling $D_{QL} \propto \phi^2$). The diffusion coefficient becomes significant even for the bulk electrons. As a consequence, the trapping region defined by $\Delta v = \sqrt{(e\phi_0)/m}$ (cf. Fig. 4) also much broadens (bulk electrons may get accelerated and become trapped). From this point of view, there exists some analogy with recent paper of Fuchs et al. [8].

Extension of the LHW-particles interaction down to the thermal velocities will result in a more intensive damping of LHW during their penetration into the plasma core and might therefore represent a serious obstacle for Cohen's proposal. A more accurate quantitative analysis is being performed.

7. Conclusion

All our results concerning nonlinear reflection coefficient of the LH wave, the plasma bias and plasma rotation induced by the LH wave, are critically dependent on the value of the boundary plasma temperature in front of the grill. For plasma temperatures of a few tens of eV in front of the grill, the reflection coefficient of the LH wave would be unacceptably high. On the other hand, for the boundary plasma temperature approaching the order of 100 eV, the value of the nonlinear reflection coefficient will approach the values according to the linear theory. At these larger boundary plasma temperatures and correspondingly higher plasma pressures, the ponderomotive forces are not strong enough to expel the plasma with higher pressure from the space in front of the grill, and to deteriorate the wave coupling in this way. Similarly, the plasma bias and the corresponding plasma rotation decrease with the growing plasma temperature. The possibility of the growth of the plasma temperature in front of the grill is supported by experiments. This is further supported by recent theoretical results concerning acceleration of electrons in the field of the LH wave in front of the grill. The LH wave scattering results in enhanced LH wave absorption and in reflection of LH waves, before they reach the plasma center.

The diffusion coefficient obtained from the direct numerical simulation appears to significantly differ from that predicted by the quasilinear theory. This might represent a serious obstacle for Cohen's proposal.

[1] R.S. Devoto, Fenstermacher M.E.: Nucl. Fusion **30** (1990) 362.

[2] P. Pavlo, L. Krlín, Z. Tluchoř: Nucl. Fusion **31** (1991) 711.

[3] R.H. Cohen et al.: 13th Conf. Plasma Phys. and Contr. Fusion (1990), Vol. 1, 805.

[4] P. Bertrand et al.: 21st Conf. on Contr. Fus. Plasma Phys., 1994, Part III, 1082.

[5] V. Petržílka, J. A. Tataronis, F. X. Söldner and L. Krlín, Plasma biasing by radial electric fields induced in front of the lower hybrid grill, submitted to Physics of Plasmas.

[6] P. L. Andrews, V. S. Chan and C. S. Liu, Phys. Fluids **28** (1985) 1148; V. Petržílka, Czech. J. Phys. **38** (1988) 937.

[7] L. Krlín, P. Pavlo, I. Malijevský: Physics Lett. A **226** (1997) 80.

[8] V. Fuchs et al.: Phys. Plasmas **3** (1996) 4023.

Figure captions

Fig. 1. Radial electric field E_r, induced by poloidal ponderomotive forces in front of LH grill, in dependence on the boundary plasma temperature. The boundary plasma density is $n_b = 2 \times 10^{18}$ m^{-3}, the wave frequency $f = 5$ GHz, the toroidal magnetostatic field $B_z = 5$ T, the poloidal magnetostatic field $B_\theta = 0.5$ T, the wave field profile in front of the grill is assumed in the form $(0.1 + (r/a)^s)^t$, $s = 2$, $t = 5$, the plasma minor radius $a = 2$ m, and the wave field amplitude in front of the grill is assumed as 5.5 kV/cm, which corresponds to the coupled wave power of the order of tens of kilowatts per cm^2, depending on the wave reflection coefficient.

Fig. 2. Broadening of LH spectral power density $P(N_\parallel)$ [a.u.] at various minor radii r for the case of LH wave, which was partially scattered by plasma fluctuations at the plasma boundary. The minor radius $a = 100$ cm, plasma temperature at the boundary $T_b = 30$ eV, magnetostatic field $B = 5$ T, LH wave frequency $f = 5$ GHz, and central plasma density $n(0) = 10^{20}$ m^{-3}, $N_\parallel$ is the parallel index of refraction – denoted as N_{par} in the Figure.

Fig. 3. The diffusion coefficient for the potentials indicated.

Fig. 4. Average velocity of the collection of particles after their passage through RF region.
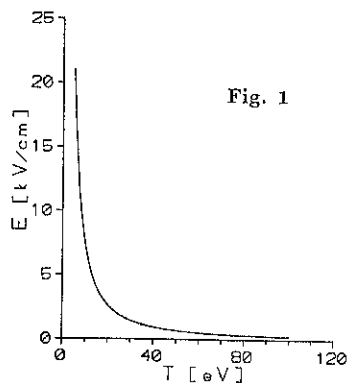
Fig. 1
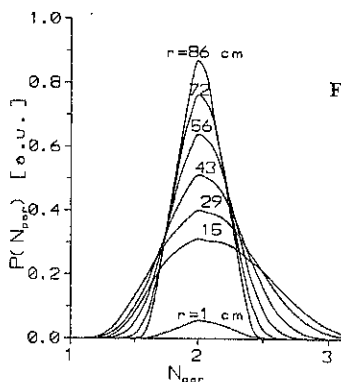
Fig. 2
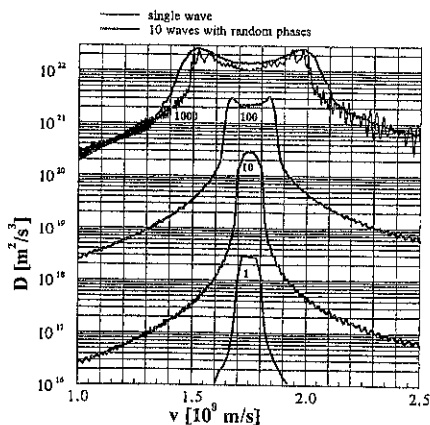
Fig. 3
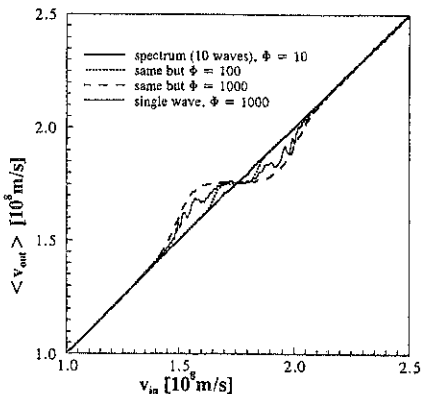
Fig. 4

Co-counter Asymmetry in Fast Wave Heating and Current Drive and Profile Control in NSTX

E.F. Jaeger, M.D. Carter, L.A. Berry, D. B. Batchelor, P. M. Ryan, C.B. Forest,*
H. Weitzner,† and R. Majeski‡

Oak Ridge National Laboratory, Oak Ridge, Tennessee 37831-8071
*General Atomics, San Diego, California 92186-5608
†Courant Institute of Mathematical Sciences, New York University, New York, NY 10012
‡Princeton Plasma Physics Laboratory, Princeton, New Jersey 08543

1. Introduction

Different plasma responses to neutral beam injection in directions co and counter to the plasma current have long been accepted as well understood in neutral beam heating of tokamak plasmas [1]. Similar differences have now been observed in electron heating and current drive experiments with toroidally phased antenna arrays in the ion cyclotron range of frequencies (ICRF) on the DIII-D tokamak [2]. Initially, such differences are puzzling because almost all radio frequency (RF) heating models are based on the homogeneous plasma dielectric tensor [3], which exhibits no obvious asymmetry for propagation in different longitudinal directions. But coupling of power between the antenna and the plasma is also a critical part of the problem, and it is here that the asymmetries become apparent. First, even for the homogeneous case, there are up-down (i.e., poloidal) asymmetries in wave propagation caused by the direction of Hall currents with respect to the applied magnetic field. This is observed as a shift in the poloidal spectrum of power radiated from the antenna in a magnetized plasma column with straight magnetic field lines [4]. The shift is symmetric in the longitudinal wave number, but symmetry is broken when a poloidal magnetic field is applied. This was first noticed in the ST tokamak [5] when split eigenmodes were observed for each value of the toroidal wave number.

In this paper, full-wave ICRF coupling models are applied to understand the difference in plasma response when antenna arrays are phased to drive currents co and counter to the plasma current. The source of this difference lies in the natural up-down asymmetry of the antenna's radiated power spectrum caused by Hall currents. When a poloidal field is applied, this up-down asymmetry acquires a toroidal component. The result is that plasma absorption (i.e., antenna loading) is shifted or skewed toward the co-current drive direction, independent of the direction of the magnetic field. When waves are launched to drive current counter to the plasma current, electron heating and current profiles are more peaked on axis, and this peaking becomes more pronounced at lower toroidal magnetic fields.

2. Symmetry of the Cold Plasma Wave Equation

Consider a two-dimensional (2-D) slab plasma in Cartesian coordinates with an external magnetic field B_0 aligned along the z axis. Assuming that the component of the RF electric field parallel to B_0 is zero (zero electron mass limit, [6]) and periodic dependence of the RF fields in the z direction, a simple wave equation can be written for B_z, the RF magnetic field in the longitudinal direction:

$$\left(\frac{\omega}{c}\right)^2 B_z + i\left[\frac{\partial B_z}{\partial y}\frac{\partial}{\partial x}\left(\frac{K_x}{\left(K_\perp - n_z^2\right)^2 - K_x^2}\right) - \frac{\partial B_z}{\partial x}\frac{\partial}{\partial y}\left(\frac{K_x}{\left(K_\perp - n_z^2\right)^2 - K_x^2}\right)\right] + \nabla\cdot\left(\frac{\left(K_\perp - n_z^2\right)\nabla B_z}{\left(K_\perp - n_z^2\right)^2 - K_x^2}\right) = 0 \qquad (1)$$

The second term (in square brackets) results from Hall currents that flow from the $E \times B$ force and is proportional to density and magnetic field gradients through the dielectric tensor element K_x. When K_x and $K_\perp$ are real, Eq. (1) is invariant under the transformation $B_z(x,y) \Rightarrow B_z^*(x, -y)$ or equivalently for the RF electric fields: $E_x(x,y) \Rightarrow E_x^*(x, -y)$ and $E_y(x,y) \Rightarrow -E_y^*(x, -y)$, where * denotes complex conjugate. The condition that K_x and $K_\perp$ are real is consistent with the usual cold plasma assumption of no collisions and therefore no absorption of wave energy. When collisions are included, K_x and $K_\perp$ become complex, and the up-down symmetry of Eq. (1) is destroyed.

These conclusions are borne out by full-wave calculations with the PICES [7] global wave code including a finite parallel RF electric field and warm plasma effects. The result in Fig. 1 is for a single toroidal harmonic, $n_\varsigma = 10$, with 32 poloidal (ϑ) harmonics and 100 radial (ρ) mesh points. The geometry is that of a tokamak similar to DIII-D with no poloidal magnetic field and $B_0 = -2.0$ T (into page), $R_{axis} = 1.8$ m, $\kappa = 1.9$ (elongation), $R_{plasma} = 2.31$ m, $f = 60$ MHz, and $n_{e,0} = 3.0 \times 10^{19}$ m^{-3}. The majority ion species is deuterium with a 2% minority fraction of hydrogen. Results are calculated for (a) zero temperature and (b) finite temperature. E_ρ and E_ϑ correspond to E_x and E_y, respectively, in the slab model. Note the perfect up-down symmetry of E_ρ in (a) without absorption. When absorption is included in (b) through finite temperature, the up-down symmetry is destroyed. A plot (not shown) of the radiated power spectrum in front of the antenna shows that the direction of energy flow in (b) is down. Reversing the sign of B_0 reverses the direction of energy flow.
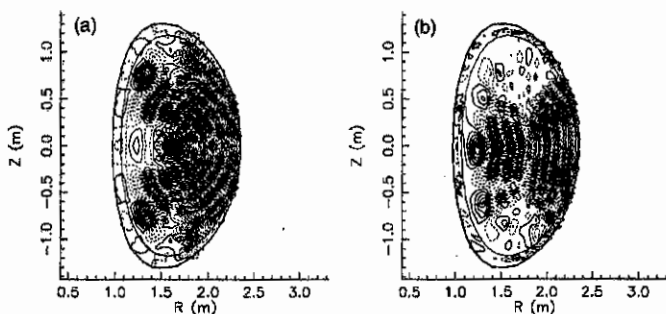
Fig. 1. Wave electric field Re(E_ρ) from the PICES code [7] for no poloidal magnetic field with (a) zero temperature and (b) finite temperature ($T_e = 20$ keV, $T_i = 8$ keV).

3. Co-counter Asymmetry

When a poloidal magnetic field is introduced, the up-down asymmetry acquires a toroidal component. In this case, the plane of the magnetic field in front of the antenna is tilted due to the pitch of the field lines. For a positive plasma current, the downward direction of energy flow in Fig. 1(b) has a toroidal component in the $-\varsigma$ or "co current" drive direction. (Note that because of the negative electron charge, waves traveling in the $-\varsigma$ direction drive current in the

+ ς direction). Thus, an antenna that is phased to launch waves in the − ς direction transfers more energy to the plasma (loads better) than the same antenna phased to launch waves in the + ς direction. This is shown in Fig. 2(a) where the spectrum of absorbed power is plotted vs toroidal mode number for $B_\varsigma < 0$ and $B_\theta > 0$. The calculation includes 100 uniformly excited toroidal modes. Parameters are those expected for the National Spherical Tokamak Experiment (NSTX) [8]: $B_0 = -0.30$ T, $R_0 = 0.8$ m, $I_p \approx 1$ MA, κ = 2.0 (elongation), $R_{wall} = 1.39$ m, $f = 41$ MHz, $n_{e,0} = 3.0 \times 10^{19}$ m^{-3}, $T_{e,0} = 2.0$ keV and $T_{i,0} = 1.0$ keV. In NSTX, the co-counter asymmetry is particularly strong because of the large poloidal magnetic field near the antenna.
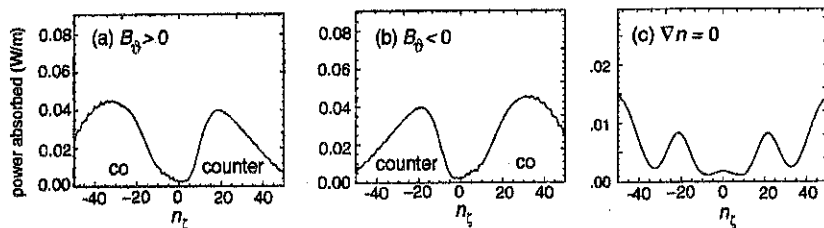
Fig. 2. *Spectrum of absorbed power in NSTX with $B_\varsigma < 0$ and (a) $B_\theta > 0$. In (b) $B_\theta < 0$, and in (c) the density gradient is set to zero.*

When the sign of B_θ is reversed in Fig. 2(b), the asymmetry is also reversed. But in this case, the plasma current also changes sign so that co and counter directions reverse, and loading remains highest for the co direction. The general conclusion is that plasma absorption and hence antenna loading are always shifted or skewed toward the co-current drive direction independent of the direction of the applied magnetic field. When density gradients are forced to zero as in Fig. 2(c), both up-down and co-counter asymmetries are eliminated because the Hall terms in Eq. (1) are proportional to density gradients.

Current drive efficiency is also affected by the direction that waves are launched relative to the plasma current. Figure 3 shows radial profiles of the driven current density $J(\rho)$ and integrated current $I(\rho)$ for the example of Fig. 1, but includes a positive poloidal magnetic field.
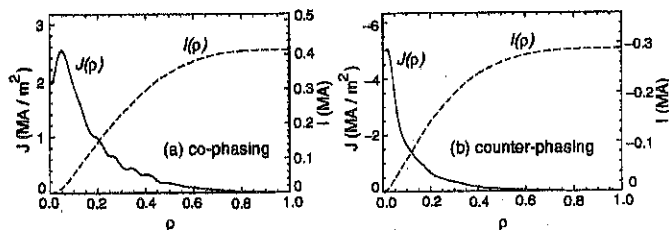
Fig. 3. *Driven current profiles for the case of Fig. 1 but with a positive poloidal magnetic field and a smaller toroidal magnetic field (B = −1.7 T): (a) co-phasing; (b) counter-phasing.*

Although the total current is slightly higher for co-phasing in (a), the current density profile is more peaked near the axis for counter-phasing in (b). This peaking is more pronounced at low toroidal magnetic fields because the Hall terms in Eq. (1) are proportional to the magnitude of

the $E \times B$ drift velocity (E/B).

4. Current Profile Control in NSTX

The ideas in this paper suggest new ways for optimizing antenna performance in advanced tokamaks such as NSTX. The discussion in Secs. 2 and 3 suggests that poloidal phasing and/or poloidal positioning of the antenna could be used to partially cancel or reinforce the natural up-down shift of the antenna's radiation pattern. Also, RF power can be used to control the total current profile shape by driving current co or counter to the bootstrap current. An example is shown in Fig. 4 where a fast wave current of about 100 kA is used to partially cancel or reinforce the bootstrap current ($\approx$ 200 kA) in NSTX. The ohmic current is adjusted in both cases to keep the total plasma current constant at about 1 MA. Depending on the direction of the fast wave current

Fig. 4. Total current density profile in NSTX for the case of Fig. 2(a). The RF power is phased co and counter to the bootstrap current. Integrated current is 1 MA for both cases.

relative to the bootstrap current, two distinctly different current profiles are obtained in Fig. 4. This provides a unique opportunity to use RF power in advanced tokamaks to influence turbulence and stability properties as well as to control transport barriers.

Acknowledgments

References

[1] J. A. Rome, J. D. Callen, J. F. Clarke, Nucl. Fusion 14 141 (1974).

[2] C. C. Petty, et al., "Direct Electron Absorption of Fast Waves on the DIII-D Tokamak" in *Radiofrequency Heating and Current Drive of Fusion Devices,* (Proc. Euro. Top. Conf., Brussels, 1992) Vol 16E, EPS, p. 177 (1992).

[3] T. H. Stix, *Waves in Plasmas* (American Institute of Physics, New York, 1992)

[4] A. M. Messiaen, et al., Nucl. Fusion 15 75 (1975) .

[5] J. Adam, et al., "Wave Generation and Heating in the ST-Tokamak at the Fundamental and Harmonic Ion Cyclotron Frequencies", in *5th Conf. on Plasma Physics and Controlled Nuclear Fusion Research,* Tokyo, IAEA-CN-33/A3-2, 1974.

[6] E. F. Jaeger, D. B. Batchelor, H. Weitzner, J. H. Whealton, Comput. Phys. Commun. 40, 33 (1986).

[7] E. F. Jaeger, D. B. Batchelor, D. C. Stallings, Nucl. Fusion 33 179 (1993) .

[8] M. Ono, Phys. Plasmas 2 4075 (1995) .

Alfvèn Current Drive in Tokamaks with Aspect Ratio in the Range $1.05 \leq R/a \leq 10$

S.Cuperman, C.Bruma and K.Komoshvili
School of Physics and Astronomy, Tel Aviv University
Ramat Aviv, 69978 Tel Aviv, Israel

Abstract. Alfvèn Wave Current Drive (AWCD) in simulated low-field-side of tokamaks with aspect ratio in the range $1.05 \leq R/a \leq 10$ is considered within the framework of a resistive MHD model; equilibrium profiles with shear and toroidicity effects are used. In the case of low aspect ratio (viz., $R/a = 1.25$, representative for a START-like device), neoclassical conductivity effects have been also considered.

Introduction

In this paper we investigate the aspect ratio dependence of the current drive generated by Alfven waves in *simulated* tokamak (low-field-side) plasmas in the range $1.1 \leq R/a \leq 10$. The following basic features are included: (i) we treat the case of a current carrying cylindrical plasma (of radius a) with periodic boundary conditions at the ends; (ii) the plasma is surrounded by a helical sheet-current antenna of radius r_A and by a perfectly conducting wall of radius r_w ($a < r_A < r_w$); (iii) toroidicity effects are simulated by identifying the equilibrium axial magnetic field with the toroidal field component $B_{0,\phi}(r)$ and by using the actual tokamak r-dependence for the $B_{0,z}$ - component; (iv) shear as well as finite poloidal magnetic field effects are properly accounted for; (v) a full wave ($E_\parallel \neq 0$) and resistive (two fluid) MHD equations are consistently solved; (vi) all three components of the current drive related to plasma flow, dynamo and helicity injection are considered ; (vii) efficiencies and radial profiles of the rf current drive corresponding to several illustrative combinations of antenna parameters are calculated and compared. Some simpler cases have been considered in [1]-[3]. Also, in view of the recent interest in the small aspect ratio tokamaks we investigated the same problem for a START-like device ($R/a = 1.25$) with consideration of neoclassical effects.

Equilibrium Magnetic Fields

In cylindrical coordinates, $(\hat{\mathbf{r}}, \hat{\boldsymbol{\theta}}, \hat{\mathbf{z}})$, the equilibrium magnetic field is

$$\boldsymbol{B}_0(r) = B_{0z}(\hat{\mathbf{z}} + \hat{\boldsymbol{\theta}}\delta), \qquad \delta(r) \equiv B_{0\theta}(r)/B_{0z}(r) . \tag{1}$$

With the illustrative equilibrium profiles ($h_n = 0.99$, $h_T = 0.75$, $x \equiv r/a$)

$$n(x) = n(0)(1 - h_n x^2), \quad T(x) = T(0)(1 - h_T x^2), \quad j_{0z}(r) = j_{0z}(0)\left[1 - x^2\right]^2, \tag{2}$$

from Maxwell's and force balance equations one can obtain $\bar{B}_{0\theta}(x)$ and $\bar{B}_{0z}(x)$.

We "simulate" toroidal effects and define an equivalent inverse aspect ratio, $\epsilon \equiv a/R_0$, by identifying B_{0z} of the cylindrical configuration considered here with a Shafranov-type solution for the toroidal field component in a tokamak, $B_{0\phi}$ satisfying the relation $RB_{0\phi} = const.$ ($R = R_0 + r\cos\theta$) . With the notation $\bar{B}_{0\phi} \equiv B_{0\phi}/B_{0z}(0)$, one has $\bar{B}_{0\phi}(x, \theta) = 1/(1 + \epsilon x\cos\theta)$.

Thus, identifying $\bar{B}_{0z}$ with $\bar{B}_{0\phi}$ and requiring $\bar{B}_{0z}(1) = \bar{B}_{0\phi}(1,0)$, one obtains an equivalence condition, from which it follows $(\beta(x) \equiv 8\pi p_0(x)/B_0^2(x))$

$$\epsilon_{eq} = \left\{ 1 + \beta(0)[(h_n + h_T) - h_n h_T)] - 4.7\alpha^2 \right\}^{-1/2} - 1. \tag{3}$$

The wave equation and boundary conditions

In local magnetic coordinates, the equations for the e.m. field components are

$$\mathcal{A}(\mathbf{U}/dr) = \mathbf{A} \cdot \mathbf{U}, \qquad \mathbf{U} \equiv \mathbf{U}\left(\mathcal{B}_{\parallel}, E_{\parallel}, E_{\perp}, \mathcal{B}_{\perp}\right), \tag{4}$$

where the matrix elements A_{ij} are functions of the elements of the resistive dielectric tensor and equilibrum profiles.

Boundary Conditions at $r = 0$. We express the elements A_{ik} in the form $A_{ik}(r) = r^{\alpha_{ik}} a_{ik}(r)$, $a_{ik}(0) \equiv \hat{a}_{ik} \neq 0$. and we look for regular solutions of the the form: $\mathbf{U}(r) = \mathbf{U}(r)\left(r^{\xi}\hat{\mathcal{B}}_{\parallel}(r), r^{\zeta}\hat{E}_{\parallel}(r), r^{\eta}\hat{E}_{\perp}(r), r^{\kappa}\hat{\mathcal{B}}_{\perp}(r)\right)$, where $\hat{\mathcal{B}}_{\parallel}$, $\hat{E}_{\parallel}$, $\hat{E}_{\perp}$ and $\hat{\mathcal{B}}_{\parallel}$ have non zero values at $r = 0$, and ξ, ζ, η and κ are some arbitrary powers. Then, upon retaining in the quantities $a_{ik}(r)$ only the terms that do not vanish in the limit $r \to 0$, after some tedious algebra, one obtains a set of equations which must be satisfied at $r = 0$. A systematic search of these equations leads to the solution $\xi = |m|$, $\quad |m| \geq 0$, and consequently, $E_{\parallel}(0) = \mathcal{B}_{\parallel}(0) = 0$.

Boundary Conditions at $r = a$. The consistent solution of the problem requires the continuity of the solutions of the wave equation in the plasma region, $0 \leq r \leq a$ and those holding in the surrounding region, $a \leq r \leq r_w$, within which the wave emitting antenna is situated. In the domain $a \leq r \leq r_w$, exact analytical solutions for the field components which contain only two arbitrary constants, C_1 and Q_1, can be obtained. Thus, the continuity conditions at $r = a$ provides two relations between the four field components, representing the required two boundary conditions at $r = a$.

Power absorption and current drive

The power absorption by the plasma system is calculated by the following equivalent expressios [1] (L_z – the lentgh of the plasma column) :

$$P_1 = \frac{acL_z}{4}Re(E_{\parallel}^* B_{\perp} - E_{\perp}^* B_{\parallel})_{r=a}, \; P_2 = \int_{V_p} dV \; p_L(r) = 2\pi L_z \int_0^a r p_L(r) dr, \tag{5}$$

where, $p_L(r) \equiv \frac{1}{2}Re(\mathbf{E} \cdot \mathbf{j}^*)$ is the locally absorbed power density. For the RF current drive we use

$$j_{0z}^{RF} = j_{0z}^{HI} + j_{0z}^{MT} + j_{0z}^{PF}, \tag{6}$$

where the quantites j_{0z}^{HI}, j_{0z}^{MT} and j_{0z}^{PF} indicate, respectively, contributions due to helicity injection, momentum transfer and plasma flow[4].

Computations and results

We are faced with the solution of a system of four 1st order differential equations for the field components $\mathcal{B}_{\parallel}$, $E_{\parallel}$, $E_{\perp}$ and $\mathcal{B}_{\perp}$, subject to two boundary conditions given at $r = 0$ and two boundary conditions given at $r = a$. This represents a *two-point boundary value problem* which we solved by relaxation techniques. Thus, the differential

equations are replaced by finite difference equations on a mesh of 2000 points that cover the integration range $0 \leq r \leq a$. As initial conditions, exact analytical vacuum solutions obtained for the same configuration are used. The relaxation process is stopped when the sum of the changes in the local values of any of the field components at two consecutive time steps, divided by the maximum peak to valley value, becomes smaller than 10^{-10}. Some illustrative results obtained in this work are presented in Figs. 1.

The START-like case with neoclassical conductivity

From the numerical solution of the MHD equations with neoclassical conductivity obtained for START [5], by adequate best fit techniques, we obtain consistent equilibrium profiles. These results correspond to the following START-parameters: invers aspect ratio, $\varepsilon = 0.697$; elongation of plasma boundary, 1.3; triangularity of plasma boundary, 0.3; toroidal B-field (axis)), 0.4895 T; central electron temperature, $T_e(0) = 0.18$ keV; central ion temperature, $T_i(0) = 0.15$ keV; central electron density, $n(0) = 0.25 \ 10^{21} \ m^{-3}$. Also, the following prescribed profiles were used: current density: $j_0(x) = j_0(0)(1-x)$; $n_s = n_i = n(0)(1-x)^{0.8}$ and $T_l(x) = T_l(0)(1-x)^{0.8}$ $(l = e, p)$. For $(\theta = 0)$, low–field–side case illustrative solutions of the full wave equation $(E_{\parallel} \neq 0)$ for the cases of neoclassical (dashed curves) and classical (solid curves) conductivities are shown in Fig.2.

Concluding Remarks

The results of this investigation support the following conclusions: 1. The generation of the momentum transfer, helicity injection and plasma flow components of AWCD is demonstrated for the entire range of relevant aspect ratio values. 2. For the physical parameters considered in this work, the helicity injection CD component dominates ; the other (smaller) CD components are comparable. 3. In the case of small (large) aspect ratio configurations, the maximum efficiency of AWCD increases (decreases) with increasing poloidal wave number, $|m|$ $(m = -|m|)$, and with decreasing toroidal wave number, $|n|$ $(n = -|n|)$. 4. When $n = -1$, the frequency value corresponding to maximum efficiency value equals that corresponding to the lower edge of the continuum, $\omega_L(\varepsilon, T, m, n)$ (this, independently of the actual aspect ratio, temperature and poloidal wave number values used in this work); when $| n | > 1$, this frequency shifts to higher values, $\omega > \omega_L$, especially in the lower aspect ratio cases. 5. The radial distance of the conversion layer is determined by the lower edge frequency, $\omega_L(\varepsilon, T, m, n)$. Its value decreases with increasing aspect ratio and toroidal wave number as well as with decreasing poloidal wave number.

For START-like devices with *neoclassical conductivity* the following hold: (a). The total power absorption is almost unaffected by neoclassical effects and increases with n and $|m|$-values. (b) The total AWCD decreases below the values based on classical conductivity; for example, in the case $m = 1, n = 4$ and $\omega = \omega_{LA}$ the maximal decrease (about 50 %) is found for the helicity injection ACWD-component, j^{HI}.

References

[1] Cuperman, S., Bruma, C., Komoshvili, K. 1996 *J. Plasma Physics*, **56**, part 1, 149.

[2] Komoshvili, K., Cuperman, S., Bruma, C. 1997 *J. Plasma Physics*, **58**, part 3, 1

[3] Bruma, C., Cuperman, S. and Komoshvili, K. 1997 *J. Plasma Physics*, in press.

[4] Elfimov, A. G., Petrzilka, V. and Tataronis, J. A. 1994 *Phys. Plasma*, **1**, 2882.

[5] Wilson, H. R., SCENE—Simulation of Self-Consistent Equilibra with Neoclassical Effects, *Fusion Theoretical and Strategic Studies Depart.* Culham Lab. July, 1994.
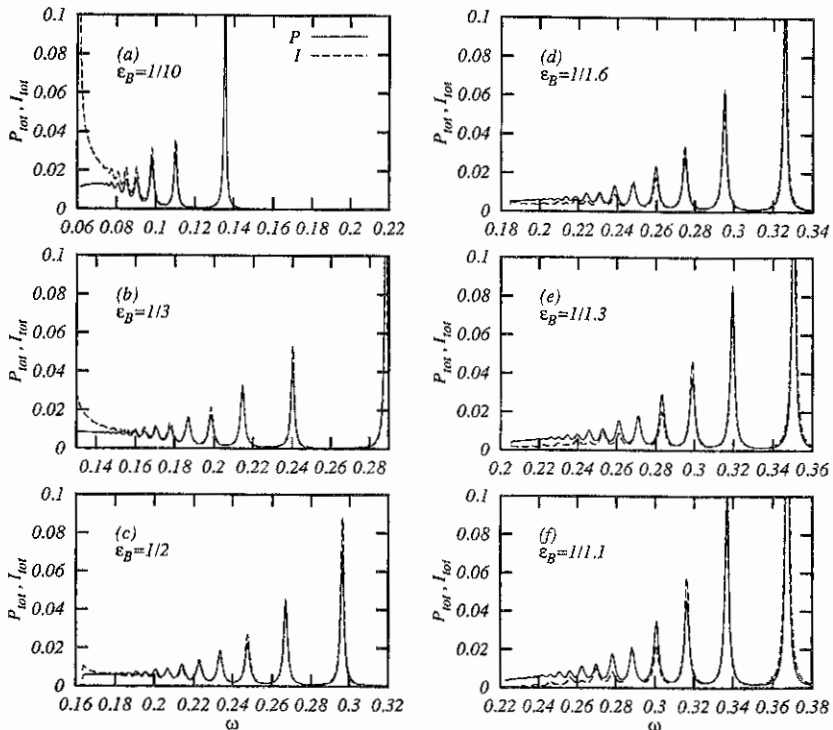
Fig.1. Frequency spectra of the total power absorption $P(\omega)$ (solid) and current drive, $I(\omega)$ (dotted) for different aspect ratios. The other parameters are $T=100eV$, $n(0)=10^{14}$ cm^{-3}, $B(0)=1T$, $m=-1$, $n=-2$.
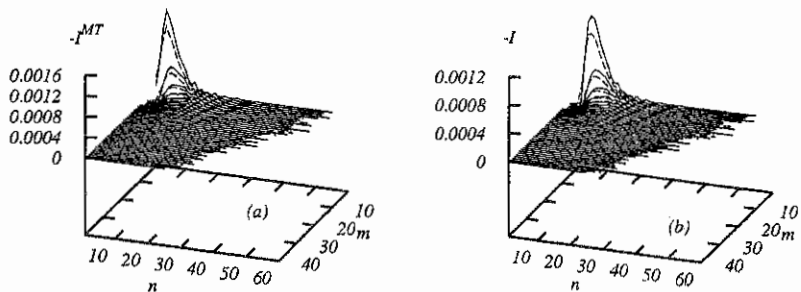
Fig.2. (m,n)-dependence of the integrated AWCD: solid (dashed) curves correspond to classical (neo-classical) conductivity. (a) momentun transfer component, $-I_{0z}^{MT}$; (b) total AWCD. (Integral on eq. (6)).

Fokker-Planck Simulation of the Electron-Cyclotron Heating and Electron-Cyclotron/Lower-Hybrid Current Drive Synergy for TdeV

M. Shoucri, I. Shkarofsky, Y. Peysson[*],
Y. Demers, A. Côté, C. Côté

Centre canadien de fusion magnétique,
Varennes J3X 1S1, Québec Canada

Electron-cyclotron heating and electron-cyclotron/lower-hybrid current drive synergy experiments are currently planned for TdeV [1], with available power of 1 MW of LH at 3.7 GHz and 1 MW of EC power at 110 GHz (harmonic 2 ω_{ce}). We present in this work a study using a bounce averaged Fokker-Planck code for this problem. The code uses the collision operator recently discussed in Ref. [2]. The Fokker-Planck equation is discretized in velocity space and solved using a five-point solver algorithm which has been previously presented [3], or using a more recent nine-point algorithm solver [4]. Previous results for electron-cyclotron heating and electron-cyclotron/lower-hybrid current drive synergy have been presented in Ref. [5] without trapping. The version of the code used here is extended to include bounce averaging. The equation is written in divergence form assuming circular flux surfaces as follows:

$$\frac{\partial f}{\partial t} + \frac{1}{p_0^2}\frac{\partial}{\partial p_0}\left(p_0^2 S_{p_0}\right) - \frac{1}{p_0}\frac{\partial}{\partial \mu_0}\left(\sqrt{1-\mu_0^2}\ S_{\mu 0}\right) = I_0 \tag{1}$$

where p_0, $\mu_0 = \cos \vartheta_0$ represent the coordinate system in momentum space at the position of minimum magnetic field of the flux surface (on the outer equatorial plane for up-down symmetric situations). The fluxes in Eq. (1) are written in the form

$$S_{p_0} = S_{Ecp_0} + S_{LHp_0} + S_{Ep_0} + S_{colp_0}; \qquad S_{\mu 0} = S_{Ec\mu_0} + S_{LH\mu_0} + S_{E\mu_0} + S_{col\mu_0} \tag{2}$$

The different fluxes in Eq (2) represent the contributions from electron cyclotron, lower-hybrid, electric field and collisions, which are obtained by appropriate bounce averaging of the local coefficients [6]. For the EC contribution, for instance, we have:

$$S_{Ecp_0} = -D\left(1-\mu_0^2\right)\left[\frac{B}{B(0)}\frac{\partial f}{\partial p_0} + \frac{1}{p_0\mu_0}\left(\frac{B}{B(0)}\left(1-\mu_0^2\right) - \frac{n\omega_{ce}}{\omega\gamma}\right)\frac{\partial f}{\partial \mu_0}\right] \tag{3}$$

[*] CEA Cadarache, St-Paul-Lez-Durance, France

$$S_{Ec\mu_0} = D \frac{\left(1-\mu_0^2\right)^{1/2}}{\mu_0} \left(\frac{B}{B(0)}\left(1-\mu_0^2\right) - \frac{n\omega_{ce}}{\omega\gamma} \right) \frac{\partial f}{\partial p_0}$$
$$+ \frac{D}{p_0} \frac{\left(1-\mu_0^2\right)^{1/2}}{\mu_0^2} \frac{B(0)}{B} \left(\frac{B}{B(0)}\left(1-\mu_0^2\right) - \frac{n\omega_{ce}}{\omega\gamma} \right)^2 \frac{\partial f}{\partial \mu_0} \tag{4}$$

The coefficient D is written for the harmonic $2\omega_{ce}$ in the form

$$D = D_{cy} \frac{\gamma}{|p_\parallel|} p_\perp^2 \exp\left(-\left(\left(\gamma - \frac{2\omega_{ce}}{\omega} \right) \Big/ p_\parallel\beta_{th} - N_\parallel \right)^2 \Big/ \Delta N_\parallel^2 \right) \tag{5}$$

where $\quad p_\perp^2 = p_0^2 \left[B/B(0)\right]\left(1-\mu_0^2\right), \quad p_\parallel^2 = p_0^2 - p_\perp^2, \quad N_\parallel = k_\parallel c/\omega, \quad \beta_{th} = v_{th}/c \tag{6}$

$B/B(0) = (1+\varepsilon)/(1+\varepsilon\cos\theta)$, where θ is the poloidal angle on the flux surface. $\varepsilon = R_{min}/R_{maj}$, where R_{min} is the radius of the flux surface and R_{maj} is the major radius of the tokamak. Details on other terms can be found in Refs. [3, 6]. For the harmonic $2\omega_{ce}$, there is a factor $p_\perp^2$ in Eq. (5) which results from the small argument expansion of the Bessel functions [7]. For the LH wave, we have

$$S_{LHp_0} = - D_{LH}\mu_0 \left(\mu_0 \frac{\partial f}{\partial p_0} + \frac{1-\mu_0^2}{p_0} \frac{\partial f}{\partial \mu_0} \right); \quad S_{LH\mu_0} = \left(1-\mu_0^2\right)^{1/2} D_{LH} \left(\mu_0 \frac{\partial f}{\partial p_0} + \frac{1-\mu_0^2}{p_0} \frac{\partial f}{\partial \mu_0} \right) \tag{7}$$

where the quasilinear LH diffusion coefficient is given by $D_{LH} = D_0$ for $v_1 \leq p_\parallel/\gamma \leq v_2$ and $D_{LH} = 0$ otherwise. For the lower-hybrid wave alone with $D_0 = 0.5$, $v_1 = 3$, and $v_2 = 8$, we get a current of $j = 0.181$, $P_{abs} = 9.49 \times 10^{-3}$, for a ratio $j/P_{abs} = 19.07$. We present in Table 1 the results for the electron cyclotron wave alone when $N_\parallel = 0.4, 0.5, 0.6$ and together with the lower-hybrid wave. Fig. 1 shows the distribution function obtained for the electron cyclotron wave alone, with the parameters $D_{cy} = 0.025$, $N_\parallel = 0.4$, $\Delta N_\parallel = 0.03$, $T_e = 4$ keV, $Z = 1$ and $R_{maj} = 83$ cm for TdeV. We consider a flux surface of radius $R_{min} = 5$ cm, at a poloidal angle $\theta = 30°$. In this case $B/B(0) = 1.0076$, $2\omega_{ce}/\omega = 0.95$. The current obtained is $j = 8.2 \times 10^{-3}$, $P_{abs} = 7.85 \times 10^{-4}$, yielding a ratio of 10.44. The synergy between the previous EC wave and LH is presented in Fig. 2 and in Table 1. We show in Fig. 3 and Table 1 the results obtained

for the EC wave alone, with $N_{\parallel} = 0.5$, and all other parameters remain identical to those of Fig. 1. The synergy with the same LH wave is presented in Fig. 4 and Table 1. Finally, we give in Fig. 5 and Table 1 the results obtained for the EC wave alone and with $N_{\parallel} = 0.6$. The synergy with the LH current is presented in Fig. 6 and in Table 1. We note the synergy for the current obtained at $\theta = 30°$ and $R_{min} = 5$cm increases with $N_{\parallel}$. However, preliminary results for higher values of θ indicate less synergy and more heating for the distribution function in the transverse direction.

Table 1   Current density and absorbed power calculated at
poloidal position $R_{min} = 5$cm, $\theta = 30°$

		$N_{\parallel} = 0.4$		$N_{\parallel} = 0.5$		$N_{\parallel} = 0.6$	
	LH	EC Fig. 1	EC + LH Fig. 2	EC Fig. 3	EC + LH Fig. 4	EC Fig. 5	EC + LH Fig. 6
j	0.181	0.0082	0.227	0.0187	0.2646	0.0195	0.2972
P_{abs}	0.00949	0.00078	0.013	0.0022	0.0166	0.003	0.017
j/P_{abs}	19.07	10.44	17.63	8.5	15.9	6.38	17.38

(current density is normalized to $en_e v_{th}$ and P_{abs} is normalized to $n_e m_e v_{th}^2 \nu$)

Acknowledgments

References

[1]   A. Côté, Y. Demers *et al.*, Proc. 16th IAEA Fusion Energy Conf., (Montréal, 1996).

[2]   I. Shkarofsky, Phys. Plasmas, July 1997.

[3]   M. Shoucri, I. Shkarofsky, Comp. Phys. Comm. 82, 287 (1994).

[4]   Y. Peysson, M. Shoucri, Comp. Phys. Comm., to be published.

[5]   M. Shoucri, I. Shkarofsky, CCFM Report 467 (1996).

[6]   E. Westerhof, A. Peeters, W. Schippers, "RELAX", FOM-Inst. Report 92-211 (1992).

[7]   M. Shoucri, I. Shkarofsky, *et al*, Comp. Phys. Comm. 55, 253 (1989).

$N_{\parallel} = 0.4$

BC

EC + LH

Figure 1

Figure 2

$N_{\parallel} = 0.5$

BC

EC + LH

Figure 3

Figure 4

$N_{\parallel} = 0.6$

BC

EC + LH
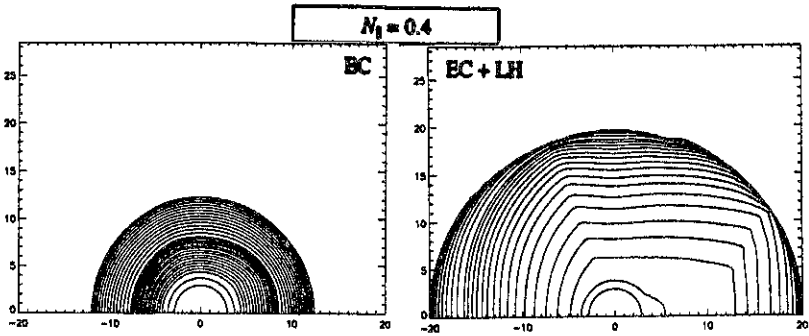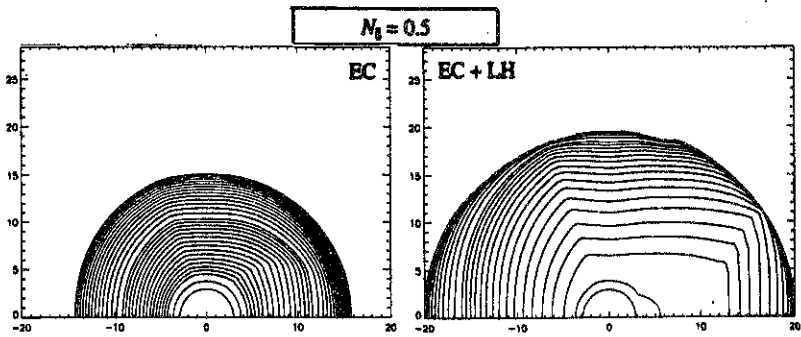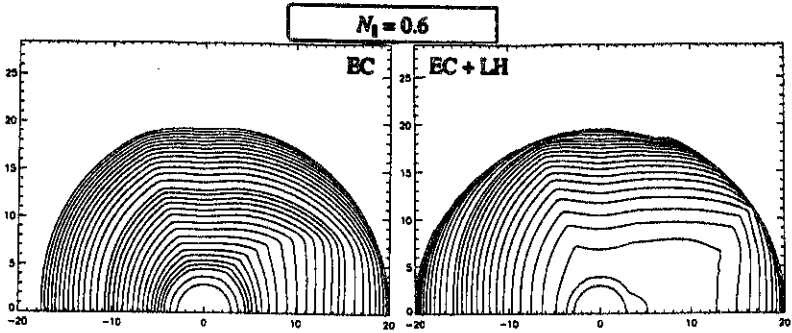
Figure 5

Figure 6

Experimental investigation of oscillating magnetic field current drive in an inductively coupled plasma device

S. Xu, Weiyi Luo, Hanshi Li, and S. Lee

Division of Physics, School of Science, Nanyang Technological University

469 Bukit Timah Road, Singapore 259756

Introduction

Theoretical analysis has shown that steady-state plasma currents can be driven using a low-frequency, transverse oscillating magnetic field (OMF)[1][2][3]. We present here an experimental investigation of the OMF current drive technique made on a low-frequency, low power, inductively coupled spherical device.

OMF current drive

Using an immobile uniform ion model, Brotherton-Ratcliffe and Xu solved the appropriate current drive equations for a spherical plasma (see Fig. 1) by method of vector spherical harmonics expansion. They found that the interaction of the applied OMF with the vertical field generates: (1) a steady-state toroidal plasma current, (2) a rotating magnetic field, (3) a bi-directional toroidal, and (4) a frequency- doubled harmonics.

Experimental set-up

A schematic diagram of the experimental setup is shown in Fig. 2.
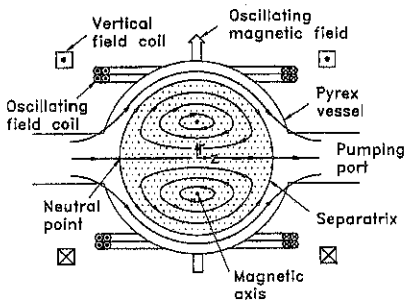
Fig. 1 Model of OMF current drive in a plasma sphere.
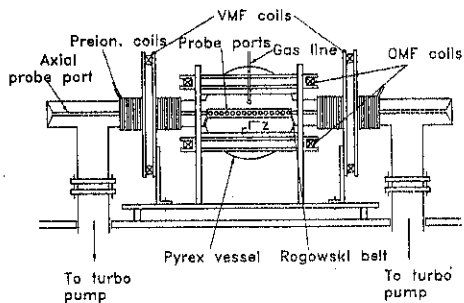
Fig. 2 Schematic diagram of the inductively coupled RF plasma device

The spherical discharge vessel had an inner diameter of 28 cm. Access for magnetic and electric probes was provided by a machined ceramic block cemented over a slit cut in a poloidal (r-z) plane. The oscillating magnetic field was generated by a pair of parallel circular coils fed by a RF current pulse of frequency (490 kHz) and 7 ms pulse duration from a MOSFET transistorized RF power generator. The equilibrium (vertical) field was produced by a pair of circular coils fed with a constant current. In this paper, the vertical field was characterized by its steady value, B_v, at $r = z = 0$ in the absence of a plasma. The working gas, Argon, was weakly pre-ionized by passing a 20 ms HF current pulse through two coils wound around each pumping arm of the discharge vessel. The pre-ionization pulse overlapped the start of the main RF pulse by 2 ms.

A Rogowski belt was used to measure the toroidal driven current. The steady-state magnetic field and the time-varying magnetic field in the discharge vessel were measured using Hall-effect magnetic probes and miniature wire-wound coils, respectively. A floating double Langmuir probe was employed to measure the electron number density and electron temperature.

Experimental results

• Driven current with vertical field

The toroidal driven current was measured as a function of the magnitude and orientation of the applied vertical field, and is shown in Fig. 3. There was a clear linear dependence of the toroidal driven current I_ϕ on the applied vertical field. It is worth pointing out that the steady toroidal current was zero when the vertical field was absent, and it reversed its direction when the polarity of the applied vertical field was changed. This was in accord with the theoretical predictions and was in contrast to the conventional RMF current drive[4] where a significant current was observed even if there was no applied vertical field. The production of a reversed magnetic field configuration generated by the driven current was also observed.

• Bi-directional toroidal field

Theoretical studies showed that there should exist a steady bi-directional toroidal field generated by the poloidal current loops in a similar way to the RMF case. This field had a $\sin(2\theta)$ dependence and an opposite polarity in each half hemisphere. This field was readily measured using the B_ϕ Hall probe, as shown in figure 5. The measured data were fitted with polynomial regression.
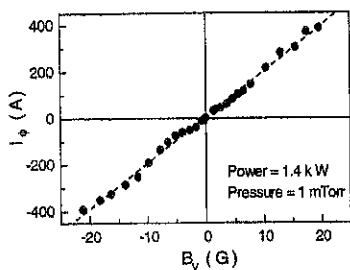
Fig. 3 Driven current versus the applied
vertical field.
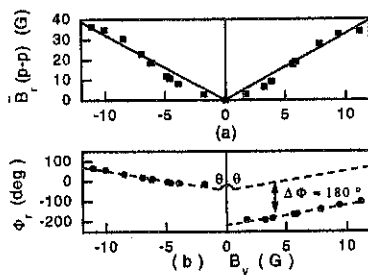
Fig. 4 The amplitude (a) and phase (b) of $\widetilde{B}_r$ as a
function of the vertical field at $z = 0$, $r = 3$ cm
for power $= 640$ W and pressure $= 3.3$ mTorr.
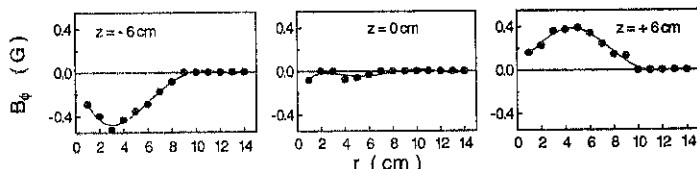
Fig. 5 Steady toroidal field B_ϕ at the $\phi = 0$ plane for
power $= 640$ w, pressure $= 2.0$ mTorr and $B_v = 8.24$ G.

- **Frequency-doubled oscillating field**

A number of theoretical mechanisms exist for the generation of frequency-doubled field harmonics. To verify this, the $\widetilde{B}_z$ wire-wound probe was inserted into the axial glass probe guide and a strong frequency-doubled term was then observed.

- **Rotating magnetic field**

The phase of the rotating field signal was measured with respect to a Pearson current signal of the oscillating field coils. The magnitude and the phase of the $\widetilde{B}_r$ component of the rotating magnetic field measured as a function of the applied vertical field at $z = 0$, $r = 3$ cm are shown in figure 4. Solid and dashed lines in this figure were fits of the measured data using linear regression. It was clearly shown that the phase was changed by 180 degrees when the applied vertical field was reversed. Both the amplitude and the phase of the rotating magnetic field changed in a linear fashion with the changing in the vertical field.

Fig. 4 (b) showed that when the vertical field was reversed the driven current changed its direction. This implied that the direction of the generated rotating magnetic field varied as a function of the applied vertical field.

- **Electron number density n_e and temperature T_e**

Fig. 6 shows both n_e and T_e values as a function of the applied vertical field. It is shown that the plasma density increased significantly as the vertical field was increased. This was because of the improvement of the plasma confinement.
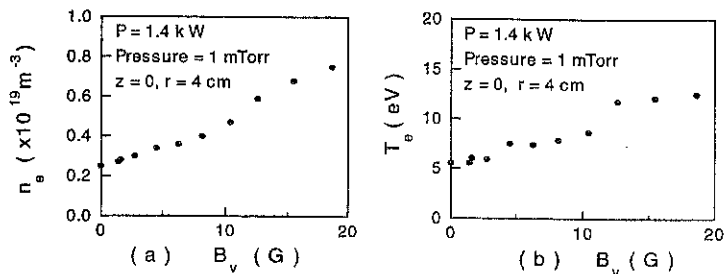
Fig. 6 Electron (a) density and (b) temperature versus vertical field.

Conclusion

We have experimentally studied the OMF current drive technique. The experimental results are in good agreement with the theoretical analysis. The measured electron number density n_e and electron temperature T_e conclusively showed that both the density and the temperature increased with an increase in the applied vertical field. This resulted in an increase in the toroidal driven current, which enhanced the confinement to the plasma.

The present current drive mechanism implies that a magnetic field confinement could be properly applied to effectively raise the plasma density and it may open an avenue for exploring novel low-frequency, inductively coupled RF plasma sources for materials processing.

Acknowledgments

References

[1] D. Brotherton-Ratcliffe and S. Xu, *Plasma Phys. Contr. Fusion*, **31**, 595 (1989).

[2] S. Xu and D. Brotherton-Ratcliffe, *Plasma Phys. Contr. Fusion*, **30**, 1905 (1988).

[3] S. Xu and I.R. Jones, *Plasma Phys. Contr. Fusion*, **35**, 531 (1993).

[4] I.R. Jones, Flinders University Report **FUPH-R-151**, (1979).

EC RAY TRACING WITH RELATIVISTIC EFFECTS

L. K. Kuznetsova *Institute of Nuclear Fusion, RRC "Kurchatov Institute", Moscow, Russia*
R. W. Harvey, *COMPX, Del Mar, California, US*

1. Introduction

Relativistic effects are well known to be of large importance in the interaction of electron cyclotron radiation with modern tokamak plasmas (see for example [1,2]). Propagation of EC waves is mainly described within geometrical optics in cold plasma approximation for dispersion relation whereas relativistic effects are taken into account in absorption and current drive calculations. Extensions of geometrical optics on inclusion of diffraction effects for a beam propagation in a dispersive anisotropic medium and ray-tracing problem near EC resonance have been made [3,4]. H.Bindslev [5] and E.Mazzucato [6] founded that relativistic change of electron mass can play a significant role in the propagation of extraordinary waves in plasmas with parameters similar to those of existing tokamaks even under conditions of negligible wave absorption.

Bindslev [7] made a comparison of different existing models for accounting of relativistic effects in refractive index being of importance for determination of propagation, cutoffs, transformations and polarization of EC waves. These models are listed in order of decreasing of accuracy or generality and increasing of calculation speed [7]: *1) fully relativistic, 2) weakly relativistic, 3) reduced weakly relativistic, 4) modified cold* and *5) cold.*

The account of the relativistic effects according to method [6] (*modified cold - 4*)) is based on the cold-plasma approximation for the components of the dielectric tensor with replacement of the electron rest mass m_0 by $m_e = m_0 \cdot \left(1 + 5/\mu\right)^{1/2}$, where $\mu = m_0 c^2 / T_e$ in expressions for plasma and electron cyclotron frequencies ω_{pe}, ω_{ce} (*c* is the velocity of light, T_e is electron temperature). This method is quite correct for determination of X-mode propagation in perpendicular direction to magnetic field and is in excellent agreement with the results of fully relativistic theory for $0.7 < \omega_{ce}/\omega < 0.9$ and $\omega_{ce}/\omega < 0.25$ and $T_e \leq 10\,keV$ [8]. The approximation [6] is not good in application for wave propagation at large oblique angles to the magnetic field and near EC resonances.

The *reduced weakly relativistic* model takes into account (in contrast with modified cold one) first order corrections in Larmor radius as well as anomalous dispersion effects.

The goal of this work is to developed a compact numerical ray-tracing code ABSORB-MC which takes into account the relativistic effects at the levels 3) and 4) mentioned above. ABSORB-MC had to be convenient for fast calculations of EC energy deposition, current drive as well as for analyzing the experimental data on the absorption at first and second EC harmonics. The specific purpose of the work is to scan the conditions of extraordinary EC waves input into D-III-D tokamak plasma for wide region of parameters.

2. Numerical modelling

2.1. Model. The ray-tracing ABSORB code was constructed for study EC-propagation, absorption, EC heating and current drive in T-10, T-15 tokamaks and ITER [9-12] and was tested by comparison with results of DIII-D obtained by TORAY modeling. In ABSORB code: a) waves propagation is calculated in geometrical optics approximation by standard routine for ray-tracing calculations; b) refraction and wave polarization is accounted in the cold plasma approximation for dispersion relation; c) absorption calculations take into account two relativistic effects: 1) modification of resonance conditions for EC-radiation, 2) modification of electron energy distribution function.

ABSORB-MC in contrast to previous ABSORB-code takes into account both 1) the relativistic mass corrections in components of dielectric tensor (*modified cold* model) [6] and 2) so named *reduced weakly relativistic* model including Dnestrovskii function [13] calculation, terms in first order in $\lambda = (k_\perp \rho)^2$ ($k_\perp$ - is wave vector and ρ - is Larmor radius). The last model allows to investigate in more details anomalous dispersion near EC resonance and region of X-mode transformation. Moreover the expression for refractive index is explicit (no root search). The explicit expression for the refractive index in these models makes it possible to calculate this value one or two orders of magnitude faster than more accurate but transcendental model (see [7]). The calculations of absorption in ABSORB-MC needs only in small modifications as compared with the code ABSORB that is in a modification of refractive indexes.

The calculations of refractive index and the results of parameter scans on DIII-D like plasmas are presented below. The relativistic corrections in ray propagation X-mode for both cases of first harmonic (inside launch f=60 GHz, B_0=2.1 T) and second harmonic (outside launch f=110 GHz, B_0 =2.1 T) are taken into account.

2.1 Refractive index

Real (a,b) and imaginary (c) parts of refraction index for X-mode as function of ω_{pe}^2/ω^2 (a) and ω_{ce}/ω (b,c) are shown in Figs.1a,b,c for perpendicular propagation and T_e=5, 10, 15, 20 keV. Fig.1 are relevant for analysis of dispersion for second harmonic in DIII-D plasmas. It follows from Fig.1a, that the temperature increase leads to relativistic shift of the R_{cutoff} and more deep ray penetration as compared with the cold plasma approximation. One can see that the cold plasma approximation leads to the underestimation of the electron density profile as it has been pointed by Bindslev [5] in reflectometry calculations. It is seen from Figs.1b,c that reduced weakly relativistic model decribes in more details the EC frequency domain as compared with cold or modified cold ones.
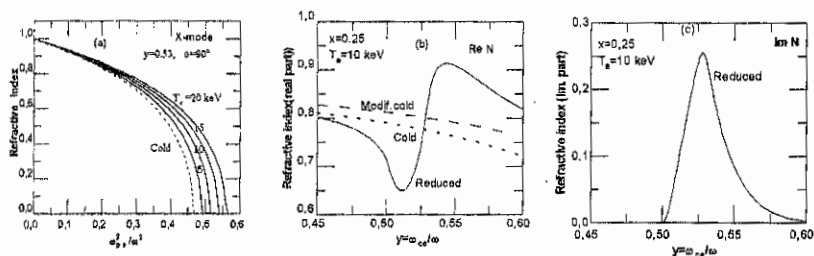
Fig.1.a)Refractive index of X-mode as a function of ω_{pe}^2/ω^2 for different temperatures T_e: $y = \omega_{ce}/\omega = 0,53$, calculated by cold and modified cold models; b) comparison real parts of refractive index obtained by cold, modified cold and reduced weak relativistic models; c) imaginary part of refractive index depend on $y = \omega_{ce}/\omega$ (ABSORB-MC code calculations).

2.2 X-mode first harmonic. Inside launch(f=60 GHz, B =2.1 T).

The fundamental X-mode inside launch from a point with R=100 cm and Z=15 cm in a perpendicular direction to toroidal magnetic field is considered. The calculations are performed for n_{e0} =0.1÷0.7 · 10^{14} cm^{-3} and for the profiles of electron density and temperature: n_e=(n_{e0}-n_{ea})·(1-a^2)+n_{ea}, T_e=(T_{e0}-T_{ea})·(1-a^2)+T_{ea}, where n_{e0}, T_{e0} are the corresponding values at plasma

center, and n_{ea}, T_{ea} are their values at the edge of plasma, and a is normalized radius. It is also suggest that $I_p = 2$ MA. The elongation $\lambda = 1,7$, Shafranov shift is $\Delta(a) = 10\,cm$, triangularity is equal to $\delta = 4\,cm$.

The results of calculations for $T_e = 1$, 5, 10 keV are shown in Figs.2a,b. Calculations demonstrate that there are strong discrepancy between cold and mass corrected rays (modified cold model). It is connected mainly with a shift of ray turning point into the region of larger values of magnetic field in relativistic case as compared with cold one. That is why the rays in relativistic approximation are turned out to be reversed at the periphery region of plasmas (more large values of magnetic field).
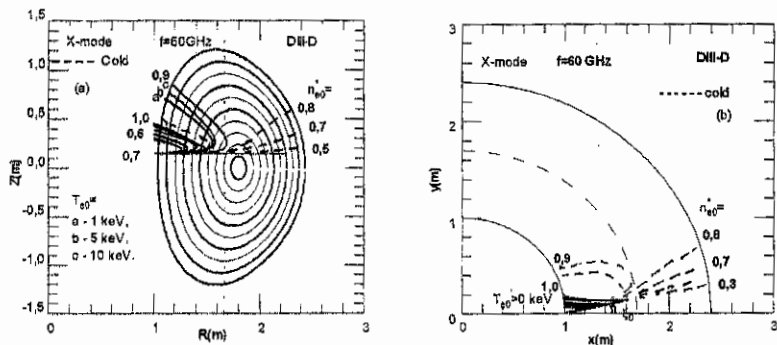
Fig.2. Cold (dashed) and mass corrected (full) curvers X-mode ray tracing projection for inside input (f=60 GHz) on planes (z,R) (a); (x,y) (b) for different electron densities ($n_{e0} = n_{e0}^M \cdot 10^{14} cm^{-3}$) and temperatures ($T_{e0}$).

2.3 X-mode second harmonic. Outside launch (f=110 GHz, B = 2.1 T).

It is considered the X-mode second harmonic input from Z=65 cm, R=235 cm. The toroidal angle varies ξ_0 is examined from 0^0 to 25^0. The poloidal angle ψ_0 is variated from $+10^0$ upward to -40^0 downward. The four groups of rays for $n_{e0} = 0,3 \cdot 10^{14}\,cm^{-3}$; $0,5 \cdot 10^{14}\,cm^{-3}$;
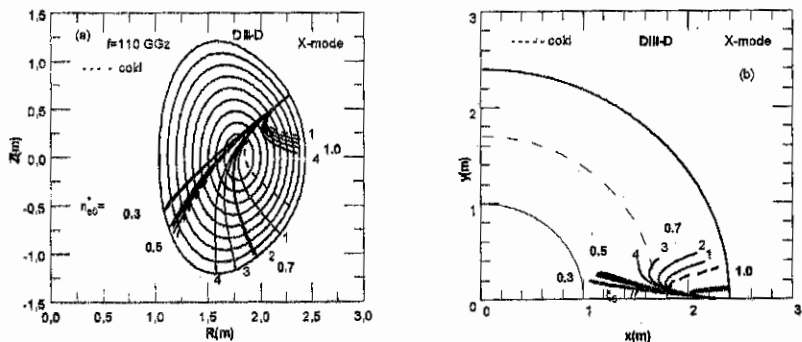
Fig.3.The same as in Fig.2 for X-mode second harmonic (f=110 HGz) in the case of outside input.

$0,7 \cdot 10^{14}\, cm^{-3}$; $1 \cdot 10^{14}\, cm^{-3}$ is considered. There are 5 rays with T_{e0}=0, 5, 10, 15 and 20 keV in each group. The results of one of the calculations are shown in Figs.3(a,b). The results of calculations for T_e=1, 5, 10 keV are shown in Figs.3a,b. Calculations demonstrate that there are strong discrepancy between cold and mass corrected rays (modified cold model). It is connected mainly with a shift of ray turning point into the region of larger values of magnetic field in relativistic case as compared with cold one. That is why the rays in relativistic approximation are turned out to be reversed at the periphery region of plasmas (more large values of magnetic field).

Results and conclusions

The calculations show that the mass corrections are of no importance for ray propagation for poloidal injection angle from $\psi_0 = 10^0$ to $\psi_0 = 0^0$ for arbitrary ξ_0, which was considered. In this case ray propagates toward periphery of plasmas, where density and temperature are low and mass corrections give small effect. Mass corrections are also not essential if $n_{e0} = 0,1 \cdot 10^{14}\, cm^{-3}$ or $n_{e0} = 0,3 \cdot 10^{14}\, cm^{-3}$ independ-ently of injection angle, because of low level of density. The relativistic corrections are most expressive for $n_{e0} = 0,5;\ 0,7;\ 1,0 \cdot 10^{14}\, cm^{-3}$, namely under the conditions: a) $n_{e0} = 0,5 \cdot 10^{14}\, cm^{-3}$, $\psi_0 = -20^0 \div -40^0$ and $\xi_0 = 25^0$; $\psi_0 = -40^0$ and $\xi_0 = 15^0$ being weak for $\psi_0 = -40^0$ and $\xi_0 = 5^0$. b) $n_{e0} = 0,7 \cdot 10^{14}\, cm^{-3}$, $\psi_0 = -10^0 \div -40^0$ and $\xi_0 = 0^0 \div -40^0$. c) $n_{e0} = 1,0 \cdot 10^{14}\, cm^{-3}$, $\psi_0 = -10^0 \div -40^0$ and $\xi_0 = 0^0$; $\psi_0 = 0^0 \div -30^0$ and $\xi_0 = 5^0$; $\psi_0 = -10^0 \div -40^0$ and $\xi_0 = 15^0$. The relativistic effects are essential for the parameters mentioned but they are not so dramatic because the density is high enough and rays do not achieve central region of plasma. For ITER input geometry the relativistic effects are mainly important for absorption and current drive accounted in ABSORB code [14] but not for ray tracing. The last effects are essential for reflectometry measurements near regions of cut-offs.

As conclusion the mass corrected numerical code ABSORB-MC providing the fast routine for ray-tracing calculations in modern tokamaks is developed. Test calculations in the wide domain of plasma parameters and input geometry for the specific case of DIII-D are in reasonable agreement with more refined calculations.

References

1. M.Bornatici, R.Cano, O.De Barbieri, and F.Engelmann, Nuclear Fusion, 23,1153, (1983).
2. D.B.Batchelor, R.C.Goldfinger, Phys.Fluids, 27, (12), 2835, (1984).
3. A.G.Peeters, Phys. Plasmas 3, (12), 4386, (1996).
4. E.Westerhof, Proc. of the EC10 Workshop, 6-11 April 1997 (to be published)..
5. H.Bindslev, Plasma Phys. Controlled Fusion, 33, 1775, (1991).
6. E.Mazzucato, Phys.Fluids B 4 (10), 3461 (1992).
7. H.Bindslev, in Proc.of Joint Int. Workshop EC-9, Borrego Springs, January, 585, 1995.
8. H.Bindslev Phys.Fluids B 5(8), 3108, (1993).
9. V.V.Alikaev, S.V.Bazdencov, L.K.Kuznetsova, V.V.Parail, ITER Working session, Garching,Febr.1989, ITER-IL-Ph-6-9-S-1,5p.
10. L.K.Kuznetsova, ITER Working session, Garching, March,1990, ITER-IL-Ph-06-0-S-4.
11. L.K.Kuznetsova, Strong Microwaves in Plasmas, Vol.1, 246, (1991), IAP, Nizhny Novgorod, USSR (Proc.of Intern.Workshop "Strong microwaves in plasmas", Suzdal, USSR, Sept.18-23, 1990).
12.. L.K.Kuznetsova, V.V.Parail, A.G.Shishkin, A.P.Smirnov. in Proc. of 17 th EPS Conf. on Controlled Fusion and Plasma Heating, 25-29, June 1990, Amsterdam, vol. 14B., 1247.
13. Yu.N.Dnestrovskiy, D.P.Kostomarov,N.V.Skrydlov, Sov.Phys.Tech.Phys.., 8, 691(1964)
14. Yu.N.Dnestrovskiy, S.E.Lisenko, L.K.Kuznetsova , Technical Meeting and Workshop Plasma Heating and Current Drive, Cadarache, France, 1994

Reconstruction of transport coefficients and ECRH power deposition profile from SXR intensity in tokamak T-10.

Andreev V.F., Dnestrovskij Yu.N., **Sushkov A.V.**, Razumova K.A.
RRC "Kurchatov Institute" 123182 Moscow, Russia.

1. Introduction.

A new statement of the problem of recovering of transport coefficients in the plasma from experimental data as a mathematical inverse coefficient problem for parabolic differential equations is represented [1]. The values of temperature at number of points along the radius at various instants of time are known from T-10 experiment. The heat conduction coefficient, convective heat flux velocity and the heat source are found from the minimum of discrepancy functional.

2. Statement of a problem.

Let us suppose that the heat flux Γ in one dimensional parabolic equation for electron temperature $T(r, t)$ has the following structure:

$$\Gamma = -n\chi \frac{\partial T}{\partial r} + \frac{5}{2} nuT \tag{1}$$

Determination of a heat conduction coefficient $k = n\chi$, convective velocity $v = nu$ and the power sources in the thermoconductivity equation $Q(r,t)$ is the goal of a given study.

Let the temperature would be known from the experiment at the internal points

$r = r_i, i = 1, \overrightarrow{N}$ along the segment [0,a] at the instants of time

$$T^{exp}(r_i, t_j) = f_i^j, \quad t = t_j, j = 1, \overrightarrow{M} \tag{2}$$

Let us choose the discrepancy functional in the following form:

$$J = 1/ 2 \cdot \sum_{j=1}^{M} \sum_{i=1}^{N} \rho_i \left[T(r_i, t_j) - f_i^j \right]^2, \tag{3}$$

One needs to find such k, v, Q_{OH} and Q_{add} that the solution $T(r, t)$ of the following differential boundary problem

$$\frac{\partial}{\partial t}\left(\tfrac{3}{2} nT\right) = \frac{1}{r} \frac{\partial}{\partial r}\left(rk \frac{\partial T}{\partial r}\right) - \frac{1}{r}(rvT) + Q_{OH} + Q_{add} \tag{4}$$

$$0 < r < a, 0 < t < t_0, \frac{\partial T}{\partial r}(0, t) = 0, T(a, t) = T_a, T(r,0) = T_0(r) .$$

would minimize the functional.

3. Numerical algorithm.

We use the polinomial parameterization for sought functions k(r) and v(r) and some "natural" representations for Q_{OH} and Q_{add}, where ρ_j is a weight factor which takes into account various reliabilities of experimental data.

$$Q_{OH}(T, r, t) = C_q(r, t)[T_S(r) / T_S(0)]^3 / T^{3/2}(r, t)$$
$$Q_{add}(r) = C_d \, exp(-\beta_d(r - r_0)^\alpha) \tag{5}$$

where r_0 and β_d are the known parameters $T_s(r)$ is a steady-state temperature distribution before the change in additional heating. As a result the inverse problem is reduced to the search of the set of polynomial coefficients and of unknown parameters C_q, C_d. The analysis of calculations has shown that $C_q(r,t)$ can be approximated by the following simple expression.

$$C_q(r, t) = C_{q0} + C_q f(t),$$
$$f(t) = \begin{cases} t, & 0 < t < t_x \\ 1 - t, & t_x < t < 1 \end{cases} \tag{6}$$

The ECRH starts at t=0 and finishes at $t=t_x$.

4. Results of numerical calculations.

The change of $T_e(r,t)$ at the beginning or/and at the end of ECRH pulse may be used as the initial experiment information. In some experiments [2] the measurements of $T_e(r,t)$ with the help of ECE diagnostic are used. However, this method has some defects:

1. The measurements of P_{EC} are impossible near EC resonance position where they are extremely needed

2. In the case of oblique EC waves injection the electron distribution function $f_e(E_e)$ is not a Maxvellian one and the information on $T_e(r)$ becomes not local [3].

In this paper the soft x-ray intensity distribution, $I_{SXR}(r)$, measurement is proposed instead of the ECE method. This method is free from mentioned above lacks but to use the algorithm described beyond we need in before hand transformation of chords data I_{SXR} into local data $T_e(r)$.

On T-10 the I_{SXR} was measured along 40 chords with the space resolution Δr=1-1.5 cm and time resolution $\Delta t \approx 40$ μs. After Abel reconstruction of I_{SXR} and transformation I_{SXR} in T_e in accordance with relation:

$$I_{SXR} \propto \frac{1}{\sqrt{T_e}} \int_0^\infty e^{-\frac{E}{T_e}} \varphi(E)dE, \tag{7}$$

the value of $T_e(r,t)/T_{e0}(r)$ is used in described above calculation. Here $\varphi(E)$ is an energy dependence of the SXR detector sensitivity (Fig 1) and Maxwellian distribution is suggested; $T_{e0}(r)$ is the temperature of electrons before P_{EC} is changed. The task become more complicate in the case of ECCD experiments, as $f_e(E_e)$ becomes non Maxwellian and EC power may be absorbed by a suprathermal tail of $f_e(E_e)$. In this case we need to register I_{SXR} in a wide enough energy range up to 100 keV and to know the form of $f_e(E_e)$ from SXR (spectra diagnostic). As at T-10 we have measured I_{SXR} in energy range only up to 10 keV, the $P_{HF}(r)$ might be measured for transverse to B_z wave launch or for low power wave launch only. The experimental data and results of proceeding for oblique wave lunch with low power are presented on Fig. 2,3,4. The calculations of $\chi_e(r)$ from experimental results with higher P_{ECCD} for Co and Counter direction of current generation are presented on Fig.5. One can see the difference in $\chi_e(r)$ distribution for different $j(r)$ but the difference sems to be not exeed error bars.

4.Conclusion.

The method of determination electron transport coefficients, $\chi_e(r)$ and EC power deposition profile which uses $I_{SXR}(r)$ measured is developed.

First implementation of this method for proceeding T-10 experimental data indicates satisfactory correspondence with numerical calculation by ASTRA code, although limited amount of proceeding data not allow us to discuss received physical results.

References.

1. Andreev V.F., Dnestrovskij Yu.N., Popov A.M., Reconstruction of Transport Coefficients from Tokamak Experimental Data, Nuclear Fusion, 33, N3 (1993) 499-504.

2. M.Rome, V.Erckmann, U.Gpario, et al. Plasma Phys. Control Fusion, 39, 1997, p.117.

3. A.V.Sushkov, A.A.Bagdasarov, D.A.Kislov, K.A.Razumova, A.V.Timofeev, Production of an "illusory image" in the measurements of Te(r) profile by the ECE diagnostic under ECCD in T-10 tokamak. The proceedings of this conference.
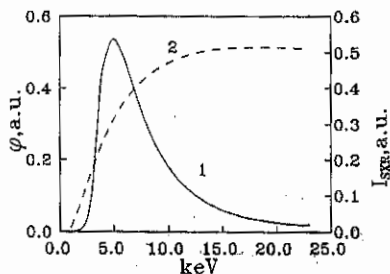
Fig.1. 1. The efficiency of the SXR
detector as function of photon
energy.
2. The dependence of SXR
intensity on T_e.

Fig.2. The X-ray intensity for different
chords.
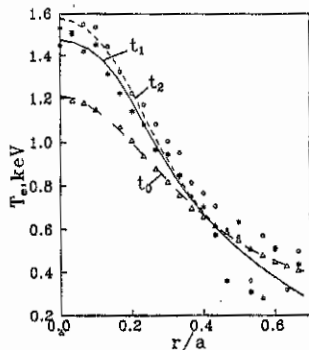
Fig.3. Radial dependencies electron
temperature $T_e(r)$ for different time.
Shot #62727, I_p=140kA, B_0=2.45T,
ECRH switch on t_0.

Fig.4. Radial dependences $Q_{add}(r)$ for
shot #62727, ECRH power
Q_{EC}=0.3MW heat conductivity $\chi_e(r)$
(solid line #62727, dash line
#62728).
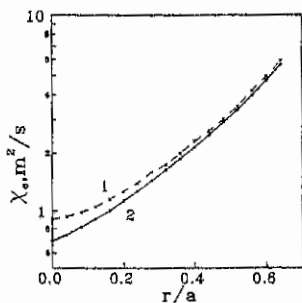
Fig.5. Radial dependences heat
conductivity $\chi_e(r)$.
1 - shot #60834 Co direction of
current generation,
2 - shot #60836 Cntr direction of
current generation.
I_p-140kA, B_0=2.45T, Q_{EC}=0.78MW.

Full Wave-Vlasov Analysis of Alfvèn Wave Current Drive in Simulated Low Aspect Ratio Tokamaks

K.Komoshvili, S.Cuperman and C.Bruma
School of Physics and Astronomy, Tel Aviv University
Ramat Aviv, 69978 Tel Aviv, Israel

Abstract. Alfvèn Wave Current Drive (AWCD) in low aspect ratio ($A \equiv R/a = 1/\varepsilon \gtrsim 1$) tokamaks (LART's) is studied numerically within the framework of Vlasov theory. For this, the full-wave equation ($E_{\parallel} \neq 0$) is solved by relaxation techniques, subject to appropriate boundary conditions at the plasma center and at plasma-vacuum interface, as well as at the concentric antenna current sheet and at the external metallic wall. Illustrative results are presented and discussed.

Introduction

The contribution of Alfvèn Wave Current Drive (AWCD) to the non-inductive current drive required for the steady state operation of magnetically confined thermonuclear plasmas has been considered *either* for large aspect ratio tokamaks (in both MHD and kinetic limits; see, e.g., [1]) *or* for small aspect ratio tokamaks (in the ideal and resistive MHD limits, [2]-[4]). The combined kinetic, toroidicity and shear effects in current carrying plasmas in small aspect ratio tokamaks — for which the large aspect ratio asymptotic expansions do not hold — have not yet been considered; their investigation is just the purpose of this work.

Thus, the full-wave equation ($E_{\parallel} \neq 0$) with a Vlasov-based dielectric tensor is solved by relaxation techniques, subject to appropriate boundary conditions at the plasma center and at plasma-vacuum interface, as well as at the concentric antenna current sheet and at the external metallic wall.

Physical Model

We consider a current-carrying cylindrical plasma of radius a and length $2\pi R$, with periodic boundary conditions at the ends, surrounded by a helical sheet-current antenna of radius r_A and by a perfectly conducting wall of radius r_w ($a < r_A < r_w$). In cylindrical coordinates, $(\hat{r}, \hat{\theta}, \hat{z})$ the equilibrium magnetic field is

$$\mathbf{B}_0(r) = B_{0z}(\hat{z} + \delta\hat{\theta}), \qquad \delta(r) \equiv B_{0\theta}(r)/B_{0z}(r) < 1. \tag{1}$$

The antenna current density is

$$\mathbf{j} = \mathbf{j}_A \delta_D(r - r_A) exp[i(m\theta + k_z z - \omega t)], \qquad \mathbf{j}_A = (\hat{\theta} k_z - \hat{z} m/r_A)J_0, \tag{2}$$

(J_0 is half the amplitude of the total current).

The strong toroidicity effects existing in small aspect ratio tokamaks are here simulated by using for B_{0z} the following r-dependence:

$$\bar{B}_{0z}(x) = 1/(1 + \varepsilon x), \tag{3}$$

where $\bar{B}_{0z} = B_{0z}/B_0$, $\varepsilon = a/R$, $R = R_0 + r \cos\theta$, $x = a/r$. For the low-field side case ($\theta = 0$), $\cos\theta = 1$.

The kinetic elements of the dielectric tensor used are those derived in [5], namely:

$$\epsilon_{NN} = \left[\frac{c^2}{v_A^2} \left(1 - \frac{11}{8} k_\perp^2 \rho_i^2 \right) + \frac{3}{8} \frac{d}{dr} \left(\frac{c^2}{v_A^2} \rho_i^2 \right) \frac{1}{r} \frac{d}{dr} r \right] G^{-1}, \tag{4}$$

$$\epsilon_{N\perp} = -\epsilon_{N\perp} = \left[i \frac{c^2}{v_A^2} \left(\frac{\omega}{\omega_{ci}} - \frac{11}{8} \rho_i^2 \frac{k_\perp}{r} \frac{d}{dr} r \right) + i \frac{3}{8} \frac{d}{dr} \left(\frac{c^2}{v_A^2} \rho_i^2 \right) k_\perp \right] G^{-1} - i k_\parallel \mu, \tag{5}$$

$$\epsilon_{\perp\perp} = \left[\frac{c^2}{v_A^2} \left(1 - \frac{3}{8} k_\perp^2 \rho_i^2 \right) + \frac{11}{8} \frac{d}{dr} \left(\frac{c^2}{v_A^2} \rho_i^2 \right) \frac{1}{r} \frac{d}{dr} r \right] G^{-1} + \mu\lambda, \tag{6}$$

$$\epsilon_{\parallel\parallel} = \frac{c^2}{v_A^2} \left(k_\parallel \rho_s \right)^{-2} \left[1 + \frac{\omega}{|k_\parallel| v_{Te}} Z \left(\frac{\omega}{|k_\parallel| v_{Te}} \right) \right], \tag{7}$$

where ω_{ci} and ρ_i stand for the ion cyclotron frequency and Larmor radius, respectively; $k_\perp$ and $k_\parallel$ denote the perpendicular and the parallel (to the equilibrium magnetic field) components of the wave vector $\mathbf{k}$; $\rho_s = c_s/\omega_{ci}$ ($c_s^2 = T_e/m_i$) and Z represents the plasma dispersion function. Also, the following notations were used:

$$G = 1 - (\omega/\omega_{ci})^2, \quad \mu = [(r\delta)'/r]/(1 + \delta)^2, \quad \lambda = [r(\delta/r)']/(1 + \delta)^2. \tag{8}$$

The other elements of the dielectric tensor are negligible [5].

The local (P_{loc}) and total (P_{tot}) power absorptions were calculated by the formulas

$$P_{loc} = (i\omega/8\pi) \left(\epsilon_{ij}^* - \epsilon_{ji} \right) E_i E_j = (\omega/4\pi) \, Im \left(\epsilon_{\parallel\parallel} \right) |E_\parallel|^2, \quad P_{tot} = \int P_{loc} \, dV. \tag{9}$$

The AWCD density components were evaluated by the expressions [6], namely

$$j_{HI} = -\frac{B_{0z}}{2en_e B_0 \eta_\parallel \omega} \left\{ \frac{B_{0\theta}}{B_0} \frac{1}{r^2} \frac{d}{dr} \left[r^2 Re \left(i j_r^* E_\theta \right) \right] + \frac{B_{0z}}{B_0} \frac{1}{r} \frac{d}{dr} \left[r Re \left(i j_r^* E_z \right) \right] \right\}, \tag{10}$$

$$j_{MT} = -\frac{B_{0z}}{2en_e B_0 \eta_\parallel \omega} \left\{ \frac{B_{0\theta}}{B_0} \frac{m}{r} + \frac{B_{0z}}{B_0} k_z \right\} P_{loc}, \tag{11}$$

$$j_{PF} = \frac{B_{0z}}{2en_e B_0 \eta_\parallel \omega} \left\{ \frac{B_{0\theta}}{B_0} \frac{1}{r^2} \frac{d}{dr} \left[r^2 Re \left(j_r^* \frac{\omega}{\omega_{pe}^2} \frac{j_\theta}{\epsilon_0} \right) \right] + \frac{B_{0z}}{B_0} \frac{1}{r} \frac{d}{dr} \left[r Re \left(j_r^* \frac{\omega}{\omega_{pe}^2} \frac{j_z}{\epsilon_0} \right) \right] \right\}. \tag{12}$$

Here, the subscripts HI, MT and PF indicate, respectively, the helicity injection, momentum transfer and plasma flow components of the AWCD; $\eta_\parallel$ is the electrical conductivity parallel to the magnetic field and m and k_z are the poloidal and the "toroidal" wave numbers, respectively. As indicated above, the full-wave equation $(E_\parallel \neq 0)$ with a Vlasov-based dielectric tensor was solved by relaxation techniques, subject to appropriate boundary conditions at the plasma center and at plasma-vacuum interface, as well as at the concentric antenna current sheet and at the external metallic wall.

Illustrative Results

For illustration, (and moreover, for comparison) we chose to study a case corresponding to a tokamak device for which, within the Vlasov equation formalism, the wave equation was solved and (only) the absorption power frequency spectra were computed *upon neglecting toroidicity effects* (i.e., the assumption $\varepsilon = 0$ was used) [5]. Thus, consider the

following equilibrium profiles, as used in [5] for the PLT device:

$$q(x) \equiv [ax/R\delta(x)] = 1.1\,(1 - 1.5x^2 + x^4 - 0.25x^6), \tag{13}$$

$$n_0(x) = n_0(0)\,(1 - 0.98x^2), \quad T_{e,i}(x) = T_{e,i}(0)\,(1 - 0.95x^2)^2. \tag{14}$$

Also, use the following specific parameters characterizing the device: $R = 1.3\,m$, $a = 0.45\,m$, $n_0(0) = 5 \times 10^{19}\,m^{-3}$, $T_e(0) = 2\,keV$, $T_i(0) = 1\,keV$, $B_0(0) = 4.5\,T$, $\varepsilon = 0.346$.

Then, with the assumption $\varepsilon = 0$ (as used in [5]), we obtained the absorption power spectrum $\bar{P}(\bar{\omega})$ shown in Fig.1a ($\bar{\omega} \equiv \omega/\omega_{LA}$). This spectrum consists of an extended "Alfvèn-continuum" domain (the almost straight portion of the curve), a GAE (Global Alfvèn Eigenmode) region situated just below ω_{LA}, a narrow Kinetic Alfvèn Wave (KAW) domain at about ω_{LA} and the SQEW (Surface Quasi-Electrostatic Wave) region situated at the right of the Alfvèn continuum.

The computed AWCD components (Fig.1b) indicate the helicity injection, j_{HI} and the momentum transfer, j_{MT}, to be *dominant*; the plasma flow component, j_{PF}, is negligibly small.

When the restrictive assumption $\varepsilon = 0$ is removed and the actual value is used, namely $\varepsilon = 0.346$, the results shown in Fig.1c,d are found. Thus, the Alfvèn continuum range shrinks and the SQEW modes shift down towards lower frequencies; the same holds for the AWCD components, with j_{MT} being the dominant component. Here, current peaks due to SQEW are present.

Consider now the small aspect ratio case, $\varepsilon = 0.7$ (see Fig.1e,f). The changes in the direction already found in the case of intermediate ε-values, become even more important with j_{MT} still making the largest contribution.

In conclusion, we showed that the combined kinetic and toroidicity effects strongly affect the non-inductive AWCD in low aspect ratio tokamaks.

These illustrative kinetic results, holding for the set of antenna parameters $m = -1, n = -2$, should be supplemented by additional, systematic ones, having as purpose the optimization of the power absorption and especially of the core-localization and relative direction of the AWCD in specific small aspect ratio tokamaks.

References

[1] *Fast Wave Current Drive in Reactor Scale Tokamaks. Proc. IAEA Techn. Comm. Meet., Arles (France)*, 1991.

[2] Cuperman, S., Bruma, C., Komoshvili, K. 1996 *J. Plasma Physics*, **56**, part 1, 149.

[3] Komoshvili, K., Cuperman S. and Bruma C. 1997 *J. Plasma Physics*, **58**, part 3, 1.

[4] Bruma, C., Cuperman, S. and Komoshvili, K. 1997 *J. Plasma Physics*, (*in press*)

[5] Ross, D.W., Chen, G.L., Mahajan, S.M. 1982 *Phys. Fluids* **25**, 652.

[6] Elfimov, A. G., Petrzilka, V. and Tataronis, J. A. 1994 *Phys. Plasma*, **1**, 2882.
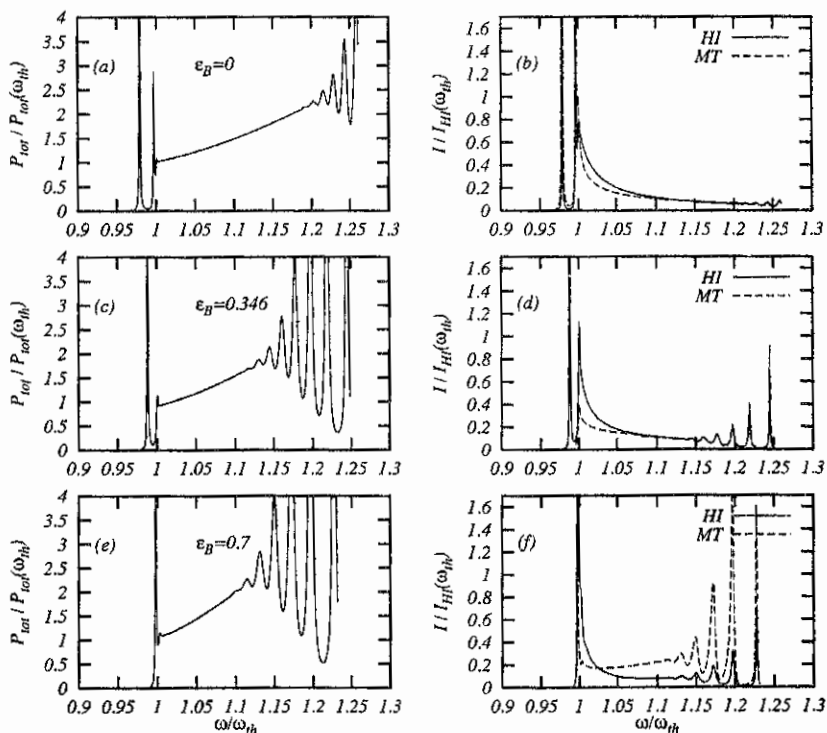
Fig.1. Frequency spectra of the power absorption $P(\omega)$ (left) and the current drive components, j_{MT} and j_{HI}, (right). From top to bottom: $\varepsilon_B=0$, $\varepsilon_B=0.346$ and $\varepsilon_B=0$; in all cases, $m=-1$, $n=-2$.
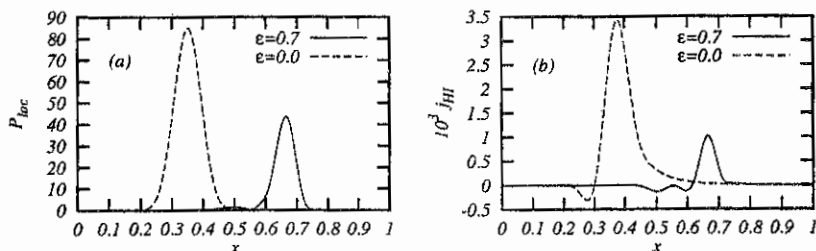
Fig.2. Profiles of (a) local power absorption and (b) helicity injection current component for $\varepsilon_B=0.7$ (solid) and $\varepsilon_B=0$ (dashed); $m=-1$, $n=-2$, $\omega/\omega_{th}=1.01$.

ICRF Heating and Current Drive in Low and High Beta Tokamaks

J.E. Scharer, M.H. Bettenhausen, and R.S. Sund
Electrical and Computer Engineering Department
University of Wisconsin-Madison, Madison, WI, USA   53706

Abstract. Comparison with experimental results and methods for utilizing ion cyclotron range of frequencies power to provide the heating and current profile control for low (TFTR) and high beta operation are considered. Mode conversion current drive in TFTR and the planned large aspect ratio, high beta machine LCT-2 is considered. Minority heating for startup from ohmic conditions is considered for the Pegasus low aspect ratio, high beta machine under construction at University of Wisconsin. The results presented show that ion cyclotron range of frequency methods are attractive for use in either low or high beta regimes.

I.   Mode Conversion Current Drive in D-T in TFTR

We consider the recent experiments for D-T supershots in which lithium-7 pellets have been replaced by lithium-6 for wall conditioning. We utilize the nonlocal large gyro-radius code SEMAL [1] which solves an integrodifferential equation for global wave fields and incorporates large ion gyroradii. We have previously found that small fractions of ^{7}Li (0.5-0.7%) have given rise to strong absorption due to the D-^{7}Li two-ion resonance lying on the low field side of the D-T two-ion resonance for 30 MHz mode conversion experiments on TFTR. This greatly reduced the mode conversion efficiency for coupling to electrons. The use of ^{6}Li changes this process so that much more power is available to couple to the electrons in moderate temperature TFTR plasmas.

We consider the recent supershot series of D-T experiments on TFTR and the role of the alphas, tritium, deuterium and electron absorption on the mode conversion efficiency. We have considered $T_{i0} = 30\text{-}10$ keV with parabolic squared temperature and parabolic density profiles. The alphas are modelled by equivalent Maxwellians whose profiles are parabolic to the fourth power for density and parabolic for temperature.

The equivalent Maxwellian temperature is $T_{\alpha 0} = 800$ keV and the peak density for $T_{i0} = 30$ keV is taken to be $n_{\alpha 0} = 0.2\%$. Figure 1 illustrates one of the runs for $k_z = 8$ m^{-1}, $T_e = 6.5$ keV, $n_{e0} = 4.5 \times 10^{19}/\text{m}^3$, $n_D = 0.4\ n_e$, $n_T = 0.32\ n_e$, $n_H = 0.1\ n_e$ and $n_C = 0.03\ n_e$, $R_0 = 2.62$ and $B_0 = 5.1$ T. The code is a global wave code such that reflections from the high field side are taken into account in the total absorption.   Note that the integrated tritium absorption at these high temperatures is 58%, the electrons 17%, the alpha particles 15% and the deuterium absorption is 9%. When the ion temperatures are reduced to 20 or 10 keV corresponding to some of the shots, the fractional tritium absorption is reduced and the electron fraction is increased. It is interesting to note that for these parameters, the alpha absorption is competitive with the electrons and the tritium ion absorption is substantial.

II.   LCT-2 High Aspect Ratio, High Beta Tokamak

We have considered radiofrequency antenna coupling, heating, current drive, and plasma rotation concepts and analyses for the proposed LCT-2 large aspect ratio tokamak at UCLA [2]. This machine has several features which make it attractive for high beta research. Since it is a large aspect ratio machine with a large plasma size, antennas can be mounted on the high field side or the

low field side. The large surface access available for antennas permits a low coupled rf power density and the potential for good spectrum control using antenna array factors. The magnetic field line curvature is also reduced compared to the low aspect ratio machines allowing a 1-D nonlocal description of the wave heating and current drive scenarios. Our research has explored low and high field side antenna coupling, plasma heating at lower ohmic densities and magnetic fields, concepts for localized current drive for profile control (including two-ion mode conversion schemes with the wave launched from the high field side) and high harmonic current drive. We have also examined concepts and Fokker-Planck calculations for plasma minority ion ejection to produce a radial electric field which drives plasma rotation and can produce classical ion transport and stabilize MHD ballooning and kink instabilities.

To illustrate some of the results for this machine, we consider the generation of localized radiofrequency non-inductive electron currents needed for profile control. We considered a high field current drive launch scenario with 20% hydrogen in a ^{4}He high beta (T = 1 keV, n = 1×10^{13}/cm^3) plasma at 0.25 T and a launched frequency of 3.5 MHz with a $k_\parallel = 3$ m^{-1}. Figure 2 illustrates the results of the run utilizing SEMAL which solves an integro-differential equation for the wave fields and incorporates large ion gyroradii. It illustrates that electron current drive via mode conversion which is localized in a 15 cm half-width can be produced with a small amount of hydrogen heating. This method produces the localized current drive required for profile control during the transition from moderate to high beta conditions.

III. Pegasus Low Aspect Ratio, High Beta Tokamak

ICRF physics in low aspect ratio, high beta tokamaks is complicated by increased toroidicity, magnetic field and plasma pressure profiles which are very different from the profiles in conventional tokamaks. To obtain initial estimates of the effects of the differences in the radial magnetic field and pressure profiles on ICRF waves, we have modified the 1-D code SEMAL to use profiles calculated with MHD equilibrium codes. We have examined the effects of stable MHD equilibria utilizing the TOQ code [3] for the Pegasus low aspect ratio tokamak [4] under construction at Wisconsin.

We examine a 1-D slice of the profiles along the midplane of the tokamak. We consider a case of a moderate beta for this machine of 20% which modifies the magnetic field profile to produce a magnetic well as shown in Fig. 3. Also shown is the corresponding electron density profile which is obtained from the plasma pressure profile by specifying the ratios of the ion to electron density, ion to electron temperature and electron density = 1, ion to electron temperature = 2 and electron density to electron temperature. The peak ion temperature is 700 eV for this case. Figure 4 shows the absorption profiles at this increased beta and $k_\parallel = 3$ m^{-1}. The beta allows the second harmonic majority ^{4}He species to dominate the minority hydrogen and electron absorption locally and the absorption profile is broadened from the ohmic case. In addition an electron absorption peak due to mode conversion at the H-^{4}He two ion hybrid resonance is observed on the high field side. Note that in this case 38% of the wave power is absorbed by the majority ^{4}He, 14% by the minority hydrogen and 49% by the electrons. At low beta (1%), greater than 50% of the power is absorbed by the minority hydrogen.
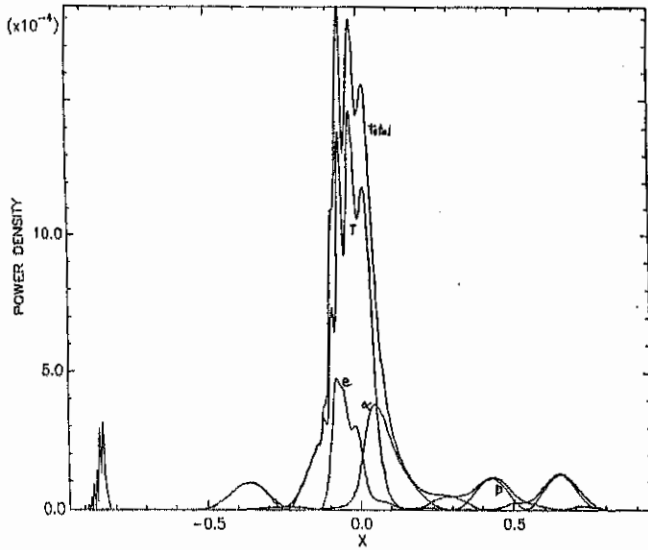
Fig. 1. D-T mode conversion current drive for TFTR
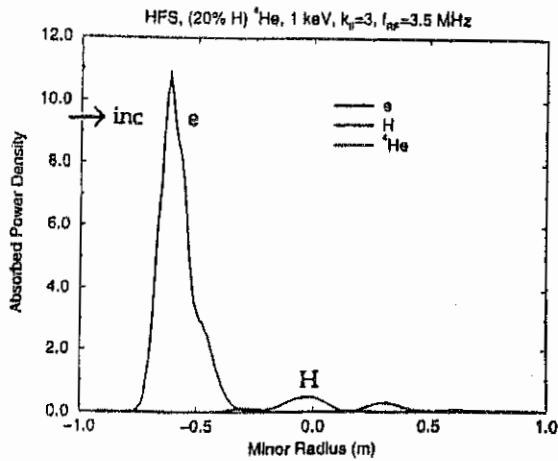
Fig. 2. High beta mode conversion

948

Acknowledgments

The authors thank Drs. R. Majeski, C. Phillips, R. Wilson and R. Taylor for many stimulating discussions on ICRF heating and current drive issues. This research was supported in part by DOE.

References

[1] O. Sauter and J. Vaclavik, Nucl. Fus. **32**, 1455 (1992).
[2] R. Taylor, et al, Unity Beta Tokamak LCT-2 proposal, private communication, (1996).
[3] Kruger, S.E., C.C. Hegna and J.D. Callen, "Stability of Pegasus – Ideal MHD and Neoclassical MHD," Sherwood Theory Meeting, Madison, WI (1997).
[4] Fonck, R. et al., "The Pegasus Low Aspect Ratio Proposal" (1997).
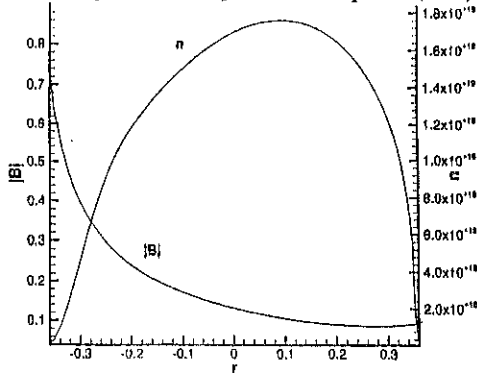
Fig. 3. Magnetic well and density profile for Pegasus $\beta = 20\%$ equilibria
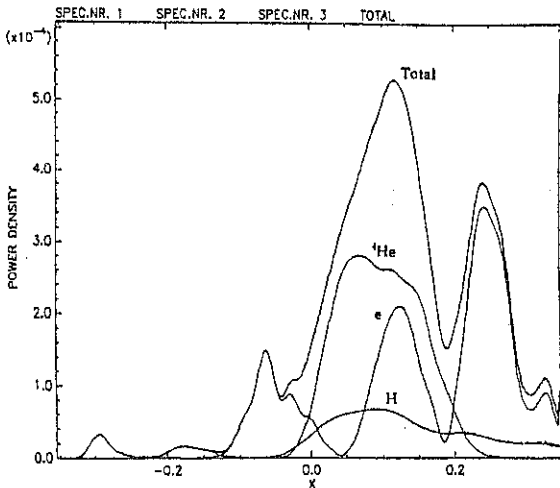
Fig. 4. Pegasus $\beta = 20\%$ absorption profile for $\omega = \omega_{CH} = 2\,\omega_{CH}{}^4He$

Production of an "illusory image" in the measurements of Te(r) profile by the ECE diagnostic under ECCD in T-10 tokamak.

Sushkov A.V., Bagdasarov A.A., Kislov D.A., Razumova K.A., Timofeev A.V.

Well known fenomenon of sawtooth oscillations was investigated on T-10 tokamak during experiments with ECCD. For this purpose two diagnostic were used: 1. Multichord XR pin-hole camera calibrated in space and having the accuracy of referencing to the geometrical position $\Delta R=1$-1.5 cm. 2. The ECE diagnostic with resolution in the major radius direction $\Delta R=1.5$-2cm for plasma regions not very closely located to the centre.

In OH and ECRH experiments, both diagnostics give coinciding values for the phase inversion surface radius. In the experiments with a current drive at the second ECR harmonic, in the measurements of spatial-temporal electron temperature behaviour by the ECE technique the following effects were observed:

1. The phase inversion zone for sawtooth oscillations is shifted towards a lower magnetic field in comparison with that registered by SXR, i.e. as if "illusory image" of that event emerged. Fig.1.

2. The phenomenon does not depend on the plasma current direction, in spite of that the direction of the EC receiving horn antenna was declined by 3 degry in the horizontal direction. So the effect does noe related with longitudinal motion of electrons.

3. The "illusory image" displacement delta is the greater, the greater the power of the EC waves absorbed in the plasma. Fig.2.

4. The "illusory image" displacement delta is greater, when the EC wave absorption zone is shifted towards r_s (under high magnetic fields). Fig.3.

5. The effect exists under current drive at the first harmonic too, but at greater power. Fig.2.

6. The effect rises with a reduction in the plasma density.

The mentioned dependencies make us to think that the observed phenomenon is related with the radiation of suprathermal "tails" in the electron energy distribution under ECCD. The X-ray radiation spectrum under ECCD is given in Fig.4. The dotted line represents the spectrum observed under similar conditions in the process of the EC wave launch perpendicular to the magnetic field. The dependence of amount of suprathermal electrons (I_{tl}) on the EC power deposited into the plasma at the fundamental harmonic and at the second one under oblique power launch,[1] is given in Fig.5.

Thus one can conclude that the suprathermal tails, under ECCD, in the electron distribution function, $f_e(E)$, somehow result in the radiation at the reduced frequency. The relativistic frequency reduction for the electron radiation with the suprathermal tail energies 20 - 30 keV could be the simplest explanation. However, the plasma in those experiments was rather "black" and one could not expect that the radiation at the reduced frequency would pass through 5-7cm of such a plasma on its way to the receiving horn installed on the side of a weak magnetic field. The radiation intensity, Io at the ordinary wave - for which the plasma is transparent - is very low: $I_0 / I_{ex} \sim T_e / m_0 c^2$, ($T_e$, m_0 are electron temperature and mass)

The EC radiation receiver located at the low field side has the polariser tuned to the reception of an extraordinary wave at the horizontal field direction. The errors in the tuning and a small magnetic field slope respective to the horizontal, in the vicinity to the horn, due to plasma current magnetic field can allow one to register an ordinary wave with the efficiency of a few per cent. In the experiments the "illusory" fluctuations related with sawtooth oscillations are of about 10% of the maxvellian plasma radiation intensity at this frequency. It is hard to explain such a great signal by radiation at the ordinary wave .

We propose another explanation to this effect. The radiation intensity at a given frequency, ω, is great at the plasma region, where the resonance condition, $\omega = 2\omega_{Be}$, is satisfied (ω_{Be} is the larmore electron frequency). The radiation source intensity configuration at some frequency, ω, is schematically given in Fig.7. The right-hand side wing of this function is related with the Doppler broadenning due to a finite angle of the receiver antenna. A relativistic frequency reduction - considerable for suprathermal electrons - makes its contribution in to the left-hand side wing, along with the similar Doppler effect. The left-hand side wing configuration depends on how $f_e(E)$ is changed along the radius. If the plasma is hot and its blackness is great, the receiver located on a weak magnetic field side can register waves arriving from the zone I (Fig.7) only. The radiation from the central part (zone 2) - which corresponds to $\omega = 2\omega_B$ - will be locked because of strong absorption. In that case, a fraction of the radiation outgoing from the plasma at a given frequency will not be proportional to the plasma temperature, T_e. This explains the very fact that, as seen in Fig.8, the result is reduced in the measurements of $T_e(r)$ by the ECE technique in comparison with that produced by other methods (say, SXR), since in the ECE measurement it is usually assumed that the radiation intensity is proportional to the temperature, and the normalisation to the OH conditions, when $T_e(r)$ is well known, is done .Calculations gives possible shift of these two curves about 1.5cm for given parameters. The radiation as an extraordinary wave from the zone 3 also does not

pass to the detector, but it freely propagate towards a greater magnetic field, enters the metallic chamber wall, where it is reflected and depolarised. As a result, after reflection, roughly speaking, a half of the flax, as an ordinary wave, passes through the plasma - practically, without absorption - and can be registered with the horn, with the efficiency of a few per cent. This radiation carries on some mixed information about the central part of the plasma, being prescript by us to the resonance zone, $\omega = 2\omega_B(r)$. Some rough estimates show that under typical experiment conditions the radiation related with suprathermal electrons having the conventional temperature two - three times higher than that for bulk electrons may exceed the radiation of the bulk electrons in the same plasma volume, and as a result, make a noticeable contribution - after reflection - into total registered intensity.

Thus one can conclude that it is possible to measure, by the ECE technique, the temperature profile with a not too important systematic error under ECCD condition, when f(E) has essential deviations from the maxvellian one [2], but it is hard to interpret its temporal changes which can give an information about the plasma in the higher magnetic field region.

In order to avoid such errors, it is better to install an EC wave absorber upon the inner (high field side) tokamak chamber wall. and/or carefully to tune the polariser, in front of the detector, to the extraordinary wave.

The suggested explanation undoubtedly needs some additional experimental verification by finer polariser tuning, and/or by installing a HF wave absorber upon an inner chamber wall.

[1] Yu.V.Esipchuk, N.A.Kirneva, A.A.Martynov, V.M.Trukhin, Fisika plasmy, 1995, v.21,p.57.
[2] M.Iontano,R.Pizzoli,E.V.Suvorov. IL NUOVO CIMENTO,v.63.B,N2,p.29.
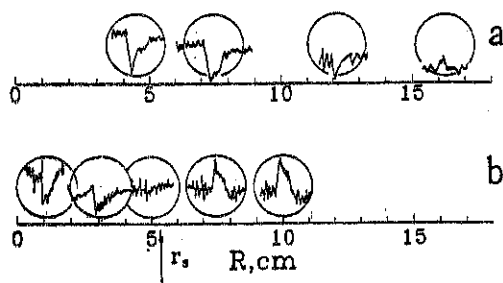
Fig.1. Phase inversion zone of sawtooth oscillations:
a) under measurement with an ECE harmonic;
b) under measurement of soft X radiation intensity. A typical signal behaviour under internal disruption at the designated R-value is given in circles.
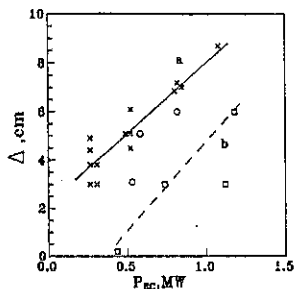
Fig.2. Phase inversion point
displacement, Δ, vs. EC power pulse
under oblique wave launch.
a) for ECCD at the second
harmonic (circles - for an inverse
sign of a current in the plasma).
b) for ECCD at the fundamental
harmonic.
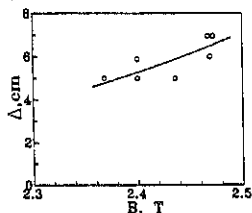
Fig.3. Δ vs. EC power absorption zone
position, dependent on the magnetic
field magnitude.
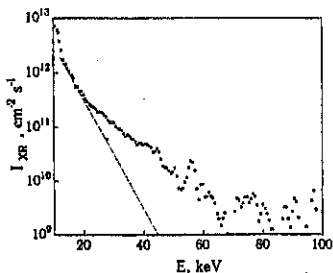
Fig.4. X radiation spectrum, registered
under ECCD at the second harmonic.
The dotted line is the maxvellian
distribution intensity behaviour at the
temperature of the bulk plasma
component [1].
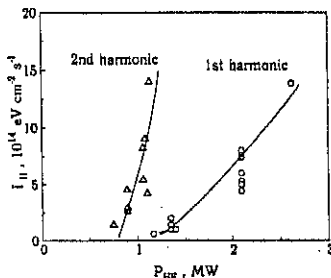
Fig.5. The suprathermal electron amount
dependence on EC power P_{HF}.
$I_{ij} = \int (I_{XR} - I_{max}) dE$, where I_{XR} is the
X radiation intensity, I_{max} is an
intensity, corresponding to the
maxvellian distribution [1].
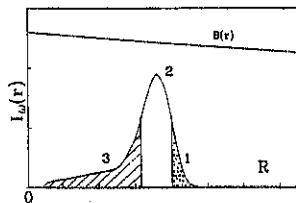
Fig.6. Schematically depicted radiation
source profile at a given frequency, ω.
1 - Zone, from which the radiation
escapes into the low magnetic field
region
2 - Zone of locked radiation
3 - Zone, from which the radiation
escapes forwards the high magnetic
field side only.
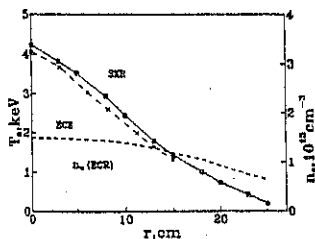
Fig.7. Typical plasma density profiles,
n_e, and electron temperature ones,
T_e, for the experiments with ECCD
at the second ECR harmonic,
measured from the X radiation
spectrum and from the radiation at
the second harmonic of cyclotron
resonance.

Author Index

Author Index

Author Index

Author Index

Author Index

Author Index

Author Index

Author Index

Author Index

Author Index

Author Index

Author Index

Author Index

Author Index

Author Index

Author Index

Author Index

Author Index

L

Author Index

Author Index